Search for supersymmetric particles in final states with jets and missing energy with the ATLAS Experiment at the LHC

Dissertation zur Erlangung der Doktorwürde
Vorgelegt von

Janet Dietrich

Freiburg, November 2010

Fakultät für Mathematik und Physik
Albert-Ludwigs-Universität Freiburg

Dekan:	Prof. Dr. Kay Königsmann
Leiter der Arbeit:	Prof. Dr. Gregor Herten
Referent:	Prof. Dr. Gregor Herten
Koreferent:	Prof. Dr. Karl Jakobs
Tag der Verkündigung des Prüfungsergebnisses:	07.02.2011

Abstract

With the start of the Large Hadron Collider (LHC) at CERN it is now possible to study physics at the TeV-scale for the first time. At this unprecedented energy range it is expected that the Standard Model of particle physics will reach its limits and new phenomena can appear. One of the main goals of the ATLAS experiment is the search for physics beyond the Standard Model. This includes observing supersymmetric particles, which are predicted to have masses of several hundred GeV up to a few TeV.

The subject of this thesis is the search for supersymmetric particles in final states with jets and missing transverse energy and the evaluation of the ATLAS discovery potential for supersymmetric particles in the Minimal Supersymmetric Standard Model (MSSM) parameter space for these channels. Different centre-of-mass energies of $\sqrt{s}$ = 14 TeV, 10 TeV and 7 TeV are assumed.

For many R-parity conserving SUSY models, the decay of supersymmetric particles leads to detector signatures characterised by missing transverse energy and multi-jets, sometimes accompanied by leptons. In this thesis, SUSY searches with $\geq$ 2 - 6 jets and 0 - 2 leptons (electrons, muons) are studied, with a focus on 0-lepton channels, that are expected to be sensitive in large areas of the SUSY parameter space. The search strategies for supersymmetric particles are applied on a sets of differently constrained SUSY models and on several hundred SUSY signals, generated within the pMSSM subspace of the MSSM. The goal of this work is to explore the reach of the performed SUSY searches for completely different decay signatures. It will be shown that the ATLAS SUSY searches cover a large parameter space of SUSY models.

The first p-p collisions at a centre-of-mass energy of $\sqrt{s}$ = 7 TeV in March 2010 allow a comparison of the measured data with the Monte Carlo predictions, in order to see how well the detector response is understood in the context of SUSY specific variables used in the 0-lepton analyses. All measurements are found to be in agreement with the Standard Model expectations within the associated systematic uncertainties. The results indicate that the ATLAS SUSY searches cover a large parameter space and it is possible to discover or exclude some SUSY models already with a few pb^{-1} of integrated luminosity.

Contents

1. Introduction

For generations, we try to answer questions like: "What is our universe made of ? What are the constituents of nature and what are the laws that govern their behaviour ?" To our present knowledge, three generations of quarks (u, d, s, c, t, b) and leptons (e, ν_e, μ, ν_μ, τ, ν_τ) are the elementary constituents of matter, which interact via four elementary forces: electromagnetism, gravity, and the strong and weak force. All discovered particles and all known forces, except for gravity, could be incorporated in a gauge theory, known as the *Standard Model of Particle Physics (SM)*. Since its invention in the 1970s, the Standard Model has been successfully validated by high precision measurements at energies up to hundred GeV. Until now, no strong deviations have been found between the experimental measurements and the theoretical predictions of this model. The only predicted Standard Model particle, that has not been observed yet, is the Higgs boson.
Despite the success of this model, some fundamental questions remain unanswered and point to its limitations. For example the Standard Model does not incorporate gravity and and will break down at energy scales, where gravity is no longer negligible (Planck scale). It also does not explain the unknown "dark matter" in the universe. This leads particle physicists to believe that the Standard Model is not the final theory, and only a low-energy approximation of a more fundamental one. The discovery of physics beyond the Standard Model is one of the main goals of high energy physics. Several models have been proposed in the past years. Supersymmetry is considered as one of the most plausible and attractive extensions as it provides answers to some of the open questions of the Standard Model. The model predicts the existence of a superpartner for each Standard Model particle that differs in the spin. Since no supersymmetric particles have been observed so far, it cannot exist in its most fundamental form and must be a broken symmetry. The resulting SUSY particles have masses higher than the SM particles of the order of $\mathcal{O}$(1 TeV), and their decay leads to characteristic signatures in colliders that could be measured at particle colliders reaching the energies needed.
The Large Hadron Collider was built to probe the physics of the Standard Model and beyond. It has provided in March 2010 first p-p collisions at centre-of-mass energies of $\sqrt{s} = 7$ TeV, which are the highest collision energies ever reached in experiments thus far. In the coming years, this energy will be increased to 14 TeV. The design of the multipurpose detector ATLAS, which is installed at the LHC, is driven by the the need to detect interesting physics events like Supersym-

metry in the challenging LHC environment. If SUSY is present at the TeV scale, as favoured by several arguments, the ATLAS detector will observe these particles within the first few years of data taking.

This thesis presents a new search strategy for R-parity conserving supersymmetric particles of the Minimal Supersymmetric Standard Model (MSSM) with the ATLAS detector at the LHC. The goal of the analyses was to determine the ATLAS discovery potential in the SUSY parameter space. The studies are based on simulated data at a centre-of-mass energy of 14 TeV, 10 TeV and 7 TeV and an integrated luminosity of 1 fb^{-1}, 0.2 fb^{-1} and 0.5-2 fb^{-1}, respectively. In order to cover a wide range of different SUSY signatures, the SUSY searches are performed in channels with different numbers of jets (≥ 1, ≥ 2, ≥ 3, ≥ 4) and leptons (exactly 0, 1 or 2). The focus of the work is on 0-lepton analyses, that are expected to be sensitive in large areas of the SUSY parameter space. Channels with very high jet multiplicities (≥ 5 and ≥ 6 jets) have also been considered in these studies, which are especially important for SUSY models with very large squark and gluino masses (> 1 TeV).

The SUSY analyses are applied on different constrained MSSM grid models as well as on several hundred SUSY signals generated within the phenomenological MSSM parameter space to explore the reach of the SUSY searches. It is shown that ATLAS could discover SUSY models at a mass scale below $\mathcal{O}(1\text{ TeV})$ with an integrated luminosity of 1 fb^{-1} for a centre-of-mass energy of $\sqrt{s} = 14$ TeV and squarks and gluinos with a mass of $600-700$ GeV for $\mathcal{L} \approx 0.2\ (0.5-1.0)\ \text{fb}^{-1}$ at $\sqrt{s} = 10$ TeV ($\sqrt{s} = 7$ TeV). The results indicate that the ATLAS SUSY searches cover a large SUSY parameter space and it is possible to discover first SUSY models already with $\mathcal{O}(100)$ pb^{-1} of integrated luminosity. The 0-lepton channel was shown to be the one with the highest discovery potential.

In the second part of this work, p-p collision events for an integrated luminosity of about 70 nb^{-1} at a centre-of-mass energy of $\sqrt{s} = 7$ TeV are studied. In this thesis a comparison of the measured data with the Monte Carlo predictions for the main SUSY specific variables used in the 0-lepton analyses is presented. All measurements are found to be in agreement with the Standard Model expectations within the associated systematic uncertainties.

This work is organised as follows:

Chapter 2 provides the theoretical background to this thesis and gives a brief introduction to the Standard Model and to Supersymmetry, in particular to the studied Minimal Supersymmetric Models. This is followed by an overview of the phenomenology of p-p collisions, that are relevant for experimental studies at the LHC. The design of the ATLAS detector and the physics goals of the ATLAS experiment are discussed in Chapter 3. A description of the different Monte Carlo generators, the event generation and the produced Monte Carlo datasets used, is given in Chapter 4. Several hundred SUSY signals have been produced for the estimation of the ATLAS discovery reach. The different SUSY signal grids are explained at the end of the same chapter. An overview of the ATLAS search strategy is presented in Chapter 6. The different reconstruction algorithms of the resulting physics objects of the proton-proton collision in the ATLAS detector are summarised in Chapter 5. The object selection criteria and the SUSY analysis cuts for the performed SUSY searches for the different LHC centre-of-mass energies are explained in Chapter 7. A summary of the used global SUSY specific variables and the statistical methods used to estimate the ATLAS

discovery potential can be found in the same chapter. Chapter 8-11 present the analysis results for the different centre-of-mass energies and for the first data studies.
The understanding of the Standard Model backgrounds is crucial for every SUSY discovery. The main methods for the SM background determination in the 0-lepton channel are summarised in Chapter 12. Finally, a summary of the results of this thesis and prospects for future analyses are given in Chapter 13.

2. Theoretical Aspects

The Standard Model (SM) of particle physics [1–4] represents one of the greatest achievements in the field of elementary particle physics in the last decades that attempts to describe the fundamental constituents of matter and their interactions among them. Despite the remarkable agreement between the theoretical predictions of this model and the experimental observations until today, there are some experimental and theoretical hints indicating that this model will have to be extended to describe the physics at even higher energy scales. Supersymmetry (SUSY) [5–7] is one attractive scenario for the possible extension of this model.
This chapter briefly summarises the main aspects of the Standard Model and Supersymmetry, which are important for the understanding of this thesis. A complete description of these models is far beyond the scope of this thesis and are given in various books, for example in Ref. [8–12] for an introduction to the SM and Ref. [13–18] for an introduction in Supersymmetry. The second part of this chapter gives an introduction to the phenomenology of p-p collisions including the calculation of cross sections and the luminosity.

It should be noted that the following definitions are used within the thesis: The reduced Planck's constant $\hbar \equiv \frac{h}{2\pi}$ and the speed of light c are $\hbar \equiv c \equiv 1$. The dimensions of the basic quantities like energy, mass and momentum will be given in units of *electron volt* - eV.

2.1. The Standard Model

The Standard Model of particle physics describes the known 12 fundamental matter particles (fermions) and three of the four fundamental forces - electromagnetic, weak and strong (by leaving apart the gravitational interactions) which are mediated by gauge boson particles (bosons). The fermionic elementary particles are to today's knowledge point like, structureless constituents that carry a spin S = $\frac{1}{2}$ and can be classified into leptons and quarks. The known leptons are electron e^-, muon μ^- and tau τ^-, all with the electric charge Q = -1. For every lepton exists a corresponding neutrino ν_e, ν_μ, ν_τ with Q = 0. The 6 quarks have different flavours: *u, d, s, c, b, t* and fractional charges Q = $\frac{2}{3}$, $-\frac{1}{3}$, $-\frac{1}{3}$, $\frac{2}{3}$, $-\frac{1}{3}$, $\frac{2}{3}$, respectively. The three generations of quarks and leptons are summarised in Table 2.1. The intermediate interaction particles - the gauge bosons,

fermions	**generation**			**Q** [e]	$\mathbf{T}_3$	$\mathbf{SU(3)_C}$	$\mathbf{SU(2)_L}$	$\mathbf{U(1)_Y}$
quarks	$\begin{pmatrix} u \\ d' \end{pmatrix}_L$	$\begin{pmatrix} c \\ s' \end{pmatrix}_L$	$\begin{pmatrix} t \\ b' \end{pmatrix}_L$	$\frac{2}{3}$ $-\frac{1}{3}$	$\frac{1}{2}$ $-\frac{1}{2}$	**3**	**2**	$\frac{1}{3}$
	u_R	c_R	t_R	$\frac{2}{3}$	0	**3**	**1**	$\frac{4}{3}$
	d_R	s_R	b_R	$-\frac{1}{3}$	0	**3**	**1**	$-\frac{2}{3}$
leptons	$\begin{pmatrix} \nu_e \\ e \end{pmatrix}_L$	$\begin{pmatrix} \nu_\mu \\ \mu \end{pmatrix}_L$	$\begin{pmatrix} \nu_\tau \\ \tau \end{pmatrix}_L$	0 -1	$\frac{1}{2}$ $-\frac{1}{2}$	**1**	**2**	-1
	e_R	μ_R	τ_R	-1	0	**1**	**1**	-2

Table 2.1: The fermions of the Standard Model. The symbols refer to: Q = charge, T_3 = 3^{rd} component of the weak isospin, $SU(3)_C$ = number of QCD colour states, $SU(2)_L$ = number of spin states, $U(1)_Y$ = hypercharge. The left handed (L) and right handed (R) eigenstates mix and build the mass eigenstates. The symbols d', s', b' indicate the eigenstates of the electroweak interaction that are connected by the Cabibbo-Kobayachi-Maskawa-Matrix to the mass eigenstates d, s and b. The left-handed fermions form $SU(2)_L$ doublets, while right-handed fermions form $SU(2)_L$ singlets.

have an integer spin S = 1 and are listed in Table 2.2. The photon γ is the exchange particle of the electromagnetic interactions, the 8 gluons mediate the strong interactions among the quarks and the three bosons W^+, W^- and Z^0 correspond to the weak interactions.
In the Standard Model the interactions between the particles are described by gauge theories[1], that can be formulated with the Lagrangian L, a function that formulates the dynamics of the system. Every gauge theory is characterised by a group of transformations of the field variables, called gauge transformations, that leave the basic physics of the quantum field unchanged. This means, the Lagrangian is invariant under the gauge transformations (gauge invariance). This condition gives the theory a certain symmetry. Every gauge invariance, caused by a symmetry, implies a conservation law (Noether's theorem [19]) and leads to the introduction of a new gauge boson. For example quantum electrodynamics (QED) is a relativistic quantum field theory of electromagnetic interactions with the symmetry group $U(1)_{\text{em}}$. It describes all interactions of electrically charged particles by means of the electromagnetic force. The physics observables are invariant in the chosen electromagnetic potential. This leads to the law of the conservation of the charge. The introduced gauge boson is the massless spin-1 photon. In much the same way, gauge invariance requirements in the electroweak theory lead to the other mentioned gauge bosons.
The SM is a quantum field theory (QFT) that is based on the gauge symmetry of:
$SU(3)_C \otimes SU(2)_L \otimes U(1)_Y$. The strong interactions are hereby described by the **Quantum Chro-**

[1] A gauge theory is a quantum field theory, in which fields and potentials are described by a symmetry group - the gauge group.

modynamics (QCD), which is a gauge theory with the $SU(3)_C$ symmetry group, that gives rise to the force fields, named colour. Every quark gets an additional quantum number, the *colour* of three possible types[2] [20], generically denoted as q_i (i = 1, 2, 3). The electrically neutral, massless spin $-$ 1 gluons, which also carry a colour quantum number (every gluon carries colour-anti-colour charge) mediate the interactions, between the quarks. As a consequence of the gluons being coloured is that they interact not just with the quarks, but also with themselves (non-Abelian gauge theory). Since colour is not experimentally observed, the elementary quarks must be confined to colourless composite particles, the hadrons. Dependent on the number of quarks hadrons are classified into baryons (three quarks) like a proton and mesons ($q\bar{q}$) e.g. a pion. Inside a hadron quarks and gluons behave like free particles and interact with a high-energy probe at very short distances.

field	**boson**	**Q** [e]	$\mathbf{T}_3$	$\mathbf{S}U(3)_C$	$\mathbf{S}U(2)_L$	$\mathbf{U}(1)_Y$
$U(1)_Y$ gauge field	B	0	0	**1**	**1**	0
	W^1	1	1			
$SU(2)_L$ gauge field	W^2	-1	-1	**1**	**3**	0
	W^3	0	0			
$SU(3)_C$ gauge field	G^1 ... G^8	0	0	**8**	**1**	0
Higgs field ϕ	ϕ^+	1	$\frac{1}{2}$	**1**	**2**	1
	ϕ^0	0	$-\frac{1}{2}$			

Table 2.2: The bosons of the Standard Model. The symbols refer to: Q = charge, $T_3 = 3^{rd}$ component of the weak isospin, $SU(3)_C$ = number of QCD colour states, $SU(2)_L$ = number of spin states, $U(1)_Y$ = hypercharge. The gauge fields have spin 1 and a hypercharge of 0, while the Higgs field carries a spin of 0 and a hypercharge of 1.

The quark mass eigenstates as presented in Table 2.1 are not the weak eigenstates. They are mixed states where a unitary 3×3 matrix, called Cabibbo-Kobayashi-Maskawa (CKM) matrix [21,22] governs the transformation. The implies CP-violation (see for instance Ref. [21,23]).
The electromagnetic interactions and electroweak interactions are described by a unified **electroweak theory** (EW) $SU(2)_L \otimes U(1)_Y$ that was initially proposed by Glashow, Weinberg, and Salam [1,3,4]. The symmetry group $U(1)_{em}$ is hereby "included" in this group definition. The requirements of the gauge invariance in the electroweak theory represent the weak isospin or chiral symmetry (T) and the weak hypercharge (Y) symmetry. The index "L" for the $SU(2)$

[2] In the symmetry group $SU(3)_C$ the *C* refers to the colour and the number *3* refers to the three possible colour states.

component denotes that the symmetry is only for the left-handed part of the fermion fields, while the $U(1)$ component acts on right- and left-handed components. The symmetry of the unified electroweak theory comprises four massless vector fields, three associated with $SU(2)_L$ denoted as W_μ^i (with i = 1, 2, 3) and one associated with $U(1)_Y$ denoted as B_μ. The gauge fields B_μ and W_μ^i mix among themselves to build the physical fields: W_μ^1 and W_μ^2 form the two charged fields $W_\mu^\pm$ while B_μ and W_μ^3 mix to form A_μ and Z_μ:

$$W_\mu^\pm = \frac{1}{\sqrt{2}}(W_\mu^1 \mp i\, W_\mu^2) \tag{2.1}$$

$$A_\mu = B_\mu \cos\theta_W + W_\mu^3 \sin\theta_W \tag{2.2}$$

$$Z_\mu = -B_\mu \sin\theta_W + W_\mu^3 \cos\theta_W \tag{2.3}$$

with $\cos\theta_W$ the weak mixing angle (Weinberg angle). The field A_μ defines the photon field of the Standard Model and forms the γ-boson, while the vector bosons $W^\pm$ and Z^0 are obtained from Z_μ and $W_\mu^\pm$.
The equations of motion for the SM particles can then be derived by using the "principle of least action" [24], where every action is represented as an integral over time, taken along the path of the system between the initial time and the final time of the development of the system. Feynman has generalised this principle to the path integral formulation and the so-called Feynman diagrams [25,26]. This allows to determine the equations of motion by minimising $S = \int d^4x\, L_{\mathrm{SM}}$. The Feynman diagrams provide a description of the interactions of particles in all allowed ways represented by particle paths, which join and split as described by the diagram.
The combined $SU(3)_C \otimes SU(2)_L \otimes U(1)_Y$ symmetry group, together with the gauging principle and equations of motion are often seen as the basis of the SM. However, in the description of the vector bosons is a problem related to restriction, that the gauge bosons should be massless. Experimental results have shown that $W^\pm$ and Z^0 are selfinteracting, massive particles. Only the photon is massless and non-selfinteracting. On the other hand every mass term would violate the chiral symmetry $SU(2)_L$.
In the Standard Model, the $W^\pm$ and Z^0 bosons get masses by the spontaneous symmetry breaking of the electroweak symmetry group $SU(2)_L \otimes U(1)_Y$ caused by the Higgs mechanism [27,28]. This can be realized linearly by a scalar field, which acquires a non-zero vacuum expectation value.

It should be noted that a system is called *symmetric*, if it has several equally likely outcomes with the same probability. Spontaneous symmetry breaking (SSB) occurs when a system falls into a vacuum state that is not symmetric, such that a specific outcome appears with the probability 1 (one element of the symmetry group is distinct). In the quantum field theory a spontaneously broken system has a Lagrangian that is invariant under the symmetry transformations, but the vacuum of the theory is not.

2.1.1. The Higgs mechanism

Higgs suggested that the gauge invariance could be *spontaneously broken* by adding of (at least) one complex scalar $SU(2)_L$ doublet, the Higgs field ϕ (see Ref. [29])

$$\phi = \begin{pmatrix} \phi^+ \\ \phi^0 \end{pmatrix} = \frac{1}{\sqrt{2}} \begin{pmatrix} \phi_1^+ - i\phi_2^+ \\ \phi_1^0 - i\phi_2^0 \end{pmatrix} \tag{2.4}$$

with the corresponding Higgs potential, that is the key to the spontaneous symmetry breaking:

$$V(\phi^\dagger\phi) = \mu^2\phi^\dagger\phi + \lambda(\phi^\dagger\phi)^2 \tag{2.5}$$

Depending on the sign of the mass parameter μ^2 in the Higgs potential, there are two possibilities for the vacuum expectation value $<0|\phi|0>$ that minimises the potential V(ϕ). Figure 2.1 shows the Higgs potential V of a single-complex scalar Higgs field ϕ for $\mu^2 > 0$ and $\lambda > 0$ (left plot) and for $\mu^2 < 0$ and $\lambda > 0$ (right plot). The vacuum state corresponds to a certain state within the continuous circular minimum. For the first case $\mu^2 > 0$ the expectation value is $<0|\phi|0> = 0$. The vacuum is $SU(2)_L \otimes U(1)_Y$ symmetric and therefore no symmetry breaking occurs. For $\mu^2 < 0$ a non-zero vacuum expectation value of the scalar field ϕ is found:

$$\phi = \frac{1}{\sqrt{2}} \begin{pmatrix} 0 \\ v \end{pmatrix}, \qquad |\phi^2| \equiv \frac{v^2}{2} = -\frac{\mu^2}{2\lambda}. \tag{2.6}$$

Once this particular vacuum state is chosen the symmetry $SU(2)_L \times U(1)_Y$ will be broken.
However, perturbation calculations converge only, if ϕ is expanded by "small oscillations" around the vacuum state. This can be parametrised by adding small fields like:

$$\phi_0 = \frac{1}{\sqrt{2}} \begin{pmatrix} 0 \\ v + h(x) \end{pmatrix}. \tag{2.7}$$

The resulting spectrum contains massive intermediate vector bosons $W^\pm$ and Z^0, a massless gauge boson γ, but also the neutral scalar field of the Higgs particle. The Higgs boson, with an expectation value for its mass of $m_H = \sqrt{-2\mu^2}$, is the only free parameter of the four degrees of freedom of the introduced complex scalar field, which is not discovered so far. Searches for the Higgs boson at the Large Electron-Positron Collider (LEP) at CERN [30] and at the Tevatron collider [31, 32] have been conducted to limits for the Higgs mass. LEP has defined a lower limit for the Higgs boson mass of $m_H > 114.4$ GeV [33], while the Tevatron experiments DØ and CDF have recently excluded with 95% C.L. a Higgs boson mass of about $158 < m_H < 175$ GeV [34]. These limits leave only a small range in case of a very light Higgs boson for future Higgs searches, if the Standard Model is the correct theory.
The main advantage of the picture of symmetry breaking is the fact that an explicit and consistent

formulation exists and any observable can be calculated perturbatively. It should be noted that the additional Higgs field not only generates the masses of the gauge bosons. The mass terms for the fermions are also generated by so called Yukawa interaction terms (Yukawa couplings) between the fermions to the scalar Higgs fields. The coupling strength of the Higgs boson to a fermion is hereby proportional to the fermion mass.

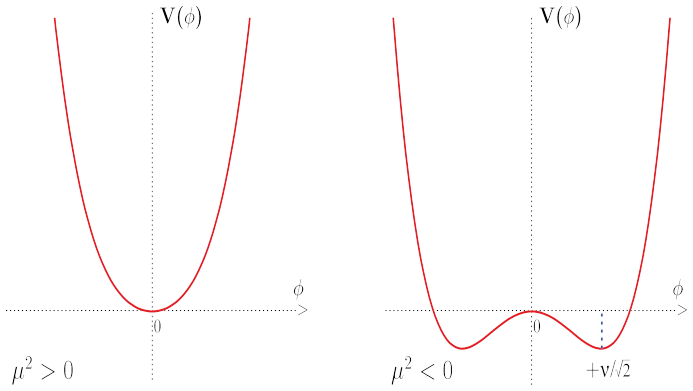

Figure 2.1: The Higgs potential V in the symmetric phase (left plot) and in the spontaneously broken phase (right plot). Figure is taken from Ref. [29].

2.1.2. The Lagrangian of the Standard Model

The Lagrangian L_{SM} of the Standard Model comprises all the discussed contributions - the strong interaction L_{QCD}, the electroweak interaction L_{EW} and the term from the Higgs boson L_{Higgs} and its interactions L_{Yukawa} and can be written in the form as defined e.g. in Ref. [35]:

$$L_{\mathrm{SM}} = L_{\mathrm{QCD}} + L_{\mathrm{EW}} + L_{\mathrm{Yukawa}} + L_{\mathrm{Higgs}}. \tag{2.8}$$

The dynamics of the quarks and gluons are controlled by the gauge invariant quantum chromodynamics Lagrangian, that describes the propagation of the quarks L_{quarks}, the dynamics of the gluon fields L_{gluons} and the interaction between quarks and gluons L_{int} (see Ref. [35])

$$\begin{aligned} L_{\mathrm{QCD}} &= L_{\mathrm{quarks}} + L_{\mathrm{gluons}} + L_{\mathrm{int}} \\ &= \sum_{\text{flavors f}} \bar{q}_f (i D_\mu \gamma^\mu - m_f) q_f - \frac{1}{4} G^i_{\mu\nu} G_i^{\mu\nu} \end{aligned} \tag{2.9}$$

The term $L = -\frac{1}{4} G^i_{\mu\nu} G_i^{\mu\nu}$ is the Lagrange density of the eight gauge (gluon) fields and their self-interactions, where $G^i_{\mu\nu}$ denotes the gluon field-strength tensor that describes the gluon field potentials with the colour i = (1, ..., 8). The gauge interactions among the quarks and gluons are in the term $\bar{q}_f (i D_\mu \gamma^\mu - m_f) q_f$ with $D_\mu = \partial_\mu - i g_s \frac{\lambda_i}{2} G^i_\mu$, where λ_i are the generators of the $SU(3)_C$

gauge group. The variable g_s is the dimensionless coupling constant of the strong interactions and q_f denotes the coloured quarks triplets of the flavour f (see Table 2.1). More details about QCD can be found in e.g. in Ref. [36].
The Lagrangian of the electroweak interactions, based on the gauge group $SU(2)_L \otimes U(1)_Y$, has the form (see Ref. [29]):

$$L_{\mathrm{EW}} = \bar{L} i\gamma^\mu D_\mu L + \bar{R} i\gamma^\mu D_\mu R - \frac{1}{4} W_i^{\mu\nu} W^i_{\mu\nu} - \frac{1}{4} B_i^{\mu\nu} B^i_{\mu\nu} \tag{2.10}$$

"L" denotes the left-handed weak isospin fermion doublets and "R" the corresponding right-handed isospin fermion singlets. W^i_μ (i= 1,..., 3) and B_μ are the vectorfields associated with $SU(2)_L$ and $U(1)_Y$, respectively, which describe the interactions between the W and the B particles. D_μ is the covariant derivative defined as $D_\mu = \partial_\mu + igT_i W^i_\mu + ig' \frac{Y}{2} B_\mu$, with g and g' the coupling constants of $SU(2)_L$ and $U(1)_Y$. T_i, $\frac{Y}{2}$ are the symmetry group generators [37]. The isospin T_3 and the hypercharge Y satisfy the relation with the electrical charge Q = T_3 + $\frac{1}{2}Y$.
The Lagrangian of the Higgs mechanism and the trilinear Yukawa couplings of the fermions to the Higgs field are (see Ref. [35]):

$$\begin{aligned} L_{Higgs} &= |\, D_\mu \phi \,|^2 - V(\phi^\dagger \phi) && (2.11) \\ &= |\, D_\mu \phi \,|^2 - \mu^2 \phi^\dagger \phi - \lambda (\phi^\dagger \phi)^2 \\ L_{Yukawa} &= -g_f \left[\bar{L} \phi R + \bar{R} \phi_c L \right] && (2.12) \end{aligned}$$

D_μ is the same as defined in the Lagrangian for the electroweak interaction and g_f is the Yukawa coupling strength which is proportional to the fermion mass and may vary for each fermion.
In the simplest version of the Standard Model are 19 a priori unknown parameters: 9 fermion masses (quarks and charged leptons), 4 quark-mixing matrix (CKM) quantities, 2 gauge boson masses (for example the Z and Higgs boson masses), 3 coupling constants, and 1 strong CP parameter.

2.1.3. Problems of the Standard Model

The SM is one of the best verified theories in physics. With addition of an extra term to give neutrinos masses[3] all experimental measurements up to energies of the order of 100 GeV can be described so far [39]. This shows the remarkable success of this model. The top mass could for example be predicted several years before it was discovered. Nevertheless, it seems evident that the SM will have to be extended to describe physics also at higher energy scales. In the following some reasons suggesting a physics model beyond the SM are listed.

[3] Due to neutrino oscillation the neutrinos have small, but non-zero masses [38].

- **Gravitation**

  Gravitation is one of the fundamental forces found in nature, but evades its integration in form of a quantised theory. Thus one of the strongest arguments for believing the SM is not a complete theory is that the SM disregards all gravitational effects, because it cannot be integrated into the framework of the gauge theories. This approximation is not problematic for the so far explored energy scale since current experiments are operating at the electroweak scale ($\mathcal{O}(100)$ GeV) where gravity is very weak. However gravitational interactions become more important and are comparable in magnitude to the gauge interactions at the Planck scale ($M_{\text{Planck}} \approx 10^{19}$ GeV) [40].

- **Gauge coupling unification**

  The electromagnetic and weak nuclear forces have been combined to the electroweak force and the corresponding couplings unify at about 100 GeV. The idea of the gauge coupling unification is the basic motivation of the gauge unification theory - "Grand Unified Theory" (GUT). It assumes that the three SM gauge couplings, which define the electromagnetic, weak and strong interactions, merge through the use of the renormalisation group equations (RGEs) at very high energies, called GUT scale, of about $M_{\text{GUT}} \approx 10^{15}$-$10^{16}$ GeV to one single interaction characterised by a larger gauge symmetry and one coupling constant [41]. The symmetry group is broken at lower energies, that leads to the known Standard Model $SU(2)_C \times SU(2)_L \times U(1)_Y$ symmetry group. However, experimental results of the values of the low energy gauge couplings and their extrapolations to higher energies show that the SM can not unify the gauge couplings accurately. The coupling constants approach each other, but do not meet at the same energy as shown in Figure 2.2 (left plot). Therefore a unification is only possible within a model beyond the SM, e.g. with Supersymmetry (see Figure 2.2, right plot).

- **Dark matter (dark energy)**

  Only a very small part of the matter in the universe can be described with the SM, while nearly 1/4 is considered to be cold dark matter. Cosmological observations have established the existence of cold dark matter in the universe e.g. the rotational speed of spiral galaxies [42] or anisotropy measurements of the cosmic microwave background [43–45]. In the past, several possible dark matter candidates have been already discussed, but many were discarded or only account for a small fraction of dark matter [46]. One most likely idea is that an unknown particle is responsible for dark matter, called weakly interacting massive particle (WIMP), that has been produced in the big bang and would have survived until today. The SM in its current form does not provide any candidate for cold dark matter.

- **The gauge hierarchy and fine-tuning problem**

  Probably one of the most serious theoretical issues is the instability of the Standard Model against the huge hierarchies of different scales relevant to describe high energy particle physics. For example the mass of the neutrinos (eV range [47]) is much smaller than the mass of the top quark (around 172 GeV [47]) and the electroweak scale at the order of

100 GeV is tiny compared to the Planck scale that is about 17 orders of magnitude larger. The problem of the mass differences is related to the fact that in contrary to what the basic QFT Lagrangian show, the particles do have a mass which characterises the different types of particles. With the Higgs mechanism mass was given to both the electroweak bosons and to the fermions. In addition a Higgs boson, which is for many reasons believed to be light, is predicted. This view is strongly supported by global electroweak fits and unitarity constraints, which suggest that the SM Higgs mass m_H could be around 115 GeV [32,47,48].

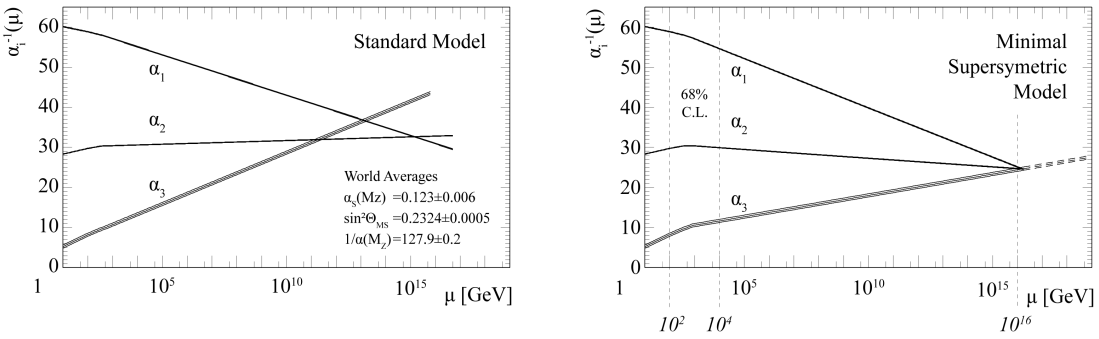

Figure 2.2: Extrapolated unification of the three gauge coupling constants corresponding to the $U(1)_Y \otimes SU(2)_L \otimes SU(3)_C$ symmetries of the electromagnetic/hypercharge (α_1), the weak (α_2) and strong forces (α_3) at the GUT scale for the Standard Model (left plot) and assuming Supersymmetry (right plot). Figures are taken from Ref. [49].

The introduction of the Higgs boson leads to the *fine tuning problem*. Radiative corrections to the mass of the Higgs boson and thus also to the gauge bosons, need to be calculated up to the energy scale Λ, a cut-off parameter that sets the scale for new physics (e.g. at the GUT or Planck scale). All dimensionless couplings and fermion masses are logarithmically sensitive to the scale Λ. The Standard Model particles and all unobserved particles, that couple to the Higgs field, contribute to these corrections. This implies quantum loop corrections to the squared Higgs mass that are quadratically divergent at the order of $\mathcal{O}(\Lambda^2)$.
The observed Higgs mass m_H is thus:

$$m_H^2 = m_0^2 + \delta m_H^2 \tag{2.13}$$

with m_0 the bare Higgs mass and δm_H the quantum corrections due to virtual particle loops. For example the one-loop contribution to the Higgs mass as shown in Figure 2.3 (left plot, figure a) is:

$$\delta m_H^2 \approx N_f \frac{|\lambda_f|^2}{8\pi^2}\left[-\Lambda^2 + 6m_f^2 ln\frac{\Lambda}{m_f} - 2m_f^2\right] + h.c. \approx \mathcal{O}(\Lambda^2) \tag{2.14}$$

where N_f is the number of fermions, m_f is the mass of the fermion, λ_f is the Yukawa coupling strength of the Higgs boson to the fermion (see Ref. [50]). It is hereby assumed that the fermion is very heavy.
If also scalar particles contribute (see Figure 2.3, right plot (b)) these corrections become extraordinary, assuming that the Standard Model is valid up to the Planck Scale. In order to remove the quadratic dependence of the Higgs mass on the high energy scale and to leave the Higgs with a mass of the order of the electroweak scale, the correction term needs to be cancelled with a precise tuning of the squared bare Higgs mass with an accuracy of about 10^{-34}. This seems to be very unnatural [51].
Under the assumption that the Higgs couplings of the scalar particles with the mass m_b are related to the Higgs-fermion couplings, one gets (see Ref. [50]):

$$\delta m_H^2 \approx \frac{N_f \mid \lambda_f \mid^2}{4\pi^2} \cdot \left[(m_f^2 - m_b^2) \cdot ln\left(\frac{\Lambda}{m_b}\right) + 3m_f^2 ln\left(\frac{m_b}{m_f}\right) \right] + \mathcal{O}(\frac{1}{\Lambda^2}) \tag{2.15}$$

The quadratic divergences in equation 2.14 disappear and only the logarithmic divergences are still present. Bosons and fermions provide hereby corrections to the Higgs mass with a different sign. The divergence completely disappears, if one assumes $m_f = m_b$. Therefore a possible solution to the fine tuning problem could be that new physics enters not much above the electroweak energy scale and regularises the quadratic divergences.

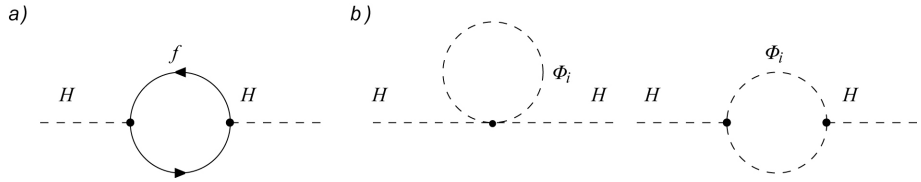

Figure 2.3: Diagram for the contribution of the fermions (a) and scalars (b) to the Higgs boson mass. Figure is taken from Ref. [50].

A "symmetry" which enforces that the scalar particle masses are equal to the fermion mass, would "protect" the Higgs boson mass. This could be realized by contributions of additional particles e.g. by introducing fermionic partners to W/Z and Higgs bosons and by adjusting their couplings to the Higgs boson. However, to keep the Higgs mass at the range of the electroweak scale the mass difference between the SM and the "new" particles has to be very small - O(1 TeV). There are also several other theoretical points where the SM does not give satisfying answer, for example the number of various free parameters in the SM, which are determined by measurements, but are lacking a fundamental explanation, the incorporation of neutrino masses or the hierarchical pattern of the quark masses $m_t, m_b \gg m_c, m_s \gg m_u, m_d$ or of the leptons $m_\tau \gg m_\mu \gg m_e$.

2.2. Supersymmetry

A variety of theoretical models have been proposed in the last decades, addressing the discussed limitations of the Standard Model. Supersymmetry (SUSY) is considered to be one of the most promising scenarios for the extension of the Standard Model [5–7]. It offers an attractive solution to the discussed hierarchy problem by assuming a symmetry that is connecting fermions and bosons, such that all fermion quantum correction terms contributing to the scalar mass of the Higgs boson are accompanied by corresponding scalar terms (which have opposite sign). This solution requires additional particles, the superpartners to the Standard Model particles, called sparticles. They are identical to their corresponding Standard Model particles in all quantum numbers except the spin (and mass as discussed later), that provides the required relative minus signs in the loop contributions. The superpartners of the fermions are the scalar sfermions and the superpartners of the gauge bosons are fermionic gauginos. The new SUSY particles also alter the RGEs in such a way that the three gauge couplings would merge at around 10^{16} GeV. These modifications to the RGEs are quite generic and parameter independent, if the SUSY particles are not too heavy [52]. Figure 2.2 (right plot) illustrates this unification. The gravitational field is introduced naturally for models that require invariance of the Lagrangian under local supersymmetry transformations.
Furthermore, in many supersymmetry models the lightest supersymmetric particle with a mass of $\mathcal{O}(1\,\text{TeV})$ provides a suitable WIMP candidate for dark matter [43, 53–55]. Although Supersymmetry adds more complexity to the Standard Model, this theory can also solve many of the discussed open questions of the Standard Model.

In the following section, the main concepts of Supersymmetry will be explained. A comprehensive description can be found in Ref. [56–59].

2.2.1. Theoretical framework

Since Supersymmetry is a symmetry between fermions and bosons, there exists a supersymmetric operation that transforms bosonic states (spin S = 0, 1) into fermionic states (spin S = $\frac{1}{2}$) and vice versa with the operator Q:

$$\text{Q} \mid \text{Boson} > = \mid \text{Fermion} > \qquad \text{Q} \mid \text{Fermion} > = \mid \text{Boson} > \tag{2.16}$$

If Q is a real symmetry operator, it has to commute with the Hamiltonian:

$$[Q, H] = 0 \tag{2.17}$$

It follows that Q and its hermitian conjugate $\bar{Q} \equiv Q^{\dagger}$ must have fermionic character. Within the easiest supersymmetric extension, the two generators Q_a and Q_b (type Q with indices a, b) satisfy the constraints of anticommutation and commutation relations [17]:

$$\{Q_a, Q_b\} \quad = \quad \left\{\bar{Q}_a, \bar{Q}_b\right\} = 0 \tag{2.18}$$

$$\{Q_a, \bar{Q}_b\} = (2\sigma^\mu)_{ab} P_\mu \quad (2.19)$$
$$[Q_a, P_\mu] = [\bar{Q}_a, P_\mu,] = 0 \quad (2.20)$$

with σ^μ the Pauli Spin matrices, P_μ the momentum generator of space-time translations. The formula directly implicates the supersymmetric algebra:

- The action of Q or $\bar{Q}$ on one state will modify the spin by 1/2.
- The operator P^μ commutes with the generators Q and $\bar{Q}$ which leads to states in a so called "supermultiplet". A supermultiplet contains bosonic or fermionic states and their respective superpartners with opposite spin statistics.
- Superpartners in a supermultiplet must have equal mass and must have the same gauge quantum numbers since the supersymmetry generators Q and $\bar{Q}$ also commute with the generators of the gauge transformations (gauge symmetry groups).
- The bosonic and fermionic degrees of freedom of each supermultiplet are related by: $n_b = n_f$ since a two SUSY transformation "Boson $\rightarrow$ Fermion $\rightarrow$ Boson" maps the bosonic subspace onto itself.

The simplest possible supermultiplet that is consistent with the discussed properties is called a "chiral supermultiplet" (matter supermultiplet). It consists of a left handed spinor field χ (single Weyl fermion with two spin helicity states) and two real scalar fields. The two scalars are typically assembled into a complex scalar field ϕ. The supersymmetric scalar particle states receive an "s" as prefix to their names ("sfermions") to distinguish them from the Standard Model particles. The next-simplest combination, called gauge or vector supermultiplet, are the gauge supermultiplets with a massless spin-1 vector boson and massless spin S = $\frac{1}{2}$ fermion as superpartner. These superpartners of the gauge bosons are called "gauginos". Depending on the supersymmetric model there are also other possible constellations. Some of the SUSY particles and the SUSY mass spectrum will be discussed in Section 2.2.2.

In the following, only the Minimal Supersymmetric Standard Model will be considered, which has been probed in Chapter 8-11.

2.2.2. The Minimal Supersymmetric Standard Model

The Minimal Supersymmetric Standard Model (MSSM) [60–62] represents the simplest possible supersymmetric extension to the SM and contains the minimal number of couplings and fields. The resulting MSSM multiplets, that form the particle content of the MSSM, can be found in Table 2.3:

- **Chiral supermultiplets**
  The Standard Model fermions and their corresponding superpartners are members of chiral supermultiplets. The scalar SUSY particles, the sfermions $\tilde{f}$, are called in the same way as the SM fermions, but get a prefix "s" (for scalar) and tilde "$\sim$" added to the symbol to indicate them, e.g. the superpartner of quarks and leptons are called squarks $\tilde{q}$ and sleptons $\tilde{l}$. Each SM fermion (except the neutrinos[4]) has two helicity states, a left-handed and right-handed component (see Table 2.1). These states transform differently under the gauge group transformations and therefore belong to different chiral supermultiplets. The consequence is that each fermion has two complex scalar superpartners- one for the right- and one for the left-handed part. For example the electron has two superpartners called selectrons: $\tilde{e}_L$ and $\tilde{e}_R$. The helicity symbol "R" and "L" refers to the chiral component (handedness) of the SM particle they are associated with, not to the superpartner, that are scalar spin-0 particles. For convenience, all fermions in the chiral supermultiplets are defined in terms of left-handed Weyl-spinors. Conjugations are therefore applied to the right-handed fields (see Table 2.3).

- **Gauge supermultiplets**
  The Standard Model gauge bosons (see Table 2.2) and their fermionic superpartners, referred as gauginos, form the gauge supermultiplets including: 8 gluons for the $SU(3)_C$ gauge group and the accompanied spin-1/2 gluinos, which form a colour-octet, the vector gauge bosons $W^{\pm}$, W^0 and B^0 for the electroweak gauge symmetry with the associated spin-1/2 superpartners called winos and bino. Again every SUSY partner has the name of the associated gauge bosons with an appended "ino" and a tilde in the symbol (see Table 2.3).

It is most convenient to describe the MSSM in terms of the gauge eigenstates, in which the particles can be treated as massless.
It should be noted that by imposing a local supersymmetry invariance an additional field which describes gravity has to be introduced. The corresponding SUSY field is called supergravity [63] (see Section 2.2.9) and the additional supermultiplet contains the spin-2 graviton and its spin-3/2 superpartner called "gravitino".

2.2.3. R-Parity

An additional quantum number is introduced by Supersymmetry, called R-parity [64, 65]. It is calculated from the baryon number B, the lepton number L and the spin S of a particle:

$$R \equiv (-1)^{3B+L+2S} \tag{2.21}$$

The Standard Model particles and their supersymmetric partners can be distinguished due to this multiplicative quantum number - all Standard Model particles have R-parity +1, while all supersymmetric particles have R-parity of -1.

[4] Neutrinos have only a left-handed component.

chiral supermultiplets		**spin** S = 0	**spin** S = $\frac{1}{2}$	**S**$U(3)_C$	**S**$U(2)_L$	**U**$(1)_Y$
squarks, quarks	Q	$(\tilde{u}_L, \tilde{d}_L)$	(u_L, d_L)	**3**	**2**	$\frac{1}{3}$
(3 families)	$\bar{U}$	$\tilde{u}_R^\dagger$	$u_R^\dagger$	$\bar{\mathbf{3}}$	**1**	$-\frac{4}{3}$
	$\bar{D}$	$\tilde{d}_R^\dagger$	$d_R^\dagger$	$\bar{\mathbf{3}}$	**1**	$\frac{2}{3}$
slepton, leptons	L	$(\tilde{\nu}_{e_L}, \tilde{e}_L)$	(ν_{e_L}, e_L)	**1**	**2**	-1
(3 families)	$\bar{E}$	$\tilde{e}_R^*$	$e_R^\dagger$	**1**	**1**	2
Higgs, Higgsinos	H_u	(H_u^+, H_u^0)	$(\tilde{H}_u^+, \tilde{H}_u^0)$	**1**	**2**	1
	H_d	(H_d^0, H_d^-)	$(\tilde{H}_d^0, \tilde{H}_d^-)$	**1**	**2**	-1
gauge supermultiplets		**spin S =** $\frac{1}{2}$	**spin** S = 1	**S**$U(3)_C$	**S**$U(2)_L$	**U**$(1)_Y$
gluino, gluon		$\tilde{g}$	g	**8**	**1**	0
wino, W boson		$\tilde{W}^\pm, \tilde{W}^0$	$W^\pm, W^0$	**1**	**3**	0
bino, B boson		$\tilde{B}^0$	B^0	**1**	**1**	0

Table 2.3: Chiral (top) and gauge (bottom) supermultiplets in the MSSM and the transformation properties under the SM gauge group $SU(3)_C \otimes SU(2)_L \otimes U(1)_Y$; Q and L present the supermultiplets containing $SU(2)_L$ doublets, $\bar{U}$, $\bar{D}$ and $\bar{E}$ contain the corresponding conjugate right-handed singlet states.

Whereas in the Standard Model baryon- and lepton-numbers are automatically conserved, the MSSM theoretically allows interaction terms that violate this symmetry. To avoid this undesired effect, the conservation of R-Parity will be assumed. From this it follows that there cannot be any mixing between the sparticles and the SM particles and every interaction vertex will contain an even number of R $= -1$ sparticles. The consequences of this new conservation are of great importance for the design of inclusive search channels in collider experiments:

1. Supersymmetric particles are only produced in pairs:
   $R_{total} = R_1^{SUSY} \cdot R_2^{SUSY} = (-1)^2 = R_1^{SM} \cdot R_2^{SM} = 1.$

2. Each sparticle decays into a state that contains an odd number of SUSY particles (usually one) and cannot decay into SM matter only.

3. There must be a lightest supersymmetric particle (LSP) that is stable and does not decay further into another SUSY particle.

It should be mentioned that there is no measurement that rules out the R-parity violation (RPV) SUSY models. However, there are several bounds that constrain these models, like the so far not observed proton decays[5] as well as constraints from collider experiments (e.g. see Ref. [66,67]). In this thesis only MSSM models with R-parity conservation are discussed.

The lightest supersymmetric particle in R-Parity conserving models

Since no exotic or electromagnetic bound states have been observed so far and taking cosmological constraints on the LSP into account to provide a viable candidate for cold dark matter [46,68], it can be assumed, that the LSP should be neutral, colourless and interacts weakly. The detector signature of an LSP is thus similar to that of a neutrino. It escapes direct detection resulting in an imbalance of the energy measured in the detector, called missing energy. However this still leaves several possible candidates in the supersymmetric parameter space, specifically the sneutrino with spin S = 0, the neutralino with spin S = 1/2, and the gravitino with spin S = 3/2. The sneutrino would have relatively large coherent interactions with heavy nuclei, and experiments searching directly for the scattering of massive dark matter particles on nuclei exclude a stable sneutrino weighting between a few GeV and several TeV - in the cosmologically interesting regions [69]. The possible very light sneutrino was excluded by measurements of the invisible Z-boson decay rate at LEP [70]. Gravitinos might be cold dark matter, however due to its very weak interactions, the gravitino itself would not be seen directly and only the next-to-lightest supersymmetric particle (NLSP) could be measured at colliders. For most models the LSP is assumed to be the lightest neutralino $\tilde{\chi}_1^0$ that will be discussed in Section 2.2.6.

2.2.4. The supersymmetric Lagrangian

The basic principles of constructing the total supersymmetric Lagrangian are similar to those used for the SM. According to the action principle $S = \int d^4x\, L$ the Lagrangian must stay invariant under any symmetry transformation, that leads to the gauge fields and provides the basis for the strong and electroweak forces. In addition, invariance under the supersymmetry transformation, that turns bosons into fermions and vice versa, is needed.
The SUSY invariant Lagrangian density, that describes the chiral and gauge supermultiplets as

[5] Proton decay channels are forbidden by either B or L conservation. R-parity violation is connected with the baryon- or lepton-number violation. As long as both B and L are not violated simultaneously in the model, there is no problem with proton decays.

well as the interactions between the gauge fields of the gauge supermultiplets and the matter fields of the chiral supermultiplets has the form (see Ref. [17]):

$$
\begin{aligned}
L_{SUSY} &= L_{\text{chiral}} + L_{\text{gauge}} + L_{\text{interactions}} \qquad (2.22)\\
L_{\text{SUSY}} &= \underbrace{(D_\mu \phi_i)^\dagger (D^\mu \phi_i)}_{\text{scalars}} + \underbrace{\mathrm{i}\, \psi_i^\dagger \bar{\sigma}^\mu D_\mu \psi_i}_{\text{fermions}} - \underbrace{\frac{1}{4} F^a_{\mu\nu} F^{\mu\nu a}}_{\text{gauge bosons}} + \underbrace{\mathrm{i}\, \lambda^{\dagger a} \bar{\sigma}^\mu D_\mu \lambda^a}_{\text{gauginos}} + \\
&\quad \underbrace{\frac{1}{2} D^a D^a + W_i^\dagger W_i}_{\text{scalar potential}} - \underbrace{\frac{1}{2} \left[\frac{\partial^2 W}{\partial \phi^{\dagger i} \partial \phi^{\dagger j}} \Psi^{\dagger i} \Psi^{\dagger j} + \frac{\partial^2 W}{\partial \phi_i \partial \phi_j} \Psi_i \Psi_j + h.c. \right]}_{\text{fermion mass term and Yukawa coupling}} \\
&\quad \underbrace{-\sqrt{2} g [(\phi_i^\dagger T^a \Psi_i) \lambda^a + \lambda^{\dagger a} (\Psi_i^\dagger T^a \phi_i)] - g (\phi_i^\dagger T^a \phi_i) D^a}_{\text{additional couplings}}.
\end{aligned}
$$

where ϕ_i , ψ_i denote scalar, fermionic fields, respectively with the index i running over all gauge and flavour degrees of freedom; D is a real scalar field and D_μ the gauge covariant derivative; λ_a denotes a fermion gaugino with the index a running over the representation of the gauge group: a = 1, ..., 8 for $SU(3)_C$ colour gluons and gluinos, a = 1, 2, 3 for the $SU(2)_L$ weak isospin; a = 1 for the $U(1)_Y$ weak hypercharge. The variable $F_{\mu\nu} = \partial_\mu A_\nu - \partial_\nu A_\mu - g A_\mu \times A_\nu$ is the Yang-Mill field strengths (gauge field tensor) with the gaugino coupling g and A_μ the gauge vector field; $\bar{\sigma}^\mu$ are the Pauli matrices. T^a is the gauge group transformation operator and D^a the bosonic auxiliary field, that ensures the invariance of the Lagrangian under a global supersymmetry transformation with $D^a = g \sum_i \phi_i^\dagger T^a \phi_i$. W^i is derived from the superpotential W. In a renormalizable supersymmetric field theory, the interactions and masses (before symmetry breaking) of all particles are determined just by their gauge transformation properties and by the superpotential W, given by: $W = \frac{1}{2} M_{ij} \phi_i \phi_j + \frac{1}{6} y_{ijk} \phi_i \phi_j \phi_k + f^i \phi_i$, with M_{ij} the symmetric mass matrix for the fermion fields, that can be interpreted as mass and y_{ijk} the Yukawa couplings of the fermion fields with the scalar one and f^i that is describing the parameters with dimensions of the mass^2. The superpotential contains only bilinear and trilinear scalar coupling terms and no fermionic contributions. The form of the superpotential is restricted by the requirement of the gauge invariance.
The **scalar potential** can be written as:

$$
\begin{aligned}
V(\phi_i, \phi_i^\dagger) &= |\, W_i \,|^2 + \sum_a \frac{1}{2} (D^a)^2 \qquad (2.23)\\
V(\phi_i, \phi_i^\dagger) &= |\, W_i \,|^2 + \frac{1}{2} \sum_G \sum_a \sum_{i,j} g_G^2 (\phi_i^\dagger T_G^a \phi_i)(\phi_j^\dagger T_G^a \phi_j) \geq 0.
\end{aligned}
$$

In this term more than one gauge group G enters, usually as for $SU(3)_C \otimes SU(2)_L \otimes U(1)_Y$ in the SM with different couplings g_G and generators T_G. The first term in equation 2.23 is called "F-term", because it is determined by the fermion mass term M_{ij} and the Yukawa coupling

$W_i = \frac{\partial W}{\partial \phi_i}$, the second term is determined by the gauge interactions and called the "D-term". For every field configuration is $V \geq 0$ and it is the only scalar potential independent of other terms appearing in the Lagrangian.
The term -$\sqrt{2}g[...]$ in equation 2.22 is important in case the chiral multiplet (ϕ_i, Ψ_i) are the Higgs supermultiplets H_u, H_d. These terms are responsible that mixing will appear among the fields of binos/winos $(\tilde{B}, \tilde{W}^0)$ and $(\tilde{H}_u^0, \tilde{H}_d^0)$ as a consequence of the electroweak symmetry breaking. The resulting neutral mass eigenstates are called neutralinos (see Section 2.2.6).

2.2.5. Supersymmetry breaking

Supersymmetry requires that all particles and sparticles have identical masses and only differ in their spin. Thus superpartners would have been extremely easy to detect at previous colliders. However, sparticles have not yet been observed. This implies that if supersymmetry is realized in nature, it must be a broken symmetry, such that the sparticles can be heavier than the corresponding Standard Model partners. In order to still solve the problems of the Standard Model, the breaking mechanism should preserve the renormalizability of the theory and it must ensure that quadratic divergences of the loop corrections to the squared Higgs mass, that are naturally cancelled by introducing supersymmetry, are not reintroduced.
Currently the exact breaking mechanism is unknown and it is one of the open question that searches for supersymmetric particles need to answer. There are two possible ways to break a symmetry in a field theory: By explicit symmetry-breaking terms in the Lagrangian or spontaneous symmetry breaking as it occurs for example in the Standard Model via the Higgs mechanism. The idea of the spontaneous symmetry breaking mechanism for Supersymmetry is hereby that it works similar to the electroweak symmetry breaking in the SM. The Lagrangian of the underlying model should be invariant under supersymmetry, but the vacuum state is not.

Spontaneously broken SUSY in the MSSM

As discussed for the SM, the symmetry in a field theory is spontaneous broken, if the field, which is not invariant under the symmetry, has a vacuum expectation value $\neq$ from 0 ($< 0|H|0 > \neq 0$), with H the Hamiltonian of the theory considered. Assuming the kinetic energy parts of the Hamiltonian do not contribute to the vacuum energy $< 0|H|0 > = < 0|V|0 >$, it can be seen that the scalar potential V = 0 (see eq. 2.23, scalar potential) corresponds to the SUSY-invariant case. However in the MSSM, the MSSM fields need a vacuum expectation value of 0 in order to not violate gauge invariance. Therefore the spontaneous SUSY breaking is communicated down to the observable MSSM sector via hypothetical flavour-blind messenger fields. These basic properties can be realized by adding a so-called "soft-breaking" term in the Lagrangian density, so that equation 2.22 becomes:

$$L = L_{SUSY} + L_{\text{soft}}$$

where L_{SUSY} contains all of the gauge and Yukawa interactions as discussed before and preserves the supersymmetry invariance, while L_{soft} contains mass terms and coupling parameters with positive mass dimension that breaks explicitly supersymmetry. This term results in the corrections

to the Higgs scalar masses that are logarithmic in the ultraviolet momentum cutoff Λ (and not quadratic as in the SM).
The theory itself remains renormalizable and the resulting mass terms are also small enough [71]. The following mass terms can be introduced to the Lagrangian:

- scalar mass terms $\sim m_a^2 \phi^\dagger \phi$
- mass term for the gauginos $\sim m_b \lambda_k \lambda_k$
- trilinear scalar interactions originated from the superpotential W(ϕ)

The soft-breaking term of the MSSM can than have the general form as defined in Ref. [17]:

$$\begin{aligned} L_{\text{soft}}^{\text{MSSM}} &= -\frac{1}{2}(M_3 \tilde{g}\tilde{g} + M_2 \tilde{W}\tilde{W} + M_1 \tilde{B}\tilde{B}) + h.c. \\ &\quad -(\tilde{\bar{U}} \mathbf{a_U} \tilde{Q} H_u - \tilde{\bar{D}} \mathbf{a_D} \tilde{Q} H_d - \tilde{\bar{E}} \mathbf{a_E} \tilde{L} H_d) + h.c. \\ &\quad -\tilde{Q}^\dagger \mathbf{m}_{\tilde{\mathbf{Q}}}^{\mathbf{2}} \tilde{Q} - \tilde{L}^\dagger \mathbf{m}_{\tilde{\mathbf{L}}}^{\mathbf{2}} \tilde{L} - \tilde{U}^\dagger \mathbf{m}_{\bar{\mathbf{U}}}^{\mathbf{2}} \tilde{U} - \tilde{D}^\dagger \mathbf{m}_{\bar{\mathbf{D}}}^{\mathbf{2}} \tilde{D} - \tilde{E}^\dagger \mathbf{m}_{\bar{\mathbf{E}}}^{\mathbf{2}} \tilde{E} \\ &\quad -m_{H_u}^2 H_u^\dagger H_u - m_{H_d}^2 H_d^\dagger H_d - (b H_u H_d) + h.c. \end{aligned} \tag{2.24}$$

The first line represents the mass terms of the gauginos for each gauge group (binos, winos and gluinos) with the mass parameter M_1, M_2, M_3. The second line contains the scalar superfields $\tilde{Q}, \tilde{\bar{U}}, \tilde{\bar{D}}, \tilde{L}, \tilde{\bar{E}}$ and the cubic scalar couplings, each $a^{ijk} = \mathbf{a_U}, \mathbf{a_D}, \mathbf{a_E}$ is a complex 3×3 matrix, that result in additional mass terms corresponding to the Yukawa couplings from the superpotential. All three generations contribute. The third line gives the additional squared scalar mass term $(m^2)^i_j$ for squarks and sleptons with hermitian 3×3 matrices that generate $\mathbf{m}_{\tilde{\mathbf{Q}}}, \mathbf{m}_{\bar{\mathbf{U}}}, \mathbf{m}_{\bar{\mathbf{D}}}, \mathbf{m}_{\bar{\mathbf{E}}}, \mathbf{m}_{\tilde{\mathbf{L}}}$. In the last line is the soft breaking contribution from the squared Higgs-mass terms $m_{H_u}^2$ and $m_{H_d}^2$ to the Higgs potential and the bilinear coupling b. The scalar and gaugino terms break the symmetry by giving masses to the associated particles.
This Lagrangian demonstrates the complexity of the spontaneously broken MSSM. In total there are about 105 new parameters introduced due to the soft breaking including masses, mixing angles CP-violating phases in the squark and slepton sector and in the Higgs-sector, which cannot be removed or associated to measured SM parameters [72]. However not all of these parameters are independent that reduces the number of freedom degrees. In order to solve the hierarchy problem, introduced masses should have $\lesssim \mathcal{O}(1\ \text{TeV})$.

2.2.6. The mass spectrum of MSSM particles

The masses of the supersymmetric particles are derived from the Lagrangian L_{soft} (see equation 2.24) in form of a combination of their couplings to the two Higgs fields and the direct mass terms. The mass parameters (32 in the general MSSM, not including the gravitino), defined at some very high energy scale Q, are than evolved down to the electroweak scale using the renormalisation group equations (RGE). The effective quantities at the electroweak scale come hereby from the loop diagrams, which can be large and must be re-summed in this process. Therefore all couplings and masses are treated as "running" parameters, which evolve as the energy scale

changes according to the RGEs [17]. Figure 2.4 shows the RGE running of scalar and gaugino masses for two SUSY models with $\tan\beta = 1.65$ and $\tan\beta = 50$. The running gaugino masses are solid blue lines, the running squark and slepton masses are the red dotted lines and the green lines are the running values of the quantities $\mu^2 + H_u^2$ labeled as m_1 and $\mu^2 + H_d^2$ labelled as m_2. The terms can run to negative values due to the large Yukawa couplings. The parameter values at the electroweak scale can be used to extract e.g. the physical masses. Several available programs perform these RGE running for various SUSY models. The tool mostly used within ATLAS and in this thesis is called ISAJET [73] (see Section 4.2.1).

The mass matrices of the gauginos, squarks and sleptons as result of the RGE are discussed in the following. The different mass eigenstates are listed in Table 2.4.

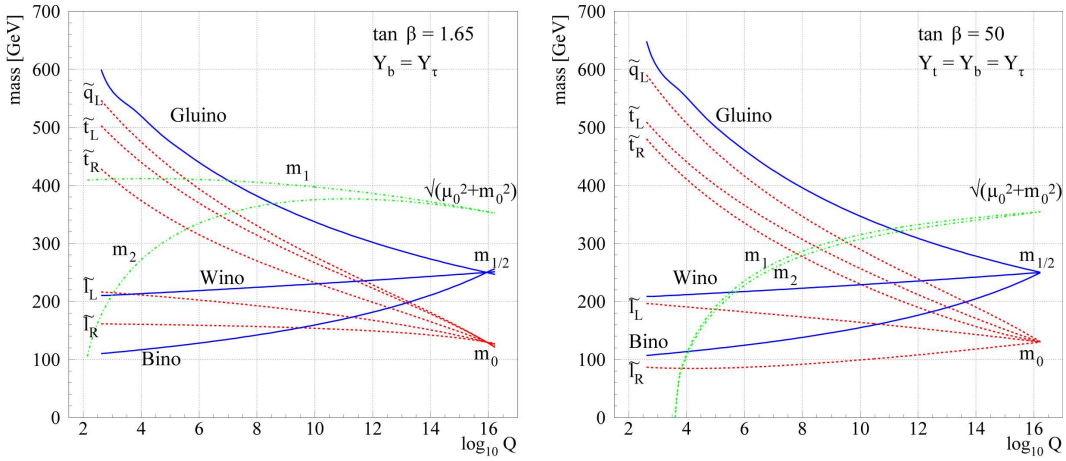

Figure 2.4: RG evolution of scalar and gaugino mass parameters in the MSSM for two typical SUSY models (mSUGRA models) with $\tan\beta = 1.65$ (left plot) and $\tan\beta = 50$ (right plot). The quantity $\mu^2 + H_u^2$ is labelled as m_1 and $\mu^2 + H_d^2$ is labelled as m_2 and can get negative values, provoking electroweak symmetry breaking. The Figures are taken from Ref. [74].

Gluinos

The gluino $\tilde{g}$ is the only octet fermion, and since $SU(3)_C$ is unbroken, it cannot mix with any other MSSM particle. Its mass arises from the soft SUSY-breaking gluino mass term (see equation 2.24):

$$L_{\text{MSSM}} \subset -\frac{1}{2}(M_3 \tilde{g}\tilde{g}) + \text{h.c.} \qquad \text{a} = (1...8) \tag{2.25}$$

where a is the colour index and M_3 is the positive mass term ($M_3 = \mid M_3 \mid$) that can be considered as the running mass parameter with an implicit dependence on the RG scale Q.

name	spin	R-parity	gauge eigenstates	mass eigenstates
Higgs boson	0	+1	$H_u^0, H_d^0, H_u^+, H_d^-$	$h^0, H^0, A^0, H^\pm$
squarks	0	-1	$\tilde{u}_L \quad \tilde{u}_R \quad \tilde{d}_L \quad \tilde{d}_R$ $\tilde{s}_L \quad \tilde{s}_R \quad \tilde{c}_L \quad \tilde{c}_R$ $\tilde{t}_L \quad \tilde{t}_R \quad \tilde{b}_L \quad \tilde{b}_R$	$\tilde{u}_L \quad \tilde{u}_R \quad \tilde{d}_L \quad \tilde{d}_R$ $\tilde{s}_L \quad \tilde{s}_R \quad \tilde{c}_L \quad \tilde{c}_R$ $\tilde{t}_1 \quad \tilde{t}_2 \quad \tilde{b}_1 \quad \tilde{b}_2$
sleptons	0	-1	$\tilde{e_L} \quad \tilde{e_R} \quad \tilde{\nu}_e$ $\tilde{\mu}_L \quad \tilde{\mu}_R \quad \tilde{\nu}_\mu$ $\tilde{\tau}_L \quad \tilde{\tau}_R \quad \tilde{\nu}_\tau$	$\tilde{e}_L \quad \tilde{e}_R \quad \tilde{\nu}_e$ $\tilde{\mu}_L \quad \tilde{\mu}_R \quad \tilde{\nu}_\mu$ $\tilde{\tau}_1 \quad \tilde{\tau}_2 \quad \tilde{\nu}_\tau$
neutralinos	$\frac{1}{2}$	-1	$\tilde{B}^0, \tilde{W}^0, \tilde{H}_u^0, \tilde{H}_d^0$	$\tilde{\chi}_1^0, \tilde{\chi}_2^0, \tilde{\chi}_3^0, \tilde{\chi}_4^0$
charginos	$\frac{1}{2}$	-1	$\tilde{W}^\pm, \tilde{H}_u^+, \tilde{H}_d^-$	$\tilde{\chi}_1^\pm, \tilde{\chi}_2^\pm$
gluino	$\frac{1}{2}$	-1	$\tilde{g}$	$\tilde{g}$

Table 2.4: Supersymmetric particles in the MSSM with spin, R-parity, the gauge and mass eigenstates. The mixing of the sfermions for the first two families was assumed to be negligible.

Neutralinos and charginos

The neutral gauginos $\tilde{B^0}$ and $\tilde{W^0}$ would have given masses just by the soft SUSY breaking term: $-\frac{1}{2}(M_2\tilde{W}\tilde{W} + M_1\tilde{B}\tilde{B} + c.c.)$ in case there is no electroweak symmetry breaking. However as result of the broken symmetry bilinear combinations are generated by parts of the gauge interaction term (D-term), that causes mixing of the four fields - the neutral higgsinos $\bar{H}_u^0$ and $\bar{H}_d^0$ and the neutral gauginos $\tilde{B^0}$ and $\tilde{W^0}$ (see Table 2.4). The resulting four neutral mass eigenstates are called *neutralinos* $\tilde{\chi}_i^0$ (i = 1, 2, 3, 4). They are ordered according increasing masses: $\tilde{\chi}_1^0 < \tilde{\chi}_2^0 < \tilde{\chi}_3^0 < \tilde{\chi}_4^0$. The charged states H_u^+, H_d^-, W^+, W^- mix and form two mass eigenstates with charge $\pm$ that are called *charginos* ($\tilde{\chi}_1^\pm, \tilde{\chi}_2^\pm$), where the lowest index denotes the lightest sparticle of the two $\tilde{\chi}_1^\pm < \tilde{\chi}_2^\pm$.
In the gauge-eigenstate basis $\tilde{G^0} = (\tilde{B^0}, \tilde{W^0}, \tilde{H_d^0}, \tilde{H_u^0})$ the neutralino mass of the Lagrangian is: $L_{\text{neutralino}} \subset -\frac{1}{2}(\tilde{G^0})^T M_{\tilde{G^0}} \tilde{G^0}$ + h.c., where:

$$M_{\tilde{G^0}} = \begin{pmatrix} M_1 & 0 & -c_\beta s_W m_Z & s_\beta s_w m_Z \\ 0 & M_2 & c_\beta c_w m_Z & -s_\beta c_w m_Z \\ -c_\beta s_W m_Z & c_\beta s_W m_Z & 0 & -\mu \\ s_\beta c_W m_Z & -s_\beta c_W m_Z & -\mu & 0 \end{pmatrix} \tag{2.26}$$

with $c_\beta \equiv \cos\beta$, $s_\beta \equiv \sin\beta$, $c_W \equiv \cos\theta_W$, $s_W \equiv \sin\theta_W$.

This mass matrix can be diagonalised to obtain the neutralino mass eigenstates.
The terms $M_{1,2}$ come from the mass terms in L_{soft}, the value of μ corresponds to the higgsino mass terms and the terms proportional to m_Z are from the mixing terms between higgsinos and gauginos. In general the parameter can have complex phases, but it is possible to choose a convention that M_1 and M_2 are real and positive. Usually μ is taken to be real, but "sign(μ)" can be positive or negative.
In models that assume gaugino unification fixed M_1, M_2 values are implied. For example in models that satisfy with unification at the GUT scale (see equation 2.37), the prediction goes to $M_1 \approx \frac{5}{3}\tan^2\theta, M_2 \approx 0.5 M_2$
and the neutralino masses and mixing angles depend on only three parameters.
From equation 2.26 one can see that $\tilde{\chi}^0_{1,2}$ are close to the eigenstates of bino and wino (if the m_Z dependent mass terms are small), respectively with masses close to M_1 and M_2, while Higgsinos are mixed by the μ entries.

For the charged analoges of the neutralinos- the charginos- is the Lagrangian
$L_{\text{chargino}} \subset -\frac{1}{2}[\tilde{g}^{+T} X^T \tilde{g}^- + \tilde{g}^{-T} X \tilde{g}^+]$ + h.c. with the gauge-eigenstate basis (see Ref. [17]):

$$\tilde{g}^+ = \begin{pmatrix} \tilde{W}^+ \\ \tilde{H}_u^+ \end{pmatrix} \qquad \text{and} \qquad \tilde{g}^- = \begin{pmatrix} \tilde{W}^- \\ \tilde{H}_d^- \end{pmatrix} \tag{2.27}$$

where:

$$\mathbf{X} = \begin{pmatrix} M_2 & \sqrt{2} s_\beta m_W \\ \sqrt{2} c_\beta m_W & \mu \end{pmatrix} \tag{2.28}$$

Since $\mathbf{X} \neq \mathbf{X^T}$ (unless $\tan\beta = 1$) two distinct 2×2 matrices are needed to determine the mass eigenstates:

$$\tilde{\chi}^+ = \mathbf{V}\tilde{g}^+ = \begin{pmatrix} \tilde{\chi}_1^+ \\ \tilde{\chi}_2^+ \end{pmatrix} \qquad \text{and} \qquad \tilde{\chi}^- = \mathbf{U}\tilde{\mathrm{g}}^- = \begin{pmatrix} \tilde{\chi}_1^- \\ \tilde{\chi}_2^- \end{pmatrix}.$$

$\mathbf{X}$ can than be diagonalised by the operation $\mathbf{U^* X V^{-1}}$ that gives the chargino masses (assuming M_2 and μ to be real):

$$m^2_{\tilde{\chi}^\pm_{1,2}} = \frac{1}{2}|M_2|^2 + \frac{1}{2}|\mu|^2 + m_W^2 \mp \frac{1}{2}\sqrt{(M_2^2 + |\mu|^2 + 2m_W^2)^2 - 4|\mu M_2 - m_W^2 \sin(2\beta)|^2}. \tag{2.29}$$

The following expressions are used within this thesis:
The region in the parameter space where $|\ \mu\ | \gg M_i \gg m_Z$ (i = 1, 2) is called "gaugino region", because the field content of the lightest chargino and neutralinos is dominated by wino and bino contributions:

$$\begin{array}{ll} m_{\tilde{\chi}_1^0} \approx M_1 & m_{\tilde{\chi}_1^\pm} \approx M_2 \\ m_{\tilde{\chi}_2^0} \approx M_2 & m_{\tilde{\chi}_2^\pm} \approx |\mu| \\ m_{\tilde{\chi}_{3,4}^0} \approx |\mu| & \end{array}$$

If $M_1 < M_2 \ll \mid \mu \mid$ the neutralino mass-eigenstates are called "bino-like", $\tilde{\chi}_1^0 \approx \tilde{B}^0$, while if $M_2 < M_1 \ll \mid \mu \mid$ the neutralino mass-eigenstate is "wino-like" with a chargino only very slightly heavier. The chargino mass eigenstates are called wino-like for $m_{\tilde{\chi}_1^\pm} \approx M_2$ ($M_2 \ll \mid \mu \mid$). The other two neutralinos $\tilde{\chi}_{3,\,4}^0$ and the $\tilde{\chi}_2^\pm$ are in the gaugino region "higgsino-like" with mass-eigenstates $m_{\tilde{\chi}_{3,4}^0} \approx m_{\tilde{\chi}_2^\pm} \approx |\mu|$.
For the condition $\mid \mu \mid \ll M_i$ (i = 1, 2), the lightest neutralinos are dominantly by higgsinos, thus the region is called "higgsino region". The $\tilde{\chi}_2^0$ and $\tilde{\chi}_1^\pm$ are often not much heavier than $\tilde{\chi}_1^0$: $m_{\tilde{\chi}_1^0} \approx m_{\tilde{\chi}_2^0} \approx |\mu|, m_{\tilde{\chi}_3^0} \approx M_1$.

Higgsinos

The spin-0 SM Higgs boson is naturally accommodated in the chiral supermultiplet along with its "Higgsino" superpartner (again denoted by adding the tilde symbol). However the SUSY theory requires more than one complex Higgs doublet: At least two Higgs supermultiplets are necessary in order to avoid gauge anomalies as known from the SM and to induce the necessary Yukawa couplings to all up- and down-like quarks and to give also mass to the fermions [60]. The two (SM) Higgs $SU(2)_L$ -doublet complex scalar fields come with weak hypercharge Y = 1 and Y = -1 and are called H_u and H_d, respectively:

$$\begin{pmatrix} H_u^+ \\ H_u^0 \end{pmatrix} \qquad \text{and} \qquad \begin{pmatrix} H_d^+ \\ H_d^0 \end{pmatrix} \tag{2.30}$$

In total there are 4 complex or 8 real degrees of freedom in the Higgs doublets (2 Higgs doublets + conjugates). In the Standard Model three phases are absorbed by Goldstone bosons[6] to give mass to Z^0 and $W^\pm$, the remaining 5 are used to produce massive Higgs bosons (real scalar Higgs fields) consisting of: two neutral CP – even scalars- h^0 (often referred as h), a light neutral scalar Higgs particle and H^0, a heavy neutral scalar Higgs particle A^0; a neutral CP-odd pseudoscalar Higgs particle and two charges scalars $H^\pm$. By convention, h^0 is lighter than H^0.
The masses of the Higgs bosons can be determined from the Higgs scalar field V, that should have a well defined local minimum and vacuum expectation values unequal to 0. Without loss of generality, one can chose $H_u^+ = H_d^- = 0$ at the local minimum of V, implying that the charged components of the Higgs scalars cannot get vacuum expectation values. The values H_u^0 and H_d^0 have to be real and positive, so that the vacuum expectation values have opposite phase:
$v_u = < H_u^0 >$ and $v_d = < H_d^0 >$ with the ration $\tan\beta = \frac{v_u}{v_d}$ (with $0 \leq \beta \leq \frac{\pi}{2}$). The values are related to the known mass of the Z^0 boson and the electroweak gauge couplings via: $v^2 = {v_u}^2 + {v_d}^2 = \frac{2m_Z^2}{g^2+g'^2}$,

[6] Goldstone bosons are hypothetically massless particles, which occur in the context of spontaneous symmetry breaking.

where g is their coupling constant of $SU(2)_L$ and g' is the SM hypercharge gauge coupling. The masses of the higgsinos are (see e.g. Ref [56]):

$$m^2_{A^0} = 2 \mid \mu \mid^2 + m^2_{H_u} + m^2_{H_d} \quad (2.31)$$

$$m^2_{H^\pm} = m^2_{A^0} + m^2_W \quad (2.32)$$

$$m^2_{h^0,H^0} = \frac{1}{2}\left(m^2_{A^0} + m^2_{Z^0} \mp \sqrt{(m^2_{A^0} + m^2_{Z^0})^2 - 4 m^2_{Z^0} m^2_{A^0} \cos^2(2\beta)} \right) \quad (2.33)$$

The mass equations imply an upper bound on the mass of the lightest neutral Higgs boson:

$$m_{h^0} \leq m_Z \mid cos(2\beta) \mid \leq m_Z \quad (2.34)$$

With this mass limit the lightest Higgs boson of the MSSM would have been already discovered. However due to e.g. quantum corrections from top quark and top squark loops for the squared mass term and other important corrections (see Ref. [75–78]) is the upper bound in the MSSM $m_{h^0} \lesssim 135$ GeV. This limit assumes that all sparticles that can contribute to $m^2_{h^0}$ in the loops have masses below 1 TeV. For SUSY masses above 1 TeV the lightest neutral Higgs boson should be lighter than about 150 GeV [56].
There is also a "constraint" on $\cos\beta$ if one requires that the running bottom and tau Yukawa couplings do not become non-perturbatively large. The rough upper bound on $\tan\beta$ is $\lesssim 65$ [79].

Squarks and sleptons

The scalar partners of the SM fermions form the largest collection of new particles, all together there are 21 new sfermion fields. The part in the Lagrangian that mostly contributes to the mass eigenstates is $L_{sfermion} \subset -\tilde{f}^\dagger \mathbf{m^2_{\tilde{f}}} \tilde{f}$, where $f = (\tilde{f}_L, \tilde{f}_R)$ stands for the different left- and right-handed sfermions with mass $m_{\tilde{f}_L}$ and $m_{\tilde{f}_R}$ and $\mathbf{m^2_{\tilde{f}}}$ for the corresponding symmetry matrices:

$$\mathbf{m^2_{\tilde{f}}} = \begin{pmatrix} m^2_f + M^2_L + m^2_Z \cos(2\beta)(T^3_f - Q_f sin^2\theta_W) & m_f(A_f - \mu\kappa) \\ m_f(A_f - \mu\kappa) & m^2_f + m^2_{\tilde{f}_R} + m^2_z cos(2\beta) Q_f sin^2\theta_W \end{pmatrix} \quad (2.35)$$

with $\kappa = \cot\beta$ for "up-type" squarks ($\tilde{u}_L, \tilde{u}_R, \tilde{c}_L, \tilde{c}_R, \tilde{t}_L, \tilde{t}_R$) and $\kappa = \tan\beta$ for "down-type squarks" ($\tilde{d}_L, \tilde{d}_R, \tilde{s}_L, \tilde{s}_R, \tilde{b}_L, \tilde{b}_R$) and the charged sleptons. The variable m_f is the mass of the fermion f with the electromagnetic charge Q_f and the isospin T^3_f. The quantities $M_L, m_{\tilde{f}_R}$ and A_f denote the soft-breaking parameters ($M_L = m_{\tilde{Q}}, m_{\tilde{L}}$; $m_{\tilde{f}_R} = m_{\tilde{U}}, m_{\tilde{D}}, m_{\tilde{E}}$; $A_f = A_u, A_d, A_e, ..$; see Section 2.2.7).
In principle, any scalars with the same electric charge, R-parity and colour quantum numbers can mix with each other, across the families via the soft SUSY breaking parameters. Since most of these mixing angles for the flavour-blind soft symmetry breaking MSSM parameters are small, mixing of the sfermions in the first two families is generally neglected and the off-diagonal terms in equation 2.35 do not contribute. The third family squarks and sleptons can have substantial mixing between the left-handed and right-handed states ($\tilde{t}_L, \tilde{t}_R$), ($\tilde{b}_L, \tilde{b}_R$), ($\tilde{\tau}_L$,$\tilde{\tau}_R$) due to the large masses

of top and bottom quark and tau lepton. The sfermion mass matrices can than be diagonalised by 2×2 rotation matrices with the mixing angle θ_f, which turn the eigenstates $\tilde{f}_L$ and $\tilde{f}_R$ into the mass eigenstates $\tilde{f}_1$ and $\tilde{f}_2$, where '1" denotes the lightest particle $m_{\tilde{f}_1} < m_{\tilde{f}_2}$:

$$\begin{pmatrix} \tilde{f}_1 \\ \tilde{f}_2 \end{pmatrix} = \begin{pmatrix} cos\theta_f & sin\theta_f \\ -sin\theta_f & cos\theta_f \end{pmatrix} \begin{pmatrix} \tilde{f}_L \\ \tilde{f}_R \end{pmatrix} \tag{2.36}$$

The mixing effect is very strong for large values of the mass parameter $A_f - \mu\kappa$ that contributes to the sfermion mass $m^2_{\tilde{f}_{1,2}}$. For example for large values of $\tan\beta$ and $|\mu|$ the mixing in the sbottom or stau sectors can contribute significantly and generates a mass splitting, which makes the $\tilde{b}_1$ and $\tilde{\tau}_1$ mass eigenstates much lighter than their first- and second-family counterparts. Similar effects are for $\tilde{t}_1$. The $\tilde{t}_1$ and $\tilde{b}_1$ are than the lightest squarks and the $\tilde{\tau}_1$ is the lightest slepton compared to the other sleptons. The very light $\tilde{\tau}_1$ enhances the τ-lepton rate in supersymmetric decay chains. Also the mass difference between the selectron and stau ($m_{\tilde{e}_R} - m_{\tilde{\tau}_1}$) is for large $\tan\beta$ significant, because of a large τ Yukawa coupling. For small values of $\tan\beta$ is $\tilde{\tau}_1$ predominantly $\tilde{\tau}_R$ and not much lighter than the first and second generation sleptons.
In addition to all these terms there are also contributions to the sfermion mass from the SUSY-invariant D-term, which arises as a result of the electroweak symmetry breaking.
Due to large Yukawa and soft couplings have the third generation squarks and sleptons very different masses compared to the first- and second-family sfermions. The first- and second-family squarks and sleptons have negligible Yukawa couplings and end up in nearly degenerated, unmixed pairs.
It is noteworthy that the left-handed squarks $\tilde{u}_L, \tilde{d}_L, \tilde{s}_L$ and $\tilde{c}_L$ and charged sleptons $\tilde{e}_L$, $\tilde{\mu}_L$ are likely to be heavier than their right-handed ones $\tilde{u}_R, \tilde{d}_R, \tilde{s}_R$, $\tilde{c}_R$ due to the larger RGE contributions from $SU(2)_L$ gauginos values.

2.2.7. Phenomenological MSSM models

The MSSM Lagrangian (see Section 2.2.5) has a high number of free input parameters. Including at least 105 new parameters added to the 19 parameters of the SM, the model can be described by 124 parameters[7] that need to be determined. However, often only a subsets of these parameters are relevant for experimental processes.
The number of the free choosable parameters, which imply flavour mixing or CP violating processes, can be significantly reduced or restricted by considering experimental results. For example the boundaries on violation of the lepton number e.g. from the muon decay process $\mu \rightarrow e\gamma$ [80] limit the slepton mixing and imply constraints on the off-diagonal entries of the slepton mass matrices. The experimental limits for squark (flavour) mixing from flavour changing neutral current (FCNC) measurements, e.g. from the K^0 system as well as from the neutral D-system and e.g. from the process $b \rightarrow s\gamma$ affect the d-squark and s-squark mixing and the squark matrices as well as the off-diagonal elements of the matrices $\mathbf{a_U}$, $\mathbf{a_D}$ and $\mathbf{a_E}$. All these processes would be allowed by flavour mixing soft-symmetry-breaking MSSM terms (see equation 2.24). Strict constraints on

[7] The MSSM is therefore often referred as MSSM-124.

CP-violating phases [81] follow e.g. from limits on the electric dipole moments of the neutron and electron. There are several other experimental results that have an influence on the parameter (see e.g. discussion in Section 6.3.1).
Models based on these similar constraints are referred to as **phenomenological MSSM (pMSSM)** [82]. A phenomenologically viable MSSM model can be defined by making the following three assumptions:

1. All the soft SUSY-breaking parameters are real and therefore there is no new source of CP-violation generated in addition to the one from the CKM matrix.

2. The matrices for the sfermion masses and for the trilinear couplings are all diagonal, implying the absence of flavour changing neutral currents (flavour-blind). The trilinear couplings of three scalars $\mathbf{a_U}, \mathbf{a_D}, \mathbf{a_E}$ are proportional to the Yukawa coupling.

3. First and second sfermion generation have no effect on the running of the SUSY-breaking parameters and can be assumed as universal at low energy.

Making these three assumptions will lead to 19 model parameters (see Ref. [82]):

- 3 gaugino masses M_1, M_2, M_3
- 5 sfermion masses of the first two generations $m_{\tilde{e}_R}, m_{\tilde{u}_R}, m_{\tilde{d}_R}, m_{\tilde{q}}$ and $m_{\tilde{l}}$
- 5 sfermion masses of the third generation $m_{\tilde{\tau}_R}, m_{\tilde{b}_R}, m_{\tilde{t}_R}, m_{\tilde{Q}}$ and $m_{\tilde{L}}$
- 3 trilinear couplings for 3rd generation: A_t, A_b, A_τ
- 3 parameters for the Higgs sector m_A^0 (m_A), $\tan\beta$, μ

The parameter $\mid \mu \mid$ and the soft SUSY-breaking bilinear Higgs term are determined through the electroweak symmetry breaking conditions. The trilinear sfermion couplings are mostly only important in the case of the third generation.

2.2.8. Constrained MSSM models

For practical purposes to carry out phenomenological analyses often constrained MSSM models (CMSSM) are studied. They are based on a number of assumptions e.g. about the SUSY breaking mechanism at the grand unification scale. The common approach in supersymmetry breaking models is to assume that the MSSM soft terms arise indirectly or radiatively. The idea is that the theory is splitted into at least two sectors - a hidden and a visible (observable) sector. The visible sector contains the SM fields and their superpartners and in the hidden sector is SUSY spontaneously broken by a dynamical mechanism. The fundamental scale of supersymmetry breaking Q is much larger than the TeV scale, depending on the model it can be e.g. at the GUT scale. Within this framework, SUSY breaking is than mediated between the two sectors via interactions involving a set of fields, called the mediator or messenger fields. The main characteristics of the different

SUSY breaking models arise from the choice of the mediation mechanisms (messenger fields), the soft supersymmetry breaking terms and the energy scales at which the soft terms are generated. All models predict new particles and interactions usually at high mass scales of $\mathcal{O}(1-2\,\text{TeV})$. The most common SUSY models, that are also discussed in this thesis, are:

- Gravity Mediated Supersymmetry Breaking (mSUGRA)
- Gauge Mediated Supersymmetry Breaking (GMSB)
- Anomaly Mediated Supersymmetry Breaking (AMSB)

Gravity mediated supersymmetry breaking models propose gravitational interactions, which are associated to the new physics that enters close to the Planck scale. The simplest realisation of such a framework is the minimal supergravity model (mSUGRA) [83,84], that is described in the next section.
Gauge-mediated SUSY breaking models [85,86] assume that SM gauge interactions are responsible for the appearance of soft supersymmetry breaking in the MSSM. The basic idea is to introduce some new chiral supermultiplets, called messengers, that couple to the source of supersymmetry breaking, and also couple indirectly to the (s)quarks and (s)leptons and Higgs(inos) of the MSSM through the $SU(3)_C \otimes SU(2)_L \otimes (U(1)_Y$ associated gauge boson and gaugino interactions. There are also gravitational interactions between the MSSM and the source of the supersymmetry breaking, but the effect is relatively unimportant compared to the gauge interactions. As a result of the spontaneous SUSY breaking, the physical spectrum of GMSB models contains the spin-3/2 partner of the graviton, the gravitino defined by the parameter $m_{3/2}$.
Since the superpartners of the Standard Model particles get their masses via gauge interactions that are are flavour-blind, there are no flavour changing neutral currents, which can be problematic in gravity mediated models. The minimal GMSB (mGMSB) [86] is a very promising alternative to the mSUGRA model based on the hypothesis that the soft SUSY-breaking occurs at relatively low energy scales. Typically the scale of supersymmetry breaking in the GMSB is of the order of $\approx O(10^4 - 10^5)$ GeV. Moreover, the gravitino gets a mass in the eV to keV range and is therefore the LSP. This can be crucial for SUSY signatures at collider experiments, because the next lightest LSP (NLSP) can decay into its SM partner plus a gravitino. There can be a long-lived neutralino $\tilde{\chi}_1^0$, that decays outside the detector and leads to the usual SUSY signature of large missing energy plus leptons and/or jets or the neutralino decays into a gravitino and a photon inside the detector. The NLSP may however also be a slepton e.g. a stau that can decay into long-lived charged particles or τ leptons. MGMSB models can be described by six free parameters, that include e.g. the scale of gauge unification Λ and the messenger mass scale M_{mess}, that determines the low-energy spectrum.
It is also possible that the MSSM and the supersymmetry breaking sectors are in different dimensions, such that a MSSM brane and a hidden brane exist. This can be accomplished by assuming that there are extra spatial dimensions, so that a physical distance separates the visible and hidden sectors. **Anomaly mediated supersymmetry breaking models** [87–89] assume that the gauge

supermultiplet fields are confined to the MSSM brane and the SUSY breaking is conveyed to the observable sector by the super-Weyl anomaly. Anomaly mediation is a special case of gravity mediation with no tree-level couplings between the superfields of the hidden and the observable sectors. AMSB scenarios have several features with important phenomenological consequences. The gravitino is rather massive, the LSP can be either a wino-like $\tilde{\chi}_1^0$, which is nearly mass degenerate with $\tilde{\chi}_1^{\pm}$ or the $\tilde{\nu}$. Another feature of AMSB models is that they predict negative mass squares for the sleptons. In the minimal AMSB model this problem is solved by adding a universal constant mass term m_0^2 to the squared scalar masses, chosen such to allow the sleptons to have positive squared masses. The set of common parameters, which parameterises the minimal AMSB framework is than: $m_{3/2}, m_0$, $\text{sign}(\mu), \tan\beta$.
Another type of models called **NUHM** [90] assumes that the soft supersymmetry-breaking masses of the Higgs multiplets are non-universal. Compared with the mSUGRA model, that requires gaugino mass equality at GUT scale, the Higgs mixing parameter μ and the pseudoscalar Higgs mass m_{A_0} are free in the NUHM model and phenomena in the mSUGRA parameter space could become more general.

2.2.9. Minimal gravity mediated SUSY breaking model (mSUGRA)

Many of the results in this thesis are interpreted for the minimal gravity mediated SUSY breaking model [83,84], that is a simplified phenomenological model based on a set of universal boundary conditions at the GUT scale. In mSUGRA models, gravitational-strength interactions, as specified by Supergravity, mediate the breaking of Supersymmetry between the hidden sector, that is postulated at the Planck scale M_{Planck}, and the visible sector at the TeV scale. Therefore the name minimal SUper GRAvity. This messenger field also comprises a new particle, the graviton (S = 1/2) and its superparter the gravitino (S = 3/2). The soft SUSY breaking terms in mSUGRA models naturally emerge if the Supergravity interactions are flavour-blind through a so-called "super Higgs" effect, where the massless gravitino becomes massive by using the spin 1/2 component of a chiral super Higgs multiplet.
In order to obtain SUSY masses at the desired TeV scale, to get unification at the GUT scale and to prevent Higgs mass divergences, the SUSY breaking scale $\sqrt{< F >}$ should be around 10^{11}-10^{12} GeV. The Lagrangian includes terms of unbroken Supersymmetry and the soft breaking terms, but with couplings constants that are anti-proportional to the Planck scale and therefore negligible [56]. Assuming unification of the gauge coupling constants g_1, g_2, g_3 of the gauge groups at the GUT scale $M_{GUT} \sim 2 \times 10^{16}\ GeV$, the following set of assumptions emerges that lead to simple model parameters at the GUT scale:

- The gaugino masses unify to a common gaugino mass $m_{1/2} \equiv M_3 = M_2 = M_1$
- The sfermion and Higgs masses that contribute to the soft SUSY-breaking scalar mass term unify to a common scalar mass $m_0\mathbf{1} = m_{\tilde{Q}}^2 = m_{\tilde{U}}^2 = m_{\tilde{D}}^2 = m_{\tilde{L}}^2 = m_{\tilde{E}}^2$, with $\mathbf{1}$ for the unity matrix in the family space and $m_0^2 \equiv m_{H_u}^2 = m_{H_d}^2$
- All trilinear couplings unify to a common trilinear coupling A_0:
  $\mathbf{a_U} = A_0 y_U, \mathbf{a_D} = A_0 y_D, \mathbf{a_E} = A_0 y_E$

- The sign of the Higgs mass parameter sign(μ) and the ratio of the vacuum expectation values of the Higgs fields $\tan\beta$.

All soft SUSY breaking parameters in the MSSM Lagrangian L_{soft} (see equation 2.24) are determined by these 5 parameters. The terms that imply flavour-changing and CP-violating processes are removed in the mSUGRA model by the constraints discussed in Section 2.2.7.
Variations in the mSUGRA model parameters have important and predictable effects, e.g. larger values of m_0^2 will result in higher masses of squarks and sleptons compared to the neutralinos, charginos and gluino. Moreover the mass spectra of squarks and sleptons will be very close together.
Since the entire MSSM particle spectrum at the electroweak scale can be calculated from these parameters using renormalisation group equations (RGEs) (see e.g. Figure 2.2), mSUGRA models are highly predictive models and are thus used for many experimental searches e.g. at the Tevatron [31]. However, due its constraints, it also a very restrictive model.
As a result of the unification of the gauge couplings at the GUT scale M_{GUT}, a common assumption is that the gaugino masses also unify near this scale with a value called $m_{1/2}$:

$$\frac{M_1}{g_1^2} = \frac{M_2}{g_2^2} = \frac{M_3}{g_3^2} = \frac{m_{1/2}}{g_{GUT}^2}. \tag{2.37}$$

(2.38)

Since the gluino mass parameter M_3 is related to the bino and wino mass parameters M_1 and M_2, this leads to the relation $M_3 : M_2 : M_1 \approx 6 : 2 : 1$ at the electroweak scale for minimal supergravity models [56]. M_3 grows relatively fast with the RG evolution, because the QCD coupling is larger than the electroweak gauge couplings and is larger than M_1 and M_2. In many models the gluino mass is thus considerably the heaviest gaugino.

2.3. Phenomenology of p-p collisions

2.3.1. Partonic structure of hadrons

Protons (hadrons) are composite particles that consist of quarks and gluons, usually referred as partons. Their properties like the quantum numbers are primarily determined by the so-called valence quarks, however every hadron contains also an indefinite number of virtual quarks and anti-quarks. Therefore collision of two incoming hadrons must be considered as interactions between the parton pairs, that are essentially independent of each other.
The longitudinal component (direction along the beam pipe) of the initial momentum that a parton carries is unknown in the parton-parton interactions, however the transverse momentum is zero. Since the total transverse momentum is conserved, the resulting products of every parton-parton interaction can be described by the transverse momentum and the transverse energy.
Depending on the momentum transfered, the parton-parton interactions are called “hard-scattering”, if the transfered momentum is large and “soft collisions”, if the transfered momentum is small.

The last one makes the majority of all p-p interactions, however the most interesting physics is characterised by high momentum transfer. Since the colliding partons take only a fraction x_1 and x_2 of the total momentum of the initial hadrons, the effective centre-of-mass energy $\sqrt{\hat{s}}$ of hard scattering process is reduced compared to the initial centre-of-mass energy $\sqrt{s}$ provided by the collider.

2.3.2. Cross section and parton distribution function

In order to specify interactions of elementary particles quantitatively, a cross section can be calculated. It can be seen as the probability that an interaction will occur between two initial state particles resulting in a given final state.
The production cross section can be calculated in the framework of the parton model. The cross section $\sigma_{a+b\to c}$ of the parton subprocess $a+b\to c$ can be obtained with the invariant matrix element M which is derived from the interaction Lagrangian of the theory and relates the initial and the final states of the interaction:

$$d\sigma_{a+b\to c} = \frac{1}{2\hat{s}}\frac{1}{(2\pi)^2}\int \frac{d^3p_c}{2E_c}\delta^4(p_a+p_b-p_c)\cdot F_{\text{color}}\cdot F_{\text{spin}}\sum_{\text{colour, spin}}|M|^2. \tag{2.39}$$

The sum runs over all possible initial and final spin and colour states. F_{colour} and F_{spin} are the factors, which result from averaging over the initial colour and spin states and $\hat{s}$ is the centre-of-mass energy of this process.
Assuming a and b are the constituents of the protons A and B, the hadronic process:

$$A+B\to c+X \tag{2.40}$$

where c is for example a vector boson and X are the hadronic remnants of the interaction, can be related to the parton subprocess:

$$a+b\to c \tag{2.41}$$

The cross section of the parton subprocess $\sigma_{a+b\to c}$ can be translated into the hadronic cross section $\sigma_{A+B\to c+X}$ according to:

$$d\sigma_{A+B\to c+X} = \sum_{a,\,b}\int_0^1 dx_a \int_0^1 dx_b f_A^a(x_a,Q^2)\cdot f_B^b(x_b,Q^2)\; d\sigma_{a+b\to c} \tag{2.42}$$

where the sum extends over all possible initial partons a and b that can produce the final state c. The sum of all parton momenta of a and b results in the total momentum of the hadron. The variables $f_A^a(x_a,Q^2)$ and $f_B^b(x_b,Q^2)$ are the so called "parton distribution functions (PDF)". It includes a logarithmic dependence on Q^2, the scale of the hard scattering subprocess.

Parton distribution function (PDF)

The parton distribution function[8] (PDF) $f_A^a\left(x_a, Q^2\right)$ is used to describe the substructure of the hadrons. It gives the probability to find a parton "a" within the hadron "A" carrying a particular fraction x of the total hadron momentum evaluated at the scale Q^2 of the hard scattering process.

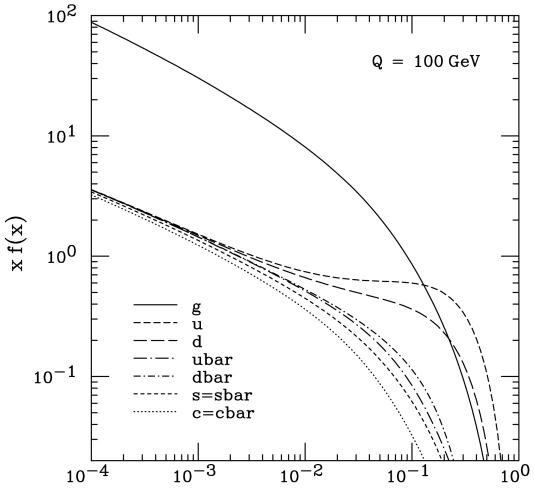

Figure 2.5: Product of the parton momentum fraction x and the quark or gluon parton distribution functions f(x, Q) for the scale Q = 100 GeV determined by the CTEQ group [91]. The distributions are generated from PDF version CTEQ6M.

PDFs cannot be calculated and have to be determined by global fits (see e.g Ref. [91]), for instance using the data from deep inelastic scattering experiments. Figure 2.5 shows the products of the parton momentum fraction x and the quark or gluon PDFs, as obtained by the CTEQ group [91] for the scale Q = 100 GeV.

This approach of separating the interaction in a short-distance hard-scattering part, which can be calculated by perturbation theory, and a long-distance part represented by the PDFs, is called factorisation and the scale Q^2 is referred to as factorisation scale.

Usually hard parton processes are calculated in leading order or, in some cases, in next-to-leading order perturbation theory. However, the leading order (LO) calculation are not sufficient and can have large uncertainties. A more precise result is achieved by including next-to-leading order (NLO) contributions in form of radiation of real particles or virtual corrections. Beside the inclusive cross sections also final states and kinematics are influenced by these higher order corrections.

[8] Usually the momentum-weighted combination $x_a \cdot f_A^a\left(x_a, Q^2\right)$ is used.

Additional processes in p-p collisions

The following processes can be relevant and contribute to the final state topology of an event produced at a hadron collider:

- **Initial and Final State Radiation**:
  Since the quarks carry colour charge, they radiate gluons, which themselves create new $q\bar{q}$ pairs resulting in a cascade of partons. Such parton showers can originate from the initial state partons, referred as initial state radiation (ISR). In addition every coloured and/or charged objects in the final state can emit additional particles, known as final state radiation (FSR). ISR and FSR can significantly affect the cross section of the involved process and increase the number of objects in the final state that can lead to large corrections to the overall topology of events, e.g. starting from a basic $2 \rightarrow 2$ process, this kind of corrections will generate $2 \rightarrow 3$, $2 \rightarrow 4$, and so on.

- **Hadronisation**:
  The final state particles of the discussed processes are leptons, quarks, gluons and electroweak bosons. However quarks or gluons are coloured partons and not experimentally observable. They are grouped together into colour-singlet hadrons, in a process called "hadronisation". This complex processes cannot be treated with a perturbation theory, but several phenomenological models exist such as the Lund string or the cluster fragmentation models (see Ref. [92]).

- **Beam remnants**:
  The partons involved in the hard scattering interactions carry only a fraction of the momentum of the colliding hadrons. The remaining momentum is carried by the so-called "remnants", which are not colour neutral, can hadronise and lead to additional particles. This can effect the final event topology.

Figure 2.6 illustrates some of these discussed processes. The time evolution of this event goes from bottom to top. In addition minimum bias events and underlying events can occur in a bunch crossing:

Minimum bias events The cross section of inelastic interactions at the LHC energy is several orders of magnitude larger than the cross section of the hard interactions. Therefore, the vast majority of the parton interactions are not hard scattering. Usually the low p_T events, that are dominated by soft interactions are commonly called "minimum bias events" (MB). Multiple events of this type can occur per bunch crossing, its number varies with the luminosity.

Underlying event In hadron-hadron collisions is a relatively high probability that beside hard interactions also other parton pairs from the same collision can undergo an interaction, and hence contribute to the overall event activity especially at low p_T. These additional interactions are referred as underlying event. The underlying event has been studied and compared to MC simulation

in detail at the Tevatron [93]. A study on predictions for minimum bias and the underlying event at the LHC can be found in Ref. [94].

The non-perturbative effects mentioned above, the hadronisation as well as the description of the parton shower and the underlying event, can currently only be described by phenomenological models that have to be tuned on data from previous collider experiments and are extrapolated to LHC energies. This can lead to large uncertainties since different models can predict different cross sections [95], hence these models have to be tuned on LHC data in future.

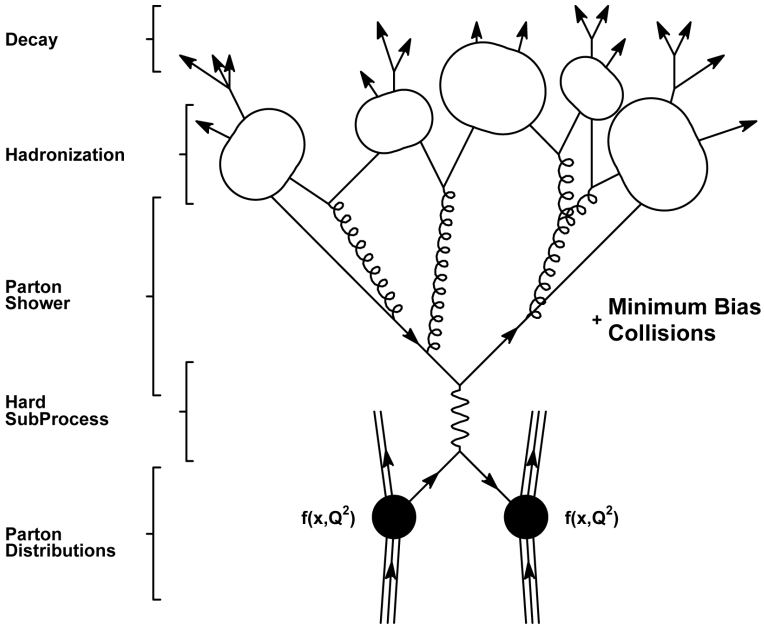

Figure 2.6: Phenomenological model of a hard proton-proton interaction. The time progresses from the bottom to the top of the graphic. Initial state radiation is not shown for simplicity. The figure is taken from Ref. [92].

The cross section of the SUSY particles

Searches for Supersymmetry rely heavily on Monte Carlo simulations of the cross sections and event topologies. Several Monte Carlo generators exist to generate hadron-hadron collisions including SUSY processes as described in Section 4.2.1. However most generators compute the production cross sections for pairs of supersymmetric particles only for LO hard parton processes (Born level calculations) [96]. There are many arguments to take NLO SUSY-QCD corrections into account. First of all LO cross sections have a strong dependence on the a priori unknown renormalisation and factorisation scale. Therefore the theoretical predictions have in general an

uncertainty that is almost as large as the cross section itself. The implementation of NLO corrections can substantially reduce this scale dependence. Higher order corrections for SUSY signals usually increase the production cross sections and thereby improve the experimental exclusion limits. For example in the mass ranges considered, the SUSY QCD corrections can reach a level of 30-50% [97], if gg initial state dominates. If, in contrast, the $q\bar{q}$ initial state dominates, the corrections are smaller. This has an influence on the lower mass bounds for squarks and gluinos[9].

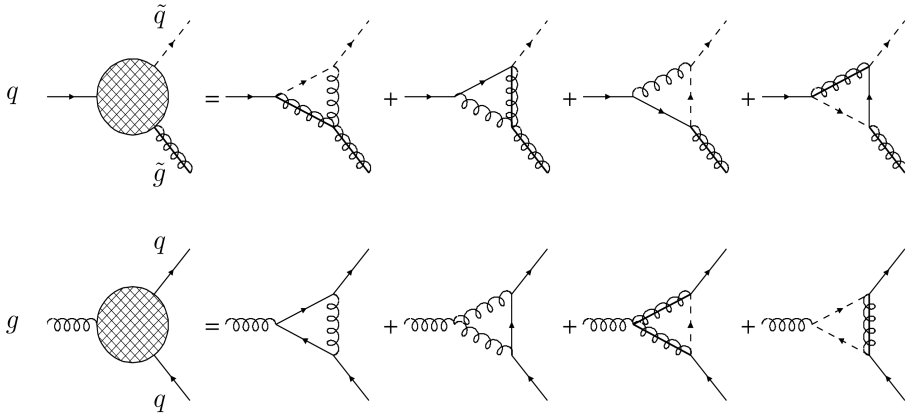

Figure 2.7: Feynman diagrams for the virtual NLO SUSY-QCD corrections to the quark-squark-gluino vertex (Yukawa coupling) and the quark-quark-gluon vertex (gauge coupling). Taken from Ref. [98].

This occurrence of large corrections indicates also that the computation of higher order terms of the perturbative expansion is necessary in order to achieve precise theoretical predictions and make a precision comparison of data and theory possible. In case of the discovery of Supersymmetry, a good knowledge of the total cross sections is required to determine the masses of the particles, especially if an exact mass determination of the squark and gluino masses is limited by the measurement of the invisible LSP's.
At the partonic level many different subprocesses contribute at LO and NLO, corresponding to the flavours/chiralities of the squarks and the initial-state partons, e.g. NLO SUSY-QCD corrections comprise virtual corrections (consisting of self-energy corrections, vertex corrections, and box diagrams; see also Figure 2.7 as an example), real-gluon radiation (with an additional gluon attached to the LO diagrams) in the initial and final state, Coulomb corrections due to the exchange of gluons and the radiation of a massless quark.
Several calculations that include contributions through next-to-leading order in QCD have been performed in the last years e.g. for the production of squarks and gluinos, top squark pairs, slepton pairs, gaugino pairs and the associated production of gauginos and gluinos. An example for

[9] An enhancement of the cross section would lead to a higher mass bounds for squarks and gluinos by +10 GeV to +30 GeV [98].

the virtual NLO SUSY QCD corrections to quark-squark-gluino vertex and the quark-quark-gluon vertex is given in Figure 2.7. Computer programs like for example PROSPINO [99–101] (see Section 4.2.1) can calculate next-to-leading order cross sections for the different production processes of supersymmetric particles at hadron colliders. Figure 2.8 shows the LO and NLO cross sections for the different production processes for a centre-of-mass energy of $\sqrt{s} = 14$ TeV and $\sqrt{s} = 7$ TeV. For the studied SUSY benchmark signals (see Section 4.5.2) in most studies NLO cross sections are used. For some SUSY signals in the different SUSY signals grids (see Section 4.5.2) the LO and NLO cross section are compared (see Section B). The results indicate that LO and NLO cross sections are in agreement for most studied SUSY signals and the differences are smaller than the systematic uncertainties considered in all studies.

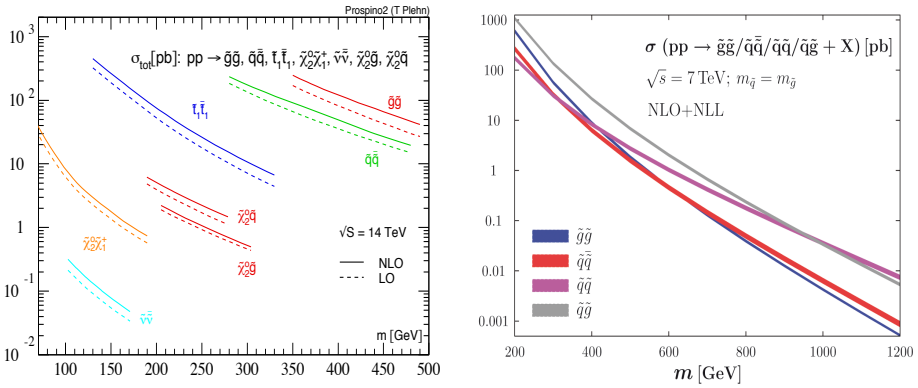

Figure 2.8: Leading-order (LO) and next-to-leading-order (NLO) SUSY-QCD predictions for different SUSY pair production processes at the LHC for a centre-of-mass energy of $\sqrt{s} = 14$ TeV (left plot) and for $\sqrt{s} = 7$ TeV (right plot). The figures are taken from Ref. [101] (left plot) and Ref. [102] (right plot).

2.3.3. Beam backgrounds

Further processes that can contribute to the final event topology are e.g. pile-up or beam-halo events. They are referred as "beam background" events.

Pile-up Due to the large protons density in the LHC beams it is possible that more than one proton per beam will undergo an inelastic interaction. If detector readout system is not fast enough, the events are overlaid with the ones from the previous beam particle interaction. This superposition of several inelastic proton-proton collisions is called piling-up. The ATLAS detector has latencies that exceed the small LHC bunch spacing of 25 ns[10]. Therefore when an "interesting physics" event is triggered, additional detector signals can arise from previous bunch-crossings.

[10] The expected number of minimum bias events per bunch crossing at $L = 10^{34} cm^{-2} s^{-1}$ is 23, for $L = 2 \cdot 10^{33} cm^{-2} s^{-1}$ it is about 4.6.

These hits represent a serious background to physics events. It has a strong impact on the technical design of all LHC detectors and also influences physics analyses [103,104]. The effect of pile-up events is often included during the event generation by overlaying the hard scattering events with minimum bias events.

Beam halo and beam gas Protons from the LHC can produce beam-induced backgrounds in the experimental areas, resulting from proton losses, including gas impurities in the beam pipe and collimator effects. The interactions of beam particles with the gas molecules in the imperfect vacuum are called beam gas collisions. A beam halo is an unavoidable characteristic of high-intensity beams that can arise from a number of possible interactions in the accelerator and contributes to the backgrounds of physics signals. Under certain conditions a small fraction of particles can acquire enough transverse energy within the beam and lead to uncontrolled beam loss. For a well-controlled stable beam such a loss is typically associated with the low-density halo surrounding beam core. In order to minimise uncontrolled beam loss or to improve the performance of an accelerator, it is very important to understand what are the sources of halo formation. ATLAS studies concentrate on the suppression of this beam-induced backgrounds to physics analyses [105].

2.3.4. Luminosity L

The design of the LHC is driven by physics aims, namely the discovery of rare processes. Two critical parameters can maximise the number of events of a certain physical process: the collision energy and the luminosity L.
The expected rate of physics processes with a given cross section σ observed in the time t is given by:

$$R = \frac{dN}{dt} = \sigma \cdot L \tag{2.43}$$

where L is the instantaneous luminosity and σ is the cross section of the physics process under study at the centre-of-mass energy $\sqrt{s}$, that increases with the beam energy. The instantaneous luminosity is primarily a function of the beam shape and currents. It is defined by the beam parameters such as the number of particles per bunch N_p, the number of bunches per beam n_B and the revolution frequency f_{rev} as:

$$L = \frac{n_{B1} N_{p1} \cdot n_{B2} N_{p2} f_{rev}}{A_{eff}} \tag{2.44}$$

where n_{B1}, n_{B2} are the number of bunches per beam 1 and beam 2, respectively. N_{p1}, N_{p2} are the number of particles contained in every bunch of the beam 1 and 2 (e.g. 1.5×10^{11} protons), which are f_{rev} in the effective collision area A_{eff}. Assuming a perfectly Gaussian beam profile transverse to the beam direction, the luminosity is given by:

$$L = \frac{n_{B1} N_{p1} \cdot n_{B2} N_{p2} f_{rev}}{4\pi\sigma_x\sigma_y} \tag{2.45}$$

The high peak luminosity of $10^{34} cm^{-2} s^{-1}$ at the LHC (see next section) can be achieved by a large number of bunches $n_B = 2808$, a small bunch spacing $1/f_{rev}$= 25 ns and a high number of protons per bunch $N_p = 1.15 \cdot 10^{11}$ as well as the good beam focus. The number of measured events N with a cross section σ is given by:

$$N = \sigma \cdot \int L dt = \sigma \cdot \mathscr{L} \tag{2.46}$$

The quantity

$$\mathscr{L} = \int L dt \tag{2.47}$$

is called the integrated luminosity and has the dimension of cm^{-2}, or more commonly *barn* b where 1 barn = 10^{28} m^2 (1fb = 10^{-39} cm^2). Running with the design luminosity, the LHC will provide an integrated luminosity of about 100 fb^{-1} per year.

Luminosity block (LB)

A luminosity block is the shortest time interval for which the integrated luminosity, corrected for dead-time and pre-scale effects, can be determined and can be seen as an interval of "constant" data taking conditions. The length of the luminosity block represents stable conditions in the data-taking and depends on the machine luminosity. On the one hand each luminosity block should contain enough data such that the uncertainty of the luminosity determination is limited by systematic effects, not by the available statistics in the interval. On the other hand a luminosity block should be as small as possible to avoid to much data loss in case of detector failures, so that data can be rejected from the boundary of the last luminosity block known to be unaffected. For ATLAS this interval is in the order of minutes (for $L = 10^{31}$cm^{-2}s^{-1} it is about 60 s). The LB provides the smallest granularity at which various data will be monitored and available for physics analysis.

3. The ATLAS Experiment at the Large Hadron Collider

The ATLAS experiment is designed to measure the decay products of proton-proton collisions provided by the Large Hardon Collider (LHC). Since March 2010 till the beginning of September 2010 the collider has already provided data corresponding to an integrated luminosity of more than 3 pb^{-1}. Until the end of the year 2011, an integrated luminosity of about 1 fb^{-1} is expected to be recorded.
This Chapter provides a brief description of the LHC and the relevant ATLAS detector components for the discussed analyses. First in Section 3.1 and 3.2 the accelerator chain and the LHC experiments are introduced, followed by a presentation of the ATLAS detector components in Section 3.3. The ATLAS trigger system is discussed in Section 3.4.

3.1. The Large Hadron Collider

The **L**arge **H**adron **C**ollider(LHC) [107, 108] is the world's most powerful collider designed to provide proton-proton (p-p) collisions up to a centre-of-mass energy of $\sqrt{s} = 14$ TeV. In addition to protons, the LHC will also accelerate and collide lead ions ($^{208}Pb^{82+}$) up to beam energy of 2.76 TeV per nucleon[1].
The collider is installed in the former Large Electron-Positron Collider (LEP[2]) [30] ring tunnel of 26.7 km circumference, roughly 90 m under the Earth's surface, at the site of the European Organisation for Nuclear Research (CERN[3]), at the French/Swiss border near Geneva. A schematic view of CERN accelerator complex and the LHC ring is shown in Figure 3.1. A comprehensive description of the technical design of the LHC machine can be found in Ref. [108], as well as in the Design Reports [109–111]. A brief overview is given in the following.
The LHC is a double-ring collider with superconducting magnets, comprising eight sections and

[1] This number corresponds to nominal magnetic field configurations in the dipole magnets. First collisions of lead ions are scheduled for November 2010.
[2] The **L**arge **E**lectron **P**ositron collider was decommissioned in 2000 after running for 11 years.
[3] The **C**onseil **E**uropéen pour la **R**echerche **N**ucléaire

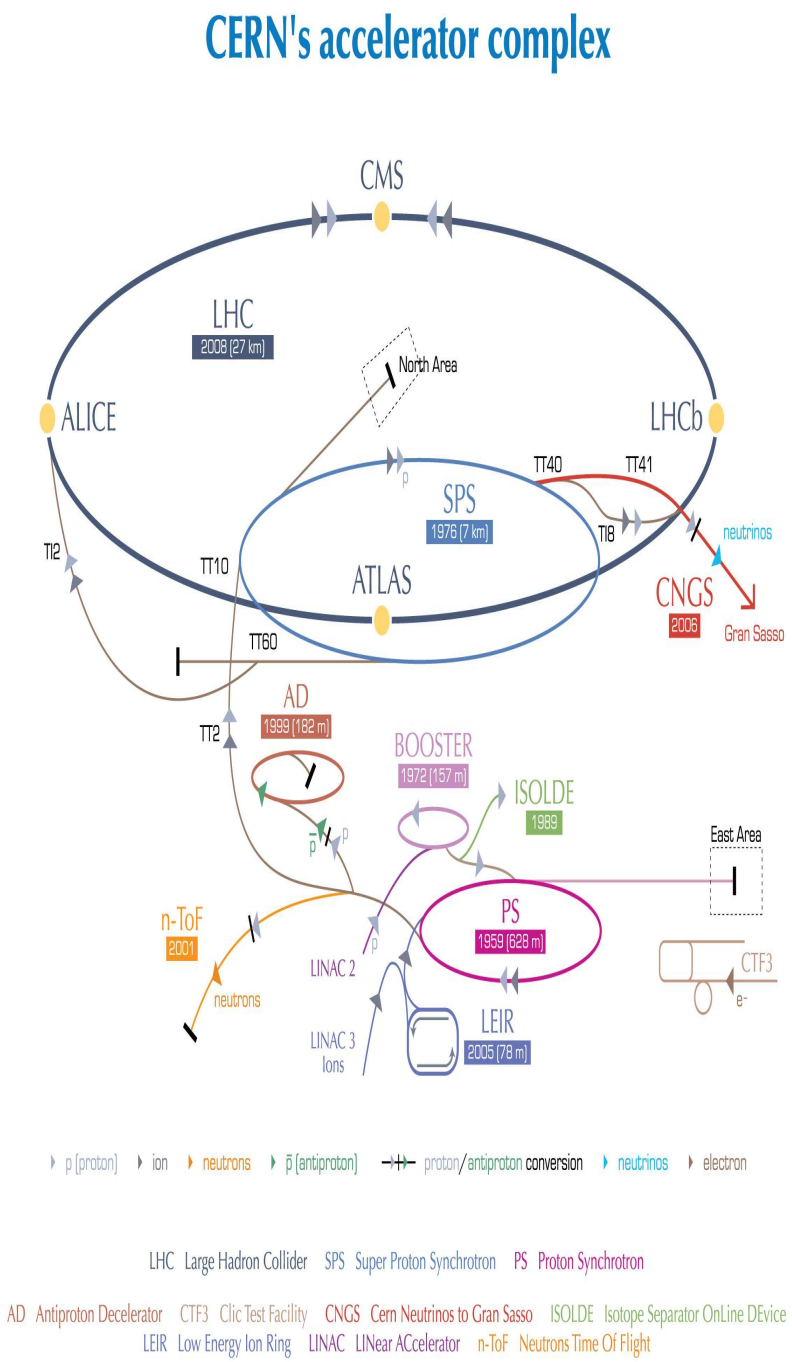

Figure 3.1: Schematic view of the accelerator complex at CERN with the four LHC experiments. The Figure is taken from Ref. [106].

four interaction points (see Figure 3.1). Predominantly, both rings are accommodated in the same magnet line.
More than 1230 dipole magnets are installed along the LHC ring to keep the protons on the circular track. They provide a magnet field strength up to 8.33 T at a temperature of 1.9 K. The special design of the magnets (see Figure 3.2) allows the simultaneous acceleration of protons in both directions.

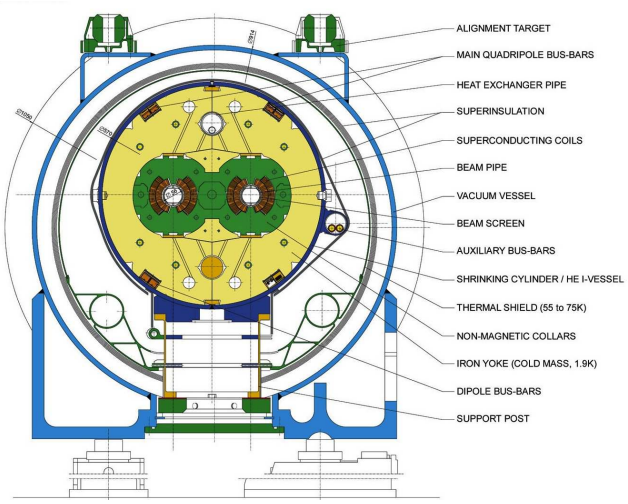

Figure 3.2: Cross section diagram of a LHC dipole magnet. The two apertures for the beams can be seen, as well as the various support structures and services. The Figure is taken from Ref. [108].

The CERN's accelerator complex is a succession of particle accelerators (see Figure 3.1), each accelerator boosts the energy of a beam of particles, before injecting it into the next one in the sequence. Initial protons are obtained by removing electrons from hydrogen atoms. They are supplied by a linear accelerator (LINAC2) with E = 50 MeV. Starting from the injector chain LINAC2, the preparatory work for LHC is divided into the following three parts, dealing with the PSB, the PS complex and the SPS, respectively [108].The **P**roton **S**ynchrotron **B**ooster (PSB) accelerates the particles to E = 1.4 GeV, before they are injected into the **P**roton **S**ynchrotron (PS), where they are bunched to the LHC time spacing of 25 ns and accelerated to E = 26 GeV. After that, the protons are given their LHC injection energy, E = 450 GeV, by the **Su**per **P**roton **S**ynchrotron (SPS) and extracted to the Large Hadron Collider ring clockwise and counter-clockwise via TI2 or TI8. After that the particles are accelerated to their final energy, which was in the year 2010 3.5 TeV. Protons circulate in the LHC several minutes (for $\sqrt{s}$ = 14 TeV for about 20 minutes) before reaching the maximum speed and energy [108].
Lead ions (heavy ion beams) for the LHC start from a source of vapourised lead and enter LINAC3 before being collected and accelerated in the Low Energy Ion Ring (LEIR). They then follow the same route to maximum acceleration as the protons.
To produce rare processes at an acceptable rate, the LHC is designed to collide particles at an ex-

tremely high rate, up to a designed luminosity of $L = 10^{34}$ cm^{-2} s^{-1} for protons ($L = 10^{27}$ cm^{-2} s^{-1} for lead ions), resulting in approximately a billion collisions per second[4]. To achieve this design luminosity, 2808 bunches with $\sim 10^{11}$ protons per bunch need to be accelerated in each direction leading to bunch crossings every 25 ns ($\simeq$ bunch length 7.5 cm) and a proton bunch-crossing rate of 40 MHz[5] at the interaction points. The main design parameters of the LHC accelerator are summarised in Table 3.1.

beam parameters	
main collision type	proton-proton
centre-of-mass energy	14 TeV
bunch-crossing rate	40.08 MHz
number of bunches (n_B)	2808
number of protons per bunch (N_p)	$1.15 \cdot 10^{11}$
beam current	0.58 A
stored energy per beam	362 MJ
luminosity related parameters	
RMS bunch length	7.55 cm
RMS beam size	16.7 μm
geometric luminosity reduction factor	0.836
nominal peak luminosity L	10^{34} cm^{-2}s^{-1}
p-p collisions per bunch-crossing (at nominal peak luminosity)	$\mathcal{O}(20)$

Table 3.1: Summary of the key LHC design parameters; the luminosity related parameters are specific for the ATLAS interaction points.

3.1.1. First collisions at the LHC

The LHC accelerator was completely built and commissioned in September 2008 and became first operational on 10^{th} September 2008. Although no p-p collisions took place in 2008, all the major LHC experiments, described in the next Section 3.2, observed events resulting from protons colliding with deliberately placed beam stops and the low-density gas remaining in the beam pipe. Unfortunately nine days later an accelerator incident happend, caused by a faulty

[4] On average about 23 inelastic proton-proton collisions will take place at each bunch crossing. Thus, each interesting physics event will be overlaid by so-called pile-up events (see Section 2.3.3).

[5] Due to the accelerator mechanism protons are grouped in several bunches inside the accelerator tunnels. This has the result that p-p collisions occur at discrete time intervals, rather than in a continuous manner.

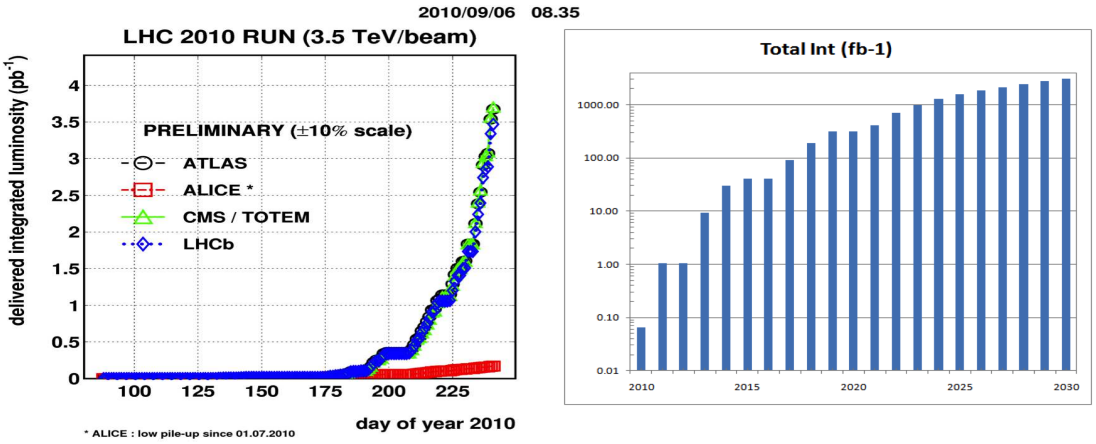

Figure 3.3: The achieved luminosity measured till September 2010 (left plot) and expected (right plot) luminosity for the LHC experiments. The results have been presented on the ICHEP conference in July 2010 (see Ref. [112]) and in LHC status report meeting (see Ref. [113]).

electrical connection between two of the accelerator's magnets. This resulted in a mechanical damage of several superconducting magnets (see Ref. [114]). Following major repairs to sections of the accelerator, particle beams have been once again circulated on 20^{th} of November 2009 with first collisions at $\sqrt{s}$ = 900 GeV three days after. At the end of December 2009 collisions at 2.36 TeV have been recorded before the LHC has been stopped to prepare for higher energy collisions. On March 30^{th} 2010 for the first time beams collided at 7 TeV. For the next 18 to 24 months the LHC will probably operate at a centre-of-mass energy of $\sqrt{s}$ = 7 TeV for safe commissioning of the accelerator to deliver a wealth of data to the experiments. The resulting interactions will allow physicists to study new fields of physics. Subsequently, the centre-of-mass energy will be increased up to the design value of 14 TeV. At the beginning the LHC will also operate at relatively low instantaneous luminosities of $L = 10^{30} - 10^{32}$ cm^{-2}s^{-1}. After this initial phase, the luminosity will first be increased to $L = 10^{33}$ cm^{-2}s^{-1} before the LHC will finally reach its designed luminosity of 10^{34} cm^{-2}s^{-1}, which corresponds to an integrated luminosity of about 100 fb^{-1} per year. Figure 3.3 shows the achieved luminosity till the beginning of September 2010 (left plot) and the expected luminosity (right plot) as a function of the time for the next years. In this thesis the first $\sqrt{s}$ = 7 TeV ATLAS results for an integrated luminosity of $\mathscr{L} = 70$ nb^{-1} collected till July 2010 are presented (see Chapter 11) and an outlook for about 3 pb^{-1} of measured data is given (see Chapter 13.2).

3.2. Collider experiments at the LHC

At the LHC it is expected to discover many new phenomena, both within and beyond the Standard Model of particle physics. All LHC experiments are designed to probe the energy and luminosity frontiers showing maximum sensitivity to many potential signatures, which may characterise this new physics. Four different experiments are installed at the four interaction points covering a broad range of experimental studies:

- The two general-purpose detectors, ATLAS (**A** **T**oroidal **L**HC **A**pparatu**S**) [115] and CMS (**C**ompact **M**uon **S**olenoid) [116] will provide information on precision measurements of Standard Model processes and are intended for searches of new phenomena in p-p collisions. The ATLAS experiment and its goals are described in more detail in the next Section 3.3. Of the three other LHC experiments, CMS is the most similar to ATLAS in its physics aims and overall design, but the two experiments use different technologies and thus can be used to cross-check each other's results.

- LHCb (**L**arge **H**adron **C**ollider **b**eauty) [117] experiment is a single arm spectrometer, designed to measure CP violation and rare decays of B-mesons.

- ALICE (**A** **L**arge **I**on **C**ollider **E**xperiment) [118] is a general-purpose detector, which is optimised for heavy ions collisions to study strongly interacting particles and the quark-gluon plasma[6] at high densities and temperatures.

Furthermore, the LHC hosts two smaller experiments, which provide complementary physics measurements in the forward regions, using the same collisions as the general purpose experiments:

- LHCf [119] (measurement of forward neutral particle production for cosmic ray research) is an experiment dedicated to measure neutral particles emitted in the very forward region of the LHC collisions at extremely low angles. It consists of two small calorimeters each one placed about 140 m away from the ATLAS interaction point. Its results will help to improve simulations of cosmic ray interactions in the Earth atmosphere.

- TOTEM experiment [120] (**TOT**al cross section, **E**lastic scattering and diffraction dissociation **M**easurement at the LHC), positioned near the CMS detector, studies physics processes in the region very close to the particles beam [121] and measures the proton-proton interaction cross section, as well as elastic and diffractive scattering at the LHC for a better understanding of the proton structure.

[6] The quark-gluon plasma is a hadronic state where quarks and gluons are not in bound states like protons anymore, but move freely in the plasma. It is expected that the extreme energy density in the heavy ion collisions is sufficient to create this state of matter for a fraction of a second.

3.3. The ATLAS Experiment

3.3.1. Overview

ATLAS is a multi-purpose high energy physics experiment, designed to exploit the discovery potential of the LHC and to study a broad spectrum of physics processes, ranging from precise measurements of Standard Model parameters to the search for new physics phenomena like Supersymmetry. The high luminosity and increased cross sections at the LHC enable also high precision tests of QCD, electroweak interactions, and flavour physics as well as the search for the origin of electroweak symmetry breaking. It is the world's largest particle detector with a weight of approximately 7000 tonnes, installed 92.5 m underground in a huge cavern, situated in Switzerland at point 1 on the LHC ring (see Figure 3.1). The first technical proposal for the ATLAS experiment [122] was published in 1994, the detector construction started 1997 and was finalised in 2008, just before the very first LHC beam. The dimension of this large physics project is represented by the number of scientist, technicians and engineers: at the moment more than 3000 people from about 37 different countries work together in the ATLAS collaboration.
The design of the ATLAS detector was driven by the main physics goals and a set of general requirements for the LHC detectors. The unprecedented energy and extremely high collision rate of the LHC require ATLAS to be larger and more complex than any detector ever built. The detectors technologies and electronics as well as the sensor elements should be fast and radiation-hard. The detector should have a large acceptance in pseudorapidity and a almost full azimuthal angle coverage. A high detector granularity is needed to handle the particle fluxes and to reduce the influence

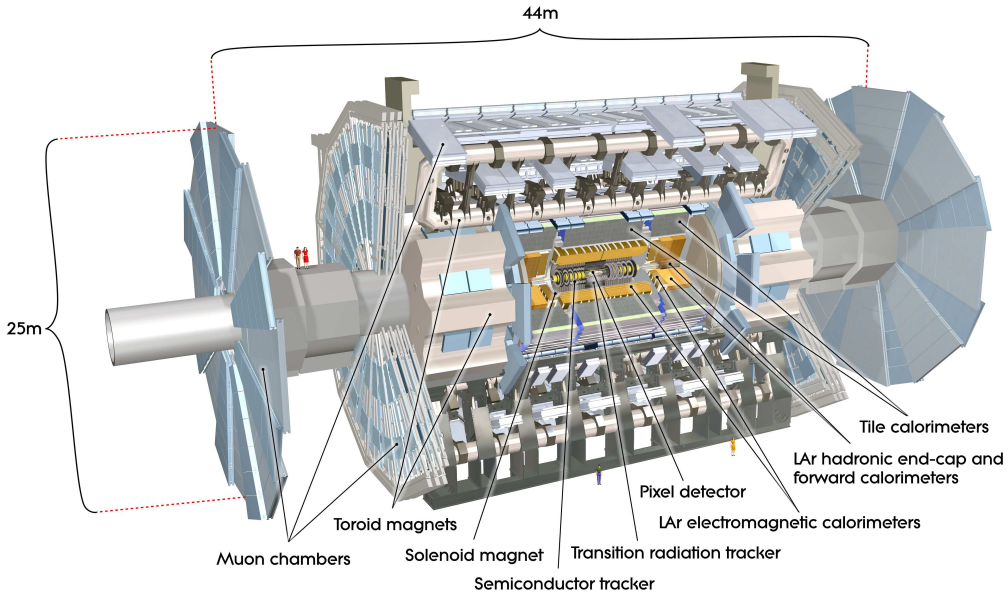

Figure 3.4: Cut-away view of the ATLAS detector. Figure is taken from Ref. [115].

of overlapping events. To achieve an acceptable trigger rate, for most physics processes of interest ATLAS uses a highly efficient trigger system, which provides strong reduction of the event rate while efficiently selecting interesting physics events. It will be introduced in Section 3.4.
Requirements for the ATLAS detector system have been defined using a set of physics processes (benchmark physics studies) to ensure that the detector concept is suited for a large range of physics scenarios and covers new phenomena which one can hope to observe at the TeV scale.

- Precision measurements: Already at low integrated luminosities precise measurements of the W- and Z-boson masses and production cross sections are possible and allow the calibration and performance measurement of all detector components. The expected top-quark production at the LHC is significantly larger than at the Tevatron [123] [124]. This allows very precise measurements of the top mass, its cross section and decay branching ratios and provides the opportunity to test its couplings and spin.

- Higgs physics: The LHC provides access to a mass range up to 1 TeV for searches for the Higgs boson in the Standard Model and beyond. The search for the Standard Model Higgs boson has been used as a benchmark to establish the performance of important sub-systems of ATLAS. Should the Higgs boson be discovered, it would need to be studied in several modes, regardless of its mass, in order to fully disentangle its properties and establish its credentials as belonging to the Standard Model or an extension thereof [115].

- Beyond the Standard Model: Many signatures of various new physics processes beyond the Standard Model will be searched for by ATLAS. Supersymmetry (SUSY), one of the favoured models, has not been observed yet experimentally. The discovery of supersymmetric particles could be already possible with an integrated luminosity of $O(100\ \text{pb}^{-1}$ for favourable combinations of model parameters [125, 126], because of the relatively large production cross sections of some SUSY particles (see also Chapter 2 and Ref. [56]). The decays of supersymmetric particles, such as squarks and gluinos, would result in a clear signature in the ATLAS detector, for example significant large missing transverse energy due to the lightest supersymmetric particle (LSP), in combination with Standard Model particles. Other new phenomena discoverable by ATLAS beside Supersymmetry are, for instance, new heavy gauge bosons W' and Z', quark compositeness, rare decays of heavy quarks and leptons as well as extra dimensions and mini black holes. If there are new physics processes or new particles produced by the LHC collisions, whatever form these processes or particles take, ATLAS has to be able to detect them and measure their properties.

However, QCD jet production cross sections dominate over the rare processes mentioned above and a high rate of inelastic events will accompany every candidate event. All these searches for existing Standard Model physics and new phenomena require therefore good particle-identification capabilities of the detector for the final state objects like electrons, muons, photons, jets (from τ leptons, b-quarks and light flavours) and missing transverse energy, good b-tagging performance as well as a precise tracking and momentum measurement and identification of experimental signatures like secondary vertices over a wide kinematical range of a few TeV.

In the following, the ATLAS detector is introduced and its main sub-detectors are briefly described. A comprehensive description can be found in Ref. [115] as well as in the Technical Design Reports (TDRs) for the overall technical design [127] and the expected performance [103].
The detector, that is almost as large as the cavern where it is placed, has a cylindrical design around the beam pipe: 25 m in diameter and 44 m in length and consists of several sub-detectors arranged radially around the interaction point. Its overall layout is shown in Figure 3.4. From the inside to the outside the main detector systems provide:

- Inner Detector: Tracking and precise momentum measurement of charged-particles; for offline tagging of τ-leptons and b-jets, observation of secondary vertices.
- Calorimeter System: Electron and photon identification and energy measurements, hadronic jet and missing transverse energy measurements.
- Muon Spectrometer: Muon identification, tracking as well as stand-alone momentum and charge measurement of muons.

The design performances of the different subsystems are listed in Table 3.2.

detector component	**required resolution coverage**	η **range**
inner detector	$\frac{\sigma_{p_t}}{p_T} = 0.05\% \cdot p_T \oplus 1\%$	≤ 2.5
electromagnetic calorimeter	$\frac{\sigma_E}{E} = \frac{10\%}{\sqrt{E}} \oplus 0.7\%$	≤ 3.2
hadronic calorimeter		
barrel/end-cap	$\frac{\sigma_E}{E} = \frac{50\%}{\sqrt{E}} \oplus 3\%$	≤ 3.2
forward region	$\frac{\sigma_E}{E} = \frac{100\%}{\sqrt{E}} \oplus 10\%$	$3.1 <\mid \eta \mid < 4.9$
muon spectrometer	$\frac{\sigma_{p_T}}{p_T} = 10\%$ at p_T = 1 TeV	≤ 2.7

Table 3.2: Design performance of the ATLAS detector subsystems [115].

3.3.2. The coordinate system

The following coordinate system described below will be used throughout this thesis.
The righthanded cartesian coordinates x, y, z of the ATLAS coordinate system are chosen such that the origin is the nominal interaction point within the ATLAS detector $(x, y, z) = (0, 0, 0)$. The LHC beam direction defines the z-axis (z > 0 towards south-east), the x-y plane is transverse to the beam direction. The x-axis points from the interaction point to the centre of the LHC tunnel, while the y-axis defined as pointing upwards, slightly tilted with respect to vertical from the general tilt of

the tunnel due to the curvature of the tunnel. Figure 3.5 shows a schematic view of the coordinate system used to describe the ATLAS detector.

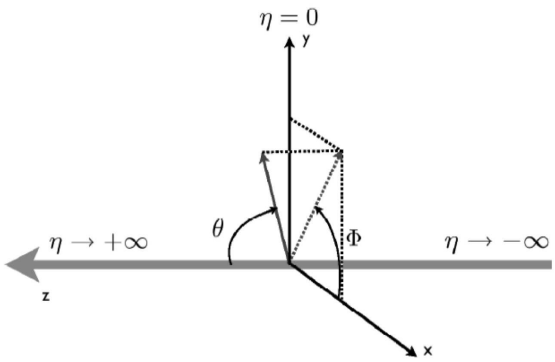

Figure 3.5: Schematic view of the ATLAS cartesian coordinate system.

Spherical coordinates are defined in the standard way. The radial distance r from the origin is:

$$r = \sqrt{x^2 + y^2 + z^2} \tag{3.1}$$

The azimuthal angle ϕ is the angle measured around the beam axis in the x-y plane with respect to the positive x-axis, the polar angle θ is defined with respect to the positive z-axis:

$$\begin{aligned} \theta &= arc\,tan\left(\frac{\sqrt{x^2+y^2}}{z}\right) \\ \phi &= arc\,tan\left(\frac{y}{x}\right) \end{aligned} \tag{3.2}$$

The distance ΔR in the pseudorapidity-azimuthal angle space, often used to describe the separation between particles in the plane, is defined as:

$$\Delta R = \sqrt{\Delta\eta^2 + \Delta\phi^2}$$

An important variable in high-energy physics at hadron colliders is the so-called pseudorapidity η and for massive objects the rapidity y:

$$y = \frac{1}{2} ln\left(\frac{E+p_z}{E-p_z}\right) \tag{3.3}$$

$$\eta = \frac{1}{2} ln\left(\frac{p+p_z}{p-p_z}\right) = -ln\left[tan\left(\frac{\theta}{2}\right)\right] \tag{3.4}$$

with $p = \mid \vec{p} \mid$ the magnitude of the momentum vector.
The pseudorapidity is 0 for particle tracks perpendicular to the beam pipe ($\theta = 90°$). For all measured particles the relativistic energy of a particle in the labour system is defined as

$$E = \sqrt{p^2 + m^2}$$

In proton-proton collisions, the momentum of the colliding partons is unknown[7], thus the centre-of-mass system of the interaction is not known. However, the momentum components in x- and y-direction (transverse to the beam axis) can be assumed to be zero. Therefore quantities defined in the transverse (x-y) plane to the beam axis are of particular importance. Transverse variables used throughout this work are for instance: the transverse momentum p_T, the transverse energy E_T and the missing transverse energy E_T^{miss}. They are defined as variables perpendicular to the LHC beam axis and can be obtained by the projection onto the x-y plane, for example

$$p_T = \sqrt{p_x^2 + p_y^2}$$

In experimental particle physics, missing energy refers to the energy E_T^{miss}, which is not detected in the detector, but is expected because of conservation of energy and conservation of momentum. It is commonly used to infer the presence of non-detectable particles such as neutrino although apparent missing energy may be caused by mis-measurement of the energy/momentum of detected particles. E_T^{miss}, that is expected to be a signature of many new physics events, is defined in the transverse plane by:

$$E_T^{miss} = \sqrt{\left(\Sigma E_x^{miss}\right)^2 + \left(\Sigma E_y^{miss}\right)^2} \tag{3.5}$$

3.3.3. The Magnet system

The magnetic field is essential to bend charged particle tracks to measure their momenta. Figure 3.6 shows the complex superconducting magnet system of the ATLAS detector. It consists of one central solenoid and three toroids (two end-caps and one barrel) and drove most of the design of the ATLAS detector due to its unusual configuration and large size of 22 m in diameter and 26 m length.

Central Solenoid (CS)

The **C**entral **S**olenoid surrounding the inner tracking detector cavity is designed to provide a 2 T axial magnetic field for the inner detector at a nominal operating current of approximately 7.7 kA

[7] The energy of each hadron is split and constantly exchanged between its constituents.

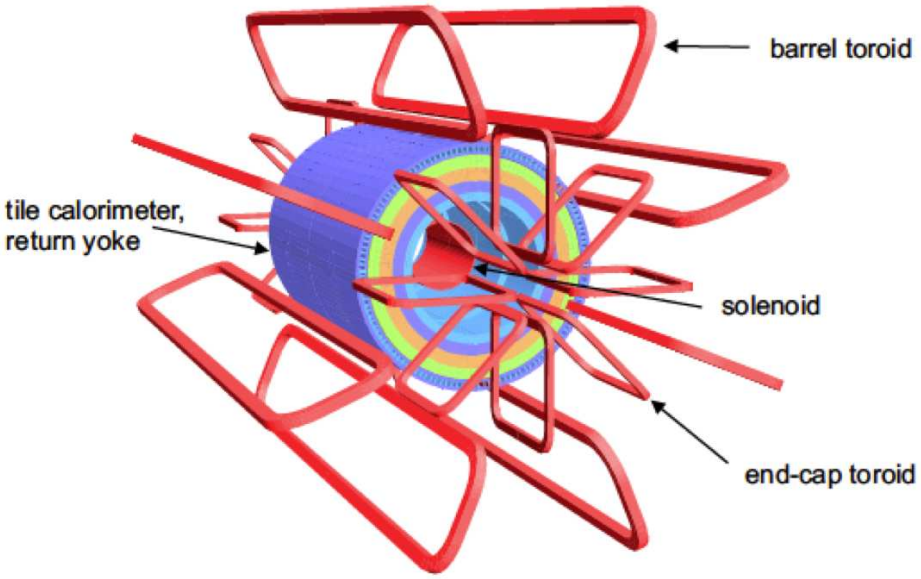

Figure 3.6: The general layout of the ATLAS magnet windings. The solenoid windings are situated inside the calorimeter volume. The tile calorimeter is modelled by four layers with different magnetic properties, plus an outside return yoke. The Figure is taken from Ref. [115].

[115, 128]. The solenoid coil, which is operated at a temperature of 4.5 K, is located in between the tracking detector and the electromagnetic calorimeter. It extends 5.8 m in axial length and 2.56 m in outer diameter and has a mass of about 5.4 tonnes. To achieve a good performance of the electromagnetic calorimeter (LAr calorimeter, see Section 3.3.5), the design of the CS has to minimise the amount of material in order to allow for a precise energy measurement of particles reaching the calorimeter. Therefore, the solenoid shares one vacuum vessel with the electromagnetic calorimeter exploiting its iron absorbers as return yoke.

Barrel Toroid (BT) and End Cap Toroids (ECTs)

The **B**arrel **T**oroid (see Figure 3.7) and the two **E**nd-**C**ap **T**oroids (ECT) generate the magnetic field for the muon detectors in the central and end-cap regions, respectively. The air-core superconducting magnets are situated outside the calorimeter and within the muon system and consist of eight superconducting coils powered by 20.5 kA power supply [115, 129, 130]. The overall size of the barrel toroid is 25.3 m in length, 9.4 m in inner and 20.1 m in outer diameter and has a total weight is 830 tonnes. Each of the barrel toroid coils is encased in an individual stainless-steel vacuum vessel. The two end-cap toroids are placed in the forward regions of the detector inside the barrel toroid and have an axial length 5.0 m, a outer diameter of 10.7 m and inner bores of 1.65 m. Every ECT has a weight of about 240 tonnes and were some of the heaviest objects to be lowered

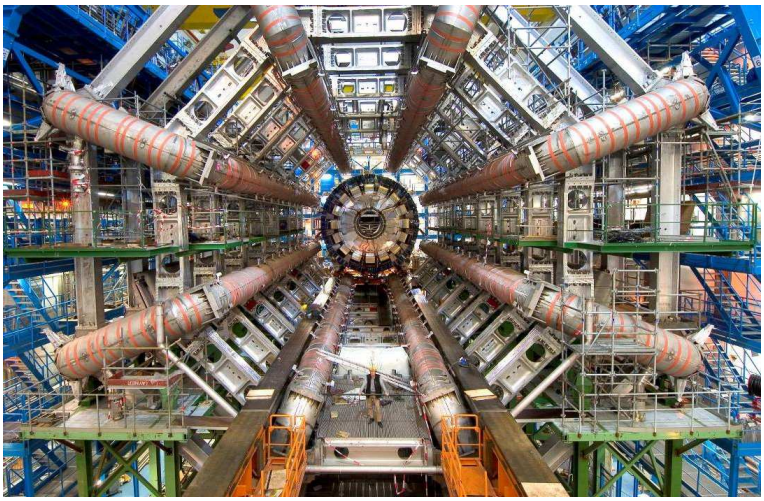

Figure 3.7: The barrel toroid as installed in the underground cavern. Figure is taken from Ref. [115]. The temporary scaffolding and green platforms were removed once the installation was complete. Also visible are the stainless-steel rails carrying the barrel calorimeter with its embedded solenoid, which await translation towards their final position in the centre of the detector.

in the cavern. The magnet coils of every end-cap toroids are housed in the same vacuum vessel (one per side) and assembled radially and symmetrically around the beam axis. The End-Cap coils systems are rotated with respect to the BT in order to provide radial overlap and to optimise the bending power in the interface regions of both coil systems. The field varies depending on the radius r and the azimuth angle ϕ:
Over the range $\mid \eta \mid$, magnetic bending is provided by the large barrel toroid and varies from 0.15T to 2.5T, with an average value of 0.5T. The end-cap toroids provide a field of approximately $0.2-3.5$T in the region $1.6 <\mid \eta \mid < 2.7$. In the transition region $1.4 <\mid \eta \mid < 1.6$ where the magnetic fields overlap, the field of one magnet cancels the bending power of the other one and so the total field strength is lower.

3.3.4. The Inner Detector

Due to the high energy of the proton-proton collisions a large number of particles are generated in one interaction and multiple interactions are expected in one collision of the proton bunches. At the LHC design luminosity of $10^{34} cm^{-2} s^{-1}$, about every 25ns approximately 1000 tracks will emerge from the collision creating a large track density in the detector. This demands the use of fast and highly granular detectors achieved through silicon technology and straw tube gaseous detectors that also tolerate large radiation doses. The **I**nner **D**etector (ID) [115,131,132]), illustrated in Figure 3.8, is the sub-detector closest to the beam pipe and p-p interaction point. It is immersed within a cylindrical envelop of 7m total length and with a radius of 1.15m, in a 2T solenoidal

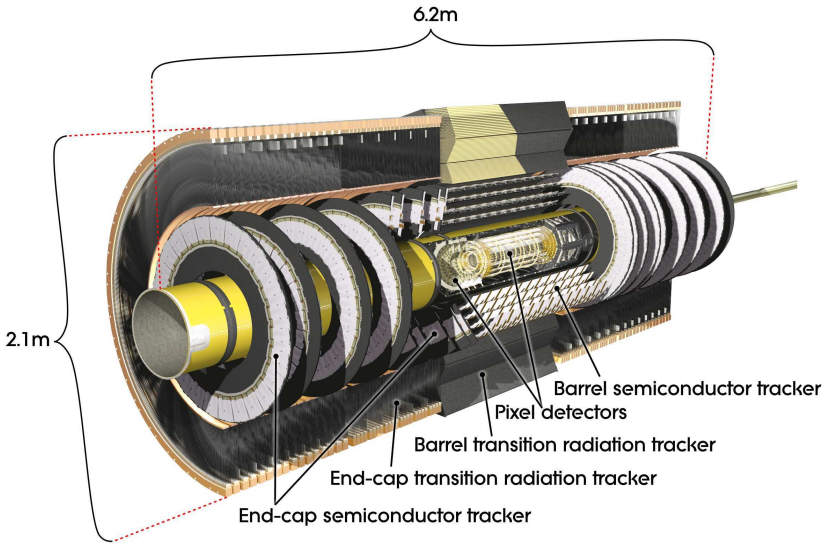

Figure 3.8: Cut-away view of the ATLAS inner detector. Figure is taken from Ref. [115].

magnetic field[8] positioned on the inner face of the electromagnetic calorimeter. The detector consists of a three independent, but complementary sub-detectors: the high-resolution semiconductor pixel detector (Pixel), a silicon microstrip semiconductor tracker (SCT) and a straw-tube tracking detector-transition radiation tracker (TRT); all three in order of decreasing granularity from the interaction point. It is also divided along the beam direction into a barrel region (see Figure 3.8) and two end cap sections in order to minimise material for traversing particles coming from the interaction region at its centre. The tracking detectors - Pixel and SCT in the barrel section are arranged on co-axial cylinders around the beam axis, while in the end-cap regions the detectors are on disks perpendicular to the beam axis.The high-radiation environment imposes conditions: The silicon sensors must operate at low temperatures (-5 to -10°C, coolant temperature around -25°C) to maintain an adequate noise performance, while the transition radiation tracker work at room temperatures. The ID layout reflects the performance requirements:
The inner detector is designed to provide high-precision momentum measurements of charged particles (between ≈ 0.5 GeV and ≈ 150 GeV) in the environment of numerous tracks within a pseudorapidity range $|\eta| < 2.5$, as well as an accurate primary and secondary vertex reconstruction by combining tracks to vertices. It is also used for electron identification over $|\eta| < 2.0$ and to find short-lived particles such as b-quarks and τ-leptons. A detailed description of the ATLAS ID can be found in Ref. [115], in the ATLAS Inner Detector Technical Design Reports [131,132] and ATLAS Pixel Detector Technical Design Report [133], as well as in the articles [134–136].

[8]The field is considerably weaker near the ends of the ID cavity due to the finite length of the solenoid.

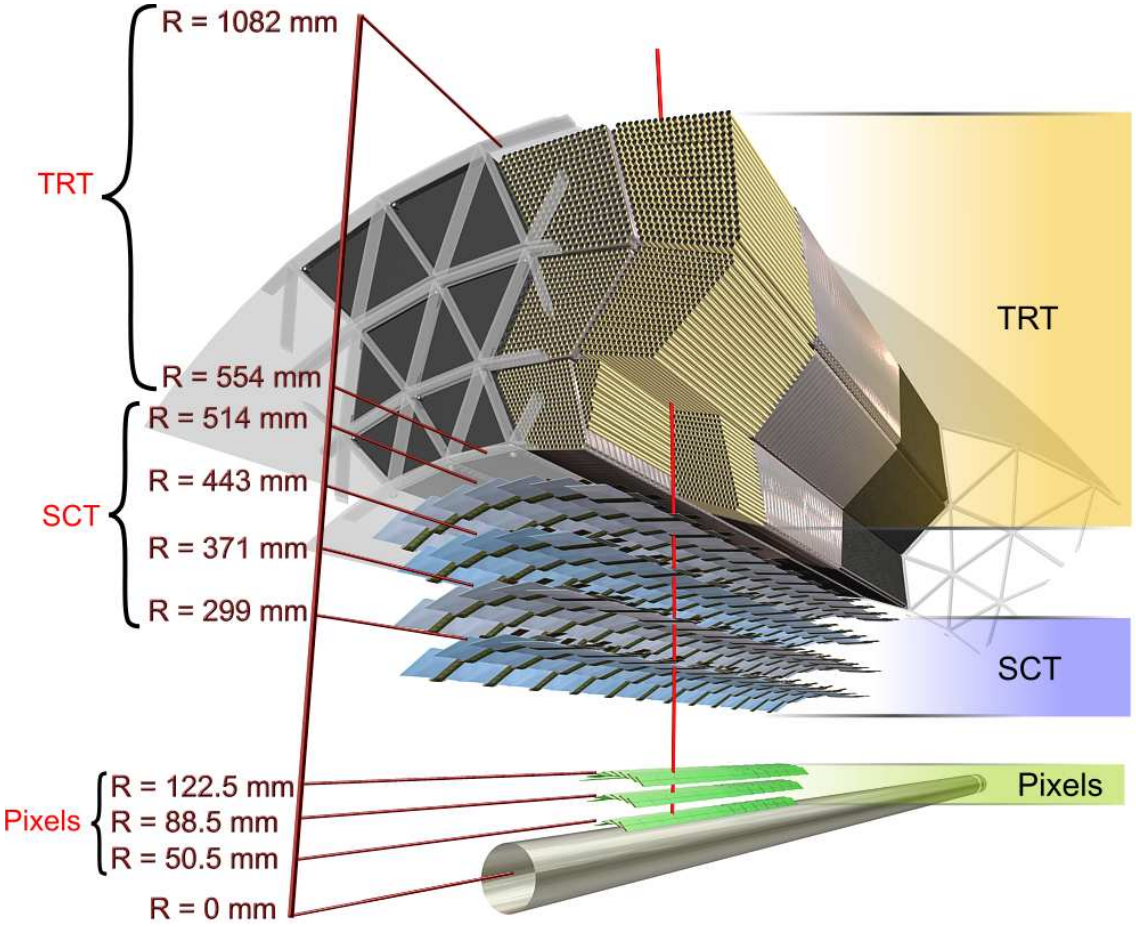

Figure 3.9: The sensors and structural elements traversed by a charged track of $p_T = 10$ GeV in the barrel inner detector ($\eta = 0.3$). Figure is taken from [115].

Pixel Detector

Closest to the beam pipe is the pixel detector (PIXEL), that provides the highest granularity and the highest precision measurements for charged particles using silicon sensors (pixels). The detector consists of pixel layers that are segmented in R-ϕ and z in pixel modules of the size of 62.4 mm×21.4 mm, where every model consists of about 46000 pixel most of the size of 50×400 μm^2 in R-ϕ×z direction[9] and are 250 μm^2 thick.
The pixel detector has in the barrel region three silicon barrel layers at average radii of $\sim$ 5 cm, $\sim$ 9 cm and $\sim$ 12 cm from the interaction point (1456 modules) with modules with their long side positioned parallel to the beam and in the end-cap region the three discs are arranged on each side with radii of 9 cm and 15 cm (288 modules) [137]. Here the modules are with the long side positioned radially in the disks. In total the pixel detector has approximately 80.4 million readout

[9] About 10% of the pixels have a size 50×600 μ^2.

channels. Typically three pixel layers provide three space points per particle track over the full acceptance (see Fig. 3.9).

Semiconductor Tracker (SCT)

The **S**emi **C**onductor **T**racker is a p-in-n silicon-microstrip detector [135] designed to provide eight precision measurements per track in the intermediate radial range. It is surrounding the pixel detector and has a similar geometry as the pixel detector, but silicon microstrips made of silicon pixel are used to cover the larger area. In the barrel region, four cylindrical double layers with silicon detectors are arranged between $299\,\text{mm} < R < 514\,\text{mm}$ such each track crosses eight SCT strip layers (four space points). In the end-cap regions the pixels are located on nine end-cap disks (on each side of the two endcaps) at $85\,\text{mm} < z < 272\,\text{mm}$. Every layer can read out the track position in two dimensions and provide precision space-point coordinates.
In the barrel region, the detectors have small-angle (40 mrad, $\pm$ 20 mrad around the geometrical centre of the sensor) stereo strips to measure both coordinates R-ϕ and z, with one set of strips in each layer parallel to the beam direction (measuring R-ϕ). In the end-cap region, the detectors are very similar in construction, but consist of a set of strips (tapered strips) running radially and a set of stereo strips at an angle of 40 mrad to give the required space-point resolution in R-ϕ and R. One silicon detector is about $6.36 \times 6.40\,\text{cm}^2$ with about 768 readout strips [131]. The SCT consists in total of 4088 modules. This high granularity entails a large number of readout channels- about 6.3 million channels in the SCT.
The strips provide a position resolution of $17\,\mu$m in the transverse direction (in R-ϕ) and of $580\,\mu$m in the longitudinal direction (z-direction), respectively. Tracks can be distinguished if they are separated by more than 200 μm [115, 135].

Transition Radiation Trackers (TRTs)

The outermost part of the inner detector, are the **T**ransition **R**adiation **T**rackers (TRTs), which consist of straw tubes (drift tubes) and cover the range up to $|\,\eta\,| < 2.0$. Straw tubes can operate at very high rates due to their small diameter and the isolation of the sense wires within individual gas volumes. Therefore the TRT contributes significantly to the momentum measurement: the lower precision per point is compensated by the larger number of tubes and the longer measured track length. Due to the high number of hits per track, the TRT provides continuous tracking to enhance the pattern recognition.
The TRT is divided into two regions: barrel region and the end-cap region. The barrel TRT has 73 layers and is divided into three rings with 32 modules each. Every module has between 329 and 793 straws, covering the radial range from 56 to 107 cm. The end-cap TRT consist of two set of wheels. The set closer to the interaction point has 12 wheels between $848 \leq \text{z} \leq 1705\,\text{mm}$, the outer set contains eight wheels between $1740 \leq \text{z} \leq 2710\,\text{mm}$. Each wheel has eight layers (in total 160 layers). The layers are interleaved with fibres in the barrel and foils in the end-caps, that provide transition radiation for the electron identification. In the barrel region, the straw tubes in the layers are parallel to the beam and have a length of 144 cm, while in the end-cap region, the

37 cm long straws are arranged radially in wheels.
Every straw cylindrical tube has a diameter of about 4 mm. The straw tube wall acts as a high-voltage cathode. In the centre of the straw is a 30 μm diameter gold-plated tungsten wire, supported at the straw end by an end-plug, which acts as anode. The wires of the barrel straw tubes are divided into two halfes near the centre (at approximately $\mid \eta \mid = 0$) and read out at both ends, to reduce the occupancy. Each long barrel straw is therefore inefficient near its centre over a length of 2 cm. The straws in the end-cap are readout at the outer radius. All straws are filled with a xenon-based gas mixture that enhanced the electron identification capability.
At the LHC design luminosity the straw counting rate will reach 20 MHz in the most critical regions. The total number of TRT readout channels is approximately 420 thousand. Each channel provides a drift time measurement, giving an intrinsic resolution of 130 μm in the R-ϕ plane, and two independent thresholds. These allow the detector to discriminate between tracking hits, which pass the lower threshold, and transition radiation hits, which pass the higher one. On average, 36 hits are provided by the TRT: charged tracks with $p_T > 0.5$ GeV and $\mid \eta \mid < 2.0$ will traverse at least 36 straws, except in the barrel-end-cap transition region ($0.8 < \mid \eta \mid < 1.0$), where this number decreases to a minimum of 22 crossed straws. For electrons with energies above 2 GeV seven to ten hits from transition radiation are expected.

Summary

The inner detector system provides tracking measurements (momentum and direction) of charged particles in a range up to $\mid \eta \mid < 2.5$ with full coverage in ϕ. The momentum of the charged particle tracks is measured through the curvature in a magnetic field (see Section 3.3.3). At inner radii, high-resolution pattern recognition capabilities are available using discrete space-points from silicon pixel layers and stereo pairs of silicon microstrip (SCT) layers. At larger radii, the transition radiation tracker (TRT) comprises many layers of gaseous straw tube elements interleaved with transition radiation material.
Typically for each track the pixel detector contributes three, the strips four space points and at larger radii the transition radiation tracker provides about 36 tracking points.
The combination of precision trackers at small radii together with the TRT at larger radii gives robust pattern recognition and high precision in both R-ϕ and z coordinates. The detector has been designed to provide a transverse momentum resolution of ≈ 5 % at $p_T \sim 100$ GeV, in the plane perpendicular to the beam axis [115]: $\frac{\sigma_{p_T}}{p_T} = 0.05\% \cdot p_T \oplus 1\%$.
In 2008 the inner detector participated in different data-taking periods from single-beam LHC runs as well as cosmic-ray runs. After the initial detector alignment the relative momentum resolution was measured to be [138]: $\sigma_{p_T}/p = (4.83 \pm 0.16) \times 10^{-4}\text{GeV}^{-1} \times \text{p}_\text{T}$ for high momentum tracks.
To measure the primary vertex location is essential for different physics channels i.e. for the measurement of the Higgs mass. The semiconductor trackers allow impact parameter measurements and vertexing for heavy-flavour. The secondary vertex measurement performance is enhanced by the innermost layer of pixels (B-layer), at a radius of about 5 cm.
The ID is not part of the Level 1 trigger (see Section 3.4), digitised data events are just stored in buffers of sufficient length and passed to off-detector electronics after.

3.3.5. The Calorimeter

The ATLAS calorimeter system, shown in Figure 3.10, covers a range of $|\eta| < 4.9$ and is divided into two main parts: the electromagnetic calorimeter (ECAL) and the hadronic calorimeter (HCAL). The ECAL is designed to measure mainly the energy of electromagnetic showers, while the HCAL is optimised to measure hadronic showers that penetrate more deeply than electromagnetic showers.

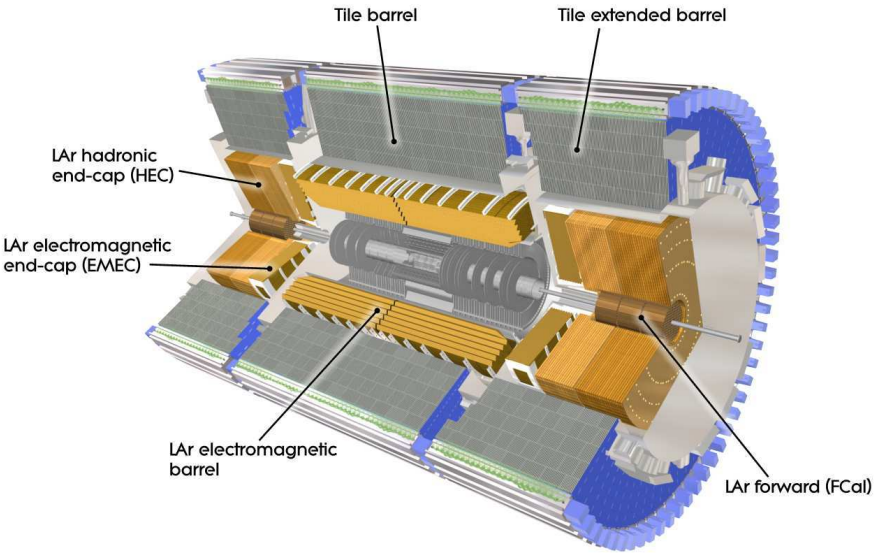

Figure 3.10: Cut-away view of the ATLAS calorimeter. Figure is taken from Ref. [115].

The purpose of the calorimeter system is manifold. It is designed to measure the energy and the direction (position) of charged and neutral particles like electrons, photons, isolated hadrons, taus and jets within its acceptance. Especially over the η range matched to the inner detector, the fine granularity of the EM calorimeter is ideal for precise measurements. Beside this it provides a "measurement" of E_T^{miss}, which is important for many physics signatures and in particular for SUSY particle searches. The calorimeter also contributes in the particle identification e.g. to distinct between particles like electrons, photons and hadrons, as well as for the muon momentum reconstruction [139].
The geometry of a calorimeter is also chosen such, that a fast extraction of the signal is also possible. The calorimeters closest to the beam-line are housed in three cryostats. The barrel cryostat contains the electromagnetic barrel calorimeter. Each of the two end-cap cryostats contains an electromagnetic end-cap calorimeter (EMEC), a hadronic end-cap calorimeter (HEC) calorimeter, that is installed behind the EMEC and a forward calorimeter (FCal) to cover also the region closest

to the beam. All calorimeter sub-detectors have full ϕ-symmetry coverage around the beam axis. In the following, the sub-detectors of the electromagnetic and the hadronic calorimeter are briefly described. A full description of ATLAS calorimeter system can be found in Ref. [115] and in the ATLAS calorimeter TDRs [140–142].

LAr electromagnetic Calorimeter (ECAL)

The **E**lectromagnetic **Cal**orimeter is a liquid-argon (LAr) sampling detector divided into a barrel electromagnetic calorimeter ($0 <| \eta |< 1.475$) and two end-caps (EMEC) ($1.375 <| \eta |< 3.2$), each of the components housed in their own cryostat.
The ECAL consists of absorbers and electrodes and is longitudinally segmented to measure shower evolution as a function of depth. This accordion geometry in ϕ offers uniform detection of electromagnetic particles without any dead regions, a good shower reconstruction and energy calibration. The electrodes of the ECAL consist of capton plated copper plates, which are segmented into strips that constitute the read out cells. The passive material is steel plated lead. The gap between electrodes and absorber plates is filled with liquid argon as the active medium. Liquid argon is an intrinsically linear, radiation-hard medium, which has good energy resolution and a stable response over the time.
The ECAL has more than 170 thousand readout channels and can be divided into three precision-measurement regions: Within $| \eta |< 2.5$ (corresponding to the inner detector acceptance) are three principal longitudinal segments or layers, two layers are in the region $2.5 <| \eta |< 3.2$ and in the overlap region between the barrel and the electromagnetic end-cap calorimeter[10].
The design was chosen to achieve uniform coverage over ϕ (without any azimuthal cracks), the folding angle, absorber thickness and wave amplitude all vary with radius and η to optimise linearity and resolution for every layer.
The first layer is finely segmented in η (η-strip layer), the segmentation granularity (thickness) varies in $| \eta |$ providing a precise position measurement in that direction. It is used for a sensitive measurement of the fine structure of the electromagnetic shower shape. With the separation of electron/photons from hadronic showers as well as the two γs originating from the π^0 decay, it also enhances the particle identification. The second layer absorbs most of the electromagnetic energy in a shower or jet and is the largest layer. It is transversally segmented into square towers and builds the thickest part with ≈ 16 radiation length. The granularity in η and ϕ of the cells is: $\Delta\phi \times \Delta\eta = 0.025 \times 0.025$. The 2nd layer is used together with the first one i.e. to determine η-direction of photons with the position of the photon cluster in the layers. The third layer, just in front of the hadronic calorimeter, is less segmented in η and collects possible energy tails of EM showers from the rear of this calorimeter. In the region $| \eta |< 1.8$ there is in addition, a fourth, pre-sampling, instrumented argon layer (”pre-sampler detector”) in front of the first layer. It is used to estimate and correct the energy losses for electrons and photons in the material of the inner detector, cryostats and the coils before reaching the calorimeter.
The total thickness of the EM calorimeter is > 22 radiation lengths in the barrel and > 24 in

[10] In the region $2.5 <| \eta |< 3.2$ the design of the two longitudinal layers is similar, but with a coarser granularity.

the end-caps [115] and can thus limit the punch-through into the muon system well below the irreducible level of prompt or decay muons.

Barrel electromagnetic Calorimeter The position of the central solenoid in front of the EM calorimeter demands optimisation of the material in order to achieve a good calorimeter performance. The barrel electromagnetic calorimeter [143,144] is divided into two identical half-barrels, centred around the z-axis (z = 0), separated by a small gap (4 mm): One half-barrel covers the region with $z > 0$ ($0 < \eta < 1.475$) and the other one the region with $z < 0$ (-1.475 $< \eta <$ 0). Each half-barrel is made of accordion-shaped absorbers, interleaved with readout electrodes and has a length of 3.2 m. It is complemented with a liquid-argon pre-sampler detector, placed in front of its inner surface. Their inner and outer diameters are 2.82 m and 4 m respectively. For ease of construction every half-barrel has been divided into 16 modules, each covering a $\Delta\phi = 22.5°$. The total thickness of a module increases with η - up to 33 radiation lengths in $|\eta| = 1.3$.

End-cap electromagnetic Calorimeter (EMEC) Each EMEC [144] consist of two wheels, one on each side of the electromagnetic barrel covering the region $1.375 <|\eta|< 3.2$. Each end-cap wheel is 63 cm thick, weights 27 tonnes and consists of two co-axial wheels: an inner and an outer wheel with a boundary at $|\eta| = 2.5$ (3 mm width). Every wheel is subdivided into eight wedge-shaped modules without any discontinuity along the azimuthal angle. It contains 768 absorbers interleaved with readout electrodes in the outer wheel and 256 absorbers in the inner wheel. The total radiation lengths of an end-cap calorimeter is greater than 24 (except for $|\eta| < 1.475$) and increases with $|\eta|$ up to 36 radiation length. In the transition region between the barrel and the end-cap calorimeters a liquid-argon pre-sampler, that consists of 32 identical azimuthal sectors, is implemented in front of the end-cap calorimeter, covering the range $1.5 <|\eta|< 1.8$ to improve the radiation lengths and thus the energy measurement in this region.

Transition region between barrel and endcap sections The region of transition between barrel and endcap sections in the EM calorimeter ($1.37 <|\eta|< 1.52$) is expected to be more challenging in terms of calibration and reconstruction due to the increased dead material (for support structures etc.) in this region. While scintillators are in place to estimate losses, it is assumed in this thesis, that this region will not be well enough understood for precision measurements in early data. Therefore events with electron candidates in this region are not analysed.

Hadronic Calorimeter (HCAL)

The **H**adronic **Cal**orimeter is placed directly outside the EM calorimeter, surrounding the barrel and end-cap region and covers the range $|\eta| < 4.9$. The HCAL is be composed of three main parts: one central barrel ($|\eta| < 1.0$), two extended barrels covering the region $0.8 <|\eta|< 1.7$, and two hadronic end-caps (HEC) covering the region $1.5 <|\eta|< 3.2$. An additional Forward Calorimeter (FCal) covers the range $3.1<|\eta|< 4.9$. Different technologies are used in different regions of the hadronic calorimeter to provide a good calorimeter depth. The central barrel and extended barrels are sampling tile detectors and are named Tile barrel and Tile extended barrels. The HEC

and FCal are sampling LAr detectors. Each part consists of at least three samplings for shower profile measurements. Their purpose is to completely stop and absorb all strongly interacting particles produced in every collision to avoid hadronic punch-through into the muon system and the measurement of jets. With at least 10 interaction lengths over almost the complete angular range, hadronic jets should be well contained. This enables also a good E_T^{miss} resolution. The total thickness of the HCAL is about 11 interaction lengths at $\eta = 0$ including the outer material.

Tile Calorimeter The tile calorimeter [141] is a steel-scintillator-sampling calorimeter and uses plastic scintillator with photo-multiplier as the active medium (scintillating tiles), and steel plates as the passive medium. It is located behind the liquid argon electromagnetic calorimeter and consists of three parts: one central barrel ($|\eta| \lesssim 1$) with a length of 5.8 m and two 2.6 m long extended barrels ($0.8 \lesssim |\eta| \lesssim 1.7$). Radially, the tile calorimeter extends from an inner radius of 2.28 m to an outer radius of 4.25 m. The barrel and extended barrels are divided azimuthally into 64 modules, each made of steel plates and scintillator tiles and of size, and longitudinally they segmented into three layers. The segments in the first two layers are $\Delta\eta \times \Delta\phi = 0.1 \times 0.1$ and $\Delta\eta \times \Delta\phi = 0.2 \times 0.1$ in the last layer. The scintillation light in the tiles is read out via wavelength shifting fibres by photomultiplier tubes (PMTs) positioned behind each calorimeter module.
The scintillator tiles are oriented radially and normal to the beam line. This allows the almost seamless azimuthal calorimeter coverage. A small plug calorimeter, made of steel-scintillator sandwiches is used to estimate energy losses in the transition region ("crack region") between the barrel and extended barrel sections [115].
Together with the electromagnetic barrel calorimeter, the tile calorimeter focuses on precise measurements of hadrons, jets, taus and the missing transverse energy.

LAr end-cap Calorimeter (HEC) The **H**adronic **E**nd-**C**ap Calorimeter (HEC) [145–147] is a copper/liquid-argon sampling calorimeter located directly behind the end-cap electromagnetic calorimeter in the intermediate region ($1.5 < |\eta| < 3.2$). To reduce the drop in material density at the transition between the end-cap and the forward calorimeter, the HEC overlaps slightly with the forward calorimeter (around $|\eta| = 3.1$) and with the tile calorimeter ($|\eta| < 1.7$). Due to the more intense radiation environment, a liquid argon technology is used as the active medium, similar to the EM calorimeter, but with copper absorbers to provide the necessary density of material.
The HEC consists of two independent wheels per end-cap (front wheel HEC1 and rear wheel HEC2) and shares with the electromagnetic end-cap (EMEC) and forward (FCal) calorimeter the same LAr cryostats. Each HEC wheel is cylindrical with an outer radius of 2030 mm, divided into two longitudinal layers in depth (four layers per end-cap) and constructed of 32 identical wedge-shaped modules. Similar to the tile calorimeter, the read out cells of the HEC are arranged in a grid with the granularity $\Delta\eta \times \Delta\phi = 0.1 \times 0.1$ (0.2×0.2) in the region $1.5 < |\eta| < 2.5$ ($2.5 < |\eta| < 3.2$).
The HEC is responsible for the jet measurements [145, 148], but it can also detect muons and measure any radiative energy loss with its more than 5000 read-out channels.

LAr Forward Calorimeter

The **F**orward **Cal**orimeter (FCal) [149] measures both- hadronical and electromagnetical activities and covers the range $3.1 <| \eta |< 4.9$. The FCal is placed by about 1.2 m with respect to the EM calorimeter front face, about 4.7 m from the interaction point in the same cryostats as the end-cap calorimeters.
The HEC and the FCal overlap in the high η region. This minimises energy losses in cracks between the calorimeter systems and also reduces the radiation backgrounds, which could reach the muon system. Since a high particle density is expected close to the beam line, the FCal has due to its location and size a high density design with a relative fine segmentation. This allows a good forward jet reconstruction and provides an important contribution to the missing transverse energy measurement.
The FCal is about 10 interaction lengths deep and consists of three 45 cm deep longitudinally separated modules in each end-cap. The first module-the electromagnetic module (FCal1) has copper absorbers stacked one behind the other one and is optimised for electromagnetic measurements. The other two modules (FCal2 and FCal3) are hadronic ones, optimised for a high absorption length. They have tungsten absorbers to minimise the lateral spread of hadronic showers and are primarily for measuring hadronic energy deposits. A copper shield has been installed behind FCal3 to reduce the background in the end-cap muon system.

Trigger system

The readout electronics for the EM calorimeter have been designed to provide the signals to the first level (L1) trigger system, and to measure for L1-triggered beam crossings the energy deposit in each calorimeter cell. The readout should proceed without any appreciable dead-time up to a trigger rate of 75 kHz (see also Section 3.4) and allows having a high radiation tolerance and dynamic range (signals range from 10 MeV to 3 TeV). To satisfy all these requirements, signal amplification and digitisation is handled by the front-end electronics of the detector, which also provide analogue sums of deposits in trigger "towers" of size $\Delta\eta \times \Delta\phi = 0.1 \times 0.1$ for the Level 1 calorimeter triggers. The readout of the hadronic and forward calorimeter systems mirrors that of the electromagnetic calorimeter-signals, they are read out from the side of FCal1 nearer to the interaction point and from the sides of FCal2 and FCal3 farther from the interaction point (front-end and back-end electronics). Like the EM calorimeter, the system provides energy deposite in pseudo-projective trigger towers for the Level 1 trigger decision. More details are described in the Section 3.4 and in the Ref. [115].

Summary

The ATLAS calorimeter system provides accurate energy and position measurements of electrons, photons, isolated hadrons, taus and jets. The electromagnetic calorimeter is the main detector to measure the electron and photon energy in the central part of the ATLAS detector and to provide a good energy reconstruction performance for electrons and photons. The desired energy resolution

for the ECAL [115] is:

$$\frac{\sigma_E}{E} = \frac{10\%}{\sqrt{E}} \oplus 0.7\%.$$

In the barrel part of ATLAS, together with the electromagnetic barrel calorimeter, TileCal focuses on precise measurements of hadrons, jets, taus and the missing transverse energy (E_T^{miss}). The performance requirements are driven by the ATLAS physics programme: The desired energy resolution of the hadronic calorimeter is [115]:

$$\begin{aligned} \frac{\sigma_E}{E} &= \frac{50\%}{\sqrt{E}} \oplus 3\% \qquad \text{for} \qquad |\eta| < 3.2 \\ \frac{\sigma_E}{E} &= \frac{100\%}{\sqrt{E}} \oplus 10\% \qquad \text{for} \qquad 3.1 < |\eta| < 4.9 \end{aligned}$$

Studies of the Tile hadronic calorimeter performance using random triggers, calibration data, data from cosmic ray muons and single beam data have shown, that the hadronic calorimeter operated at the end of 2009 with 99.1% of cells functional for readout. The calibration systems' precision is well below the design of 1%. The determination of the global energy scale was performed with an uncertainty of 4% [139].
During the April and May 2010 data taking, about 20 out of 1524 optical links of the electromagnetic calorimeter readout system were non-working, in addition approximately 0.05% of single channels were affected by readout problem or noise and masked during reconstruction [150].

3.3.6. The Muon Spectrometer

The **M**uon **S**pectrometer (MS) defines the outermost and largest (in terms of detector volume) subdetector of the ATLAS detector (see Ref. [151] and references therein). It is designed to provide a precise momentum measurement of charged particles based on the magnetic deflection of tracks in the toroidal magnetic field (see Section 3.3.3) up to a pseudorapidity of $|\eta| < 2.7$. Due to the depth of the calorimeters, muons are typically the only charged particles exiting the barrel and end-cap calorimeters and passing through the muon systems. Air-core toroids (see Section 3.3.3) have been chosen to minimise the material the muons have to traverse and hence the multiple scattering to allow a stand-alone measurement of the muon momentum and direction with the MS. The magnetic field is mostly orthogonal to the muon trajectories minimising the degradation of resolution.
The MS can provide stand-alone measurements with good momentum resolution and charge identification for low p_T muons (~ 3 GeV), as well as for high momentum muon tracks (~ 3 TeV). A stand-alone transverse momentum resolution with a precision of approximately 10% for 1 TeV tracks is expected. However, in order to achieve always the highest precision, also the inner detector and calorimeter measurements are used for the muon track reconstruction (see Section 5.5.1).
The MS is not only a high-precision tracking detector, it is instrumented with trigger chambers

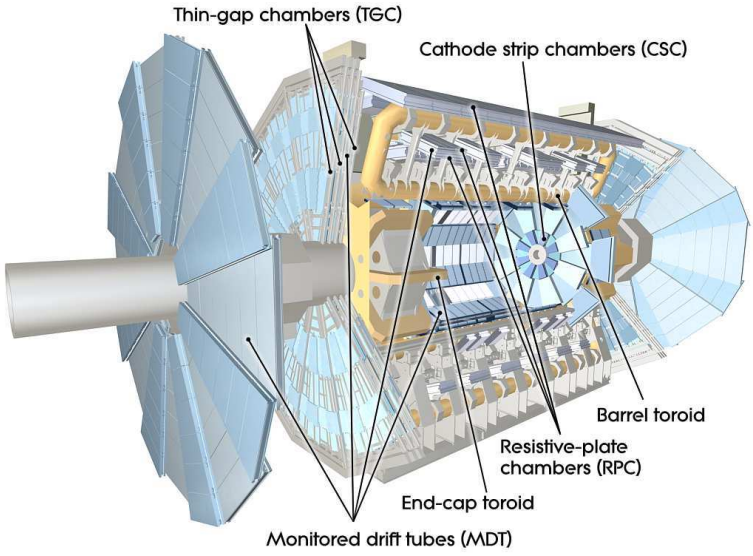

Figure 3.11: Cut-away view of the ATLAS muon system. Figure is taken from Ref. [115].

with Level 1 trigger capability, that cover the pseudorapidity range $|\eta| < 2.4$, roughly corresponding to the inner detector acceptance. Beside this, it is also used e.g. for bunch-crossing identification and the identification of cosmic ray particles.
The ϕ symmetry of the toroids is reflected in the symmetric structure of the muon chamber system. Its main components are displayed in Figure 3.11. The muon chambers are arranged projectively in three stations (layers) for both barrel and endcap regions. Each layer is subdivided in different sectors with slightly different lateral extensions. This leads to a region of overlap in ϕ that minimises gaps in detector coverage. The geometrical design of the MS was optimised such, that a typical muon originating from the interaction point with $|\eta| \approx 2.5$ could be registered by each of the layers.
In the barrel region, the muon chambers are located between and on the eight coils of the superconducting barrel toroid magnet and arranged in three cylindrical layers around the beam axis at radii of approximately 5 m, 7.5 m, and 10 m, whereas the chambers in the end-cap regions are in front and behind the two end-cap toroid magnets. They form large wheels installed in four planes perpendicular to the beam (z-axis) at distances of $|z| \approx 7.4$ m up to 21.5 m from the interaction point. In the centre of the detector ($|\eta| \approx 0$), a gap in chamber coverage has been left open to allow for services to the solenoid magnet, the calorimeters and the inner detector. Its size varies from sector to sector, the angular range, seen from the interaction point, where a high momentum track is not recorded is about $\pm 4.8°$ ($|\eta| \leq 0.08$) in the large and $\pm 2.3°$ ($|\eta| \leq 0.04$) in the small sectors.
In the following the main characteristics of the MS sensors as well as the regions of their coverage are discussed: The muon spectrometer is instrumented with dedicated Trigger Chambers, Resistive Plate Chambers (RPC) in the barrel region and with Thin Gap Chambers (TGC) in the end-cap

region. Monitored Drift Tube (MDT) chambers and Cathode Strip Chambers (CSC) serve as high precision tracking chambers.

Monitored Drift Tube Chambers (MDT)

The precision momentum measurement of the track coordinates is performed by the **M**onitored **D**rift **T**ube chambers (MDTs). These chambers consist of three to eight layers of individual drift tubes with an average resolution of 80 μm per tube and about 35 μm per chamber. Every tube is mechanically isolated, which guarantees the high mechanical precision of the chambers and a high level of operational reliability. The layer dimensions and the chamber sizes increase in proportion of their distance from the interaction point. The chambers are rectangular in the barrel and trapezoidal in the end-cap. Their shapes and dimensions were chosen to optimise solid angle coverage, while respecting the envelopes of the magnet coils and support structures. In the barrel and end-caps the tubes are arranged along the ϕ-direction, the centre points of the tubes are tangential to circles around the beam axis. All tubes of a barrel chamber have the same length (with the exception of some chambers with cut-outs), while in the end-cap chambers the tube lengths changes along R.
In some sections of the barrel, special chambers were designed to keep the acceptance losses due to the ATLAS support structure ("feet") to a minimum. The MDT's cover the pseudorapidity range $|\eta| < 2.7$ and $|\eta| < 2.0$ in the innermost end-cap layer. In the toroidal field, muons are bend in the η direction, which is therefore the direction that the precision chambers measure. In the forward region ($2 < |\eta| < 2.7$), Cathode-Strip Chambers (CSC) are used in the innermost tracking layer, because they show a higher rate capability and time resolution (see next Section). More details about the chamber dimensions and parameters as well as the construction can be found in [152] and [153].

Cathode-Strip Chambers (CSC)

The **C**athode-**S**trip **C**hambers are multiwire proportional chambers with cathode planes segmented into strips in orthogonal directions and with the wires oriented in the radial direction (wires are parallel to the central wire, which points in the radial direction). This allows to measure both coordinates from the induced-charge distribution. In the forward region ($2 < |\eta| < 2.7$) they are used in the innermost tracking layer. In the region $|\eta| > 2.0$ in the first layer of the end-cap the MDT counting rates will exceed the limit for safe operation (about 150 Hz/cm^2). Therefore the MDT's are replaced by cathode-strip chambers, which have a high time and double track resolution and low neutron sensitivity and can withstand the demanding rate and background conditions.
The CSC system consists of two disks, each has eight chambers (eight small and eight large) and is segmented into large and small chambers in ϕ. Each chamber has four plans that gives four independent measurements in ϕ and η along a track. The resolution of the chambers depends on the signal-to-noise ratio and the readout pitch. It is about 40-60 μm in the bending plane and about 5 mm in the transverse plane, where the difference in resolution between the bending and non-bending planes is due to differences in the readout. More detailed information on chamber

parameters are available in Ref. [153].

Trigger Chambers (TGC and RPC)

One of the main design criteria for the muon system was the trigger capability of muon tracks to deliver track information within a few nanoseconds. Therefore beside the precision-tracking chambers a trigger system has been installed: **R**esistive **P**late **C**hambers (RPCs) cover the pseudorapidity range in the barrel region $|\eta| < 1.05$, while in the end-cap ($1.05 < |\eta| < 2.4$) **T**hin **G**ap **C**hambers (TGCs) are used. Both chamber types consist of independent detector layers, have an excellent time resolution of about 1.5-4 ns and provide bunch-crossing identification with a very high probability.
The trigger chambers for the muon spectrometer also serve another purpose: they measure the muon track coordinates in the bending (η) and in the non-bending (ϕ) plane in the direction orthogonal to that determined by precision-tracking chambers.
The RPC system consists of three concentric cylindrical layers around the beam axis and makes it possible to select high momentum tracks with a transverse momentum p_T = 9-35 GeV (high p_T-trigger), as well as to measure with the two inner chambers the low-p_T tracks (low-p_T trigger, p_T = 6-9 GeV)). In case a track goes through all three stations six measurements of η and ϕ are delivered. This track measurement helps to reject fake tracks from noise hits and improves the trigger efficiency, because not all coincident hits need to be used. The TGC's provide the muon trigger capability in the end-cap and determine the azimuthal coordinate to complement the measurement of the MDTs in the bending (radial) direction. In the end-cap the MDT's are complemented by seven layers of TGC's, in the inner layer are two TGC layers, that are segmented radially into two non-overlapping regions: the end-cap and forward region (also known as the small wheel). The end-cap TGC,s are mounted on support structures of the barrel toroid coils. The azimuthal coordinate in the outer MDT wheel, i.e. the coordinate along the tube, has to be obtained by the extrapolation of the track from the middle layer, which can be done accurately because there is no magnetic field.
The main characteristics of the MS sensors as well as the regions of their coverage can be found in Ref. [115].

Summary

The design of the ATLAS detector is optimised for muon identification, with an efficiency greater than 95%. Muon momenta are independently measured in the inner detector and the muon spectrometer. The deflection of muons in the magnetic field generated by a system of air core toroid coils in the muon spectrometer is measured by layers of precision drift tube (MDT) chambers in combination with the cathode strip chambers (CSC) at the entrance of the muon spectrometer. The layers of resistive plate chambers (RPC) in the barrel region and the thin gap chambers (TGC) in the end caps provide the muon trigger and also measure the muon trajectory in the non-bending plane of the spectrometer magnets. The algorithms for the reconstruction of muons in p–p collisions at 7 TeV have been optimised with Monte-Carlo simulations. The performance goal of the

muon spectrometer is a transverse momentum resolution better than 3% over a wide transverse momentum range and approximately 10% for 1 TeV tracks.
In order to study the performance of the muon reconstruction of the ATLAS detector and the reliability of the Monte-Carlo simulation about 0.6 nb^{-1} integrated luminosity of $\sqrt{s} = 7$ TeV p-p collisions, corresponding to the data acquired with minimum bias triggers, have been analysed [154]. The inner detector momentum resolution for muons with $6\,\text{GeV} < p_T < 20$ GeV is dominated by multiple scattering. A fractional momentum resolution of 2% is reached in the barrel region, which increases to about 5% in the forward end-cap region. The muon momentum resolution is dominated by energy loss fluctuations for $p_T \leqslant 10$ GeV and by multiple scattering above 10 GeV, a fractional momentum resolution of 5% is expected for muons with $p_T \leqslant 10$ GeV. The shapes of the distribution obtained from the first data events are in general similar to the Monte-Carlo simulation [154].

3.3.7. The Forward Detectors

The ATLAS detector includes also several forward detector systems: the **M**inimum **B**ias **T**rigger **S**cintillators (MBTS), the **LU**minosity **C**herenkov **I**ntegrating **D**etector (LUCID), the **Z**ero-**D**egree **C**alorimeters (ZDC) and the **A**bsolute **L**uminosity **F**or **A**TLAS) (ALFA) Roman pots.
The **Minimum Bias Trigger Scintillators** were designed to provide a Level 1 minimum bias trigger for the early data taking period and consists of two sets of sixteen scintillation counters, which are installed on the inner face of the end-cap calorimeter cryostats at about 3.6 m from the interaction point. The scintillators are read out by TileCal photomultipliers connected to the standard TileCal. The MBTS has been extremely valuable in early data taking, especially for the first ATLAS physics publication using 900 GeV data [155].
About 17 m either side of the interaction point in the ATLAS end-cap regions is the Cerenkov detector called **LUCID** [156–158]. Luminosity can be measured by several detectors in ATLAS, but LUCID is the only detector, which is primarily dedicated to online luminosity monitoring of the instantaneous luminosity and beam conditions. It consists of an array of Cerenkov tubes and detects inelastic p-p scattering in the forward direction. At the LHC design luminosity, most bunch-crossings will result in multiple p-p interactions. The number of interactions per beam-crossing must be known in order to determine the luminosity. LUCID assumes, that the number of interactions in a bunch-crossing is proportional to the number of particles detected in this detector. This holds true even when most of the detected particles originate from secondary interactions. The LUCID detector was optimised for high luminosity, but performed very well in early data taking with a luminosity of less than $10^{27}\text{cm}^{-2}\text{s}^{-1}$.
The **Zero-Degree Calorimeter** [156] is located at a distance of $\simeq \pm 140$ m, where the LHC beam-pipe is divided into two separate pipes and is embedded in the TAN (Target Absorber Neutral) absorber. The primary purpose of the ZDC is to detect forward neutrons and photons at very low angle $|\,\eta\,| > 8.3$ in both proton-proton and heavy-ion collisions. The ZDCs play a key role in determining the centrality of heavy ion collisions, but they also increase the acceptance for diffractive processes of ATLAS central and forward detectors and provide an additional trigger for minimum bias events during low luminosity running.

The ALFA detector [156] consists of scintillating-fibre trackers located inside four Roman pots [159] that are placed very close to the beam (≈ 1 mm) at a distance of approximately $\sim$240 m from the interaction point. The system measures elastic Coulomb scattering at small angles to obtain the most accurate calibration and to measure the luminosity with an uncertainty of better than 5%. These extremely small scattering angles are smaller than the nominal beam divergence. The measurements can therefore only be performed with specially prepared beam conditions, which are also used for calibration of the LUCID detector.

3.3.8. The status of the ATLAS Detector 2010

In December 2009, the ATLAS detector recorded its first collision events from LHC runs at the centre-of-mass energies of 0.9 TeV and 2.36 TeV. All detector components were fully operational and all levels of the trigger and data acquisition system performed as expected. The obtained performance for the different detector components was close to its design goals although most of the measured events have been low energy particles, an energy range the detector has not been optimised for. Details can be found in Refs. [160]. The operational fractions of the various detector systems at the beginning of the year 2010 are [161]:

- about 98% of the inner detector are tested and work (97.4% pixels, 99.2% SCT, 98.0% TRT)
- about 99% of all calorimeter cells are tested and work (97.3% Tile calorimeter, 98.5% ECAL, 99.9% HEC and 100% FCal)
- about 98.5% of all muon detector systems are tested and work (99.7% MDT, 98.5% CSC, 97.0% RPC, 98.6% TGC)

3.4. The ATLAS Trigger System

The proton-proton interaction rate with approximately 1 GHz is much higher than the offline computing power and storage capacity that limits the event data recording. Therefore a trigger system is employed to identify and to capture the physics signatures of interest with high efficiency. It must provide a sufficient rejection factor of 5×10^6 against minimum-bias events to reduce the rate to 200 Hz while maintaining maximum efficiency for the new physics.
The ATLAS trigger and data acquisition system (TDAQ), schematically shown as block diagram in Figure 3.12, is based on three distinct levels of online event selection: Level-1 (L1), Level-2 (L2), and event filter (EF) [104, 162, 163]. L2 and EF together form the high-level trigger (HLT). Each trigger level refines the decision made at the previous level and reduces the data rate gradually by adding additional selection criteria. As soon as an event fails all trigger criteria of a given processing level, it is rejected and cannot be resurrected subsequently. Accepted events have passed through all processing steps. This approach saves valuable processing time. In the following, a brief overview is presented, also introducing the data acquisition system (DAQ).

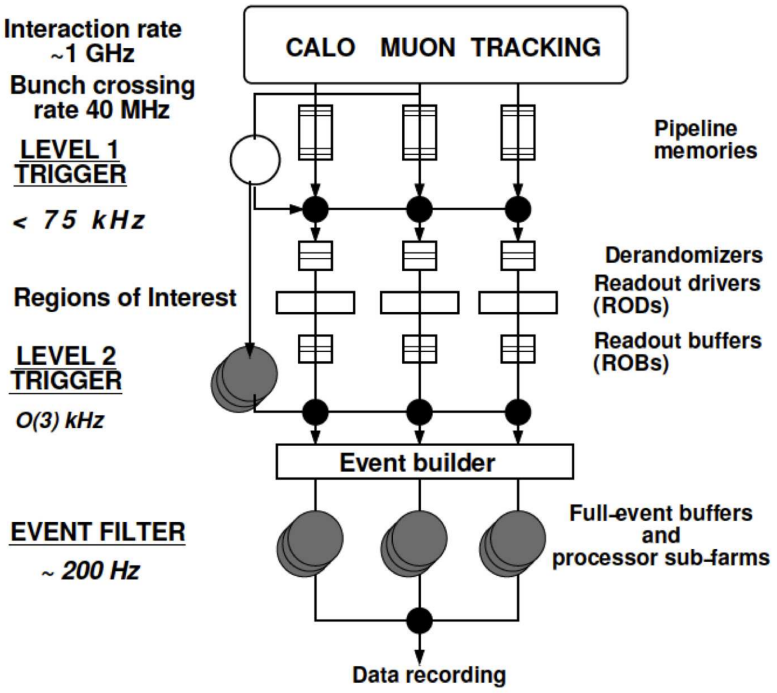

Figure 3.12: Schematic view of the ATLAS TDAQ system, taken from Ref. [162].

3.4.1. Level-1 Trigger

The Level-1 (L1) trigger system is a hardware trigger, based on detector electronics, that uses the reduced-granularity information from a subset of the total detectors - the calorimeter sub-systems and the muon detectors[11] and performs the initial event selection based on it. The L1 calorimeter trigger uses the information from all the calorimeters/calorimeter trigger towers (electromagnetic and hadronic; barrel, end-cap and forward, see Section 3.3.5) and aims to identify high-E_T objects such as electrons and photons, jets, and τ-leptons decaying into hadrons, as well as events with large E_T^{miss}. The electron/photon and τ triggers extend out to $|\eta| = 2.5$, which is the limit for precision measurements with the inner detector and electromagnetic calorimetry, the jet trigger to $|\eta| = 3.2$ and the E_T^{miss} and total transverse-energy triggers include the forward calorimetry, and extend to $|\eta| = 4.9$. This also allows the FCal to be used for forward-jet triggers.
The L1 muon trigger is based on signals in the muon trigger chambers (see Section 3.3.6): RPCs in the barrel ($|\eta| < 1.05$) and TGCs in the end-caps ($1.05 < |\eta| < 2.4$, except the innermost plane covers only $1.05 < |\eta| < 2.4$) and searches for patterns of hits consistent with high-p_T muons originating from the interaction region.
In addition to the main ATLAS detector, L1 trigger signals are provided by the beam pickups, beam conditions monitor, Zero Degree calorimeter, the luminosity monitors ALFA and LUCID

[11] The ATLAS ID and the precision muon chambers (MDTs) are not used in the L1 trigger, because of speed reason.

(see Section 3.3.7) and forward scintillators designed to detect minimum bias events. More information can be found in the Trigger Technical Design Reports [162,163].
The Level 1 trigger needs to be very fast, to cope with a bunch crossing rate of 40 MHz. The available system bandwidth limits the combined output rate for all L1 triggers to around 75 kHz, which may be upgraded to 100 kHz. The L1 latency, the time from the proton-proton collision until the L1 trigger decision is completed, is about 2.5 μs. The L1 decision must reach the front-end electronics after the bunch-crossing within this time.
The L1 accept decision is made by the Central Trigger Processor (CTP) that combines the information of the different object types. The selection of the signals used from all signals available at the input boards is programmable, the currently foreseen input signals sum up to 150 bits [115]. The CTP uses look-up tables to form trigger conditions from the input signals. The trigger conditions are combined to form up trigger items. Every trigger item has a mask, a priority and a pre-scaling factor. A trigger item is for example: at least two muons and at least one jet have passed a particular threshold. A L1 Accept signal (L1A) is generated by the CTP of all logical OR trigger items. When there is a L1A decision, the CTP sends the information about the trigger decision for all trigger items to the L2 trigger (RoI builder), where it is used by the HLT and the data acquisition system.

3.4.2. Level-2 Trigger and Event Filter

The subsequent two levels, that form together the High-Level Trigger (HLT), are the Level-2 (L2) trigger and the event filter. The HLT is a software based trigger, almost entirely based on computers and networking hardware running on a computer farm.
The **L2 algorithms** provide a refined analysis of the L1 data based on detector information and calibration that is not available at L1 e.g. reconstructed tracks from the inner detector to receive results with improved resolution. The L2 trigger selection is largely based on Regions-of-Interest (RoI's), the regions of the detector where the L1 trigger has identified possible trigger objects within the event, and uses fine-grained data from the detector for a local analysis of the L1 candidate. The RoI information provided by the L1 trigger sub-systems for every event is i.e. information on coordinates, energy and type of signatures.
In the first step of the L2 trigger process a seed is constructed for each trigger accepted by L1 that consists of a p_T threshold and an η-ϕ position. The L2 algorithms use this seed to construct an RoI window around the seed position. The size of the RoI window is determined by the L2 algorithms depending on the type of triggered object (for example a smaller RoI is used for electron triggers than for jet triggers). A coherent set of selection criteria is applied on the derived informations to determine, if the candidate object should be retained. After confirmation, additional features may be searched for in the other detector systems. In this way information from individual sub-systems can be matched to provide additional rejection and higher purity at L2. The information can be also combined to form more specialised global trigger objects, which become candidates for leptons, jets, photons and E_T^{miss} as well as B-physics objects. This allows to distinguish for the first time between electrons and photons.
The ability to move, unpack, and analyse the local data only around the seed position greatly re-

duces both the processing times and the required data bandwidth. Using only the data located in the RoI's limits the amount of data, which must be transferred from the detector readout. The L2 system only is designed to provide an event rejection factor of about 40 (compared to L1) and to reduce the final data-taking rate from ∼75 (40) kHz to about 2 (1) kHz [104] during nominal (startup) operations. On average, the L2 can initiate the processing of a new event every 10 μs, the average event processing time should be less than 40 ms including the time for data transfers. If the event is accepted by the L2 trigger, the results of the L2 triggers analysis are built into the final event and subsequently used by the event filter to seed its selection.
The final online selection is performed by the **Event Filter** (EF) that receives events accepted by L2. Each L2 trigger that has been accepted can be used to seed a sequence of EF algorithms. Since the EF selection is performed after the event building step, it has direct access to the complete data for a given fully-built event using the full granularity of the detector. The EF classifies events and stores accepted events for a further offline analysis. For this it uses offline analysis procedures e.g. vertex reconstruction or track fitting that provide a more refined and complete analysis to further select events down to a rate which can be recorded for subsequent offline analysis. The output rate from the Event Filter is limited by the offline computing budget and storage capacity. It must provide the additional rejection factor of about 30 to reduce the output rate to 200 Hz, corresponding to about 300 MB/s, with an average processing time of 4 s per event.

Trigger for the Monte Carlo studies

The trigger used for some of the Monte Carlo studies presented in this thesis is the combined `J70_XE70` High-Level trigger, that requires at least one jet which has passed the 70 GeV threshold and missing energy which exceeds the the 70 GeV threshold.

The ATLAS **jet trigger** is based on the selection of jets according to their transverse energy E_T at the three trigger levels. The Level-1 jet reconstruction uses so-called jet elements, which are towers formed from the electromagnetic and hadronic calorimeter cells with a granularity of $\Delta\phi \times \Delta\eta = 0.2 \times 0.2$. The jet finding is based on a sliding window algorithm (see Section 5.1.1) that identifies the jet-RoI. The jet transverse energy is computed in a window of configurable size around it. If a Level-1 jet candidate passes a given transverse energy threshold, the Level-2 jet trigger continues by requesting calorimeter data around the L1 jet RoI position and runs an iterative cone algorithm with a radius of R = 0.4 [104]. The event filter jet algorithm is based on the offline algorithm using trigger towers, but is configured for the online environment.
The ATLAS **missing transverse energy trigger** ("XE" signatures) select events based on E_x and E_y and requires that the magnitude of the vector sum of all transverse energies exceeds some threshold. The L1 missing transverse energy trigger uses the L1 calorimeter measurements done with all calorimeters. Trigger towers are defined, which correspond to the sum of all calorimeter cells in an (η, ϕ) range and all found jet elements are summed up. The High Level E_T^{miss} trigger consists of a set of software-based algorithms, which perform E_T^{miss} reconstruction from the detector input once per event. At L2 the L1 results are refined by applying a correction taking into account muons reconstructed at L2. In a last step at EF-level, contributions from both calorimeters

and muon spectrometers are recomputed. A noise cut is applied on the calorimeter cell energy to improve the resolution.

Trigger for first LHC collisions

The trigger menus that consist of many trigger chains, where each chain defines the L1 and HLT selection for a single physics signature, have been evolved several times through the commissioning periods. For example for the LHC collision running in 2009 and 2010, the trigger was commissioned in several steps, the procedure is discussed for example in Ref. [164–166].
The trigger selections criteria during the ATLAS startup phase were loose selections at each stage. The HLT operated in a pass-through mode, which entails executing the trigger algorithms, but accepting the event independent of the algorithmic decision. This allows the trigger selections and algorithms to be validated to ensure that they are robust against the varying beam and detector conditions. All events that passed the ATLAS L1 hardware-based triggers, e.g. the calorimeter jet trigger are processed and have been written to the L1Calo stream. As the luminosity increases, the use of higher thresholds, isolation criteria and tighter selections at HLT become necessary to reduce the background rates. For particularly high rates a pre-scaling was be applied, where pre-scaling indicates that only 1 in every X events are passed to the next levels of the trigger system.
For the collision data analysed in this thesis (see Chapter 11) the events have passed the L1 jet-trigger `L1_J15` that requires at least one ROI of a jet type, which has passed the 15 GeV threshold. The trigger efficiencies of the used triggers are discussed in Section 7.4.

3.4.3. Data Acquisition System (DAQ)

The data acquisition system (DAQ) controls all data movements down the trigger selection chain. Its main components are: readout, L2 trigger, event-building, event filter, configuration, control and monitoring. In addition, the DAQ provides configuration, control, and monitoring of the TDAQ and ATLAS detector during data-taking. As explained in the previous sections the DAQ receives and buffers the event data from the detector-specific readout electronics after a L1 trigger accept. Requested event information are transfered to the L2 trigger, and in case of an accept, all parts of the event data are assembled in the event builder nodes. The full event data are then moved by the DAQ to the EF trigger. Finally, in case of an EF accept, the full event data are moved to permanent storage. The DAQ interfaces the DAQ/HLT to CERNs central data-recording facility, and decouple the data-taking process from possible variations in the central data-recording service: At a peak event rate of up to 400 Hz events are record in extra files. Under normal operating conditions, this storage capacity is only partially used. In case of a failure in the transmission of data to CERNs central data recording service, there is a local storage capacity to buffer all events locally for up to 24 hours.
All recorded events are saved in ATLAS-defined data streams, for example events that passed the L1 calorimeter jet trigger are written to the L1Calo stream. Each event can be recorded in one or more files depending on the stream classification made by the event-filter processing task. In addition to these data streams, a subset of the events is also written to calibration streams and

an express stream. The express stream is a subset of the events selected by the event filter and additional criteria which select the events as being useful for monitoring the quality of the data and the detector. The calibration stream provides the minimum amount of information needed for detector calibration. These events will only contain a subset of the event data.

3.4.4. ATLAS computing model

LHC Computing Grid

The data volume recorded by the LHC will be roughly 15 Pbyte per year and exceeds that of any other experiment in the world [167]. This enormous amount of data cannot be stored and processed by one local computing centre alone anymore, also because thousands of scientists around the world want to access and analyse this data. Therefore, CERN operates a distributed computing and data storage infrastructure: the worldwide computing framework -LHC Computing Grid (LCG) [168]. The Grid is a distribution network that combines the computing resources of more than 130 computing centres in 34 countries to harness the power of several thousand CPUs to process, analyse and store data produced from the LHC. The physics event informations are stored in different file formats, beginning with RAW and processing through reconstruction to ntuples used for the analysis [169–172]. They are briefly summarised in Section G.

ATLAS stages of data-taking

The Tier-0 facility at CERN receives the RAW data from the Event Filter and is responsible for archiving it before it is processed and distributed to large computing sites around the world known as Tier-1 centres. On the Tier-0 the first calibration/alignment and prompt reconstruction is performed (express streams). This first calibration loop takes about 24-48 hours after a data run has ended, the newly calculated constants are later used for the bulk reconstruction and physics streams. The derived datasets (ESD, primary AOD and TAG sets) are distributed from the Tier-0 to the Tier-1 facilities.
The eleven Tier-1 institutions have several important tasks. They take responsibility to host and to provide long-term access and archival of a subset of the RAW data, for which they serve as a backup repository for CERN. The Tier-1 centres also provide the capacity to perform the reprocessing of the RAW data: After the new calibration and alignment constants are determined, the data is reprocessed in the Tier-1 centres where the “slow” calibration/alignment procedures as well as the reconstruction with a better calibration/alignment and/or algorithms are running. The derived ESDs, AODs and TAG datasets (see explanation in The Appendix Section G) are ATLAS-wide accessable - with the most up-to-date versions stored on disk and the previous version stored “on tape”. The Tier-1s also host a secondary copy of the current ESD, AOD and TAG samples from another Tier-1, and the simulated data samples from Tier-2 facilities to improve access and provide fail-over. Analysis jobs of the physics and detector groups run in the Tier-1 centres and produce e.g. derived physics datasets (DPDs) and samples on which user analysis will be performed. Parts of the AODs/DPDs are copied after to Tier-2 facilities for further analysis.
More than 150 Tier 2 institutions are connected to the Tier 1 institutions, where all user analyses

are running. The Tier-2 facilities may take a range of significant roles in ATLAS such as providing calibration constants, simulation and analysis. They typically host about one third of the available current primary AOD and the full TAG samples as well as some of the physics group DPD samples, most likely in accordance with local interest. In addition, the Tier-2 centre provide simulation capacity for the experiment and analysis capacity for physics working groups and subgroups. More information about the ATLAS computing model can be found in Ref. [169–172].

Athena Framework

ATHENA [171,173,174] is an offline software framework developed by the ATLAS collaboration for simulation, reconstruction and physics analyses in ATLAS. It is an implementation of the component-based architecture Gaudi responsible for handling the configuration and execution of several $C++$ packages through python scripts.
The great advantage of this package is the possibility to use all the functionalities provided by the framework in the default input formats (RAW, ESD, AOD, DPD). This includes for example tools used for the event reconstruction for fitting, calibration, track extrapolation, geometry and magnetic field mapping. The framework performs the reconstruction of physics objects, takes care of the execution order and data flow, provides common tools for the physics analysis as well as incorporates with event simulation packages.

4. Event simulation and Monte Carlo samples

Theoretical predictions are a fundamental part of any particle physics experiment. On one hand, they can help to design the detectors and to define the experimental strategies, on the other hand they can be used to extract non-computable parameters of a theoretical model or for an unambiguous interpretation of the experimental results and e.g. help to decide whether some new physics phenomena has been observed or not. To serve this purpose, the predictions must reproduce as close as possible the collision processes taking place in real detectors and generate events as detailed as they could be observed by a perfect detector.
Since the ATLAS detector recorded its first LHC collisions in December 2009, simulated data events are an important part of this thesis. The SUSY studies, described in the following chapters have been developed and tested on Monte Carlo samples. Only in the Chapter 11 first measured data are analysed.
This chapter briefly describes the main production steps of the data event generation and simulation. Section 4.2 gives a short overview of the Monte Carlo event generators used to simulate the physics processes. In Section 4.3 the different ATLAS detector simulations are discussed. Finally the simulated signal and background samples, which are relevant for the SUSY analyses are detailed in Section 4.5.
Part of this thesis was the production of the different SUSY signal grids described in Section 4.5.2, including the generation of the SUSY spectra and the complete production chain (generation, simulation) with the help of the LHC computing grid (see Section 3.4.4).
Throughout this thesis simulated data samples will be referred to as "Monte Carlo samples".

4.1. Overview

The production of simulated data can be generally divided into three steps:
Monte Carlo event generation $\rightarrow$ the simulation of the detector response for the produced particles and physics interactions (gas ionisation, showering etc.) $\rightarrow$ digitisation of the energy deposited in the sensitive regions of the detector into voltages and currents for comparison to the readout of

the ATLAS detector. The full simulation chain is demonstrated in Figure 4.1. The output of this chain can be presented in either an object-based format or in a format identical to the output of the ATLAS data acquisition system (DAQ). Thus, both the simulated and real data from the detector can then be run through the same ATLAS trigger and reconstruction packages to transform the digital output of detector into physics objects.
The ATLAS detector geometry used for the simulation, digitisation, and reconstruction is built from databases containing all the information needed to emulate a single data-taking run of the real detector including the the physical construction and detector conditions. Large computing resources are needed to model the complex detector geometry and physics descriptions in the standard ATLAS detector simulation. This has led to the development of faster simulations that are described in Section 4.3.2.
In contrast to real data events MC events contain also so called "truth" information, that can help to understand better the physics and reconstruction processes within the detector and supports the development of new analysing methods. In the event generation the information about the decay chain producing the final state particle including incoming and outgoing particles[1] is recorded for every particle, whether the particle is to be passed through the detector simulation or not, while in the simulation jobs, truth tracks and decays for certain particles are stored.

4.2. Event generation

Monte Carlo (MC) generators simulate the physics processes resulting from a particle interaction using theoretical calculations such as matrix elements for the generation of selected processes and input from previous experimental results. They are developed independently of the experiments and are written in general by third parties. The simulation is usually not done in one step, but rather by "factorising" the full problem into a number of components, each of which can be handled reasonably accurately. Basically, this means that the simulation starts with the hard interaction process and the result is thereafter left to hadronise (see Section 2.3.2). Most event generators include initial state radiation, final state radiation, beam remnants and further decays (parton shower method). The output of an event generator is in the form of "events" including the four-vectors and position of the produced particle, with the same average behaviour and the same fluctuations/frequency the events are expected to appear in the real physics process (real data). In Monte Carlo generators special techniques are used to select all relevant variables according to the desired probability distributions, and thereby ensure (quasi-)randomness in the final events. However, some loss of information is entailed in this method. The simulated events can therefore only used to predict a limited number of observable and are not a complete description of actual events taking place in real detectors.

[1] Informations about the parents and grandparents are available for every final state particle as well as for the children for each parent particle.

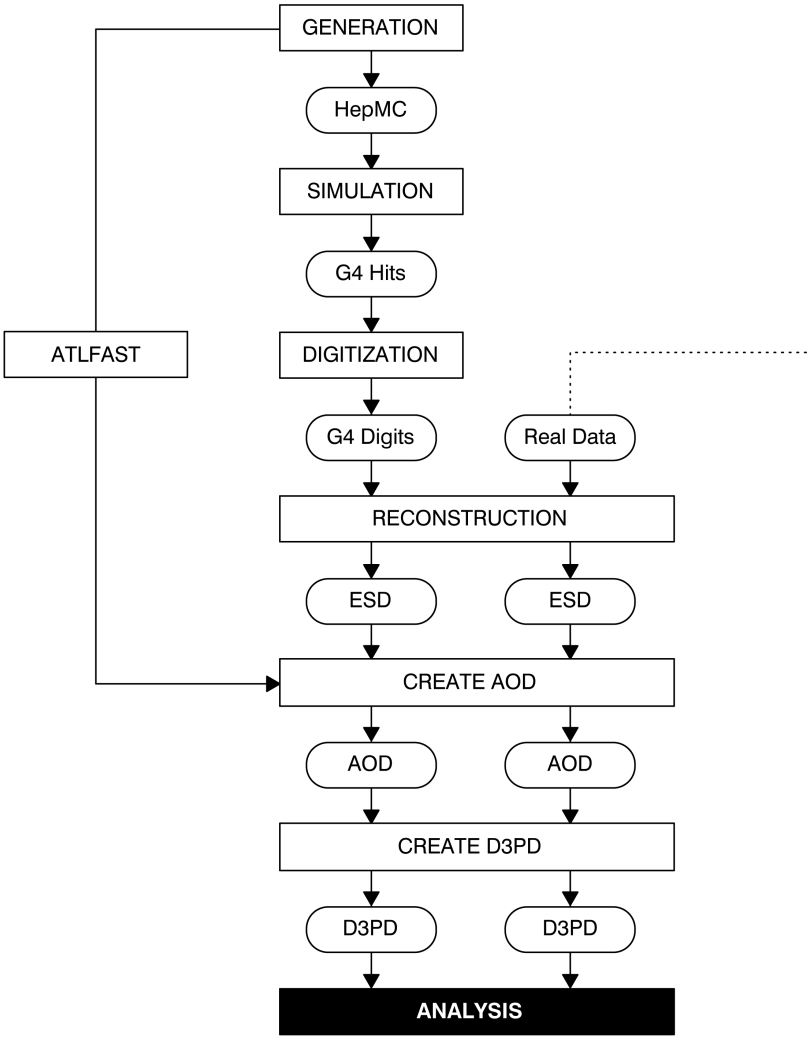

Figure 4.1: Flowchart to demonstrate the main production steps of the event simulation as presented in Ref. [175], starting from the event generation to the production of Analysis Object Data (AOD). After the digitalisation step both simulated and real measured data run through the same reconstruction steps. The main processing steps are illustrated in rectangles, the output formats of the steps are shown in ovals.

4.2.1. Monte Carlo generators

A long list of generators (see e.g. Ref. [176]) are used by ATLAS. The generators running within ATHENA can be grouped in three categories. The first group of generators, the full generators, include parton shower and fragmentation, for example PYTHIA [177], HERWIG [178–181], SHERPA [182], ACERMC [183], ALPGEN [184], MadGraph/MadEvent [185] and MC@NLO [186–188]. A second type of interfaces exist, so called Matrix Element generators ("Les Houches" type generators) that can run standalone, only generate the particles produced in the hard scattering process and write ASCII file containing partonic four-vectors in the "Les Houches" event format [189]. The output is passed to PYTHIA or HERWIG for parton showering and hadronisation. Specific purpose add-on packages to generators like TAUOLA [190][2] or PHOTOS [191][3] represent the third group. A brief description of the employed MC generators for this thesis is given in the following, details about the datasets (generator filter settings, production cross sections etc.) are described in Section 4.5.

PYTHIA The PYTHIA MC event generator [177] can be used to generate high energy physics events of high-energy collisions, comprising a coherent set of physics models for the evolution from a few-body hard process to a complex multi-hadronic final state. The objective of this tool is to describe as good as possible event properties, within and beyond the Standard Model, where strong interactions play a role and multi-hadronic final states are produced, e.g. it is used to simulate QCD jets. PYTHIA contains a library of hard processes and models for initial- and final-state parton showers, multiple parton-parton interactions, beam remnants, string fragmentation and particle decays. It also has a set of utilities and interfaces to external programs.
For most simulated processes only the leading order matrix elements are used, combined with parton showering to take ISR and FSR into account. There are only some cases where higher-order matrix elements are included e.g. the case of W production at a hadron collider. PYTHIA is the default generator in ATLAS, the FORTRAN version PYTHIA 6.4 is used.

HERWIG HERWIG is as PYTHIA a general-purpose event generator [178–181], that provides a full-simulation of hard lepton-lepton, lepton-hadron and hadron-hadron scattering together with ISR, FSR, hadronization and decays. HERWIG is a flexible generator with a large number of built in processes and has been tuned to agree with the Tevatron data [192–194]. ATLAS uses HERWIG 6.5, the last release of the FORTRAN HERWIG package, which is now superseded by HERWIG++ (see below), together with the JIMMY generator [180, 195] for hard and soft scattering processes in a single event in order to simulate underlying event activity.
The HERWIG MC event generator is often employed for the simulation of SUSY processes in combination with the ISAWIG and ISAJET [73] packages that provide pre-generated input tables (SUSY particle masses, particle spectra, decay modes/branching ratios) for these processes. It is also used to generate electroweak boson pair samples (WW, ZZ, WZ).

[2] TAUOLA is utilised for the simulation of τ-lepton decays.

[3] The radiation of photons from charged leptons is also treated separately, using the PHOTOS QED radiation package that is called by TAUOLA. TAUOLA cannot be used without PHOTOS.

HERWIG++ HERWIG++ [196, 197] (version 2.4.2) is the C++ based replacement for HERWIG and uses the MRST 2007 *LO** proton parton density distributions [198]. It contains important processes from the Standard Model, the universal extra dimensions model and supersymmetric models as well as leptoquarks models and many more. The user can add additional decay models as well as additional hard scattering processes can be used via Les Houches input from specialised generators. HERWIG++ was used for the generation the SUSY signal SU4 (see Section 4.5.2) for the 7 TeV MC sample for which it includes full spin correlations and QCD radiation in the supersymmetric decay chains. The current version of HERWIG++ also incorporates an underlying event model based on the extension of Jimmy to include soft scatters [199].

JIMMY JIMMY [180] is a library of routines, which should be linked with the HERWIG Monte Carlo event generator that allows to generate multiple parton scattering events in hadron-hadron, photon-photon or photon-hadron events.

ALPGEN ALPGEN [184] is a "Les Houches" type generator that is used for the generation of Standard Model processes in hadronic collisions, for example for the W and Z boson production in association with up to five jets. It is designed for final states with several well-separated hadronic jets, where the fixed order matrix element for multiparton hard processes in hadronic collisions, at leading order in QCD and electroweak interactions, is expected to give a better approximation than the shower approximation of PYTHIA or HERWIG.
The parton multiplicity in the calculated matrix element (N = 1 to 6) has to be specified before running ALPGEN, therefore the simulation of the physics process is sliced in N-partons samples. Showering, hadronisation and simulation of the underlying event can be performed by interfacing with HERWIG and JIMMY. In order to perform the parton showering and matrix element matching ALPGEN provides an algorithm to prevent double counting of parton emission either through the matrix element or the parton shower by event rejection- the MLM matching technique [200]. This technique vetoes events, where the parton shower generates jets that have already been generated by the ALPGEN matrix elements. This process can be very inefficient for final states with large numbers of jets, and the generation time can be significant.
Since exclusive matching is applied, the matched samples (each with N-partons) can be added, and the inclusive sample is obtained after summing up all N-partons samples. Also the total (inclusive) cross section is given by the sum over all cross sections, each multiplied by its MLM matching efficiency.

MC@NLO The MC@NLO generator [186–188] is a Les Houches type generator that runs standalone to produce ASCII files. It is one of the few MC tools that uses fundamental (hard scattering) processes evaluated at the next to leading order (NLO) in QCD perturbation theory. The inclusion of the NLO QCD corrections provides a good description of the final state kinematics for events with up to one additional QCD jet. As a consequence of the one loop corrections, generated events appear with negative and positive weights, which have to be carefully considered in the analysis.
Since only hard scattering processes are provided, the parton showering and hadronization is per-

formed by interfacing the generator with HERWIG together with JIMMY, that is utilised for the simulation of the underlying event.
MC@NLO has been used for large-scale production, e.g it was employed for the production of the primary $t\bar{t}$ sample (top events) as MC@NLO gives a better representation of the transverse momentum distribution of top quarks than PYTHIA or HERWIG.

ACERMC The ACERMC [183] is a "Les Houches" type Monte Carlo event generator dedicated for the generation of the Standard Model background processes, primarily W or Z bosons, with several jets, including jets originating from b-quarks in p-p collisions at the LHC. The program provides a FORTRAN library of the massive matrix elements and phase space modules for generation of a set of selected processes. The initial and final state radiation, hadronisation and decays have to be simulated either with PYTHIA or HERWIG Monte Carlo event generators.

gg2WW The program gg2WW [201] is used to calculate the loop-induced gluon-fusion process $gg \rightarrow W^*W^*l\bar{\nu}\bar{l}'\nu'$, including intermediate light and heavy quarks. Previous calculations have been extended by including the contribution from the intermediate top-bottom massive quark loop and the Higgs signal process. The program can be used to calculate cross sections with any set of cuts or any kind of differential distribution, or to generate weighted or unweighted events for experimental analyses.

SUSY spectrum generators

In order to study supersymmetric models, the expected spectrum of the superpartner, the Higgs boson masses and the couplings need to be calculated. The studied models in this thesis are supersymmetric quantum field theories specified by the gauge symmetry, (super-)field content and the Lagrangian with softly broken supersymmetry at the TeV scale. The Supersymmetry-Lagrangian is derived from the more fundamental superpotential and for non-renormalisable models from the gauge kinetic function [202]. The SUSY breaking effect is encoded in the Lagrangian soft SUSY breaking terms similar to what was described in Chapter 2. The Lagrangian parameters are usually specified at very high scales (e.g. M_{GUT} or M_{Planck}), such that renormalisation group equations (RGEs) are used to connect this scale to the energy scale at which the effective theory and Lagrangian parameters are valid and should be tested/measured. As soon as the Lagrangian parameters are known at the weak scale, the physical (s)particle masses are calculated, often by diagonalising the relevant mass matrices. Higher order perturbative corrections to the mass eigenstates- at minimum 1-loop-corrections are included to gain sufficient accuracy in the predictions. The most common SUSY spectrum calculator codes are ISAJET/ISASUGRA [73], SUSPECT [203] or SOFTSUSY [204].
The multi-purpose event generators like ISAJET, PYTHIA, HERWIG or PROSPINO have a complete library of tree-level SUSY particle production reactions and are used to calculate tree-level sparticle production cross sections. Different programs like ISASUSY/ISAJET can calculate all sparticle and Higgs boson $1 \rightarrow 2$-body and $1 \rightarrow 3$-body decay widths and branching fractions that can be input to the event generators used in ATLAS via the LHA input/output files.

HERWIG/PYTHIA can partly read branching fraction inputs, but mostly compute them internally by themself as it is done for the SUSY models used in this thesis.

ISAJET/ISASUGRA ISAJET [73] is a FORTRAN program used in conjunction with HERWIG to generate supersymmetric events. It simulates p-p, p-$\bar{p}$, and e^+–e^- interactions at high energies. It is based on perturbative QCD plus phenomenological models for parton and beam jet fragmentation. The program provides hard-scattering processes, ISR, FSR, hadronisation and additional beam jets assuming that these are identical to a minimum bias event. ISAJET incorporates ISASUSY, a subprogram of ISAJET, which evaluates the branching ratios for the minimal supersymmetric extensions of the SM and calculates also the sparticle mass spectra given a set of soft SUSY breaking parameters at the weak scale. ISASUSY includes 1-loop corrections to all sparticle masses, while for the Higgs masses and couplings the 1-loop potential is minimised at an optimised scale choice, which accounts for leading 2-loop effects from the results obtained from ISASUGRA. Yukawa couplings, which are necessary for the loop calculations are evaluated using simple SM running mass expressions [73,205].
ISAJET is also interfaced with IsaTools, which contains subroutines to evaluate dark matter constraints (see Section 6.3.1) such as the relic density of (stable) neutralino dark matter in the universe, the supersymmetric contributions to Δa_μ or the branching fraction for $b \to s\gamma$.
ISASUGRA comes with each version of ISAJET and determines the weak-scale parameters via the full set of 2-loop RGEs using an iterative approach e.g. it generates the masses and decay modes for supersymmetric models, which ISASUSY uses to find the branching ratios. The weak scale threshold corrections, which depend on the entire SUSY mass spectrum are hereby included. The output file of ISAJET can be loaded into HERWIG that generates the complete final states. For the SUSY signal samples simulated, the ISAJET version 7.75 (for 14 TeV, 10 TeV samples, 7 TeV mSUGRA samples) and version 7.79 (for 10 TeV MSSM sample) was used.

SoftSusy, micrOMEGAs SoftSusy [204] is a C++ program that calculates the SUSY particle spectrum in the CP-conserving Minimal Supersymmetric Standard Model parameter space. Weak-scale gauge coupling and the fermion masses are used as a boundary condition, as well as radiative electroweak symmetry breaking. The program solves the renormalisation group equations with theoretical constraints on soft supersymmetry breaking terms.
SoftSusy can be used in conjunction with other programs for many different particle physics calculations. For the production of MSSM SUSY signal points in this thesis, SoftSusy (version 2.0) was used together with micrOMEGAs [206] (version 2.2.), a program that was originally developed to calculate Dark Matter properties including the relic density, direct and indirect rates in a general supersymmetric model and other models of new physics.

Suspect SUSPECT [203, 207] is Fortran program, which calculates the Supersymmetric and Higgs particle spectrum in the Minimal Supersymmetric Standard Model (MSSM). The calculation can be performed in constrained models with universal boundary conditions at high scales such as the gravity (mSUGRA), anomaly (AMSB) or gauge (GMSB) mediated breaking models,

but also in the non-universal MSSM case with R-parity and CP conservation. It is used to generate phenomenological MSSM models with 19 + 3 free parameters, where the additional 3 parameter are from the 1st and 2rd generation trilinear couplings.

PROSPINO PROSPINO [99–101] is a FORTRAN-program that computes all $2 \rightarrow 2$ supersymmetric production cross sections at both leading order (LO) and next-to-leading order (NLO) at hadron colliders. All next-to-leading order SUSY-QCD corrections to all possible final states are included e.g. squark, gluino, stop, neutralino/chargino, and slepton pair production as well as the associated production of squarks with gluinos and of neutralinos/charginos with gluinos. The program allows to calculate beside the total cross section also differential distributions (in p_T and rapidity y) of one of the outgoing particles. PROSPINO reads SUSY "Les-Houches-Accord" files (SLHA) [208,209], a standardarised output format of many SUSY event generators. In this file the masses of the SUSY particles as well as the coupling spectra, branching ratios and decay modes are defined for the generated SUSY model. In this thesis PROSPINO version 2.1 is used to calculate NLO cross sections for the SUSY signals.

Changes for the 7TeV data studies

PDFs (see Section 2.3.2) are used by all the event generators as external inputs. ATLAS uses the Les Houches Accord PDF Interface (LHAPDF) [210] library with a large repository of PDFs. CTEQ [211,212] PDFs are used by default. All datasets employed in the present work for 14 and 10 TeV used the PDF sets CTEQ6L [213] for leading order (LO) MC event generators, and CTEQ6M [213] for the next-to-leading order (NLO) MC event generator MC@NLO [214]. For the 7 TeV simulations ATLAS has updated the parton density functions (PDFs) to those including new measurements and theoretical developments [215]. It was decided to use the MRST LO^* parton density functions [198] for mass production of Monte Carlo data. The new PDFs are especially developed for the use in MC event generators with the aim, that the cross sections and the shapes of many differential distributions should become more similar to the next-to-leading order calculation when they are used with leading order matrix elements, such as implemented in PYTHIA and HERWIG. This requires also a modification of phenomenological model parameters (tuning) to describe existing data. Therefore ATLAS has developed new tunes for underlying event (UE) and minimum bias (MB) distributions of the main shower MC generators, PYTHIA and HERWIG with the aim to constrain the model predictions as much as possible by adding the most recent data and new theoretical developments to the tuning effort [215]. The tunes are based on the physics models and parton distribution functions derived from published datasets. Special studies on the performance of these tunes are presented in the Ref. [215].
For the NLO generator MC@NLO the PDF CTEQ6.6 [216] was used. Again this generator was only running with the tuned HERWIG/JIMMY generators.

4.3. Detector simulation

In order to study the detector response for physics processes, a detailed simulation is needed that carries events from the event generation through to the output in a format which is identical to that of the true detector. The produced variables of the simulation step are later used as an input for the reconstruction, thus the detector simulation is an essential ingredient of the Monte Carlo production and important for the validation and understanding of the detector components and their response. In ATLAS exist several approaches to simulate the detector. In the following two simulations are briefly discussed: A detailed detector simulation called full simulation (FULLSIM) and a simplified simulation referred as fast simulation (ATLFAST) [214].

4.3.1. Full simulation

The ATLAS full detector simulation is based on the GEANT4 particle simulation toolkit, which is integrated into the ATLAS software framework [217–219]. The GEANT 4 software propagates particles (elementary particles and ions, both stable and unstable) through any geometrical arrangement of material and simulates the processes of these particles, founded both theoretically and experimentally, within matter. The software was used together with the ATLAS software to built an accurate model of the geometry and the material of the ATLAS detector to describe the reactions of all generated particles in the detector. This includes all interactions with the material e.g. ionisation, bremsstrahlung or multiple scattering as well as the simulation of the measured energies and the electronics used for the read-out. During the commissioning this "ideal" detector geometry underwent continuous updates to better match to the real ATLAS detector geometry, including a more detailed description of the magnetic field and the detector material as well as alignment and placement shifts and material distortions. The configuration and layout of the detector can be set at run time by the user. Several additional options are also available e.g. the non-uniform magnet field can be enabled. During the simulation process several cuts and transformations can be made to the event, e.g. the vertex position can be smeared. The output of the simulation process is a file, containing some metadata describing the configuration of the simulation during the run, all requested truth information of the particles, and a collection of hits for each subdetector. The hits are records of energy deposition, with position and time, during the simulation, that are converted to "digits" during the digitalisation.
Because of the complicated detector geometry and detailed physics description used, the simulation step is very CPU intensive and particularly slow, taking up to $\sim$ 30 minutes per event. Most of the full simulation time is thereby spent for simulating particles traversing the calorimetry or for simulating electromagnetic particles [214].

4.3.2. Fast simulation

The detailed detector description is very useful to study e.g. detector effects in detail, but many physics studies require a large amount of statistics that cannot be achieved with the full simulation within a short time period. For this ATLAS has developed two fast simulation packages to

complement the GEANT4 simulation and facilitate the production of large signal and background event samples.

ATLFAST2

The ATLFAST2 package [220–222] simulates the input to the standard ATHENA reconstruction algorithms to mimic the full simulation. It is developed to provide a fast simulation with large statistics to supplement full simulation. The simulation package is still in development and consists of several components and options to run. It includes for example the fast track simulation package FATRAS [223] (Fast ATLAS Tracking Simulation) to simulate tracks in the inner detector, a fast calorimeter simulation (FastCaloSim) [224, 225] and a muon parametrisation can be applied. Optionally, any subdetector can be simulated with the full GEANT4 simulation to provide the higher level of accuracy without the same CPU time consumption as the full simulation of the entire detector. Depending on the packages used, a factor of 10 over the full simulation time can be achieved.
Because ATLFAST2 is running the standard reconstruction, it is possible to work with a combination of full and ATLFAST2 simulated events without modifying any analysis code. The reconstructed output includes all the properties associated with a reconstructed object e.g. the energies in the calorimeter cells. The FastCaloSim package provides a parametrised simulation of the particle energy response and energy distribution in the calorimeter to reduce the calorimeter simulation. The parametrisation is based on GEANT4 simulations of photons and charged pions in a fine grid of simulated particle energies and directions. As input for its simulation, it uses the truth information of all interacting particles at the end of the inner detector volume.

ATLFAST1

ATLFAST1 [221, 226, 227] is a ATLAS Fast Simulation package, that replaces the full detector simulation and reconstruction phases of the Monte Carlo reconstruction chain and tries to simulate the final physics objects after all simulation, reconstruction and identification steps. It has been developed for physics parameter space scans and studies that require very large statistics, but do not require the level of detail contained in the full simulation [214, 226]. For example ATLFAST1 was used for the production of some large SUSY signal grids in this thesis. Studies requiring detector-based quantities, such as calorimeter sampling energies and track hit positions are not possible with this fast simulation. ATLFAST1 only provides momenta for the reconstructed objects without any detailed simulation of efficiencies and fakes, with two exceptions: fake b-jets and taus are simulated.
In order to provide physics objects similar to those after reconstruction, smears the fast simulation the generated MC truth objects directly with the detector resolutions measured in full simulation studies and corrects it for reconstruction and identification efficiencies. The detailed detector simulation is in this way replaced with the parameterisations of the desired detector and reconstruction effects.
The software package can run using any generator that works in ATHENA. While the speed at

which ATLFAST runs, depends on many factors (available CPU, output file format, input file format, complexity of physics channel, etc.), a factor of 1000 speed increase over full simulation[4] is achieved with sufficient detail for many general studies.

ATLFAST1 correction

Due to the simplified detector simulation in ATLFAST1, there usually exist residual differences between ATLFAST1 and the full simulation. The general expectation is that for all SUSY processes the differences between ATLFAST1 and FULLSIM (ATLFAST2) are independent of the process. This allows to calculate so called "transfer functions" and to apply the same corrections to all fast simulated processes. The transfer functions are used to simulate the behaviour of the full detector simulation for SUSY points where no full simulation data was available, in order to ensure that the performance of the reconstructed physics objects in ATLFAST1 samples correctly matched the performance observed using full simulation samples.
For the 14 TeV MC studies full simulated background samples have been used. Electron efficiency corrections have been applied by comparing ATLFAST1 simulations with the corresponding FULLSIM distributions. For the studies at a centre-of-mass energy of 10 TeV most background samples are ATLFAST2 simulated samples. Hence all ATLFAST1 samples are corrected such that they reproduce the results obtained with the ATLFAST2 simulation.

Electron correction ATLFAST1 tends to reconstruct electrons more efficiently than the full simulation or ATLFAST2. Thus the electron identification was corrected in all ATLFAST1 samples (for 14 TeV and 10 TeV) in order to reproduce results obtained with the more detailed simulation (FULLSIM/ATLFAST2).
The main idea of the transfer function is to veto electrons in order to get a lower efficiency. For this, both the efficiencies of the full and the fast simulation are calculated as 2D functions of p_T and η. Correction factor are determined by calculating:

$$f_{\text{corr}}(p_T,\eta) = \frac{\varepsilon_{\text{FULL}}(p_T,\eta)}{\varepsilon_{\text{FAST}}(p_T,\eta)}, \tag{4.1}$$

with $\varepsilon_{\text{FULL}}$ the selection efficiencies of the full simulation (ATLFAST2) and $\varepsilon_{\text{FAST}}$ the efficiencies of the ATLFAST1 simulation.
The correction is applied by calculating a random number "a" between 0 and 1 for every object. If $a > f_{\text{corr}}(p_T,\eta)$ and $f_{\text{corr}}(p_T,\eta) < 1$ the electron was removed in the fast simulated sample.
For the correction of the p_T spectrum of the electrons, the relative resolution was calculated:

$$\frac{p_{T,\text{FAST}} - p_{T,\text{FULL}}}{p_{T,\text{FULL}}} \tag{4.2}$$

with $p_{T,\text{FAST}}$ the transverse momenta of the simulated ATLFAST1 object and $p_{T,\text{FULL}}$ the transverse momenta of the corresponding object in the full (ATLFAST2) simulation. In order to determine a correction factor, the spectra of the relative resolution were constructed in bins of p_T

[4] To produce one event takes in average less than 1/10 of a second.

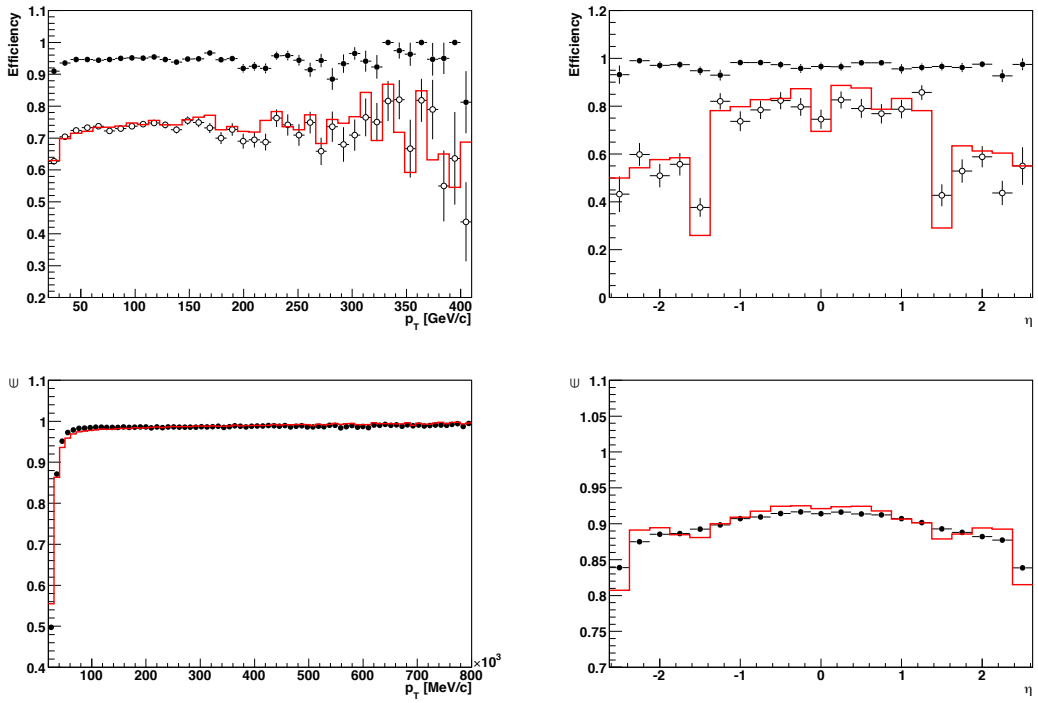

Figure 4.2: Upper plots: Electron efficiencies as a function of p_T for the SU3 sample (left plot) and as a function of η for the process Z $\rightarrow$ ee + 1 jet (right plot); red line: FULLSIM; black dots: uncorrected ATLFAST1; open dots: corrected ATLFAST1. Bottom plots: Jet efficiencies as a function of p_T (left plot) and as a function of η (right plot) for the SU3 sample; red line: FULLSIM; black dots: corrected ATLFAST1. Figures are taken from the Ref. [104,228].

and η. The PDFs for the final p_T ATLFAST1 correction were obtained by normalising this spectra to 1. The correction was applied by generation a random number "b" according to the PDFs and the p_T of the corrected object is recalculated as:

$$p_{T,\text{corr}} = (1+b) \cdot p_T .$$

Figure 4.2 (top plots) shows the reconstruction efficiency distribution for electrons as a function of p_T for the SUSY signal point SU3 (left plot) and as a function of η for the process $Z \rightarrow \text{ee} + 1\text{jet}$ (right plot) obtained from 14 TeV samples. Three lines are compared: The red lines shows the distribution for the full simulated sample, the black dots the distribution of the uncorrected ATLFAST1 sample and the open dots the fast simulated sample after applying the correction.
For the 10 TeV Monte Carlo samples a similar, but more simplified method with a correction factor determined from the comparison of the p_T distributions from ATLFAST2 and ATLFAST1 simulated samples, was used. The p_T (left plot) and η (right plot) electron distributions for the SUSY signal point SU4 at a centre-of-mass energy of 10 TeV are presented in Figure 4.3 (top plots). The

ATLFAST1 simulated sample (blue dots), the ATLFAST2 simulated sample (black line) and the corrected ATLFAST1 simulated sample (red dots) are compared. Both figures (Figure 4.2 and Figure 4.3) illustrate that the ATLFAST1 samples describes the ATLFAST2/FULLSIM performance more accurately after applying the correction.

Jet correction During the ATLFAST1 simulation of 14 TeV samples the merging-splitting algorithm, which takes care that the reconstructed jets do not overlap, was turned off. As a consequence one truth jet could be reconstructed as several jets sharing the total energy of the truth jet. This effect was corrected by merging ATLFAST1 jets: the four vectors of the reconstructed jets, that are matched to the same truth jet have been added to build one jet. No further efficiency and resolution correction have been applied. Figure 4.2 shows the reconstruction efficiency of the jets for the SUSY signal point SU3 as a function of p_T (left plot) and η (right plot), comparing the full simulation (red line) and the corrected ATLFAST1 simulation (black dots). The merging correction is sufficient to obtain a good agreement of ATLFAST1 and FULLSIM jets.
For the 10TeV samples small changes in the ATLFAST1 package have been applied with the result, that the jet distributions (see Figure 4.3, upper plots) looked very similar for ATLFAST1 (blue dots) and ATLFAST2 (black line) simulation. Therefore no correction was applied.

Muon correction The p_T (left plot) and η (right plot) muon distributions for the SUSY signal point SU4 at a centre-of-mass energy of 10 TeV are presented as an example in Figure 4.3 (bottom plots). The distributions of the ATLFAST1 simulated sample (blue dots) and the distributions of the ATLFAST2 simulated sample (black line) are in agreement, no correction need to be applied. A very similar result was obtained comparing the full simulated and ATLFAST1 simulated muon distributions for the 14 TeV samples.

4.4. Digitisation

The ATLAS digitisation software takes hit output from simulated events: hard scattering signal events, minimum bias events, beam halo events, beam gas events (see Section 2.3.3, and cavern background events and converts it into detector signals e.g. voltage and time: “digits” that are read after by the reconstruction software (see Chapter 5).
During digitisation detector noise is added to the event, e.g. each type of event can be overlaid with “pile-up” (see Section 2.3.3). The first level trigger (see Section 3.4.1), installed in hardware on the real detector, is also simulated, no events are discarded, but each trigger hypothesis is evaluated.

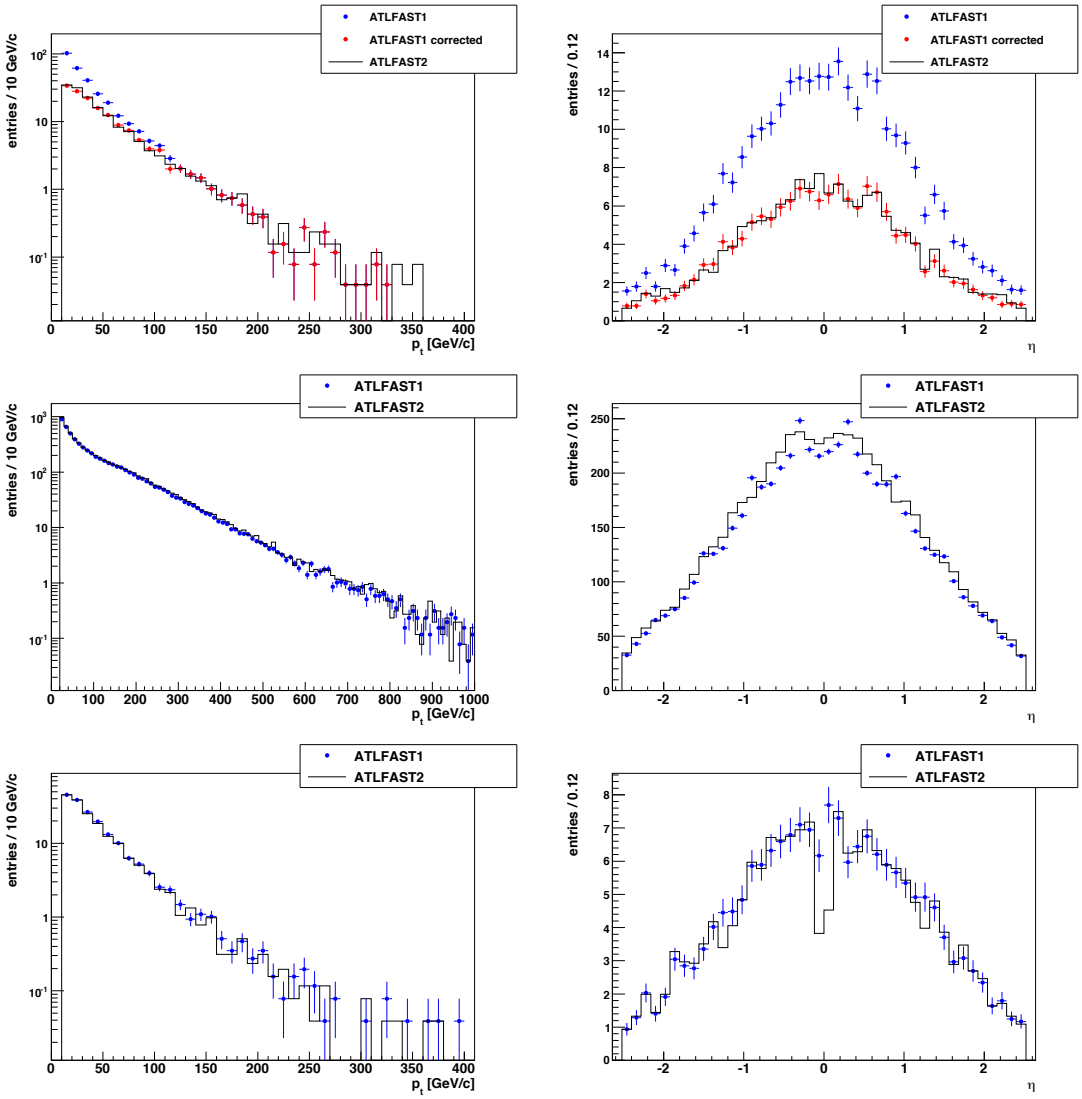

Figure 4.3: The p_T (left plots) and η (right plots) distributions for electrons (upper plots), jets (middle plots) and muons (bottom plots) for a SUSY point SU4 at a centre-of-mass energy of 10 TeV. Shown are the ATLFAST1 (blue dots) and ATLFAST2 simulation (black line) and the effect of the corrections applied for electrons (red dots).

4.5. Monte Carlo samples used in this thesis

In the following the samples used for first studies at centre-of-mass energy of 14 TeV will be referred as "14 TeV MC samples", the sets of MC samples modelling a centre-of-mass energy of 10 TeV will be called "10 TeV MC samples". For the studies at a centre-of-mass energy of $\sqrt{s} = 7$ TeV different MC samples have been used: First Monte Carlo studies have been performed with pdf reweighted 10 TeV MC samples in order to prepare the analyses for the first collision data. These reweighted 10 TeV MC samples are only used for the performed Monte Carlo studies. The third set referred as "7 TeV MC samples" was produced for $\sqrt{s}$ = 7 TeV and is used to compare MC expectations with the measured ATLAS data events.
The results presented in this thesis correspond to an integrated luminosity of $\mathscr{L}$ = 1 fb^{-1} for the $\sqrt{s}$ = 14 TeV studies and to an integrated Luminosity of $\mathscr{L}$ = 200 pb^{-1} for $\sqrt{s}$ = 10 TeV. The MC studies for a centre-of-mass energy of 7 TeV assume an integrated luminosity $\mathscr{L}$ = 0.5 - 2 fb^{-1}.
All simulated samples have been officially produced and validated by the ATLAS production team within the ATHENA frameworks and passed through the GEANT4 detector or the fast simulation. No pile-up or cavern background simulations have been imposed on the SUSY signal or Standard Model events. All used datasets are also free of duplicated events (see Ref. [229] for more details). available, MC generators and tools are taken from the LHC computing grid generator services. Furthermore, a common definition of the particle masses is used among all generators, e.g. for all simulated datasets of SUSY events in the present work a top quark mass m_{top} = 175.0 GeV for the 14 TeV samples and m_{top} = 172.5 GeV for the 10 TeV and 7 TeV samples was used. The Monte Carlo generators were running in the ATHENA software release 12 for 14 TeV studies, ATHENA software release 14 for 10 TeV studies and ATHENA software release 15 for 7 TeV studies.

4.5.1. Standard Model background processes

The Standard Model background processes most relevant for the SUSY studies are $t\bar{t}$, W + jets, Z + jets, single top, diboson and QCD jet production processes. Different MC generators are used for the different processes, in an attempt to estimate a reliable SM background. All used SM background and their corresponding effective cross sections[5] for the different centre-of-mass energies are listed in the Appendix in Section D (see Table D.1 for 14 TeV samples, Table D.2 for 10 TeV samples, Table D.3 for 7 TeV samples). For each dataset the ID number, the event generator, the cross section, the number of generated events and the integrated luminosity are listed. A short summary is given in Table 4.1 in the following.
The $\sqrt{s}$ = 14 TeV and 7 TeV Standard Model MC samples are all produced with the full detector simulation (FULLSIM), while for a centre-of-mass energy at $\sqrt{s}$ = 10 TeV only single top, Diboson samples and the leptonic top sample are full simulated, the remaining samples were simulated with the fast simulation (ATLFAST2). With the exception of the J4, J5 and J6 samples, the number of available events in Standard Model background dataset corresponds to about or higher than 1fb^{-1} of data for $\sqrt{s}$ = 14 TeV, more than 1nb^{-1} for 10 TeV and more than 1nb^{-1} for 7 TeV.

[5] The effective cross section is calculated as: $\sigma_{eff} = \sigma \times EF_{efficiency}$, if a filter with an efficiency $EF_{efficiency}$ is applied on generator level.

physics process	generator/simulation for $\sqrt{s}$ = 14 TeV	generator/simulation for $\sqrt{s}$ = 10 TeV	generator/simulation for $\sqrt{s}$ = 7 TeV
top pair	MC@NLO+JIMMY FULLSIM	MC@NLO+JIMMY FULLSIM –leptonic top ATLFAST2 –hadronic top	MC@NLO+JIMMY FULLSIM
single top	-	ACERMC FULLSIM	-
W+jet	ALPGEN+HERWIG PYTHIA (for 2, 3 jet) FULLSIM	ALPGEN+HERWIG ATLFAST2	ALPGEN+HERWIG FULLSIM
Z +jet	ALPGEN+HERWIG PYTHIA (for 2, 3 jet) FULLSIM	ALPGEN+HERWIG ATLFAST2	ALPGEN+HERWIG FULLSIM
QCD jet	PYTHIA FULLSIM	ALPGEN ATLFAST2	PYTHIA FULLSIM
Diboson	HERWIG FULLSIM	MC@NLO (for WZ, ZZ) gg2WW+JIMMY (for WW) FULLSIM	-

Table 4.1: Summary of the Standard Model background samples for the centre-of-mass energies $\sqrt{s}$ = 7, 10, 14 TeV. The event generator and the simulation are listed.

Single top and top pair production The $t\bar{t}$ process is a dominant SM background for most of the studied SUSY channels. The `MC@NLO` generator, including full NLO QCD corrections has been used to simulate the hard process. Parton showering and fragmentation were simulated by the `HERWIG` event generator, `JIMMY` generated the underlying event. The fully hadronic decay ("hadronic $t\bar{t}$") mode was separated from the semi-leptonic and full leptonic (di-leptonic) decay mode ("leptonic $t\bar{t}$"). The division is performed with an event filter at generator level. The $t\bar{t}$ cross sections were normalised to the next-to-leading order (NLO) and next-to-leading-log (NLL) [186] resummation.
In addition to the $t\bar{t}$ process for $\sqrt{s}$ =10 TeV, single top production was simulated with the `ACERMC` generator.

W/Z + jets production As the SUSY event selection often requires many jets in the final state, it is particularly important to model multiparton final states, in order to simulate the kinematics of the additional jets as accurately as possible. For this reason, the `ALPGEN` Monte Carlo generator

has been chosen for the production of $W^{\pm}$ or Z^0 bosons in association with jets for all studies (at 14, 10 and 7TeV). At leading order in QCD and electroweak interactions, it calculates the exact matrix elements of multiparton hard processes in hadronic collisions. Samples are generated exclusively for a fixed number of jets by applying parton - jet MLM matching (see Section 4.2.1) and are later added to one inclusive sample. Jet production was generated for up to five-parton matrix elements. The generator is interfaced to HERWIG for showering and fragmentation processes and JIMMY generating the underlying event.
For the **14 TeV samples**, to increase the statistics an event filter at generation level was applied, requiring: at least four jets, each with jet transverse momentum $p_T > 40$ GeV and the hardest jet with a transverse momentum $p_T(\text{jet}_1)$ above 80 GeV and missing transverse energy E_T^{miss} above 80 GeV. These filters reflect the minimum requests for the standard ATLAS SUSY searches at 14 TeV. The LO cross sections are normalised to NNLO calculations by applying a k-factor[6] of 1.15 for W and of 1.27 for the Z samples calculated with the program FEWZ [230, 231]. The total cross section for the samples is given by the sum over all parton multiplicities. The production cross section σ, the event filter efficiency $EF_{efficiency}$ and parton - jet matching efficiency $MLM_{efficiency}$ are listed in Ref. [228].
As a result of the generator filters, ALPGEN samples were not available for jet multiplicities as low as two. Therefore for the 2- and 3-jet analyses PYTHIA samples with multijet events being approximated by parton showers, were used instead.
For the **10 TeV samples** the LO cross sections as detailed in Table D.2 and Table D.3 are used. The overall normalisations of the $W^{\pm} \to l\nu$ and $Z^0 \to \nu\nu$ processes at **7 TeV** are based on next-to-next-to-leading order (NNLO) QCD corrections estimated from FEWZ program. The same normalisation scaling factor has been applied for all ALPGEN parton multiplicities.

Diboson Diboson processes have a small cross section with respect to the previously discussed background processes. Their contribution is almost negligible as they are strongly suppressed by the typical SUSY analysis cuts requiring a large number of jets with high transverse momenta and cut on the missing transverse energy. Nevertheless these backgrounds can contribute to the multi-leptons search channels (for high luminosities).
For the studies at **14 TeV** the WW, ZZ and WZ processes were generated at leading order with the HERWIG MC generator. The samples are normalised to NLO cross sections obtained with the MCFM program [232, 233]. An event filter at generation level was applied, requiring at least one electron or muon with a transverse momentum of about 10 GeV and within $|\eta| < 2.8$.
For **10 TeV** ZZ, WW and WZ are simulated with the MC@NLO generator, whereas the gg2WW [201] generator was used for gluon induced WW production. The samples are normalised to LO cross section.
Due to the small cross sections and the relative small luminosity, no Dibosons MC samples are used for the comparisons with real data at $\sqrt{s}$ **= 7 TeV**.

[6] Since the calculation of NLO cross sections can take rather long, NLO (or NNLO) cross sections are often approximated by multiplying the LO cross section with a k-factor. The k-factor is defined as $k = \frac{\sigma_{(N)NLO}}{\sigma_{LO}}$.

QCD jet production Multijet production via QCD processes is one of the dominant processes at the LHC and an important background in SUSY searches with jets, E_T^{miss} and no leptons in the final state. Even if NLO corrections are partially known, the uncertainties from missing higher-order corrections can remain large. Therefore only LO cross sections have been used. To cover the uncertainties, large errors were assigned.
For similar reasons to the W/Z + jets generation, the use of multiparton generators is desirable for the QCD production. ALPGEN samples are generally regarded to be the most appropriate choice for the background prediction in SUSY studies, but it is also important to have samples with large statistics. For practical reasons, it was not always possible to generate ALPGEN QCD samples with sufficient statistics within a short time scale. Therefore for the studies at **14 TeV** and **7 TeV** PYTHIA samples have been used, while for **10 TeV** a large set of ALPGEN samples was available.
A large sample of inclusive jet events has been generated with PYTHIA. The hard interaction of the event is modelled via $2 \rightarrow 2$ matrix elements at leading order in the strong coupling constant. The samples are produced in p_T slices (denoted as J1, J2, etc.) of the hard-scattering. The production of top quarks is not included in this sample and instead a dedicated sample has been produced (see above). Additional initial and final state radiation are generated by a parton shower algorithm in the leading logarithm approximation. In order to increase the statistics for the **14 TeV samples**, especially for the high p_T jets that are visible in the interesting region of the SUSY analysis, a filter at generation level was applied, requiring at least two jets with the hardest transverse momentum $p_T(\text{jet}_1)$ above 80 GeV and a second jet $p_T(\text{jet}_2)$ with transverse momentum above 40 GeV. The missing transverse energy E_T^{miss} should be above 100 GeV.
For **10 TeV** ALPGEN + HERWIG samples were used to generate the QCD processes. The generation was splitted according to the type of quark produced (b-quarks or light quarks), the number of partons in the final state and the p_T of the leading parton. In order to reduce the size of the final samples, events where the p_T of the leading parton was less than 140 GeV were filtered at truth level and kept when passing one of the following requirements :
at least one truth jet reconstructed with a cone algorithm (cone size of R = 0.4, see Section 5.2) with $p_T > 120$ GeV and $|\eta| < 2.8$ and at least one truth jet with $p_T > 60$ GeV plus a minimum of two additional truth jets with $p_T > 25$ GeV. After the event generation the samples are produced using ATLFAST2.
For the **7 TeV** PYTHIA samples the modified leading order distributions of MRST 2007 LO* [198] parton density functions were used. Addionally to this, the PYTHIA QCD prediction has been compared to a QCD prediction calculated with the ALPGEN generator. The ALPGEN samples used for this comparison are generated with up to five-parton matrix elements for the light quarks and up to four-parton matrix elements for *b*-quark production. After scaling the overall normalisation of the prediction to the data luminosity in the QCD control region, the remaining differences between PYTHIA and ALPGEN are smaller than the current total experimental uncertainties (see Figure 7.4 in Section 7.5.3).

Reweighting of the 10 TeV samples to $\sqrt{s} = 7$ TeV

For the Monte Carlo studies at $\sqrt{s} = 7$ TeV reweighted 10 TeV samples are used in order to update the 10 TeV results (see Section 9 and Ref. [234, 235]). For this the 10 TeV Standard Model and SUSY signal samples have been corrected using the LHAPDF software package [210], which calculates for every event an event "weight". The applied procedure is discussed in the Appendix in Section E.4.

4.5.2. SUSY models

SUSY benchmark points

In order to study "typical" experimental signatures of SUSY models and to investigate the achievable experimental precisions and the sensitivities of the studied SUSY analyses, theoretically well motivated parameters of certain SUSY-breaking scenarios are chosen and define so-called "benchmark points". These benchmark scenarios should account for a wide variety of SUSY phenomenologies [236].
ATLAS has defined several SUSY "benchmark points" for example in the mSUGRA parameter space[7] (see Section 2.2.9), that provide a wide range of possible decay topologies. For all selected points the predicted cosmological relic density of the neutralinos was required to be consistent with the observed cold dark matter density. In the mSUGRA parameter space with $\text{sign}(\mu) > 0$ this can be only realised in special reduced regions, where the annihilation of the neutralinos is enhanced e.g. through mass relationships or in a region where the lightest neutralino has a large higgsino component. For the selected benchmark points the gluino mass is less than 1 TeV, $M(\tilde{g})/M(\tilde{\chi}_1^0) =$ 6-8 and for nearly all points the squark and gluino masses are comparable (except for the point SU2). The decay signatures of the benchmark points are relatively general among different SUSY models and are not specific for the selected mSUGRA model. This makes it possible to use the SUSY benchmark points for different SUSY analyses. A list of all ATLAS SUSY benchmark points as well as their SUSY particle masses can be found in the Appendix in the Section A. In this thesis most often the two ATLAS SUSY point SU3 and SU4 are presented in the distributions as SUSY signal. The SUSY point SU4 was used in the kinematic distributions of first LHC collision data and in the MC studies at 10 TeV and 7 TeV to illustrate the prediction of a low mass point close to the Tevatron limits [237, 238]. The two benchmark points are defined in terms of the mSUGRA parameters at the GUT scale:

SU3 $m_0 = 100$ GeV, $m_{1/2} = 300$ GeV, $A_0 = -300$ GeV, $\tan\beta = 6$, $\text{sign}(\mu) > 0$
Bulk region: relatively light sleptons enhance LSP annihilation
SU4 $m_0 = 200$ GeV, $m_{1/2} = 160$ GeV, $A_0 = -400$ GeV, $\tan\beta = 10$, $\text{sign}(\mu) > 0$
Low mass point close to the Tevatron bound.

All SUSY particles are produced with the generator ISAJET (see Section 4.2.1) in combination with the HERWIG/HERWIG++ MC generator. No event filter at generator level was applied. Ta-

[7] ATLAS has also defined benchmark points in AMSB and GMSB parameter space, not discussed in this thesis.

ble 4.2 summarises for the SUSY points SU3 and SU4 the used generators, number of generated events as well as the cross sections at the different centre-of-mass energies. For a centre-of-mass energy of 14 TeV the top quark mass was set to 175.0 GeV, for 10 TeV and 7 TeV studies m_{top} = 172.5 GeV. The inclusive SUSY production cross section is calculated at leading order by HERWIG/HERWIG++ and by PROSPINO at next-to-leading order[8]. All generated SUSY samples include always all decay channels which are possible for the selected SUSY model.

process	$\sqrt{s}$ [GeV]	**generator**	**simulation**	N_{events}	σ^{LO} [pb]	σ^{NLO} [pb]
SU3	14	ISAJET 7.75 HERWIG 6.5	FULLSIM	500 K	18.6	27.7
SU4	14	ISAJET 7.75 HERWIG 6.5	FULLSIM	200 K	262.0	402.3
SU4	10	ISAJET 7.75 HERWIG 6.5	ATLFAST2	53 K	107.6	164.6
SU4 point	7 (data studies)	ISAJET 7.75 HERWIG++	FULLSIM	50 K	42.3	59.9

Table 4.2: Summary of the used generators, the number of generated events, the cross sections and the top quark mass for the SUSY mSUGRA benchmark points SU3 and SU4 at $\sqrt{s}$ = 14, 10 and 7 TeV.

SUSY signal grids

It is impossible to study Supersymmetry in general. Even a model with the minimal particle content (MSSM) has many free parameters. In order to have a better grasp of the situation less model dependent discovery strategies for SUSY signals are developed. To reduce prejudice and to minimise the dependence on model assumptions of the selected SUSY benchmark points, the analyses are not optimised for one specific SUSY model point (benchmark point). Several different so called "grids" of SUSY points are generated. A "SUSY grid" is a set of points generated in the parameter phase space of a specific SUSY model.
In the last years different SUSY grids have been generated for the validation and optimisation of the search strategies. Because of these large number of free parameters, first studies are performed in more constrained frameworks making assumptions about the breaking mechanism of Supersymmetry (studies at 14 TeV), later various different MSSM SUSY samples with a higher number of variable free parameters are used to determine the ATLAS discovery potential (studies

[8]For the 10 TeV SU4 SUSY signal no NLO cross section was used.

at 10 TeV). In the following, the different SUSY samples are described. All studied scenarios assume that the R-parity quantum number (see Chapter 2) is conserved. Only SUSY signal models with a neutralino as LSP and SUSY mass scales within the reach of early LHC running are considered. Since there is no unique model of SUSY-breaking, all these models should be viewed only as possible patterns of LHC signatures, not as complete theories.

It should be noted that due to the large number of generated SUSY signal points (> 1000 points) only LO cross sections have been used for the studied SUSY signal grids. However, LO and the NLO order cross sections are compared for some of these grid points (see Section B) and have shown a satisfying agreement.

SUSY signal grids for the 14 TeV studies

Six different SUSY grids have been produced for different regions of the SUSY parameter space and using different generators. All models emanates from the MSSM, using GUT assumptions to limit the number of parameters:

- Minimal SUGRA with $\tan\beta = 10$; equidistant spacing in m_0 and $m_{1/2}$
- Minimal SUGRA with $\tan\beta = 50$; equidistant spacing in m_0 and $m_{1/2}$
- Minimal SUGRA with random sampling. In the random sampling procedure constrains from experimental measurements and dark matter bounds are taking into account.
- Non-universal Higgs masses (NUHM)
- Gauge-Mediated Supersymmetry Breaking (GMSB)
- Anomaly-Mediated Supersymmetry Breaking (AMSB)

For each SUSY signal point the mass spectrum and the decay modes of the SUSY particles were generated with ISAJET version 7.75 (m_{top} = 175.0 GeV) and read into HERWIG that produced the proton-proton scattering events. The ATLAS detector response was simulated using the fast ATLAS simulation ATLFAST1 with corrections (see Section 4.3.2) to match the efficiencies and resolutions of the full ATLAS simulation.

mSUGRA fixed grids with $\tan\beta = 10$ and $\tan\beta = 50$

Two 25×25 rectangular mSUGRA grids with fixed mSUGRA parameters $A_0 = 0$, $\tan\beta$ = 10 (50) are produced. The physics predicted by the mSUGRA model at large $\tan\beta$ is substantially different from the one expected at lower values. Large $\tan\beta$ increases the mixing of $\tilde{b}_{L,R}$ and $\tilde{\tau}_{L,R}$, leading to enhanced b and τ production.
For the $\tan\beta = 10$ grid the parameter sign$(\mu) > 0$ and the parameter m_0 is varied from 60 GeV to 2940 GeV in step size of 120 GeV, and $m_{1/2}$ from 30 GeV to 1470 GeV in 25 steps of 60 GeV.

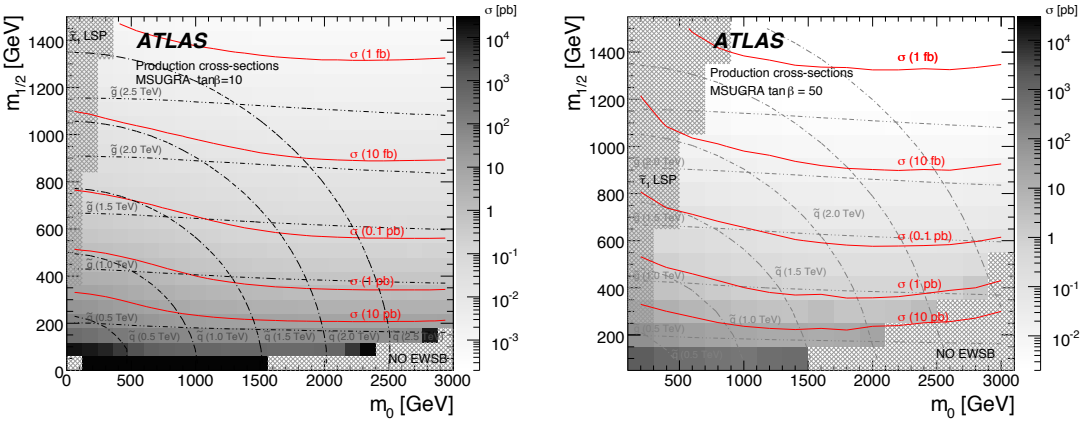

Figure 4.4: Leading order cross sections (in picobarn) for the mSUGRA grid with $A_0 = 0, \tan\beta = 10$ and $\text{sign}(\mu) > 0$ (left plot) and with $A_0 = 0,\ \tan\beta = 50$ and $\text{sign}(\mu) < 0$ (right plot) in the m_0-$m_{1/2}$ parameter space. The dashed regions are theoretically not viable due to a lack of electroweak symmetry breaking or a charged LSP. Grey lines illustrate the gluino and squark masses.

From the 625 possible grid points only for 600 a spectrum could be successfully generated with ISAJET, every point with 20 k events. For the other 25 points the spectrum generation failed due to theoretical limits e.g. production of "tachyonic particles" or "no Electroweak (EW) symmetry breaking".
The $\tan\beta = 50$ grid has been generated with $\text{sign}(\mu) < 0$, m_0 is ranging from 200 to 3000 GeV in steps of 200 GeV and with $m_{1/2}$ is ranging from 100 to 1500 GeV in steps of 100 GeV. The points at low $m_{1/2}$ (m_0) and relatively large m_0 ($m_{1/2}$) are theoretically excluded. Figure 4.4 shows the leading order cross section, as calculated by HERWIG in picobarn (grey background level and red lines) for the $\tan\beta = 10$ (left plot) and the $\tan\beta = 50$ (right plot) grid. The hashed grey regions are not theoretically allowed due to lack of electroweak symmetry breaking or the production of a charged LSP. The grey dashed lines illustrate the squark (with stop and sbottom mass) and gluino masses. The cross sections reflect the squark and gluino masses and are between $2{\cdot}10^{-3}$ and $2{\cdot}10^{4}$ pb.

mSUGRA random grid with dark-matter constraints

In order to include dark matter and constrains from collider experiments two limited regions in the mSUGRA parameter space were sampled:

Both regions are found in Ref. [239] to have a large probability to agree with current experimental data. The first region was set to the 68% probability interval of the mSUGRA parameters, the second sample was selected with relatively high probability (95%) and with relatively low squark and gluino masses, which lead to higher cross sections of about 0.1 - 10^4 pb. In both regions

region 1:		**region 2:**	
m_0	0-2 TeV	m_0	< 0.4 TeV
$m_{1/2}$	0.5-1.3 TeV	$m_{1/2}$	0.5-1.0 TeV
A_0	-0.34-2.4 TeV	A_0	$-2.5 - 2.5$ TeV
tan β	39-55	tan β	5-38.5

four mSUGRA parameters were chosen randomly (with sign$(\mu) > 0$) for each generated SUSY point. The mass spectra, mixings and branching ratios of all supersymmetric particles are determinded using ISASUGRA/ISAJET 7.75 together with the branching ratios $BR(b \to \mu^+\mu^-)$ and $BR(b \to s\gamma)$ and the anomalous magnetic momentum of the muon $(g_\mu - 2)$. In parallel, the relic density was evaluated using ISARED [240]. The derived values have been compared with experimental constraints e.g. from LEP, Tevatron and cosmological observations (WMAP) and only points with acceptable values have been selected[9]. All selected points satisfy the LEP Higgs mass limit of about 114 GeV [33]; the WMAP total dark matter limit, $\Omega h^2 < 0.14$ [241]; within 3σ the branching ratio limits for $BR(b \to s\gamma)$ [242], within 3σ the limits for $BR(B_s \to \mu^+\mu^-)$ [243]; and within 3σ of the muon anomalous magnetic moment measurement a_μ [244–246]. About 180 point have been selected and are generated with 5000 events per point. Figure 4.5 shows the selected points in the Ωh^2-m_0 plane (left plot) and in the Ωh^2-$m_{1/2}$ parameter space (right plot). The cross section is between $4 \cdot 10^{-4}$ and $8 \cdot 10^4$ pb.

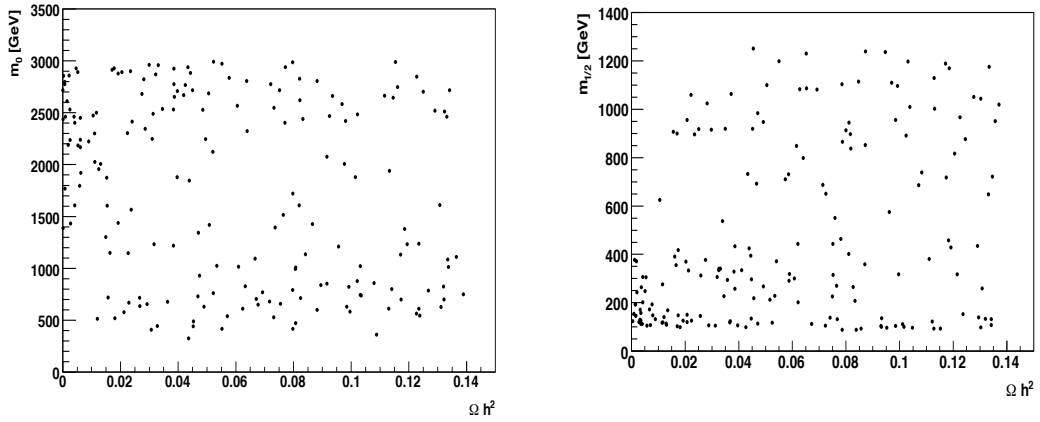

Figure 4.5: The mSUGRA points of the dark-matter constraint grid in the Ωh^2-m_0 and Ωh^2-$m_{1/2}$ parameter space.

[9] It should be noted that the constraints of the year 2006/2007 have been used. They are looser than the actual limits discussed in Section 6.3.

NUHM

In the constrained minimal Supersymmetry Standard Model (CMSSM) (see Section 2.2.8) like e.g. the mSUGRA model all soft breaking scalar masses are set to be universal at the GUT scale. The non-universal Higgs masses (NUHM) model [90] is similar to the mSUGRA model, but does not assume that the Higgs masses unify with the squark and slepton ones at the GUT scale. Hence it generalises the CMSSM model by letting the Higgs masses be non-universal. This allows more gaugino/Higgsino mixing at the weak scale and so relaxes the mSUGRA dark matter constraints. One can choose the Higgs mixing parameter μ and the pseudoscalar Higgs mass m_{A^0} as free parameter. The scan uses a step size of 100 GeV in both m_0 and $m_{1/2}$, varies m_0 between 100 GeV and 900 GeV and $m_{1/2}$ between 150 and 950 GeV. For each point the values of μ and m_A^0 at the weak scale are adjusted to give acceptable cold dark matter. About 72 points with 5000 events per point and a cross section between $7 \cdot 10^{-2}$ and 375 pb have been generated.

GMSB

Gauge Mediated Supersymmetry Breaking (GMSB) [247] models provide a possible mechanism to mediate supersymmetry to the visible sector via gauge fields (see Section 2.2.8). It is described by 5 + 1 parameters:

$$M_{\text{mess}} \ , \ \Lambda \ , \ N_{\text{mess}} \ , \ C_{\text{grav}} \ , \ \tan\beta \ , \ \text{sign} \ \mu$$

Here M_{mess} is a mass scale of the messenger fields, Λ is the scale of SUSY breaking, N_{mess} is the number of $SU(5)$ messenger multiplets, and $\tan\beta$ is the usual ratio of vacuum expectation values. C_{grav} is the gravitino mass factor in $m_{3/2} = C_{\text{grav}}(\ \Lambda M_{\text{mess}}/\sqrt{3}M_{\text{Pl}})$.

Table 4.3: GMSB parameters varied for the 14 TeV grid.

Λ	$\tan\beta$	M_{mess}	N_{mess}	C_{grav}	sign μ
10-80 by step 5TeV	5-40 by step 5	500 TeV	5	1	> 0

The phenomenology of the GMSB models is determined by the next lightest SUSY particle and by its lifetime to decay. The selected models under study only consider $N_{\text{mess}} = 5$ and $C_{\text{grav}} = 1$, giving a slepton NLSP decaying promptly. The grid parameters are given in Table 4.3. The main difference from mSUGRA at the point of final states is that event fraction associated with di-leptons is large and E_T^{miss} is relatively small. The SUSY mass scale is dominantly determined by Λ and the gluino is always slightly heavier than squarks, because of the choice of N_{mess}. About 116 points with 5000 events per point and a cross section between $1 \cdot 10^{-2}$ and 370 pb have been generated.

AMSB

In Anomaly Mediated Supersymmetry Breaking (AMSB) [87–89] (see Section 2.2.8), SUSY breaking is taking place on another brane different from our 3-brane world and is transmitted to the observable sector via the super Weyl anomaly. The minimal AMSB model is very predictive and expressed by 3 + 1 parameters,

$$m_{3/2}\ ,\ m_0\ ,\ \tan\beta\ ,\ \text{sign}\ \mu$$

The parameter $m_{3/2}$ is the gravitino mass and the other parameters are already explained in the previous sections. Only models with $\tilde{\chi}_1^0$ LSP case with $\Delta M(\tilde{\chi}_1^\pm - \tilde{\chi}_1^0) > m_\pi$ will be studied. Since $\tilde{\chi}_1^0$ is wino-like, the $\tilde{\chi}_1^0$ mainly comes from the lightest chargino associated with a soft charged pion.
The minimal AMSB parameter space scan is performed on a $m_{3/2}$-m_0 plane with $m_{3/2}$ varied from 10 to 150 TeV in steps of 10 TeV, m_0 from 100 to 3700 GeV in steps of 200 GeV. For the studies 557 AMSB model points with 5000 events per point and a cross section between $1 \cdot 10^{-6}$ and 1900 pb are generated.

SUSY signal grids for the 10 TeV studies

In the following the SUSY signal grids - the mSUGRA grids and the phenomenological MSSM (pMSSM) [82] grids (see Section 2.2.7) that are studied in this thesis for a LHC energy scenario of 10 TeV are briefly described.

process	**generator**	**simulation**	$\mathbf{N_{points}}$	$\mathbf{N_{events}}$ per point	**cross section** [pb]
mSUGRA $\tan\beta = 10$	ISAJET 7.75 + HERWIG 6.5	ATLFAST2	76	30000	0.2 - 1900
mSUGRA $\tan\beta = 50$	ISAJET 7.75 + HERWIG 6.5	ATLFAST2	23	30000	0.3 - 6750
pMSSM with constraints	SuSpect 2.34 PYTHIA 6.4	ATLFAST1	159	30000	1.1 - 1000
unconstrained pMSSM	ISAJET 7.79 + HERWIG 6.5	ATLFAST1	220	30000	0.1 - 3400
8 parameter pMSSM	SoftSusy 2.0 + micrOMEGAs2.2 + PYTHIA 6.4	ATLFAST1	935	30000	0.1 - 80

Table 4.4: The generators, the detector simulations, the number of points, the number of events per point and the cross section ranges for the pMSSM grid samples produced at $\sqrt{s}$ = 10 TeV.

The SUSY spectra for the MSUGRA points are generated with ISAJET 7.75, SuSpect or SoftSusy 2.0 (+ micrOMEGAs2.2), produced with HERWIG 6.5 or PYTHIA 6.4 generators and run through the ATLAS detector simulations ATLFAST1 or ATLFAST2. ATLFAST1 has only been used for pMSSM points, while the mSUGRA grid points are simulated with ATLFAST2. Table 4.4 summarises the Monte Carlo generators and detector simulation used for the different samples. The top mass was set to 172.5 GeV for all SUSY signals.
Following the ATLAS policy for parameter scans, one point was processed by the ATLAS production team, while the other points were produced privately. It was shown that the local setup gave identical results to the official production. Technical details concerning the signal grids and lists of LO and NLO cross sections can also be found on the ATLAS wiki pages [248].

mSUGRA grids

In order to cover a large parameter space and to reduce the number of SUSY points mSUGRA grids were made in "radial coordinates", i.e. points along outgoing radial lines in the $(m_0, m_{1/2})$ plane for $\tan\beta = 10$ and 50. The other mSUGRA parameter are set to $A_0 = 0$, $\text{sign}(\mu) > 0$ for all signals. Figure 4.6 shows the HERWIG cross sections for the mSUGRA grids as a function of the minimal susy mass min.$(m_{\tilde{u}}, m_{\tilde{d}}, m_{\tilde{s}}, m_{\tilde{c}}, m_{\tilde{g}})$. The total SUSY signal cross sections was also calculated in next-to-leading order (NLO) using PROSPINO 2.1, the comparison between the LO and the NLO cross sections can be found in the Appendix in Section B. For most of the points good agreement was found between the HERWIG and leading-order PROSPINO cross section predictions.

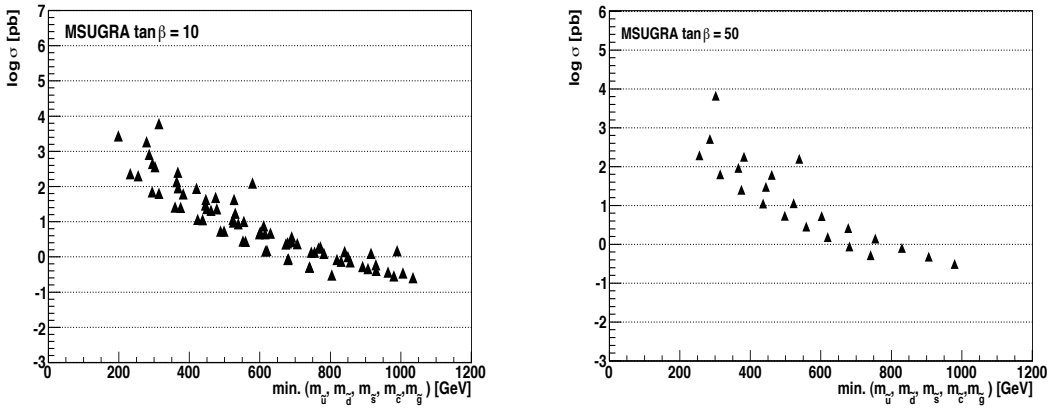

Figure 4.6: The total cross sections as predicted by HERWIG as a function of the minimal susy mass (min. $(m_{\tilde{u}}, m_{\tilde{d}}, m_{\tilde{s}}, m_{\tilde{c}}, m_{\tilde{g}})$) for the mSUGRA grid points with $\tan\beta = 10$ (left plot) and $\tan\beta = 50$ (right plot).

MSSM grids

The objective was to study the discovery potential of ATLAS for SUSY models that were not considered in the previous studies e.g. in the mSUGRA signal studies and to enlarge the range of possible mass patterns by studying different models. In order to cover a larger parameter space for the SUSY signal, different phenomenological MSSM models as a potential signal for the SUSY analyses have been chosen.
The following three samples of pMSSM SUSY signals (grids) are selected :

- **MSSM points fulfilling contraints from experiments**: about 150 pMSSM points which satisfy various experimental bounds from collider experiments at LEP and Tevatron as well as the WMAP dark matter density upper bound and constraints from direct Dark Matter detection searches
- **unconstrained pMSSM grid**: about 220 pMSSM points to scan the pMSSM parameter space without applying any constraints than LEP-1 limits
- **8 parameter pMSSM grid**: about 935 pMSSM points were selected from a model with universal gaugino masses which satisfy various experimental constraints such as those from collider experiments at LEP and also the WMAP Dark Matter density upper bound and bounds from direct Dark Matter detection searches. Only 7 parameters of the 19 free soft SUSY breaking pMSSM parameters and the top mass were varied.

Figure 4.7 shows the total cross section for the unconstrained pMSSM points (top left plot) and the 8 parameter points (top right plot) calculated using HERWIG and PYTHIA, respectively, and the total PYTHIA cross sections for the MSSM points with constraints (bottom plot). The cross sections vary between 0.1 and $\approx$ 3400 pb for the unconstrained pMSSM points, between 1.1 and 100 pb for the MSSM signal grid with constraints and is between 0.1 pb and 80 pb for the 8 parameter grid points. For the pMSSM grid fulfilling constraints from Dark Matter and direct searches (bottom plot) the total SUSY signal cross sections was also calculated in next-to-leading order using PROSPINO. For most of the points good agreement is found. The remaining differences are understood and are due to low mass chargino and neutralino processes. The large HERWIG cross sections for some of the unconstrained pMSSM points (left upper plot in Figure 4.7) are due to direct neutralino and chargino production.
For the unconstrained pMSSM points no NLO cross sections could be calculated with PROSPINO since the points are generated with ISAJET that did not produce "Les-Houches-Accord" files[10]. However the LO cross section distributions are similar to the results of MSSM points with constraints. Hence one could expect the same behaviour for the NLO distributions.

[10]This option was added by the authors in the recent versions.

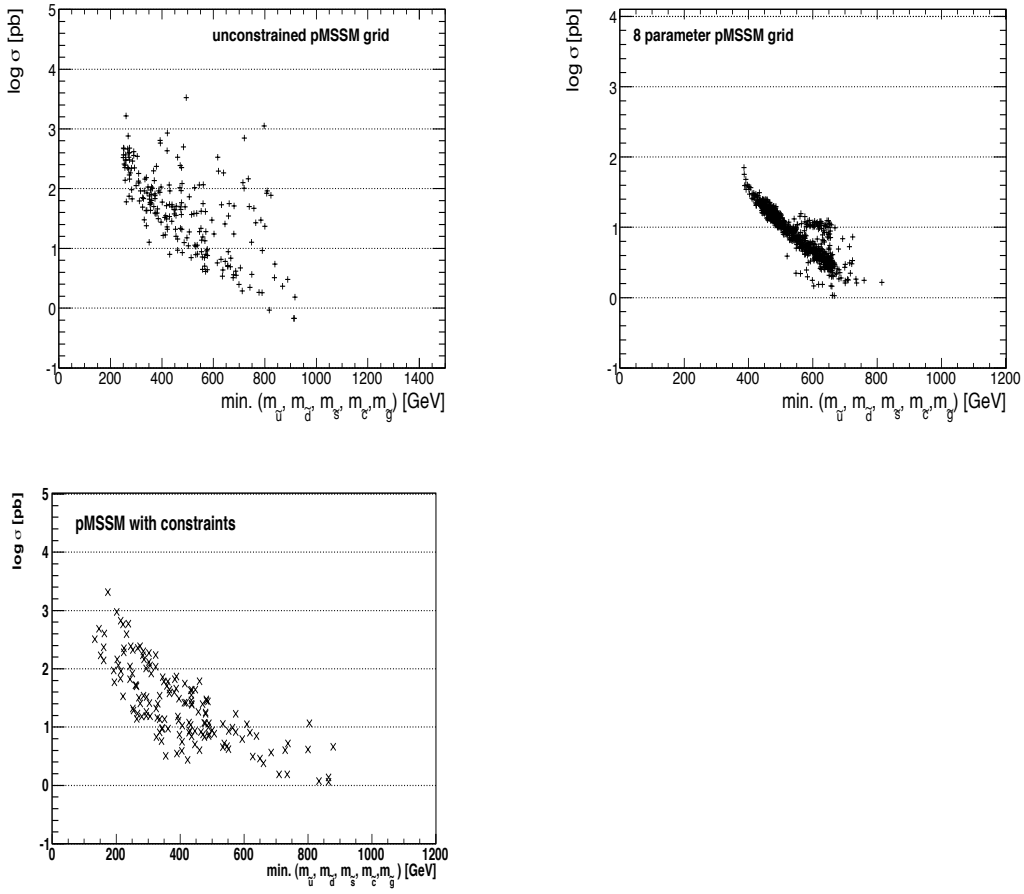

Figure 4.7: The total cross sections as predicted by HERWIG for the unconstrained pMSSM grid points (left upper plot) and as predicted by PYTHIA for the 8 parameter pMSSM grid points (right upper plot) and for the MSSM points with constraints (bottom plot) as a function of the minimal mass of the light squarks and the gluino min. $(m_{\tilde{u}}, m_{\tilde{d}}, m_{\tilde{s}}, m_{\tilde{c}}, m_{\tilde{g}})$.

MSSM points fulfilling constraints from experiments

The grid points are generated in the phenomenological MSSM (pMSSM) parameter space with 19 free soft SUSY breaking parameters. The parameter space was sampled with a flat prior distribution within certain theoretical limits and a mass scale of $< 1\,\text{TeV}$ (so called flat prior grid) as described in Ref. [249]. The parameter range is listed in Table 4.5. Only points are chosen, which satisfy various experimental constraints such as those from collider experiments at LEP and Tevatron and also the WMAP dark matter density upper bound and bounds from direct Dark Matter detection searches (see Section 6.3).

parameter	**lower bound**	**upper bound**
higgsino mass parameter μ	50 GeV	1000 GeV
gaugino mass M_1, M_2	50 GeV	1000 GeV
gaugino mass M_3	100 GeV	1000 GeV
common sfermion mass $m_{\tilde{l}}, m_{\tilde{q}}$	100 GeV	1000 GeV
3rd gen. triliniar coupling A_t, A_b, A_τ	-1000 GeV	1000 GeV
$\tan\beta$	1	50
pseudoscalar Higgs mass m_A^0	43.5 GeV	1000 GeV

Table 4.5: Lower and upper bound of the MSSM parameters varied for the constrained pMSSM grid.

For about 200 randomly selected points events were generated with SUSPECT 2.34 and PYTHIA 6.4 and simulated with the ATLFAST1 detector simulation. About 41 points with a mass difference between the $\tilde{\chi}_1^0$ and $\tilde{\chi}_1^+$ of 300 MeV or less were removed from the production as they lead to longlived charginos, which cause problems in the PYTHIA fragmentation and are not simulated within ATLFAST1. Figure 4.8 shows the mass distributions of the various SUSY particles for the analysed points.

8 parameter pMSSM grid with gaugino mass unification

Using a Markow chain Monte Carlo approach these points are generated in the pMSSM parameter space with eight free soft SUSY breaking parameters [250]. In this model, universality conditions at the GUT scale are imposed on the gaugino sector. The mass of the first and second squark generations are set to be equal to avoid strong flavour-changing neutral current constraints. All input parameters are defined at weak scale. The model assumes common slepton masses and common squark masses for all three generations. The universality of the gaugino masses is assumed at the GUT scale.

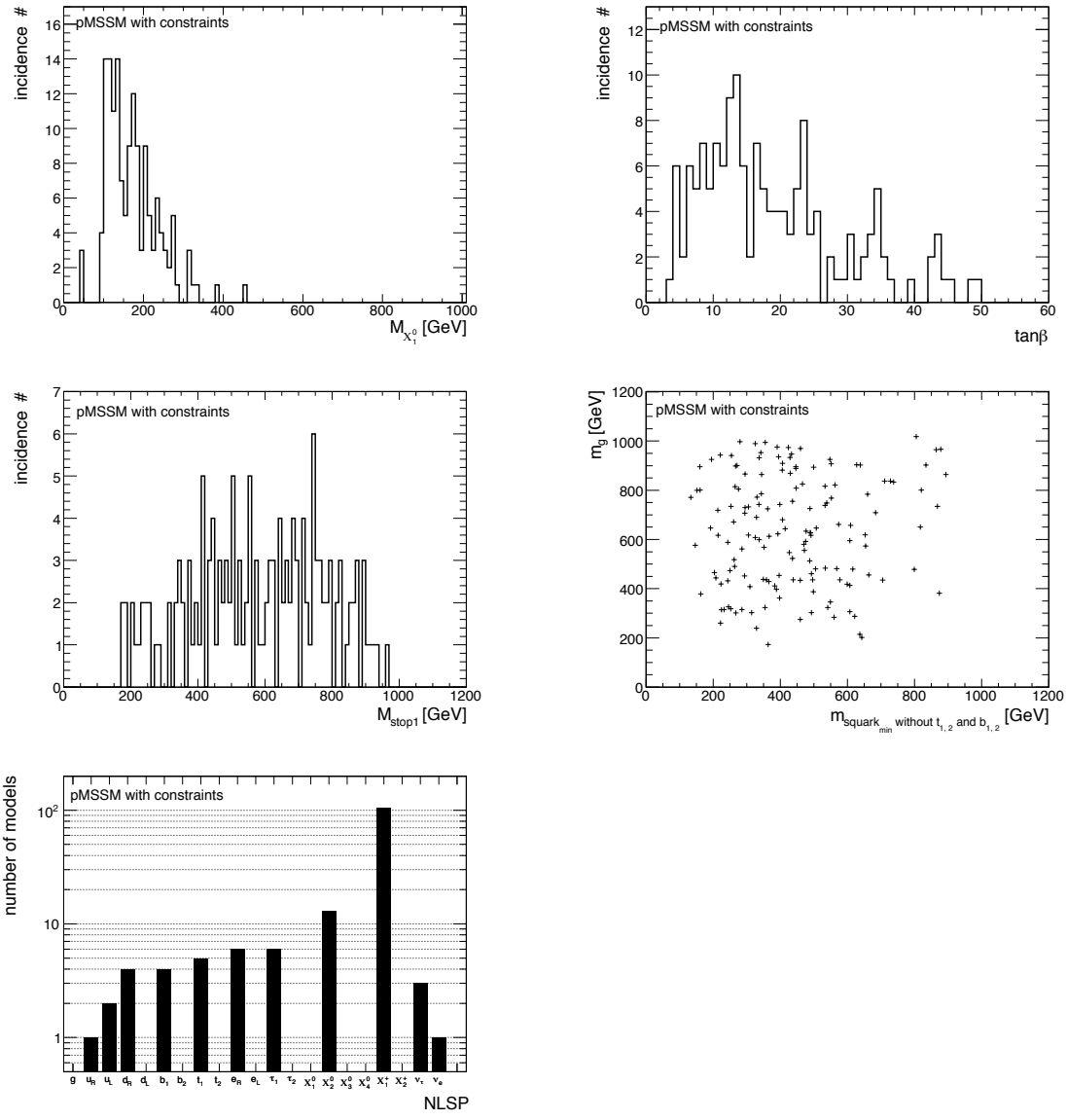

Figure 4.8: Parameters of the MSSM with constraints grid. Mass of the neutralino $\tilde{\chi}_1^0$ (top left plot), distribution of $\tan\beta$ (top right plot), mass of the stop $\tilde{t}_1$ (middle left) and gluino versus mass of the 1st and 2nd family squarks (middle left plot). The distribution of the next LSP (NLSP) type for the MSSM with constraints (bottom plot).

This implies the following relation: $M_2 = 2M_1 = M_3/3$ as one can find e.g. for models with minimal supergravity. The free varied parameters of the MSSM model with unified gaugino masses are: $\mu, M_2, m_{\tilde{q}}$ and $m_{\tilde{l}}, A_t, \tan\beta, M_{A^0}, m_{top}$. The parameter range is listed in Table 4.6. Only points are chosen, which satisfy various experimental bounds such as those from collider experiments at LEP, the WMAP Dark Matter density upper bound and bounds from direct Dark Matter detection searches. The generated models have squark and gluino masses within the reach of the LHC. A more detailed explanation of the sampled parameter space and the selected SUSY models can be found in Reference [250].
The particle spectra of the SUSY signals in this grid are computed with SoftSusy 2.0 and fed to micrOMEGAs 2.2 [206] for the computation of all DM observables and the constraints on the parameters of the supersymmetric models. From the points produced in Ref. [250], 935 points were randomly selected with cross section between 0.1 pb and 80 pb (see Table 4.4 and Figure 4.7). The events were generated with PYTHIA and simulated with the ATLFAST1 detector simulation. Distributions of some of the most important SUSY parameters of the analysed models are shown in Figure 4.9. It is interesting to see that the gluino mass (left plot in the 4th row of Figure 4.9) is restricted to a corridor, due to a combination of the universal gaugino mass at the GUT scale and the Dark Matter constraint. This constraints indirectly the gluino mass scale.

parameter	**lower bound**	**upper bound**
higgsino mass parameter μ	-3000 GeV	3000 GeV
gaugino mass M_2	30 GeV	2000 GeV
common slepton mass $m_{\tilde{l}}$	50 GeV	4000 GeV
common squark mass $m_{\tilde{q}}$	50 GeV	4000 GeV
stop triliniar coupling A_t	-3000 GeV	3000 GeV
$\tan\beta$	5	65
pseudoscalar Higgs mass m_{A^0}	100 GeV	2000 GeV
mass of top quark m_{top}	165 GeV	180 GeV

Table 4.6: Lower and upper bounds of the 8 parameters varied for the pMSSM grid with constraints.

unconstrained pMSSM grid

MSSM points without applying any constraints were produced in order to study the discovery potential of the SUSY analyses for typical representations of the phenomenological MSSM model without excluding any decay chains in the parameter space.

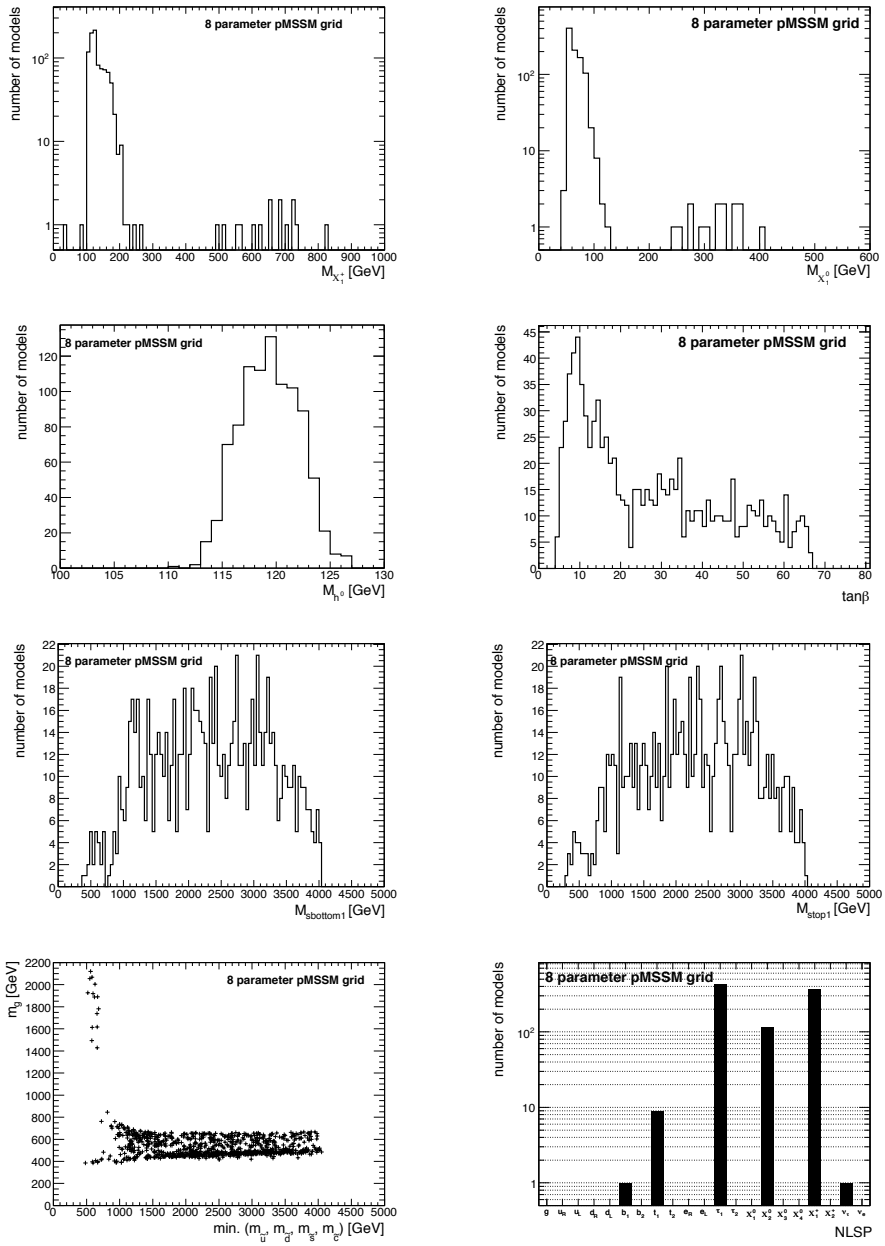

Figure 4.9: Parameters of the 8 parameter pMSSM grid. The mass of the chargino χ_1^+ (top left plot), the mass of the neutralino χ_1^0 (top right plot), the mass of the lightest higgs (2nd row left plot), the distribution of $\tan\beta$ (2nd row right plot), the mass of lightest sbottom (3rd row left plot), the mass of the lightest stop (3rd row right plot), the distribution gluino versus minimal mass of the 1st and 2nd family squarks (bottom left plot) and next LSP type (NLSP) for the selected SUSY models (bottom right plot).

parameter	lower bound	upper bound
gluino mass $m_{\tilde{g}}$	250 GeV	1000 GeV
U(1) gaugino mass M_1	−1000 GeV	1000 GeV
SU(2) gaugino mass M_2	−1000 GeV	1000 GeV
higgsino mass parameter μ	−1000 GeV	1000 GeV
pseudoscalar Higgs mass m_A^0	100 GeV	1000 GeV
$\tan\beta$	2	55
1st and 2nd gen. squark mass $m_{\tilde{q}} = m_{\tilde{u}_R} = m_{\tilde{d}_R}$	250 GeV	1000 GeV
1st and 2nd gen. slepton mass $m_{\tilde{l}}$	70 GeV	1000 GeV
left handed squark mass 3rd gen. $m_{\tilde{Q}}$	90 GeV	1000 GeV
right handed sbottom $m_{\tilde{b}_R}$	90 GeV	1000 GeV
right handed stop $m_{\tilde{t}_R}$	90 GeV	1000 GeV
3rd gen. lepton $m_{\tilde{L}}$	80 GeV	1000 GeV
stop triliniar term A_t	−1000 GeV	1000 GeV
sbottom triliniar term A_b	−1000 GeV	1000 GeV
stau triliniar term A_τ	−1000 GeV	1000 GeV

Table 4.7: Lower and upper bounds of the MSSM parameters used for the unconstrained pMSSM grid.

Of course any true theory must obey such constraints. It is often possible, however, to modify the SUSY parameters in order to satisfy the constraints while keeping the basic phenomenology unchanged (e.g. by extending the Higgs sector of the MSSM). The "unconstrained" pMSSM grid is an extension of previously studied pMSSM grid, where Dark Matter constraints are enforced ("MSSM points fulfilling constraints from experiments"). These constraints are now relieved.
The ranges of the varied input parameters are shown in Table 4.7. The masses of the left and right handed 1st and 2nd generation, squarks and sleptons, respectively, were set to the same value to make sure that the first and second sfermion generation have no effect on the SUSY-breaking parameters. This assumption can be assumed as universal at low energy scale. The total number of parameters of this reduced MSSM model is thus 15. The lower mass constraints are set such that the generated squark, gluino and slepton masses start slightly lower than the current PDG exclusion limits [47] for mSUGRA type scenarios. The resulting mass relations are in general very different to mSUGRA type of models (see Section 2.2.9), e.g. in the MSSM points all squark/gluino mass relations appear. The upper constraints are set such that the cross sections are still high enough to produce some events with the target integrated luminosity of 200 pb^{-1}. All selected SUSY models have a cross section between $\sigma = 0.1$ pb and 3400 pb. The other parameters are varied within the theoretically favoured regions [73]. SUSY points were chosen randomly within

those range, a flat prior is assumed. The SUSY spectra for all points were generated using ISAJET 7.79 and using HERWIG 6.5 for the fragmentation. The pMSSM was defined as the MSSM implementation of ISASUSY at the electroweak scale. The top mass was set to 172.5 GeV for all samples. In total 220 points were selected, which fulfilled the requirement that ISASUSY [205] did not produce any 'MSSM warning' message. These messages are produced with the SSTEST routing in ISAJET that checks if the branching ratio of the Z boson to neutralinos does not exceed the upper bounds from LEP-1, and if the Z decay to charginos or squarks and sleptons is allowed. For the simulation ATLFAST1 was used, however this program does not properly treat stable particles. Therefore points with a mass difference between the chargino χ_1^+ and the neutralino χ_1^0 of less than 300 MeV were also removed. Those points lead to a quasi-stable χ_1^+. The selected points have all a squark and gluino mass between 250 GeV and 1000 GeV. Distributions of some of the parameters of the unconstrained MSSM models are presented in Figure 4.10.

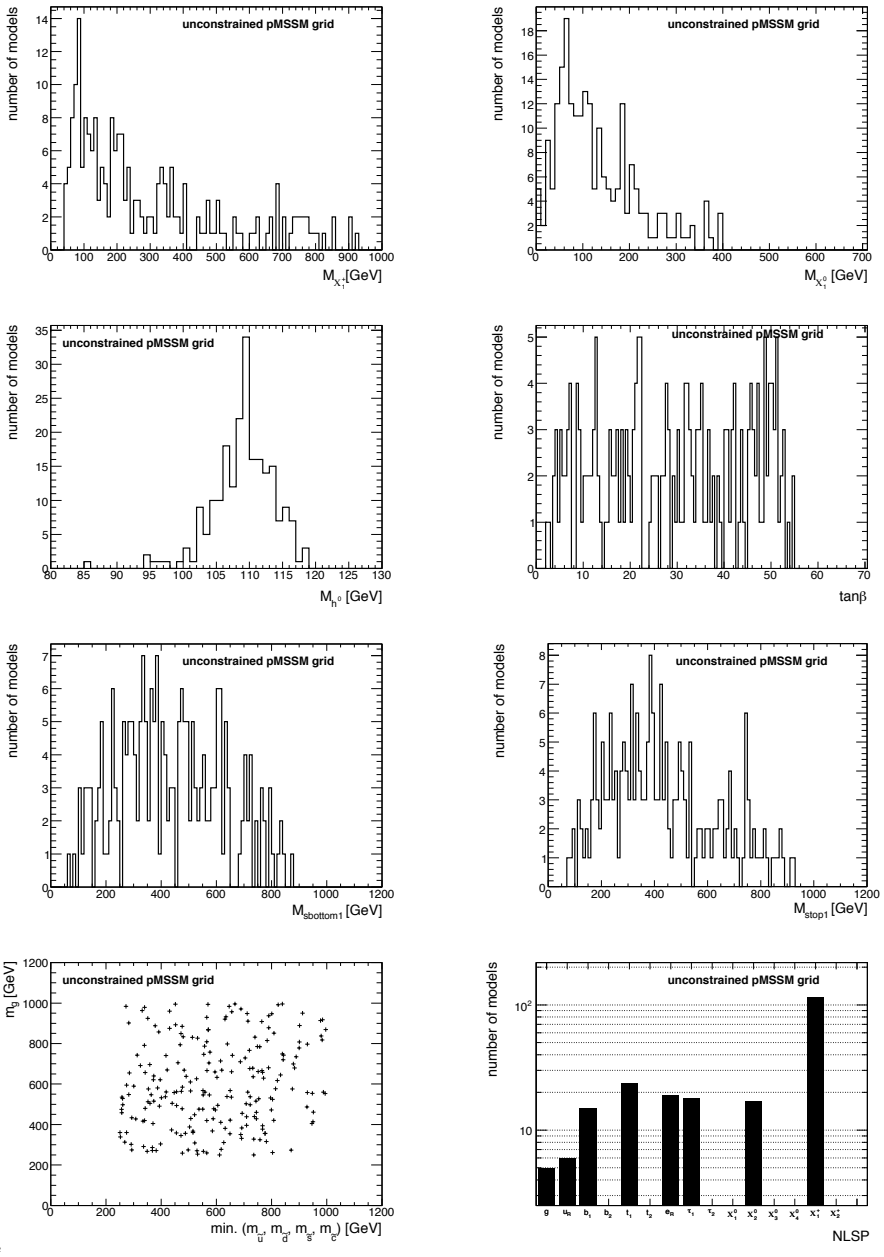

Figure 4.10: Parameters of the unconstrained pMSSM grid. The mass of the χ_1^+ (top left), mass of the χ_1^0 (top right), mass of the lightest higgs (2nd row, left), distribution of $\tan\beta$ (2nd row, right), mass of lightest sbottom (3rd row, left), mass of lightest stop (3rd row, right). The distribution gluino versus minimal mass of the 1st and 2nd family squarks (bottom, left), next LSP type (NLSP) for the pMSSM models (bottom, right).

5. Particle reconstruction in the ATLAS detector

An excellent particle identification capability is necessary for most physics studies at the LHC, especially for searches for new physics. The ATLAS detector with its subsystems, described in Chapter 3.3, is designed to provide this requirement. In this chapter the offline reconstruction algorithms for the relevant physics objects such as electrons, muons, jets and missing transverse energy, used for the SUSY analyses in this thesis will be briefly described. Further standard ATLAS object reconstruction algorithms, which are not used in the present work like for example jet b-tagging, τ–lepton or photon reconstruction are discussed in the References [104,115]. The criteria used to define the relevant particle objects for the Monte Carlo studies are those recommended by ATLAS for the CSC exercise [104]. The selection criteria applied for the first data studies (see Chapter 11) are similar to the ones used in earlier Monte Carlo studies, however the reconstruction algorithms including the calibration have slightly changed (see Section 5.2.2 and 5.3.2).

5.1. Offline reconstruction

After the digitalisation (see Section 4.4) the raw data consists of about 1.6 MB/event detector signals. This information has to be converted by the offline reconstruction software into information that can be interpreted in terms of particle interactions with the detector to perform the physics analyses. Specialised software tools for the raw signal conversion, the calibration and alignment of the different systems, and the reconstruction and identification of physics objects have been developed within the ATHENA framework. The discussed object reconstruction algorithms are executed once per event and are based on clusters and tracks, that are observed in different detector systems. The output is a collection of tracks, calorimeter clusters and reconstructed particle candidates.

5.1.1. Cluster reconstruction

The electromagnetic and hadronic calorimeters of the ATLAS detector (see Section 3.3.5) provide accurate measurements of the energies and positions of electrons, photons, and jets as well as of the missing transverse energy. They are segmented in layers and consist of several thousand cells of different sizes ($\Delta\eta \times \Delta\phi$). Incoming particles usually deposit their energy in many calorimeter cells, in both – the lateral and longitudinal direction. Clustering algorithms are designed to group these cells and to sum the total deposited energy within each cluster. The cluster energies are then calibrated to account for the energy deposited outside the cluster and in dead material.
The calibration depends on the incoming particle type: electrons and photons or jets. The first step in reconstructing this calorimeter clusters is to locate suitable cluster seeds. Two different types of clustering algorithms are used in ATLAS:

- sliding-window algorithm ("CaloTowers")

- topological algorithm ("TopoClusters")

The **sliding-window algorithm** is running on "CaloTowers" within the precision region of the calorimeter [251]. A tower is hereby the sum of all calorimeter layers add in a grid of cells within a fixed-size rectangular window[1]. The position of the window is adjusted such that its contained transverse energy is a local maximum. The clustering algorithm proceeds in the following three steps: tower building, pre-cluster (seed) finding, and cluster filling, whereas pre-cluster finding and cluster filling occur in a single step for combined clusters, but are two separate steps for EM clusters. The sliding window tool is often used for the reconstruction of electromagnetic showers and jets from tau-lepton decays. Since the cluster size is fixed, it allows a very precise cluster energy calibration.

The **topological algorithm** starts with a seed cell and iteratively adds to the cluster the neighbour of a cell, if the energy in the new formed cell has a significant energy and is above a threshold defined as a function of the expected noise. As a result, topoclusters that have a variable number of cells, in contrast to the fixed-size cluster algorithm described before, are produced. The clustering consist of two steps: the cluster maker and the cluster splitter. The first step forms topological clusters from a list of calorimeter cells: The signal-to-noise ratio should be $\Gamma = E_{cell}/\sigma_{noise,cell} > 4$ for the seed cell[2], neighboring cells are added, whose threshold is $\Gamma > 2$ (2σ significance) until no further cells are found to have a significant energy. A cluster includes (usually) the eight surrounding cells within the same calorimeter layer. Optionally, the set of neighbours can also include cells overlapping partially in η and ϕ (see Ref. [251]) in adjacent layers/calorimeter systems. Two types of cluster exist:
The *electromagnetic cluster*, that uses only electromagnetic calorimeter cells and the *combined cluster*, that uses all calorimeter cells. In endcaps and forward calorimeters clusters can grow to

[1] Different types of towers exist: CaloTower of the size $\Delta\eta \times \Delta\phi = 0.025 \times 0.025$ defined within $|\eta| < 2.5$ and combined tower $\Delta\eta \times \Delta\phi = 0.1 \times 0.1$ within $|\eta| < 5$.
[2] 4σ is the standard deviation of the fluctuation for the measured energy in the calorimeter cell due to noise.

cover large areas of the detector, if sufficient energy is present between incident particles.
The cluster splitting algorithm is designed for this described situation. It can separate two individual particles, if two local maxima in the calorimeter exist (E $>$ 500 MeV, energy is great than any neighbour cell energy, number neighboring cells within the parent cluster is above the threshold ≥ 4 [251]). After all initial clusters are identified, they are analysed for multiple local signal maxima. In case of more than one maximum in a given cluster, it is split into smaller clusters (again in three dimensions) along the signal valleys. Contrary to the signal tower algorithm, topological cell clustering includes noise suppression, meaning that cells with no signal at all are most likely already not included in the cluster. This results in substantially less noise. It is therefore very efficient for jet and missing transverse energy reconstruction.

5.1.2. Track reconstruction

The process can be subdivided into several steps (see also Ref. [115,252]: It begins with the identification of clusters using the pixel detector and the first layer of the SCT, that are than transformed into space-points by combining the cluster information from opposite sides of a SCT module. The second step is the "track-finding" process, in which different tracking strategies, optimised to cover different applications, are implemented [252]. The default tracking algorithm uses the pixel and SCT detector information to find prompt tracks originating from the interaction region. The track seeds are formed from a combination of space-points in the three pixel layers and the first SCT layer. Additional hits from the SCT are then added to these seeds using a loose selection to form a track candidate. Next, a fitter is applied using a special filter technique. Outlying clusters are removed, ambiguities in the cluster-to-track association are resolved and tracks deemed to be fakes are rejected. For this, quality cuts e.g. on the number of associated clusters with explicit limits on the number of clusters shared between several tracks and the number of silicon sensors crossed by a track without generating any associated cluster. The remaining tracks are then extended/extrapolated using the calibrated drift-circles. Finally the tracks are refitted with the full information of all three detectors. The unused TRT track segments can also be extrapolated back into the SCT and pixel detectors to locate further secondary tracks ("back-tracking"). On average, a track consists of 3 pixel hits, 4 space-points in the silicon micro-strip detector and about 36 hits in the Transition Radiation Tracker (TRT).
The clusters and tracks observed are combined to identify physics objects (e.g. jets, leptons, photons) and to measure their properties like momentum, position and charge as accurately as possible. The reconstruction of these objects is performed by dedicated algorithms, discussed in the following.

5.2. Jets

A precise jet reconstruction with a high reconstruction efficiency is very important for nearly all physics analyses performed at the LHC. It is also of great importance for all SUSY studies, since squarks and gluinos are expected to decay in many jets. Therefore jets are one of the physics objects used in nearly every SUSY analysis to define the SUSY final states. The most important

detector for the jet reconstruction is the ATLAS calorimeter system (see Section 3.3.5). ATLAS followed in its jet reconstruction strategy the concepts from the Tevatron (see Ref. [253] and Ref. [254]) and tried to consider theoretical and experimental guidelines such as infrared safety, collinear safety and detector independence.
Different jet finding algorithms are used by ATLAS. The most commonly used jet-clustering algorithms are the seeded fixed cone finder with split-and-merge [255], the sequential recombination algorithm like k_T [256–259] and the anti-k_T [260] algorithm. Since there cannot be one universal jet finder preferred by all physics analysis, the available algorithms tried to cover the wide spectrum of hadronic final states in all event topologies of the physics processes. Every algorithm has a modular and generic design and can be run on every object having a four-momentum representation like calorimeter signal towers, topological cell clusters in the calorimeters, reconstructed tracks, and generated particles and partons, to be able to combine the different jet constitutes.

5.2.1. Jet reconstruction

Two different jet-reconstruction processes are available in ATLAS to combine the different calorimeter cells to larger signal four-momenta objects: *calorimeter towers* (seeded fixed-cone algorithm) and *topological cell clusters* (successive recombination algorithm). The clustering is already described in detail in the previous section and just shortly summarised here for jets:

- Calorimeter towers:
  The cells of the calorimeter are collected and formed to towers of the size:
  $\Delta\eta \times \Delta\phi = 0.1 \times 0.1$ in the acceptance region of the calorimeters ($\mid \eta \mid < 5, -\pi < \phi < \pi$).
  The signal from the cells is taken at the basic EM energy scale without applying any corrections or calibrations. Cells that are not fully covered by one tower, contribute a fraction of their signal corresponding to the geometrical overlap. This summing is non-discriminatory, all calorimeter cells are used to build towers. Towers with negative signals are dominated by noise and cannot be used. They are combined with neighbour signals-towers until the final signal is positive and has a valid physical four-vector (“noise cancellation”).

- Topological cell clusters:
  This is an attempt to reconstruct three-dimensional energy depositions in the calorimeter [115] based on collecting the nearest neighbours around seed cells.Since cells with no signal are not used for the cluster, this algorithm is efficient at suppressing noise.

The calorimeter towers and cell clusters are both used to define the basic cell signals at the EM energy scale. Optionally, in a second step clusters can be calibrated to a local hadronic energy scale. The main difference between the algorithms is the number of calorimeter cells used. Towers include all cells of the calorimeters, while the clusters use considerably fewer cells. Historically, calorimeter tower jets have been used in ATLAS e.g. for all Monte Carlo studies presented in this thesis, but topological cell clusters seem to show better results due to the noise suppression, meaning that cells with no signal at all are most likely already not included in the cluster. They are used for all data studies discussed in Section 11.

In the following the three jet-finding algorithms "cone", "k_T" and "anti-k_T", that define the jet objects in the SUSY analysis, are described. A summary of the available jet algorithms and their performance in the ATLAS detector is for example in Ref. [261].

Jet-finder algorithms

Fixed cone algorithm The aim of a fixed cone algorithm is to maximise the energy (or p_T) in a geometric cone. It is iterative and relies upon a seed in order to initiate the first candidate cones. The algorithm needs two parameters, the transverse energy threshold for a seed, E_T = 1 GeV for all cone jets and a cone size R_{cone}. In a first step all input objects (cluster, towers or partons, particles from simulated data) are arranged in decreasing order according to their transverse energy E_T. If the object with the highest E_T is above the seed threshold, a cone is build with an radius R_{cone}[3] around it and all object within this cone with $\Delta R = \sqrt{\Delta\eta^2 + \Delta\phi^2} < R_{cone}$ are collected and combined with the seed. R_{cone} is hereby fixed e.g. $R_{cone} = 0.4$ for narrow jets and $R_{cone} = 0.7$ for wide jets. Narrow jets are used for example for W + jets, $t\bar{t}$ measurements (but more meaningful for final states like W/Z + 1 jet than with 2 or 3 jets) or for events containing large multiplicities of jets such as in supersymmetric models. After combining the objects with the seed a new cone direction is calculated with all combined four-momenta in this cone and a new cone is centered around it to refine the centre of the cone. The objects around this new centre are (re-)collected, and again the direction is updated. This process continues until the direction of the cone does not change after any additional recombination of the momenta. If so, the cone is considered to be stable and is called a jet. This iterative procedure is repeated for all input objects from the transverse energy E_T list until no more seeds are available with a transverse energy above the seed threshold.
It is possible that the finally found jets share constituents. In order to resolve these overlaps, all jets are revised in a split-and-merge step. Overlapping jets with shared E_T above a given threshold (typically 50%) are hereby merged. If the shared E_T is below this threshold, the jets will be split. Some signal objects contributing to the cone at the first iterations can get lost again due to the recalculation of the direction at a later iteration. Therefore parts of the input signals might not be used by any jet and result in so-called "dark towers". It should be noted that this algorithm is not infrared safe and can be only partly recovered by the described split and merge step after the jet formation is done.

K_T-algorithm The k_T-algorithm in ATLAS is implemented following the suggestions in Reference [259] to avoid a pre-clustering step and to be also efficient even for a rather large number of input objects. It is successfully used in electron–positron annihilations, in electron–proton deep inelastic scatterings and, recently, even in hadron-hadron collisions. The algorithm introduces a distance measure d_{ij} between particles, and repeatedly recombines the closest pair of particles until some stopping criterion is reached. All pairs of input objects (towers, clusters, partons, particles, etc.) are first listed and than analysed following a special routine until all objects are merged to jets. A short summary of this procedure can be found in the Appendix in Section F.1.

[3] For simplicity R instead of R_{cone} will be used in the following chapters of this thesis.

As a results all original input objects end up to be either part of a jet or to be jets by themselves. In contradiction to the cone algorithm described earlier, no objects are shared between jets. The procedure is infrared safe and also collinear safe. Moreover no initial seed is needed. The radius parameter R, which is the only free parameter in this routine, controls the size of the jets. Default values in ATLAS are R = 0.4 for narrow and R = 0.6 for wide jets, with similar physics performance to the one of the corresponding cone algorithm.

Anti-k_T algorithm Another infrared and collinear safe algorithm is the anti-k_T jet algorithm [259]. It uses sequential recombination to build the jet as the k_T algorithm, is essentially the same algorithm, but a different recombination of the physics objects is done (see Appendix Section F.2). This is due to an additional parameter p that was added to the radius parameter R. For the k_T algorithm p = 1, while for the anti-k_T algorithm to p = -1. The different parameters produce different peculiarities between the two algorithm. While the k_T algorithm starts in general merging a soft object to the spatially closest one, anti-k_T process starts recombining a hard object to the spatially closest one. Soft objects that are within a certain radius R of a high k_T object will be merged to an anti-k_T object and the final jet will have very regular shape (almost a circle around the high k_T object). It should be noted, that soft particles contribute only a modest component of the overall jet momentum, and the algorithm remains flexible in its adaptation to hard (sub)structure in the jets.

Summary

A default set of configurations for jet-finding strategies is provided. Due to the relatively large multiplicity of jets in SUSY events always narrow cone was used with cone size 0.4 for all SUSY studies. The algorithm reconstructing jets for the SUSY analyses was "Cone4Tower" for all Monte Carlo studies at 14, 10 and 7 TeV. For the first data SUSY studies the available anti-k_T jet finder algorithm using topological clusters "Anti-k_T-Topojets" was used.

5.2.2. Jet calibration

Ideally, the clusters allow to associate together calorimeter signals produced by the same hadron shower. Reconstructed jets are calibrated as a baseline to the energy scale measured by the calorimeters, called the electromagnetic (EM) scale. The electromagnetic energy scale is established using test-beam measurements for electrons and muons in the electromagnetic and hadronic calorimeters [139]. This energy scale accounts correctly for the energy of photons and electrons, but it does not correct for calorimeter non-compensation or instrumental (detector) effects including energy losses in inactive regions of the detector (dead material), particles which are not totally contained in the calorimeter (leakage) or that fall out of the reconstructed jet, but are included in the truth jet or inefficiencies in calorimeter clustering and jet reconstruction. Therefore, after the jets are identified, a calibration scheme must be applied to correct for these effects.
The most widely used calibration in the ATLAS collaboration is the so-called "H1-style" method or "global cell weighting" [262,263], which is based on cell signal weighting. The approach can

be applied to both tower and cluster jets. The strategy is similar to the original approach developed for the H1 calorimeter. The basic idea of this algorithm is, that the shower produced by a jet is composed of an electromagnetic and a hadronic component. The hadronic component is broader and less dense than the electromagnetic one that is a compact, highly dense, energy deposit. This fact can be used to correct the energy measurement to recover for the non-linear calorimeter response to the hadrons. Low signal densities in the calorimeter indicate a hadronic signal in a non-compensating calorimeter, while high signal densities are more likely to be generated by EM showers. To compensate for this, hadronic showers are weighted by a factor of the order of the electron/pion signal ratio.
The calibration is made in two steps. First the cell weighting, which mainly improves the resolution and makes the response linear to within 10%. The cell weighting step corrects for energy lost in material in front of the calorimeters and that the response of the calorimeter to hadronic energy is smaller than the response to electrons. Once the cells are weighted, the jet energy is calculated from it to obtain a jet energy at the hadronic energy scale. The mean jet energy is now closer to the truth (the electromagnetic energy scale), but residual corrections are needed to ensure that the reconstructed jet has the correct energy on average. In a second step these corrections account for effects such as the loss of low energy particles from the jet due to absorption in material in front of the calorimeter or the bending of charged particles in the magnetic field. A scalar factor depending on η and p_T of the jet after the cell weighting step scales each jet.
The performance of the calibration in terms of jet linearity and resolution has been assessed in a variety of physics processes like QCD dijets, top-pairs and SUSY events, that are characterised by a different structure of events (different colour structure, different underlying event). The final correction is at the level of few percent (up to 5%) in the crack and gap calorimeter region, while it is of the order of 1-2% (depending on the jet algorithm) in the rest of the p_T–η phase space [115].

Jet calibration for the first data events

ATLAS has developed several calibration schemes with different levels of complexity and different sensitivity to systematic effects. The algorithms are undergoing commissioning at the moment and will be part of the default energy scale in future. For first collision events analysed in this thesis in Chapter 11, the simplest calibration is used, the so-called "EM + JES calibration" to convert the electromagnetic calibration scale of the ATLAS calorimeters to the calibrated hadronic scale [264]. It is a jet by jet scheme that corrects for the non-linear correlation between the energy reconstructed in the calorimeter and the energy of the particles forming jets. The jet energy scale calibration is derived as a global function depending on p_T and η used to restore the jet response to unity, starting from the jet response at the electromagnetic scale: $R^{EM} = \frac{p_T^{jet,EM}}{p_T^{MC,\text{truth jet}}}$.
The jet finding, selection and binning are performed in rapidity y and ϕ coordinates of the jets, since reconstructed jets obtain a mass via the recombination scheme. The calibration is done in η–ϕ coordinates due to detector effects. Only jets satisfying the following kinematic criteria are used: $p_T > 20$ GeV, $|\eta| < 2.8$.
The calibration constants are calculated from the Monte Carlo simulation from the jet response of truth jets, that is transformed to a response function of reconstructed jets and can be applied to the

towers or clusters, that form the jets at the electromagnetic scale. The final correction is defined as the inverse of the response function and applied inclusively to all jets, including non-isolated jets. The calibrated transverse momentum of the jet is calculated as:

$$p_T^{jet} = \frac{1}{R^{EM}(p_T^{jet,EM},\eta)} \cdot p_T^{jet,EM}$$

Details about the particular steps of the jet calibration can be found in Ref. [264].
The advantage of this calibration technique compared to other available schemes is that it relies on very few details of the description of the calorimeter response. Only basic properties of the energy deposits in the calorimeters are used. Although it does not show the best performance, it allows the most direct evaluation of the systematics and is less demanding in terms of agreement between the simulated detector predictions and the real data.
However, the calibration assumes that the jet direction does not change. This leads to a tiny difference between energy response and p_T. Figure 5.1 shows the jet energy scale correction as a function of jet transverse momentum at the electromagnetic scale for jets in the central barrel (black circles) and endcap (red triangles) regions for anti-k_T, R = 0.6 jets, built from topoclusters. The p_T range is 20 to 300 GeV.

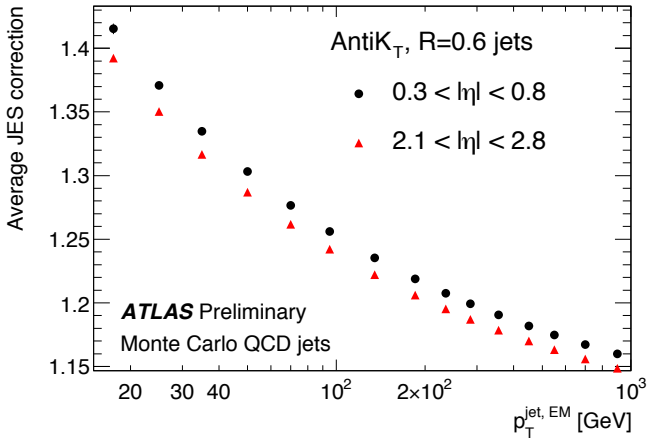

Figure 5.1: Jet energy scale correction as a function of jet transverse momentum at the electromagnetic scale $p_T^{\text{jet,EM}}$ for jets in the central barrel (black circles) and endcap (red triangles) regions, averaged in $p_T^{\text{jet,EM}}$ bins and η regions. Figure is taken from Ref. [264].

Jet energy scale (JES) uncertainty The JES systematic uncertainty is derived from single pion test-beam measurements and Monte Carlo simulation test samples generated with different conditions to take into account the uncertainties on the material budget of the calorimeter (e.g. dead material), electronic noise, the theoretical model uncertainty used in the Monte Carlo generation, fragmentation, underlying event, the comparison of test beam data for the hadronic shower model used in the simulation, and other effects such as a shifted beam spot and the electromagnetic scale uncertainty for the calorimeters. All these variations are expected to provide a conservative

estimate of the systematic effects contributing to the JES uncertainty. The total jet energy scale uncertainty has been derived by considering all the individual contributions:

$$\Delta_{JES}(p_T^{jet}, \eta^{jet}) = \mid 1 - \frac{R_{var}}{R_{nom}} \mid$$

with R_{var} as the systematic variation response and R_{nom} the nominal one. The JES uncertainty will be applied to the full jet four-momentum, the largest Δ_{JES} in each bin derived from energy or transverse momentum response is considered as the contribution to the final JES. The absolute electromagnetic energy scale contribution from the electromagnetic and hadronic calorimeter is weighted by the average electromagnetic and hadronic energy content and added in quadrature to this. Due to the limited MC statistics for high jet p_T this method becomes insufficient in some regions. Therefore for these high p_T bins the uncertainty from the last bin is used. The final relative jet energy scale systematic uncertainty as a function of jet p_T and η is shown in Figure 5.2. The light blue area is the total uncertainty, the other colours are the individual contributions with statistical errors from the fitting procedure if applicable. The relative JES uncertainty is in the central region for jets wih a $p_T < 60$ GeV about 9.4% and about 7% for jets with a larger transverse momentum. The uncertainty increases with η and reaches for $2.1 < \mid \eta \mid < 2.8$ in the endcap region its maximum of about 10% (7.6%) for jets with $p_T < (>)$ 60 GeV. This is also due to the fact that the JES uncertainty for the endcap is extrapolated from the barrel uncertainty, with the contribution from the η intercalibration between central and endcap jets in data and Monte Carlo added in quadrature. The study was repeated for anti-k_T jets with distance parameter R = 0.4 with a comparable slightly smaller JES uncertainty as result: about 8% for low p_T jets and 6% for larger ones. More details can be found in Reference [264].
The JES correction is at the moment a conservative approach and can be reduced using e.g. in-situ methods. For future high intensity LHC runs, also the fraction of the multiple proton-proton interactions (pile-up) needs to be considered. This additional energy has not been taken into account in the jet energy scale. However, for the initial data taking period discussed in this thesis, the effects are expected to be much smaller compared to the jet energy scale uncertainties considered.

5.2.3. Jet performance

Figure 5.3 shows the linearity, defined as the ratio of reconstructed cone R = 0.4 tower jet energy to the matching truth jet energy, as a function of energy for three pseudorapidity regions (top left plot) and of the pseudorapidity for three transverse energy bins (right top plot) for cone 0.4 tower jets in SUSY SU3 events. The bottom plots illustrate the expected jet fractional energy resolution as a function of the mean transverse energy E_T of the reconstructed jets with $\mid \eta \mid < 3$ (left bottom plot) and $\mid \eta \mid$ (right bottom plot) for cone-tower jets with a cone size of R = 0.7 and 0.4. The linearity is overall good, in the central region a deviation from 1 of maximum 4% is observed at low jet energy. Apart from the expected dip at η = 1.5 that corresponds to detector transition regions, a good uniformity of the linearity as a function of the pseudorapidity is observed. At large pseudorapidity ($\mid \eta \mid > 3.5$), the linearity is off by 5-6%. For dijet events the linearity differs by up to 5% from 1 in the central region.
The expected jet energy resolution shown in the bottom plots can be fitted using a three-parameter

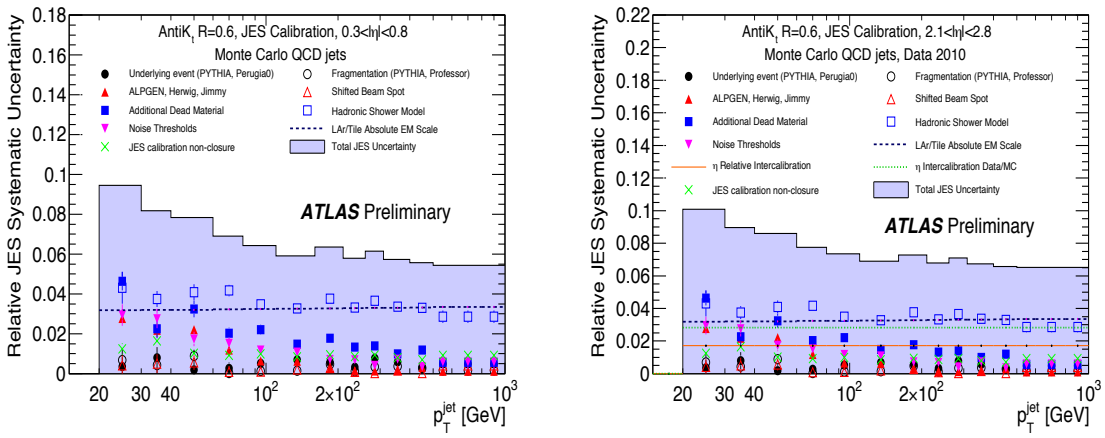

Figure 5.2: Relative jet energy scale systematic uncertainty as a function of p_T^{jet} for jets in the pseudorapidity region $0.3 < |\eta| < 0.8$ in the calorimeter barrel (left plot) and in the endcap $2.1 < |\eta| < 2.8$ (right plot). The total uncertainty is shown as the solid light blue area. The individual sources are also presented, with statistical errors if applicable. The figures are taken from Ref. [264].

function:

$$\frac{\sigma}{E} = \frac{a}{\sqrt{E(GeV)}} \oplus \frac{b}{E} \oplus c \tag{5.1}$$

The jet energy resolution is η dependent due to the increasing readout-cell size and the change in calorimeter technology in the hadronic calorimeters from the low-noise tile calorimeter to the higher noise LAr calorimeter. Term a is due to the statistical, poissonian, fluctuations in the energy deposits in the calorimeters. It increases from the barrel to the end-cap η-ranges. The term c reflects the effect of the calorimeter non-compensation and all the detector non-uniformities involved in the energy measurement. The noise term b describes the noise contribution to the energy measurement. For central jets in the region $0.2 <| \eta |< 0.4$, the term a is $\approx 60\%\sqrt{E(GeV)}$, the noise term varies around 3-4% [261] and the high energy limit is $\approx$ 2-3% [261, 265]. The efficiency for jets tower and cluster jets with a $p_T > 40$ GeV is very similar and about 0.98 -1. For lower values of p_T, the cluster jets are found with higher efficiency [265].

Performance of the first $\sqrt{s} = 7$ TeV data events

Before a jet is calibrated, it has to pass several selection criteria which are discussed in detail in Ref. [266] and are particularly discussed in Section 7.3.1. Figure 5.4 shows for 7 TeV data events collected in April / May 2010 the transverse momentum (left plot) and rapidity distribution ($p_T >$ 30 GeV) (right plot) for the topocluster jets calibrated with the Monte Carlo-based p_T and η jet calibration together with simulated events after applying the event cleaning cuts. The expectation from the Monte Carlo simulation is superimposed and normalised to the number of events in

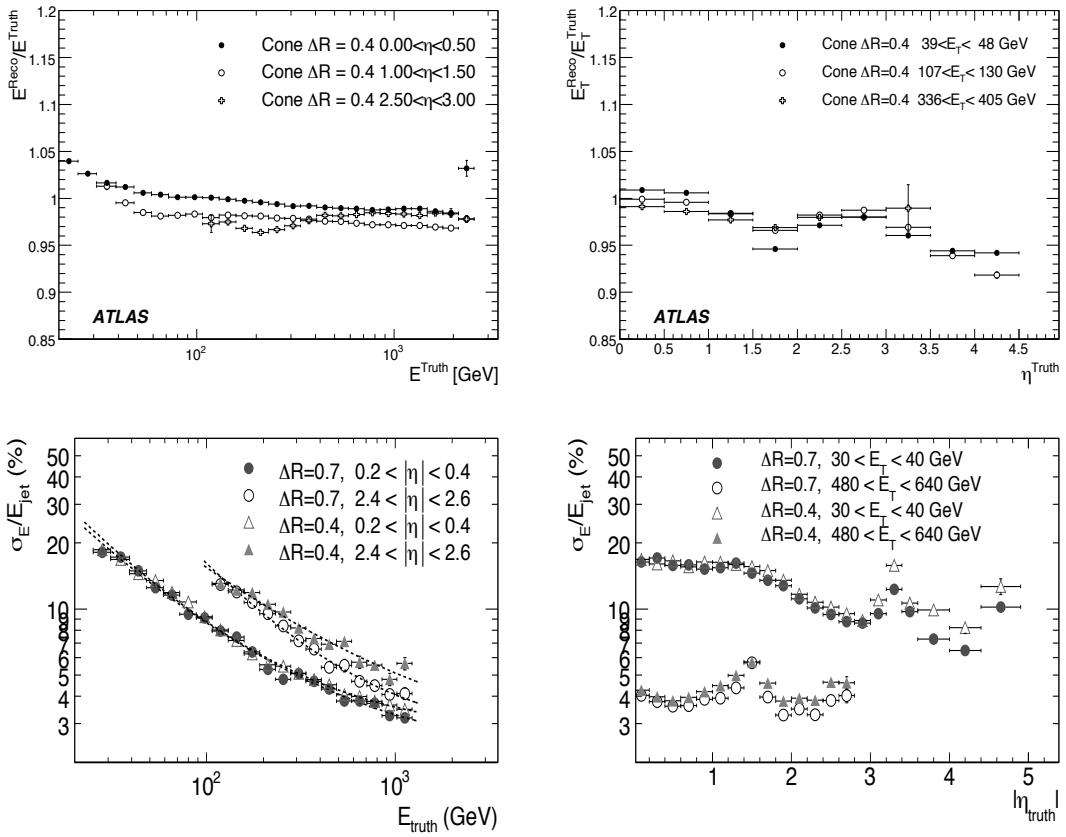

Figure 5.3: Linearity as a function of energy for three pseudorapidity regions (left top plot) and linearity as a function of the pseudorapidity for three transverse energy regions (right top plot) for cone-tower jets with a cone size of R = 0.4 in SU3 SUSY events. Expected jet fractional energy resolution as a function of energy (left bottom plot) and $|\eta|$ (right bottom plot) for cone-tower jets with a cone size of R = 0.7 and 0.4. Figures are taken from Ref. [104] (upper plots) and from Ref. [115](bottom plots).

data. In general a reasonable agreement between measured data and Monte Carlo simulation was found. Small differences can be seen with increasing jet p_T, that may reflect the limitations of the description of the hard-scattering process provided by the Monte Carlo generator PYTHIA [267]. In the rapidity y the distributions are well described by the Monte Carlo simulation. A slight structure can be observed in the number of reconstructed jets as a function of y jet, which is related to the jet reconstruction efficiency and the accuracy of the Monte Carlo-based calibration constants.

The relative good agreement between data and Monte Carlo simulation reflects the description of noise in the context of jets, jet reconstruction efficiencies and jet energy scale in the simulation. A slightly higher energy density is observed in the Monte Carlo simulation than in the data in the electromagnetic calorimeter. These results will be considered in the future tuning of the Monte

Carlo generators for ATLAS. With additional data the commissioning of the jet calibration will continue to establish a jet energy scale uncertainty for the different calibration schemes.

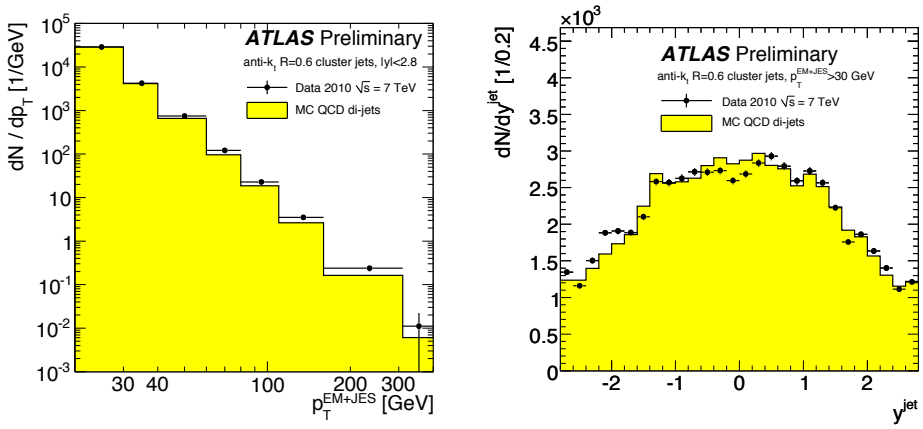

Figure 5.4: Transverse momentum p_T (left plot) and rapidity y (right plot) distributions of the calibrated topological cluster jets using the described EM + JES calibration for first 7 TeV collision data events. The expectation from the Monte Carlo simulation is superimposed and normalised to the number of events in data. Figures are taken from Ref. [267]

5.3. Missing transverse energy

Missing transverse energy is one of the most important variables for all the SUSY searches discussed in this thesis. A fundamental requirement on the measurement of E_T^{miss} is to minimise the impact of tails induced by the limited detector coverage, finite detector resolution, presence of dead regions - in particular hot/noisy or dead calorimeter cells and other sources of noise that can produce fake E_T^{miss}. The challenge is in a precise E_T^{miss} measurement in terms of linearity and accuracy. The calorimeter plays a crucial role in this measurement, the forward calorimeters cover large η regions and extend the pseudorapidity angles of the detector, however the imperfect detector coverage e.g. in the transition regions of the calorimeters as well as detector malfunction in some cells is unavoidable. ATLAS has developed two E_T^{miss} reconstruction algorithms – a cell-based and a object-based algorithm. Only the cell based reconstructed E_T^{miss} is used for the SUSY analyses and will be described in the following. More information can be found in Ref. [104].

5.3.1. E_T^{miss} reconstruction

The cell-based E_T^{miss} algorithm starts from energy E_x and E_y deposited in the calorimeters after a noise suppression procedure is applied[4] The algorithm (cell based method) used is robust, since it

[4]To classify energy deposits in the calorimeter cells, schemes to calibrate hadronic showers such as “H1-like” calibration utilise the energy density in a cell.

does not rely on any reconstructed objects. It further corrects for energy losses in the cryostat and takes muon energy into account. The total missing energy in x- and y-direction is calculated as:

$$E_{x,y}^{miss} = E_{x,y}^{miss,\,Calo} + E_{x,y}^{miss,\,muon} + E_{x,y}^{miss,\,Cryo} \tag{5.2}$$

The total transverse energy E_T^{miss} is given by the equation:

$$E_T^{miss} \equiv \sqrt{(E_x^{miss})^2 + \left(E_y^{miss}\right)^2} \tag{5.3}$$

The calorimeter term $E_{x,y}^{miss,\,Calo}$ is calculated from the energies measured in the topological clusters (topocells) at the electromagnetic scale [268].

$$E_T^{miss,\,Calo} \equiv \sqrt{\left(E_x^{miss,\,Calo}\right)^2 + \left(E_y^{miss,\,Calo}\right)^2} \tag{5.4}$$

with:

$$E_x^{miss,\,Calo} \equiv -\sum_{i=1}^{N_{\text{topocells}}} E_i \sin\theta_i \cos\phi_i \qquad \text{and} \qquad E_y^{miss,\,Calo} \equiv -\sum_{i=1}^{N_{topocells}} E_i \sin\theta_i \sin\phi_i \tag{5.5}$$

with E_i the cell energy, θ_i the polar angle and ϕ_i the azimuthal angle. All topological cluster cells within the pseudorapidity range $|\eta| < 4.5$ are summed up.
In equation 5.2 two additional terms can be added to the $E_{x,y}^{miss,\,Calo}$ term:
In case of a high p_T muon was measured in the event, a muon $E_{x,y}^{miss,\,muon}$ term has to be calculated separately and added to the calorimeter term, since due to limited coverage of the muon spectrometer (apart from the loss of muons outside the acceptance of the muon spectrometer $|\,\eta\,| > 2.7$) some muon energy would not be measured. The muons reconstructed from the inner detector and calorimeter energy deposits could be used to recover these muon energy. The final E_T^{miss} performance is only marginally affected by the muon term due to the good identification efficiency and resolution of the ATLAS muon system. However, unmeasured, badly measured or fake muons can produce fake E_T^{miss}.
Additionally, the reconstruction accounts for the so-called cryostat term $E_{x,y}^{miss,\,Cryo}$, which corrects for the energy lost from hadronic showers in the cryostat between the barrel LAr electromagnetic and tile calorimeters. The reconstruction algorithm uses the correlation of energies between the last layer of the LAr calorimeter and the first layer of the hadronic calorimeter. A similar correction for the end-cap cryostats is applied. The cryostat correction contributes at the level of $\sim 5\%$ per jet with p_T above 500 GeV [104].

5.3.2. E_T^{miss} calibration

In the final (optional) calorimeter refinement step, a calibration of E_T^{miss} is performed. In this step calorimeter cells are associated with reconstructed and identified high-p_T objects (object based

method), in a chosen order: electrons, photons, muons, hadronically decaying τ-leptons, b-jets and light jets. The refined calibration of the identified object is then used in $E_{x,y}^{miss}$ (see equation 5.2) to replace the initial global calibration cells, since the calibration of these objects has a higher accuracy than the global calibration and can improve the E_T^{miss} reconstruction. For the calorimeter cell association maps are used. The final calorimeter E_T^{miss} term is than calculated as follows:

$$\begin{aligned} E_{x,y}^{miss,\,Calo} &\equiv -\left(E_{x,y}^{RefElec} + E_{x,y}^{RefTau} + E_{x,y}^{Refbjets} + E_{x,y}^{RefJets} + E_{x,y}^{RefMuon} + E_{x,y}^{Refcells}\right) \\ E_{x,y}^{RefCalib} &\equiv E_{x,y}^{miss,\,Calo} \end{aligned} \tag{5.6}$$

with $E_{x,y}^{Refcells}$ calculated from the cells in topoclusters, which are not included in the reconstructed objects (no associated cells). After this final calorimeter refinement step, the total E_T^{miss} from equation 5.3 is calculated as:

$$\begin{aligned} E_T^{miss} = E_T^{RefFinal} &= \sqrt{\left(E_x^{miss}\right)^2 + \left(E_y^{miss}\right)^2} \\ &= \sqrt{\left(E_x^{RefCalib} + E_x^{Cryo} + E_x^{muon}\right)^2 + \left(E_y^{RefCalib} + E_y^{Cryo} + E_y^{muon}\right)^2} \end{aligned} \tag{5.7}$$

where E_T^{miss} is often referred as $E_T^{RefFinal}$. The refined algorithm for the reconstruction of the missing transverse energy $E_T^{RefFinal}$ was used in all Monte Carlo studies.

Noise suppression

There are many sources such as the underlying event, multiple interactions, pile-up (see Section 2.3.3) and coherent electronics noise that lead to additional energy deposits. Two different approaches can be taken in order to suppress calorimeter noise. The "standard noise suppression method" only uses calorimeter cells with energies larger than a threshold corresponding to a certain number of σ_{noise}. The threshold is optimised for the E_T^{miss} resolution, the scale of E_T^{miss}, the total transverse energy in the calorimeters and the highest transverse momentum jet. Only calorimeter cells are included to the E_T^{miss} calculation that significantly exceed this noise threshold e.g. $\mid E_{cell} \mid > 2\sigma_{noise}$. The second method - the "noise suppression using topoclusters" method only uses the cells in the 3-dimensional topological calorimeter clusters (topocells), which include already a noise cut (see Section 5.2.1). This set of thresholds is optimised to suppress electronics noise as well as pile-up from minimum bias events, while keeping the single pion efficiency as high as possible.

Missing transverse momentum in the first data events

For the physics analysis with the first data, E_T^{miss} includes only the contributions from transverse energy deposits in the calorimeters and is computed just from calorimeter cells belonging to topological clusters at the electromagnetic scale $E_{x,y}^{miss,\,Calo}$ (see Ref. [268, 269]). Since the global

cell energy-density weighting calibration was still under study and a more refined calculation of E_T^{miss} was just commissioned, no corrections for the different calorimeter response of hadrons and electrons/photons or for dead material losses are applied. The transverse missing momentum components $E_x^{miss,\,Calo}$ and $E_y^{miss,\,Calo}$ are defined as in equation 5.4 and 5.5 and E_T^{miss} in the topocells is calculated from the scaler sum of E_T^{miss} of all calorimeter cells (see equation 5.3). In the following definitions the missing transverse momentum two-vector is defined by:

$$p_T^{miss} \equiv (E_x^{miss}, E_y^{miss}). \tag{5.8}$$

The performance of the missing transverse momentum reconstruction during the data-taking period is described in Ref. [268, 269]. Events in which undetectable particles are produced can be expected to have large E_T^{miss}.

5.3.3. Fake E_T^{miss}

The fake missing transverse energy is defined as the difference between the reconstructed and true E_T^{miss}. While true E_T^{miss} is produced by particles that interact weakly with the detector, the fake constituent can have many different source:

- beam-gas scattering, beam halo and other machine backgrounds
- hot, noisy, or dead calorimeter cells/regions
- inefficiencies in reconstructing a high p_T muon, fake muon due to e.g. hits from high p_T jet punch-throughs from the calorimeter to the muon chambers
- mis-measurements in the detector e.g. mis-measured hadronic jets, taus, electrons or photons in the calorimeter mainly due to escape of high p_T particles outside the fiducial acceptance of the detector, undetected energy deposits in detector (crack, gaps in the transition regions, inactive material), limited detector resolution and fluctuations in large energy deposits in non-instrumented regions such as the cryostat between the liquid argon and tile calorimeters
- mis-modeling of material distributions and instrumental failures
- cosmic rays showers
- pile up, LHC beam conditions
- hardware problems

Fake missing transverse energy can induce significant backgrounds as shown in Figure 5.5. It dominates at lower values and has a larger tail. For a good E_T^{miss} measurement it is important to understand its sources and to develop strategies to remove or suppress it. A detailed discussion of such strategies for early data can be found in Ref. [115, 270]. The main concepts considered a minimum azimuthal angular separation between the reconstructed E_T^{miss} and all jets in the event.

The left plot of Figure 5.5 shows the overall fake rate (red dots) and true E_T^{miss} (blue triangles) before applying a $\Delta\phi$ cut, the right plot shows the distribution after requiring a $\Delta\phi$ separation between E_T^{miss} and the leading high-p_T jet in the event. The fake rates can be strongly reduced. It should be noted that this cut is also applied in the SUSY analyses to suppress fake E_T^{miss} from Standard Model backgrounds like in QCD processes.

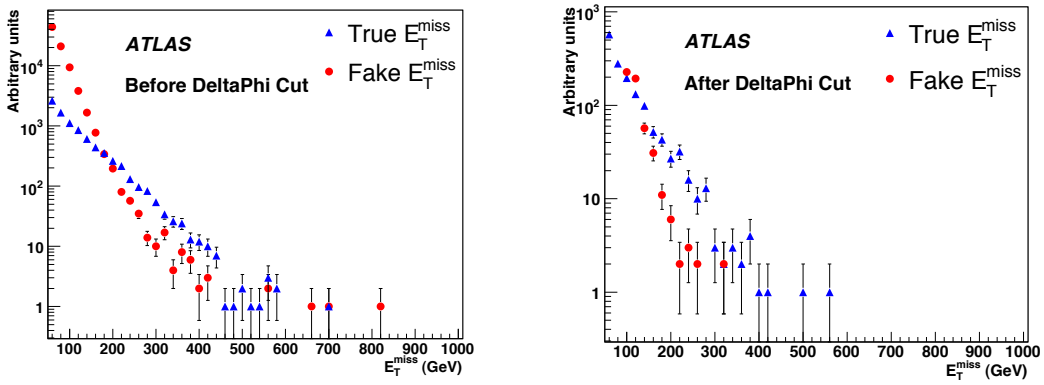

Figure 5.5: The rates of the fake E_T^{miss} and the true E_T^{miss} in the QCD sample with $560 < p_T^{jet} < 1120\ GeV$. The left plot shows the overall fake rate (red dots) and true E_T^{miss} (blue triangles), the right plot shows the distribution after requiring a $\Delta\phi$ separation between E_T^{miss} and the leading high-p_T jet in the event. Figures are taken from Ref. [104].

5.3.4. E_T^{miss} performance

Figure 5.6 (left plot) shows the E_T^{miss} response linearity, defined as the difference of the true to the reconstructed E_T^{miss} normalised to the true E_T^{miss} as a function of the true E_T^{miss} for different physics processes. The reconstructed E_T^{miss} based on globally calibrated cell energies including reconstructed muons gives a linearity within 5%. The calibration together with the muon and cryostat corrections terms shows a E_T^{miss} linearity below 1%. In the right plot of Figure 5.6 is the E_T^{miss} resolution σ as a function of $\sum E_T$, the scalar sum of the transverse energies of the calorimetric cells. The resolution is obtained from a Gaussian fit to the difference of the reconstructed to the true E_T^{miss} in each E_T^{miss} bin. A fit $\sigma = a \cdot \sqrt{\sum E_T}$, which describes the observed stochastic behaviour of the E_T^{miss} resolution, was applied, the parameter a varies between 0.53 and 0.57 for $\sum E_T$ between 20 and 2000 GeV for the different physics processes[5]. SUSY events are characterised by large values of ΣE_T, but the simulations show a similar behaviour to that of the Standard Model processes with the same value of this variable. Small deviations are observed for low values of $\sum E_T$, where the contribution of noise is important and for very large values of $\sum E_T$, where the constant term in the resolution of the calorimetric energy measurement dominates. For the Standard Model background this resolution is expected, because E_T^{miss} can come from either events with

[5]The points from $A \rightarrow \tau\tau$ are for masses m_A ranging from 150 to 800 GeV.

true missing energy (neutrinos) or from fake E_T^{miss}, that produces non-gaussian tails in the missing energy distribution. Requiring a minimum angular separation between the E_T^{miss} vector and the leading jets in the event as discussed, can strongly suppresses fake missing transverse energy and contributions from jets containing hard neutrinos from the leptonic decays of charmed and beauty mesons.

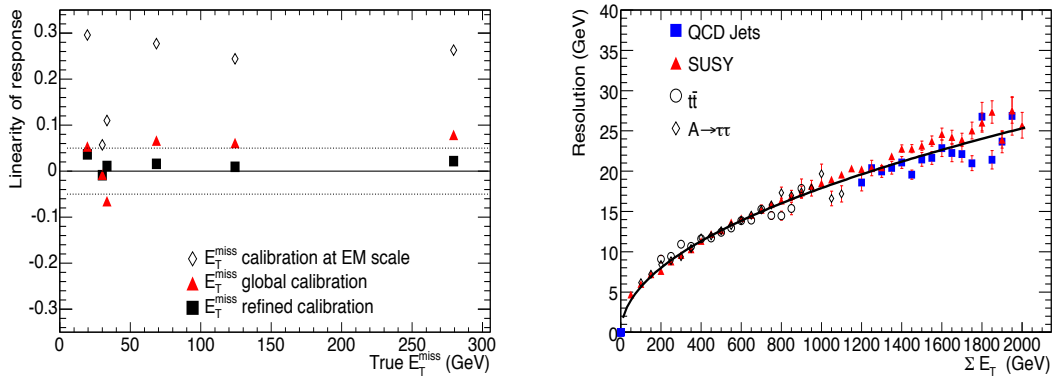

Figure 5.6: Left plot: Linearity of the reconstructed E_T^{miss} as a function of the average true E_T^{miss} for different physics processes. The values are determined from the physics processes $Z \rightarrow \tau\tau$ for the data point with average E_T^{miss} of 20 GeV, $W \rightarrow e\nu$ and $W \rightarrow \mu\nu$ for the data point at 35 GeV, semi-leptonic top decays for the point at 68 GeV, $A \rightarrow \tau\tau$ for the point at 124 GeV and SUSY decays with a typical mass scale of 1 TeV for about 280 GeV. Right plot: Resolution of the two components of the E_T^{miss} variable with a refined calibration as a function of the total transverse energy $\sum E_T$ in the calorimeter for different processes. The best fit $\sigma = 0.53 \sum E_T$ through the points from $A \rightarrow \tau\tau$ events is shown. Both figures are taken from Ref. [115].

Performance in the first data events

Figure 5.7 (left plot) presents the measured E_T^{miss} distribution for $\mathscr{L} = 0.3$ nb^{-1}. The Monte Carlo expectations are superimposed and have been normalised to the number of events in data. It can be seen that the measurement shows good agreement with the expectations from the Monte Carlo simulation. Above 10 GeV, the data distribution is systematically higher than the Monte Carlo, reaching up to 20%. One outlier event at $E_T^{miss} = 52$ GeV was found. This is due to a multi-jet event in which one of the jets points to a crack and appears to have been mis-measured. This feature could be reproduced in the Monte Carlo simulation. The E_T^{miss} resolution curve, presented in the same figure (right plot), increases as a function of $\sum E_T$. Higher values than 250 GeV could not be provided since the number of events was too small to apply a good fit. A reasonable agreement between data and Monte Carlo was found, a fit gives $\sigma(E_x^{miss}, E_y^{miss}) = 0.41 \cdot \sqrt{\sum E_T}$ for the data and $\sigma(E_x^{miss}, E_y^{miss}) = 0.43 \cdot \sqrt{\sum E_T}$ for the Monte Carlo with a negligible statistical uncertainty for both [268]. The differences in the resolution curve are less than 5%, that is probably also due to the imperfect description of the underlying physics in the PYTHIA MC sample used. The small

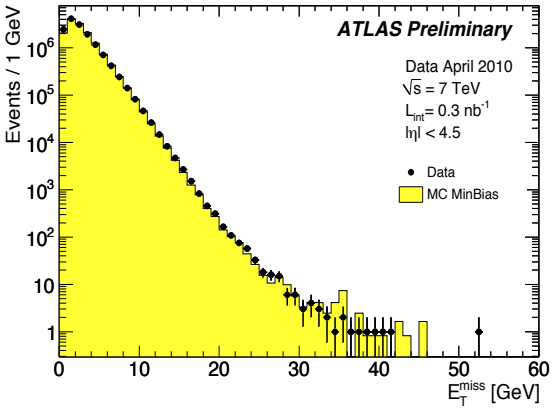

Figure 5.7: E_T^{miss} distribution (left plot) and the E_T^{miss} resolution as a function of the total transverse energy ($\sum E_T$) (right plot). Both distributions show the measured data of 14.4 million selected minimum bias events (dots) at $\sqrt{s} = 7$TeV recorded in April and May 2010 ($\mathscr{L} = 0.3$ nb^{-1}. In the calculation only topological cluster cell are used with energies calibrated at the electromagnetic scale. The expectation from the Monte Carlo simulation is superimposed and normalised to the number of events in data. The line in the right distribution represents a fit to the resolution obtained in the Monte Carlo simulation and the full dots represent the results from data taken. Both figures are taken from the Ref. [268].

discrepancies between the data and the Monte Carlo in the E_T^{miss} distribution are more pronounced in events containing high p_T jets. Comparisons, where different calibration methods are used (see Ref. [269]), demonstrate that E_T^{miss} reconstruction and calibration are well under control and reach the expected performance.

Further investigations are done at the moment in the presence of identified particles and jets for a refined E_T^{miss} reconstruction using a "global cell energy-density weighting calibration scheme" (Global calibration or GCW) [268]. This new calibration will be used for upcoming physics analyses. Studies are also ongoing to measure E_T^{miss} based on reconstructed tracks [271], since due to the increasing LHC luminosity the number of pile-up events will increase and a vertex-by-vertex estimation of E_T^{miss} disentangle many collision vertices in one proton-proton bunch crossing event.

5.4. Electrons

Electrons produced within the ATLAS detector will pass through the inner detector and leave due to the large amount of material most of its energy deposit in the electromagnetic calorimeter. The goal of the ATLAS electromagnetic calorimeter was to measure electrons within a large energy range of 5 GeV up to 5 TeV with a linearity better than 0.5%.

5.4.1. Electron reconstruction

For this challenge two different electron reconstruction algorithms are available in the ATLAS framework, both use electromagnetic calorimeter clusters and inner detector tracks. The first algorithm is optimised for low energy electrons and relies more on the electron identification capabilities of the inner detector. It uses good-quality tracks as a seed and constructs a cluster around the extrapolated impact point in the calorimeter.
The ATLAS default algorithm, used in the SUSY studies presented in this thesis, starts from clusters in the EM calorimeters and matches an inner detector track from the inner detector to them. For this electron reconstruction the "sliding window" clustering, described in Section 5.1.1, is applied. It forms a rectangular seed corresponding to 5×5 cells in the middle layer of the electromagnetic calorimeter and reconstructs a cluster of fixed size and position with significant energy deposition around it. The size of the selected cells depends on the seed position in the electromagnetic calorimeter. In order to reject calorimeter clusters corresponding to photons, tracking information is exploited. The clusters are required to match with a track within $\Delta\eta \times \Delta\phi = 0.05 \times 0.10$ such that the momentum of the associated track p and the cluster energy E is $E/p < 10$ (see Ref. [115]). The matched track is afterward checked that it does not overlap in a solid angle with a photon conversion reconstructed in the inner detector. If all criteria are fulfilled, an electron candidate is formed.

Identification

After the electron reconstruction, the identification of electrons is performed using the combined information of the calorimeters and the inner detector, including the discriminating techniques of the TRT. Three levels of electron qualities are defined: loose, medium, tight, based on simple box-cuts. In this thesis electrons are required to pass the medium cuts (see Chapter "Reconstruction and Identification of Electrons" in Ref. [104]).

Medium electrons For the "medium cuts" the shower shape variables (lateral and longitudinal shower profiles), calculated using the fine granularity of the electromagnetic calorimeter as well as the fraction of the electron energy deposited in the hadron calorimeter are used in order to suppress misidentified jets and to reduce backgrounds from electrons within a hadronic jets. In addition track-quality cuts are applied e.g. the matching track is required to have at least one hit in the pixel detector and in total at least nine hits in the pixel and SCT detectors to reject poorly reconstructed tracks. All cuts are explained in detail in Reference [104, 115].
Hadronic jets form the main background to the electron identification. On top of this selection, electrons are required to be isolated in order to reduce the misidentification rate of jets as electrons by reducing the rate of non-isolated electron candidates. The default calorimeter-based isolation variable for the selection of isolated electrons collects all calorimeter energy not belonging to the electron cluster deposited in a cone around the electron candidate. For the SUSY studies the transverse isolation energy in a cone of size $\Delta R < 0.2$ is require to be below 10 GeV. The used electron identification and reconstruction algorithms can be summarised as "EGamma" algorithm

[104,115]. They are recommended by ATLAS to separate electrons from hadronic jets [228].

Electrons in first data events

The electrons are reconstructed by an algorithm that provides a good separation between isolated electrons and a fake signature from hadronic jets, with a medium level selection criteria as discussed before. The calorimeter energy of an electron is required to be less than 10 GeV within a cone of radius $\Delta R < 0.2$ as used for the Monte Carlo studies to obtained more isolated electrons. Only electrons with $\mid \eta_2^{clus} \mid < 2.47$ are studied. In contradiction to the Monte Carlo studies the η_2^{clus} of the electrons is considered as the η value of the second sampling layer of the electromagnetic calorimeter. The SUSY analyses performed with first data events, that are discussed in this thesis (see Chapter 11) do not consider events with an electron.

5.4.2. Electron performance

The electron performance has been studied for different SUSY and Standard Model samples at different centre-of-mass energies. The following results will be presented for the SUSY signal sample SU3 and leptonically decaying top quarks[6]. For a further in-depth treatment on the electron performance see Ref. [272].
The electron energy resolution measures the quality of the reconstruction algorithm. Figure 5.8 shows the mean value of the electron resolution as a function of the transverse momentum (left top plot) and pseudorapidity $\mid \eta \mid$ (top right plot). It was found that SUSY signal (black dots) and top events (red triangles) show a very similar behaviour: At low p_T the truth transverse momenta for electrons are underestimated of about 3% of the reconstructed momentum value and remains slightly below 0 for electrons with higher p_T. The η distribution shows poorer performance in the barrel-end-cap transition region (crack region). Here the truth p_T is, on average, up to about 15% higher than the actual measured value [228]. This resolution degradation with respect to the more central values is expected. Therefore for all SUSY analyses events with an electrons in this region are excluded. The electron energy resolutions for different $\mid \eta \mid$ are fitted using the function (see Ref. [104]): $\sigma/E = a/\sqrt{E(GeV)} \oplus b/E \oplus c$
with a stochastic term (a), a noise term (b), and constant term (c). The stochastic term was found to be around 10.0% (for $\mid \eta \mid = 0.3$), 15.1% (for $\mid \eta \mid = 1.1$) and 14.5% (for $\mid \eta \mid = 2.0$) [104] for the electrons in the three η-values. The significant increase observed is due to the much larger amount of material in front of the EM calorimeter. The electron identification performance, estimated from reconstructed electron candidates in close proximity within a cone of $\Delta R < 0.02$ to a isolated truth electron, as a function of true transverse momentum and true pseudorapidity is presented in the bottom plots in Figure 5.8. The electron efficiency in SUSY SU3 events (black points) is slightly lower than the efficiency of the leptonically decaying top quarks (red points). This is an understood feature due to the higher level of hadronic activity generated in the long SUSY decay chains. Considering the left plot first, the efficiency increases to a plateau just above 70%, starting from a p_T of about 40 GeV ($\mid \eta \mid < 1.4$) and remains almost stable throughout to high values.

[6] Leptonically decaying top quarks constitute a major background for SUSY analyses with leptons.

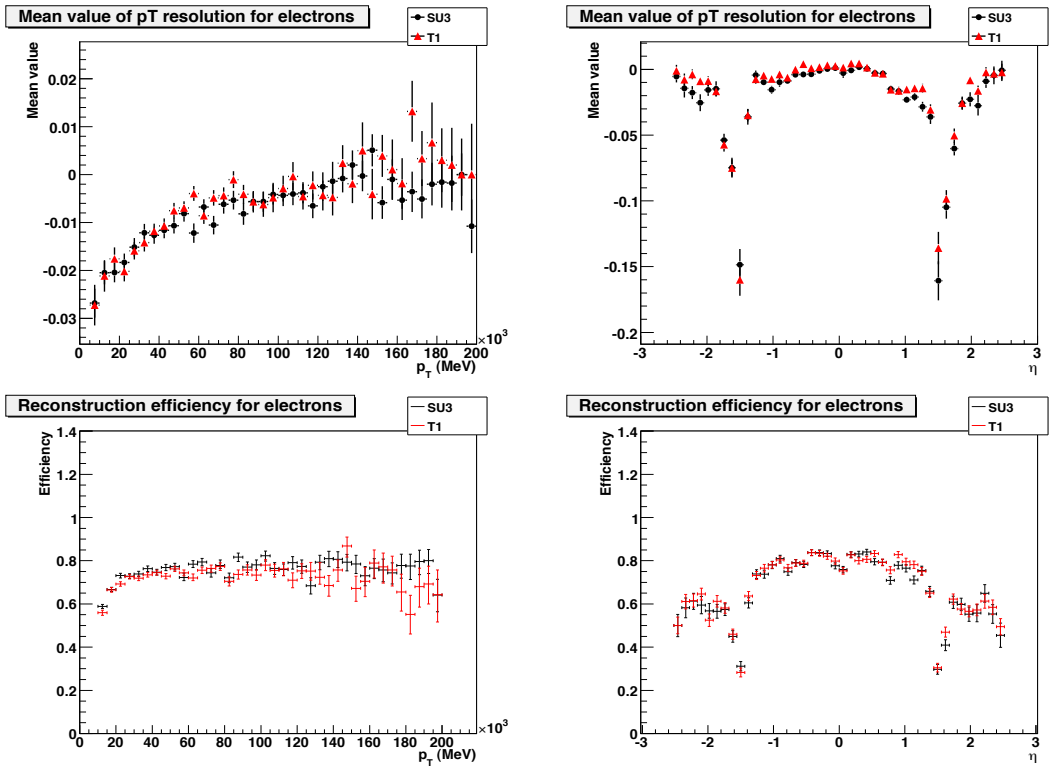

Figure 5.8: Mean value of the transverse momentum resolution for electrons as a function of transverse momentum (top left plot) and pseudorapidity (top right plot; transverse momentum required to be > 5 GeV). The bottom plots show the reconstruction efficiency of isolated electrons as a function of true transverse momentum (left bottom plot) and true pseudorapidity (right bottom plot, transverse momentum required to be > 10 GeV) for the SUSY signal SU3 (black) and leptonically decaying top quarks samples (red). The figures are taken from Ref. [273].

The η dependency of the efficiency (right plot) mirrors as expected the geometry features of the detector, showing an efficiency of roughly 80% in the barrel region ($|\eta| < 1.4$), worse performance of approximately 60% in the end-cap region due to the larger amount of material and substantial drops around the cracks ($|\eta| \approx 1.35$). Also the half-barrel transition at $\eta \approx 0$ is visible. Again both processes show a very similar behaviour. Other samples studied in Ref. [272] show similar results such that one can conclude that the reconstruction efficiency is almost sample independent. The uncertainty on the electron efficiency is expected to be around 0.5% for an integrated luminosity of 1 fb^{-1} [272] obtained from the $Z \rightarrow ee$ decay using the so-called tag-and-probe method [274]. For all studied SUSY analyses the requirement of a high p_T electron is associated with additional requirements on jets and E_T^{miss}. Therefore jet backgrounds are normally already reduced before requiring a lepton and relatively soft electron identification cuts can be applied. The minimum 10 GeV (20 GeV) threshold for the lepton transverse momentum p_T (see Section 7.1) is a good

compromise between the need to have reasonable lepton acceptance at relatively low p_T values, and the requirement to keep the contamination from non-prompt leptons to an acceptable level and leads to a significant gain in efficiency especially for searches involving many leptons.

5.4.3. Electron fake rate

Every isolated reconstructed electron, which cannot be matched to a truth one within a cone of $\Delta R < 0.02$ is considered a be fake. Contrary to the case for the efficiency, the truth electron does not need to be isolated as it often emits Bremsstrahlung, which compromises its factual isolation. One then tries to match those fake electrons to either jets or taus within a cone of $\Delta R < 0.2$. Consequently, the fake probability (*fake rate*) is defined as the number of true jets/taus, which fake electrons divided by the total number of true jets/taus. The probability for jets to fake electrons peaks at around p_T = 40 GeV for the SUSY signal and the $t\bar{t}$ background sample and decreases for higher energetic electrons since harder jets have a stronger leakage into the hadronic calorimeter and are therefore less prone to be misidentified as electrons. On average, the overall fake probability amounts to about 0.1% for both samples (see Ref. [228]) and is as expected higher in the crack regions. The overall probability for a tau to fake an electron is about 2%, which is roughly 10 times higher than the jet fake rate.

5.5. Muons

The ATLAS detector is designed to provide a precise measurement of muons over a wide range of momenta and angles. Muons are identified and measured primary in the muon spectrometer (see Section 3.3.6), but also in the inner detector (see Section 3.3.4) and calorimeters (see Section 3.3.5).
The muon spectrometer covers the pseudorapidity range $|\eta| < 2.7$ and allows the identification of muons with a momentum above 3 GeV and a precise determination up to the TeV range (about 3 TeV for precise measurements, see Ref. [275]). The magnetic field hereby guarantees excellent momentum resolution even at the highest values of η. The muon system also triggers on muons within $|\eta| < 2.4$ as described in Section 3.3.6.
The calorimeters can detect muons and other charged particles with hermetic coverage for $|\eta| < 2.5$ and can thus give an important confirmation of the muons found by the muon spectrometer over that pseudorapidity range. The energy measurements in the calorimeters can also help in the muon identification, since the direct the energy loss is measured [276]. At low and intermediate momenta the best muon resolution is obtained by the inner detector.
There are several detector regions where the different detector systems overlap and provide an important confirmation of the found muons. Combining the information from each subsystem in the reconstruction algorithm also improves the muon identification efficiency and momentum resolution. In the p_T-range between 30 GeV and 200 GeV the combined muon momentum measurements from the inner detector and muon spectrometer give a precision better than either alone. Over most of the acceptance, the inner detector measurements dominate below this range, and the spectrometer above it.

5.5.1. Muon reconstruction

A variety of strategies for the muon identification and reconstruction exist. The main three track-strategies are:

- Stand-alone muons: Direct approach to reconstruct muons. The track reconstruction is based on finding tracks in the muon spectrometer up to the range of $|\eta| < 2.7$ and the extrapolation to the beam line.
- Combined muons: Matching standalone muons with inner detector tracks and combination of the measurements from both systems over the range of $|\eta| < 2.5$.
- Tagged muons: Combination of an inner detector track with a muon-spectrometer segment. Inner detector muon tracks are extrapolated to the muon spectrometers and matched to hits/segments.

Several independent algorithms have been developed to implement these muon reconstruction strategies. For each of the three approaches, two competing algorithms, that are grouped into two families, are available in the ATLAS framework. The collections (and families) are named after the algorithms used for the combined muons: **STACO** [277] and **MUID** [278]. Every processed event includes these two collections of reconstructed muons.
The STACO collection was the default one for physics analysis recommended by ATLAS. It is used for all SUSY analyses performed in this thesis.
In the following the reconstruction strategies mentioned above are shortly described.

Standalone muons

The standalone algorithms builds tracks segments in each of the three muon stations, starting from the outer and middle stations. The track segments are hereby defined as straight lines in a single muon station. In a next step it extrapolates these segments through the magnetic field to the segments reconstructed in the other stations. When a reasonable match is found, the segment is added to the track candidate. The track-fitting finally links the segments in each of the three muon stations to form the final tracks. It hereby takes into account the full geometrical description of the traversed material and the magnetic field inhomogeneities along the muon trajectory. The track is then propagated back to the interaction point and the momentum is corrected for multiple scattering and the energy loss in the calorimeters (and in the inner detector). The **STACO**-family algorithm, that finds the spectrometer tracks and extrapolates them, is called *Muonboy* [277]. The algorithms that provides stand-alone muon reconstruction for the MUID group is called *Moore* [279]. Muonboy assigns energy loss based on the material crossed in the calorimeter, while Moore additionally uses calorimeter energy measurements.
The standalone algorithms covers the region $|\eta| < 2.7$ (compared to 2.5 for the inner detector), but there are holes in the coverage at $|\eta| = 0$ (due to inner detector cables, cryogenic lines) and at $|\eta| \approx 1.3$ (acceptance is degraded around $1.1 < |\eta| < 1.7$). Very low momentum muons (of few GeV) may be also difficult to reconstruct, because they do not penetrate to the outermost stations.

Combined muons

In both algorithms (STACO and MUID) stand-alone tracks that are reconstructed in the muon spectrometer are combined with inner detector tracks to identify combined muons. This procedure is limited by the geometrical acceptance of the inner detector to $|\eta| < 2.5$. The method is expected to considerably improve the momentum resolution for low p_T muons (<100 GeV) [104] and helps to suppress fake muon background arising from pion punch-through or pion and kaon decays in flight. A matching χ^2, defined as the difference between outer and inner track vectors weighted by their combined covariance matrix, is calculated (for details see e.g. Ref. [104], page 166). The STACO algorithm hereby does a statistical combination of the inner and outer track vectors to obtain the combined track vector. For the SUSY searches the track segment match χ^2 was loosely required to be smaller than 100 ($\chi^2 < 100$) to select good track pairs.
It should be noted that stand-alone muons, that are combined/matched with more than one inner detector track, are not recorded separately. If more than one track in the inner detector matched a track from the muon spectrometer, only the one with best match (smallest distance ΔR) was kept. It is flagged as "best match".

Tagged muons

Two algorithms are implement for the muon spectrometer tagging strategy: *MuTag* [277], that is part of the STACO family and *MuGirl* [280], that is grouped with the MUID algorithms. Both propagate all inner detector tracks with sufficient momentum, out to the first station of the muon spectrometer, search for nearby segments and extrapolate the tracks to the inner muon stations. The extrapolated tracks are there associated to the muon segments. The last step, the matching or tagging, is implemented differently by the two algorithms. MuTag defines a χ^2 using the extrapolated track prediction and nearby segments, whereas MuGirl employs a neural network to select muon segments. Therefore, muons reconstructed by MuTag (STACO) do not overlap, which is not the case for muons identified by MuGirl (MUID). In both cases, if a segment is sufficiently close to the predicted track position, then the inner detector track is tagged as corresponding to a muon. The tagged muons can significantly improve the overall muon reconstruction efficiency, since the tagging algorithm can identify muons, which have been missed by the stand-alone reconstruction.

Combined algorithms

The overall muon finding efficiency (and fake rate) can be increased by including muons found by multiple algorithms, but overlaps must be removed. In the STACO collection, the tagged and combined muons do not overlap by construction. To merge stand-alone and tagged muons, muons are required to have different inner detector tracks and stand-alone muons are merged, if they are too close to one another.
For all SUSY analyses STACO muons found with the combined algorithms are used. In addition to all the discussed requirements, the total calorimeter energy deposited in a cone of $\Delta R < 0.2$ around the reconstructed muon should be less than 10 GeV to make sure that muons are isolated.

Muons in first data events

The same algorithm as for the Monte Carlo studies was used to identify muon candidates. Muons are reconstructed by the discussed STACO-algorithms. They are required to have a best matched-χ^2 smaller than 100, an isolated muon is obtained by requiring calorimeter energy around the muon to be less than 10 GeV within a cone of $\Delta R = 0.2$. Muons are selected for the final analyses if they pass these requirements and if they have $p_T > 10$ GeV and $|eta| < 2.5$. The SUSY analyses performed with first data events presented in this thesis, veto events with an reconstructed muon.

5.5.2. Muon performance

Figure 5.9 (top plots) shows the expected fractional momentum resolution, as a function of $|\eta|$ averaged over ϕ (top left plot) and as a function of ϕ (top right plot) for single muons with $p_T = 100$ GeV as obtained for stand-alone (black squares) and combined muon tracks (white squares). The average combined muon resolution is close to 3%. The degradation of the resolution in the region $1.1 <|\eta|< 1.7$ is due to the absence of the middle muon stations in the barrel/end-cap transition region. At larger values of η the lower bending power of the magnetic field in the transition region between the barrel and end-cap toroids, and at large ϕ values the extra material of the coils of the end-cap toroids cause also a small resolution degradation. The resolution plots as a function of p_T (excluding the η region $1.1 <|\eta|< 1.7$) in the same figure (bottom plots) indicate in which region the resolution improves, when the muon spectrometer and inner detector measurements are combined. As expected, the gain is most pronounced in the low-p_T regime, the optimal resolution is achieved at $\sim$100 GeV. At lower transverse momenta is the stand-alone muon resolution dominated by fluctuations in the energy loss in the calorimeters, whereas the combined muon resolution reflects the dominant performance of the inner detector. The energy scale and the energy resolution of the muons are expected to be understood and known to 0.3% and 4%, respectively for 1 fb^{-1} of integrated luminosity [104].
The muons in the events can originate from several sources e.g. they are produced in the decays of "heavy" particles like SUSY particles, Z and W bosons, τ leptons or from fragmentations of heavy and light flavoured jets. It is also possible that muons are radiated in Bremsstrahlung processes. The muon efficiencies were studied for different samples and can be found in Reference [272]. The performance studies within the SUSY group concentrated on studying the STACO muon efficiencies for the SUSY signal samples SU1, SU3 and SU4, and on leptonically decaying top quarks, which constitute a major background for SUSY analyses with leptons. Pile-up and cavern background simulations were not included in the mentioned signal and background samples, only statistical errors on the available event statistics are considered using the default STACO-algorithm.
Figure 5.10 shows the muon efficiency as a function of p_T (left plots) and of η (right plots) for SUSY SU3 signal events (top plots) and for the leptonically decaying $t\bar{t}$ (T1) events (bottom plots) studied for a centre-of-mass energy scenario of $\sqrt{s} = 14$ TeV. Only STACO muons with $p_T >$ 20 GeV and $|\eta| < 2.5$ are considered. The efficiency is defined as the fraction of reconstructed

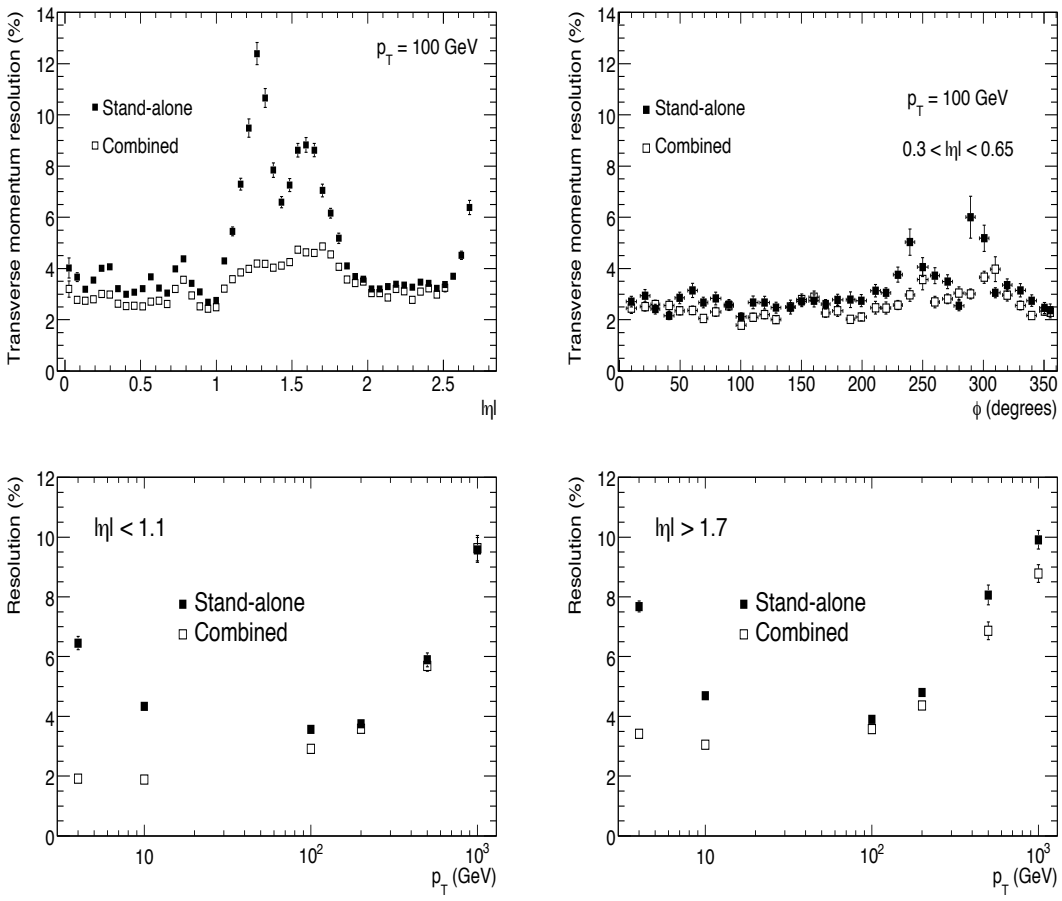

Figure 5.9: Expected STACO muon stand-alone and combined fractional momentum resolution as a function of $|\eta|$ (top left), ϕ (top right) and p_T in the barrel (bottom left) and end-cap (bottom right). The Figures are takes from Ref. [115]. For the two top plots only simulated single muons with p_T = 100 GeV are used.

and matched muons to the number of simulated muons, where the matching requires a geometrical agreement within a cone of size $\Delta R = 0.02$. The efficiency of the SUSY SU3 events is similar to the efficiency of the top sample of about 0.9. After applying an overlap removal between jets and muons, that removes muons found in a distance ΔR <0.4 from reconstructed jets (see discussion in the next Section), the average efficiency decreases to ≈ 0.85 for the studied SUSY signals and 0.87 for the top sample. In terms of η this reduction is mostly in the central barrel region $|\eta| < 1.5$. For both samples the efficiency drops at $\eta \sim 0$ and around 1.3 due to the gap for services and the transition region as mentioned earlier. The uncertainty of the muon efficiency is expected to be around 2-7% for an integrated luminosity of 1 fb^{-1}.

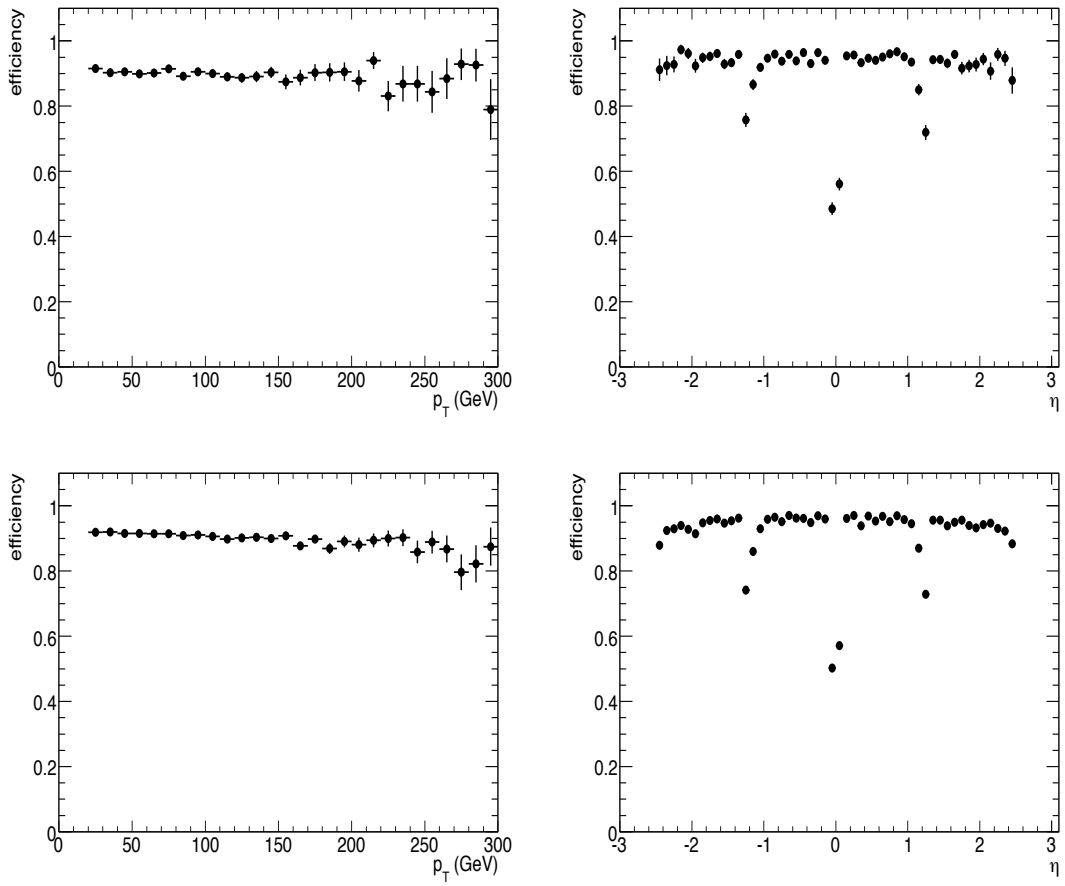

Figure 5.10: STACO muon efficiency as a function of p_T (left plot) and η (right plot) for SUSY SU3 signal events (top plots) and for the leptonically decaying $t\bar{t}$ (T1) events (bottom plots) at $\sqrt{s} = 14$ TeV. The muon transverse momentum is required to be $p_T > 20$ GeV and the pseudorapidity $|\eta| < 2.5$, no isolation requirement $\Delta R(\mu, \text{jet}) > 0.4$ was applied.

5.5.3. Muon fake rate

Low-momentum tracks can be an irreducible sources of fake stand-alone muons. Most of them can be rejected by a cut on their transverse momentum $p_T > 5$ GeV. For the SUSY searches a minimal cut of $p_T = 10$ GeV and $|\eta| < 2.5$ was required. The fake rates are in the order of 10^{-4}-10^{-5} mostly due to contribution of reconstructed muons coming from jets. If a very tight isolation requirement $\Delta R(\mu, \text{jet}) > 0.4$ is applied, the fake rate is reduced by $\sim 85\%$ for the top sample and $\sim 80\%$ for the SUSY SU3 sample. The stronger reduction for top events is expected as they have two b-jets.

5.6. Overlap between physics objects

It is noteworthy that the reconstruction algorithms discussed in this section can produce overlapping objects, such as a jet and an electron both with the same calorimeter cluster or jets with muons. To avoid double counting an object, this issue is dealt with by a so-called overlap removal procedure, which is discussed in the next Chapter in Section 7.1 for every object individually.

6. Searches for Supersymmetry with the ATLAS detector at the LHC

The LHC has an excellent potential to discover significant parts of the SUSY parameter space. A variety of theoretical models have been proposed in the last decades that may be realized at the LHC and ask for their investigation. The focus of this thesis is on R-parity conserving SUSY models, which have a high potential to be probed at the LHC within the first years of running.
This chapter gives a brief overview of the expected patterns of supersymmetric production and the subsequent decay chains at the LHC. The experimental bounds and theoretical constraints for SUSY searches are sketched, and the ATLAS SUSY search strategy for R-parity conserving SUSY models is described.

6.1. Production processes of Supersymmetric particles at the LHC

At hadron colliders, sparticles can be induced by parton collisions of electroweak or QCD strength. Squarks and gluinos are mainly produced via the strong interaction from gluon-gluon and quark-gluon fusion as well as from quark-antiquark annihilation and quark-quark scattering as demonstrated in Figure 6.1, that shows the leading-order Feynman diagrams for the processes $gg \rightarrow \tilde{g}\tilde{g}$, $gg \rightarrow \tilde{q}_i\tilde{q}_j^*$ and $gq \rightarrow \tilde{g}\tilde{q}_i$. The feynman diagrams for the processes $q\bar{q} \rightarrow \tilde{g}\tilde{g}$, $q\bar{q} \rightarrow \tilde{q}_i\tilde{q}_j^*$ and $qq \rightarrow \tilde{q}_i\tilde{q}_j$ can be found e.g. in Ref. [56]. Charginos, neutralinos as well as sleptons can be directly produced via the weak interaction from quark-antiquark annihilation e.g. in the processes $q\bar{q} \rightarrow \tilde{\chi}_i^0\tilde{\chi}_j^0$, $q\bar{q} \rightarrow \tilde{\chi}_i^+\tilde{\chi}_j^-$, $q\bar{q} \rightarrow \tilde{l}_i^+\tilde{l}_j^-$ and $q\bar{q} \rightarrow \tilde{\nu}_l\tilde{\nu}_l^*$ as presented in Figure 6.2.
As one can see in the feynman diagrams the charginos and neutralinos get e.g. contributions from electroweak vector bosons in the s-channel, while the squarks and gluinos production processes get for instance contributions from the t-channel exchange of an appropriate squark or gluino [56]. Since the couplings of the SUSY particles are identical to the couplings of their Standard Model partners, the production cross sections of SUSY particles depend only on the parton density functions (PDFs) evolved to the appropriate Q^2-scale at the hadron collider and on the mass spectrum,

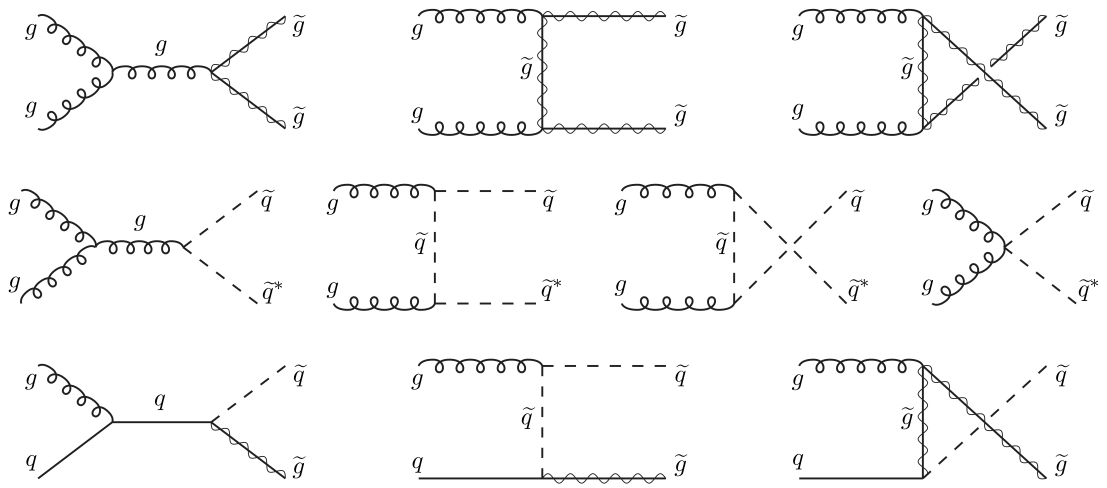

Figure 6.1: Leading-order feynman diagrams (leading-order) for gluino and squark production from gluon-gluon and gluon-quark fusion, taken from Ref. [56].

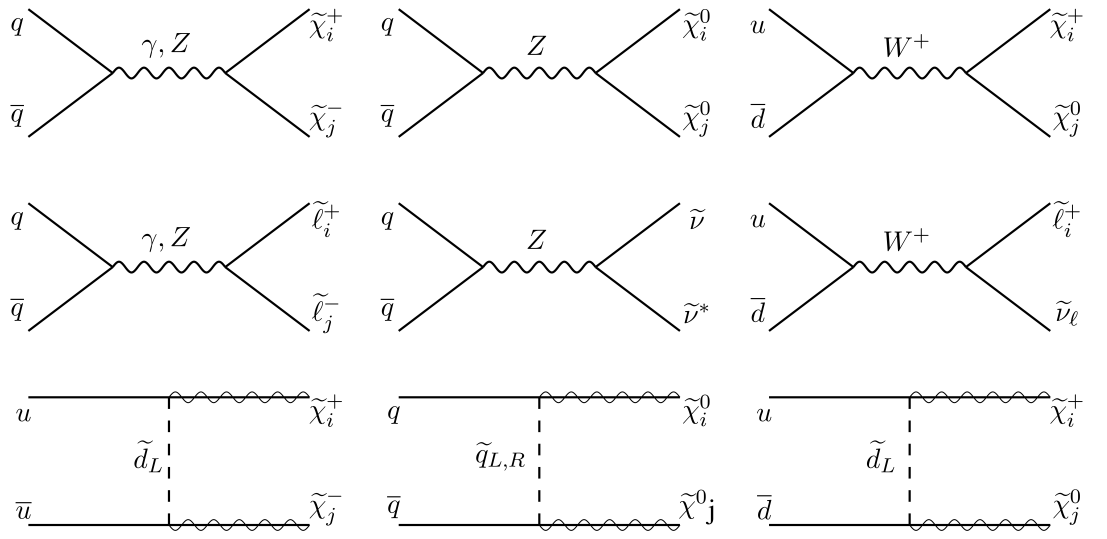

Figure 6.2: Leading-order feynman diagrams for electroweak production of supersymmetric particles from quark-antiquark annihilation, taken from Ref. [56].

mainly on the squark and gluino masses, of the produced SUSY particles [281]. There are no further strong dependencies on the SUSY parameters. Thus, if squarks and gluinos are sufficiently light, the strong production processes $\tilde{g}\tilde{g}$, $\tilde{g}\tilde{q}$ and $\tilde{q}\tilde{q}$ usually dominate at the LHC due to the high centre-of-mass energy, unless the gluino and squarks are heavier than ≈ 1 TeV, followed by the electroweak production of charginos and neutralinos.

6.2. Decay of SUSY particles

The supersymmetric particles interact similarly to their SM superpartners, however an important feature of the models under discussion is that the superpartners are not necessarily the mass eigenstates of the theory (see Section 2.2.6). Due to the mixing the mass eigenstates, sparticles can receive couplings belonging to several sparticles. This has consequences for the possible sparticles decays. The lone exception is the gluino, which is a colour octet fermion and therefore does not have the appropriate quantum numbers to mix with any other particle.
Within R-parity conserving models (see Section 2.2.3), SUSY particles are produced in pairs and decay through several chains to the lightest supersymmetric particle (LSP). Assuming that the squarks and gluinos are heavy, this decay can proceed through several chains of decays into gradually lighter sparticles ("cascade decay"), accompanied typically by additional high energy quarks, gluons and possibly other Standard Model particles. Since all decay modes end with the LSP production, the SUSY signatures are characterised mainly by the nature of the next-to-lightest SUSY particle (NLSP) and next-next-to-lightest SUSY particle (NNLSP).
The main decay modes of SUSY particles will be summarised in the following paragraph. It is assumed that the lightest neutralino $\tilde{\chi}_1^0$ is the LSP.

Chargino and neutralino decays

Charginos and neutralinos are mixed mass eigenstates of the gauginos ($W^{\pm}, \tilde{B}^0, \tilde{W}^0$) and higgsinos ($H_u^+, H_d^-, \bar{H}_u^0, \bar{H}_d^0$). If sleptons or squarks are light, they can thus decay either into a slepton and a lepton or a squark and a quark. If the mass difference between the neutralinos/chargino and a lighter neutralino is large enough, another possible two body decay is into any lighter neutralino or chargino plus a Higgs scalar or an electroweak gauge boson, with the subsequent decay into a possible fermion pair, such as:

$$\begin{aligned}\tilde{\chi}_2^0 &\rightarrow Z\tilde{\chi}_1^0; W^{\pm}\tilde{\chi}_1^{\mp}; h_0\tilde{\chi}_1^0; l\tilde{l}; \nu\tilde{\nu}; q\tilde{q}\\ \tilde{\chi}_2^{\pm} &\rightarrow Z\tilde{\chi}_1^{\pm}; W^{\pm}\tilde{\chi}_1^0; h_0\tilde{\chi}_1^{\pm}; \nu\tilde{l}; l\tilde{\nu}\end{aligned}$$

with the notation ν ($\tilde{\nu}$) for a (s)neutrino, l ($\tilde{l}$) for a charged (s)lepton and q ($\tilde{q}$) for a (s)quark. If the two-body chargino and neutralino decay modes are kinematically forbidden, three-body decays through the same (but now off-shell) gauge bosons, Higgs scalars, sleptons, and squarks into any

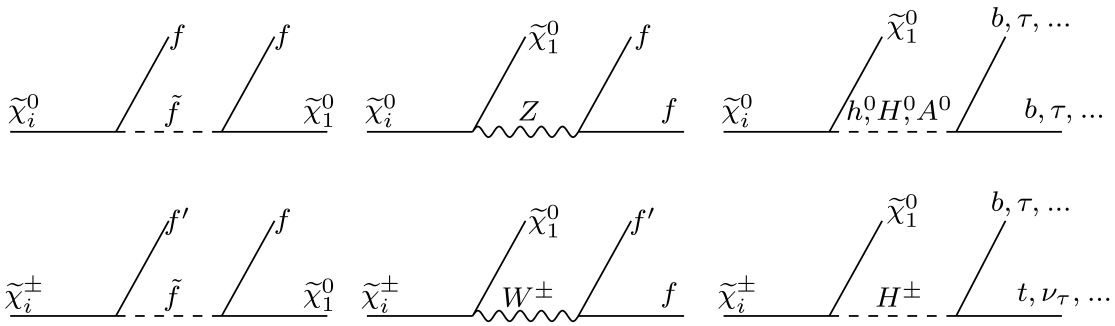

Figure 6.3: Neutralino and chargino decays with a $\tilde{\chi}_1^0$ in the final state, taken from Ref. [56]. The scalar or vector boson in each decay can be either on-shell or off-shell, depending on the sparticle mass spectrum.

lighter neutralino or chargino and leptons (l^+, l^-) or jets (j) are also possible, for example: $\tilde{\chi}_2^0 \to jj\tilde{\chi}_1^0, \tilde{\chi}_1^\pm \to jj\tilde{\chi}_1^0; \tilde{\chi}_2^0 \to l^+l^-\tilde{\chi}_1^0$.

The Feynman diagrams for the neutralino and chargino decays with a $\tilde{\chi}_1^0$ in the final state are illustrated in Figure 6.3. The variable f (f') denote a (anti)fermion and are distinct members of one $SU(2)_L$ multiplet. If the $\tilde{\chi}_2^0 \to jj\chi_1^0$ decay goes through an h^0, b-jets are produced. This mode dominates, if the mass difference between $\tilde{\chi}_2^0$ and $\tilde{\chi}_1^0$ is larger than the Higgs boson mass.
In many SUSY models sleptons are probably lighter than squarks, so the lepton + slepton decays dominate. As discussed in the previous chapter (see Section 2.2.6), the masses and field content of the staus can be different from the values for the other two slepton generations, which leads often to larger branching ratios for final states with taus than for final states with electron or muons.
The detector signatures which result from the neutralino or chargino decays are characterised by missing transverse energy in addition with various combinations of jets and charged leptons, for example 4 jets only, 2 jets and two charged leptons or three or four charged leptons only. The final state with three charged leptons (trilepton final state) is the most promising channel for searches for charginos and neutralinos at the Tevatron due to the relative small Standard Model background. The neutralino or chargino decays into quark partons are possible signatures studied in the 0-lepton channel.

Slepton decays

If the sleptons are heavy, sneutrino $\tilde{\nu}$ and slepton $\tilde{l}$ decays can be important. Each charged lepton has two scalar partners, the right and left-handed charged scalar sleptons $\tilde{l}_R, \tilde{l}_L$ (see Section 2.2.6). The dominant slepton decay modes for them are: $\tilde{l}_L^\pm \to \tilde{\chi}_j^0 + l^\pm$, $\tilde{l}_L^\pm \to \tilde{\chi}_j^\pm + \nu$, $\tilde{\nu} \to \nu + \tilde{\chi}_j^0$, $\tilde{\nu} \to l^\pm + \tilde{\chi}_j^\mp$, where j can be 1 or 2. Right-handed sleptons do not couple to winos, but to the bino and therefore prefer the decay into a $\tilde{l}_R^\pm \to l^\pm + \tilde{\chi}_1^0$, if it is more bino-like.

The slepton production and decays described, can lead to signatures with the simplest event topology: two leptons + missing transverse energy. In the case of indirectly produced sleptons, topologies with with single, three or four leptons are also possible (with and without jets).

Squark and gluino decays

The primary production at the LHC comes from cascade decays of pair-produced squarks $\tilde{q}$ and gluinos $\tilde{g}$. Their decay modes are controlled by the mass-relations between each other. They can decay into a 2-body final state through the strong interaction or they decay to gaugino plus quark(s): $\tilde{q} \to q + \tilde{\chi}_j^0$; $\tilde{q} \to q' + \tilde{\chi}_j^\pm$. Left-handed and right-handed squarks have hereby different preferences. The decays into a neutralino $\tilde{\chi}_1^0$ is favoured for the right-handed squarks, since $\tilde{\chi}_1^0$ is mostly bino-like, while left-handed squarks prefer decays into heavier and more wino-like neutralinos (see Section 2.2.6). Squark decays to higgsino-like charginos and neutralinos are less important, except in the cases of stops and sbottoms, which have sizable Yukawa couplings. In many models stop and sbottom quarks are much lighter than the other squarks, that leads to stop/sbottom production with an additional b/t quark. If the decay of stops into a gluino or $\tilde{\chi}_1^0$ are kinematically forbidden $\tilde{t}_1 \to t + \tilde{g}, \tilde{t}_1 \to t + \tilde{\chi}_1^0$, than the lighter top squark may decay only into charginos $\tilde{t}_1 \to b + \tilde{\chi}_1^\pm$. In case this decay is also not kinematically possible, only the flavour-suppressed decay to a charm quark $\tilde{t}_1 \to c + \tilde{\chi}_1^0$ and the four-body decay $\tilde{t}_1 \to b + f + f' + \tilde{\chi}_1^0$ are possible. These decays can be very slow resulting in a quasi-stable stop $\tilde{t}_1$.
A coloured gluino can only proceed through a squark, either on-shell or virtual. Typically the two body decay $\tilde{g} \to q + \tilde{q}$ is dominant when the gluino is heavier than the squarks. For models when the squarks are heavier than the gluinos, the gluino will decay only through off-shell squarks (see Figure 6.4).
The produced squarks, neutralinos and charginos in all these final states will then decay as discussed before, so there can be many competing gluino decay chains. Some of the decays are shown in Figure 6.5. Due to the high number of possible cascade decays, the final-state branching fractions are individually small and quite sensitive to the model parameters.
The gluino and squark decays lead to many different detector signatures with missing transverse energy and $0, 1, 2$ or more charged leptons in addition to two or more hadronic jets.

6.3. Experimental constraints on SUSY searches

In the past decades many experiments have been searching for new particles or indirect effects via radiative corrections or gravitational influence. The most significant direct constraints on the masses of the supersymmetric particles have been obtained with the e^+e^- collisions at LEPII by the ALEPH, DELPHI, L3 and OPAL collaborations [30, 282] and with the $p\bar{p}$ collider at Tevatron by the DØ [283] and CDF [284] collaborations. So far, at 95% confidence level no signal consistent with supersymmetry has been found by any collider experiment.

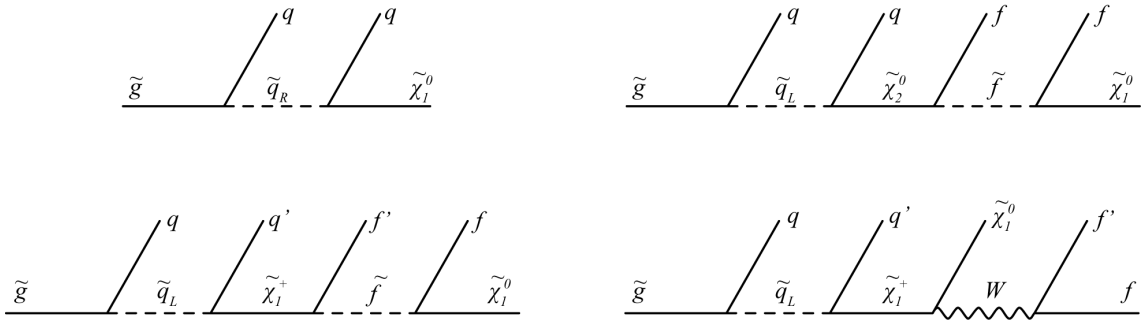

Figure 6.4: Some examples for a gluino cascade ending with a neutralino $\tilde{\chi}_1^0$ in the final state. The squark can be either on-shell or off-shell depending on the mass spectrum of the SUSY model. Figure is taken from Ref. [56].

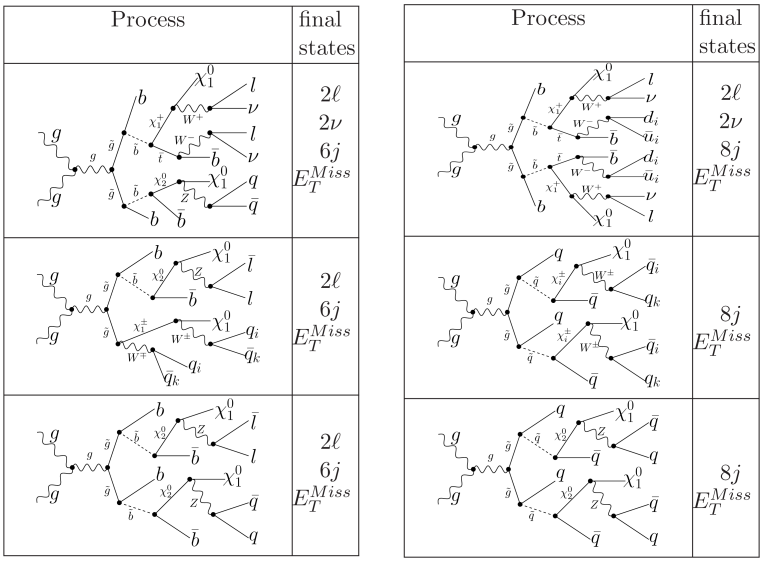

Figure 6.5: Examples for possible decay chains for gluino pair production processes with a $\tilde{\chi}_1^0$ in the final state. Figure is taken from Ref. [74].

6.3.1. Constraints from collider experiments

A wide variety of searches has been carried out at LEPII in the MSSM parameter space with R-parity conservation. The resulting limits on the chargino, neutralino and slepton production cross section have been translated into limits on the masses of these particles, typically near the kinematic production threshold. The mass constraints are than interpreted within a specific SUSY model in the CMSSM (see Section 2.2.8) parameter space. The lower mass limits for charged sparticles from the LEP experiments are nearly half of the beam energy, which reached a centre-of-mass energy of 209 GeV. Figure 6.6 (left plot) shows the combined exclusion limit in the slepton-neutralino ($m_{\tilde{l}_R} - m_{\tilde{\chi}_1^0}$) plane of the four LEP experiments, obtained from the combination of the direct searches for selectrons, charginos and neutralinos. Smuon and stau masses lower than $m_{\tilde{\mu}} \approx 95$ GeV, $m_{\tilde{\tau}} \approx 82$ GeV [47,285], depending on the $\tilde{\chi}_1^0$ mass and the mass difference between the $\tilde{\chi}_1^0$ and the slepton, can be excluded by LEP for the studied constrained MSSM models. Selectrons are excluded with masses below $m_{\tilde{e}} \approx$ 100GeV [285,286]. In the case of staus, the enhanced mixing of left and right-handed components has to be considered as well as the decays of the τ lepton that lead to reduced selection efficiencies. Stau masses smaller than 82 GeV are excluded, depending again on the $\tilde{\chi}_1^0$-mass and assuming a $\tilde{\tau}_R$-$\tilde{\chi}_1^0$ mass difference of at least 15 GeV [47]. The right plot in Figure 6.6 shows the 95% exclusion limit for the lightest chargino mass as a function of the sneutrino mass. For large slepton/sneutrino masses the lower bound on the chargino mass is $m_{\tilde{\chi}_1^+} >$103.5 GeV [47,287]. Assuming unification of gaugino masses at the GUT scale, the chargino lower mass bound is about 93 GeV [47]. LEP has also studied the mSUGRA parameter space for different values of sign(μ) and $\tan\beta$. Due to the combination of the results of the searches for charginos, sleptons and the Higgs bosons[1] a lower limit on $m_{1/2}$ as a function of m_0 could be calculated. Figure 6.7 (left plot) presents the exclusion regions within the mSUGRA m_0-$m_{1/2}$ plane for $\tan\beta = 10$, sign(μ) > 0 and $A_0 = 0$ (see Ref. [289]). For large values of m_0, the chargino searches exclude $m_{1/2}$ values up to ≈ 160 GeV. Including the results from the Higgs boson searches regions up to $m_{1/2} \approx 300$ GeV for $m_0 = 0$ could be excluded. The limit is decreasing to $m_{1/2} \approx 180$ GeV for increasing m_0 values up to 1000 GeV. The combined results could be also used to set a lower constraints for the mass of the lightest neutralino in the corresponding model. For the studied mSUGRA framework, the LSP lower mass limit is found to be 48 GeV for any value of $\tan\beta$, m_0 and A_0 [47,289] (see Figure 6.7, right plot). Further constraints can be found in Ref. [47].

Several mass limits arise from the Tevatron Run II data. At the $p\bar{p}$ collider in large parts of the mSUGRA parameter space (not ruled out by the LEP constraint on the lightest chargino mass) the gluinos are too heavy, therefore direct chargino pair and chargino/neutralino associated productions dominate. The three leptons + missing transverse energy final state was studied by both experiments CDF and DØ. The recent exclusion limits in the mSUGRA parameter space with $\tan\beta = 3, A_0 = 0$ and sign(μ) > 0 are chargino masses $m_{\tilde{\chi}_1^+} > 165$ GeV [290].

Figure 6.8 shows the exclusion regions in the studied m_0-$m_{1/2}$ mSUGRA parameter space published by the DØ-collaboration [290].

[1] A set of constraints on the MSSM Higgs sector is imposed by the LEPII data. Limits are provided in detail by the LEP Higgs Working Group (see Ref. [288]).

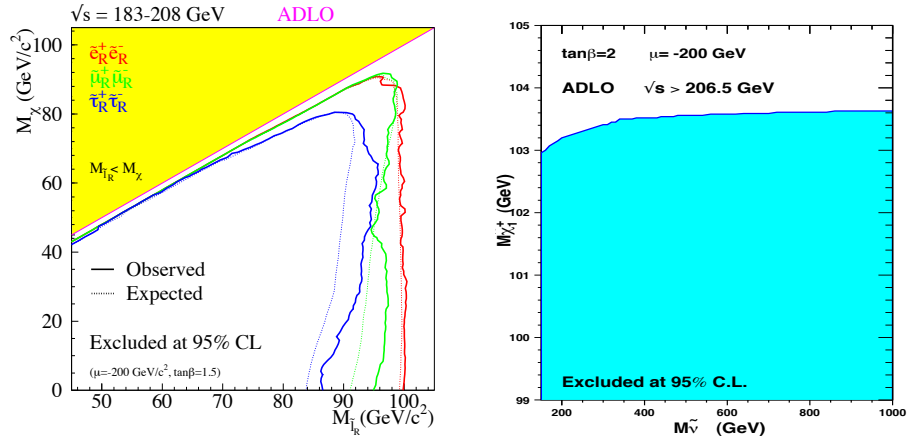

Figure 6.6: LEP combined lower limits on the slepton masses $m_{\tilde{l}_R}$ as a function of the mass of the lightest neutralino $m_{\tilde{\chi}_1^0}$ (left plot) and limits on the chargino mass $m_{\tilde{\chi}_1^+}$ as a function of the sneutrino mass $m_{\tilde{\nu}}$ (right plot) for constraint MSSM models. The figures are taken from the Ref. [285,287].

New restrictions are imposed also on the squark and gluino masses, arising from the null result of the multijet plus missing energy searches performed by DØ [238] and CDF [291]. The limits for the squark and gluino masses, presented in Figure 6.9 (left plot), are based on an integrated luminosity of 2.1 fb^{-1} and exclude $m_{squark} < 379$ GeV and $m_{gluino} < 308$ GeV within the framework of minimal supergravity with $\tan\beta = 3$, $A_0 = 0$ and sign(μ) <0 [238].
The CDF collaboration has set limits for the mSUGRA parameter space $\tan\beta = 5$, $A_0 = 0$ and sign(μ) < 0 parameter space analysing 2.0 fb^{-1} of data to $m_{gluino} = m_{squark} > 392$ GeV [291]. The exclusion region together with previous results from other experiments is presented in the right plot of the same Figure 6.9. The obtained constraints can be translated into an exclusion region in the m_0-$m_{1/2}$ mSUGRA parameter space, as shown in the left plot of Figure 6.10. Recently both experiments set also limits in the neutralino-sbottom [292] as well as in the neutralino-stop parameter space [293]. Figure 6.10 (right plot) shows the exclusion limits of the DØ collaboration in the neutralino-sbottom plane. The highest observed Tevatron sbottom mass limit for neutralino masses $m_{\tilde{\chi}_1^0}$ below 70 GeV is about 230 GeV [292]. The exclusion limits assuming a 100% decay of the stop into charm quark and a neutralino, is for stop masses up $\approx$ 180 GeV, if the neutralino mass is below $\approx$ 90 GeV [293]. Further exclusion regions e.g. in the GMSB parameter space can be found for example in Ref. [283,284].
The search for the Higgs boson is also a possible window to new physics and exclusion limits can impose a stringent constraint on supersymmetric models. A lower limit on m_{h^0} can be translated into a lower limit on $\tan\beta$. The limit on the mass of the SM-like Higgs boson is set by LEPII of $m_{h^0} > 114.1$ GeV obtained at the 95% confidence level [294]. Figure 6.11 shows the allowed regions in the mSUGRA parameter space for low $\tan\beta = 10$ (left plot) and high $\tan\beta = 50$ (right plot) values. It can be seen that the LEP Higgs boson mass limit (red line) already ruled out lower

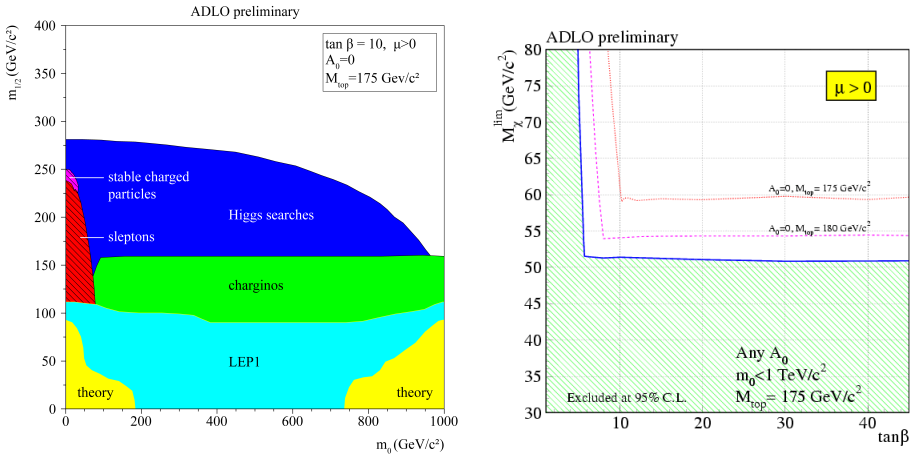

Figure 6.7: Exclusion region in the mSUGRA m_0-$m_{1/2}$ parameter space for $\tan\beta = 10$, $\text{sign}(\mu) > 0$, $A_0 = 0$ and $m_{top} = 175$ GeV (left plot). The LEP combined lower limit on the LSP mass in the same mSUGRA parameter space are presented in the right plot. The figures are taken from the Ref. [289].

$\tan\beta$ models. The largest one-loop correction to the Higgs boson mass is due to top and stop loops. The stop mass depends mostly on $m_{1/2}$ as discussed in Section 2.2.6, thus a lower bound on m_{h^0} yields a lower bound on $m_{1/2}$. This limit almost entirely excludes the so called "bulk region" in the mSUGRA parameter space. Also the Tevatron experiments work on MSSM Higgs exclusion limits. The result are used to infer new exclusion limits in the two-dimensional space of $\tan\beta$-m_A [295,296].

Indirect constraints SUSY matter may also reveal itself through indirect effects, as in contributions to rare decays such as $b \to s\gamma$ or $B_s \to \mu^+\mu^-$, or via contributions to the magnetic momentum of the muon. A number of limits have been set, some are briefly summarised in the following sections.

Measurement of the rare decays Indirect limits on the SUSY parameter can arise from processes that are either very rare or forbidden in the SM like for example $b \to s\gamma$, $\mu \to e\gamma$, or neutral meson mixing. Since these processes can have contributions from sparticle loops in SUSY models their branching ratios can be considerably enhanced in a way that they become sensitive to new physics. For example the approximate agreement between the measured value of the branching ratio of the decay of the B–meson into a strange meson and a photon, that has been measured by CLEO, Belle and BABAR [299], with the theoretical predictions from the Standard Model imposes constraints on the supersymmetric one-loop contributions, namely, they should cancel. This leads to constraints in the SUSY parameter space [300]. The green area in Figure 6.12 is favoured by this constraint.

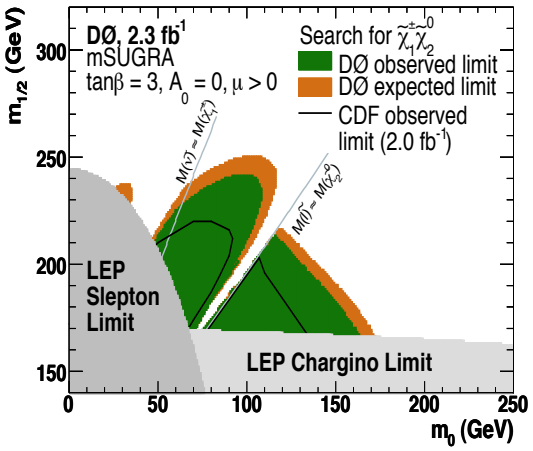

Figure 6.8: Exclusion region in the m_0-$m_{1/2}$ parameter space from the combination of the DØ analyses (green), from chargino (light grey) and slepton (dark grey) LEP searches and CDF searches (black line). The assumed mSUGRA parameters are $\tan\beta = 3$, $A_0 = 0$ and $\mu > 0$. The figures are taken from the Ref. [290].

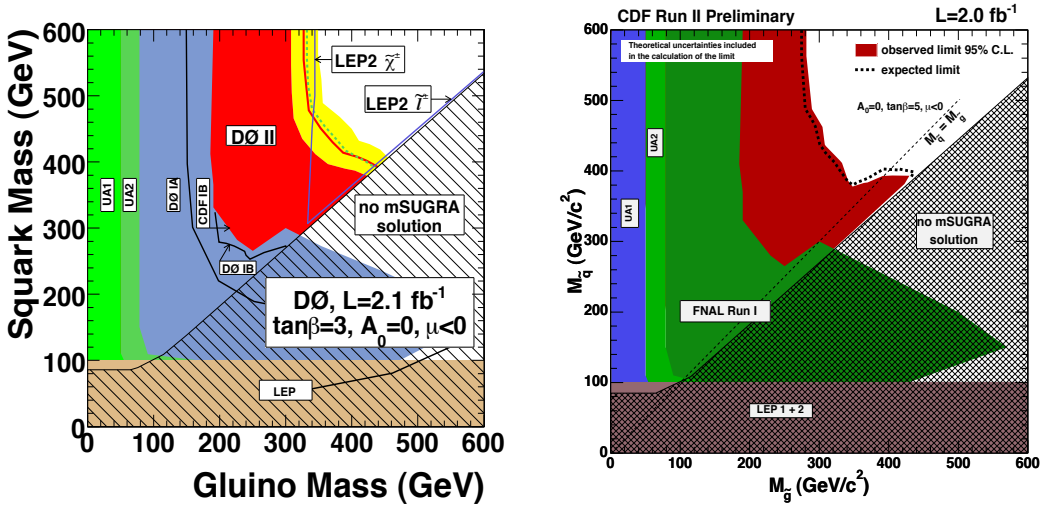

Figure 6.9: Exclusion region in the gluino-squark ($m_{\tilde{g}}$-$m_{\tilde{q}}$) parameter space for mSUGRA scenarios with $A_0 = 0$, $\mathrm{sign}(\mu) < 0$ and $\tan\beta = 3$ (left plot) and for $\tan\beta = 5$ (right plot). The figures are taken from Ref. [238, 291].

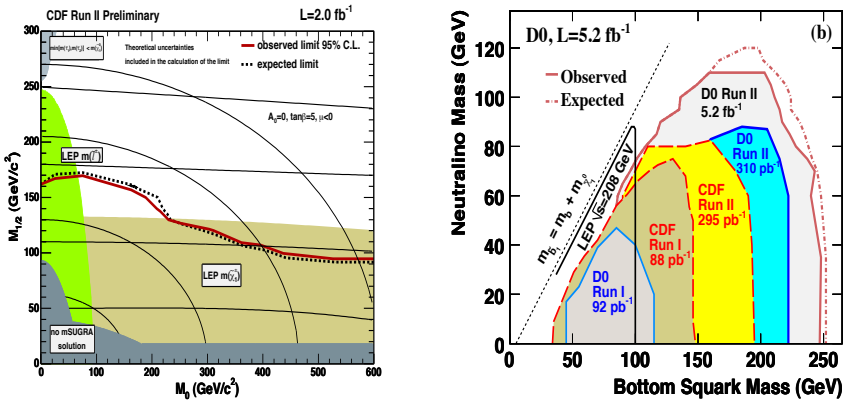

Figure 6.10: Left plot: Excluded parameter space in the m_0-$m_{1/2}$ mSUGRA parameter space with $\tan\beta = 5, A_0 = 0$ and sign$(\mu) < 0$. The thin black lines represent the mass curves for the gluinos and squarks respectively, for 150, 300, 450, and 600 GeV. The figure is taken from the Ref. [238,291]. Right plot: Exclusion region for sbottom and neutralino masses at 95% C.L. The figure is taken from the Ref. [292].

Searches by the Tevatron experiments have defined combined 95% C.L. upper limits for the branching ration $B_s \rightarrow \mu^+\mu^-$ of about 5.8×10^{-8} [301, 302], that is about one orders of magnitude from the theoretical predictions. Contributions from non-SM-like neutral Higgs bosons can enhance this decay and set limits in the SUSY model parameter space [301,302].

Measurement of muon g-2 The precision measurement of the anomalous magnetic momentum of the muon $a_\mu = (g-2)_\mu/2 = (11659208 \pm 6) \times 10^{-10}$ [244–246] by the E821 experiment (BNL) differs from the recently updated prediction of the SM by about 2-3σ [303], depending on the evaluation of the hadronic contribution to the theoretical value. Consequently, the reproduction of the experimental value constitutes an additional constraint for model building. Supersymmetric contributions to a_μ value involve chargino-sneutrino and neutralino-smuon loops and can set limits on the SUSY parameter space, as well as on the measurement of the branching ratio of the rare decays like for example $B_s \rightarrow \mu^+\mu^-$ [301,302]. The $g_\mu - 2$ favours is the "shaded pink region" in Figure 6.11 (left plot).

Constraints from dark matter

One key issue of many SUSY searches is to address the consistency of the signal with astrophysical and non-accelerator constraints on SUSY Dark Matter. New inspiring results have been obtained by neutrino experiments like K2K and WMAP in the field of astro-particle physics.
It is established by precision measurements of temperature anisotropies in the cosmic microwave background radiation (CMBR) from the Wilkinson Microwave Anisotropy Probe (WMAP) [304, 305] that a large fraction of the matter content of the Universe has to be non-baryonic, that cannot be fully explained with the Standard Model. The particle that is considered most often as a suitable

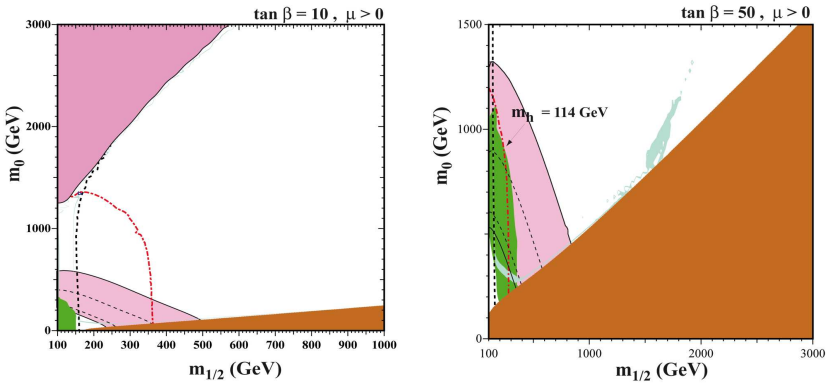

Figure 6.11: Theoretical, phenomenological, experimental and cosmological constraints in the $m_{1/2} - m_0$ parameter space for mSUGRA models with $\tan\beta = 10$ (left plot) and $\tan\beta = 50$ (right plot) and $\text{sign}(\mu) > 0, A_0 = 0$. Regions are excluded by $b \rightarrow s\gamma$ (green shaded area), by the cosmological constraint $0.097 < \Omega h^2 < 0.122$ (narrow turquoise strip), by LEP constraints on chargino mass (dashed black line) and by higgs searches (red line), the LSP would be charged (brown shaded), electroweak vacuum inconsistency (dark pink shaded region at large m_0), $g_\mu - 2$ favours (shaded pink region). The figures are taken from the Ref. [297] and [298].

candidate [53,54] is the lightest neutralino. If $\tilde{\chi}_1^0$ should explain the dark matter, the relic density of the LSPs, which results from the production in the early universe and the annihilation into Standard Model particles, has to agree with the measured value for the current Dark Matter relic density. However, this value depends on the SUSY particle mass spectrum and their couplings. Thus the measurements of the dark matter density can be reinterpreted as measurements of SUSY parameters and used to constrain the parameters of MSSM models. At each point in the MSSM parameter space the SUSY mass spectrum, branching ratios and decay widths may be calculated and the LSP relic density can be compared to the WMAP cold dark matter density. The recent precision measurements of the CMB anisotropies by the WMAP experiment [44] confirm the current Cosmic Standard Model (Λ-CDM model) and improve the obtained results to the actual cold dark matter limit of $0.1053 < \Omega_{CDM} h^2 < 0.1165$ [44], where Ω_{CDM} is the ratio of the cold dark matter density and the critical matter density that leads to a flat universe and h is the dimensionless Hubble constant.

The annihilation cross section for the lightest neutralino is dominated by slepton exchange and decreases usually with its mass. This leads to the preferred LSP mass regions in the parameter space, e.g. in the mSUGRA parameter space to a narrow band near the electroweak scale ("bulk region"). This region is also used to select the mSUGRA benchmark scenarios for study, discussed in Section 4.5.2. Fig. 6.11 shows the mSUGRA parameter space as a function of m_0 and $m_{1/2}$ for constant values of A_0, $\text{sign}(\mu)$ and $\tan\beta = 10$ taking into account a cold dark matter density consistent with WMAP data [45] (narrow turquoise strip). The locations of these WMAP "strips" do vary significantly with the choices of other supersymmetric parameters, as can be seen by comparing the cases of $\tan\beta = 10$ and $\tan\beta = 50$ of the same figure. It is important to point out

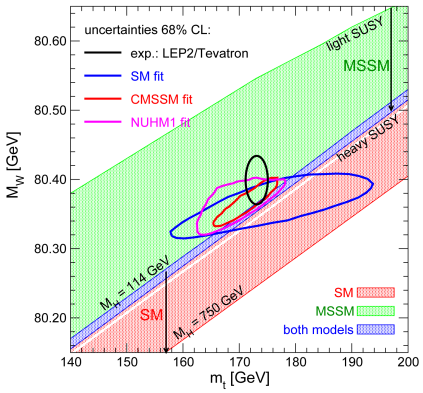

Figure 6.12: Predictions for m_{top} and m_W on the basis of low-energy precision data in the Standard Model (blue curve), the constrained MSSM (red curve) and a NUHM model (violet curve) compared with the experimental measurements at LEP and the Tevatron (black ellipse). The figures are taken from the Ref. [298].

that the different SUSY models can predict completely different relic dark matter density (LSP densities) that can lead to different CDM relic density compatible regions in the SUSY parameter space without changing much the predictions for collider experiments. Thus, the dark matter limit must be taken with care.

Theoretical constraints

A set of theoretical constraints are "rather standard" and used for all studied SUSY models within this thesis. They are "automatically" applied while generating the sparticle spectrum with the different Monte Carlo generators: the sparticle spectrum must be tachyon free [306] and cannot lead to colour or charge breaking minima in the scalar potential [307].

6.4. ATLAS search strategy

There are many viable SUSY models, that differ for example in their supersymmetry breaking processes and have independent parameters, that may vary by orders of magnitude. The high number of possible SUSY decay chains lead to many different detector signatures. The ATLAS search strategy for R-parity conserving SUSY models was developed taking the following two approaches:

1. Inclusive search strategy

At the LHC the production of squarks and gluinos dominates in a large fraction of the parameter space. The decay chains of the SUSY particles depend mainly on the details of the SUSY model under consideration, such as mass spectra and branching ratios. If R-parity is conserved

the cascade decays of these sparticles lead to events with a E_T^{miss} (from the LSP $\tilde{\chi}_1^0$), high p_T jets and possibly a number of leptons, photons or b-jets. The inclusive search strategy therefore concentrates on these signatures and looks for a deviation of the measured data events to the Standard Model events.

2. Exclusive searches

The challenge at the LHC is not only to discover SUSY, but also to make measurements of sparticle masses and other quantities like the spin of the new (s)particle to subsequently constrain the model parameters and to determine, which particular SUSY model is realised in nature. Since the decay products of the R-parity conserved SUSY particle contains a LSP that escapes the detection, no mass peaks can be directly reconstructed. Therefore masses must be inferred from kinematic endpoints and other properties of the events. Developing methods to do this is also an emphasis of the ATLAS SUSY group studies.
The focus of this thesis is the inclusive search strategy that will be described in the following. More information about exclusive searches can be found for example in Ref. [103,104,308–311].

Inclusive searches

Two different approaches have been used to develop the inclusive search strategy in ATLAS. First, promising SUSY decay final states and their relevant SM background processes are analysed for specific SUSY points like SU3 or SU4 (referred as "benchmark point"; see description in Section 4.5.2). A number of inclusive search channels have been defined, all based on the generic SUSY detector signature: missing transverse energy + several high transverse momentum jets. In order to simplify the procedure of combining results, the different search modes are classified exclusively, with respect to each other, in the number of the additional leptons. The inclusive SUSY analyses are:

- **zero-lepton channel**: The presence of multiple jets together with large E_T^{miss}; electrons and muons are vetoed. Especially SUSY models with large squark masses decay into final states with many jets. In this thesis SUSY searches with $\geq$ 2 -6 jets are studied. Main SM backgrounds are from QCD and $W/Z+$jets processes.

- **one-lepton channel**: Multiple jets together with exactly one lepton and E_T^{miss} are required. The QCD multijet background is almost negligible, remaining backgrounds are $t\bar{t}$, $W+$jets and Z+jet productions.

- **two-lepton channels**: The 2-leptons in addition to multiple jets and E_T^{miss} requirement lead to a small number of SM background events. For the two leptons channels, signatures with two leptons with opposite charge (opposite-sign) and same charge (same-sign lepton) are distinguished. The first process can arise e.g. from neutralino $\tilde{\chi}_2^0$ decays in a $\tilde{\chi}_1^0$ ($\tilde{\chi}_2^0 \rightarrow \tilde{\chi}_1^0 l^+ l^-$), while the same-sign leptons can appear from processes where two gluinos subsequently decay to same-sign charginos which decay leptonically. The two lep-

tons with opposite sign should be of the same flavour in order to not induce e.g. lepton-flavour-violating interactions.

- **multi-lepton channels**: Different approaches are under study: three or more leptons + at least one very-high p_T jet and E_T^{miss} or three leptons and E_T^{miss}. The trilepton signal can arise from direct gaugino production or from squark and gluino decays.

- τ **channel** : The presence of multiple jets together with large E_T^{miss} and one τ lepton: In some models the τ decay is dominant, e.g. for SUSY models with large $\tan\beta$ or in gauge mediated SUSY breaking models with a $\tilde{\tau}$ NLSP. The searches select hadronically decaying τs, since leptonic decays are indistinguishable from prompt leptons and will be selected in the previous search modes.

- **b-jet channel**: Different approaches are studied, considered signatures have been defined exclusively or inclusively. These searches concentrate for example on SUSY models where the mass of the b-quark superpartner is significantly lower than the ones from the first and second generation that leads to decays with b-jets.

For all these channels the performance was studied in order to define the analysis cuts that can separate best a SUSY signal from the SM backgrounds (see for example Ref. [103, 228]).
The selected benchmark points are just representative of the particular SUSY model. The main purpose of the ATLAS SUSY group was to develop a general search strategy that provides sensitivity for the different SUSY decay topologies, but also covers a wide range of SUSY models in order to be as model independent as possible. The large number of free parameters in many SUSY models makes this a challenging task. Therefore, the second approach taken by the ATLAS SUSY group was to apply the insight gained from studying specific points to several subsets of SUSY models (SUSY "grids", see Section 4.5.2), to verify that the inclusive channels are also sensitive for different signals in the SUSY parameter space. The scans of different SUSY signal grids allowed to determine the performance of each inclusive search channel in the SUSY parameter space and to assess the ATLAS discovery potential.
To produce the SUSY benchmark signals and SM backgrounds a detailed ATLAS detector simulation was used. Since these detector simulations are very computing intensive and several hundred signal points must be generated, a fast parameterised simulation (ATLFAST1) has been used (see Section 4.3.2) for the SUSY grid production.

6.4.1. SUSY searches discussed in this thesis

This thesis concentrates mainly on 0-lepton analyses and their discovery potential in the SUSY parameter space. Therefore, most of the studies discussed in the following chapters, like the comparison of first $\sqrt{s} = 7$ TeV LHC collision data with Monte Carlo simulations (see Section 11) are performed just for the final states with jets, missing transverse energy and no leptons. However, in order to compare the discovery potential of the different SUSY analyses, also channels with one or two additional leptons in the final state were under investigation, but are not studied in detail and will be therefore not discussed.

6.5. SUSY searches at different centre-of-mass-energies

At the beginning of this work, ATLAS expected to measure first collisions at a centre-of-mass energy of $\sqrt{s}$ = 14 TeV. Therefore the first SUSY analyses discussed in this thesis (see Chapter 8) have been performed for the LHC design energy assuming a luminosity expected for the first year(s) of $L = 1$ fb^{-1}. After the accelerator incident in September 2008 [114] (see also Chapter 3.1.1) it was not immediately decided at which centre-of-mass energy the LHC could run. The first idea was a partial repair of the LHC machine, enabling after a short period of initial 900 GeV centre-of-mass (CM) collisions, a long physics run period between end of 2009 and end of 2010 at 10 TeV. MC studies have been performed for 10 TeV in order to update the 14 TeV results, assuming also running at a reduced machine luminosity of approximately 200 pb^{-1}. The outcomes of this study are presented in Chapter 9. In February 2009 the LHC machine team, experiments and CERN management discussed the preliminary LHC run plan for the next two years at the LHC Chamonix workshop [312]. In order to give some input for this workshop the dependency of the ATLAS discovery potential of the different LHC centre-of-mass energies was studied. To do so, the luminosity required for a 5σ discovery for three R-parity conserved SUSY scenarios for the LHC centre-of-mass energy of 4, 6, 8, 10 and 14 TeV was determined. The studies are briefly summarised in the Appendix in Section C. More details can be found in Reference [313–315]. It was found that the studied low SUSY mass points are clearly visible at > 8 TeV for $\mathscr{L} \approx 100$ pb^{-1} including a 100% systematic error (see Figure 6.13, left plot). With a luminosity of $O(100)$pb^{-1} there is no chance to discover low mass SUSY with a centre-of-mass energy of 4 TeV. At a centre-of-mass energy of 7 TeV the current Tevatron exclusion limits could be reached with about 100 pb^{-1} integrated luminosity (see Figure 6.13, right plot).

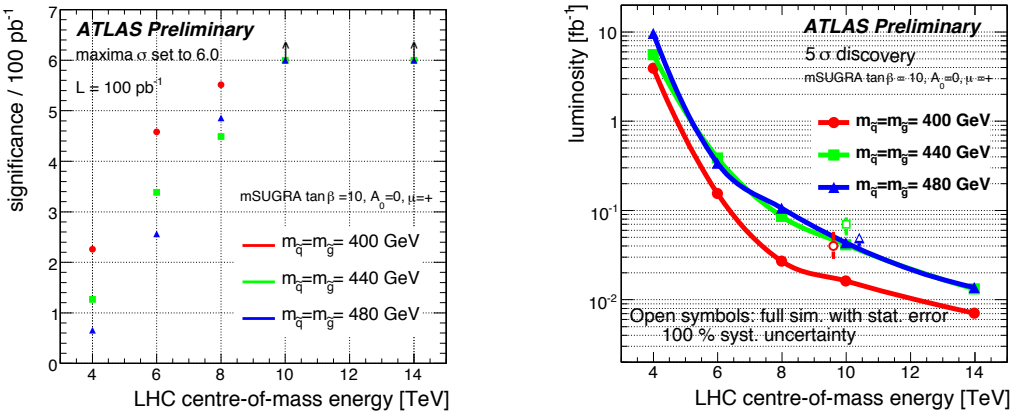

Figure 6.13: Left plot: The significance as a function of the LHC centre-of-mass energy for an integrated luminosity of 100 pb^{-1}. Right plot: The integrated luminosity needed for a 5σ discovery as a function of the LHC centre-of-mass energy for mSUGRA SUSY points with $M_{\text{squark}} = M_{\text{gluino}} = 400, 440$ and 480 GeV.

After the workshop the LHC schedule has been re-organised. It was decided that the LHC would run for 18-24 months till the end of the year 2011 at a collision energy of 7 TeV with the objective of delivering enough data to the experiments to make significant advances across a wide range of physics channels. The expected integrated luminosity of about 1 fb^{-1} (or maybe more) should be enough to explore a wide mass range and to discover SUSY particles or to define new exclusion limits. After the long run period, there will be a shutdown at the end of the year 2011 for routine maintenance, and to complete the repairs and consolidation work that is needed to reach a higher LHC energy [316] and probably continue running from 2013 till 2015 at a centre-of-mass energy of 14 TeV.
With the decision of the new LHC centre-of-mass energy the SUSY Monte Carlo studies have been repeated for $\sqrt{s}$ = 7 TeV. The predictions for different luminosities can be found in Chapter 10. First data collision results at the same centre-of-mass energy are presented in Chapter 11.

7. Event selection and statistical methods

A generic search can be constructed using simple event selections to categorise events with large E_T^{miss} by numbers of leptons and jets and let the Standard Model backgrounds and the performance of the detectors define the search ranges. ATLAS has studied various channels with different numbers of jets and leptons, but also channels with photons or b-jets. Mutually exclusive channels are defined based on the flavour of the lepton candidate that has been identified, in order to distinguish between τ- and electron/muon searches referred as "lepton channels". The word "lepton" is used to denote isolated electrons and muons. In this thesis simple and robust event signatures with ≥ 1, ≥ 2, ≥ 3, ≥ 4, ≥ 5, ≥ 6 jets and exactly 0, 1 and 2 leptons are studied, which are common for a wide range of SUSY models. Details about SUSY searches with τs, b-jets or photons can be found in the References [104,228].
This chapter describes the event and object selection for SUSY analyses performed for different LHC centre-of-mass energies and introduces the statistical methods employed for the evaluation of the signal significance. It is organised as follows. The object selection criteria and the used global SUSY specific variables like M_{eff} are summarised in Section 7.1 and Section 7.2. The event selection criteria for the different SUSY analyses and the trigger efficiencies of the used triggers are discussed in Section 7.3 and in Section 7.4, respectively. Finally the statistical procedure to derive a signal significance and the used systematic background uncertainties are described in Section 7.5. The 0-lepton analysis cuts are discussed in detail in Chapters 8-11, where also the final distributions and the estimated discovery potential are presented.

7.1. Object selection

Different object reconstruction algorithms are used to reconstruct and identify the main objects such as electrons, muons, jets and missing transverse energy. They have been described in detail in the Chapter 5 and will be only summarised here. In addition to these preselection cuts object selection criteria like a cut on the transverse momentum p_T, on η and overlap removal are applied to define the final particle candidates for the SUSY event selection.

7.1.1. Jets

To take into account the large jet multiplicity in supersymmetric events, the following algorithms have been used:

- *Monte Carlo studies*: Jets are reconstructed with a fixed-size cone algorithm (cone size radius of R = 0.4), seeded by calorimeter towers [253] (see Section 5.2.1).
- *Data studies*: The anti-k_T jet algorithm [259,317] with four-momentum recombination with the same distance parameter R = 0.4 was used (see Section 5.2.1). Inputs to the jet algorithm are topological clusters, which attempt to reconstruct the three-dimensional shower topology of each particle entering the calorimeter. The measured jet transverse momentum is determined at the electromagnetic scale (p_T^{EM}) and corrected for the lower response of the calorimeter for hadrons and the presence of dead material using a Monte-Carlo based calibration.
  Event cleaning cuts: Any event containing a bad jet or having a primary vertex with less than five associated tracks as well as fake jets resulting from calorimeter noise or cosmic ray energy deposits are rejected (see discussion about the event cleaning cuts in Section 7.3.1).
- *Monte Carlo and data studies*: Jet acceptance cuts of $p_T > 20$ GeV and $|\eta| < 2.5$ are applied.

7.1.2. Missing transverse energy

- *Monte Carlo studies*: Missing transverse energy is computed from calorimeter cell-energy and the momentum of the reconstructed muons in the muon spectrometer ($E_T^{RefFinal}$, see Section 5.3.1).
- *Data studies*: E_T^{miss} is computed from calorimeter cells belonging to topological clusters at the electromagnetic scale without applying any corrections for the different calorimeter response of hadrons and electrons/photons or for dead material losses.

7.1.3. Electrons

- "Medium" electrons as discussed in Section 5.4.1 are used.
- Electrons are required to be isolated in the calorimeter: the calorimeter energy around the electron within a cone of radius ΔR = 0.2 has to be less than 10 GeV.
- In the transition regions between the barrel and end-cap regions of the calorimeter $1.37 < |\eta| < 1.52$ ($1.37 < |\eta_2^{clus}| < 1.52$) for measured collision events[1]) the misidentification rate of jets as electrons is significantly larger compared to other detector regions. Since the reconstruction of these electrons may not be efficient in these regions, the entire event is removed if it contains one or more electrons within this η range.

[1] η_2^{clus} is the η value of the second sampling layer of the electromagnetic calorimeter.

- *Monte Carlo studies*: The p_T of electrons should exceed 10 GeV and $|\eta|$ should be less than 2.5.

- *Data studies*: The p_T of electrons should exceed 10 GeV and $|\eta_2^{clus}|$ should be less than 2.47 (see Ref. [318]).

7.1.4. Muons

- A combined reconstruction algorithm is used, which performs a combination of muon spectrometer tracks (standalone track) and the corresponding inner detector track information to reconstruct a muon candidate (STACO algorithm, see Section 5.5.1). The association between the standalone and inner detector tracks is performed using a χ^2-test. The match χ^2 provided by the algorithm should be less than 100.

- Muons should be isolated - the total calorimeter energy within a cone of $\Delta R < 0.2$ should less than 10 GeV.

- The p_T and η requirement for muons is: $p_T > 10$ GeV and $|\eta| < 2.5$.

7.1.5. Overlap removal

Since the jet reconstruction is based on calorimeter objects, energy depositions from electrons and photons are also used by the jet reconstruction algorithm. Thus the electron and jet candidates which are very close to each share the same calorimeter clusters and an overlap removal needs to be applied in order to not double count the energy.
A feature of ATHENA is that it does not remove overlap between reconstructed objects, such that each analysis can define the overlap removal dependent on the object definitions and the analysis goals. The following classification is used to remove the overlapping jet-electron and jet-muon objects. All overlap criteria are based on the simple geometric variable Δ R = $\sqrt{(\Delta\phi)^2 + (\Delta\eta)^2}$ and are applied in the following order:

- Since electrons are likely to be reconstructed also as jets, jet candidates are removed if they are found within a distance Δ R < 0.2 of a good electron candidate.

- If an electron and a jet are found within $0.2 \leq \Delta R < 0.4$, the jet candidate is kept and the electron is rejected in order to discriminate against secondary leptons from heavy flavour decays.

- If a muon and a jet are found within $\Delta R < 0.4$, the object is treated as a jet and the muon is rejected. The source of the muon is maybe a b- or c-quark, π or K decay or it is just fake muon due to reconstructing random muon chamber hits.

Note, the overlap removal procedure is always applied after the object selection described before.

7.2. Global event variables

In addtition to the physics objects defined in Section 7.1, SUSY searches rely on different event variables that are employed for example in the kinematic selection or are used to look for an evidence of Supersymmetry or to better understand the event kinematic.

Effective mass The effective mass M_{eff} is used in many SUSY searches that measures the total activity in an event in terms of momentum using visible and invisible parts. It is expected to be a very sensible variable to discriminate between SUSY and SM background events and is defined as the scalar sum of the missing transverse energy E_T^{miss} and the transverse momenta p_T of all leading jets and leptons:

$$M_{\text{eff}} \equiv \sum_{i=1}^{N_{\text{jets}}} \mid \mathbf{p}_T^{\text{jet},i} \mid + \sum_{j=1}^{N_{\text{leptons}}} \mid \mathbf{p}_T^{\text{lep},j} \mid + E_T^{miss} \tag{7.1}$$

where N_{jets} is the number of jets (2-6) and N_{leptons} is the number of leptons (0-2) as defined for each analysis. The variable $\mathbf{p}_T^{(\text{jet,i})}$ is the transverse momentum of the i^{th} jet (ordered descending in $|\mathbf{p}_T|$), $\mathbf{p}_T^{(lep,j)}$ is the transverse momentum of the j^{th} lepton (channel dependent, for 0-lepton channel it is 0) and E_T^{miss} is defined in equation 5.2.
SUSY events are presumed to be high-mass states that generate many high p_T objects in its decay chains. The M_{eff} variable, calculated with some of these decay chain objects, is therefore connected with the SUSY mass scale M_{SUSY} [319]. The effective mass distribution shows a peak, and SUSY events can be distinguished from the background events considered [320] for many SUSY models[2].

Transverse mass M_T The transverse mass is defined as the invariant mass of the lepton and E_T^{miss} in the transverse plane:

$$m_{\text{T}}^2 \equiv 2 \cdot |\mathbf{p}_{\text{T}}^{\text{lep}}||\mathbf{p}_{\text{T}}^{\text{miss}}| - 2 \cdot \mathbf{p}_{\text{T}}^{\text{lep}}\mathbf{p}_{\text{T}}^{\text{miss}} = 2|\mathbf{p}_{\text{T}}^{\text{lep}}| \cdot E_T^{miss} \cdot \left(1 - cos\left(\Delta\phi\left(\text{lep}, \text{E}_{\text{T}}^{\text{miss}}\right)\right)\right) \tag{7.2}$$

with $\Delta\phi\left(\text{lep}, \text{E}_{\text{T}}^{\text{miss}}\right)$ the azimuthal angle between E_T^{miss} and the lepton. For the W-boson and the top quarks the E_T^{miss} comes from the neutrino of the decays. The transverse mass is a usefull variable to suppress W + jet and $t\bar{t}$ events and to define a control region in the 1-lepton channel, since SUSY events are expected to populate the high M_T region. The distribution for the Standard Model backgrounds in the 1-lepton channel shows a characteristic edge structure around 90-100 GeV near the W boson mass.

[2] SUSY events and SM background events can be well distinguished, if the effective mass of the SUSY events peaks at a high M_{eff} regions.

Stransverse mass The m_{T2} variable is the generalisation of the transverse mass to pair decays [321]. For a final state consisting of two visible objects with transverse momenta $\mathbf{p}_{\mathrm{T}}^{(1)}$ and $\mathbf{p}_{\mathrm{T}}^{(2)}$ respectively, and with missing transverse momentum $\mathbf{p}_{\mathrm{T}}^{\mathrm{miss}}$, it is defined by

$$m_{T2}\left(\mathbf{p}_{\mathrm{T}}^{(1)}, \mathbf{p}_{\mathrm{T}}^{(2)}, \mathbf{p}_{\mathrm{T}}^{\mathrm{miss}}\right) \equiv \min_{\not{\mathbf{q}}_{\mathrm{T}}^{(1)}+\not{\mathbf{q}}_{\mathrm{T}}^{(2)}=\mathbf{p}_{\mathrm{T}}^{\mathrm{miss}}} \left\{\max\left(m_T\left(\mathbf{p}_{\mathrm{T}}^{(1)}, \not{\mathbf{q}}_{\mathrm{T}}^{(1)}\right), m_T\left(\mathbf{p}_{\mathrm{T}}^{(2)}, \not{\mathbf{q}}_{\mathrm{T}}^{(2)}\right)\right)\right\} \tag{7.3}$$

where m_T is the transverse mass[3] as defined before:

$$m_{\mathrm{T}}^2\left(\mathbf{p}_{\mathrm{T}}^{(i)}, \not{\mathbf{q}}_{\mathrm{T}}^{(i)}\right) \equiv 2\cdot|\mathbf{p}_{\mathrm{T}}^{(i)}||\not{\mathbf{q}}_{\mathrm{T}}^{(i)}| - 2\cdot\mathbf{p}_{\mathrm{T}}^{(i)}\cdot\not{\mathbf{q}}_{\mathrm{T}}^{(i)}, \tag{7.4}$$

and the minimisation is over all values of the two undetectable particles' possible missing transverse momenta $\not{\mathbf{q}}_{\mathrm{T}}^{(1,2)}$ consistent with the $\mathbf{p}_{\mathrm{T}}^{\mathrm{miss}} = \not{\mathbf{q}}_{\mathrm{T}}^{(1)} + \not{\mathbf{q}}_{\mathrm{T}}^{(2)}$ constraint. This variable represents an event-by-event lower bound on the mass of any pair-produced semi-invisibly decaying particle, which could have resulted in the observed state [323].

Contransverse mass This variable is useful in events, in which a pair of identical parent particles has decayed semi-invisibly producing visible daughters (with momenta $\mathbf{p}^{(1,2)}$). The contransverse mass is defined as in Ref. [324]:

$$m_{CT}^2\left(\mathbf{p}^{(1)}, \mathbf{p}^{(2)}\right) \equiv 2E_{\mathrm{T}}^{(1)}E_{\mathrm{T}}^{(2)} + 2\mathbf{p}_{\mathrm{T}}^{(1)}\cdot\mathbf{p}_{\mathrm{T}}^{(2)}. \tag{7.5}$$

It is invariant under back-to-back boosts of the parent particles, and provides a lower bound on a combination of the masses of the parent and undetectable daughter particles. The contransverse mass is sensitive to the boost of the centre-of-momentum frame of the parent particles in the laboratory transverse plane and must therefore be corrected using the procedure described in [325]. The approach involves the boosting of the four-momenta of the visible decay products back into centre-of-momentum frame with a boost factor.

Transverse sphericity S_T The transverse sphericity measures the event sphericity in terms of the momenta in the x–y–plane. It is calculated as:

$$S_T \equiv \frac{2\lambda_2}{(\lambda_1+\lambda_2)} \tag{7.6}$$

where λ_1 and λ_2 are the eigenvalues of the 2×2 sphericity tensor $S_{ij} = \sum_k \mathbf{p}_{ki}\mathbf{p}^{kj}$ computed from all jets and leptons selected, where i and j are x and y. The variable has a value between 0 and 1, where 1 corresponds to a perfect spherical event, e.g. four momentum vectors are pairwise perpendicular and all have the same magnitude. It is a very is useful variable since SUSY events are expected to be on the average more spherical than the background events ($S_T \lesssim 1$) after applying typical

[3] Following the prescription of Ref. [322] the unknown mass of any undetectable particles as well as the mass of the jets is set to zero in a search.

analysis cuts on jets and missing energy, because heavy SUSY particles subsequently emit many lighter particles in a wide range of directions within the detector. Especially QCD events tend to be found at lower S_T than SUSY events, hence a cut on this variable can suppress the abundance of QCD dijets.

Transverse thrust A convenient variable to study the event topology is transverse thrust calculated using jets in the event. In contrast to sphericity, thrust is a infrared and collinear safe variable and hence will be preferably used in the future data studies. Its definition is similar to the thrust definition (see Ref. [326]), however transformed in terms of transverse momenta. The thrust axis is found in the x–y plane via an iterative procedure, where the particle 2-momenta $\mathbf{p}_i$ are projected on the thrust axis n, and after the total sum is maximised:

$$T_T = \frac{\max(\sum_i |p_i \cdot n|)}{(\sum_i |p_i|)} \tag{7.7}$$

Transverse thrust is a Lorentz invariant quantity under the boost along the beam direction with values that range from $2/\pi$ to 1 for spherical and for pencil-like events, respectively. In order to make an easier comparison with the S_T definition possible, the variable is plotted in the distributions as $(1-T_{\mathrm{T}})/(1-\frac{2}{\pi})$.

7.3. Event selection

All analyses consist of a set of basic cuts to select events with large missing transverse energy and to reconstruct particles with large transverse momentum. The number of jets ranges from 1 up to 6 (≥ 1, ≥ 2, ≥ 3, ≥ 4,≥ 5, ≥ 6) and the number of leptons varies from 0 to 3 ($= 0$, $= 1$, $= 2$, ≥ 3), where the jet channels are inclusive and the lepton channels are exclusively[4] defined. The 2 lepton channels are separated in channels with two selected leptons that have the same charge and channels with two leptons that have opposite charge. Only the two lepton channels with different charged leptons (opposite sign leptons) are studied. Table 7.1 summarises the cuts applied for analyses asking for 0-2 leptons sorted according to the jet-multiplicity and the studied LHC energy. In the first columns are the event selection cuts used for the Monte Carlo studies, in the last column are the selection cuts used in the analysis of first data events. The defined SUSY analyses cuts are similar to those used in the ATLAS Physics TDR [103] and do not differ much for the different LHC running scenarios. The same object identification criteria are used for all studied channels as described in the previous section and e.g. in Ref. [234]. The p_T cuts on the jets are chosen according to the trigger requirements, but also to reject a sufficient amount of QCD jet background.

[4]The 3-lepton channel, studied only for a centre-of-mass energy of $\sqrt{s}$ = 14 TeV, is defined inclusively.

cut number	cut	cut definition 14 TeV (MC)	10 TeV + 7 TeV (MC)	7 TeV (data)
		1 jet analysis (in combination with 0 or 3 leptons)		
Cut 1	number of jets	≥ 1		≥ 1
		only with 3 lept.		only with 0 lept.
Cut 2	leading jet [GeV]	$p_T^{\text{jet1}} > 200$		> 70
Cut 3	subsequent jets p_T [GeV]	> 20		≤ 30
Cut 4	E_T^{miss} [GeV]	-		> 40
Cut 5	$E_T^{miss} > f \times M_{\text{eff}}$	-		-
		2 jet analysis (in combination with 0, 1, 2 leptons)		
Cut 1	number of jets	≥ 2	≥ 2	≥ 2
Cut 2	leading jet [GeV]	$p_T^{\text{jet1}} > 150$	> 180	> 70
Cut 3	subsequent jets p_T [GeV]	$p_T^{\text{jet 2}} > 100$	$p_T^{\text{jet 2}} > 50$	$p_T^{\text{jet 2}} > 30$
Cut 4	E_T^{miss} [GeV]	> 100	> 80	> 40
Cut 5	$E_T^{miss} > f \times M_{\text{eff}}$	f = 0.3	f = 0.3	f = 0.3
Cut 6	transverse sphericity S_T	-	> 0.2	-
		3 jet analysis (in combination with 0, 1, 2 leptons)		
Cut 1	number of jets	≥ 3	≥ 3	≥ 3
Cut 2	leading jet [GeV]	$p_T^{\text{jet1}} > 150$	> 100	> 70
Cut 3	subsequent jets p_T [GeV]	$p_T^{\text{jet 2,3}} > 100$	$p_T^{\text{jet 2,3}} > 40$	$p_T^{\text{jet 2,3}} > 30$
Cut 4	E_T^{miss} [GeV]	> 100	> 80	> 40
Cut 5	$E_T^{miss} > f \times M_{\text{eff}}$	f = 0.25	f = 0.25	f = 0.25
Cut 6	transverse sphericity S_T	-	> 0.2	-
		4 jet analysis (in combination with 0, 1, 2 leptons)		
Cut 1	number of jets	≥ 4	≥ 4	≥ 4
Cut 2	leading jet [GeV]	$p_T^{\text{jet1}} > 100$	> 100	> 70
Cut 3	subsequent jets p_T [GeV]	$p_T^{\text{jet 2,3,4}} > 50$	$p_T^{\text{jet 2,3,4}} > 40$	$p_T^{\text{jet 2,3,4}} > 30$
Cut 4	E_T^{miss} [GeV]	> 100	> 80	> 40
Cut 5	$E_T^{miss} > f \times M_{\text{eff}}$	f = 0.2	f = 0.2	f = 0.2
Cut 6	transverse sphericity S_T	> 0.2	> 0.2	-

Table 7.1: Event selection cuts for the SUSY analyses with 1-4jet jets: Cuts on the p_T of the leading jet, the p_T of the remaining jets, M_{eff} fraction f and transverse sphericity S_T as a function of the number of required jets and for the different studied LHC running scenarios. Additional cuts dependent on the lepton multiplicity are applied. (see Table 7.3).

The global variables used in Table 7.1 and 7.2 for the different channels are defined in Section 7.2. The cuts on the number of jets (cut 1), the transverse momentum of the jets p_T (cut 2 + cut 3), on the missing transverse energy E_T^{miss} (cut 4) and on the fraction f of the missing transverse energy to M_{eff} (cut 5) are common for all channels with different lepton-multiplicity (0-2). In addition a S_T cut was applied in some analyses (cut 6). For a centre-of-mass energy of 14 TeV a 1 jet 3-lepton channel and for first data events a 1 jet 0-lepton channel, referred to as "monojet channel", was studied (see Table 7.1).
Many SUSY signals decay into a high number of jets. Since the requirement of a high jet multiplicity strongly reduces Standard Model backgrounds, the signal-to-background ratio could be increased for such models. Thus for a centre-of-mass energy of 10 TeV (see Chapter 9) also 5 and 6 jet channels are tested. The applied cuts are listed in Table 7.2. For the 5 jet and 6 jet two lepton channel with opposite charged leptons no $|\Delta\phi(jet_i, E_T^{miss})|$ and no transverse sphericity S_T cut was applied. In addition, the p_T cut for the 5th and 6th jet was decreased to $p_T > 20$ GeV in order to increase the number of signal events.

cut	**5 jet channel**	**6 jet channel**	
number of jets	$\geq$5	$\geq$6	$\geq$6
number of leptons	0-2	0-1	2 OS
leading jet $p_T^{\text{jet 1}}$ [GeV]	> 100	> 100	> 100
subsequent jets p_T [GeV]	$p_T^{\text{jet 2-5}} > 40$	$p_T^{\text{jet 2-6}} > 40$	$p_T^{\text{jet 2-4}} > 40$ $p_T^{\text{jet 5-6}} > 20$
E_T^{miss} [GeV]	> 80	> 80	> 80
$E_T^{miss} > f \times M_{\text{eff}}$	f = 0.2	f = 0.2	f = 0.2
transverse sphericity S_T	> 0.2 (only for 0,1 lepton ch.)	> 0.2	-
$\|\Delta\phi(jet_i, E_T^{miss})\|$	>[0.2,0.2,0.2,0.0,0.0] only for 0,1 lepton ch.	>[0.2,0.2,0.2,0.0,0.0]	-

Table 7.2: Cuts on the p_T of the leading, the p_T of the remaining jets, E_T^{miss}, M_{eff} fraction f, transverse sphericity S_T and $|\Delta\phi(jet_i, E_T^{miss})|$ as a function of the number of required jets for the 5 and 6 jet 0-2 lepton channels, studied for $\sqrt{s}$ = 10 TeV.

Beside the multi-jet cuts defined in Table 7.1 and Table 7.2, additional selection criteria dependent on the required lepton multiplicity, are applied. They are detailed in Table 7.3. The event selection cuts, that define the lepton analyses, ensure that all events are disjoint with respect to the other inclusive SUSY search modes, in particular the 0-lepton and 1-lepton channels. This facilitates the combination of results obtained from the different SUSY search modes.
It should be noted that the 0-lepton channel cuts are discussed in detail in the following chapters.

channel	cuts for 14 TeV	cuts for 10 / 7 TeV
0-lepton channels	- no leptons with $p_T > 20$ GeV - cut on $\mid \Delta\phi(jet_i, E_T^{miss}) \mid$: 2 jet channel: $>$[0.2, 0.2] 3 jet channel: $>$[0.2,0.2,0.2] 4 jet channel: $>$[0.2,0.2,0.2,0]	- MC studies: no leptons with $p_T > 20$ GeV, data studies: no leptons with $p_T > 10$ GeV - cut on $\mid \Delta\phi(jet_i, E_T^{miss}) \mid$: 2 jet channel: $>$[0.2,0.2] 3 jet channel: $>$[0.2,0.2,0.2] 4 jet channel: $>$[0.2,0.2,0.2,0.0] 5 jet channel: $>$[0.2,0.2,0.2,0.0,0.0] 6 jet channel: $>$[0.2,0.2,0.2,0.0,0.0,0.0]
1-lepton channels	- one lepton with $p_T > 20$ GeV, no additional lepton with $p_T > 10$ GeV - no cut on $\mid \Delta\phi(jet_i, E_T^{miss}) \mid$ - $M_T > 100$ GeV	- one lepton with $p_T > 20$ GeV, no additional lepton with $p_T > 10$ GeV - cut on $\mid \Delta\phi(jet_i, E_T^{miss}) \mid$: 2 jet channel: $>$[0.2,0.2] 3 jet channel: $>$[0.2,0.2,0.2] 4 jet channel: $>$[0.2,0.2,0.2,0.0] 5 jet channel: $>$[0.2,0.2,0.2,0.0,0.0] 6 jet channel: $>$[0.2,0.2,0.2,0.0,0.0,0.0] - $M_T > 100$ GeV
2-lepton opposite sign (OS) channels	- two leptons with $p_T > 10$ GeV, OS - no additional lepton with $p_T > 10$ GeV - no cut on $\mid \Delta\phi(jet_i, E_T^{miss}) \mid$	- two leptons with $p_T > 10$ GeV, OS - no additional lepton with $p_T > 10$ GeV - cut on $\mid \Delta\phi(jet_i, E_T^{miss}) \mid$: 2 jet channel: $>$[0.2,0.2] 3 jet channel: $>$[0.2,0.2,0.2] 4 jet channel: $>$[0.2,0.2,0.2,0.0] 5, 6 jet channel: -
3-lepton channel	only 1 jet channel $\geq$3 leptons with $p_T > 10$ GeV - remove events w. invar. mass of same flavour opposite sign $M_{SFOS} \leq 20$ GeV	not studied

Table 7.3: Event selection criteria for the 0-3 lepton channels as a function of the number of required leptons. The cuts are applied after the object selection in addition to the jet selection cuts described in Table 7.1. The 0, 1 and 2-lepton channels are studied in combination with $\geq$ 2-6 jets (0 lepton channel also with $\geq$ 1 jet), the 3-lepton channel in combination with $\geq$ 1 jet.

7.3.1. Event selection for the collision events

For all analysed data samples presented in this thesis (see Chapter 11), stable beams at a centre-of-mass energy of about 7 TeV and optimal detector high voltage conditions were required. In addition the solenoid and toroid magnets were switched on and had their nominal fields to allow good momentum measurements for the electrons and muons. Moreover each of the sub-detectors' responses and the main criteria for electron, muon, and jet identification as well as energy and momentum computations should not deviate from their expected behaviour. This includes the systems needed for missing momentum reconstruction and the first level trigger systems required for jet selection (see Section 3.4). More than 98% of all inner detector, barrel and end-cap sub-detectors channels should be read-out or should not have read-out errors over the course of any luminosity block (see Section 2.3.4), all LAr and Tile (extended) barrel and end-cap calorimeters should have performed without major problems and not more than 1% of all events in any luminosity block are allowed to have read-out errors. Runs and luminosity blocks are flagged if there are issues which affect a large portion of a sub-detector or which have a high enough rate of currency, such that they can clearly be seen at a luminosity block or run level. Data that did not fullfill these criteria was not analysed. Moreover the events had to pass "event cleaning cuts" that are discussed in the following.

Event cleaning cuts for the collision events

In the measured collision events mis-reconstructed jets or "fake" jets arise from various sources, ranging from hardware problems (calorimeter noise), LHC beam conditions or cosmic-ray showers. Two types of mis-reconstructed jets are considered: jets not associated to in-time energy depositions in the calorimeters and jets coming from real energy depositions, where the energy measurements are of limited confidence, as the energy depositions are in calorimeter regions which have not yet been properly calibrated. These "fake" jet events show different properties with respect to real jets arising from parton fragmentation. Jet identification criteria are used to reject only jets with fake or out-of-time energy depositions as described in detail in Ref. [266]:

- **Transverse momentum** p_T: Only jets with reconstructed electromagnetic energy $p_T^{EM} > 10$ GeV are considered.
- **Single-cell jets in the HEC**: Mis-reconstructed jets are often caused by sporadic noise bursts in the hadronic endcap calorimeter, where most of the energy is in a single isolated calorimeter cell (sometimes with associated neighbouring cells due to cross-talk). Reconstructed jets with this problematics are characterised by a large jet-energy fraction in the HEC, defined by the variable "f_{HEC}" and a low number of energy-ordered cells containing at least 90% of the jet energy, known as "n90" . These fake jets are tagged with the requirement: $f_{HEC} > 0.8$ and $n90 \leq 5$.
- **Bad quality jets**: It was observed that the previous cut is not effective if the noise is overlaid with real energy deposition. For example if the noise burst affects the electromagnetic calorimeter and induces coherent noise a mis-measured jet can be reconstructed. This "bad

quality" jet is characterised by cells with bad calorimeter reconstruction quality and with large reconstructed energy, causing large fractions of jet energy in only the electromagnetic calorimeter. The variable f_{EM} describes the difference of the event pulse shape from the expected reference shape that is used to reconstruct the cell energy. In order to reject jets that have a large portion of their energy accounted for by coherent noise, the variable "$f_{quality}$" is defined, which gives the fraction of jet energy from bad-quality LAr calorimeter cells. Bad quality jets in the electromagnetic calorimeter are than selected with:
$| f_{quality} | > 0.8$ and $f_{EM} > 0.95$.

- **Out-of-time jets**: Jets reconstructed from large out-of-time energy depositions in the calorimeter, for example those due to photons produced by cosmic ray muons overlaid on a minimum bias collision event, are identified and eliminated with a loose cut on the jet time t_{jet}. This time associated to the jet is calculated as the energy squared weighted time of its constituents and is defined with respect to the event time. Jets are required to have an energy-squared-weighted cell time to be within the expected value of e.g. two beam bunch crossings. Out-of-time jets are selected with: $| t_{jet} | > 50$ ns.

- **HEC noise cleaning** Noisy cells in the hadronic endcap calorimeter (HEC) can be a dominant source of fake E_T^{miss} in the data analysed. The resulting fake jet can be removed with the discussed requirement. However, it was found that in case that the HEC noise bursts is overlaid on the real jet, the used cuts are not always efficient, because most of jet quality variables such as n_{90}, f_{HEC} and timing are smeared by the real jet. Since HEC noise produces a faster pulse shape than a normal ionisation pulse shape does, the shape quality factor from the energy reconstruction is a very powerful variable to identify HEC noise. This quality factor increases with the cell energy by $\sim E^2_{cell}$ due to the increasing differences between the actual and predicted pulse shapes, an effect which can potentially remove high energy jets. The energy deposit in bad cells with respect to the total jet energy at EM scale $f_{bad,Q}$ calculated with constant Q-factor threshold is used to suppress HEC noise overlaid events[5]. A current solution to suppress HEC noise overlaid events is to reject events having at least one jet with $f_{HEC} \geq 1 - f_{bad,Q}$ (for jets with $p_T > 10$ GeV).

- **vertex requirement** Additional background to the collision events are for example due to collisions of one proton beam with the residual beam gas within the beam pipe or muons or pions travelling in the halo of the beam ("beam halo" events, see also Section 2.3.3). Other sources are originating up-stream of ATLAS, for example caused by interactions in the tertiary collimators in the accelerator or cosmic ray muons overlapping with actual collision events. Collision candidates are rejected, if they contain no primary vertex with at least five associated tracks with minimum p_T of 150 MeV. The vertex requirement removes approximately 1.5×10^{-3} of the triggered events.

[5] A cell with a normalised quality factor > 4000 is identified as a "bad" cell.

The combined effect of all these cleaning cuts is to remove a fraction approximately 1% of triggered events. Figure 7.1 (left plot) shows the transverse momentum at electromagnetic scale of all anti-k_T, R = 0.4 jets after successive removal of single cell jets in the HEC and bad quality jets in the electromagnetic calorimeter. The cleaning selections reject most of the jets present in the tail of the inclusive distribution. The two remaining jets with a p_T at 308 GeV and 338 GeV belong to a real dijet event. In this plot the expectation from Monte Carlo simulation is superimposed and normalised to the number of jets in the data. The right plot in Figure 7.1 shows the E_T^{miss} distribution after the SUSY object selection and the L1_J15 trigger requirement (black-line), the "standard" cleaning cuts (rejection of single-cell jets in the HEC, out-of-time jets and bad quality jets) (dark blue) and the cleaning cut $f_{HEC} \geq 1 - f_{bad,Q}$ (in light blue). When a cut on the number of tracks per primary vertex is applied (light green), the number of the fake E_T^{miss} events in the tail is visibly reduced. However some events are still not rejected, e.g. an event with $E_T^{miss} = 57.5$ GeV that is overlaid with a jet with $p_T > 30$ GeV is not rejected. Figure E.10 in Section E.6 shows the event display for this event produced with the ATLAS event display software Atlantis [327,328]. Some fake E_T^{miss} events coming from HEC noise and from other sources rejected and not rejected by the applied HEC noise cut are summarised in Table E.6 and Table E.7 in Section E.6. The event with $E_T^{miss} \approx 200$ GeV is removed later by the $p_T(\text{jet1}) > 70$ GeV, veto additional jets with $p_T(\text{jet1}) > 30$ GeV requirement of the monojet data analysis.
The rate of sporadic HEC noise is expected to happen only rarely, however will increase as the luminosity goes up. Therefore some studies in the ATLAS SUSY group are also targeted to define improved cleaning cuts against HEC noise and to study the performance of such additional cuts. The defined cleaning cuts applied for the 70 nb^{-1} data samples also need to be verified with higher statistics.

Cosmic ray rejection for the monojet channel The mentioned cleaning cuts above are mostly designed for detector problems and are quite loose and simple in order to understand the detector and to avoid removing the real signal. Therefore several events induced by cosmic rays are not rejected. The monojet SUSY channel (1 jet 0-lepton channel) is most sensitive to the non-collision backgrounds due to its loose event selection of only one high p_T-jet and $E_T^{miss} > 40$ GeV. Therefore a special cut that is only used for the leading jets in the monojet analysis was designed to remove cosmic ray events.
Cosmic-ray events have been collected with the "L1_Calo_EMPTY" trigger in the CosmicCalo stream. It was found that most of the fake jets are concentrated in the central Tile calorimeter region, so the cleaning cuts requiring n90 ≤ 5 or $f_{HEC} > 0.8$ do not help to reject these cosmic-ray events. However, if a jet has 90% of its energy contained in fewer than six cells and less than 5% of its energy in the electromagnetic calorimeter, it is consistent with the signal from cosmic ray or beam halo muons (n90 ≤ 5 and $f_{EM} < 0.05$). Figure 7.2 shows for illustration purpose the E_T^{miss} distribution after the standard SUSY cleaning cuts and using the L1_J55 trigger (black line), after the monojet p_T-jet selection cuts in dark blue (leading jet with $p_T > 120$ GeV and no further jets with $p_T > 30$ GeV) and after rejecting cosmic events with the additional $f_{EM} < 0.05$ and n90 ≤ 5 cut (light blue) for data events corresponding to an integrated luminosity

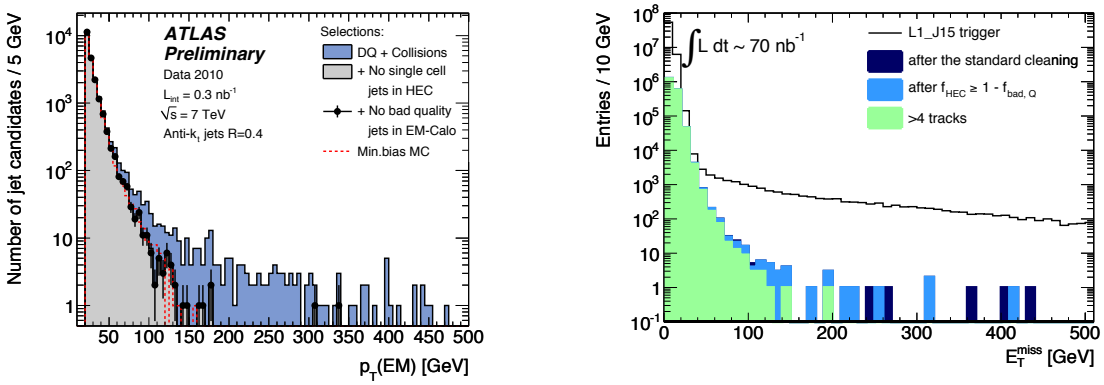

Figure 7.1: Left plot: Inclusive anti-k_T, R = 0.4, jet p_T distribution after successive cleaning cuts. The jet momenta are calibrated at the electromagnetic scale. The expectation from Monte Carlo simulation is superimposed and normalised to the number of jets in the data. Two remaining outlier jets with transverse momenta greater than 300 GeV are real jets and belong to the same dijet event. The figure is taken from Ref. [266]. Right plot: E_T^{miss} distribution after the applying the standard cleaning cuts, the HEC noise and track cuts as discussed in the text.

$\mathscr{L} = 2.95$ pb^{-1}. The estimated rejection factor is roughly 7 for a fake jet induced by cosmic rays. A more refined selection based on the relative transverse momentum carried by charged tracks associated to clusters, the activity in muon chambers and cluster shape as well as the effect of beam–induced backgrounds will be studied in the future [329].

Summary The applied event cleaning cuts used for the studies in Chapter 11 are summarised in Table 7.4. For the data studies, discussed in Chapter 11, 7 TeV proton-proton collisions events collected from March to July 2010 corresponding to an integrated luminosity of ≈ 70 nb^{-1} are analysed. The number of events rejected by this additional cleaning cut as well as event displays for this luminosity can be found in Ref. [329].
In September 2010 a "hadronic calibration workshop" was held in Pisa to review the status of the jet and E_T^{miss} reconstruction and calibration in the ATLAS experiment and to discuss recent results. As a results of this meeting tighter event cleaning cuts (bad jet criteria) are defined in order to reject the increasing number of fake jets (see Ref. [330, 331]). The SUSY group works in addition on event cleaning cuts in order to remove cosmic background events especially for the monojet channel.

Data analyses The SUSY analyses of data events proceed as follows: The events are first checked for the described event cleaning criteria and rejected if they do not pass any of the defined cuts. In a next step the object and event selection criteria as discussed are applied. The event selection requirements on jet momenta, E_T^{miss}, M_{eff} and the angle between the jets and the E_T^{miss} are detailed in Table 7.1, last column. In this thesis only data events that do not contain any recon-

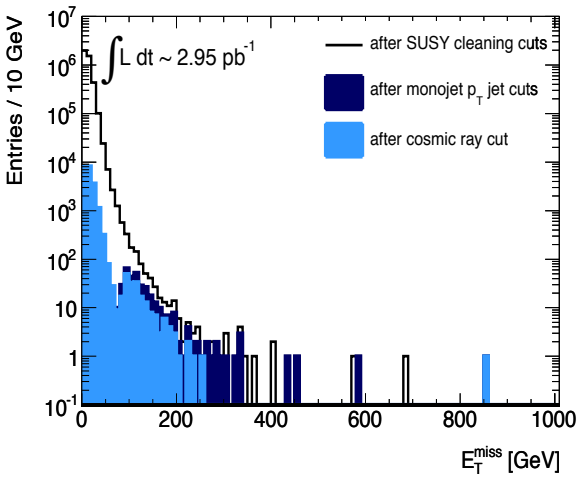

Figure 7.2: E_T^{miss} distribution after the standard SUSY cleaning cuts (black line), after the monojet selection cuts (leading jet with $p_T > 120$ GeV, no further jets with $p_T > 30$ GeV) in dark blue and after rejecting cosmic events with the f_{EM} and n90 cut (light blue) for $\mathscr{L} = 2.95$ pb^{-1}.

event rejection	**cleaning cut**
fake jets from detector failure	$\mid f_{quality} \mid > 0.8$ and $f_{EM} > 0.95$ $f_{HEC} > 0.8$ and n90 ≤ 5 $f_{HEC} \geq 1 - f_{bad,Q}$ $\mid t_{jet} \mid > 50$ ns $p_T^{EM}(jet) > 10$ GeV
fake jets from cosmic-rays/beam halo	n90 ≤ 5 and $f_{EM} < 0.05$ for the first jet in monojet channel p_T (jet1)>70 GeV prim. vertex with > 4 tracks with min. $p_T > 150$ MeV

Table 7.4: Summary of the applied cleaning cuts for the first collision events.

structed leptons (e or μ) with $p_{\mathrm{T}} > 10$ GeV (0-lepton SUSY analyses) are considered[6]. The choice of the selection criteria has been influenced by previous Monte Carlo studies. However, for the early measurements the selection thresholds have been reduced relative to the earlier Monte Carlo studies providing a larger sample of events to compare with the Standard Model expectations.

7.4. Trigger

The rate of p-p collisions at the LHC is significantly higher than the rate at which events can be read out and recorded. The ATLAS trigger system has been developed to select only the interesting events, that are required for the physics analyses (see Chapter 3.4). Dedicated triggers, that are combined to trigger menues, specify the thresholds and selection criteria for a single physics signature at each trigger level.
For the Monte Carlo studies the trigger menu, defined for an instantaneous luminosity of about 2×10^{33} cm^{-2}s^{-1} from the HLT TDR (see Ref. [162]) has been used. Reference [228] Table 1 lists the available unprescaled triggers and the obtained trigger efficiencies for the events passing the different SUSY analysis selection criteria for different samples.
The available trigger menus for the measured data events can be found in Ref. [333]. As luminosity increases the trigger menu for the collision data is updated and refined regularly.

7.4.1. Trigger efficiency for the Monte Carlo studies

The trigger efficiency with respect to the off-line event selection has been studied based on a complete simulation of the ATLAS trigger system for the SUSY benchmark points and the main Standard Model backgrounds for the initial LHC running scenario with a centre-of-mass energy of 14 TeV. The available triggers select e.g. one or multiple high p_T jets, significant E_T^{miss}, one jet + E_T^{miss} or electron or muon. The jet triggers had low efficiencies for all SUSY points. The best performance could be obtained with the jet + E_T^{miss} trigger `J70_XE70` (see Section 3.4.2) that requires a jet with p_T above 70 GeV and missing transverse energy exceeding 70 GeV. This combined trigger has an efficiency $> 95\%$ for luminosities of 1×10^{33}cm^{-2}s^{-1}. Similar results could be obtained when the trigger menu was adapted to the trigger threshholds defined for a luminosity of about $1 \times 10^{31}/1 \times 10^{32}$cm^{-2}s^{-1} for the MC studies performed at a centre-of-mass-energy of 10 TeV and 7 TeV. The ATLFAST1 simulated SUSY signal Monte Carlo samples, that are used for the discovery reach studies, did not have any trigger information included. Since the applied p_T and E_T^{miss} analysis cuts are much harsher than J70_XE70 trigger thresholds, for simplicity a trigger efficiency of 100% was assumed.

7.4.2. Trigger efficiency for the collision events

The trigger efficiency has been studied for the initial LHC running scenario by the ATLAS experiment e.g. in the Reference [334]. For the studies in this thesis the lowest available unprescaled calorimeter jet trigger (see Section 3.4.2) of the first trigger level - trigger `L1_J15` was used. The

[6] Events with one or two leptons are studied e.g. in Ref. [332].

higher trigger levels were set in a state which permitted all events passing the L1 jet trigger to pass ("pass-through mode"). The efficiency has been measured with data selected by the minimum bias trigger `L1_MBTS_1` and was compared to the Monte Carlo trigger simulation. The trigger efficiency for the L1 hardware-based trigger `L1_J15` (see Section 11) as well as for the trigger `L1_J30` and trigger `L1_J55` as a function of the calibrated p_{T} of the leading jet[7] is presented in Figure 7.3. The left plot shows the trigger efficiency for the Monte Carlo sample - SUSY signal SU4 and the right plot shows the trigger efficiency for the analysed data corresponding to $\mathscr{L} = 70$ nb^{-1}. The jet cleaning cuts, the vertex cut, electron crack veto (see previous section) as well as a electron/muon veto and a cut on the leading jet p_T larger than 70 GeV are applied. The L1_J15 trigger is fully efficient for jets with p_{T} above 50 GeV. The plateau efficiency is greater than 99% for the events analysed after applying a cut on at least one jet with $p_{\mathrm{T}} > 70$ GeV. The trigger efficiencies in data and MC simulation agree to better than 1%. Similar results are determined with the QCD samples, SU4, top pair production and vector boson samples (see studies in Ref. [329]).

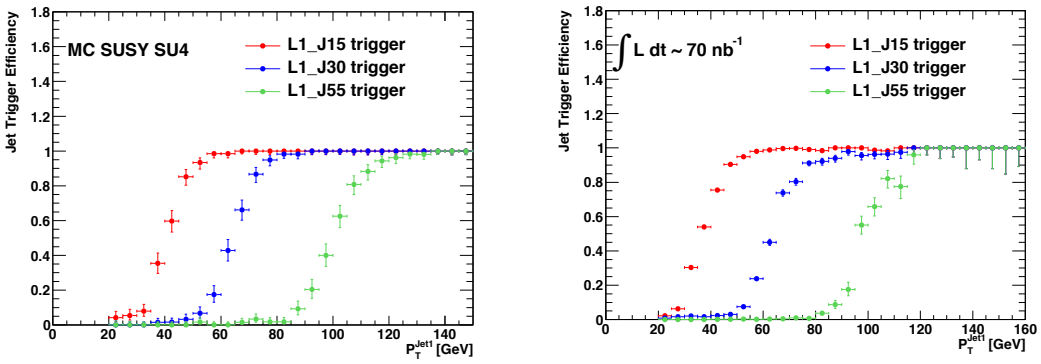

Figure 7.3: The trigger efficiency for the L1_J15, L1_J30 and L1_J55 triggers as a function of the calibrated jet p_{T} for the MC SUSY sample SU4 (left plot) and analysed data events of an integrated luminosity of $\mathscr{L} = 70$ nb^{-1} (right plot).

7.5. Statistical method

7.5.1. Significance calculation

The SUSY searches presented in the next chapters are typical examples of cut and count analyses that try to answer the question if it is possible to claim an excess of events over the expected Standard Model background. For example in order to discover a SUSY signal the measured deviation in the data from the Standard Model has to be statistically significant. This means significantly more events are detected than expected. To discriminate between a statistical fluctuation of the background and a possible presence of a real signal, and to characterise if a measured event is

[7] The trigger thresholds are defined for the jet energy at EM scale, not for the calibrated jet p_T.

unlikely to have arisen by chance and or not, the level of significance - the probability (p-value) can be calculated.
In the SUSY searches it is the probability conditional on the null hypothesis H_0 –"the measured data events are only Standard Model events" of the observed data with a value ranging from zero to one. If the obtained p-value is small, it can be said either the null hypothesis is false or an unusual event has occurred (usually if p<0.05)[8].

p-value calculation

For a random experiment with two possible outcomes, the "success" probability p for n successes in N trials (measurements) is given by the binomial distribution:

$$f(n;N,p) = \frac{N!}{n!(N-n)!} \cdot p^n (1-p)^{N-n} \tag{7.8}$$

with the expectation value N·p and the variance $N \cdot p(1-p)$.
If the number of trials is large ($N \to \infty$, for p→0), the binomial distribution can be approximated by a Poisson distribution with $\mu = N \cdot p$ the expected number of events to be observed:

$$f(n;\mu) = \frac{e^{-\mu}}{n!}\mu^n \tag{7.9}$$

$f(n;\mu)$ gives the probability that exactly n successes occur in a Poisson experiment, when the mean number of successes is μ. If the number of measured events are e.g. $n = N_{data}$, the data events found in the signal region, and μ is the number of expected events, e.g. $\mu = b$ the Standard Model events that are predicted in this region, the inconsistency of the measurement with the hypothesis H_0 is given by the p-value:

$$p = \sum_{i=n}^{\infty} \frac{e^{-\mu}}{i!}\mu^i = \sum_{i=N_{data}}^{\infty} \frac{e^{-b}b^i}{i!}. \tag{7.10}$$

The value p is the probability to measure N_{data} events or more, assuming the hypothesis H_0 is true. The smaller the p-value, the less compatible is the measurement with this null hypothesis.
If the number of expected events μ is large enough, the Poisson distribution approaches the Gaussian distribution with the probability density function:

$$f(x;\mu,\sigma^2) = \frac{1}{\sqrt{2\pi\sigma^2}} \cdot exp\left(\frac{-(x-\mu)^2}{2\sigma^2}\right) \tag{7.11}$$

with an expectation value is for a Gaussian distribution $\mu = \int_{-\infty}^{\infty} x\, f(x;\mu,\sigma^2)dx$, the variance $\sigma^2 = \int_{-\infty}^{\infty} (x-\mu)^2 f(x;\mu,\sigma^2)dx$ and the standard deviation σ.
The standard Gaussian, ($\mu = 0$ and $\sigma = 1$) and the distribution $F(a) = \int_{-\infty}^{a} f(x;\mu=0,\sigma=1)dx$ are related to the error function. Thus the calculated p-value can

[8] The common criterion for an observation is $p < 2.9 \times 10^{-7}$ (significance Z_n of 5σ or more).

be expressed in terms of the "standard-deviation" Z_n, which is commonly called significance (see Ref. [335,336]):

$$Z_n(p) = erf^{-1}(1-2p)\cdot\sqrt{2} \tag{7.12}$$

The values $Z_n(p)$ must be evaluated numerically. The deviation of 5σ corresponds to a p-value of about $\approx 10^{-7}$ and is widely used in the field of high-energy physics to claim a discovery[9].
The most simple approximation to calculate the significance Z_n of an observation is $\mathrm{N_s}/\sqrt{\mathrm{N_b}}$, where N_s is the number of signal events and N_b is the number of background events.

p-value calculation including systematic uncertainties

The so far discussed $Z_n(p)$ definition does not take into account the systematic uncertainty δN_b on the background events N_b. Including this, the probability p that N_b background events fluctuate around the measured value N_{data} can be derived from the convolution of the Poisson probability density function (pdf) to account for statistical errors with a Gaussian pdf
$f(x;\mu,\sigma^2) = G(b;N_b,\delta N_b)$. The Gaussian pdf takes the systematic gaussian uncertainties for all background events $\sigma^2 = \delta N_b$ around the mean value $\mu = N_b$ into account. The probability to measure $\mathrm{N_{data}}$ events, if N_b are expected, is:

$$p = A\int_0^\infty db\, G(b;N_b,\delta N_b)\sum_{i=N_{\mathrm{data}}}^{\infty}\frac{e^{-b}b^i}{i!} \tag{7.13}$$

The factor

$$A = \frac{1}{\int_0^\infty db\, G(b;N_b,\delta N_b)\sum_{i=0}^{\infty} e^{-b}b^i/i!}.$$

ensures that the pdf is normalised to unity. If G is replaced by a Dirac delta function $\delta(b-N_b)$, the estimator p results in a usual Poisson probability as described before.
Table 7.5 summarises as an example the number of signal events N_s for the SUSY point SU4, the number of SM background events N_b after all event selection criteria including a cut on $M_{\mathrm{eff}} > 400$ GeV for the 2, 3 and 4 jet 0-lepton channel for $\mathscr{L} = 0.5$ fb^{-1} and $\sqrt{s} = 7$ TeV. For the Z_n calculation a systematic uncertainty of 70%, applied as $\delta N_b = 0.7N_b$, and a statistical uncertainty of $\sqrt{N}$ was used.

It can be seen that without taking into acccount the systematic uncertainty, the significance $N_s/\sqrt{N_b}$ is always much larger than the correct value Z_n. In all three analyses for the selected effective mass cut $M_{\mathrm{eff}} > 400$ GeV[10] Z_n is < 5, while the value $N_s/\sqrt{N_b}$ would indicate a discovery.
Throughout this thesis the number of SUSY signal events will be always denoted by S and the number of Standard Model background events by B. For the Monte Carlo studies the value

[9] The probabilities that the measurement x is found in the range of $\mu \pm 1\sigma$ is 68.3%, for $\mu \pm 2\sigma$ it is 95.5% and for $\mu \pm 3\sigma$ it is 99.7%.

[10] For an effective mass cut $M_{\mathrm{eff}} > 800$ GeV, Z_n is more than 5 for the SUSY signal SU4 .

SUSY signal	analysis	S	B	$N_s/\sqrt{N_b}$	Z_n
SU4	2 jet 0 lepton	667.1	1563.2	16.9	3.3
SU4	3 jet 0 lepton	2412.3	1485.3	62.6	2.3
SU4	4 jet 0 lepton	1873.9	1029.9	58.4	2.6

Table 7.5: Number of signal events N_s, the number of background events N_b, the statistical significance $N_s/\sqrt{N_b}$ and the significance Z_n. All numbers are for the 2-4 jet 0-lepton channels for $\mathscr{L} = 0.5\text{fb}^{-1}$ and $\sqrt{s} = 7$ TeV. For the Z_n calculation in the last column a systematic uncertainty of 70% applied as $\delta N_b = 0.7 N_b$ and a statistical uncertainty of $\sqrt{N}$ was used.

$N_{data} = S + B$ is considered as the number of measured "data" events for the significance calculation using equation 7.13. A SUSY model "missed" or "failed" the selection for an obtained Z_n value < 5. Similarly a model is called as "discovered", when the significance is ≥ 5. The discovery reach lines presented in this thesis are always shown for SUSY signals with $Z_n \geq 5$ (referred as 5σ).

7.5.2. Correction of the significance Z_n

Especially for first data measurements relatively loose selection criteria are applied resulting in large number of events in the signal region that are expected to be still contaminated with many background events. To apply just one hypothesis test would make no sense. Therefore, several hypothesis tests, e.g. several cuts in different M_{eff} regions, are used in order to find the one with a statistically most significant deviation of the measured data compared to the MC prediction. However, looking at the different cut combinations it becomes more likely that statistical fluctuations can be misinterpreted as new physics if the number of trials is not taken into consideration. This effect is called in statistics "the problem of multiple comparisons" and can be corrected.
To determine how often a 5σ deviation arises only from Standard Model processes due to multiple tests, toy Monte Carlo experiments are performed assuming the background-only hypothesis. To do so, 50 million hypothetical histograms (e.g. M_{eff} and E_T^{miss} histograms depedent on the cuts that are tested) are generated by dicing in each bin of the "original" histogram a random number of events according to a Poisson distribution of the expected number of events in that histogram bin. This gives a huge set of histograms, each representing one possible outcome of the measurement. Each diced histogram is a possible measured result of the experiment. Finally on each of these hypothetical histograms the same set of M_{eff} cuts (see Section 7.5.4) is applied and the cut giving the largest Z_n^M value is chosen. The fraction F of histograms giving a significance larger than this highest significance value Z_n^M for the studied histogram is calculated. This procedure is done for every obtained Z_n value:

$$F = \frac{\text{number of toy Monte Carlo histograms with } Z_n > Z_n^M}{\text{number of toy Monte Carlo histograms}}$$

F gives the probability to find a deviation even bigger than the one observed in the data, assuming that only known Standard Model background events are in the data. Only this fraction F gives the correct probability to find a deviation with maximal significance $\max(Z_n)$ in the data. It can be converted into the "corrected significance Z_n" via:

$$\text{corrected } Z_n = \text{erf}^{-1}(1-2F)\cdot\sqrt{2}$$

In the following sections the expression "significance" corresponds always to the calculated corrected Z_n value.

7.5.3. Systematic uncertainties

Systematic uncertainties for the Monte Carlo studies

Any discovery of new physics can only be claimed, if the Standard Model backgrounds are understood and under control. It is expected that this cannot be achieved only with Monte Carlo predictions. In order to determine the significance in a "realistic" way, systematic uncertainties of the SM background must be considered. Data-driven methods have been developed (see Ref. [337], [338] and [104]) to reduce reliance on Monte Carlo generators and on the simulated detector performance. The effect of different uncertainties are taken into account for these studies in order to determine the total systematic uncertainty. A brief summary of these considered uncertainties is in the Appendix Section E.2, detailed informations are in Ref. [104]. As a result the expected SM backgrounds and their uncertainties could be obtained with these studies.

Uncertainties for 14 TeV Monte Carlo studies Taking recommendations from this, the systematic uncertainties corresponding to $\sqrt{s}$ = 14 TeV and $\mathscr{L}$ = 1fb^{-1} were estimated to be:

$\pm$50% for QCD jet production

$\pm$20% for the W, Z and $t\bar{t}$ backgrounds.

The uncertainty was applied as "uncertainty $\cdot$ N_b" for each histogram bin.

Uncertainties for 10 TeV and 7 TeV Monte Carlo studies Since the uncertainties are only estimated for a centre-of-mass-energy of 14 TeV and for $\mathscr{L} = 1$ fb^{-1}, for an initial sample at the centre-of-mass energy of $\sqrt{s} = 10$ TeV or $\sqrt{s} = 7$ TeV with smaller integrated luminosity, the systematic uncertainties for the Standard Model backgrounds need to be reevaluated:
The uncertainty on the background as determined with data-driven methods has a statistical component, due to the finite size of the control samples, and a systematic component, due to e.g. the detector performance uncertainties. The total error for the background determination for W, Z and top pairs typically has an equal contribution from a systematic error and a statistical error as discussed in Ref. [104]. Some parts of the loss of statistics is compensated in the control samples by making looser cuts on the transverse momenta and missing transverse energy (see Table 7.1) for the lower centre-of-mass energy studies. The systematic error is re-estimated accounting for

the expected detector performance uncertainties in early data and the lower integrated luminosity. For example conservatively an about four-five times larger systematic error for a luminosity of 200 pb^{-1} at $\sqrt{s} = 10$ TeV can be assumed. Overall, for an integrated luminosity of 1 fb^{-1} at $\sqrt{s} = 7$ TeV or for an integrated luminosity of 200pb^{-1} at $\sqrt{s} = 10$ TeV the calculated uncertainty is about 50% (statistical + systematical uncertainty) on the W, Z and top backgrounds assuming that these are determined with data-driven methods. The QCD background is not dominant for all channels (e.g. lepton channels) and the uncertainty was estimated in Ref. [104] to be about $\pm$60% for a PYTHIA sample equivalent to a luminostiy of 23.8 pb^{-1}. In conclusion, the following systematic uncertainties are estimated and used for the Monte Carlo studies at 10 and 7 TeV:

$\pm$50% for $\mathscr{L} = 0.2$ fb^{-1} at $\sqrt{s} = 10$ TeV

$\pm$70% for $\mathscr{L} = 0.5$ fb^{-1} at $\sqrt{s} = 7$ TeV

$\pm$50% for $\mathscr{L} = 1.0$ fb^{-1} at $\sqrt{s} = 7$ TeV

$\pm$35% for $\mathscr{L} = 2.0$ fb^{-1} at $\sqrt{s} = 7$ TeV

The uncertainty was applied as "uncertainty $\cdot$ N_b" for each histogram bin.
A more precise estimate of the systematic uncertainties is not possible at this point and would require further studies. They are at the moment one of the main topics to be studied with early LHC data. In order to consider the effect of different systematic uncertainties on the discovery potential the uncertainties have been varied within a range around the default values given above, for example for the Monte Carlo studies at $\sqrt{s} = 7$ TeV or for some MSSM grid studies at $\sqrt{s} = 10$ TeV for $\mathscr{L} = 200$ pb^{-1}.

Total systematic uncertainty For each bin of a distribution the statistical error of the Monte Carlo ($\sqrt{N}$), scaled according to the luminosity, is considered as an additional systematic uncertainty taking into account the limited Monte Carlo statistics for some channels. Therefore, the total systematic uncertainty increases at high E_T^{miss} and M_{eff} and for channels with low event statistics. All systematic uncertainties are taken to be uncorrelated and independent of any variable and have been added in quadrature to calculate the total systematic uncertainty. Note that this is just an approximation. Systematic effects like the jet energy scale uncertainty are common for all samples and should lead to correlated errors. This was taken into account for the studies of the collision events (see the following Section).
Note that the numbers above are determined for the 4 jet channels, but are taken as indicative uncertainties for all studied SUSY channels (e.g. 2 and 3 jet channels). No dedicated studies of background systematics have been yet performed for the 2 and 3 jet channels. However, it is expected that the lower jet multiplicity channels have larger samples of statistics to determine the backgrounds in the early data. Thus, the numbers used are likely to be a very conservative assumption for the 2 and 3 jet channels. Either way, dedicated background studies would be needed in order to properly assess the systematics for these channels.

Systematic uncertainties for data studies

For the estimation of the Standard Model prediction some of the most important sources of experimental systematic uncertainties have been studied. The statistical uncertainties are assumed to be $\sqrt{N}$ on the Monte Carlo prediction. All systematic uncertainties are added in quadrature for the estimation of the total uncertainty. The resulting total uncertainty is dominated by the uncertainties in the calorimeter energy scale and the luminosity. The comparison between the Monte Carlo predictions and the data events can be found in Chapter 11. In the following the used uncertainties are briefly discussed.

Jet Energy Scale (JES) The uncertainty associated with the calorimeter energy scale has been estimated using a parametrisation of this scale as a function of jet p_{T} and η. The method is summarised in Section 5.2.2, more details can be found in Reference [264]. The used parametrisation was evaluated by comparing the nominal results to Monte Carlo simulations using alternative detector configurations, alternative hadronic shower and physics models, and by comparing the relative response of jets across pseudo-rapidity between data and simulation. The procedure was designed to produce a conservative estimate of the uncertainty, which is about 10% for jets in the range 20 GeV $< p_{\mathrm{T}} <$ 60 GeV and $6-7\%$ for jets at higher p_{T}.
The effects of energy scale changes were determined by rescaling all jet energies and momenta in all Monte Carlo simulated samples ($p_T^{\vec{E}M}$). The missing transverse momentum E_T^{miss} was coherently recalculated using the rescaled energies of the clusters associated with the jets,

$$p_T^{miss,\ new} = p_T^{miss} + p_T^{\vec{E}M} \cdot \left[1 \pm U(p_T^{EM} \cdot JES, \eta)/JES\right] \tag{7.14}$$

where p_T^{miss} is the missing transverse momentum two-vector as defined in equation 5.8, U($p_T^{EM} \cdot JES$,η) is the relative jet energy scale uncertainty shift and *JES* is the jet energy correction factor (for the EM$\cdot$JES scale). The resulting systematic uncertainty on the number of events from the Standard Model processes that is expected after applying jet and E_T^{miss} cuts is approximately 25% for the monojet analysis (1 jet channel) and the ≥ 2 jet analysis, 40% for the ≥ 3 jet analysis and 50% for the ≥ 4 jet analysis. This estimate of the jet energy scale uncertainty for the first collision events is quite conservative and will be replaced for future analyses by in-situ methods [339,340].
The described Jet Energy Scale uncertainties do not take into account the uncertainties on the unclustered energy (cell-out term) to account for possible mis-modelling of the transverse momentum component from calorimeter cells not contained within jets.

Luminosity The uncertainty on the integrated luminosity is estimated to be $\pm 11\%$ for the $W^{\pm}$ + jets, Z^0 + jets and $t\bar{t}$ production (see Ref. [341]). The QCD multijet Monte Carlo predictions are normalised to the measured data. There is no need to apply any luminosity systematics to this contribution.

Multiple particle interactions (pile-up) effects During the data-taking period considered for this analysis, the beam intensity was increased. This could lead to a non-negligible fraction of

events where proton-proton interactions in the same bunch crossing (in-time pile-up) took place that produced soft particles overlapping with the jets produced in the hard-scatter collision. As result extra energy is added to the measured jets. To estimate the increase of pile-up events, the number of vertices reconstructed for each events was studied. For earlier runs only 6% of the events had more than one vertex, while for the high luminosity runs almost 50% of the events have at least an extra vertex.
To check for the possible pile-up effects for the final states considered, the shapes of some of the "key" distributions used in the analysis for runs with expected lower and higher pile-up content are cross checked. The studies can be found in the Appendix in Section E.6.2.
The ATLAS collaboration has developed correction techniques to account for the average increase of the jet energy due to pile-up, based on Monte Carlo that is just being commissioned with data [342]. For this initial data taking period, no additional uncertainties have been assigned for extra proton-proton interactions in the same bunch crossing (in-time pile-up). However, the effects are expected to be smaller compared to the jet energy scale uncertainties, because the selected events all contain high p_T jets and a high E_T^{miss} cut is applied. Therefore a quite conservative systematic uncertainty on the jet energy scale is applied instead to take into account an average impact of pile-up.

Theory uncertainties For the early studies no uncertainty was assigned to the the Monte Carlo generators predictions. The uncertainties on the normalisation of associated production of $W^{\pm}$ + jets and Z^0 + jets will likely be significant with increasing integrated luminosity and will be determined with data-driven techniques from control regions when more data are acquired.

Further possible uncertainties Uncertainties associated with the trigger efficiency, and lepton (electron, muon) identification efficiency are small by comparison. Therefore, no additional systematics are assigned for them. For the QCD multijet processes the PYTHIA Monte Carlo predictions have been compared to the ALPGEN distributions. Figure 7.4 shows the comparison of the two samples for the p_T distribution of the leading jets (left plot) and the missing transverse energy distribution for a 2 jet event selection (right plot). It can be concluded from these studies that the differences between ALPGEN and PYTHIA are smaller than the current systematic uncertainties. Thus, no attempt has been made to assign uncertainties on the normalisation factor related to the predictions of different QCD Monte Carlo generators. However, those differences will become more important in future with additional integrated luminosity included in the analysis.

The resulting relative systematic uncertainties on the Standard Model expectations after applying all selection criteria are:

jet Energy Scale uncertainty:	$\sim \pm 25\%$ (monojet, 2 jet 0-lepton channel)
	$\sim \pm 40\%$ (3 jet 0-lepton channel)
	$\sim \pm 50\%$ (4 jet 0-lepton channel)
luminosity uncertainty:	$\pm 11\%$

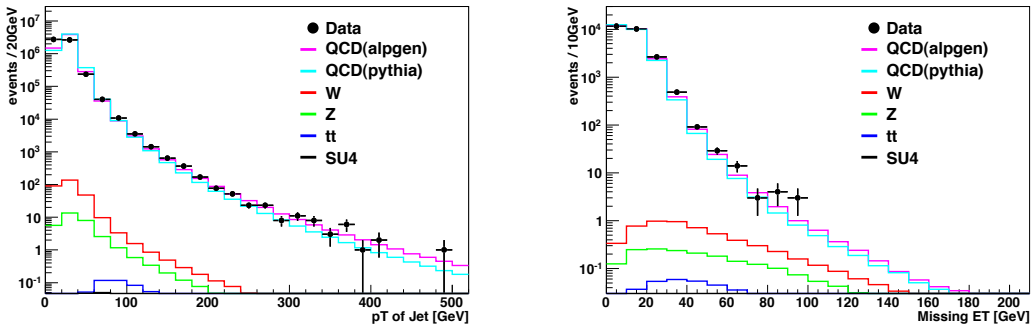

Figure 7.4: Comparison of the ALPGEN (pink line) and PYTHIA (light blue line) QCD samples with the data events (black points). The p_{T} distribution of the leading jets (left plot) and the missing transverse energy distribution for a 2 jet selection (right plot) are shown. The figures are taken from Ref. [329].

7.5.4. Scan of M_{eff}

The search for Supersymmetry is strongly influenced by the SUSY mass scale and cross sections of the SUSY signals. M_{eff} is a very powerfull variable to find an excess of data events over Standard Model background events and is used in this thesis to determine the discovery reach in the different SUSY parameter spaces. For every SUSY signal the significance can be calculated as described in Section 7.5.1 from the expected number of background and signal events in the "final" M_{eff} distribution after applying the described event selection cuts. However, these distributions show the biggest difference between signal and SM background for high M_{eff} values. Therefore an additional cut in M_{eff} should be applied to find the region with the best signal-to-background ratio. Since every SUSY signal has an individual M_{eff} distribution, a set of cuts $M_{\mathrm{eff}} \geq (400, 800, 1200, 1600, 2000)$ GeV is tested as demonstrated in Figure 7.5 (left plot). For each M_{eff} cut the significance Z_n is calculated and the cut giving the maximum significance is selected. Finally this selected significance Z_n has to be corrected for multiple testing as described in Section 7.5.2.
This procedure was done for every individual point in the studied SUSY grids. Figure 7.5 (right plot) demonstrates as an example this "scan in M_{eff}" for the M_{eff} distribution after applying the 4 jet 0-lepton cuts and the effect on the discovery reach for different mSUGRA signals in a mSUGRA tanβ=10 grid. The 5σ discovery reach lines after applying the 4 jet 0-lepton event selection (for $\sqrt{s} = 14$ TeV studies) for the different tested M_{eff} cuts are presented. For small m_0 and large $m_{1/2}$ values requiring $M_{\mathrm{eff}} \geq 2000$ GeV gives the largest reach (pink dashed line), while for larger m_0 values a lower M_{eff} cut seems to be the best (red line).
This described scan of the M_{eff} distribution is the current ATLAS baseline method to assess the best signal significance of the inclusive SUSY search channels and was used in all studies for all centre-of-mass energies. The highest significance out of the tested M_{eff} cuts is stated as the expected discovery potential for the studied SUSY signal.

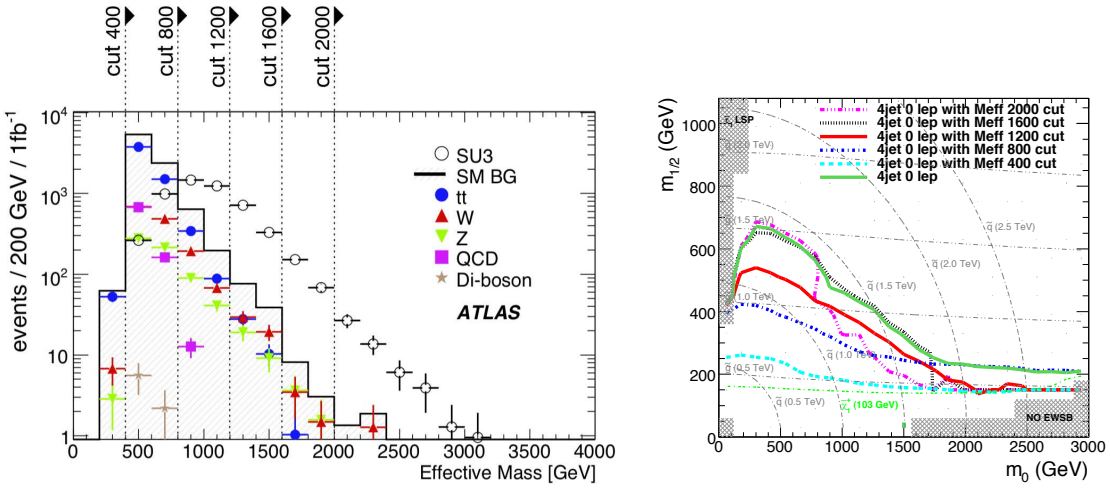

Figure 7.5: Demonstration of the M_{eff}-scan procedure (left plot) and the result in the mSUGRA grid (right plot). The significance for the 4 jet 0-lepton analysis for an integrated luminosity of 1 fb^{-1} (at $\sqrt{s}$ = 14 TeV) after a $M_{\text{eff}} > 0.4\,\text{TeV}$ (turquoise dashed lines), $M_{\text{eff}} > 0.8\,\text{TeV}$ (blue dashed line), $M_{\text{eff}} > 1.2\,\text{TeV}$ (red line), $M_{\text{eff}} > 1.6\,\text{TeV}$ (black dashed line), $M_{\text{eff}} > 2.0\,\text{TeV}$ (pink dashed line) cut and the significance taking always the largest significance of all tested cuts corrected for multiple testing (green line) are shown. All lines indicate the 5σ reach (right plot).

8. Searches for Supersymmetry at a centre-of-mass energy of 14 TeV

8.1. Introduction

This chapter describes of the SUSY discovery prospects for a centre-of-mass energy of 14 TeV. The presented studies were a part of the so-called *Computing System Commissioning* (CSC) programme and are detailed in the References [104, 228]. In the following only the inclusive SUSY strategies with 0-lepton and $\geq$ 2, 3 and 4 jets, which have been studied in detail, are discussed. The signature for these channels are a number of high p_T jets and E_T^{miss} from the cascade decays of squarks and gluinos.
First the results of the applied analysis cuts are presented for a specific SUSY signal, the SUSY benchmark point SU3 (see Section 4.5.2) together with the corresponding event numbers for the Standard Model background processes (see Section 8.3.1). In Section 8.3 the determined discovery potential is shown for several SUSY models, including parameter scans of different SUSY signal grids. Finally, Section 8.4 considers a possible cut-optimisation analysis technique, which is compared to the baseline 0-lepton analysis results. All presented distributions are normalised to an integrated luminosity of 1fb^{-1} if not indicated differently.

8.2. Experimental setup

8.2.1. Monte Carlo simulations

Fully simulated $\sqrt{s} = 14$ TeV Monte Carlo samples have been produced for the SUSY benchmark signals and the SM backgrounds, generated with PYTHIA (QCD jet production), ALPGEN (production of $W^{\pm}$ and Z^0 bosons in association with jets), MC@NLO and HERWIG (with JIMMY) ($t\bar{t}$ process, Diboson samples, SUSY signal). The different production steps are discussed in Chapter 4. The details of the samples used, are given in Section 4.5.1 and Section 4.5.2. A summary of all used sample together with the corresponding cross sections of the processes can be found in the Appendix Section D in Table A.1 and in Table A.1. Some of the Standard Model Monte

Carlo samples (referred as "background samples") are produced with generation filters to increase the statistics. The studies are not affected by these filters since the applied set of p_T-jets and E_T^{miss} event selection cuts are much tighter than the event filter cuts. It should be noted that for the 2 and 3 jet analyses $W+$jets and $Z+$jets PYTHIA samples are used instead of ALPGEN samples (see discussion in Section 4.5.1).
For the discovery reach and cut optimisation studies (see Section 8.3 and 8.4) different SUSY signal grids are produced. They are detailed in Section 4.5.2. The mass spectrum and the branching ratios of the SUSY signals are calculated using ISAJET, the events are generated using the HERWIG generator. Since all grids consist of a large number of signal points, a fast simulation was used (ATLFAST1, see Section 4.3.2), however a number of corrections are applied in order to ensure that the performance of the reconstructed physics objects matched to the performance observed using full simulation samples (see Section 4.3.2 for details).

8.2.2. Trigger

The trigger efficiency for all SUSY analysis has been studied, based on a complete simulation of the ATLAS trigger system for an instantaneous luminosity of $10^{33}\text{cm}^{-2}\text{s}^{-1}$. The trigger menu was adapted to $10^{31}/10^{32}\text{cm}^{-2}\text{s}^{-1}$ (see Section 7.4). The trigger has an efficiency of $> 95\%$ for all studied SUSY benchmark and SM scenarios. For ATLFAST1 simulated samples no trigger information was available and therefore no trigger selection could be applied. However, the results are not affected by the trigger performance, since p_T jet and E_T^{miss} values of the events that pass the J70_XE70 trigger are still below the cut values of the applied jet p_T and E_T^{miss} cuts, so a trigger efficiency of 100% can be assumed.

8.2.3. Object and event selection

The same object identification and overlap removal criteria are used for all SUSY channels. The criteria are detailed in Section 7.1 and are only summarised here. Jets are reconstructed with a seeded fixed-size cone algorithm and are required to have $p_T > 20$ GeV and $|\eta| < 2.5$. Combined muons, which are reconstructed with the STACO algorithm ($\chi^2 < 100$), and medium electrons are used. The p_T of the electrons and muons should exceed 10 GeV and $|\eta|$ should be less than 2.5. E_T^{miss} is reconstructed using the default calorimeter-based algorithm with the refined calibration and including the cryostat and muon terms.
The event selection cuts for the different lepton multiplicities (0-, 1-, 2-lepton) are very similar (see Table 7.1 and Table 7.3). In the following all results are presented for the 0-lepton channels.

0-lepton channels

A typical signal for Supersymmetry at hadron colliders are events with jets and large missing transverse energy E_T^{miss}, but no energetic isolated leptons. This signature is one of the most favoured SUSY search channels, because it can get contributions from every type of sparticle pair production, except sleptons. The multi-jet topologies are expected to give also a good statistical significance for the discovery of a large range of SUSY models, since the relevant sparticle decays have

sizable branching fractions and the requirement of high jet multiplicity strongly reduces leading backgrounds from vector boson + jet and QCD jet production. However one must choose the E_T^{miss} cut high enough to reduce backgrounds from detector mis-measurements of jet energies.
A general description of SUSY jet kinematics requires mainly three parameters, assuming that squark and gluino productions dominate: the masses of the gluino, the lightest squark and the next lightest gaugino.
Depending on the mass configuration the following strong sparticle pair-production processes can be distinguished:

- if M($\tilde{q}$) $\gg M(\tilde{g})$: $\tilde{g}\tilde{g}$ production dominates, leading to events with four parton level jets
- if M($\tilde{q}$) $\approx M(\tilde{g})$: $\tilde{q}\tilde{g}$ production dominates, leading to events with three parton level jets
- if M($\tilde{q}$) $\ll M(\tilde{g})$: $\tilde{q}\tilde{q}$ production dominates, leading to events with two parton level jets

Although lowering the jet multiplicity with a 2 and 3 jets requirement increases the levels of Standard Model backgrounds, it is conceivable that the backgrounds to the relatively simpler 2 jet and 3 jet final states may be understood more rapidly with experimental data, both due to higher event rates and more precise cross section predictions. Therefore in addition to the 4jet final states, these SUSY channels are also investigated.

Background composition

Several Standard Model physics processes with large cross sections at the LHC can also produce the E_T^{miss} + jets signature. For the studied analyses the following backgrounds need to be considered:

- **QCD**: QCD events are one of the main backgrounds in the 0-lepton channel. At the LHC there will be abundant QCD production of events with multiple high-p_T jets. Heavy flavour jets coming from b or c quarks, may decay semi-leptonically and can result in events with multiple jets and real E_T^{miss} coming from the neutrinos in these decays. Light flavour quarks do not provide events with real E_T^{miss}, but can produce fake E_T^{miss} from jet mis-measurement. In addition, fake E_T^{miss} can result from detector effects and pileup of beam halo events.
- **Top quark pairs**: Decaying top quarks lead to a b-quark and a W-boson that can decay to hadrons or a lepton and a neutrino. In consequence events with the E_T^{miss} + jets signature are produced in processes like $t\bar{t} \to b\bar{b}l\nu l\nu$ and $t\bar{t} \to b\bar{b}l\nu q\bar{q}$, where the lepton is not identified.
- **Gauge bosons**: Z and W bosons are produced individually or in diboson states (WW, ZZ and WZ), decay in final states with real E_T^{miss}: $W \to l\nu$, $Z \to \nu\bar{\nu}$ and $Z \to \tau^+\tau^-$ ($\tau \to l\bar{\nu}\nu$, $\tau \to \pi^{\pm}\pi^0\nu$), and in case of associated leptons, produce the E_T^{miss} + jets signature when the lepton is not identified.

Some general differences between SUSY signal and Standard Model events can be used to suppress the background: Events from Standard Model backgrounds typically have smaller E_T^{miss} and

fewer jets than SUSY events, while the decays of squarks and gluinos with masses ≥ 400 GeV tend to produce larger total transverse energy. Standard Model events with E_T^{miss} due to neutrinos from weak decays also typically contain charged leptons. Therefore only events with unidentified leptons contribute.
Details about the Standard Model background estimation can be found in Ref. [337], a short summary is given in Chapter 12.

Event selection

In order to improve the SUSY signal to SM background ratio for events in the 0-lepton final state, selection cuts are applied that are detailed in Table 7.1 and Table 7.3. The baseline selection for the 4 jet 0-lepton channel, as an example for the selection cuts used in the inclusive SUSY searches, is:

- ≥ 4 jets with the hardest jet $p_T > 100$ GeV and the next 3 hardest jets with $p_T > 50$ GeV
- $E_T^{miss} > 100$ GeV
- $E_T^{miss}/M_{\text{eff}} > 0.2$
- $|\Delta\phi(jet_{1,2,3}, E_T^{miss})| > 0.2$ for the three leading jets
- transverse sphericity $S_T > 0.2$
- no isolated leptons

The definitions of the used variables transverse sphericity S_T and effective mass M_{eff} are given in Section 7.2 (see eq. 7.6 and eq. 7.1). M_{eff} is defined as the scalar sum of the transverse momenta of the N_{jets} hardest jets and missing transverse energy:

$$M_{\text{eff}} \equiv \sum_{i=1}^{N_{jets}} | \mathbf{p}_T^{\text{jet},i} | + E_T^{miss} \tag{8.1}$$

where N_{jets} corresponds to the number of jets in the analysis, e.g. $N_{jets} = 4$ for the discussed 4 jet channel[1]. The effective mass distribution provides a very good sensitivity (SUSY signal to SM background ratio) for SUSY searches after applying all analysis cuts (see Section 7.2) and is later used to study the discovery reach potential.
The number of events passing the 2, 3, and 4 jet 0-lepton channel event selection cuts (for each applied cut) as well as the cut efficiencies for the SUSY benchmark points SU3 and SU4 and for the total Standard Model backgrounds are given in Table 8.1. More detailed cutflow tables for the different Standard Model background contributions for $\mathscr{L} = 1\text{fb}^{-1}$ can be found in the Appendix in Section E.1 (Table E.1 till Table E.3).
The benchmark points SU3 and SU4 are only used to model the possible SUSY signal. The points are described in the Appendix in Sectin A, however, specific details of these points are unimportant as the aim is to have an analysis that is suitable for a wide range of possible SUSY signal, not one that is optimised for a specific decay scenario.

[1] $N_{jets} = 3$ and $N_{jets} = 2$ for the 3 jet and 2 jet channel, respectively.

Table 8.1: Number of events surviving the 4 jet (top rows), 3 jet (middle rows) and 2 jet (bottom rows) 0-lepton analysis cuts. The events are normalised to 1fb^{-1}. The used selections are detailed in Table 7.1 and Table 7.3. Note that no S_T cut is applied in the 2 and 3 jet analysis.

sample	p_T *jet*+ E_T^{miss} cut	$E_T^{miss}/M_{\text{eff}}$ cut	S_T cut	$\Delta\phi$ cut	lepton veto cut	trigger cut
4 jet 0-lepton selection cuts						
SU3	9600	7563	5600	5277	4311	4301
SU4	79618	57803	46189	42408	34966	34336
total Standard Model	47805	19294	13483	8806	6655	6315
SU3 cut efficiency	35.1%	78.8%	74.0%	94.2%	81.7%	99.8%
SU4 cut efficiency	19.8%	72.6%	79.0%	91.8%	82.5%	98.1%
SM cut efficiency		40.4%	69.9%	65.3%	75.6%	94.9%
3 jet 0-lepton selection cuts						
SU3	8414.2	5391.4		4972.9	4126.8	4125.2
SU4	43782.1	18634.1		16613.1	14149.4	14125.2
total Standard Model	47731.3	4104.9		1993.7	1388.0	1374.2
SU3 cut efficiency	30.4%	64.1%		92.2%	83.0%	100.0%
SU4 cut efficiency	30.6%	42.6%		89.2%	85.2%	99.8%
SM cut efficiency		8.6%		48.6%	69.6%	99.0%
2 jet 0-lepton selection cuts						
SU3	18660.7	12519.8		12217.5	10055.2	10050.5
SU4	123088	64740.5		62258.6	52327.1	52195.8
total Standard Model	154440.5	20383.4		14010.1	10404.1	10353.4
SU3 cut efficiency	67.4%	67.1%		97.6%	82.3%	100.0%
SU4 cut efficiency	30.6%	52.6%		96.2%	84.0%	99.7%
SM cut efficiency		13.2%		68.7%	74.3%	99.5%

8.3. The ATLAS discovery potential for $\sqrt{s}$ = 14 TeV

8.3.1. Distributions for the 0-lepton channels

The resulting M_{eff} distributions after applying the different 4 jet 0-lepton event selection cuts are illustrated for the SUSY signal SU3 and the main SM backgrounds in Figure 8.1 ((a)-(e)). The SUSY point SU3 with a NLO cross section of about 28 pb was chosen as an example to show

the performance of the analysis for a SUSY signal. All used cuts have been selected based on the topologies and kinematics of the Standard Model backgrounds and the possible signals for a generic R-parity conserved SUSY event with TeV-scale sparticles. Figure 8.1 (f) presents the SM background after applying all analysis cuts together with the different ATLAS SUSY benchmark points. Before applying any cut, the main background are QCD events, where E_T^{miss} is produced

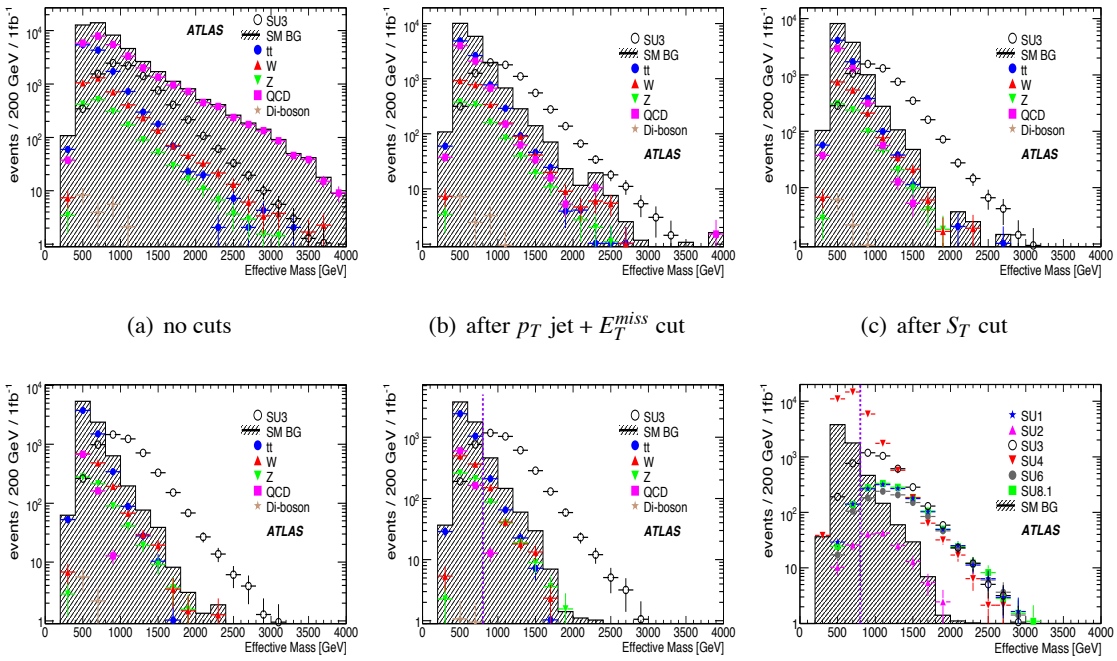

(a) no cuts (b) after p_T jet + E_T^{miss} cut (c) after S_T cut

(d) after $\Delta\phi$ cut (e) after lepton veto and trigger cut (f) all cuts, different SUSY signals

Figure 8.1: M_{eff} distributions for the cut selection of the 4 jet 0-lepton analysis. All plots show the SUSY signal (open circles), the total Standard Model background (shaded histogram), and a breakdown of the background types. The cuts are in the same order as described in the text. All numbers are normalised to 1 fb^{-1}. The error bars reflect the statistical uncertainties of the Monte Carlo samples.

either by mis-measurement of the energy of one or more jets or by a real neutrino from the decay of heavy flavour jets. After applying the p_T and E_T^{miss} cuts (see Figure 8.1 (b)), the QCD multijet production is strongly decreased. The p_T jets and E_T^{miss} cut define together with the lepton veto the signature of the final state that is being searched for, whilst the following cuts aim to reduce the SM backgrounds from events with a similar signature.

In SUSY events jets produced from the decay of heavy particles are distributed isotropically in space, whereas for the QCD events the direction of the two partons from the hard scattering provides a privileged direction. A cut on the sphericity is intended to exploit this fact (see Figure 8.1(c)).

A quantity used in nearly all SUSY searches is the ratio f of the missing transverse momentum to the effective mass. The cut was introduced with a similar idea as E_T^{miss} significance and uses the correlation between E_T^{miss} and the transverse momentum of the jets in order to suppress E_T^{miss} that arises from mis-reconstruction of the jet energies in the calorimeters or from other instrumental effects. The E_T^{miss} value in events with "real" E_T^{miss}, e.g. SUSY events, should be large compared to the average p_T value of the leading jets in the event, that are used in the M_{eff} calculation. For example for the 4 jet channel this means $E_T^{miss} > \sum_{i=1}^{4} p_T(jet_i)/4 = \frac{M_{\text{eff}} - E_T^{miss}}{4}$. This equation leads to a radio f = $E_T^{miss}/M_{\text{eff}}$ of about 0.3, 0.25 and 0.2 for the 2 jet, 3 jet and 4 jet channel, respectively. Figure 8.2 illustrates this correlation between E_T^{miss} and H_T (top plots) and E_T^{miss} and between M_{eff} (bottom plots) for the sum of the Standard Model backgrounds (left plots) and the SU3 signal (right plots) separately after applying the 4 jet p_T-jet selection cuts. H_T is the scalar sum of the p_T of the four leading jets in the 4 jet channel.

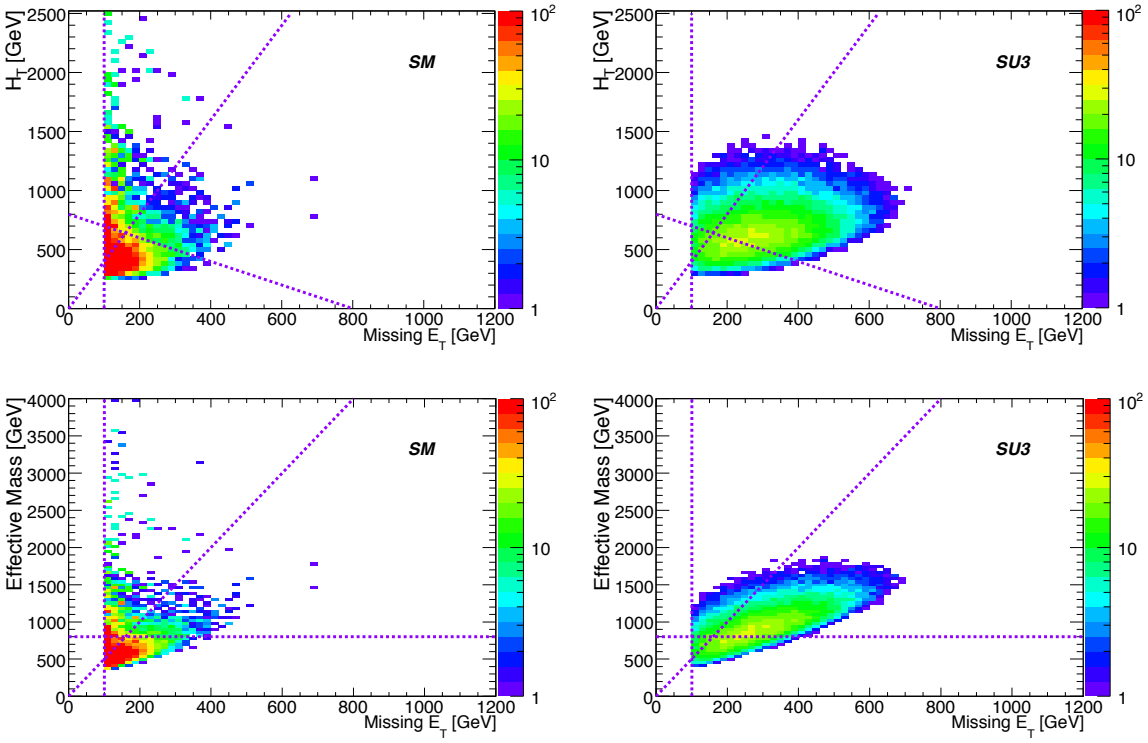

Figure 8.2: Correlation between E_T^{miss} and H_T (top plots) and E_T^{miss} and M_{eff} (bottom plots) for the sum of the Standard Model backgrounds (left plot) and the for the SUSY SU3 signal (right plot) after applying the p_T-jet selection cuts for the 4 jet 0-lepton channel. The dotted lines represent cut in E_T^{miss}, M_{eff} and $E_T^{miss}/M_{\text{eff}}$ cut.

The cut on $\Delta\phi$ between the three leading jets and E_T^{miss} removes events where the E_T^{miss} vector is close the direction of one jet that is likely to come from mis-measurements of the jets. The

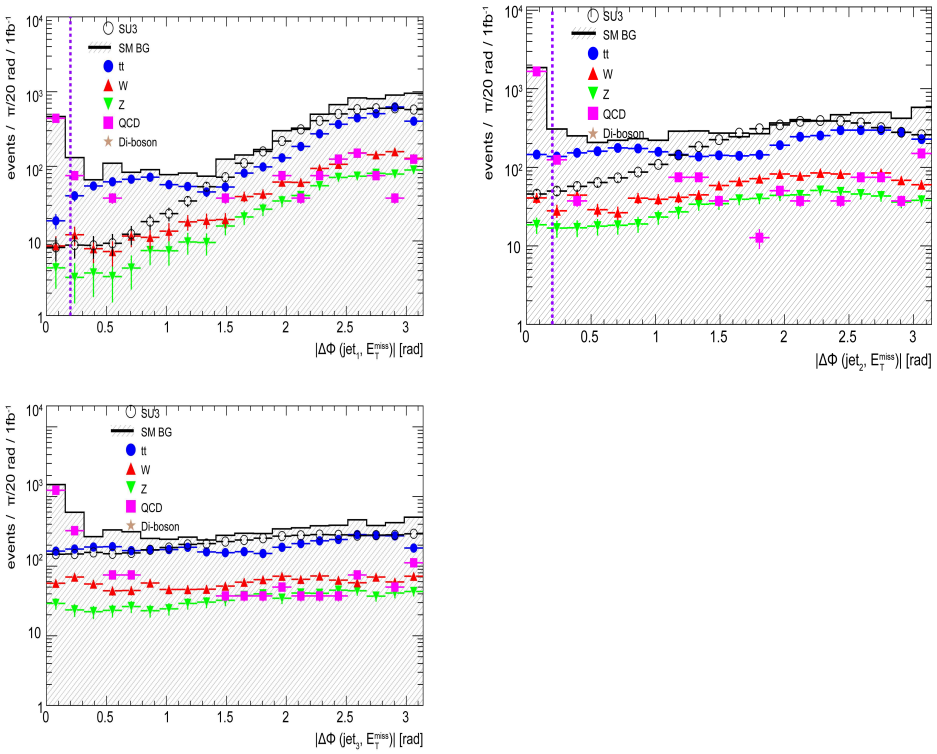

Figure 8.3: $\Delta\phi(jet_{1,2,3}, E_T^{miss})$ distributions for the three leading jets in the 4 jet 0-lepton channel after applying all event selection cuts except the $|\Delta\phi|$-cut. The error bars reflect the statistical uncertainties of the Monte Carlo samples.

$\Delta\phi(jet, E_T^{miss})$ distributions for the three leading jets after all events selection cuts except the $|\Delta\phi|$ cut are presented in Figure 8.3. The dotted line represents the cut $|\Delta\phi(jet_{1,2,3}, E_T^{miss})| > 0.2$. After the $|\Delta\phi|$ cuts the remaining backgrounds $t\bar{t}$, $W+$jets, $Z+$jets and QCD processes give all comparable contributions to the total Standard Model background (see Figure 8.1 (d)) in the high M_{eff} region. The last cut selects the events without any leptons. It can be seen from Figure 8.1(e) that this requirement mainly reduced the $t\bar{t}$ background.

The 2 and 3 jet search strategy is based on very similar analysis requirements as this "standard" 4 jet analysis, but harder cuts on the jet kinematics and E_T^{miss} have been chosen (see Table 7.1) to reduce the QCD background and the backgrounds from W/Z + jets processes. The sphericity cut was considered to be less relevant in case of lower jet multiplicities and was dropped. However, this cut was later tested in the cut optimisation studies (see Section 8.4). The other applied cuts are again used to improve the signal to background ration. The cut on $E_T^{miss}/M_{\text{eff}}$ makes sure that events with hard jets, but low E_T^{miss} do not enter the final selection and reduces the multi-jet SM background, which usually peaks at a lower $E_T^{miss}/M_{\text{eff}}$ fraction than the SUSY signal. The $|\Delta\phi(jet, E_T^{miss})|$ cuts between the 2 (3) leading jets and E_T^{miss} help to remove SM background

events with fake E_T^{miss} from mismeasured jets [338] and with real E_T^{miss} due to heavy quark decays. The M_{eff} variable for the 2 and 3 jet channel is calculated using only the two (three) hardest jets N_{jets} = 2 (3) for two (three) jet channel. In Figure 8.4 presents the final M_{eff} distributions after applying all 2 and 3 jet 0-lepton selection cuts for the SM backgrounds and the SUSY signal point SU3, while Figure 8.5 shows the M_{eff} distributions for different SUSY benchmark models (see Section A) and the combined SM background. The distributions after applying any selection cut can be found in the Appendix in Section E.1 (Figure E.1 and Figure E.2), further distributions e.g. of the cut variables are in Reference [273].
As Figure 8.1(f) and Figure 8.5 illustrate, for all studied SUSY benchmark points except SU2 (pink triangle) is an excess of the SUSY signal above the SM background clearly visible. As expected, the SUSY signal become significant at energies of about 1 TeV. For the SUSY signal SU2 direct gaugino production is dominant. This leads to signatures with leptons in the final state (see Section 6.2).

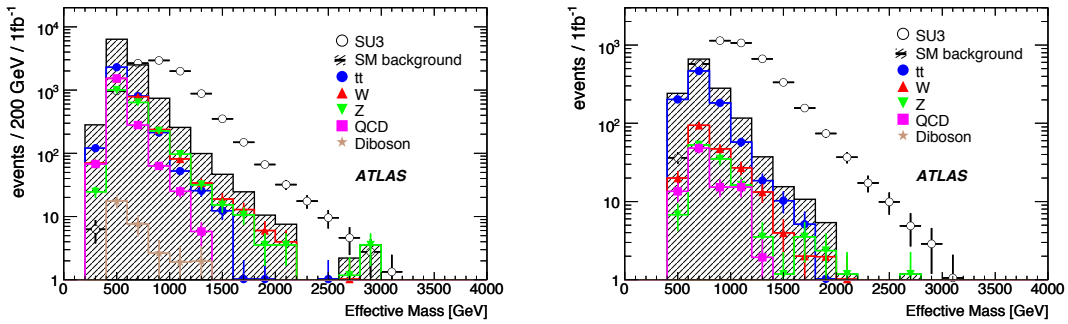

Figure 8.4: Effective mass distribution for the 2 jet (left plot) and 3 jet (right plot) 0-lepton analysis at 14 TeV. The Standard Model background (shaded histogram) are shown together with the SUSY signal point SU3 (open circles) after applying all selection cuts. All numbers are normalised to 1 fb^{-1}. The error bars reflect the statistical uncertainties of the Monte Carlo samples.

Overlap of the 0-lepton analyses Since the 2 jet, 3 jet and 4 jet analyses are all inclusive and similar selection cuts are applied, overlap of the selected events is possible. This overlap depends on the production process and the selected cuts. For example about 40% of all SU3 events selected in the 2 jet analysis are passing also the cuts of the 3 jet analysis and about 35% of them pass the cuts of the 4 jet analysis. To reduce the overlap, the 0-lepton analyses could be made more exclusive by vetoing against each other or by applying more selective cuts.

After defining the final analysis cuts for the various SUSY search channels, different SUSY signals are studied. Several grids of SUSY points were selected to verify that the analyses perform well for a wide range of possible SUSY signatures. The different grid parameters are described in detail in Section 4.5.2. The aim of this study is to estimate the possible reach of the SUSY analyses in the SUSY parameter space assuming an integrated luminosity of $\mathscr{L} = 1\text{fb}^{-1}$ at $\sqrt{s}$ = 14 TeV.

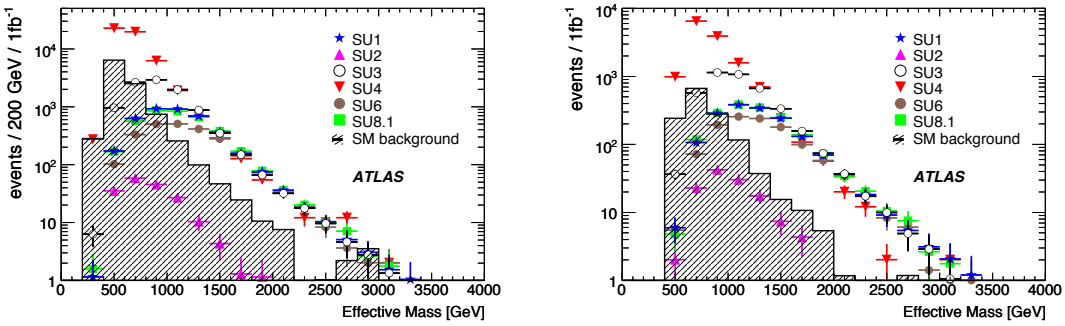

Figure 8.5: The M_{eff} distribution for the 2 jet (left plot) and 3 jet (right plot) 0-lepton analysis after applying the final analysis cuts. The shaded histograms indicate the total Standard Model background, while the points show the distribution of different mSUGRA points. The error bars reflect the statistical uncertainties of the Monte Carlo samples.

8.3.2. Determination of the discovery potential and systematic uncertainties

The significance for every SUSY signal is determined using the expected total number of background and signal events from the final M_{eff} distributions as discussed on Section 7.5.1. In addition to the "baseline" selection cuts different cuts in M_{eff} are tested (see Section 7.5.4) in order to increase the sensitivity for high-mass final states that are expected to show a peak in the M_{eff} distribution at higher values. The significance is corrected for these multiple cuts using the discussed statistical methods in Section 7.5.2. For every point the M_{eff} cut, that gives the maximal significance, was selected as the final cut.
The understanding of the SM backgrounds is essential to claim a discovery. In order to accurately determine the discovery potential of a search, the systematic uncertainties for the SM background estimation must be considered. The expected systematic uncertainties for 1 fb^{-1} on the $t\bar{t}$ and boson + jet backgrounds are 20%, for the QCD background the expected uncertainty is 50% as dicussed in Section 7.5.3. The uncertainties are taken to be uncorrelated and independent of any variable and were combined in quadrature. In addition the limited MC statistics were also taken into account. All these numbers are incorporated in the significance calculation.

It is noteworthy that the SUSY benchmark points and the Standard Model backgrounds are normalised to NLO cross section (see Appendix Table A.1). Such NLO calculations were not performed for the SUSY grids, because of the large number of grid points, each involving many subprocesses. The cross sections of signal points are therefore normalised to the leading-order values, as obtained from the HERWIG generator. Since NLO cross sections are used for the background samples and next-to-leading-order corrections increase the SUSY signal cross sections (see studies in Section B), the estimated discovery reach lines are quite conservative.

8.3.3. Discovery potential for different SUSY signal grids

In the following figures the highest significance for every studied SUSY signal is stated as the expected discovery potential for this point. Figure 8.6 shows the 5σ discovery reach potential for an

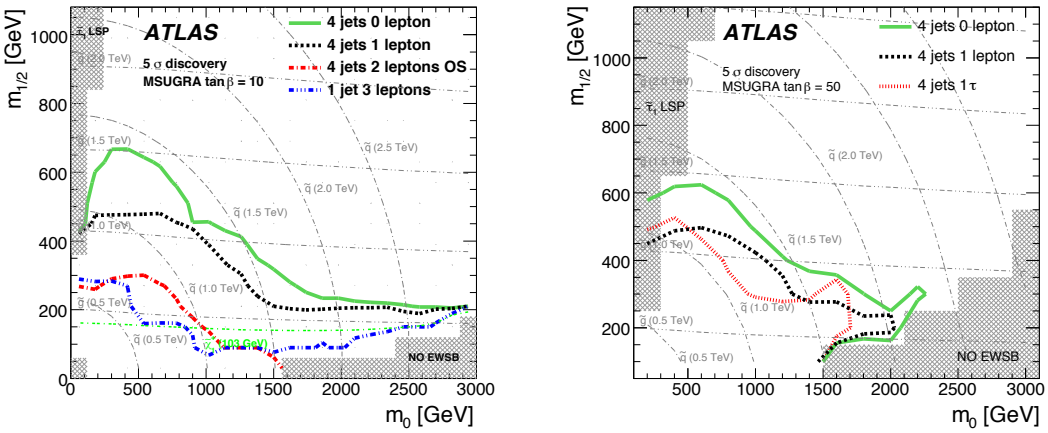

Figure 8.6: The 5σ discovery reach for the 4 jet analyses in the mSUGRA m_0-$m_{1/2}$ parameter space for $\tan\beta = 10$ (left plot) and for $\tan\beta = 50$ (right plot). The horizontal and curved grey lines indicate the gluino and squark masses, respectively.

integrated luminosity of 1 fb^{-1} in the $\tan\beta = 10$ (left plot) and $\tan\beta = 50$ (right plot) mSUGRA parameter space. The results of the 4 jet 0, 1 and 2 opposite sign lepton analyses as well as the 1 jet 3-lepton analysis are compared. The mass contours for gluinos and squarks are illustrated as grey dashed lines. It can be seen that 0-lepton mode has the best estimated reach close to $M(\tilde{g}) = M(\tilde{q}) = 1.5$ TeV. With the 1-lepton channel a smaller fraction of SUSY signals would be discovered. Only for large m_0 values (> 1.5 TeV) is the discovery reach similarly good as the 0-lepton channel. However, the 1-lepton channel is more robust against fake E_T^{miss} backgrounds resulting from detector problems, which could be an advantage especially for first data studies. In the $\tan\beta = 50$ grid, where τ production is enhanced, the discovery reach of the 0-lepton channel is still slightly better than for the 1-lepton channel and for both channels larger than the reach of the 4 jet + τ selection[2]. This result reflects the lower purity and efficiency for the τ reconstruction. One reason for the better performance in the 1-lepton channel compared to the tau-channel could be that for larger values of $\tan\beta$ tau lepton and the bottom quark Yukawa couplings become large, leading to reduced masses of τ-sleptons and b-squarks relative to their first and second generation counterparts, and to enhanced decays to τ-leptons and b-quarks (see Section 2.2.6). In the 1 and 2-lepton channels only final states with muons or electrons, but no taus are considered. Some of the taus (about 35%) decay leptonically to an electron or muon that can provide a signal for the

[2]The standard τ SUSY analysis looks for events with at least one τ in the final state. Beside this, the same cuts as for the 1-lepton channel are applied, where the lepton is just replaced by the τ.

1-lepton channel. The 0-lepton channel does not exclude taus and thus an enhancement of taus may increase also the number of signal events in this channel.
The comparison of the 2 jet, 3 jet and 4 jet 0-lepton analyses, presented in Figure 8.7 shows that the choice of ≥ 4 jets seems best for the studied mSUGRA $\tan\beta = 10$ grid. This is due to the relative high p_T jet cuts in the 2- and 3-jet 0-lepton channels.

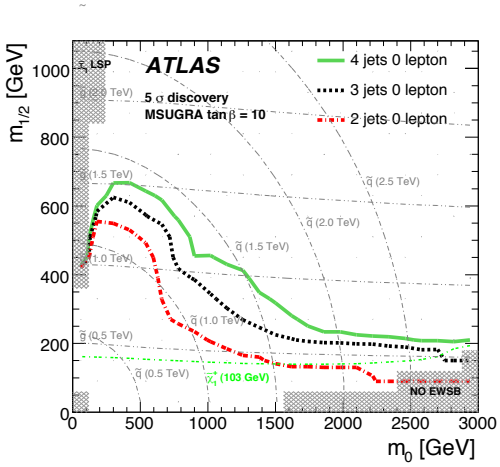

Figure 8.7: The 5σ reach contours for the 0-lepton analyses with various jet requirements as a function of m_0 and $m_{1/2}$ for the $\tan\beta = 10$ mSUGRA grid.

Beside the mSUGRA parameter space also AMSB, GMSB and NUHM signal grids are scanned. In the following only the discovery reach line of the analyses showing the best results are presented. The AMSB and NUHM models have qualitatively similar phenomenology, but different patterns of masses and decay modes (see Section 2.2.8). The 5σ discovery reach lines for the 4 jet 0 and 1 lepton channel, that show the best discovery potential in these grids, are presented in Figure 8.8. The reach of the 0 and 1 lepton analyses is essentially the same for the mSUGRA and NUHM models in the m_0-$m_{1/2}$ parameter space. This is expected since the NUHM models are characterised by slightly different mass spectra and decay modes due to the additional Higgsino mixing, that allows $\tilde{\chi}_1^0$ annihilation, but have qualitatively similar topologies as the mSUGRA signals. Exploring another SUSY-breaking mechanisms, the AMSB models are characterised by a lighter $\tilde{\chi}_1^\pm$, which is almost degenerate with the lightest $\tilde{\chi}_1^0$. This leads to "nearly invisible" decays of $\tilde{\chi}_1^\pm$ and very light leptons[3] compared to the squark masses, unless the universal scalar mass is very large. The mass specific spectra explains why the AMSB discovery reach for 4 jet 0-lepton channel is not very different from that for the mSUGRA grids, but the 1-lepton discovery potential is much smaller. The produced leptons do not pass the kinematic cuts of the lepton searches.
Models in the GMSB parameter space considered (see Figure 8.9, left plot) have a slepton as NLSP

[3]The leptons are almost invisible due to their very small p_T values.

that can decay into long-lived charged particles or τs. The studied models have therefore at least two leptons or τ's in the final state and should be easy to be distinguished from SM backgrounds. For the studied grid the 3-lepton search has a significantly better reach than the 2-lepton SUSY channels and extends well up to 2 TeV for gluinos at large $\tan\beta$.
In addition to these models a randomly selected mSUGRA signal grid that fullfills experimental constraints as discussed in Section 6.3, has been studied. As a result of these limits only SUSY signals with gluino and minimal squark masses within a limited range of the parameter space are selected. Figure 8.9 (right plot) compares the discovery potential of these models to those of the mSUGRA and AMSB scans in the gluino-min. squark ($m_{\tilde{g}}$ vs. min. $m_{\tilde{q}}$) plane. The solid points are observable with a significance ≥ 5 for 1 fb^{-1}, while open symbols indicate a smaller significance. The reach for the selected mSUGRA points is compatible to that for the generic mSUGRA grid points. This is not surprising since the SUSY production cross sections are mainly controlled by the gluino and squark masses.

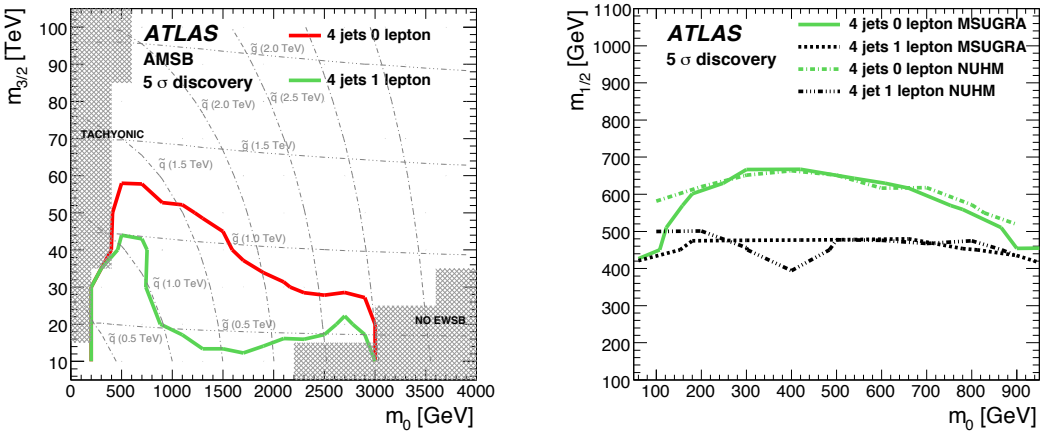

Figure 8.8: Discovery potential for the 4 jet 0 and 1-lepton channel in the AMSB (left plot) and NUHM (right plot) parameter space. The horizontal and curved grey lines indicate the gluino and squark masses respectively in steps of 500 GeV.

Summary The results of the scans of different regions in the SUSY parameter space indicate that ATLAS could discover R-parity conserving SUSY models with squark and gluino masses less than $\mathcal{O}(1\,\text{TeV})$ after having accumulated and understood the measured data with an integrated luminosity of about 1 fb^{-1}.

8.4. Cut optimisation

The goal of the performed cut optimisation was to study improvements of the discovey potential for the original 0-lepton analyses, presented in the previous sections. Since the different SUSY

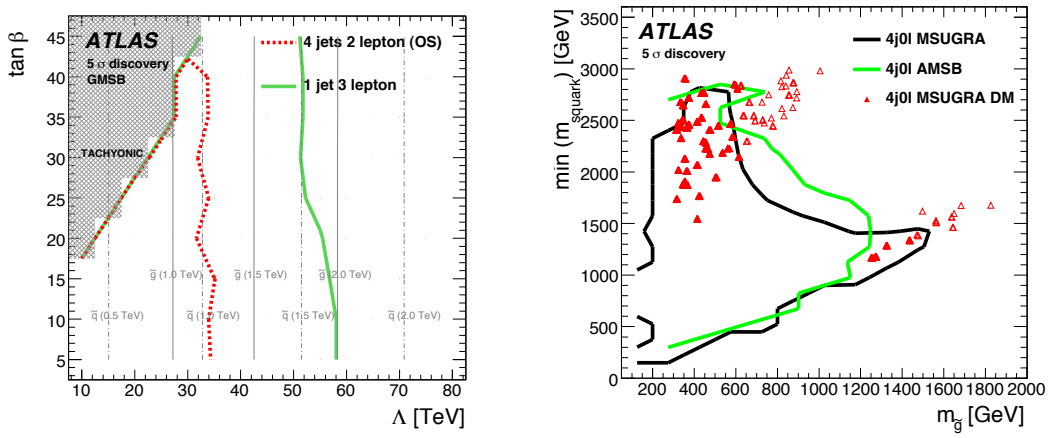

Figure 8.9: Left plot: 5σ discovery reach lines for the 4 jet 2-lepton OS and 1 jet 3-lepton analyses in the GMSB parameter space. The vertical solid and dashed grey lines indicate the gluino and squark masses respectively in steps of 500 GeV. Right plot: The 5σ discovery potential of the 4 jet 0-lepton analysis for "randomly" selected mSUGRA models and the discovery reach of the 4 jet 0-lepton analysis in the mSUGRA and AMSB parameter space presented in the gluino ($m_{\tilde{g}}$) vs. min. squark mass (min. $m_{\tilde{q}}$) plane (right plot). The solid points are observable with a significance ≥ 5 for 1 fb^{-1}, while open points show a smaller significance.

selection cuts are correlated, multidimensional cut combinations in fixed step sizes are applied to find optimal cut values. The following cut variables, shown in Table 8.2, are varied: Transverse sphericity S_T, missing transverse energy E_T^{miss}, $M_{\text{eff}}/E_T^{miss}$ and $|\Delta\phi(jet_i, jet_j)|$. The varied step size of the cuts is given in brackets. Note that the "standard" cuts on number of jets, the $p_T(jet_i)$ and the lepton veto cut have always been applied for each tested cut combination, since they define the SUSY signal and ensure that all event filters at generator level are rebuild. Also the $\Delta\phi(jet, E_T^{miss})$ is kept as "basis selection cut" since it is very efficient in removing Standard Model background events, but most of the SUSY signal events pass this cut as Table 8.1 shows.

In addition to the usual SUSY analysis cuts, a new cut variable $|\Delta\phi(jet_i, jet_j)|$ is studied. It is defined as the maximum distance in ϕ between two jets $|\ \phi(jet_i) - \phi(jet_j)\ |$, as illustrated in Figure 8.10. This cut was only tested for the 2 jet analysis. It was found that a $|\Delta\phi(jet_i, jet_j)|$ cut can be effective at removing QCD background in which the jets are back-to-back and E_T^{miss} from jet mis-measurements or heavy quark decays points to the direction of one of the jets (see Figure 8.10, right plot).

For every cut combination the full M_{eff}-scan algorithm was used, and the cuts that give the maximum significance after correcting for multiple testing, are considered. To find the best cut combination for a wide range of SUSY signals, the algorithm was run on the $\tan\beta = 10$ mSUGRA grid. The best cut combination for different SUSY signals is defined as the one, which finds the highest number of tested SUSY points with $\geq 5\ \sigma$ significance.

variable	range of cut parameters		
	4 jet 0-lepton channel	**3 jet 0-lepton channel**	**2 jet 0-lepton channel**
E_T^{miss}[GeV]	100 - 200 (50)	100 - 200 (50)	100 - 200 (50)
$E_T^{miss}/M_{\text{eff}}$	0.15 - 0.3 (0.05)	0.2 - 0.35 (0.05)	0.25 - 0.4 (0.05)
S_T	0.0 - 0.4 (0.1)	0.0 - 0.4 (0.1)	0.0 - 0.4 (0.1)
max. $\lvert\Delta\phi(jet_i, jet_j)\rvert$	-	-	2.6 - 3.1 (0.1)

Table 8.2: Range of the varied cut parameters for the 4 jet, 3 jet and 2 jet 0-lepton analyses in the cut optimisation procedure. The step size of the variation is given in brackets.

variable	optimal cuts for			
	4 jet analysis	**3 jet analysis**	**2 jet analysis**	
E_T^{miss}	100 - 150 GeV	100 - 150 GeV	100 - 150 GeV	100 GeV
$E_T^{miss}/M_{\text{eff}}$	0.15 - 0.2	0.2 - 0.25	0.25 - 0.3	0.25 - 0.35
S_T	0.2 - 0.3	0.2 - 0.4	0.1 - 0.2	0.0
max $\lvert(\Delta\phi(jet_i, jet_j)\rvert$	-	-	-	2.6 - 2.8

Table 8.3: Optimal values for the varied cut parameters for the 4 jet, 3 jet and 2 jet 0-lepton analyses, studied for $\sqrt{s} = 14$ TeV and $\mathscr{L} = 1$ fb^{-1}.

Table 8.4 lists the best cut combination for the 2, 3 and 4 jet 0-lepton analyses. It should be noted that different cuts can lead to a very similar signal-to-background ratio and thus to the same significance for a SUSY point. As a consequence the total number of discovered SUSY points (points with a 5σ probability) can be the same for different cut combinations.
Therefore the following cut combinations for the 2 jet 0-lepton and 3 jet 0-lepton analysis are selected in order to illustrate the improvement of the discovery reach (see Figure 8.11):

- 2 jet analysis : $S_T = 0.1, E_T^{miss} = 150$ GeV , $E_T^{miss} = 0.25 \cdot M_{\text{eff}}$
- 3 jet analysis : $S_T = 0.2, E_T^{miss} = 100$ GeV , $E_T^{miss} = 0.20 \cdot M_{\text{eff}}$

The solid lines in Figure 8.11 show the 5σ contour lines using the optimised cuts, the dashed lines are the 5σ discovery reach lines for the standard analyses. An additional S_T cut and a weaker $E_T^{miss}/M_{\text{eff}}$ cut for the 2 jet and 3 jet analysis can improve the significance, especially for squark masses around 1 TeV and gluino masses around 0.7-1.0 TeV. With the optimised cuts, the 2 and 3 jet analyses seem to perform as good as the 4 jet 0-lepton analysis for SUSY signas with small m_0 and large $m_{1/2}$ parameters. For the 4 jet channel the result of the optimisation algorithm are the

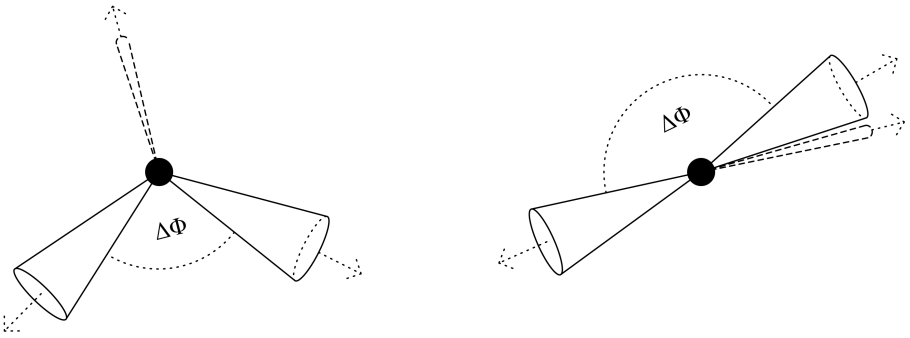

(a) 2 jet 0-lepton SUSY event

(b) 2 jet 0-lepton QCD event

Figure 8.10: Schematic drawing of a SUSY (figure a) and QCD (figure b) event in the 2 jet 0-lepton channel. The dottet cone shows the direction of the E_T^{miss} vector, the other cones illustrate the directions of the jets.

standard cut parameters: $S_T = 0.2$, $E_T^{miss} > 0.2 \cdot M_{\text{eff}}$, $E_T^{miss} > 100$ GeV. The selected cut variables seem to be already chosen quite well for the studied signatures, when the M_{eff}-scan is applied. For the studies at 10 TeV, discussed in the following chapter, the results of the cut optimisation are considered and an additional S_T cut is also applied for the 2 and 3 jet channels.

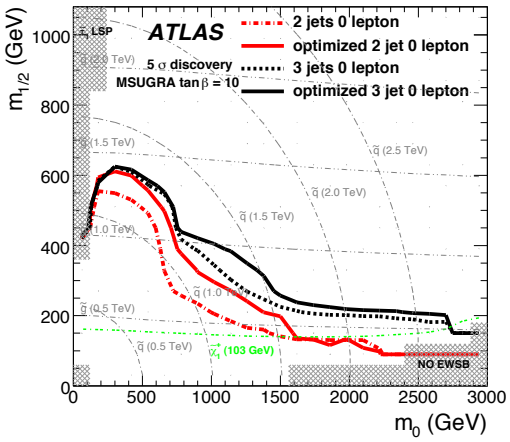

Figure 8.11: Discovery reach lines for the optimised cuts for the 2 jet and 3 jet 0-lepton channel. The solid lines are the 5σ contour lines obtained with the optimised cuts, the dashed lines are the 5σ contour lines for the standard analyses.

9. Searches for Supersymmetry at a centre-of-mass energy of 10 TeV

This chapter describes the prospects for new phenomena searches in channels with jets, leptons and missing transverse momentum assuming a LHC centre-of-mass energy of $\sqrt{s} = 10$ TeV and an integrated luminosity $\mathscr{L} = 200$ pb^{-1}. The goal of this study was to verify that the cuts proposed for a 14 TeV and $\mathscr{L} = 1$ fb^{-1} (see Chapter 8 and Ref. [104]), with a slight modification due to the reduced centre-of-mass energy and luminosity, have a large discovery potential to a broad range of SUSY models with R-parity conservation. The 14 TeV studies, presented in the previous chapter, were mostly focused on a smaller number of theoretically motivated benchmark SUSY models in order to define the SUSY analysis cuts. The analyses are run on smaller sets of generated SUSY grids in a strongly constrained SUSY parameter space to verify, that the analyses defined provide a sensitivity to a wide range of SUSY signals.
In order to increase the SUSY parameter range with respect to the previous studies, the signals investigated in this chapter are various Supersymmetry (SUSY) scenarios in the mSUGRA and in the phenomenological Minimal Supersymmetric Standard Model (pMSSM) parameter space (see Section 2.2.7).

The chapter is organised as follows: First, the studied SUSY models and Monte Carlo background samples as well as the event-, trigger- and object selection and systematic uncertainties are briefly summarised. The focus of the following sections is to present the final distributions after applying all analysis cuts and to discuss the discovery potential for the various models. New search channels, which could significantly improve the discovery reach of the ATLAS experiment are suggested.

9.1. Experimental setup

9.1.1. Monte Carlo simulations

The Standard Model background processes most relevant for the performed SUSY analyses are $t\bar{t}$, $W+$jets, $Z+$jets, single top, diboson and QCD jet production. They are generated with ALPGEN (production of $W^{\pm}$ and Z^0 bosons in association with jets, QCD processes), MC@NLO ($t\bar{t}$ process, WZ, ZZ diboson samples), gg2WW (WW diboson samples) and ACERMC (single top) and simulated partly with the full GEANT4 detector simulation (top pair production, single top and diboson samples) and partly with the faster simulation ATLFAST2 ($W+$jets, $Z+$jets, QCD jet production). The samples have been taken from the official production and are described in Section 4.5.1. A summary of all used sample together with the corresponding cross sections of the processes can be found in the Appendix Section D in Table D.2.
Different sets of SUSY signal grids are studied in order to cover a large SUSY parameter space. A summary of all generated grids is given in the Section 4.5.2. For the mSUGRA $\tan\beta = 10$ and $\tan\beta = 50$ grids the SUSY points are produced with different slopes in the $(m_0, m_{1/2})$ plane along "radial lines". The signal points were generated with ISAJET+HERWIG and simulated with ATLFAST2. The three different pMSSM parameter space grids, referred as the MSSM grid fulfilling constraints from experiments, the unconstrained pMSSM grid and the 8 parameter pMSSM grid are detailed in Section 4.5.2. The mass spectrum and the branching ratios of the SUSY signals are calculated with ISAJET, SUSPECT or SoftSusy. The points are generated after with HERWIG or PYTHIA and are run through the ATLFAST1 detector simulation. The electron identification was corrected in all ATLFAST1 SUSY signal samples in order to reproduce results obtained with the more detailed ATLFAST2 simulation (Section 4.3.2). All SUSY signal samples and Standard Model background samples are normalised to the LO cross section, except for the $t\bar{t}$ samples, where NLO cross sections are used.

9.1.2. Object and event selection

The object selection and overlap removal are discussed in Section 7.1. The same criteria have been used as for the 14 TeV studies in the previous chapter (see Chapter 8). Also the analysis cuts are similar to the selection used for the studies at a centre-of-mass energy of $\sqrt{s} = 14$ TeV, but looser cuts on the transverse momentum and missing transverse energy are applied, for example for the 4 jet channel p_T(jet 1) > 100 GeV, p_T(jet 2-4)> 40 GeV and $E_T^{miss} > 80$ GeV. For all grids, channels with $\geq 2, \geq 3, \geq 4$ jet and 0 to 2 leptons are investigated. The analysis cuts on the number of jets, the transverse momentum of the jets and the E_T^{miss}, which are common to all channels independent of the lepton-multiplicity, are detailed in Table 7.1 (2nd row) for the different jet multiplicities. The additional applied cuts dependent on the lepton multiplicity are summarised in Table 7.3. In contrast to the 14 TeV studies, the cut on the transverse sphericity $S_T > 0.2$ is now applied for all channels independent of the jet and lepton multiplicity. It was shown in Section 8.4 that this cut can improve the discovery reach for the 2 and 3 jet 0-lepton channels.
Moreover the $\Delta\phi(jet_i, E_T^{miss})$ cut, applied before only for the 0-lepton channels, is now also used

in the 1 and 2-lepton SUSY analyses. In addition to the "standard" (2-4) channels, SUSY analyses asking for ≥ 5 and ≥ 6 jets are studied. The used event selection cuts are detailed in Table 7.2. No trigger information was available for the ATLFAST1 simulated SUSY signals. The efficiency for the combined jet and E_T^{miss} trigger, studied at a centre-of-mass energy of $\sqrt{s} = 14$ TeV, was $> 95\%$ for the instantaneous luminosity of $1 \times 10^{31} \mathrm{cm}^{-2}\mathrm{s}^{-1}$ (see Section 7.4). Since similar strong analysis cuts are applied for the studies at a centre-of-mass energy of 10 TeV, a trigger efficiency of 100% was assumed for simplicity.

9.2. The ATLAS discovery potential for $\sqrt{s}$ = 10 TeV in the mSUGRA and pMSSM parameter space

9.2.1. Distributions

The kinematic distributions are shown for illustrative purpose for the SU4 mSUGRA point (see Section 4.5.2), a low mass point close to the Tevatron bound and for some selected pMSSM signal grid points assuming an integrated luminosity $\mathscr{L} = 200\ \mathrm{pb}^{-1}$. The number of passed background events for the different event selection cuts in the 4 jet 0-lepton channel are given in the Appendix in Table E.4. Figure 9.1 illustrates the contribution of the different Standard Model backgrounds for all studied SUSY channel.

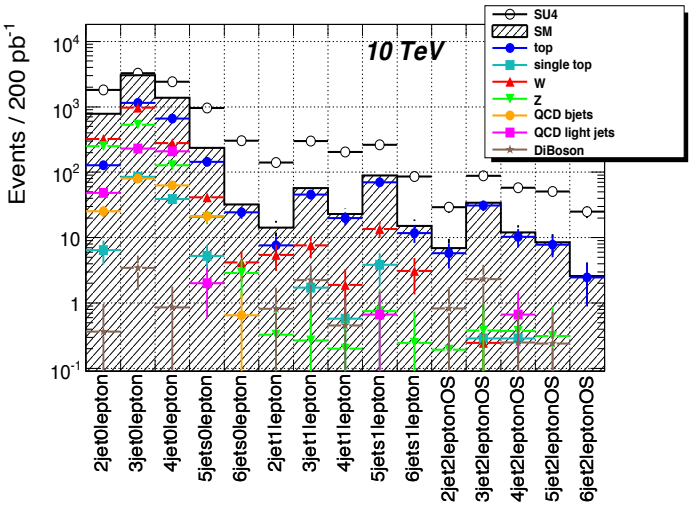

Figure 9.1: Number of expected Standard Model background and SU4 SUSY signal events for 200 pb^{-1} for the different SUSY search channels. The error bars reflect the statistical uncertainties of the Monte Carlo samples.

0-lepton channels

The M_{eff} and E_T^{miss} distributions for the 4 jet 0-lepton channel are presented in Figure 9.2. The distributions for the 2 jet and 3 jet 0-lepton channel can be found in the Appendix in Section E.3. The top row of Figure 9.2 shows the effective mass (top left plot) and the missing transverse momentum distribution (top right plot) of the SU4 mSUGRA point together with the Standard Model background. The bottom plots show the effective mass distributions for the SU4 mSUGRA point and two signal points of the unconstrained pMSSM grid (bottom left plot) and for two points of the 8 parameter pMSSM grid (bottom right plot). The minimal squark mass (with and without stop/sbottom mass), the gluino mass and the cross sections of the four illustrated pMSSM SUSY signals and the SU4 mSUGRA point are listed in Table 9.1. The four pMSSM grid points represent different regions in the SUSY parameter space of the later discussed pMSSM grids: The pMSSM point 167 has squark and gluino masses both around 550 GeV, while the pMSSM point 1101 has a factor three smaller gluino mass than a squark mass with about 280 GeV. Both points have very large cross sections and are expected to be discovered with an integrated luminosity of 200 pb^{-1}. The pMSSM grid points 2106 and 526 have gluino masses just above the Tevatron limit (about $\approx$ 490 GeV and $\approx$ 410 GeV), but very high squark masses of $\approx$ 3.5 TeV and $\approx$ 1.2 TeV, respectively. The cross sections are about factor 10-20 smaller compared to the cross section of the unconstrained pMSSM grid points.
Some SUSY models decay into a very high number of jets and could be better distinguished from the Standard Model background in searches asking for more than 5- or 6-jets. The effective mass distributions for the 5- and 6 jet 0-lepton channel for the SUSY signal SU4, the two unconstrained pMSSM grid points (light blue and dark blue lines) and the two 8 parameter pMSSM grid points (red and green line), listed in Table 9.1, are presented in Figure 9.3. As one can see all five points except the MSSM point 2106 (green line) would be discovered with the 5 jet and 6 jet 0-lepton SUSY analysis.

signal point	**SUSY model**	**min. squark mass** w/ $\tilde{t}/\tilde{b}$ [GeV]	**min. squark mass** w/o $\tilde{t}/\tilde{b}$ [GeV]	**gluino mass** [GeV]	**cross section** [pb]
SU4	mSUGRA	195.6	410.6	409.9	107.6
MSSM 167	unconstrained pMSSM	114.6	552.0	545.0	262.1
MSSM 1101	unconstrained pMSSM	324.8	617.0	277.0	199.1
MSSM 2106	8 parameter pMSSM	3489.5	3445.5	483.9	13.6
MSSM 526	8 parameter pMSSM	1222.6	1156.9	410.6	28.2

Table 9.1: The minimal squark mass (with and without minimal stop/sbottom mass $\tilde{t}/\tilde{b}$), the gluino mass and the cross section of the mSUGRA point SU4, the selected unconstrained pMSSM grid points and of the selected 8 parameter pMSSM points with constraints shown in the effective mass distribution in Figure 9.2 and 9.3.

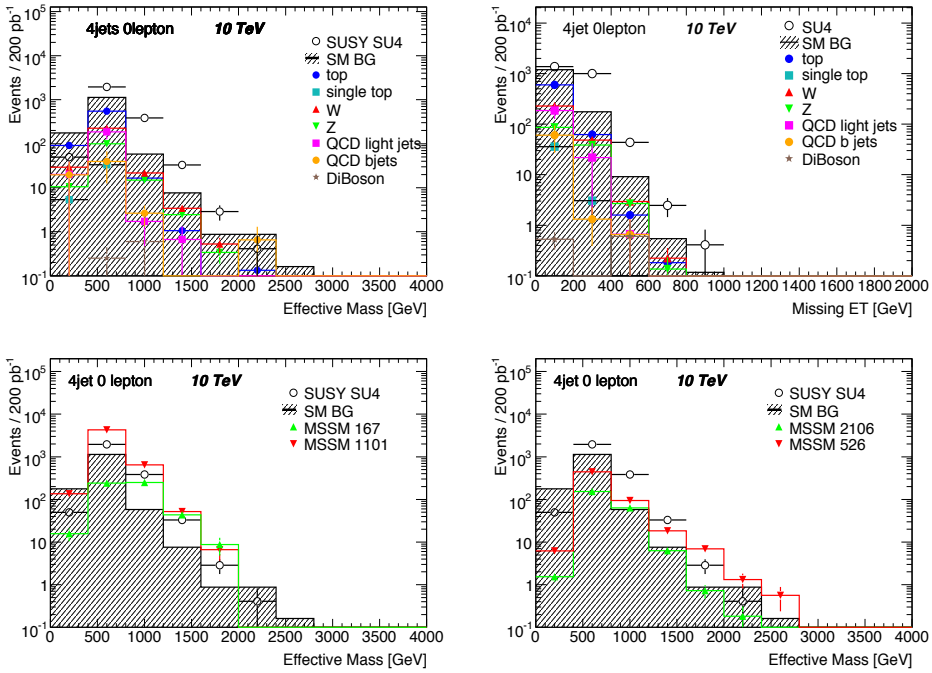

Figure 9.2: Distribution for the 4 jet 0-lepton channel. Upper plots: Effective mass distribution after applying all analysis cuts (upper left plot) and missing transverse momentum distribution after applying all analysis cuts beside the E_T^{miss} cut (upper right plot) for the mSUGRA point SU4 together with the Standard Model backgrounds. Bottom plots: Effective mass distribution for the SUSY signal SU4 and two unconstrained pMSSM signal points (bottom left plot) and SU4 together with two 8 parameter pMSSM signal points (bottom right plot). The shaded histograms indicate the total Standard Model background. The error bars reflect the statistical uncertainties of the Monte Carlo samples.

The dominating Standard Model backgrounds in the 0-lepton channels are $Z+$jets and $W+$jets for the lower jet multiplicities, whereas for events with 3 to 6 selected jets the main backgrounds are top pair and W production. Note that the W and Z-Alpgen samples have been produced only up to 5 partons. The 6 th and higher order jets come from the parton shower (see Section 4.2.1).

1-lepton channels

An example for the effective mass M_{eff} (top left plot), missing transverse energy (top right plot) and transverse mass M_T (bottom left plot; see definition for M_T in Section 7, eq. 7.2) distribution for the 4 jet 1-lepton channel can be found in Figure 9.4. The distributions for the 2 jet and 3 jet 1-lepton channel are in the Appendix in the Section E.3 (Figure E.4). For the missing transverse momentum and the M_T distributions all cuts are applied besides the cut on E_T^{miss} and M_T,

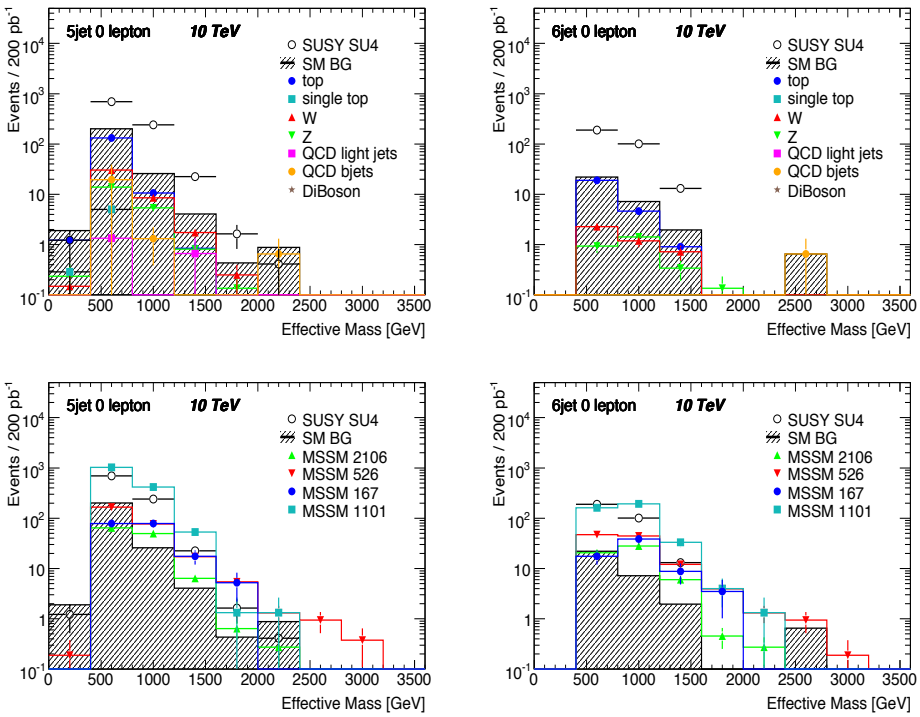

Figure 9.3: Effective mass distributions for the 5 (left plots) and 6 jet (right plots) 0-lepton channel after applying the final SUSY analysis cuts. The upper two plots show the SUSY signal SU4 together with the SM background, the lower plots show the SUSY signal SU4 together with two unconstrained pMSSM grid points and two 8 parameter pMSSM signal points. The shaded histograms indicate the total Standard Model background. The error bars reflect the statistical uncertainties of the Monte Carlo samples.

respectively. A cut on $M_T > 100$ GeV removes most of the $t\bar{t}$, W + jets background. Figure 9.5 shows the 5 jet and 6 jet 1-lepton channel effective mass distributions, in the upper plots for the mSUGRA point SU4 together with the Standard Model backgrounds and in the lower plots for the mSUGRA point SU4, two unconstrained pMSSM grid points (blue lines) and the two 8 parameter pMSSM signal points (red and green lines).
The 1-lepton channel is dominated by top pair production, while W + jets contributes significantly in the low jet multiplicity channels. The background from single top production is larger than the background from Z boson production. Diboson processes and the background from QCD events are very small for all jet multiplicities.

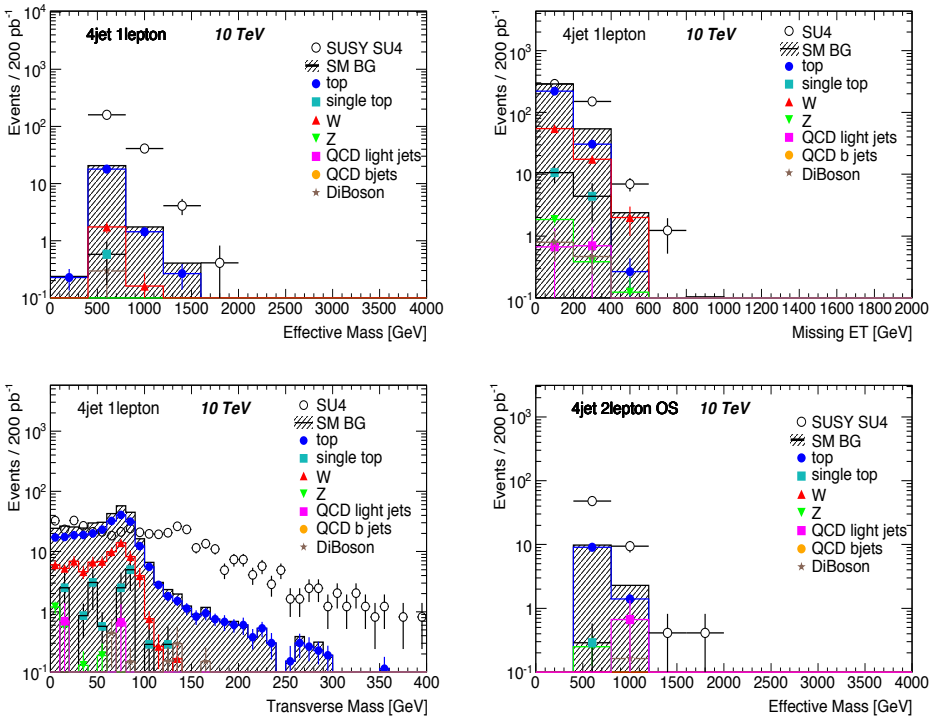

Figure 9.4: Effective mass distributions (upper left plot), missing transverse energy distribution (upper right plot) and M_T distribution (bottom left plot) for the 4 jet channel with 1 lepton. The bottom right plot shows the effective mass distribution for the 4 jet 2-lepton OS channel. The distributions are normalised to 200 pb^{-1} of integrated luminosity. For the transverse mass and E_T^{miss} distribution all cuts are applied beside the M_T and E_T^{miss} cut, respectively. All plots show the SUSY signal SU4 together with the SM background. The error bars reflect the statistical uncertainties of the Monte Carlo samples.

2-lepton opposite sign channels

The effective mass distributions for the 4 jet 2-lepton channel with opposite sign (OS) (see Figure 9.4, bottom right plot) consists mainly of top-pairs, diboson and Z production. The 2 and 3 jet 2-lepton OS effective mass distributions can be found in the Appendix in Section E.3 in Figure E.5.

9.2.2. Determination of the discovery potential and systematic uncertainties

The procedure to determine the discovery potential is the same as for the 14 TeV studies, and explained in detail in Section 7.5. The M_{eff} distribution, which yields best performance for most signals, is used to search for a deviation between the Standard Model expectations + SUSY signal ("data") and the SM expectation. Different cuts in M_{eff} (in steps of 400 GeV) are applied in order to find the optimal M_{eff} cut with the maximal significance Z_N (see Section 7.5.4). This optimisation

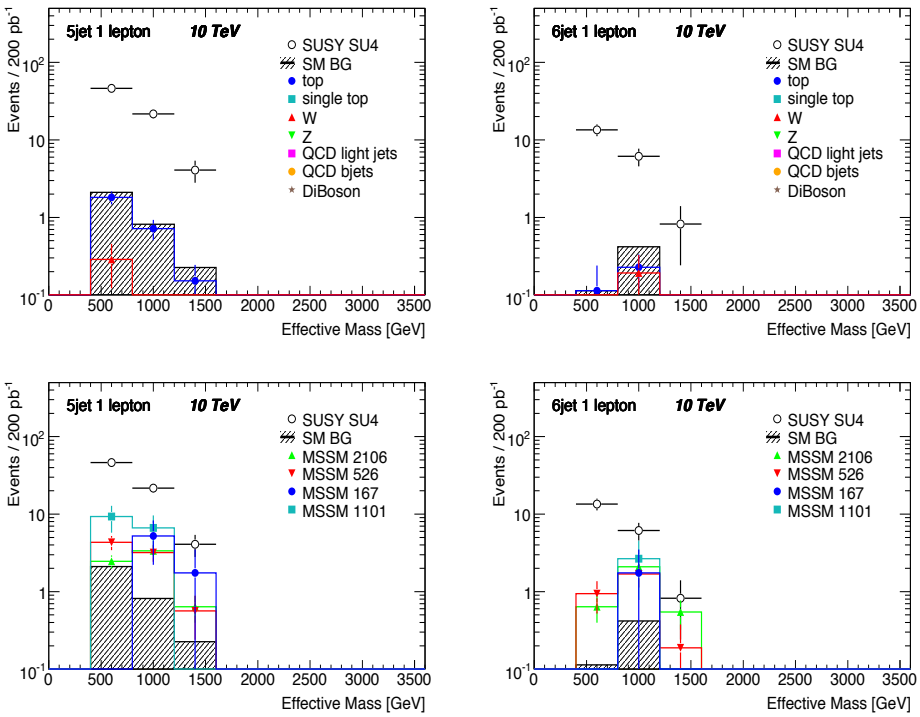

Figure 9.5: Effective mass distributions for the 5 (left plots) and 6 jet (right plots) 1-lepton channel for the mSUGRA point SU4 together with the Standard Model backgrounds (upper two plots). The lower two plots show the effective mass distributions for the 5, 6 jet 1-lepton channel for the mSUGRA point SU4 together with two unconstrained pMSSM grid points and two 8 parameter pMSSM signal points. The error bars reflect the statistical uncertainties of the Monte Carlo samples.

method was performed for each point in the selected SUSY signal grids, the determined significance for every point was corrected for the "multiple comparisons" as described in Section 7.5.2. The uncertainty in the determination of the sum of the various Standard Model backgrounds was estimated in Ref. [104] for $\sqrt{s} = 14$ TeV and $\mathscr{L} = 1$ fb^{-1} and re-evaluated for the 10 TeV studies. For a smaller energy and smaller luminosity higher uncertainties can be expected in particular for smaller datasets, as many estimates for different uncertainty sources are limited by the size of the control sample used. Taking this effect into account, a systematic uncertainty of 50% for the Standard Model background was assigned (see Section 7.5.3). To study the dependency of the discovery potential from the systematic uncertainty, a higher systematic uncertainty of 70% was also tested for some signal points. All these systematic uncertainties are just estimates, since no detailed studies have been performed for this centre-of-mass energy, luminosity and all jet multiplicities. In the following plots only the channels with the largest discovery reach for each lepton multiplicity (0, 1, 2 OS) are shown.

9.2.3. Discovery potential in the mSUGRA parameter space

Figure 9.6 presents the 5σ discovery potential for the 4 jet 0- and 1-lepton channels and the 2 jet 2-lepton channels in the mSUGRA m_0-$m_{1/2}$ parameter space with with $\tan\beta = 10$ (left plot) and $\tan\beta = 50$ (right plot), respectively. The discovery reach for the 2-lepton channel with same charge leptons (2 lepton same sign channel) is taken from Reference [235] since this channel was not studied in this thesis. As already found for a centre-of-mass energy of 14 TeV, the 4 jet 0-lepton and 4 jet 1-lepton channels have the largest reach. Scenarios with the light squarks and gluino masses up to $\approx$ 600-700 GeV could be discovered assuming an integrated luminosity of $\mathscr{L} = 200$ pb^{-1} and 50% uncertainty. In the $\tan\beta = 50$ SUSY signal grid is the discovery potential for the 0-lepton channel comparable to the reach of the 1-lepton channel, also for high m_0 regions, but with the 2-lepton channels no SUSY signals could be discovered. This was already found in the 14 TeV mSUGRA grids (see discussion in Section 8.3.3).

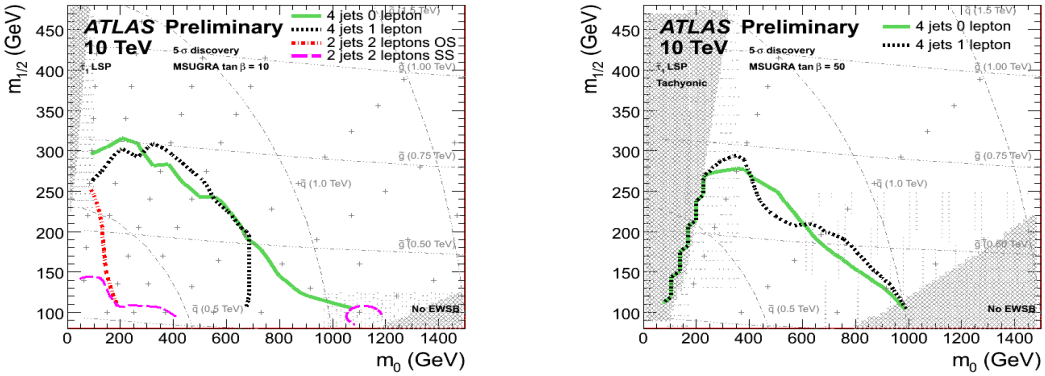

Figure 9.6: The 5σ discovery reach potential for channels with 0-, 1- and 2-leptons in the mSUGRA m_0-$m_{1/2}$ plane with $\tan\beta = 10$ (left plot) and $\tan\beta = 50$ (right plot) assuming $\sqrt{s} = 10$ TeV and $\mathscr{L} = 200$ pb^{-1}.

9.2.4. The ATLAS discovery potential in the pMSSM parameter space

SUSY models like mSUGRA cover only parts of the SUSY parameter space and predict a specific sparticle spectrum leading to distinctive signatures. Therefore only some of the kinematically possible SUSY configurations can be studied in the mSUGRA plane. To be better prepared for a potential discovery of the phenomenological manifestations of the MSSM parameter space, several hundred different pMSSM models, which yield different phenomenologies than the mSUGRA models, are explored. In total three different scans of the SUSY parameter space are performed within fixed ranges: pMSSM models fulfilling constraints from collider experiments, electroweak precision data, heavy flavour physics and cosmological considerations, pMSSM model that do not fullfill any constaints and pMSSM models with universal gaugino masses. Only SUSY signal with

label	explanation
Not found	no 5σ discovery in any of the studied channels (4 jet, 3 jet, 2 jet 0, 1, 2-lepton channel)
Not found in 4 jet channel	no 5σ discovery in any of the studied 4jet channels, but a 5σ discovery in the 2 or 3 jet channels
4 jet 0-lepton and 1-lepton	5σ discovery in the 4 jet 0-lepton and the 4 jet 1-lepton channel
4 jet 0-lepton and 2-leptons	5σ discovery only in the 4 jet 0-lepton and the 4 jet 2-lepton OS channel
4 jet 0-lepton	5σ discovery only in the 4 jet 0-lepton channel
4 jet 1-lepton	5σ discovery only in the 4 jet 1-lepton channel
2-leptons only	5σ discovery only in any of the 2-lepton channels (4 jet and/or 3 jet and/or 2 jet)

Table 9.2: Explanation of the labels used in the legends in Figure 9.7, 9.9, 9.13 and 9.14.

production cross sections that are likely at the LHC have been selected.
In the following, the ATLAS discovery reach for these SUSY signals in the pMSSM parameter space is discussed. The labels used in the legends of Figure 9.7, Figure 9.9, Figure 9.13 and Figure 9.14 are explained in Table 9.2. A summary of the used labels in the legends of Figure 9.10, Figure 9.11 and Figure 9.15 can be found in Table 9.3. The axis label "$m_{\text{min.susy}}$" in the following figures denotes the minimal mass of the 1st and 2nd generation squarks and the gluino $m_{\text{min. susy}} = \min.(\text{m}_{\tilde{\text{u}}}, \text{m}_{\tilde{\text{d}}}, \text{m}_{\tilde{\text{s}}}, \text{m}_{\tilde{\text{c}}}, \text{m}_{\tilde{\text{g}}})$ and the label "m_{LSP}" the mass of the lightest neutralino $\tilde{\chi}_1^0$. It should be noted that it is sometimes possible that a signal is hidden behind another SUSY point due to the high number of varied SUSY model parameters, the high number of SUSY signals per grid and the 2-dimensional illustration.

The ATLAS discovery reach for MSSM points fulfilling constraints from experiments

The obtained results for the studied constrained pMSSM SUSY models for an integrated luminosity of $\mathscr{L} = 200$ pb^{-1} are summarised in Figure 9.7. The green points present SUSY signals that do not have a discovery potential of at least 5σ, the red, black, blue and violet points illustrate a discovered SUSY signal in the different SUSY channels.
The upper plots show the 5σ discovery reach as a function of the total cross section and the minimal susy mass $m_{\text{min. susy}}$, in the lower plots of the same figure is the discovery reach illustrated in the minimal squark mass-gluino mass parameter space. The left plots consider stop and sbottom masses as possible lightest squark, while the right plots only take the first and second generation of squarks into account. The 4 jet 0-lepton channel (red squares) shows the highest discovery potential with about 72% generated points that could be discovered. In total about 74% of all points are discovered with the 4 jet 0- and 1-lepton analyses (black points). Only 3 points (violet triangles) are found with lower jet multiplicities (only with 2 or 3 jet channels with

label	**explanation**
Not found	no 5σ discovery in any channel (0-2 leptons, 2-6 jets)
0, 1 and 2-lepton channel	5σ discovery in any 0-, 1- and 2 lepton channel (with 2-6 jets)
0 and 1-lepton channel	5σ discovery in any 0- and 1 lepton channel (with 2-6 jets)
1 and 2-lepton channel	5σ discovery in any 1- and 2 lepton channel (with 2-6 jets)
0 lepton channel	5σ discovery in any 0 lepton channel (with 2-6 jets)
1 lepton channel	5σ discovery in any 1 lepton channel (with 2-6 jets)
2 lepton channel	5σ discovery in any 2 lepton channel (with 2-6 jets)
only found in 2 or 3 jet channel	5σ discovery only in 2 jet or 3 jet channel (with 0, 1 or 2 leptons)
4, 5 and 6 jet channel	5σ discovery only in the 4 jet, 5 jet and 6 jet channel (with 0, 1, or 2 leptons)
5 and 6 jet channel	5σ discovery only in the 5 jet and 6 jet channel (with 0, 1, or 2 leptons)
4 and 5 jet channel	5σ discovery only in the 4 jet and 5 jet channel (with 0, 1, or 2 leptons)
6jet channel	5σ discovery only in the 6 jet channel (with 0, 1, or 2 leptons)
5jet channel	5σ discovery only in the 5 jet channel (with 0, 1, or 2 leptons)
4jet channel	5σ discovery only in the 4 jet channel (with 0, 1, or 2 leptons)

Table 9.3: Explanation of the labels used in the legends in Figure 9.10, 9.11 and 9.15.

0 or 1 lepton). These SUSY signals are as expected in a region with very large gluino masses ($m_{\tilde{g}} \approx 1000$ GeV) and much smaller squark masses min.$(\mathrm{m}_{\tilde{\mathrm{u}}}, \mathrm{m}_{\tilde{\mathrm{d}}}, \mathrm{m}_{\tilde{\mathrm{s}}}, \mathrm{m}_{\tilde{\mathrm{c}}}) \approx 400$ GeV, where $\tilde{q}\tilde{q}$ production dominates. The small branching ratios for the decays to high p_T leptons for many of the studied SUSY signals lead only to very few signal events in the M_{eff} distributions of the studied lepton channels. This explains why no SUSY signals are discovered with any of the 2-lepton channels. The main conclusion of this study is that many SUSY signals can be discovered, if the cross section is larger than 10 pb and for squark and gluino masses up to 600-700 GeV. However, there are some pMSSM scenarios that are not discovered with any of the SUSY analyses under study even though the mass scale is as low as 450 GeV. This is probably due to the following reason: Some of the SUSY signals have a very similar effective mass distribution

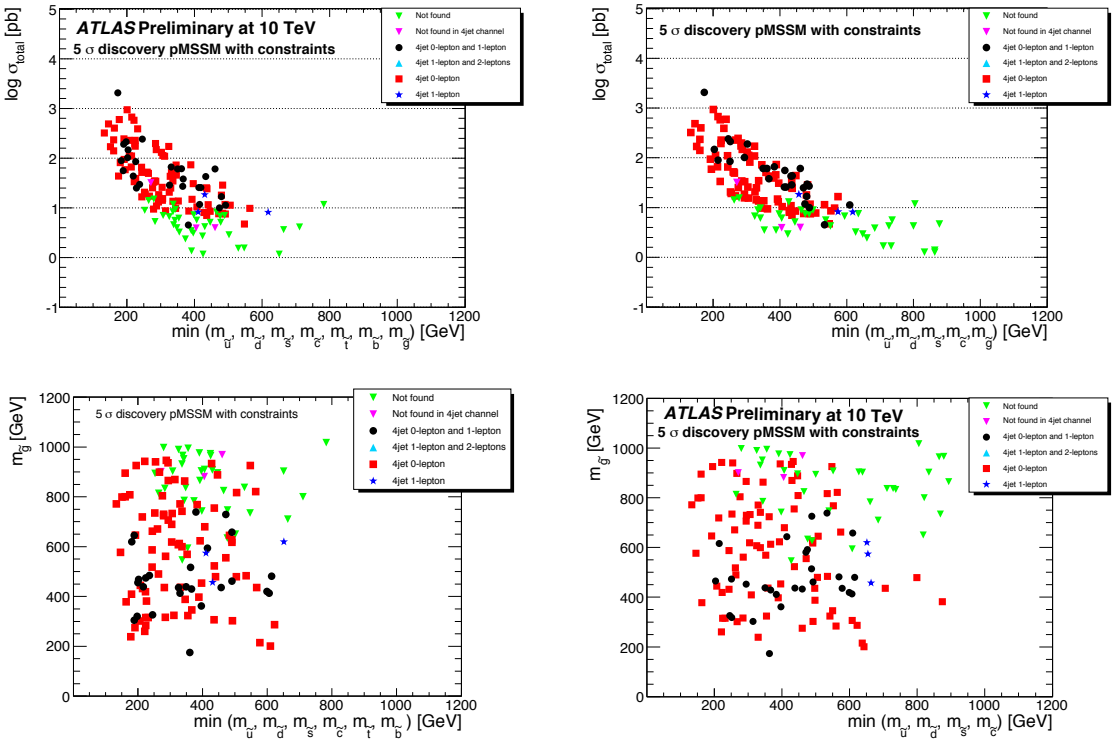

Figure 9.7: The discovery reach potential for SUSY signals of the pMSSM grid with constraints as a function of the total cross section and the minimal susy mass $m_{\text{min. susy}}$ (top plots) and as a function of the minimal mass of the squarks and the mass of the gluino (bottom plot). The presented results are for an integrated luminosity of $\mathscr{L} = 200$ pb^{-1} and a systematic uncertainty of 50%.

shape compared to the SM background distribution. As an example to illustrate this characteristic two MSSM points have been selected: the MSSM point 700 with a minimal squark mass $\text{min.}(m_{\tilde{u}}, m_{\tilde{d}}, m_{\tilde{s}}, m_{\tilde{c}}) = 489$ GeV, a gluino mass $m_{\tilde{g}} = 626.4$ GeV and a cross section of $\sigma = 7$ pb and the point MSSM point 891 with $\text{min.}(m_{\tilde{u}}, m_{\tilde{d}}, m_{\tilde{s}}, m_{\tilde{c}}) = 428$ GeV, $m_{\tilde{g}} = 546$ GeV and $\sigma = 11.8$ pb. The effective mass distributions for both points for the 4 jet 0- and 1-lepton channel and the Standard Model background events ("data") compared with the total SM distributions are presented in Figure 9.8. Due to the assumed 50% systematic error only a 3.7σ deviation is found in the 4 jet 0-lepton channel and the 4 jet 1-lepton channel yields a 4.2σ deviation for the MSSM point 700. For the point MSSM 891 a similar result was obtained. Also for this point there is no big difference between the shape of the SUSY signal and the SM background effective mass distributions as one can see in Figure 9.8 (bottom plots). The determined significance is 3.4σ and 3.9σ for the 4 jet 0- and 4 jet 1-lepton channels, respectively. A reduced systematic uncertainty would help to improve the results for those points. For example with an assumed systematic uncertainty of 30%

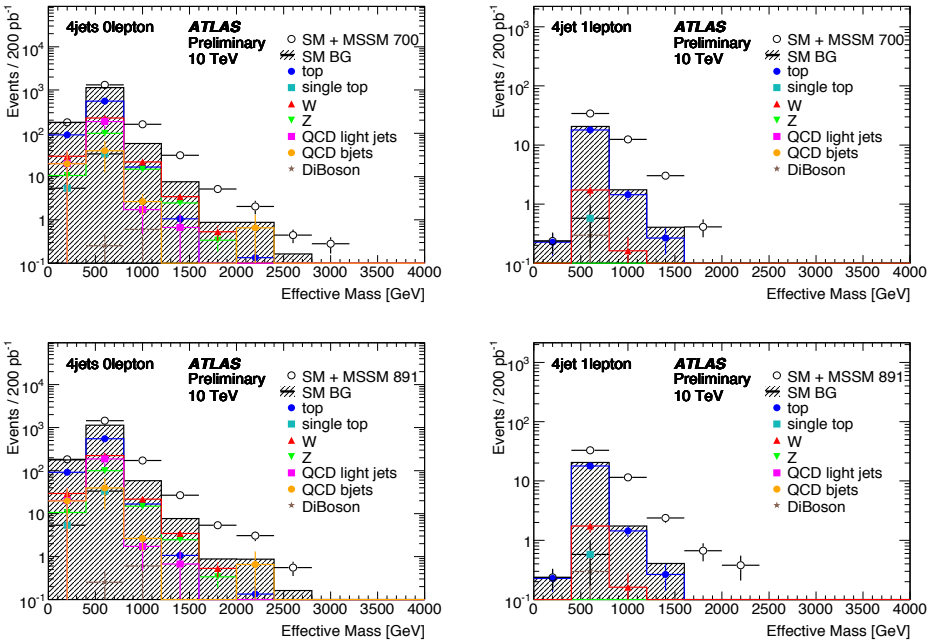

Figure 9.8: Effective mass distribution of the 4 jet 0-lepton (left plots) and 4 jet 1-lepton channel (right plot). The MSSM point 700 (upper plots) and the MSSM point 891 (lower plots) are presented together with the Standard Model background events (open circles). For both points the determined significance is below 5σ in these channels. The error bars reflect the statistical uncertainties of the Monte Carlo samples.

the MSSM 700 shows a deviation of 5.3σ in the 4 jet 0-lepton channel and of 4.8σ in the 4 jet 1-lepton channel and for the MSSM point 891 a significance of 5.5σ in the 4 jet 0-lepton channel and of 4.5σ in the 4 jet 1-lepton channel is obtained. Table 9.4 and Table 9.5 list the number of SUSY signals discovered by any of the 2-4 jet 0-lepton (top row), 2-4 jet 1-lepton (middle row) or by any of the 2-4 jet 0 or 1-lepton SUSY analyses (bottom row) when the luminosity is varied between $\mathscr{L} = 0.2, 0.3, 0.4, 0.5$ and 1.0 fb^{-1} (see Table 9.4) assuming 50% systematic uncertainties or when the systematic uncertainty is varied between 30%, 50%, 70% and 90% (see Table 9.5) assuming $\mathscr{L} = 200$ pb^{-1}. It can be seen that the systematic uncertainties used for the significance calculation play a major role in the 0-lepton channels, while the luminosity is more important for the 1-lepton channels that mainly suffer under a too small number of events due to the smaller production cross sections.
Another explanation can be found, if one compares the left and right plots in Figure 9.7. Several undiscovered SUSY signals have a very light stop or sbottom squark that can decay e.g. into b-jets that are not considered in the studied analyses.

channel	**luminosity $\mathscr{L}$ [pb^{-1}]**				
	200	300	400	500	1000
0 lepton channel	74%	77%	81%	81%	87%
1 lepton channel	21%	24%	31%	37%	48%
0 or 1 lepton channel	76%	79%	84%	85%	92%

Table 9.4: Number of discovered points in the pMSSM grid fulfilling constraints considering any of the studied 2-4 jet 0-lepton, 1-lepton and 0- or 1-lepton channels. The luminosity is varied from $\mathscr{L} = 0.2$ to 1.0 fb^{-1} assuming 50% systematic uncertainties.

channel	**systematic uncertainty [%]**			
	30	50	70	90
0 lepton channel	85%	74%	57%	48%
1 lepton channel	23%	21%	18%	14%
0 or 1 lepton channel	85%	76%	63%	54%

Table 9.5: Number of discovered points in the pMSSM grid fulfilling constraints considering any of the studied 2-4 jet 0-lepton, 1-lepton or 0- and 1-lepton channels. The systematic uncertainty is varied from 30% to 90% assuming $\mathscr{L} = 0.2$ pb^{-1}.

The ATLAS discovery reach in the pMSSM parameter space with universal gaugino masses (8 parameter pMSSM grid)

Figure 9.9 illustrates the discovery potential for the 8 parameter pMSSM grid points in the 2, 3 and 4 jet channels with 0-2 leptons. A detailed explanation of the legend can be found in Table 9.2. The left plot of the figure shows the 5σ reach as a function of the minimal SUSY mass $m_{\text{min.susy}}$ (with a zoom in the lower $m_{\text{min.susy}}$ region) and the total cross section, the right plot presents the 5σ reach as a function of the minimal squark mass and the mass of the gluino. Only SUSY signals with a minimal squark mass below $m_{\text{min.susy}} < 1000$ GeV that also have a gluino mass below $m_{\tilde{g}} < 800$ GeV can be discovered with the 4 jet 0- and/or 1-lepton channels. In total only 19 of 935 points ($\approx 2\%$) are discovered. Most points that are found have a cross sections $\sigma > 20$ pb, however there are also some points with a minimal SUSY mass $m_{\text{min.susy}} < 400$ GeV and a cross section of ≈ 30 pb that cannot be discovered (points are partly hidden under the red squares in the left plot) assuming an integrated luminosity of $\mathscr{L} = 200$ pb^{-1} and a systematic uncertainty of 50%. The 4 jet 0-lepton channel has again the best discovery potential, 11 of the 19 discovered points are found with this channel.

How much the discovery potential can be improved including the 5 and 6 jet analyses, can be see in Figure 9.10 and Figure 9.11. The legend is described in Table 9.3. For the upper two plots in

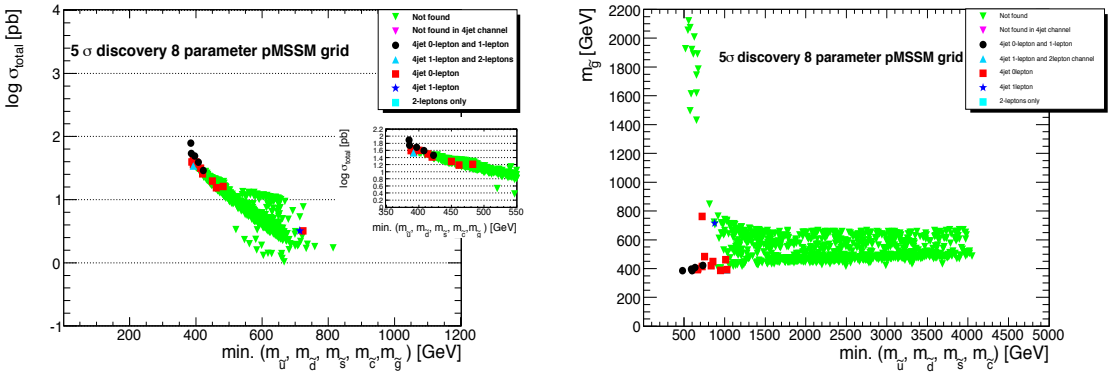

Figure 9.9: Discovery potential for the points of the 8 parameter pMSSM grid as a function of the logarithm of the total cross section and the minimal SUSY mass $m_{\text{min. susy}}$ (left plot, with a zoom in the lower $m_{\text{min.susy}}$ region) and as a function of the minimal squark mass min. $(\mathrm{m}_{\tilde{\mathrm{u}}}, \mathrm{m}_{\tilde{\mathrm{d}}}, \mathrm{m}_{\tilde{\mathrm{s}}}, \mathrm{m}_{\tilde{\mathrm{c}}})$ and the gluino mass $m_{\tilde{g}}$ (right plot). The results are presented for the studied 2, 3, 4 jet channels with 0-2 (OS) leptons assuming an integrated luminosity of $\mathscr{L} = 200\ \mathrm{pb}^{-1}$ and a systematic uncertainty of 50%.

both figures a systematic uncertainty of 50% was considered, while for the lower plots a systematic uncertainty of 70% is assumed. The discovery potential is presented for different lepton multiplicities (left plots) and for the different jet multiplicities (right plots). The scan shows that the 5 jet and 6 jet 0-lepton analyses (see right plots, red squares and light blue squares) can significantly improve the discovery reach for SUSY signals with large squark masses min. $(\mathrm{m}_{\tilde{\mathrm{u}}}, \mathrm{m}_{\tilde{\mathrm{d}}}, \mathrm{m}_{\tilde{\mathrm{s}}}, \mathrm{m}_{\tilde{\mathrm{c}}}) > 1000$ GeV and a quite small gluino mass $m_{\tilde{g}} < 800$ GeV. In total about 4% of all points (37 points) can be discovered with any of the 5 jet analyses and about 18% of all points (166 points) can be discovered with any of the 6 jet analyses. Including the 5 and 6 jet channels increased the number of discovered points by a factor of more than 10, about 28% of all signals are found with a significance of $\geqslant 5\sigma$ in any of the 2-6 jet 0-2 lepton channels in this grid. The 0-lepton channels have the highest impact on the improved discovery potential; about 24% of all SUSY models are found by any of the 2-6 jet 0-lepton SUSY analyses.
Increasing the systematic uncertainties (see Figure 9.10 and 9.11, bottom plots) from 50% to 70% has a strong influence on the results. The number of discovered points considering 2-6 jet SUSY analyses is reduced by more than 50%. Only 11% of all SUSY signals (106 points) still have a significance of $\geq 5\sigma$ and only 8% of all SUSY signals would be found with any of the 0-lepton channel. Most of these discovered SUSY signals have a minimal squark mass min. $(\mathrm{m}_{\tilde{\mathrm{u}}}, \mathrm{m}_{\tilde{\mathrm{d}}}, \mathrm{m}_{\tilde{\mathrm{s}}}, \mathrm{m}_{\tilde{\mathrm{c}}}) < 1400$ GeV and a gluino mass $m_{\tilde{g}} <$ 400-500 GeV.

Summary The results indicate that ATLAS can discover SUSY signals in the pMSSM 8 parameter grid, if they have a minimal SUSY masses less than 500 GeV and a total cross section up to 10 pb considering a 50% systematic uncertainty on the Standard Model background determina-

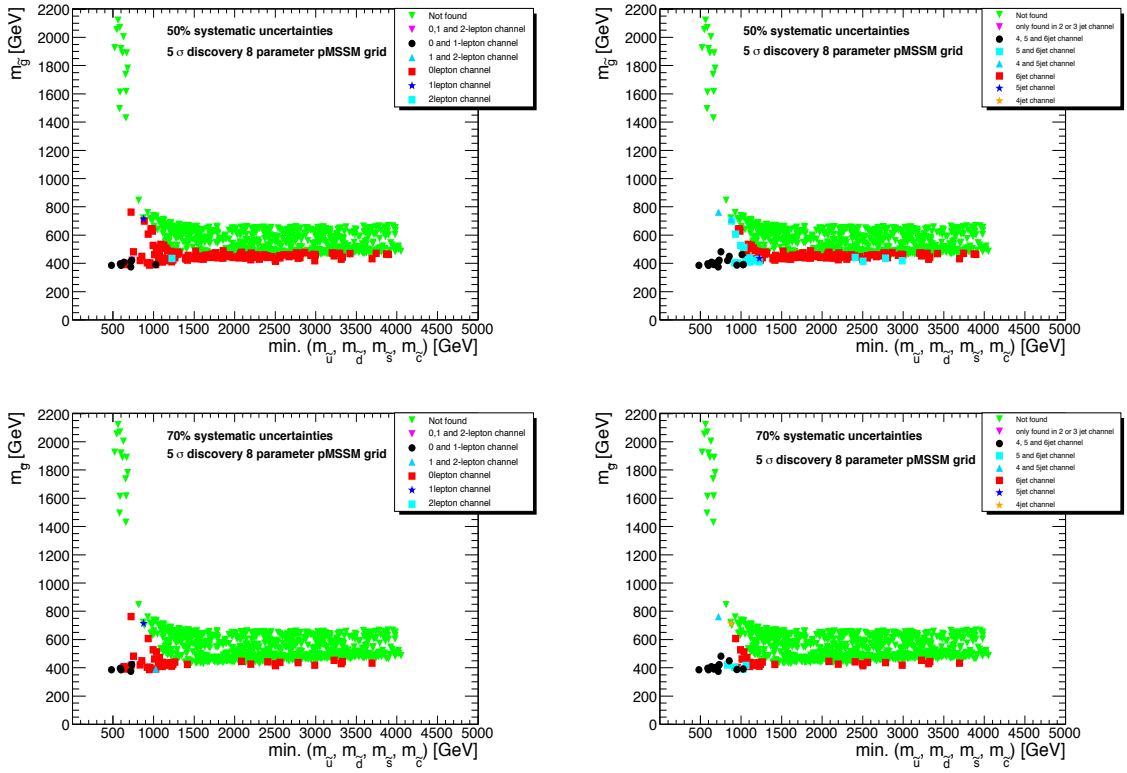

Figure 9.10: Discovery potential for the points of the 8 parameter pMSSM grid as a function of the minimal squark mass min. $(m_{\tilde{u}}, m_{\tilde{d}}, m_{\tilde{s}}, m_{\tilde{c}})$ and the gluino mass $m_{\tilde{g}}$. The 5σ reach for different jets multiplicities (right plots) and for different lepton multiplicities (left plots) assuming a 50% systematic uncertainty (upper plots) and 70% systematic uncertainties (bottom plots). The green points show SUSY signals that could not be discovered. All studied jet multiplicities 2-6 jets are considered.

tion. SUSY signals with minimal squark mass min. $(m_{\tilde{u}}, m_{\tilde{d}}, m_{\tilde{s}}, m_{\tilde{c}}) > 1000$ GeV and with gluino masses $m_{\tilde{g}} \approx 400 - 500$ GeV are mainly discovered with the 5 and 6 jet 0-lepton channels. For the different squark masses in this parameter region, the gluino mass is fixed to a certain phase space due to the gaugino mass relations and the applied dark matter constraints. This leads to dominating $\tilde{g}\tilde{g}$ production leading to a high jet multiplicity.
The are pMSSM scenarios where ATLAS does not have the sensitivity to observe the signal with the studied analyses channels, although the squark/gluino mass scale of about 450 GeV is quite low. Some these SUSY signals have a gluino mass that is much higher than the minimal squark mass ($m_{\tilde{g}} \gg$ min. $(m_{\tilde{u}}, m_{\tilde{d}}, m_{\tilde{s}}, m_{\tilde{c}})$) and an effective mass distribution with a similar shape to the Standard Model backgrounds. The reduction of the systematic uncertainty for the SM backgrounds is for those points very important in order to increase the coverage of the pMSSM model parameter

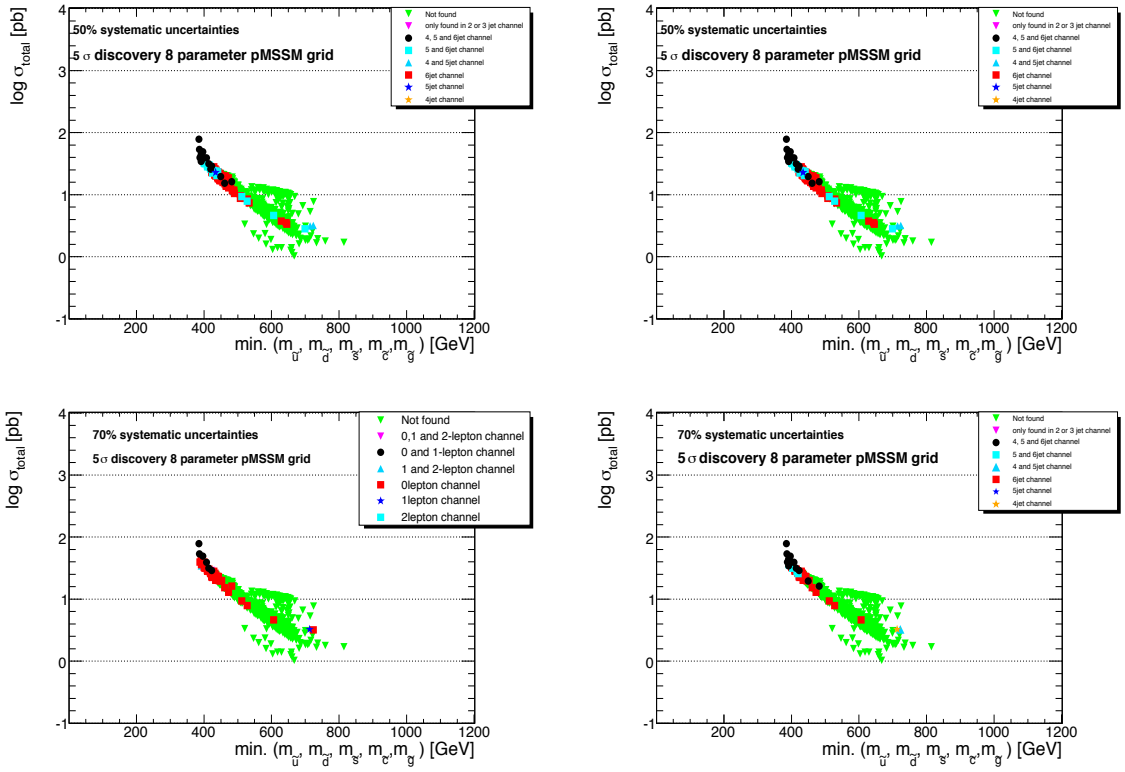

Figure 9.11: Discovery potential for the points of the 8 parameter pMSSM grid as a function of the minimal SUSY mass and the logarithm of the total cross section. The discovery reach for different jets multiplicities (right plots) and for different lepton multiplicities (left side) assuming 50% systematic uncertainties (top plots) and 70% systematic uncertainties (bottom plots). The green poins show SUSY signals that could not be discovered. All studied jet multiplicities 2-6 jets are considered.

space, as already discussed for the pMSSM grid with constraints. It was also found that many of the studied SUSY signals do not lead to significant high p_T lepton production. Thus, the 0-lepton channels are again more efficient for this SUSY grid. With an assumed 50% uncertainty on the Standard Models background a higher luminosity than 200 pb^{-1} is needed for a 5σ discovery in the lepton channels.

Discussion about points with a $\tilde{\tau}$ as NLSP

Since many of the studied 8 parameter MSSM SUSY signals have a stau as next lightest SUSY particle (see Figure 9.18, left plot), that can decay into a τ and the LSP as described in Section 6.2, one can expect a large number of τs in the final states for these points. The number of true τs with $p_T > 10$ GeV (left plot) and their transverse momenta distributions (right plot) for six different

8 parameter pMSSM grid points with gluino masses $m_{\tilde{g}}$ between 390 GeV and $\approx$ 510 GeV are shown in Figure 9.12. The minimal squark masses (without stop/sbottom squark), the gluino masses, the stau masses and the cross sections of the presented points are listed in Table 9.6. The last two columns indicate, if the points would be discovered with any of the studied 2-4 jet (5-6 jet) 0-2 lepton analyses.

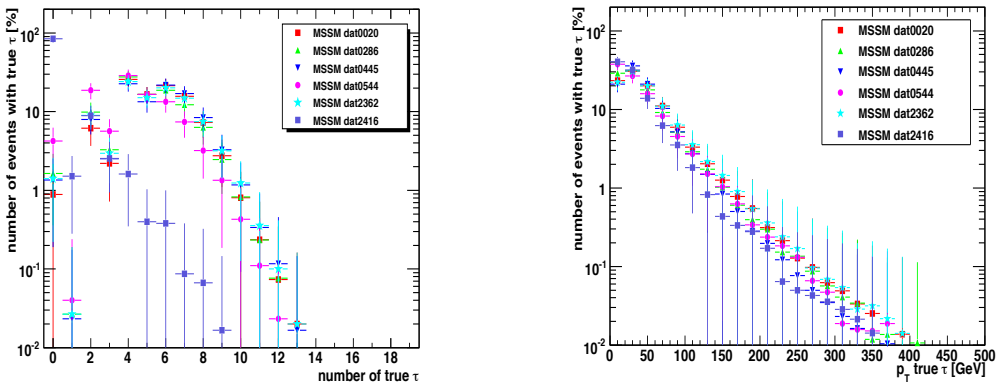

Figure 9.12: The number of true τs with $p_T > 10$ GeV (left plot) and the transverse momentum distribution of the true τs (right plot) for different 8 parameter pMSSM grid points. Both plots are normalised to unity.

The MSSM points dat0020, dat0286, dat0445, dat0544 and dat2362 have a high number of true τs with a maximum around 4-6 (see Figure 9.12, left plot). For all these points the NLSP is a stau $\tilde{\tau}_1$. For the point MSSM dat2416 (purple square), the NLSP is a chargino $\tilde{\chi}_1^{\pm}$, which can decay in a neutralino if the mass difference is large enough or in squarks and sleptons, dependent on the sparticle mass spectrum. For this SUSY signal the staus are too heavy ($m_{\tilde{\tau}_1} \approx 1456$ GeV, $\tilde{\chi}_1^{\pm} \approx 109$ GeV, $\tilde{\chi}_1^0 \approx 55$ GeV), which leads to a smaller number of τs with mainly low p_T. From these studies one can also deduce the following for the 8 parameter pMSSM grid points: if the chargino and neutralino mass are larger than the lightest stau mass $m(\tilde{\chi}_2^0, \tilde{\chi}_1^{\pm}) \gg m_{\tilde{\tau}_1}$ as this is the case for point dat0020, dat0286, dat0445, dat0544 and dat2362, but not for the dat2416 SUSY signal[1] and if tanβ is high enough, so that tau lepton Yukawa couplings become large, leading to reduced masses of τ-sleptons, one can expect an abundant production of taus in the pMSSM final states.
As already discussed in the ATLAS paper [343], the SM background in τ-channels mainly consist of $t\bar{t}$ and W + jets events. However, the ratio of signal over background should be large in channels requiring more than 1-2 τs and with enhanced stau production. Selecting events with high p_T jets and τ leptons in the final state could help to improve the discovery reach of those points.

[1] The mass of the stau is more than ten times larger than the mass of the neutralino $\tilde{\chi}_2^0$ or the chargino $\tilde{\chi}_1^{\pm}$.

point	min. squark mass w/o $\tilde{t}_1/\tilde{b}_1$ [GeV]	$m_{\tilde{g}}$ [GeV]	$m_{\tilde{\tau}_1}$ [GeV]	cross section [pb]	found w/ 2-4 jets	found w/ 5-6 jets
dat0020	2692.5	509.0	118.3	11.2	no	no
dat0286	1110.4	410.1	100.0	29.6	no	yes
dat0445	2001.5	506.4	107.4	10.0	no	no
dat0544	948.7	387.9	101.0	39.6	yes	yes
dat2362	1073.7	472.5	116.8	12.9	no	yes
dat2416	1683.2	442.7	1455.7	21.0	no	yes

Table 9.6: The minimal squark mass (without stop $m_{\tilde{t}_1}$/sbottom $m_{\tilde{b}_1}$ mass), the gluino mass $m_{\tilde{g}}$, the stau mass $m_{\tilde{\tau}_1}$ and the cross section of the selected 8 parameter pMSSM grid points that are shown in the τ distribution plots (see Figure 9.12). The last two columns indicate if the points would be discovered with any of the studied 2-4 jet (5-6 jet) 0-2 lepton analyses.

The ATLAS discovery reach in the unconstrained pMSSM parameter space

The considerations of the previous sections can be extended to the case of a more general pMSSM model. Figure 9.13 shows the discovery reach for the studied unconstrained pMSSM grid (see Section 4.5.2) as a function of the total cross section and $m_{\text{min.susy}}$ (left plot) and the 5σ discovery potential in the minimal squark mass $\text{min.}(\text{m}_{\tilde{\text{u}}}, \text{m}_{\tilde{\text{d}}}, \text{m}_{\tilde{\text{s}}}, \text{m}_{\tilde{\text{c}}})$ - gluino mass $m_{\tilde{g}}$ parameter space (right plot). It can be seen that again the 4 jet 0-lepton channel discovers with 54% of all studied models the highest fraction of SUSY signals in this grid. The majority of the found SUSY signals have a minimal SUSY mass $m_{\text{min.susy}}$ smaller than $\approx$ 800 GeV and a gluino mass smaller than $\approx$ 600 GeV. In total about 66% of all points are found with any of the 2-4 jet 0-2 lepton analyses. It is worth mentioning, that in this grid about 9% of all points have a discovery potential of $\geq 5\sigma$ only in the 2 or 3 jet 0- and 1-lepton channels (pink triangles), but are not discovered by any of the studied 4 jet analyses. These points are mainly found in the region $\text{min.}(\text{m}_{\tilde{\text{u}}}, \text{m}_{\tilde{\text{d}}}, \text{m}_{\tilde{\text{s}}}, \text{m}_{\tilde{\text{c}}}) > 600$ GeV and $m_{\tilde{g}} > 800$ GeV with a minimal squark mass lighter than the gluino mass and dominant $\tilde{q}\tilde{g}$ and $\tilde{q}\tilde{q}$ production.
In contradiction to the results found for the MSSM grid with constraints (see Section 9.2.4), there are again several SUSY signals with a cross section larger than 10 pb and with squark and gluino masses smaller than 600 GeV for which ATLAS is not sensitive with any of the studied SUSY analyses.
In order to better understand why some of these SUSY models are undiscovered, the mass difference between the LSP and the squarks and gluino was studied. Figure 9.14 illustrates the discovery reach in the plane of the logarithm of the mass difference between the minimal SUSY mass $m_{\text{min. susy}}$ and the mass of the mass of the LSP $|m_{\text{min. susy}} - m_{LSP}|$ as a function of the minimal SUSY mass (top left plot) and as a function of the LSP mass (top right plot). The bottom right (left) plot shows the logarithm of the mass difference between the minimal squark (gluino) mass and the mass of the LSP $|\text{min.}(\text{m}_{\tilde{\text{u}}}, \text{m}_{\tilde{\text{d}}}, \text{m}_{\tilde{\text{s}}}, \text{m}_{\tilde{\text{c}}}) - \text{m}_{\text{LSP}}|$ ($|m_{\tilde{g}} - m_{LSP}|$) as a function of the minimal squark

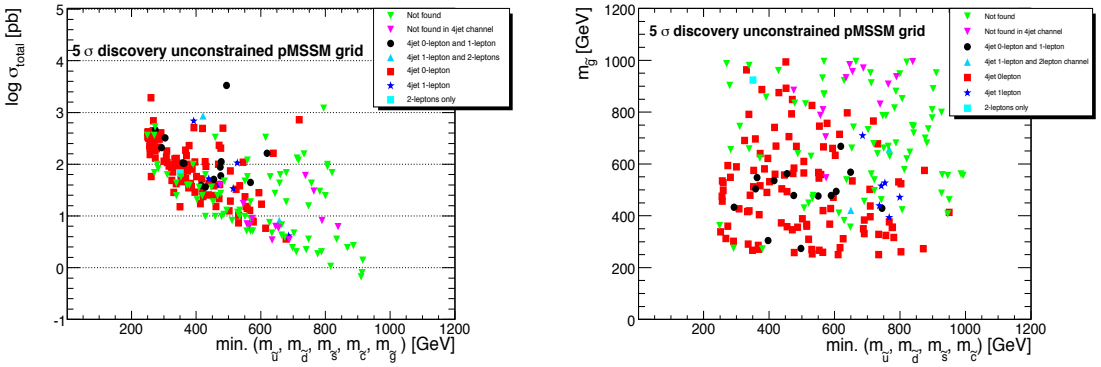

Figure 9.13: Discovery reach of the unconstrained pMSSM signal points as a function of the total cross section and the minimal SUSY mass $m_{\text{min. susy}}$ (left plot) and as a function of the minimal squark mass $\text{min.}(\text{m}_{\tilde{\text{u}}}, \text{m}_{\tilde{\text{d}}}, \text{m}_{\tilde{\text{s}}}, \text{m}_{\tilde{\text{c}}})$ and the gluino mass $m_{\tilde{g}}$ (right plot) assuming $\mathscr{L} = 200\ \text{pb}^{-1}$ and 50% uncertainty.

(gluino) mass. If $m_{\text{min. susy}}$ is less than $\approx$ 350/400 GeV, most of the SUSY signals are discovered if their mass difference $|m_{\text{min. susy}} - m_{LSP}|$ is more than $\approx$ 100-150 GeV ($m_{LSP} < 250$ GeV). For SUSY signals with larger masses ($m_{\text{min.susy}} > 400$ GeV), the mass difference $|m_{\text{min. susy}} - m_{LSP}|$ has to become also larger and needs to further increase with the SUSY mass in order to get a significance of more than 5σ. This is due to the fact that for most SUSY signals squarks and gluinos production dominate and points with light squarks/gluinos and small mass splittings with the LSP decay to rather soft jets and are thus not discovered with the studied SUSY analyses that apply high p_T jet cuts. Only very few SUSY signals with very large squark/gluino masses ($m_{\text{min. susy}} > 700$ GeV) are found. This is what one would naively expect, since in this case squark and gluino production is kinematically more suppressed that results in a smaller number of events in the final states with high p_T jets.

The discovery potential for the selected unconstrained pMSSM SUSY signals considering also the 5 and 6 jet SUSY analyses are illustrated in Figure 9.15 (legend explained in Table 9.3). The left plots show the discovery reach as a function of the different lepton multiplicities (0 - 2 leptons) and the right plots as a function of the different jet multiplicities (2 - 6 jets). The plots show only a small improvement of the discovery reach using the 5 and 6 jet analyses, 11 more SUSY signal points are discovered. (light blue and red squares in the right figures). Most SUSY signals that are found with the 4 jet 0-lepton analysis can be also found by the 5 or/and 6 jet 0-lepton analysis (black circle and light blue triangles right plot). As expected, SUSY signals with very small mass splitting are not discovered with any of the 5 and 6 jet analyses. Considering all 2-6 jet SUSY analyses about 71% of all SUSY signals in the unconstrained pMSSM grid can be found, 68% in the 0-lepton channel.

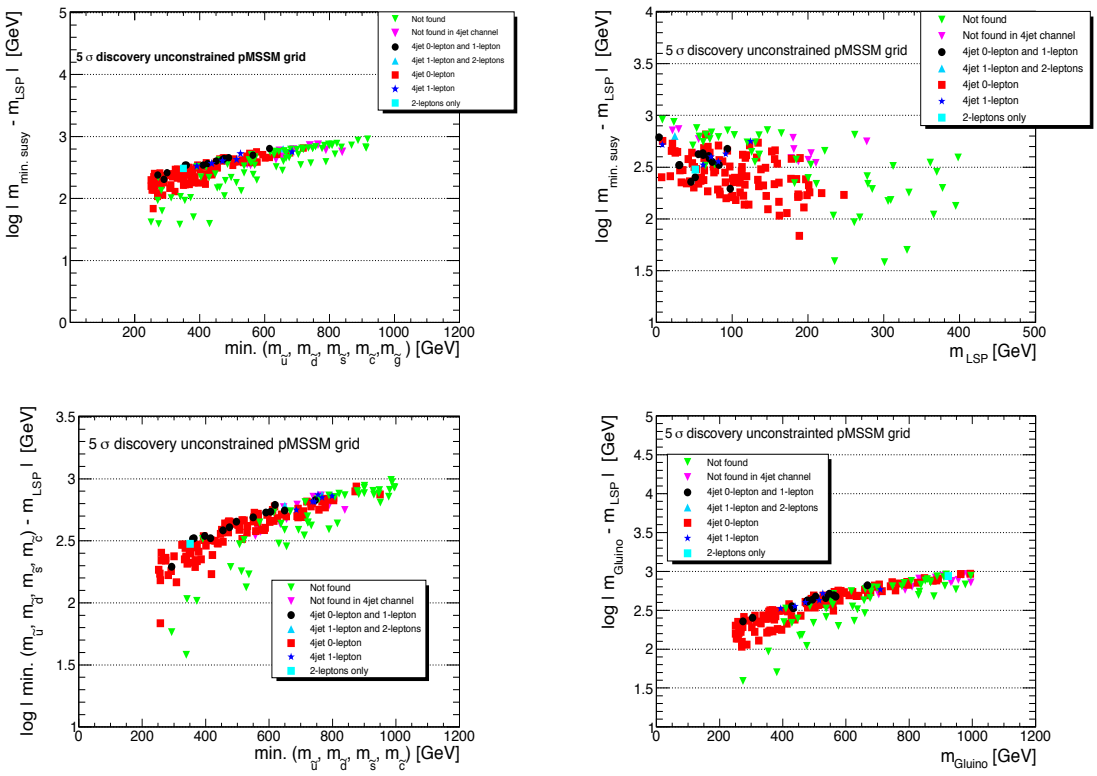

Figure 9.14: Top plots: Discovery potential for the SUSY signals of the unconstrained pMSSM grid in the $m_{\text{min. susy}}$vs. log $|m_{\text{min. susy}} - m_{\tilde{\chi}_1^0}|$ (top left plot) and in the $m_{\tilde{\chi}_1^0}$vs. log $|m_{\text{min. susy}} - m_{\tilde{\chi}_1^0}|$ (top right plot) parameter space. Bottom plots: 5σ discovery potential for the logarithm of the mass difference between the minimal squark mass and the mass of the LSP as a function of the minimal squark mass ($\log|\text{min.}(m_{\tilde{u}}, m_{\tilde{d}}, m_{\tilde{s}}, m_{\tilde{c}}) - m_{\tilde{\chi}_1^0}|$ vs. min. $(m_{\tilde{u}}, m_{\tilde{d}}, m_{\tilde{s}}, m_{\tilde{c}})$ (bottom left plot) and the logarithm of the mass difference between the gluino mass and the mass of LSP as a function of the gluino mass ($m_{\tilde{g}} - \log|m_{\tilde{g}} - m_{\tilde{\chi}_1^0}|$ plane). All plots assume $\mathscr{L} = 200\ \text{pb}^{-1}$ and 50% uncertainty. Susy analyses with 2-4 jets 0-2 leptons are considered.

Discussion about some points not discovered by the "standard" 2-4 jet analyses

As illustrated in Figure 9.15 few more points not discovered with the standard 2-4 jet analyses, can be found by the 5 and 6 jet SUSY channels. However, some of the studied SUSY signals are not only characterised by high p_T jets, they also have high p_T b-jets. In the framework of minimal supersymmetry (MSSM), the production of third generation squarks can be also favoured as the large mixing between the chiral states of the superpartners of the Standard Model fermions might yield low masses for the lightest scalar bottom and scalar top states. The SUSY sparticles scalar bottom and scalar top are expected to be produced in pairs through direct production or through

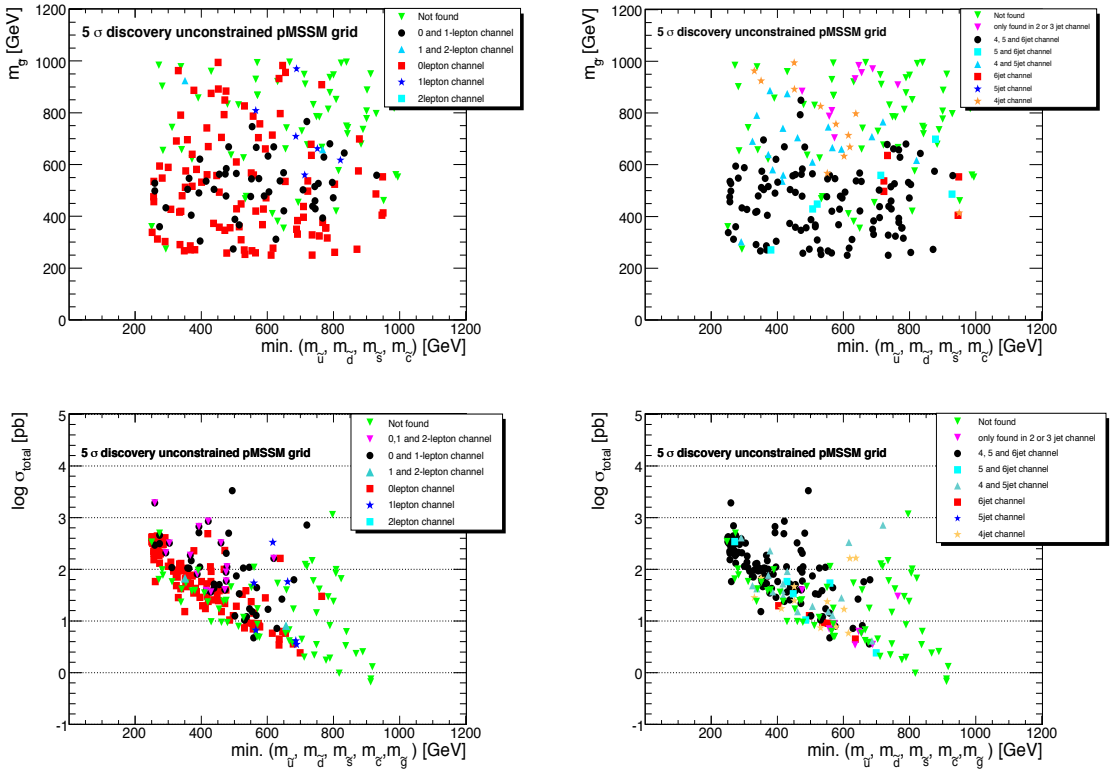

Figure 9.15: The 5 σ discovery potential of the 2-6 jet SUSY analyses for unconstrained pMSSM models in min. squark mass vs. gluino mass (min.$(m_{\tilde{u}}, m_{\tilde{d}}, m_{\tilde{s}}, m_{\tilde{c}})$-$m_{\tilde{g}}$) parameter space (top plots) and for the min. susy mass vs. the logarithm of the total cross section parameter space (bottom plots) for the different lepton multiplicities (left plots) and for the different jet multiplicities (right plots).

$\tilde{g} \rightarrow \tilde{b}b(\tilde{t}t)$ decays, if this is kinematically allowed. Two of the possible production mechanisms are shown in Figure 9.16.

To identify b-jets, usually the ATLAS default "b-tagging" algorithm can be used as described in Ref. [345]. However this algorithm was not implemented in the ATLFAST1 software. Therefore, in order to define which true jet is a true b-jet, a procedure similar to the algorithm performed on the truth level by the full-detector simulation (see Ref. [346] and [347]) was used: For all true b-quarks the smallest distance ΔR to all true jets has been calculated. In case ΔR is less than 0.3, the true jet is tagged as true b-jet. Figure 9.17 shows as example the jet multiplicity for true jets with $p_T > 10$ GeV (top left plot) and the true b-jet multiplicity for true b-jets with $p_T > 10$ GeV (bottom left plot) for four different unconstrained pMSSM signals. The transverse momentum distribution for the true jets is presented in right top plot of the same figure, while the bottom right plot shows the true b-jet probability as a function of the transverse momentum of the true jets. The

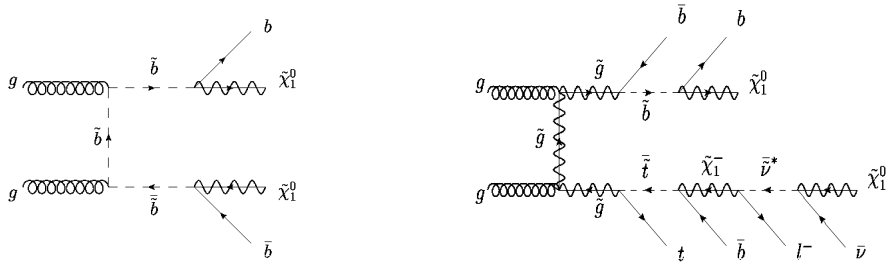

Figure 9.16: Feynman diagrams of two possible production mechanisms and subsequent decay chains involving third generation squarks. Presented are sbottom pair production and sbottom decay into b-quark and neutralinos (left plot); gluino pair production and decay into $\tilde{b}b$ and $\tilde{t}t$ (right plot). Figure is taken from Ref. [344].

minimal squark masses (with stop/sbottom), the stop masses, the sbottom masses as well as the gluino masses and the cross sections of the presented points in Figure 9.17 are listed in Table 9.7. The last two columns indicate if the points would be discovered with any of the studied 2-4 jet (5-6 jet) 0-2 lepton analyses. The points MSSM 1187 (light blue star) and MSSM 778 (pink triangle) show a high b-jet probability compared to the other two points (MSSM 893 and MSSM 922). These two points are not discovered with the standard 2-4 jet analyses. For the point MSSM 1187 the gluino decays mostly into two b-quarks[2], one with low and one with high p_T and a neutralino leading to two b-jets per event. For the point MSSM 778 the lightest squark is the stop, that can decay either into a top and a gluino or a top and a neutralino. The gluino can only decay through squarks (see Section 6.2). The produced neutralinos (and charginos) are often $\tilde{\chi}^0_{2,3}$ ($\tilde{\chi}^{\pm}_{1,2}$) which are not stable and can further decay into a $\tilde{\chi}^0_1$, jets (and leptons). Such points are also often characterised by a high jet multiplicity (beside b-jets). Therefore these points could be also discovered for example with an analysis asking for more than 4 or 5 jets, as Table 9.7 shows. The MSSM points 893 (red triangle) and MSSM 922 (blue circle) have nearly no b-jets. For these points, the stop and the sbottom mass is much bigger than the squark masses of the 1st and 2nd generation and the gluino mass. Thus the gluino decays into light quarks and squarks, which results in a signature with many jets. These points are found with the 4-6 jet 0-lepton analyses and are only shown for the comparison.

Figure 9.18 right plot (left plot) presents the number of discovered (red line, blue line for 5-6 jet analyses only) and undiscovered (green line) unconstrained MSSM SUSY models (8 parameter grid pMSSM models) as a function of the next LSP type and demonstrates the discussed results. Many SUSY signals with a sbottom $\tilde{b}_1$ (or chargino $\tilde{\chi}^{\pm}_1$) as NLSP are not discovered.

The large number of b-jets per event in the signal for many of the studied SUSY models should allow efficient signal selection through b-tagging, even if the b-tagging efficiency is relatively

[2]The gluino decays into a b-quark and a sbottom, that is not stable and decays into a b-quark and a neutralino.

low. A b-jet analysis could reduce the SM background, while leaving a substantial amount of the signal events, thus leading to a high discovery potential for 200 pb^{-1} at a centre-of-mass energy $\sqrt{s} = 10$ TeV for those points.
The ATLAS SUSY group studies inclusive SUSY analyses with b-jets in the final state (see for example Ref. [348]). Recently a paper about first measurements of supersymmetry-sensitive variables in heavy-flavour enriched final state events with jets, missing transverse energy, b-jets with and without additional leptons (see Ref. [345]) was published. These results demonstrate the good level of understanding of the ATLAS performance for jets and tracking and show that b-jet analyses provide sensitivity to new physics.

point	**min. squark mass** w/ $m_{\tilde{t}}/m_{\tilde{b}}$ [GeV]	$\mathbf{m}_{\tilde{t}_1}$ [GeV]	$\mathbf{m}_{\tilde{b}_1}$ [GeV]	$m_{\tilde{g}}$ [GeV]	**cross section** [pb]	**found w/ 2-4 jets**	**found w/ 5-6 jets**
MSSM 893	308.0	443.1	740.9	427.0	42.8	yes	yes
MSSM 922	268.0	809.2	365.8	312.0	694.7	yes	yes
MSSM 1187	239.9	239.9	261.8	429.0	57.8	no	yes
MSSM 778	691.3	691.4	836.9	404.0	19.7	no	yes

Table 9.7: The minimal squark mass (with stop/sbottom mass), the stop mass $m_{\tilde{t}_1}$, the sbottom mass $m_{\tilde{b}_1}$, the gluino mass $m_{\tilde{g}}$ and the cross section σ of the unconstrained pMSSM grid points that are presented in the b-jet distribution plots (see Figure 9.17). The last columns indicate, if the points would be discovered with any of the studied 2-4 jet (5-6 jet) 0-2 lepton analyses.

9.3. Summary and conclusion

The expected performance of the ATLAS detector for mSUGRA models as well as for SUSY signatures in the pMSSM parameter space (MSSM points fulfilling constraints, 8 parameter MSSM SUSY models with universal gaugino masses and unconstrained pMSSM models) assuming an LHC centre-of-mass energy $\sqrt{s} = 10$ TeV and an integrated luminosity of $\mathscr{L} = 200$ pb^{-1} has been studied. It is demonstrated that a discovery of mSUGRA signals (with $\tan\beta = 10$ and $\tan\beta = 50$ and $\mathrm{sign}(\mu) > 0$) is possible up to squark/gluino masses less than 600-700 GeV.
The large number of SUSY parameters in the MSSM parameter space makes it difficult to comprehend the variety of all possible signals and signatures and to evaluate the reach for all sparticle decay modes in general. However, the study of different pMSSM signal grids has shown that many different scenarios could be covered:

- **pMSSM scenarios fulfilling experimental constraints**
  Most SUSY signals can be discovered up to squark/gluino masses less than 600-700 GeV and cross sections of $\sigma > 10$ pb, but there are pMSSM signals with a mass scale as low as

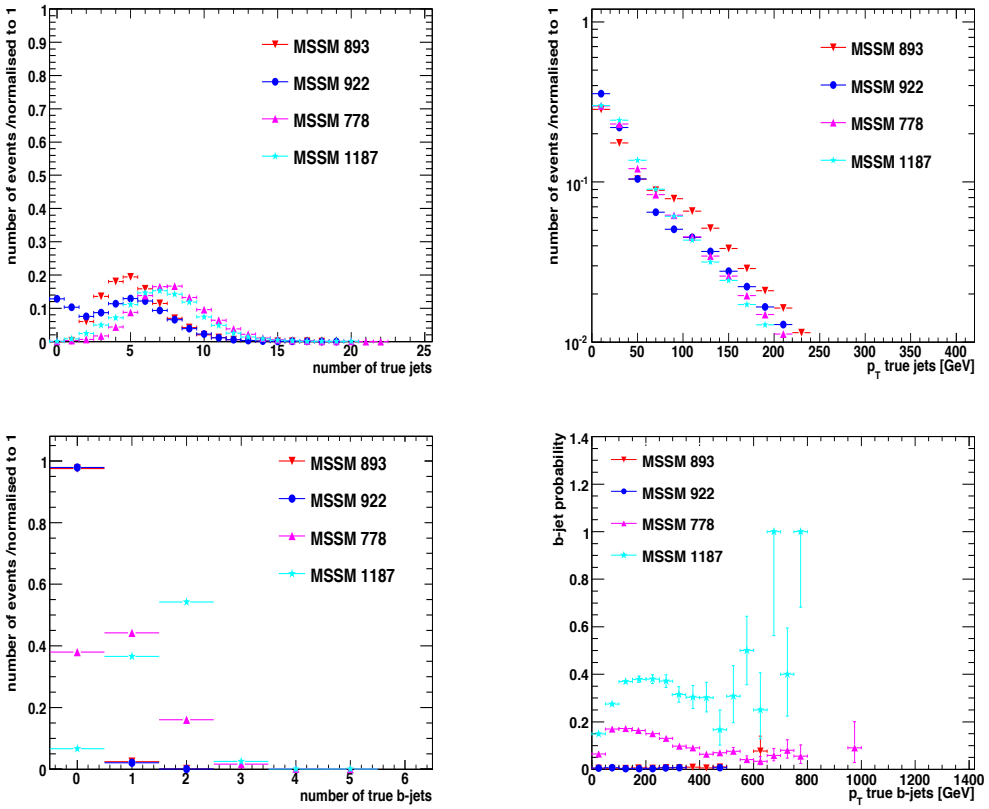

Figure 9.17: The number of true jets with $p_T > 10$ GeV (top left plot) and their transverse momentum distribution (top right plot). The bottom plots show the number of true b-jets with $p_T > 10$ GeV (bottom left plot) and their transverse momentum distribution (bottom right plot). Both plots are normalised to unity, results for four different unconstrained MSSM points are presented (see Table 9.7).

450 GeV that could not be discovered with any of the studied SUSY analyses. Several undiscovered SUSY signals show a similar shape of their M_{eff} distribution as the SM background events. A reduced systematic uncertainty would help to discover these points.

- **8 parameter pMSSM grid models**
  Similar results as for the pMSSM grid studies are obtained. Asking for a higher jet multiplicity ($\geq 5, \geq 6$ jets) could improve the discovery reach in the parameter space with gluino masses of $m_{\tilde{g}} \approx 400-500$ GeV and minimal squark masses min. $(m_{\tilde{u}}, m_{\tilde{d}}, m_{\tilde{s}}, m_{\tilde{c}}) > 1000$ GeV. Changing the systematic uncertainty influences the discovery reach. A increased systematic uncertainty from 50% to 70% reduces the number of discovered point by more than a factor

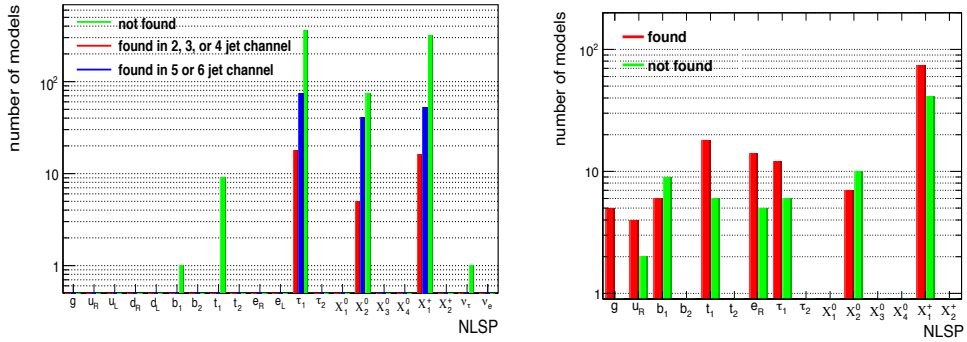

Figure 9.18: The number of discovered (red and blue line) and undiscovered (green line) 8 parameter pMSSM models (left plot) and unconstrained pMSSM SUSY models (right plot) as a function of the NLSP type. The results are for an integrated luminosity of $\mathscr{L} = 200$ pb^{-1} and 50% systematic uncertainties.

of 2. Only 11% of all SUSY signals still have a significance of $\geq 5\sigma$ and only 8% of all SUSY signals would be found with any of the 0-lepton channels. The discovered SUSY signals have min. $(m_{\tilde{u}}, m_{\tilde{d}}, m_{\tilde{s}}, m_{\tilde{c}}) < 1400$ GeV and $m_{\tilde{g}} < 400$-500 GeV. The studies indicate, that channels with higher jet multiplicity or a larger number of expected background events like the 0-lepton channels can benefit from a reduction of the systematic uncertainties. Since several undiscovered SUSY signals have a stau as NLSP, which decays mainly into a τ and a $\tilde{\chi}_1^0$, channels asking for high p_T jets and τs in the final state could improve the discovery potential in this pMSSM grid.

- **unconstrained pMSSM grid models**
  SUSY signals with a minimal SUSY mass $m_{\text{min. susy}}$ smaller than ≈ 800 GeV show a significance with $\geq 5\sigma$ in any of the studied SUSY analyses channels with 0, 1 or 2 leptons and 2-4 jets. However, there are also SUSY signals with a cross section larger than 10 pb and squark and gluino masses smaller than 400 GeV or with $m_{\text{min. susy}} < 800$ GeV that are not found. Some undiscovered SUSY signals are characterised by high p_T jets and among them, also by a high number of jets, which could be tagged as b-jets. A b-jet analysis could enhance the signal to background event ratio and could lead to a discovery especially for those points.

There are some general reasons, why some of the studied pMSSM model points failed to be observed:

- The signal cross sections for particular decay channels are to small.

- The squark and gluinos, which are dominantly produced for most SUSY signals and which have the largest production cross sections, are too heavy that causes kinematically suppressed production rates.
- Several models show a "compressed" mass spectra, that results in a reduced phase space of the possible SUSY decay channels and a decreased transverse momenta for the final state objects. For example, a small mass splitting between squarks and gluinos and the LSP can lead to the production of soft jets and leptons, that do not pass the analysis cuts.
- The systematic uncertainties used for the significance calculation play a major role in the 0-lepton channels, while the luminosity plays an important role for the lepton channels that mainly suffer under a too small number of events due to the smaller production cross sections.

The studies of the different regions in the pMSSM parameter space have shown, that ATLAS has a high discovery potential for SUSY signals at a centre-of-mass energy of $\sqrt{s}$ = 10 TeV for a luminosity of $\mathscr{L} = 200$ pb^{-1}. The estimated discovery potential is strongly dependent on the phase space of the studied SUSY models as well as on the systematic uncertainties on the Standard Model background. The majority of the discovered SUSY signals in the different pMSSM grids has minimal squark and gluino masses up to 600-700 GeV and a cross section larger than 10pb. Of course one can always find a signature that cannot be discovered even at a lower mass scale. Considering higher jet multiplicities or different SUSY signatures like τs or b-jets can improve the discovery reach and 5- and 6-jet analyses can be important in regions with mainly gluino production. Within the ATLAS SUSY group several SUSY analyses have been developed looking for signatures with taus + jets or b-jets + jets (+ leptons) to cover also signatures that could not be discovered with any of the discussed jet + E_T^{miss} + (0, 1, 2) lepton analyses, see for example Ref. [344,348].

10. Searches for Supersymmetry at a centre-of-mass energy of 7 TeV

The Tevatron experiments have set limits in the mSUGRA parameter space for squark and gluino masses at around 390 GeV [238,291] (see Section 6.3.1). The goal of the following study was to determine the ATLAS discovery reach for a centre-of-mass energy of 7 TeV just before first LHC collision events. The studies assume an integrated luminosity $\mathscr{L} = 0.5 - 2$ fb^{-1}, which could be collected in the years 2010-2011.

10.1. Experimental setup

The production of the Monte Carlo samples for a LHC centre-of-mass energy $\sqrt{s}$ = 7 TeV was still running when the analysis work started. Therefore the identical $\sqrt{s}$ = 10 TeV mSUGRA SUSY signal and Standard Model Monte Carlo samples are used (see Chapter 9) and reweighted to a centre-of-mass energy of 7 TeV. Details about the reweighting process can be found in the Appendix in Section E.4. The mSUGRA SUSY signal grid as well as the Standard Model background samples are described in Section 4.5.2 and in Section 4.5.1, respectively. The object and event selection criteria are the same as applied for the 10 TeV SUSY searches. However, for simplicity only channels with $\geq 2, \geq 3$ or ≥ 4 jets and exactly 0, 1 or 2 leptons (with opposite charge) are considered. The event selection cuts are detailed in Table 7.1 and Table 7.3.

10.2. Prospects for a discovery in the mSUGRA parameter space

Figure 10.1 shows the M_{eff} and E_T^{miss} distribution after applying the 4 jet 0-lepton selection cuts (top plots) as well as the final M_{eff} distribution for the 2 and 3 jet 0-lepton channel (bottom plots). The effective mass and transverse mass distribution after applying the 4 jet 1-lepton selection cuts are presented in Figure 10.2. Further distributions for lower jet multiplicities as well as for the results of the 2 lepton analyses can be found in the Appendix Section E.5 Figure E.7, E.8 and

E.9. All distributions are normalised to an integrated luminosity of $\mathscr{L} = 1$ fb^{-1}. The individual SM background contributions are indicated as described in the legend. The error bars in all figures reflect the statistics of the Monte Carlo samples. The M_{eff} distributions after applying all selection cuts are used to search for a deviation between signal and Standard Model background ("data events"), illustrate with white open circles and the Standard Model expectation, shown as hashed histogram in the plots.

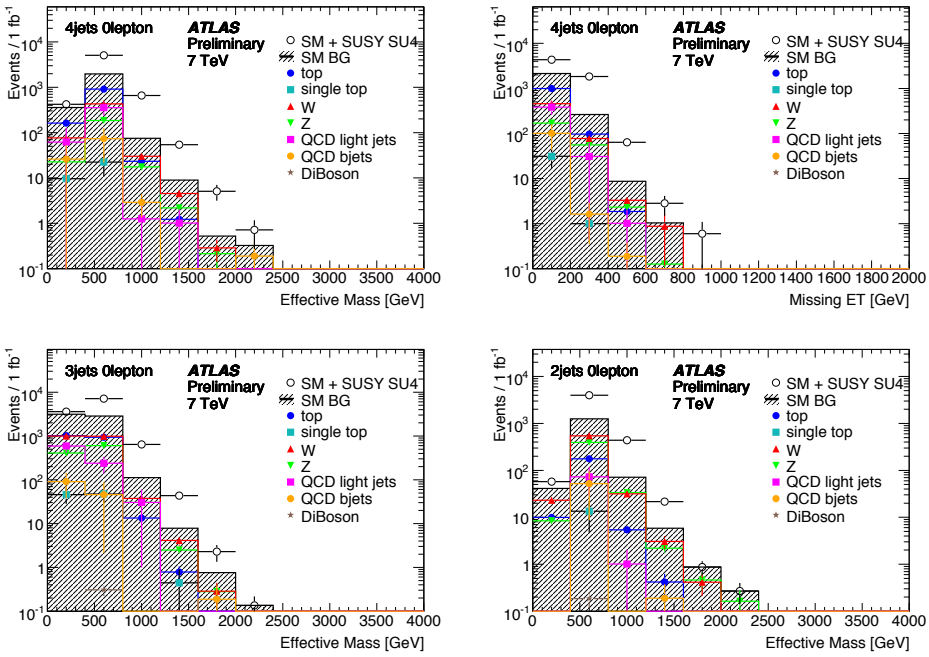

Figure 10.1: Effective mass (left top plot) and missing transverse energy (right top plot) distributions for the 4 jet channel with 0 leptons and the effective mass distribution for the 3 jet (left bottom plot) and 2 jet 0-lepton channel (right bottom plot) for $\mathscr{L} = 1$ fb^{-1}. The error bars reflect the statistical uncertainties of the Monte Carlo samples.

Table 10.1 summarises the predicted number of SU4 SUSY signal and background events scaled to an integrated luminosity $\mathscr{L} = 1$ fb^{-1} after each selection cut for the 4 jet 0-lepton channel. In the first column are the expected number of events after the object selection cuts (see Section 7.3). After applying the p_T jet and E_T^{miss} cut (2nd column) the dominating SM backgrounds are QCD jets and top quark pairs. There is also a strong contribution from associated gauge boson production. In order to isolate the SUSY signal from the SM background, a $E_T^{miss}/M_{\text{eff}}$ >0.2 cut, a $S_T > 0.2$ cut and a $\Delta\phi$ cut between the three leading jets and the missing transverse momentum are applied. The 2nd and 3rd cut reduce the multi-jet background, which have a lower $E_T^{miss}/M_{\text{eff}}$ fraction than the signal and a more more pencil-like event shape, while cut4 is the most efficient cut to reduce multi-jet background with fake E_T^{miss} from mis-measured jets.

sample name	object selection	p_T jet + E_T^{miss} cut	$\frac{E_T^{miss}}{M_{\text{eff}}}$ cut	S_T cut	$\Delta\phi$ cut	lepton cut	$M_{\text{eff}} >$ 800 GeV
$Z+$jets	4672556.3	1657.7	1067.8	725.4	661.2	227.7	19.9
DiBoson	1345.2	0.9	0.7	0.5	0.5	0.0	0.0
$W+$jets	39363268.1	5354.0	3140.4	2111.6	1891.2	539.9	35.1
QCD	1798435060.0	30375.7	5447.7	3468.5	1577.5	520.2	5.4
top pairs	395998.1	11162.6	7197.2	5424.7	4955.9	1098.4	24.6
single top	54762.2	523.5	371.1	303.5	296.3	32.0	0.0
total SM	1842922990.0	49074.4	17224.7	12034.2	9382.1	2418.2	85.0
SU4	106507.3	29761.0	21031.9	16331.7	14946.9	3810.6	637.0

Table 10.1: Cutflow table for the 4 jet 0-lepton analysis. Presented is the expected number of events for $\mathscr{L} = 1$ fb^{-1} for the different event selection cuts.

The last cut is the lepton veto cut that defines the 0-lepton signature.
The background contribution of the different Standard Model backgrounds after applying all cuts did not change much compared to the results for 10 TeV and 200 pb^{-1}. The $Z+$jets and $W+$jets backgrounds dominate the 2 jet 0-lepton selection (see Figure 10.1, bottom right plot), whereas for events with 4 selected jets and 0 lepton the background (see Figure 10.1, upper plots) is dominated by top pair production. In the 3 jet 0-lepton channel the $W+$jets and top backgrounds are found to be almost equally large. The top pair production and $W+$jets background come from a lepton that was not reconstructed, while the $Z+$jets background are mainly $Z \to \nu\bar{\nu}+$ jets events.
In the 1-lepton channel a $M_T > 100$ GeV cut was applied (see Figure 10.2, right plot and Figure E.7), that suppresses effectively top and W production background events. The QCD background is reduced to a negligible level for all jet multiplicities by the lepton and E_T^{miss} cuts. The single top production is comparable with the background from $Z+$jets. The dominating background in this channel after the final event selection is, as expected, top pair production with an increasing contribution from $W+$jets for lower jet multiplicity channels. Both backgrounds are expected to be be better understood than QCD background, especially for the first data.
The background in the opposite sign 2 lepton channels consists mainly of top-pairs. In contradiction to the 10 TeV plots (see Figure E.8 and E.9) there are no Diboson events that contribute. Although no Z-mass veto was applied the background from Z production was found to be very small.

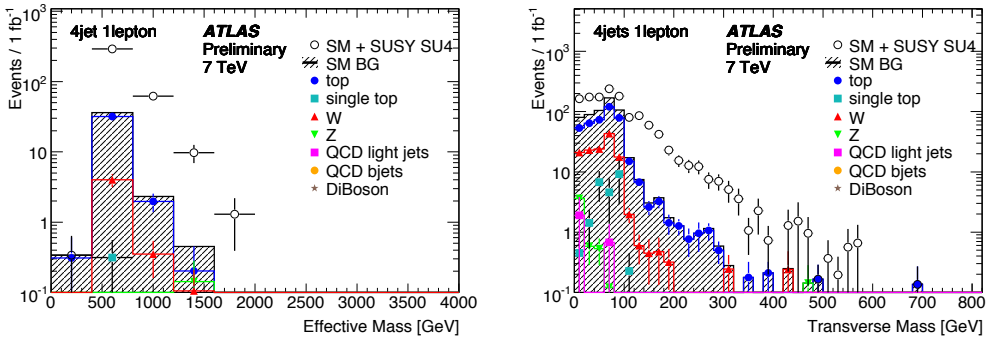

Figure 10.2: Effective mass M_{eff} (left plot) and transverse mass M_T (right plot) distributions for the 4 jet channel with 1 lepton for $\mathscr{L} = 1$ fb^{-1}. For the transverse mass distribution all cuts, beside the M_T cut, are applied. The error bars reflect the statistical uncertainties of the Monte Carlo samples.

10.2.1. Discovery potential

The discovery reach was calculated as described in Section 7.5 after applying a procedure in order to find the optimal M_{eff} cut for $\mathscr{L} = 0.5$ fb^{-1}, $\mathscr{L} = 1$ fb^{-1} and $\mathscr{L} = 2$ fb^{-1}. A systematic uncertainty of $\pm 70\%$ was used for the 0.5 fb^{-1}, $\pm 50\%$ for the 1.0 fb^{-1} and $\pm$ 35% for the 2 fb^{-1} scenario. The errors are reevaluated from the 14 TeV studies (see Section 7.5.3). These numbers are just estimates and need to be validated with first collision data. In the following, all discovery reach plots present only the channels with the largest discovery reach for each lepton multiplicity. Figure 10.3 shows the 5σ discovery potential for the 4 jet 0-lepton, the 4 jet 1-lepton and the 2 jet 2-lepton (OS and SS) channels for three different luminosities in the m_0–$m_{1/2}$ (left plots), as well as in the min. squark mass–gluino mass ($m_{\tilde{q}}$–$m_{\tilde{g}}$)[1] parameter space (right plots). The dashed line in the right plots is the line of equal squark and gluino masses. The discovery reach for the 2 jet 2-lepton same sign (SS) channel was determined and provided by the group of Wisconsin. The 4 jet 0-lepton and 1-lepton channels have the largest discovery potential for the studied mSUGRA signals. This result agrees very well with the estimates for a centre-of-mass energy of 14 and 10 TeV. For a scenario were the gluino mass is similar to the mass of the lightest squark, squark and gluino masses up to 600 (700) GeV could be discovered assuming an integrated luminosity of $\mathscr{L} = 0.5(1.0)$ fb^{-1}. For $\mathscr{L} = 2.0$ fb^{-1} the 4 jet 0 and 1-lepton analyses have a very similar discovery potential for SUSY signals with $m_0 > 500$ GeV, squark/gluino masses up to 800 GeV could be discovered (see Figure 10.3, bottom plots).
Especially for the first data also the lower jet multiplicity channels are interesting. The discovery reach lines for the 2–4 jet 0 and 1-lepton analyses for $\mathscr{L}$= 0.5 fb^{-1} and a systematic uncertainty of 70% are illustrated in Figure 10.4. The 2 jet channel seems to be slightly better than the 3 jet channel.

[1] Squark mass $m_{\tilde{q}}$ means min. squark mass under the consideration of only first and second generation squarks.

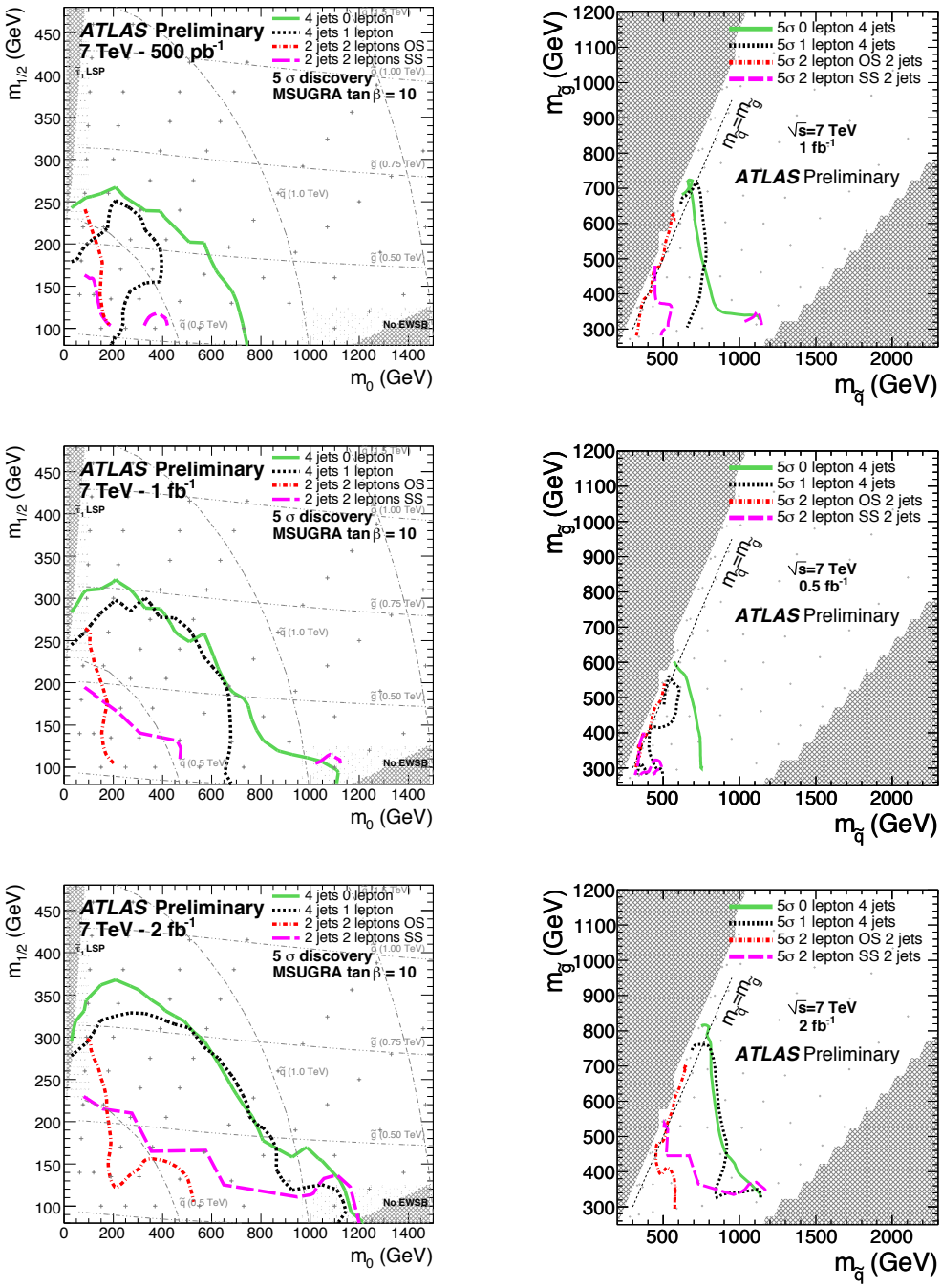

Figure 10.3: The 5σ discovery potential for the 4 jet 0, 1-lepton and 2 jet 2 lepton analyses in the m_0–$m_{1/2}$ (left plots) and $m_{\tilde{q}}$–$m_{\tilde{g}}$ (right plot) parameter space for mSUGRA models with $\tan\beta = 10$. The assumed integrated luminosity is 0.5 fb^{-1} (top plots), 1 fb^{-1} (middle plots) and 2.0 fb^{-1} (bottom plots). A systematic uncertainty of $\pm 70\%$ for $\mathscr{L} = 0.5$ fb^{-1}, of $\pm 50\%$ for $\mathscr{L} = 1.0$ fb^{-1} and $\pm 35\%$ for $\mathscr{L} = 2$ fb^{-1} was considered.

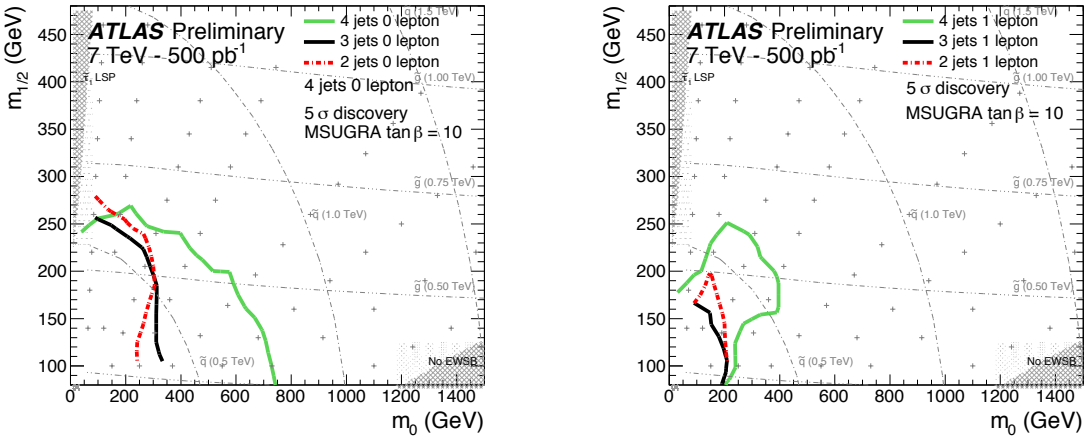

Figure 10.4: 5σ discovery potential in the m_0-$m_{1/2}$ parameter space for mSUGRA models with $\tan\beta = 10$. The results for the 2 jet, 3 jet and 4 jet 0 lepton (left plot) and 1-lepton analyses (right plot) for an integrated luminosity of $\mathscr{L} = 0.5$ fb^{-1} are presented.

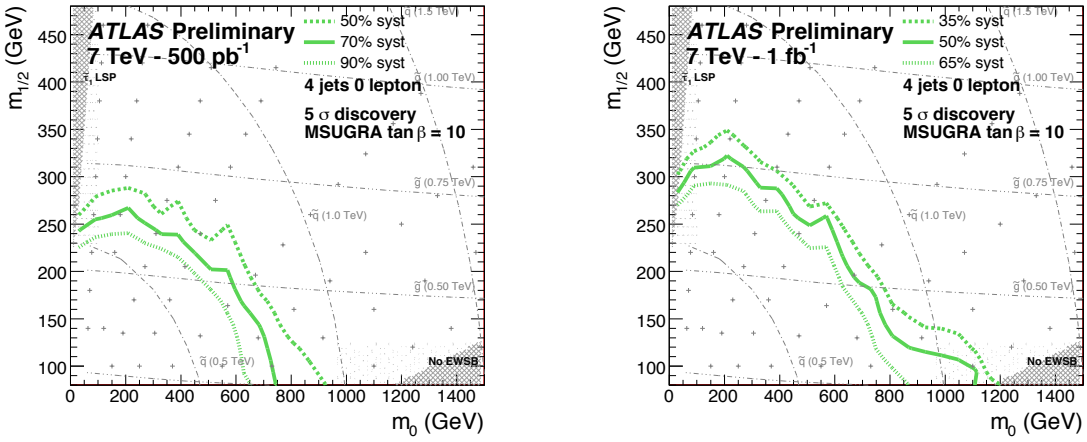

Figure 10.5: 5σ discovery potential for the 4 jet 0-lepton channel in the m_0-$m_{1/2}$ mSUGRA parameter space for SUSY models with $\tan\beta = 10$. The integrated luminosity is $\mathscr{L} = 0.5$fb^{-1} (left plot) and $\mathscr{L} = 1$fb^{-1} (right plot). Each plot shows the effect of the variation of the assumed systematic uncertainty.

This is probably due to the small squark and gluino masses of the discovered SUSY models. For most of the models with $m_0 < 200$ GeV, which could be discovered with the 2 and 3 jet 0-lepton analysis, is the squark mass lighter than the gluino mass and $\tilde{q}\tilde{q}$ production is enhanced.

The squark tends to decay into a quark and a neutralino, such that the 2 jet + E_T^{miss} topology is favoured. In order to estimate the influence of different systematic uncertainties on the discovery reach potential, the systematic uncertainty was varied around the default values given above. For an integrated luminosity of $\mathscr{L} = 0.5$ fb^{-1} a systematic uncertainty of 50% or 90% was assumed and for an integrated luminosity of $\mathscr{L} = 0.5$ fb^{-1} the discovery potential was studied taking a systematic uncertainty of 35% and 65% into account. Since similar effects appear when the systematic uncertainty is varied for the different SUSY channels, Figure 10.5 shows only the results of the variation for the 4 jet-0 lepton channel. The discovery reach lines indicate that a large systematic uncertainty can have an influence, however for the studied mSUGRA models it is a comparatively small effect on the overall discovery potential.

10.2.2. Summary

The discovery potential in the scanned mSUGRA parameter space for inclusive SUSY search channels with ≥ 2, ≥ 3 or ≥ 4 jets and 0, 1 or 2 leptons (OS) assuming an LHC centre-of-mass energy $\sqrt{s} = 7$ TeV and an integrated luminosity of $\mathscr{L} = 0.5 - 2$fb^{-1} (first year(s) LHC running scenario) indicate that ATLAS can discover signals of R-parity conserving SUSY models with squark and gluino masses less than 600-700 GeV. This mass range is clearly above recent exclusion limits defined by the Tevatron experiments.

11. Analysis of first $\sqrt{s} = 7$ TeV LHC collision events

The first collision candidate in ATLAS was observed at the end of November 2009. During the remaining weeks of 2009, LHC continued to deliver collisions at 900 GeV centre-of-mass energy, which corresponds to the injection energy from the SPS. Towards the end of the data taking in 2009, the energy was increased to 2.36 TeV. The ATLAS detector started recording first collision events at a centre-of-mass energy of $\sqrt{s} = 7$ TeV at the end of March 2010.
This chapter presents a first look at these collision events recorded between March and July 2010 and corresponding to a total integrated luminosity of $\mathscr{L} = 70 \pm 8$ nb^{-1}. The goal is not to study in detail the performance of the ATLAS detector. It is rather to compare the most important kinematical variables and physics objects for the 0-lepton supersymmetry searches, which were used in the Monte Carlo based analyses discussed in the previous chapters, with the measured data in order to see how well the simulation has reproduced them. Selections based on these variables are expected to be not only sensitive to R-parity conserving SUSY particle production involving jets and missing transverse momentum with no leptons, but also to any model in which one or more strongly-interacting particles decay semi-invisibly.

11.1. Experimental setup

11.1.1. Monte Carlo simulations

The signal and background Monte Carlo samples used for a comparison with the measured data events are generated at $\sqrt{s} = 7$ TeV with the PYTHIA (QCD jet production), ALPGEN (production of $W^{\pm}$ or Z^0 bosons in association with jets), MC@NLO and HERWIG (with JIMMY) ($t\bar{t}$ process, SUSY signal) event generators (see Section 4.2) using a special set of parameters tuned by ATLAS for the 2009 Monte Carlo generation [215] (see Section 4.2.1). All events are run through the GEANT4 based simulation (full simulation) (see Section 4.3.1). The used samples are summarised in the Appendix Section D in Table D.3 together with the corresponding cross sections of the processes. The different production steps are discussed in Chapter 4. The SUSY signal

SU4 spectrum and branching ratios were calculated using ISAJET [73] version 7.75, the events are generated using the HERWIG++ generator. The inclusive SUSY production cross section is calculated at leading order by HERWIG++ to be 42.3 pb and by PROSPINO at next-to-leading order to be 59.9 pb.

Normalisation The QCD multijet processes are the dominant background for this analysis since relatively low p_{T} jets cuts are applied. The QCD Monte Carlo used is PYTHIA and only leading order in the strong coupling constant. Therefore it is not expected that it correctly describes the absolute normalisation of the QCD cross section. To set the QCD normalisation, a control region is defined by applying the dijet cuts asking for at least two jets with $p_{\mathrm{T}} > 30$ GeV and at least one of both with $p_{\mathrm{T}} > 70$ GeV. This selection is known to be dominated by QCD production and contributions from other processes such as vector boson + jets are negligible in this region. Moreover the cuts are sufficiently close to the interesting region studied in the analyses. The total number of events measured in the control region for $\mathscr{L} \approx 70$ nb^{-1} is 108 239 and the resulting determined QCD normalisation factor from data is 0.61. This factor is applied for all jet multiplicities of all studied 0-lepton SUSY channels to obtain the QCD expectation. The PYTHIA QCD prediction has also been compared to a QCD prediction calculated with the ALPGEN generator and only small differences are found (see Figure 7.4 in Section 7.5.3).
The limited number of $W^{\pm} \to l\nu$ and $Z^0 \to \nu\nu$ events in the current data sample precludes a data-driven estimate of the normalisation. The samples are therefore normalised to the integrated luminosity accumulated using the cross sections that are listed in Table D.3. The same scaling factor has been applied for all ALPGEN parton multiplicities. For the W/Z + jets prediction the Next-to-Next-to-Leading Order (NNLO) cross sections obtained from the FEWZ program [231] was used, while the $t\bar{t}$ cross sections were normalised to the next-to-leading order and next-to-leading log result [188].
The SU4 sample presented in all figures is normalised to the next-to-leading-order cross section after the normalisation to the measured integrated luminosity.

11.1.2. Trigger

The trigger used is the calorimeter jet trigger of the first trigger level "L1_J15". The trigger efficiency has been studied for the initial LHC running scenario (see Figure 7.3 in Section 7.4) and is greater than 99% for the events with at least one jet with $p_T > 70$ GeV.

11.1.3. Object and event selection

The used SUSY object and event selection requirements are detailed in Chapter 7 and have been already extensively discussed in the previous Chapters 8-10. In the following they are only briefly summarised.

Object selection

The object selection criteria are similar to the ones used for the Monte Carlo studies discussed before, but have been slightly modified according to the detector calibration requirements obtained with the first collision data [264,268,269,339,340]: Jets are reconstructed using the infrared- and collinear-safe anti-k_T jet clustering algorithm with a radius parameter of 0.4 using the topological calorimeter clusters as input. All clusters signals are reconstructed at the 'electromagnetic' (EM) energy scale and the measured jet transverse momentum is corrected using a Monte Carlo based calibration. The jet acceptance cuts are $p_T > 20$ GeV and $|\eta| < 2.5$. Muons are reconstructed by the STACO algorithm, while electrons are required to pass the medium electron selection as discussed in Chapter 5 and defined in Ref. [104], excluding the calorimeter crack region $1.37 < |\eta_2^{clus}| < 1.52$. Both objects are selected as follows: electrons and muons with transverse momentum $p_T > 10$ GeV, and a pseudo-rapidity $|\eta_2^{clus}|$ smaller 2.47 for electrons and $|\eta| < 2.5$ for muons. In addition, electrons and muons are required to be isolated. The missing transverse energy is constructed from the vector sum of the topological calorimeter cluster cells on EM scale. An overlap removal is applied between electron and jets and muon and jets. More details about the used object selection and the overlap removal can be found in Section 7.1.

Event selection

The overall selection starts by requiring the presence of a "L1_J15" trigger object and vetoing events containing electrons or muons. For the early analysis of the collision data presented a looser set of selections relative to the earlier Monte Carlo studies is employed providing a larger sample of events to compare with the Standard Model expectations. The p_T jet cut of the leading jet is reduced to 70 GeV, the additional applied transverse momentum jet cuts to > 30 GeV. The missing transverse energy should exceed at least 40 GeV. No cut on the transverse sphericity was used. The same cut as for the MC studies on $\Delta\phi(jet, E_T^{miss})$ and $E_T^{miss}/M_{\text{eff}}$ was applied. All applied cuts are summarised in Table 7.1 (last column).
Fake missing transverse energy (fake E_T^{miss}) can result from detector problems or non-collision sources. Identification and cleaning of such events are necessary prerequisites for SUSY searches. Therefore additional quality criteria are applied to improve the rejection of events containing jets which are consistent with calorimeter noise, cosmic rays, beam-induced backgrounds or out-of-time energy deposits. All "cleaning" cuts are discussed in Section 7.3.1. The pre-selection requirements include the rejection of events that do not have a primary reconstructed vertex with at least five associated tracks.

11.1.4. Systematic uncertainties

The studied sources of systematic uncertainties on the Standard Model prediction are discussed in Section 7.5.3. For the estimation of the Standard Model prediction only the most important sources of the experimental systematic errors were considered. No attempt has been made in this early study to distinguish between errors correlated and uncorrelated between bins or selections.
The dominating uncertainty in this measurement is the jet energy scale (JES) uncertainty, de-

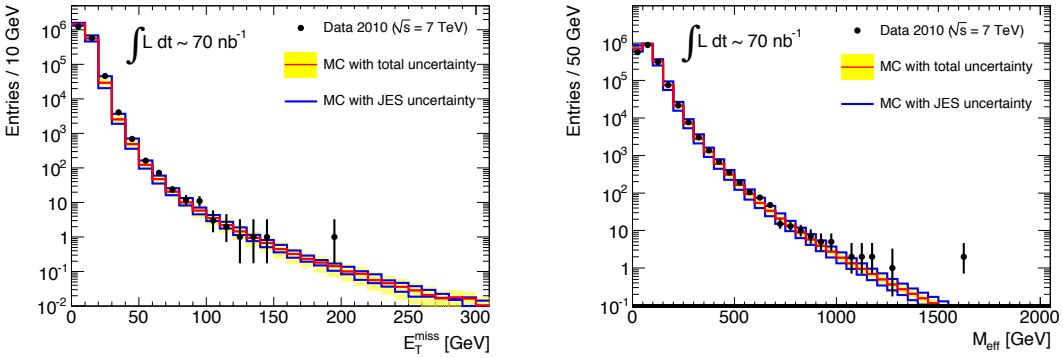

Figure 11.1: Distributions of the missing transverse energy (left plot) and the effective mass (right plot) for the 4 jet 0-lepton channel after applying the object selection and event cleaning cuts. The Monte Carlo prediction (red line) is shown together with the JES uncertainty (blue lines) and the total uncertainty (yellow band). The black points are the measured data events for an integrated luminosity of $\mathscr{L} = 70$ nb^{-1}.

termined as a function of jet transverse momentum and pseudo-rapidity. Table 11.1 details the number of data events compared to the Standard Model expectation and to the expectation for the up and down variation of the jet energy scale. After applying the $E_T^{miss} > 40$ GeV cut, in all channels the data is above the expectation, since these channels are correlated. The estimate of the JES uncertainty is typically 10% for jets in the range 20 GeV $< p_T <$ 60 GeV and about 7% for jets at higher p_T. The missing transverse momentum E_T^{miss} was coherently recalculated with the variation of the jet energy scale (see Section 7.5.3).

Further uncertainties taken into account are the uncertainty on the integrated luminosity that is estimated be $\pm$11% for the $W^{\pm}$ + jets, Z^0 + jets and $t\bar{t}$ production [341]. For this first estimation no theoretical uncertainty was assigned to the Monte Carlo generators predictions. The uncertainty on the normalisation of the $W^{\pm}$ + jets and Z^0 + jets production will be considered in future studies when more data is acquired. The selected events all contain high p_T jets, no additional uncertainty has been assigned to account for possible mis-modelling of the transverse momentum component from calorimeter cells not contained within jets.

The resulting systematic uncertainty on the number of events expected after the jet and E_T^{miss} cuts are applied is approximately 25% for the monojet analysis and the 2 jet analysis, 40% for the 3 jet analysis and 50% for the 4 jet analysis. The statistical $\sqrt{N}$ and all systematic uncertainties are added in quadrature for the estimation of the total uncertainty. Table 11.2 gives the combined statistical and systematic uncertainties for the Monte Carlo prediction for every SUSY analysis cut. Figure 11.1 presents the missing transverse energy and the effective mass distribution for the 4 jet 0-lepton channel after applying only the object selection cuts. The Monte Carlo prediction (red line) is shown together with the JES uncertainty (blue line) and the total uncertainty (yellow band). The black points are the measured data events.

channel	**DATA**	**MC**	**JES UP**	**JES DOWN**
monojet $p_T^{jet_1} > 70$ GeV, $p_T^{jets} \leq 30$ GeV	21227	22761	29601	16996
2 jet channel after $p_T^{jet_1} > 70$ GeV, $p_T^{jet_2} > 30$ GeV	108239	108267	139150	82777
3 jet channel after $p_T^{jet_1} > 70$ GeV, $p_T^{jet_{2,3}} > 30$ GeV	28697	30716	41142	22779
4 jet channel after $p_T^{jet_1} > 70$ GeV, $p_T^{jet_{2,3,4}} > 30$ GeV	5329	5592	7881	3975
monojet after p_T jet and $E_T^{miss} > 40$ GeV cut	73	46	68	36
2 jet channel after p_T jet and $E_T^{miss} > 40$ GeV cut	650	450	640	325
3 jet channel after p_T jet and $E_T^{miss} > 40$ GeV cut	325	231	337	162
4 jet channel after p_T jet and $E_T^{miss} > 40$ GeV cut	116	84	129	55

Table 11.1: Number of collision data events and Monte Carlo prediction with a change in the jet energy scale (JES) for an integrated luminosity of $\mathscr{L} = 70$ nb^{-1}. The first four rows show the number of events after applying the lepton veto and the p_T jet requirement, the last four rows after applying an additional E_T^{miss} cut.

11.2. Results

The following presented variables are expected to be sensitive and important for any model with one or more strongly-interacting particles, which decay semi-invisibly. This includes R-parity conserving SUSY models. Only final states without any leptons are considered. Similar distributions for example of the E_T^{miss}, p_T jet or $\Delta\phi(jet, E_T^{miss})$ for events with missing transverse energy and 1- and 2-lepton or b-jets in the final state can be found in the References [332, 349].

11.2.1. Number of events

A comparison of the number of events passing different stages of the event selection between data and Monte Carlo samples for every applied analysis cut is given in Table 11.2. The cutflow table of the different Standard Model contributions is presented in the Appendix in Table E.5. It can be seen that, within the uncertainties, data is in good agreement with the Monte Carlo. The ≥ 2, ≥ 3 and ≥ 4 jet analyses overlap, therefore there are correlations between the corresponding entries in the table. The QCD normalisation factor, that was calculated for the ≥ 2 jet channel and applied to all jet-selections, can be determined from the numbers in the table. The factors are in agreement for all channels and seem to provide a good description of the overall normalisation in the 0-lepton channels. Since the jet energy scale uncertainty was used to estimate the E_T^{miss} uncertainty, a change in the jet energy scale uncertainty will therefore produce a correlated change in the number of events in the various selections after the E_T^{miss} requirement. However the numbers of observed events after the E_T^{miss} cut (see Table 11.2, last row) are within $1\,\sigma$ in agreement with

the expectation.

channel		**after jet cuts**	**after E_T^{miss} cut**	**after $\Delta\phi$ cut**	**after $\frac{E_T^{miss}}{M_{\text{eff}}}$cut**
Monojet	Data	21 227	73	-	-
	Monte Carlo	$23\,000^{+7000}_{-6000}$	46^{+22}_{-14}	-	-
≥ 2 jets	Data	108 239	650	280	4
	Monte Carlo	$108\,000^{+31\,000}_{-25\,000}$	450^{+190}_{-120}	200^{+110}_{-65}	6.6 ± 3
≥ 3 jets	Data	28 697	325	136	0
	Monte Carlo	$31\,000^{+10\,000}_{-8000}$	230^{+100}_{-70}	100^{+55}_{-30}	1.9 ± 0.9
≥ 4 jets	Data	5329	116	54	1
	Monte Carlo	5600^{+2300}_{-1600}	84^{+45}_{-30}	43^{+26}_{-16}	1.0 ± 0.6

Table 11.2: Number of events observed in the data and expected contribution of the Standard Model processes for the monojet, 2 jet, 3 jet and 4 jet 0-lepton event selection for $\mathscr{L} = 70$ nb^{-1}. The numbers for the SM prediction are after rescaling the QCD background Monte Carlo sample by the normalisation factor as discussed in Section 11.1.1. The quoted uncertainties include statistical and systematic contributions. The first row shows the number of events after the p_T jet cuts, the second row the number of events after an addition E_T^{miss} cut, in the 3rd and 4th row are the number of events after a $\Delta\phi$ and $E_T^{miss}/M_{\text{eff}}$ cut as detailed in Table 7.1.

11.2.2. Non-collision background events

An estimate has been made of the remaining background in the signal selection from cosmic rays in coincidence with primary vertices from minimum-bias collisions by considering fake "jets" in LHC bunches. After the full set of cleanup cuts described in Section 7.1 about 2.3 non-collision events are expected in the monojet channel for $E_T^{miss} > 50$ GeV decreasing to 1.3 for $E_T^{miss} > 70$ GeV and to less than one for $E_T^{miss} > 100$ GeV. By measuring the apparent jet multiplicity in empty and non-colliding bunches the expected number of non-collision background events in the dijet channel is calculated to be approximately 0.1. The rate of fake jets from beam halo muons has been estimated from events recorded during the transit of unpaired LHC bunches. The contribution to the monojet channel is approximately 10 events with jet p_{T} greater than 70 GeV.

11.2.3. Distributions of the studied SUSY variables

The following distributions present the measured data events as points with error bars, which show the Poisson coverage interval corresponding to the number of data events in each bin, to estimate the statistical uncertainty. All results are compared to a normalised QCD PYTHIA prediction and

to the Monte Carlo expectation for the $W^{\pm}$ + jets, Z + jets and $t\bar{t}$ production as discussed. The SUSY signal SU4 is scaled with a factor of 10 to be better visible.

Monojet channel

Figure 11.2 (left plot) shows the distribution of the leading jet after applying the lepton veto and the p_T jet requirement: $p_T(\text{jet1}) > 70$ GeV, events with further jets with a $p_T > 30$ GeV are rejected. In the right plot of the same figure an additional missing transverse momentum $E_T^{miss} > 40$ GeV cut was applied. The measured events are well described by the Monte Carlo prediction.

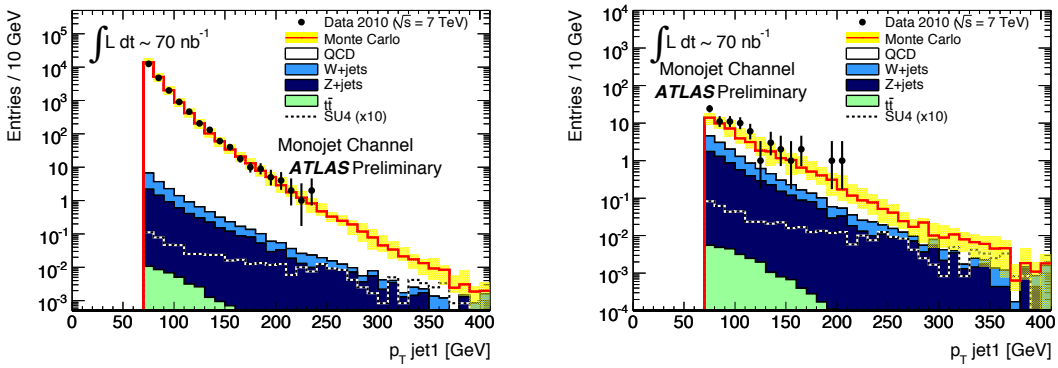

Figure 11.2: Distribution of the leading jet transverse momentum for events in the monojet channel before (left plot) and after (right plot) a cut requiring $E_T^{miss} > 40$ GeV is applied.

The distribution of the missing transverse momentum for events in the monojet channel before any E_T^{miss} requirement is presented in Figure 11.3, the M_{eff} distribution before and after applying the E_T^{miss} cut is illustrated in Figure 11.4. The dominating SM backgrounds are QCD processes, the background from $W^{\pm}$ and Z + jet(s) production becomes important at missing transverse momentum > 50 GeV. These events are predominantly $Z \rightarrow \nu\bar{\nu}$+ jets events and events with leptonic W decays, where the lepton could not be identified. All events with $E_T^{miss} > 40$ GeV have been cross checked, eleven events are candidates for beam halo interactions, in which an energetic photon has been radiated from a halo muon traversing the calorimeter, which is consistent with the expectation. These beam halo events currently contribute mainly to the tail of the distribution in Figure 11.3 and 11.4. The SUSY group works at the moment on defining new event cleaning cuts since a larger contribution of beam halo, cosmics or beam gas events can be expected with increasing luminosity. For example a cut, that is combining tracking and calorimeter information on $\Delta\phi(E_T^{miss,\,\text{calo}}, E_T^{miss,\,\text{track}})$ between the missing transverse energy from the jets and the missing transverse energy calculated from the track looks promissing. An interesting control region for the monojet channel to develop data driven Standard Model background estimation methods could be $\Delta\phi(jet_1, E_T^{miss})$ - the difference in azimuthal angle between the jet and the missing transverse momentum vector. In Figure 11.5 one can see this distribution before (left plot) and after (right plot) applying the $E_T^{miss} > 40$ GeV cut. The QCD dijet events with jets approximately

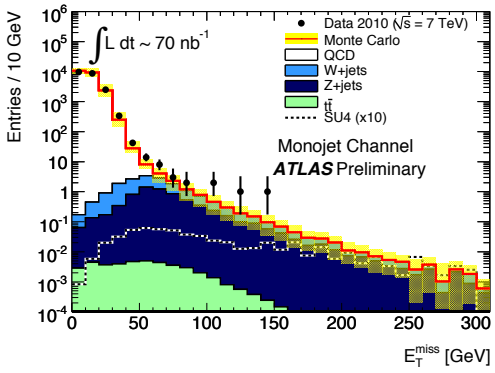

Figure 11.3: Distribution of the missing transverse momentum for events in the monojet channel. Only the jet selection cuts have been applied.

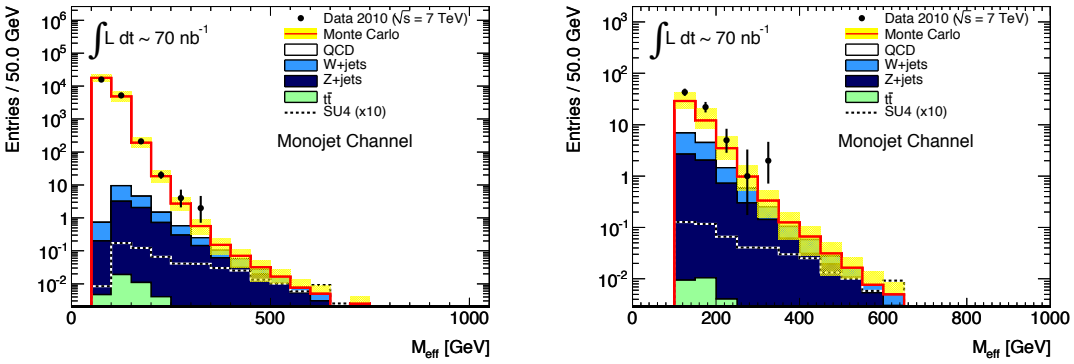

Figure 11.4: Distribution of the effective mass for events in the monojet channel. Only the jet selection cuts have been applied in the left plot. In the right figure $E_T^{miss} > 40$ GeV was required.

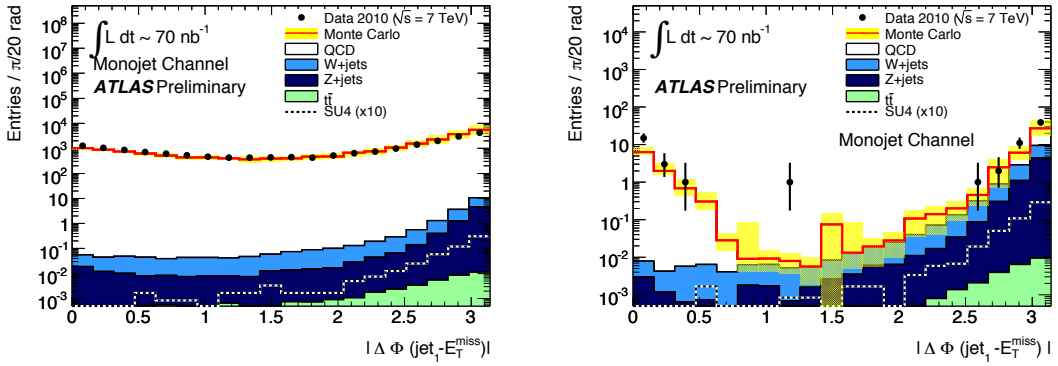

Figure 11.5: Distributions of the difference in the azimuthal angle between the jet and the missing transverse momentum vector for events in the monojet channel without (left plot) and with (right plot) a cut requiring $E_T^{miss} > 40\ GeV$.

back-to-back in the transverse plane appear in this plot at $\Delta\phi \approx \pi$ if the lower energy jet is not reconstructed or out of acceptance, but they can also contribute at $\Delta\phi \approx 0$ if the observed jet recoils against a higher-energy jet beyond the selected rapidity range. After the E_T^{miss} cut nearly only QCD events appear in the region $|\ \Delta\phi(jet_1 - E_T^{miss})\ | < 1.5$. The contributions from Z + jet(s) and $W^{\pm}$ + jet(s) events are dominated by the electroweak boson recoiling against a single jet leading to a peak at π only. Within the systematic uncertainties, which are largely correlated between the bins, the Monte Carlo prediction is in agreement with the data. This single data event with $|\ \Delta\phi(jet_1 - E_T^{miss})\ | \approx 1.18$ is probably a HEC noise event[1].

Two jet channel

The two jet selection criteria are: >1 jet with $p_{\mathrm{T}}^{(jet1)} > 70$ GeV and $p_{\mathrm{T}}^{(jet2)} > 30$ GeV. The distributions of the missing transverse momentum after applying these selection cuts are presented in Figure 11.6. Data and Monte Carlo expectations are in good agreement. It can be seen that the missing transverse momentum distribution is dominated by QCD dijet events. Figure 11.7 shows the M_{eff} distribution before (left plot) and after (right plot) applying a $E_T^{miss} > 40$ GeV cut. The selection without applying the E_T^{miss} cut defines the normalisation region for the QCD Monte Carlo sample, so the overall event numbers in data and Monte Carlo must agree by construction. The Monte Carlo provides a good description of the shape of the data within the systematic uncertainties up to large $M_{\mathrm{eff}} \approx$ 800-1000 GeV.

In the last years many studies have been performed using the contransverse mass m_{CT} and the stransverse mass m_{T2} (see e.g. Ref. [321, 324]). The stransverse mass is an event variable used to recalculate the masses of an unseen pair of particles, each of which decays to a set of (one or

[1]The event has $E_T^{miss} \approx 43\ GeV$ and M_{eff} = 129.9 GeV and its leading jet is out of the jet acceptance region (p_T = 117.0 GeV, η = -2.6) and has a bad cell in calorimeter that leads to $f_{\mathrm{bad,Q}} = 0.62$.

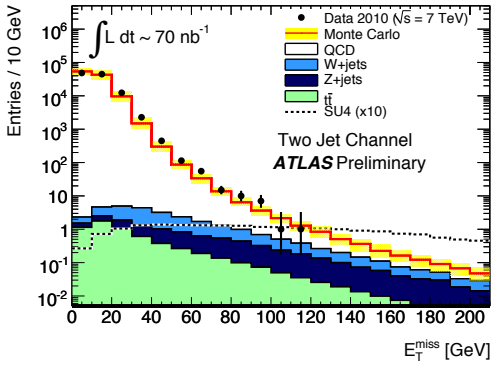

Figure 11.6: Distributions of the missing transverse momentum for events in the 2 jet channel. Only the jet selection cuts have been applied.

more) visible and (one or more) invisible daughters. It gives an estimate of the lowest upper bound of mother particles mass in the beginning of the decay chain. This topology of an unseen pair of particles is common in R-parity conserving supersymmetry models, where the lightest supersymmetric particle is very often the lightest neutralino. This variable is thus interesting for studies of event topologies in which two neutral particles are produced from the decay of two massive particles [322]. The contransverse mass measures the masses of pair-produced semi-invisibly decaying heavy particles and can be applied also to events with non-negligible boosts of the centre-of-mass frame of the heavy states in the laboratory transverse plane [324]. The equations for these variables can be found in Section 7.2 (see equation 7.5 and equation 7.3). The distributions after requiring missing transverse momentum greater than 40 GeV for this selection are shown in Figure 11.8.
Again the data are in agreement with the Monte Carlo prediction given the current size of the systematic uncertainties. For both distributions a SUSY signal would be expected to be present at high values of these variables, indication a high SUSY particle mass.
In the SUSY analyses, discussed in the previous sections, the difference in azimuthal angle between the jet and the missing transverse momentum vector for the leading and second jet are used to reduce the Standard Model background, mainly the QCD events. The distributions are shown in Figure 11.9 after the cut on the missing transverse momentum. In case one jet is mis-measured and the resulting missing transverse momentum is consistent this mis-measurement, $\Delta\phi(jet, E_T^{miss})$ is close to zero. In the analyses a cut on $\Delta\phi(jet_{1,2}, E_T^{miss})$ >0.2 for the two leading jets is applied for the later selection. Both distributions are in agreement with the Monte Carlo prediction which is dominated by the QCD processes due to the loose p_T jet and E_T^{miss} cuts.
Some variables that are sensitive to the angular distributions in the transverse plane of the produced jets are the transverse sphericity S_T and the transverse thrust T_T[2] (defined in Section 7.2, equation 7.6 and equation 7.7) that are shown in Figure 11.10. In a 2 jet event like QCD dijet

[2]It should be noted that transverse thrust is a Lorentz invariant quantity under z-boosts. The variable plotted in the distributions is $(1-T_T)/(1-2/\pi)$.

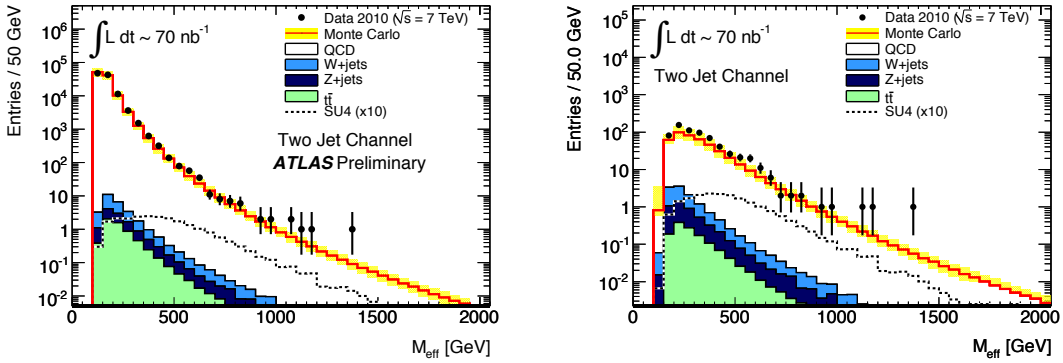

Figure 11.7: Distributions of the effective mass for events in the 2 jet channel. Only the jet selection cuts have been applied, in addition in the right plot also E_T^{miss} >40 GeV was required.

events both variables should be peaked towards zero (S_T =0, T_T = 1) due to the back-to-back configuration. The more spherical SUSY signal or events from $t\bar{t}$ production show higher values in these two quantities. Both distributions, presented after the cut on the missing transverse momentum, describe this behaviour. The data is consistent with the Monte Carlo prediction that is dominated by QCD background. The ATLAS SUSY group plans to use in future the variable transverse thrust instead of transverse sphericity since both variables show a similar Standard Model background reduction efficiency for the SUSY analyses, but the transverse thrust is in contradiction to the transverse sphericity an infrared- and collinear-safe measure of the geometrical properties [350–352].

A further quantity used in Supersymmetry searches is the ratio f of the missing transverse momentum to the effective mass. The cut was introduced to suppress E_T^{miss} that arises from misreconstruction of the jet energies in the calorimeters or from other instrumental effects (see discussion in Section 8.2.3). The distribution of this variable after applying the p_T jet and E_T^{miss} cut can be seen in Figure 11.11 (left plot). A cut on $f > 0.3$ is used for the 2 jet channel, which removes nearly all of the still dominating QCD background events. QCD events have lower f-values while processes with real missing transverse momentum show higher values of this quantity. Also for this variable is the data distribution described by the Monte Carlo prediction. The final effective mass distribution after applying the $f = E_T^{miss}/M_{\text{eff}} > 0.3$ cut and the $\Delta\phi$ cut is presented in Figure 11.11 (right plot). Four data events are found after applying all 2 jet analysis cuts consistent with the expectation of 6.6 ± 3. Note that the Standard Model expectation at high M_{eff} values are due to vector boson plus jets production.

Three jet channel

Distributions of the missing transverse momentum and the effective mass after the p_T jet requirement are presented in Figure 11.12. A cut requiring $E_T^{miss} > 40$ GeV was used for the M_{eff} distribution. Each of the two events with M_{eff} >1500 GeV in Figure 11.12 contains an additional jet

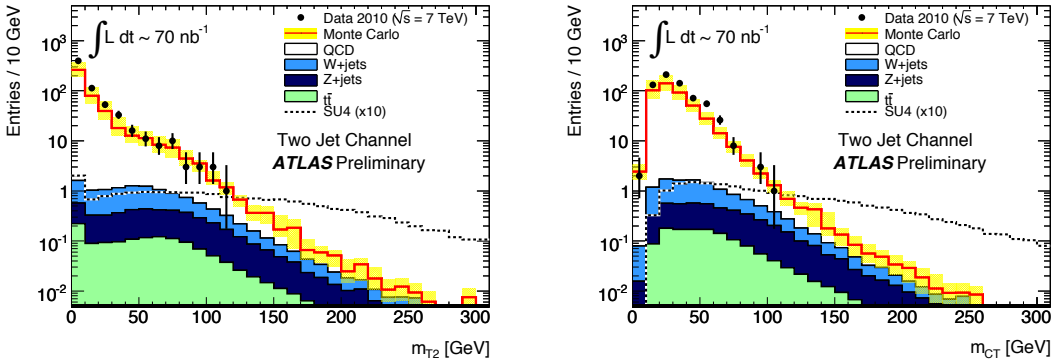

Figure 11.8: Distributions of the stransverse mass m_{T2} and the contransverse mass m_{CT} for events in the 2 jet channel. The plots require $E_T^{miss} > 40$ GeV.

thus also appears in intermediate stages of the 4 jet selection. An event display for one of these events (run number 158116, event number 5513627) can be seen in Figure 11.13. The M_{eff} is about 1.5 TeV when only the the leading three jets are included in the scalar sum and increases to about 1.65 TeV if all four high-energy jets are included. The size of the missing transverse momentum is about 100 GeV. All of the high energy jets are associated with the same primary vertex.
The $\Delta\phi(jet_{1,2,3}, E_T^{miss})$ distributions for the three leading jets and the ratio f of the missing transverse momentum to the effective mass after the $E_T^{miss} > 40$ GeV cut for the 3 jet events are illustrated in Figure 11.14. The final effective mass distribution after applying the cuts on the azimuthal angles $\Delta\phi(jet_{1,2,3}, E_T^{miss})$ for the three leading jets and after the cuts on the ratio $f > 0.25$ between E_T^{miss} and M_{eff} can be seen in Figure 11.16 (left plot). All distributions are well described by the Monte Carlo predictions, given the systematic uncertainties. No data events are found in the final M_{eff} distribution, which is consistent with the expectation of 1.9 ± 0.9.

Four jet channel

Distributions of the missing transverse momentum and the effective mass after the E_T^{miss} cut are shown for 4 jet events in Figure 11.15. Both distributions are reasonably well described by the Monte Carlo prediction, given the experimental systematic uncertainties on the prediction. The two events observed in the 3 jet channel and 4 jet channel at large M_{eff} can be seen in the upper tail of Figure 11.15 (right plot). The effective mass distribution of the remaining event after cutting on the ratio $f > 0.25$ and the difference in azimuthal angle $\Delta\phi(\text{jet}, E_T^{miss})$ is given in Figure 11.16 (right plot). The one data event found is consistent with the expectation of 1.0 ± 0.6.

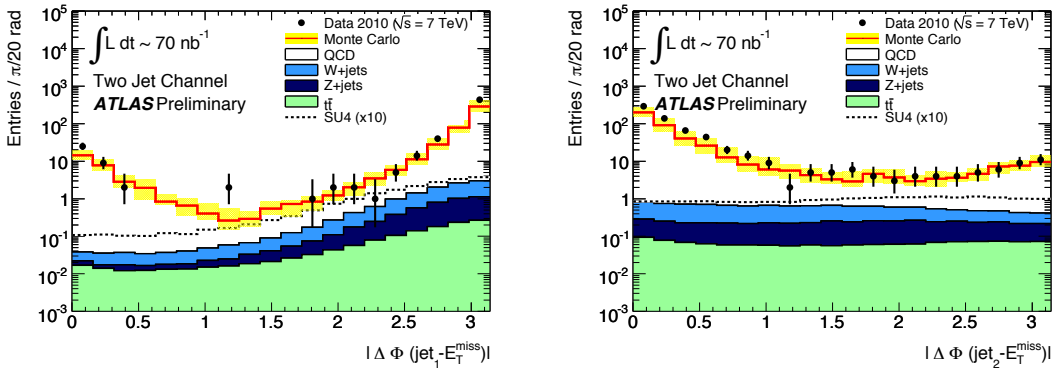

Figure 11.9: Distributions of the difference in the azimuthal angle between the jet and the missing transverse momentum vector for events in the 2 jet channel. The cut requiring $E_T^{miss} > 40$ GeV has been applied.

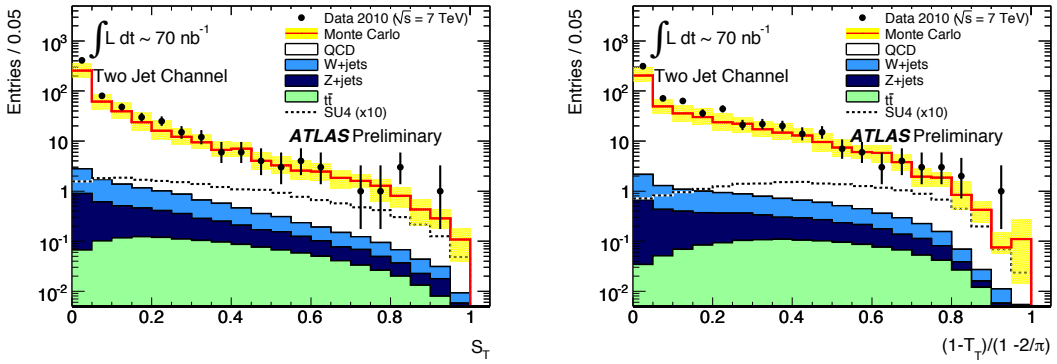

Figure 11.10: Distributions of the transverse sphericity and the transverse thrust for events in the 2 jet channel. The cut requiring $E_T^{miss} > 40$ GeV has been applied.

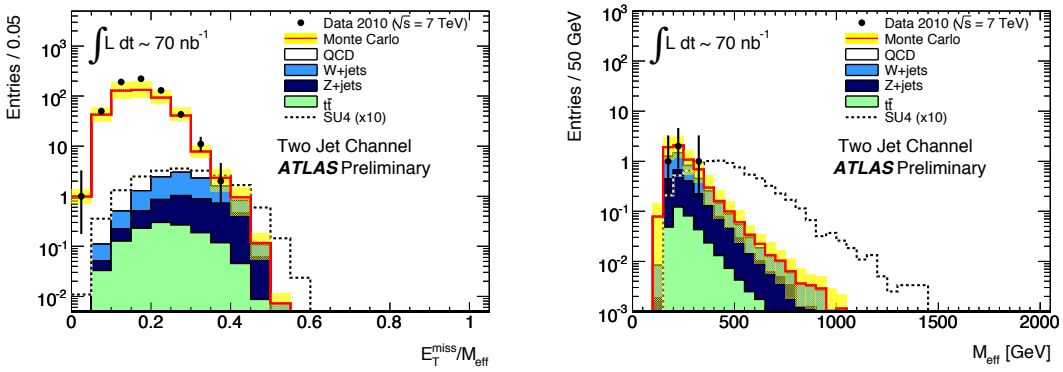

Figure 11.11: Distribution of the missing transverse momentum divided by the effective mass (left plot). A cut requiring $E_T^{miss} > 40$ GeV has been applied. The right plot shows the distribution of the effective mass for events in the 2 jet channel. The cuts on the p_T of the jets, E_T^{miss}, the azimuthal angle difference $\Delta\phi(\text{jet}, E_T^{miss})$ for the leading two jets and in addition a cut on the ratio of the missing transverse momentum over the effective mass have been applied.

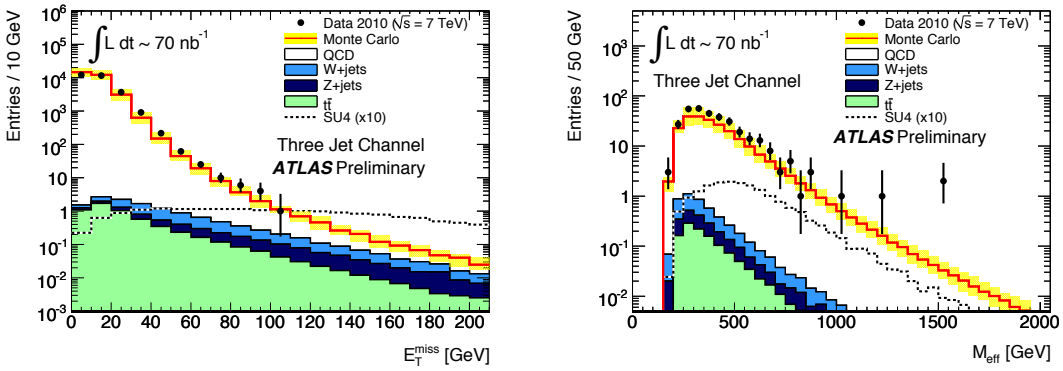

Figure 11.12: Distributions of the missing transverse momentum and the effective mass for events in the 3 jet channel. The cut requiring $E_T^{miss} > 40$ GeV has been applied in the right plot.

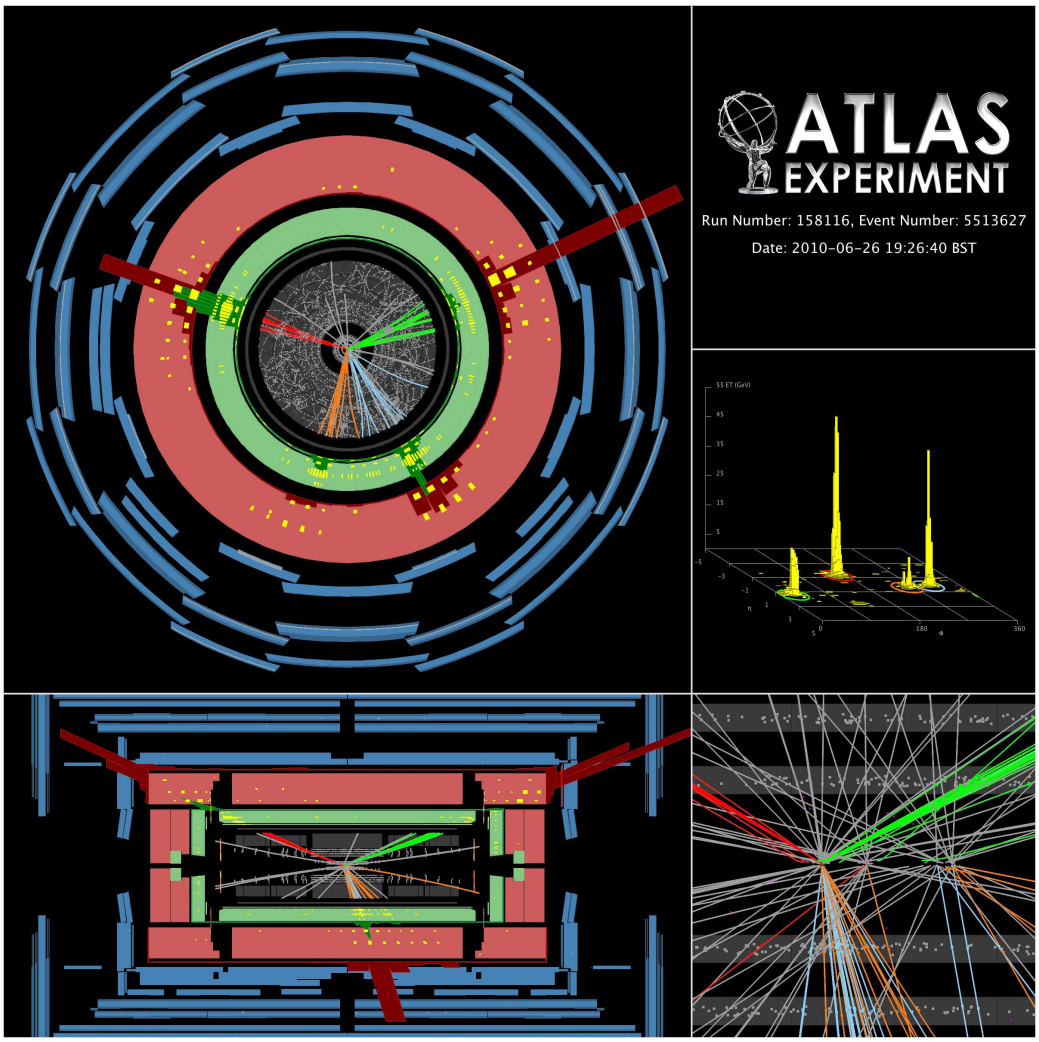

Figure 11.13: Event display of an collision event (run number 158116, event number 5513627) which has M_{eff} of about 1.5 TeV when only the leading three jets are included in the scalar sum, increasing to about 1.65 TeV if all four high-energy jets are included. The size of the missing transverse momentum is about 100 GeV. The missing transverse momentum vector lies within the radius of a jet with a secondary vertex tag. All of the high energy jets are associated with the same primary vertex. The event passed all 3 and 4 jet 0-lepton SUSY selection cuts.

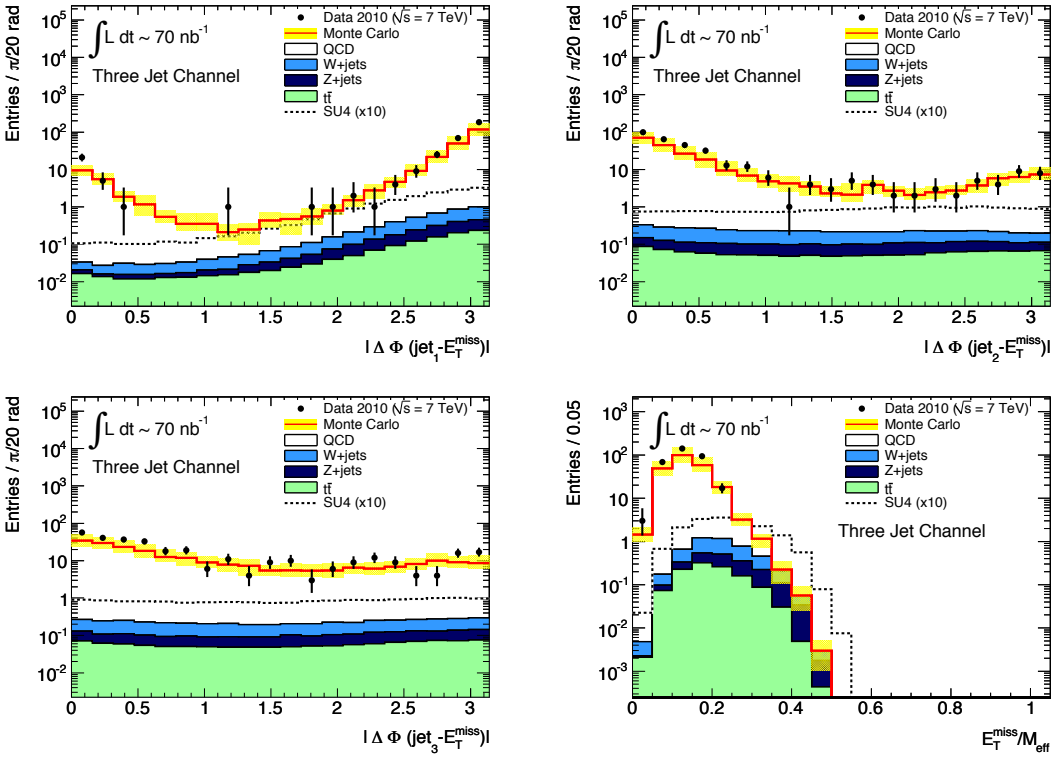

Figure 11.14: $\Delta\phi(\text{jet}, E_T^{miss})$ distributions of the three leading jets (first row and 2nd row, left plot) and the ratio of the missing transverse momentum over the effective mass (2nd row, right plot) after after applying the p_T jet cuts and a cut on E_T^{miss} >40 GeV for the 3 jet collision events.

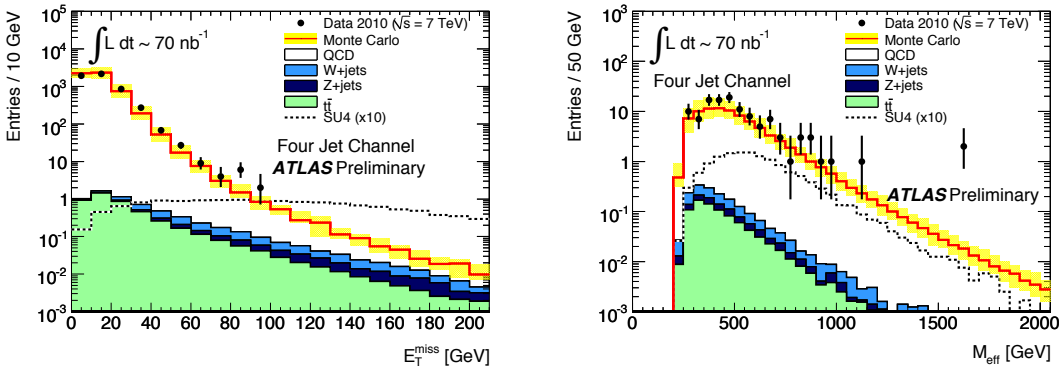

Figure 11.15: Distributions of the missing transverse momentum and the effective mass for events in the 4 jet channel. Cuts on the p_T of the jet have been applied. In the right plot $E_T^{miss} > 40$ GeV was required.

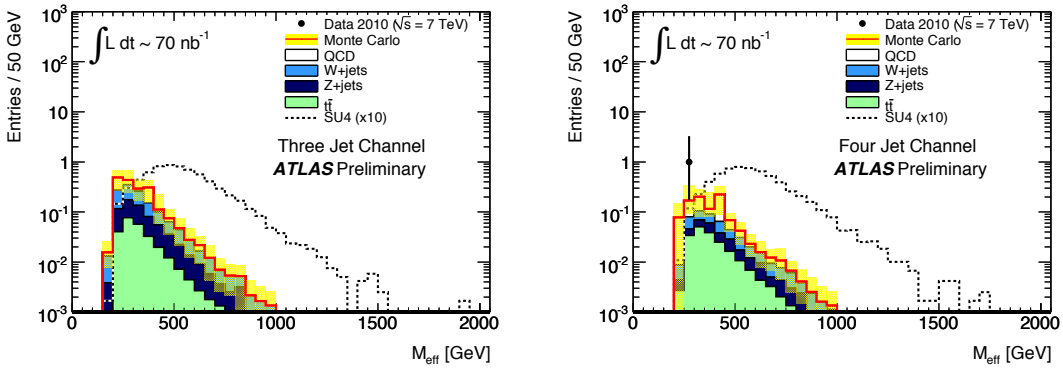

Figure 11.16: Distribution of the effective mass for events in the 3 jet channel (left plot) and 4 jet channel (right plot). The cuts on E_T^{miss}, the azimuthal difference $\Delta\phi(\text{jet}, E_T^{miss})$ and on the ratio of the missing transverse momentum over the effective mass have been applied.

11.3. Summary and conclusion

In this chapter a study of SUSY-sensitive variables for events with missing transverse energy and jets as well as the first distributions of the SUSY 0-lepton analyses have been presented for the first $\sqrt{s} = 7$ TeV collision events of an integrated luminosity of 70 ± 8 nb^{-1}. The measurements are compared to Monte Carlo predictions of Standard Model QCD, gauge boson + jets and $t\bar{t}$ processes. All measured data event distributions of the jet momenta, missing transverse momentum, effective mass, azimuthal angles, stransverse mass and contransverse mass are in agreement with the Standard Model predictions up to values of $E_T^{miss} \approx 100$ GeV, $M_{\text{eff}} \approx 1500$ GeV, $m_{T2} \approx m_{CT} \approx 100$ GeV. These results demonstrate the good level of understanding of the ATLAS detector performance for jets and tracking and that the Monte Carlo simulations describe both the underlying physics, and the detector response for jets and E_T^{miss} within the systematic uncertainties achievable so far. For future studies including larger data sets more refined techniques to estimate the Standard Model expectation and to reduce the experimental uncertainties will be used, improving our understanding of the Standard Model predictions and thereby providing increased sensitivity to new physics. The studies in this chapter are presented in a conference note, see Ref. [353].

12. The Standard Model backgrounds in the 0-lepton channels

A variety of processes exist in the Standard Model that can produce jets + E_T^{miss} in the final state and will be regarded as background to the SUSY 0-lepton signal. These backgrounds are QCD multijet events, both with and without semi-leptonic decays of heavy-flavour (b, c) quarks in jets, $Z \to \nu\bar{\nu}$ + jet events, $W \to l\nu$ + jets (where l = e, μ, τ) and $t\bar{t}$ processes.
The Monte Carlo simulations of physics processes are unlikely to describe accurately what will be seen in the measurements. The shapes of kinematic distributions of the Standard Model background events have to be understood, especially in regions where they could impact the search for new physics. Therefore data-driven methods have to be developed to determine individual background rates for every SUSY channel. Detailed studies have been performed for a centre-of-mass energy of 14 TeV and can be found in Ref. [337], data-driven background procedures for $\sqrt{s}$ = 7 TeV and lower luminosities are still in development.

In the following possible data driven methods to estimate the main Standard Model backgrounds to the 0-lepton analyses with first collision events are briefly summarised.

12.1. QCD background

Jet mis-measurements can create fake E_T^{miss} which comes mainly from mis-measured QCD dijet events. Since the QCD cross section is not determined with high precision and the kinematic distributions such as the p_T spectra or E_T^{miss} are also difficult to predict, this background is most difficult to estimate. Especially searches for SUSY signatures with large E_T^{miss} rely on the understanding of the tails of the E_T^{miss} distributions in QCD events that are very sensitive to the detector performance and to the detailed composition and kinematics of QCD events. As Figure 11.4, Figure 11.11 and Figure 11.16 (see Chapter 11) show, a large fraction of the QCD background can be removed by requiring a large amount of E_T^{miss}. Especially for the first data studies the monojet and 2 jet 0-lepton channel are most interesting since they contain only very few QCD background events. Studies to estimate QCD events are for example jet response correction methods that se-

lect back-to-back dijet events to measure response functions for Monte Carlo and data and thus obtain correction factors or jet smearing methods. Another possibility is to obtain normalisation factors (k-factors) in a defined controll region, that is for example by reversing the $\Delta\phi(jet, E_T^{miss})$ cuts, and to use these factors for the signal region assuming that the k-factor would agree in both regions.

12.2. W + jets and $t\bar{t}$ processes

The electroweak backgrounds such as $W+$jets and the $t\bar{t}$ processes are also challenges, but might be less difficult to controll. The $W+$jets and $t\bar{t}$ background in the 0-lepton channel are due to an undetected lepton and could be determined with a M_T-method similar to the one used for the 1-lepton channel as discussed in Ref. [337]. A control sample is defined, which requires one lepton and the standard jet selection. The QCD background is rejected by the lepton selection and applying an additional transverse mass $M_T < 100$ GeV cut and a cut on E_T^{miss}. The lepton is replaced and kinematic variables are recalculated ("replacement method"). Another possibility is a kinematical fit using the contransverse mass m_{CT} distribution as controll region or a combined fit methods. Both selections are imposed to estimate the shape of the M_{eff} distribution.
The largest remaining irreducible background in the 0-lepton channels stems thus from $Z \to \nu\bar{\nu} +$jets events where "true" E_T^{miss} comes from the undetected neutrinos.

12.3. $Z \to \nu\nu +$ jets background

In this thesis the 14 TeV studies for the $Z \to \nu\nu +$jets background determination (see Ref. [337]) have been repeated for a centre-of-mass energy of 10 TeV. However, this work was in an early stage and further in depth studies have not been performed due to the change of the scheduled LHC collision energy. The studied method is the most straightforward way for the background determination by measuring the same process, but with a Z boson decaying into an opposite sign same flavour lepton pair. In order to estimate the number of expected background events, the main idea is to select $Z \to l^+l^- +$jets events and to "replace" the charged leptons by neutrinos. It is hereby assumed that the neutrinos give the main contribution to E_T^{miss} such that E_T^{miss} is roughly equivalent to $p_T(Z)$ for this physics process. The analysis is performed in the following way:
$Z \to l^+l^- +$jets events that are passing the SUSY 0-lepton analysis except the E_T^{miss} cuts (and lepton veto cut), are selected. The electron and muon object selection are hereby the same as used for the 0-lepton SUSY analysis. The E_T^{miss} used for example in the $\Delta\phi(jet, E_T^{miss})$ cut is replaced by $p_T(l^+l^-) \simeq p_T(Z)$. Possible remaining backgrounds are rejected by two additional cuts: $81 < M_Z(l^+l^-) < 101$ GeV, $E_T^{miss} < 30$ GeV. In order to model the E_T^{miss} spectrum with $p_T(Z)$, the resulting distribution has to be corrected for the relative branching fraction, lepton efficiency and acceptance. The final number of events is then given by the formula:

$$N_{Z\to\nu\nu}(E_T^{miss}) = N_{Z\to l^+l^-}(p_T(l^+l^-)) \times c_{eff} \times c_{accep} \times \frac{Br(Z\to\nu\nu)}{Br(Z\to l^+l^-)}, \tag{12.1}$$

where $N_{Z\to\nu\nu}(E_T^{miss})$ is the determined number of events per bin of E_T^{miss}, $N_{Z\to l^+l^-}(p_T(l^+l^-))$ is the number of control sample events as a function of $p_T(Z)$, c_{eff} and c_{accep} are the efficiency and acceptance corrections. The ratio of branching fractions is $\sim$3. The efficiency and acceptance factors correct the reduced lepton phase space related compared to the following effects:

- e and μ leptons can not be detected beyond $\mid \eta \mid = 2.5$ (fiducial correction)
- additional cuts are applied used to select $Z \to l^+l^-$ like the Z invariant mass window, e.g. the p_T cut on leptons, E_T^{miss} cut (kinematical correction)
- lepton identification efficiency

The fiducial and kinematics correction have to be computed from simulation, whereas the lepton identification efficiency can be measured with real data events.

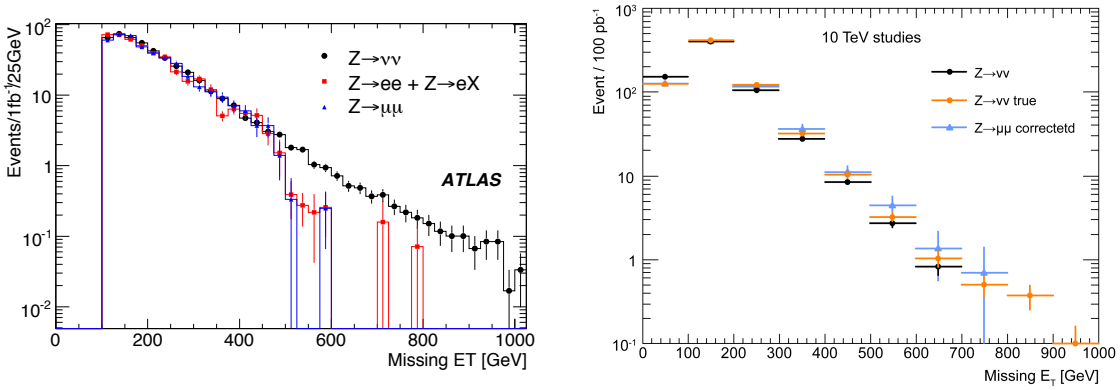

Figure 12.1: Left plot: Determined E_T^{miss} distribution from $Z \to e^+e^- + e^{\pm}X$ (red line) and $Z \to \mu^+\mu^-$ (blue line) processes together with the reconstructed $Z \to \nu\nu$ missing transverse momentum distribution (black line) for $\sqrt{s}$ = 14 TeV. The number of events corresponds to an integrated luminosity of 1 fb^{-1}, the plot is take from Ref. [337]. Right plot: Estimated E_T^{miss} distribution from the $Z \to \mu^+\mu^-$ processes (light blue line) together with the true (orange line) and reconstructed (black line) $Z \to \nu\nu$ E_T^{miss} distribution at $\sqrt{s}$ = 10 TeV. The number of events corresponds to an integrated luminosity of 100 pb^{-1}.

The main systematic uncertainty for this method is coming from the Monte Carlo generator and the variation of the renormalisation scale that affects the acceptance correction, whereas detector systematic uncertainties are related to soft part of the missing transverse energy, which is not taken into account with this method when neutrinos are replayed by charged leptons, the uncertainty of the lepton energy scale, the resolution and the reconstruction efficiency.
It should be noted that one of the main advantages of the "replacement" method is that it is a

clean signature with a negligible SUSY signal contamination due to the tight control sample event selection cuts. However due to the very limited phase space left by the SUSY preselection cuts, the total statistics are very limited. The E_T^{miss} distribution of $Z \rightarrow e^+e^-$ (red line) and $Z \rightarrow \mu^+\mu^-$ (blue line) events after applying all corrections compared to the E_T^{miss} $Z \rightarrow \nu\nu$ distribution (black line) for a centre-of-mass energy of 14 TeV and an integrated luminosity of $\mathscr{L}$ = 1 fb^{-1} is presented in Figure 12.1 (left plot). The right plot compares the determined E_T^{miss} distribution from the $Z \rightarrow \mu^+\mu^-$ sample (light blue line) with the true (orange line) and reconstructed (black line) E_T^{miss} distribution from the $Z \rightarrow \nu\nu$ sample for a centre-of-mass energy of 10 TeV and an integrated luminosity of $\mathscr{L}$ = 100 pb^{-1}. Softer p_T-jet cuts and a soft $p_T(Z)$ cut are applied to increase the event statistic in this figure. Using the default 10 TeV SUSY selection cuts listed in Table 7.1, the total number of $Z \rightarrow l^+l^- +$ jets Standard Model background events that satisfied all criteria is about 35 and about 3 events are found for $M_{\text{eff}} > 800$ GeV assuming $\mathscr{L} = 100$ pb^{-1}. The number of expected $Z \rightarrow \nu\nu +$ jets events in the same high M_{eff} region is about a factor 6 larger. Moreover, it was found that the $Z \rightarrow l^+l^- +$ jet events seem to be sensitive to the applied event and object selection criteria. Therefore this method can be only used to provide a first estimate on the number of $Z \rightarrow \nu\nu +$ jets events for first data studies and is curently used to compare first results obtained with different methods.

Alternatively to the discussed method, a similar approach can be followed with γ + jets and W$\rightarrow l\nu +$ jets as control samples. The E_T^{miss} distribution is hereby obtained by removing the identified photon or lepton and correcting for residual differences between these events and invisible Z events. Both samples have much larger cross sections and provide higher statistics than the previously studied $Z \rightarrow l^+l^- +$ jets samples. Using these sample would thus allow to apply all search selection criteria and can give an early background estimate also for lower luminosities, provided systematic uncertainties for these decay channels can be controlled. The ATLAS SUSY group is currently working on in depth studies using γ + jets and $W +$ jets samples in order to establish robust techniques to be used for ATLAS collision data.

13. Summary and Outlook

13.1. Summary

This thesis presents a search strategy for supersymmetric particles of the Minimal Supersymmetric Standard Model (MSSM) with the ATLAS detector at the LHC. Final states with jets (mainly $\geq 2-6$ jets), leptons (electron and muon, 0 - 2) and missing transverse energy are studied.
Due to the large branching fraction of the squark and gluino decays is especially the 0-lepton channel one of the most promising channels for the discovery of SUSY events, allowing also first exclusion limits on squark and gluino masses already with the early ATLAS data. The focus of this work was therefore on channels without leptons.
There have been several delays in the start-up of the LHC followed by revisions of the early physics scenarios, which have influenced the structure of this work. For this reason the analyses have been performed for different centre-of-mass energies (14 TeV, 10 TeV and 7 TeV) and integrated luminosities (ranging from 200 pb^{-1} to 1-2 fb^{-1}) to investigate the expected discovery potential of the ATLAS detector for each of the possible running conditions. The results were also interpreted in different regions of the MSSM model parameter space.
The studies assuming a $\sqrt{s}$ = 14 TeV centre-of-mass energy are performed for specific SUSY breaking models - mSUGRA models with $\tan\beta = 10$ and $\tan\beta = 50$, AMSB, NUHM and GMSB models. It was found that ATLAS can discover squark and gluino masses up to $\mathcal{O}(1\,\text{TeV})$, assuming an integrated luminosity of about 1fb^{-1}. The 0-lepton analyses lead to a discovery of the greatest fraction of the studied SUSY model points.
Since SUSY breaking models have only a simplified set of SUSY parameters, the question of how well these studies describe the true breadth of the MSSM and its possible signatures, and whether the ATLAS analyses are sensitive to the different regions of the parameter space, arose. Therefore, when assuming a centre-of-mass energy of 10 TeV, a scan in the phenomenological MSSM parameter space (pMSSM) [56], characterised by the 19 most relevant weak-scale MSSM parameters, was performed in addition to the "traditional" mSUGRA models studies. Some of these pMSSM models were subjected to a set of constraints from LEP and Tevatron collider searches, Dark Matter and some theoretical assumptions; thus the pMSSM parameter space was partly limited. In total, more than 1300 SUSY models, subdivided in three grids ("pMSSM grid fulfilling

constraints from experiments", "unconstrained pMSSM grid", "8 parameter pMSSM grid") were investigated. The models ensure large sparticle production cross sections at the LHC and a wide variety of properties and characteristic sparticle spectra. Again with the 0-lepton analyses the greatest fraction of the studied SUSY signal points could be discovered. Nevertheless, the ATLAS analysis channels also fail to observe some of the selected pMSSM models. One reason is the low luminosity of only 200 pb^{-1} and the high systematic uncertainty of 50% assumed in this study. Channels with a larger number of expected background events, like the 0-lepton channels, benefit from a reduction of the systematic uncertainties, whereas the channels with a small number of background events, like the 2-lepton channels, mostly benefit from an increased luminosity since they have less Standard Model background events. Some of the undiscovered SUSY models also have very large squark or gluino masses ($>$ 600/700 GeV). In these cases squark and gluino production is kinematically suppressed, resulting in a small number of events in the final states. Furthermore it was observed, that a fraction of models are missed by the studied 2-4 jet 0-2 lepton analyses due a different physics signature. For example a τ or b-jet SUSY analysis, as performed for the 14 TeV studies and for the first collision data, can improve the discovery potential for some regions of the studied pMSSM parameter space. Some of the studied pMSSM models with low discovery reach significance are also characterised by small mass splittings between the NLSP and LSP. They produce either rather soft jets and thus do not pass the kinematic high jet-p_T cuts for the studied channels. Finally it was shown, e.g. for the 8 parameter pMSSM grid that in regions with mainly gluino production ($m_{\tilde{g}} << m_{\tilde{q}}$) a 5 jet and 6 jet 0-lepton analyses could improve the discovery reach.

Since the final starting centre-of-mass energy of the LHC was set to $\sqrt{s} = 7$ TeV, the Monte Carlo studies in the mSUGRA parameter space were repeated just before first collision events are collected with the aim to verify that the proposed SUSY selection cuts could still lead to an early discovery for SUSY models. The results have shown that ATLAS could discover SUSY signals of R-parity conserving SUSY models with squark and gluino masses clearly above the Tevatron exclusion limits already with $\mathscr{L}$ = 0.5 -1 fb^{-1}. Studies for different luminosities and different systematic uncertainties underlined previous results that the expected discovery reach is strongly dependent on the amount of available data, how well this measured data is understood and how large is the estimated systematic uncertainty determined with data-driven methods. An overview how to estimate the Standard Model backgrounds for the 0-lepton channels is given in Chapter 12.

In the last part of this thesis a first comparison of the measured collision data with the Standard Model expectations at a collision energy of $\sqrt{s}$ = 7 TeV for an integrated luminosity of $\mathscr{L} = (70 \pm 8)$ nb^{-1} is presented in Chapter 11. This is one of the first experimental SUSY studies performed at the LHC. The most outstanding SUSY specific variables, like E_T^{miss}, M_{eff}, S_T or m_{T2} in the 0-lepton mode have been studied. All measurements are in agreement with the Standard Model expectations estimated with Monte Carlo simulations up to values of $E_T^{miss} \approx 100$ GeV, $M_{\text{eff}} \approx 1500$ GeV, $m_{T2} \approx m_{CT} \approx 100$ GeV within the associated systematic uncertainties.

It is noteworthy that all the studies discussed in thesis lead to the ATLAS publications Ref. [104, 126, 228, 234, 313, 353] as well as to the internal ATLAS notes Ref. [314, 315, 354].

13.1.1. Impact of the first ATLAS results

Recently a paper has been published (see Ref. [355]) based on the ATLAS 0-lepton channel data results of an integrated luminosity of $\mathscr{L} = 70$ nb^{-1}, showing that the reinterpreted Tevatron experiment mass limits for the gluino mass $m_{\tilde{g}} > 130$ GeV and the neutralino mass $m_{\tilde{\chi}_1^0} < 100$ GeV [356,357] can be extended by studying the gluino decay already with few luminosity of measured ATLAS data. The LHC cross section for gluinos just above current Tevatron mass limit is of the order of a few nanobarns [355]. Therefore these limits can be improved by the LHC with remarkably low luminosity and an early discovery is potentially achievable.
In this publication, only MSSM models, where the gluino is the NLSP and decays via an off-shell squark into two quarks and the neutralino (LSP) $\tilde{g} \rightarrow qq\tilde{\chi}_1^0$ leading to a signature of two jets plus missing transverse energy[1] are considered. Since there is no direct relation between the masses of $\tilde{\chi}_1^0$ and $\tilde{g}$ for these selected models, the only model independent mass constraint on the gluino mass is the one defined by LEP [358]. The multijet searches at the Tevatron apply very strong p_T jet analysis cuts, and monojet searches are typically exclusive and thus leaving a gap in the coverage of the intermediate mass-splitting region [357]. Since only low cuts on the missing energy are used in the early 0-lepton ATLAS SUSY searches, the efficiency of the selection depends on the gluino and neutralino masses and can thus be used to calculate limits. No excesses were observed in the final ATLAS M_{eff} distributions (see Section 11), therefore new limits could be inferred. It was found that the ATLAS results could improve the limits to an universal bound of $m_{\tilde{g}} >$205 GeV [358]. The determined 95% C.L. contours of the maximal allowed production cross section for $pp \rightarrow \tilde{g}\tilde{g}$X in the gluino-neutralino mass plane for direct gluino decays into two quarks and a neutralino are illustrated in Figure 13.4.
The results of this paper still need to be proven and refined by the ATLAS collaboration. However, it already shows that the possibilities for a SUSY discovery or exclusions are rapidly expanding into new kinematic regimes with the LHC.

13.2. Outlook

13.2.1. First results for $\mathscr{L} = 2.95$ pb^{-1}

In August 2010 ATLAS recorded more data than in the four previous month. This allows a first look at nearly 3 pb^{-1} of integrated luminosity, collected till the beginning of September 2010, with SUSY selections closer to the cuts forseen with the 7 TeV Monte Carlo studies presented in Chapter 10. Since the L1_J15 trigger was already prescaled with the increased luminosity[2], the lowest unprescaled jet triggers, with the highest trigger efficiency of about 99%, have been used: for the 1 and 2 jet channel the L1_J55 trigger and for the 3 and 4 jet channel the L1_3J10 trigger. The very loose p_T jet and E_T^{miss} selection criteria have been increased to p_T(jet 1) $>$ 120 GeV for the monojet channel, p_T(jet 1) $>$120 GeV, p_T(jet 2) $>$ 40 GeV for the 2

[1] The gluino can decay into a neutralino plus two quarks or a neutralino and a gluon. For simplicity it is assumed that the branching ratio for the decay of a gluino into light quarks is unity.
[2] The instantaneous integrated luminosity for the new run periods was about 40 times larger than before, ≈ 2.88 pb^{-1}

number of jets	**monojets**	**$\geq$ 2 jets**	**$\geq$ 3 jets**	**$\geq$ 4 jets**
trigger	L1_J55	L1_J55	L1_3J10	L1_3J10
leading jet p_{T} [GeV]	> 120	> 120	> 100	> 100
subsequent jets p_{T} [GeV]	veto if > 30	$>[40, 40]$	> 40 (jet 2 and 3)	>40 (jet 2 to 4)
E_T^{miss} [GeV]	> 70	> 70	> 70	> 70
$\Delta\phi(\mathrm{jet}_i, E_T^{miss})$	no cut	$> [0.2, 0.2]$	$> [0.2, 0.2, 0.2]$	$> [0.2, 0.2, 0.2]$
$E_T^{miss} > f \times M_{\mathrm{eff}}$	no cut	$f = 0.3$	$f = 0.25$	$f = 0.2$

Table 13.1: Trigger selection and evet selection cuts on the p_{T} of the leading jet, the p_{T} on the subsequent jets, the missing transverse momentum E_T^{miss} and fraction of E_T^{miss} over M_{eff}. The cuts are detailed for each of the studied jet multiplicities.

jet channel, $p_T(\text{jet 1}) > 100$ GeV, $p_T(\text{jet 2, jet 3}) > 40$ GeV for the 3 jet and $p_T(\text{jet 1}) > 100$ GeV, $p_T(\text{jet 2 - jet 4}) > 40$ GeV for the 4 jet channel and to $E_T^{miss} > 70$ GeV for all 0-lepton channels, as detailed in Table 13.1. The M_{eff} distributions for all four studied channels, after applying the final event selection cuts can be found in Figure 13.1 (for the monojet and the 2 jet channel) and Figure 13.3 (for the 3 and 4 jet channel). Figure 13.2 presents the stransverse mass m_{T2} and the contransverse mass m_{CT} after applying the p_T jet, the E_T^{miss} and the $\Delta\phi$ selection cuts for the 2 jet 0-lepton channel. All plots are for an integrated luminosity of $\mathscr{L} = (2.95 \pm 0.32)\,\mathrm{pb}^{-1}$ of measured collision data. The same event cleaning and object selection cuts are applied (see Section 7.3.1), as well as the same systematic uncertainties (see Section 7.5.3), which are used for the studies presented in Chapter 11, are considered, beside an additional uncertainty of 60% for the boson + jet Monte Carlo predictions. This conservative uncertainty of 60% is assumed to consider for example uncertainties on the predicted cross sections, the modelling of the initial- and final-state soft gluon radiation and on the PDFs, driven also by previous Tevatron measurements [359,360]. No additional systematics are assigned to the top production, since they are small compared to the jet energy scale and luminosity uncertainties considered.
It should be noted that in these figures the SUSY signal SU4 is not scaled with an additional factor as it was done in the previously presented plots, since it is now clearly visible. All figures show that the data is described by the Monte Carlo within the uncertainties, although more detailed studies still need to be investigated. For example the 2 jet channel events at very high M_{eff}, m_{T2} and m_{CT} values ($M_{\mathrm{eff}} > 800$ GeV, $m_{T2} > 300$ GeV, $m_{CT} > 300$ GeV) in Figure 13.1 (right plot) and Figure 13.2 have been studied and two events coincide with HEC noise and beam halo events. There is also one air shower event with $M_{\mathrm{eff}}(2jet) \approx 600$ GeV. The suggested new jet-cleaning definitions by the ATLAS group (see Ref. [330]) that require for example an $f_{EM} < 0.05$ cut for all jets[3] and an additional cut on the maximal fraction of energy f_{max} in one calorimeter layer for

[3] A similar, but less rejecting cut was applied for the first jet in the monojet channel in the studies presented in Chapter 11, see also Table 7.4.

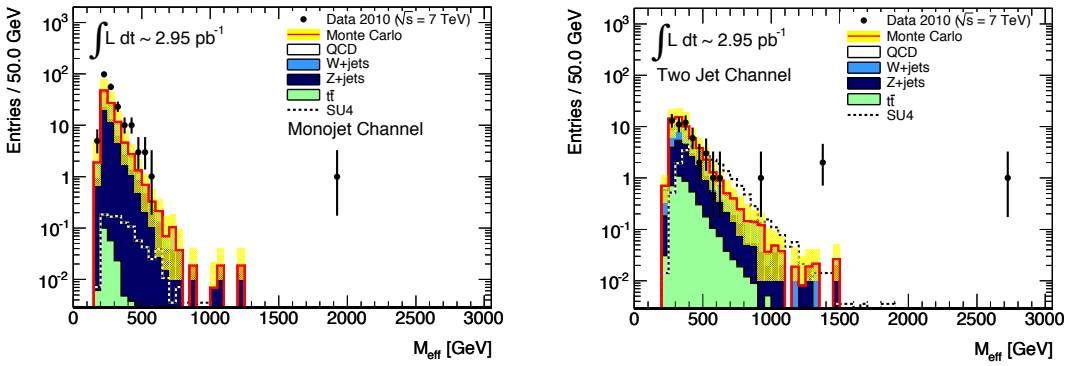

Figure 13.1: Distributions of the effective mass for events in the monojet channel after applying a $E_T^{miss} > 70$ GeV cut (left plot) and for events in the dijet channel after applying all event selection cuts (right plot).

every jet seem to remove these non-collision background events. Also using calibrated calorimeter cell energy for the E_T^{miss} calculation improves the results, e.g. the high M_{eff} event in the monojet channel (see Figure 13.1, left plot) at $M_{\text{eff}} > 1900$ GeV will be rejected using the "new" E_T^{miss} definition, because it has a $E_T^{miss}(\text{calib.}) < 70$ GeV. Although the presented plots may contain

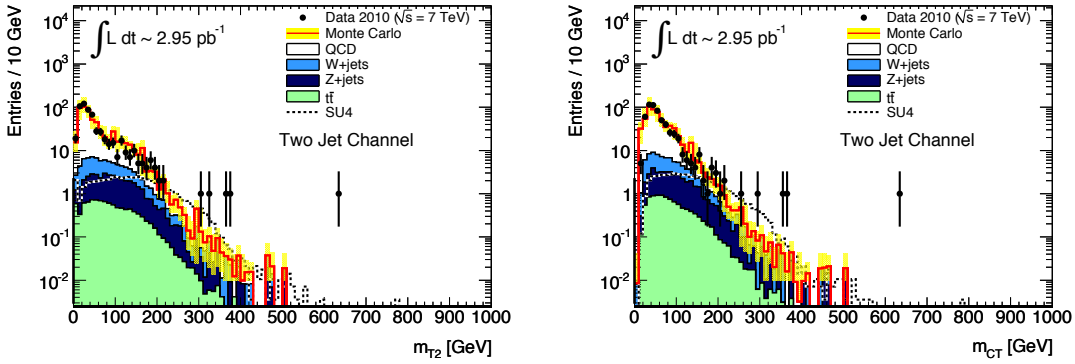

Figure 13.2: Distributions of the stransverse mass m_{T2} (left plot) and the contransverse mass m_{CT} (right plot) for events in the dijet channel after requiring the $E_T^{miss} > 70$ GeV cut and applying a cut on the azimuthal difference $\Delta\phi(\text{jet}, E_T^{miss}) > 0.2$.

some background events, it can be seen that with the increased luminosity also very interesting "real" physics events with high E_T^{miss} and M_{eff} are found, and ATLAS is becoming very sensitive to new physics, e.g. one high M_{eff} event at $M_{\text{eff}} \approx$ 700-800 GeV survives all 2, 3 and 4 jet 0-lepton channel final event selection criteria (see Figure 13.1-right plot and Figure 13.3). The event display of this events is in the Appendix Section E.6 (see Figure E.11).

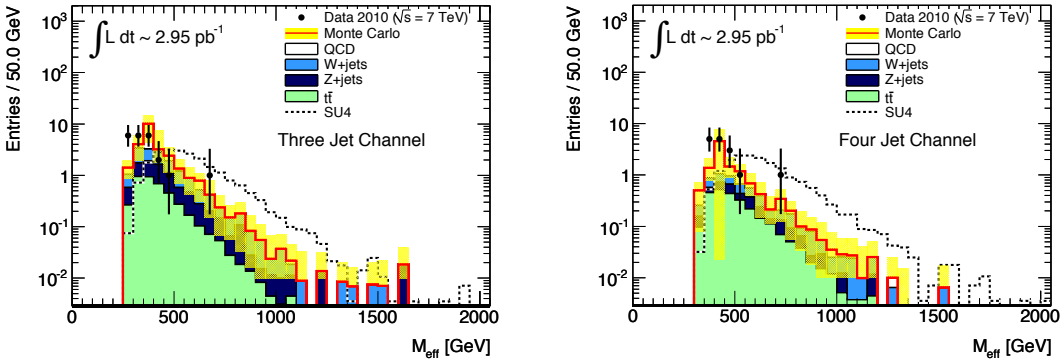

Figure 13.3: Distributions of the effective mass for events in the 3 jet (left plot) and 4 jet channel (right plot). All event selection cuts as described in Table 13.1 are applied.

13.2.2. SUSY searches at the LHC until end of the year 2011

The focus of the ATLAS collaboration in the first month of data taking was to understand the detector and its performance. A good agreement between data and Standard Model expectations estimated with Monte Carlo simulations was found.
The sensitivity of the discussed SUSY searches is at the moment mainly limited by the amount of collected data, and how our understanding of e.g. of the measured high p_T objects is and if the Standard Model backgrounds can be estimated. It is expected that the integrated luminosity will further increase in the next months to reach the goal of an integrated luminosity of about 1 fb^{-1} by the end of next year 2011. This will allow the ATLAS experiment to probe supersymmetric particle masses up to several hundred GeV and to observe or to rule out the existence of low-mass Supersymmetry. The ATLAS SUSY group works at the moment on statistical methods using a Profile-Likelihood technique (see Ref. [361–363]) to combine the different SUSY analyses with the goal of improving the sensitivity of the SUSY searches and to study the SUSY parameter space beyond Tevatron limits, already at the beginning of the next year (2011).
Figure 13.5 shows the expected 95% C.L. ATLAS exclusion limit (defined with Monte Carlo samples) for the 4 jet 0-lepton channel (black line) in the $\tan\beta = 3, A_0 = 0$ and sign$(\mu) > 0$ mSUGRA parameter space assuming $\mathscr{L} = 20$ pb^{-1}. The exclusion regions from the DØ Tevatron experiment (blue area) as well as the LEP exclusion regions (violet area, see Section 6.3) are also presented. The yellow area corresponds to the expected exclusion region in case of a 1 σ uncertainty for the expected data events. Furthermore uncertainties for the Standard Model background are considered. These predictions indicate that ATLAS has a very high sensitivity to regions of the SUSY parameter space beyond the current Tevatron limits well before 1fb^{-1} of integrated luminosity is accumulated.

In order to check if it would be already possible to exclude any SUSY signal with an integrated luminosity of 2.95 pb^{-1}, assuming that the Monte Carlo predictions describe the data, an expected

exclusion limit determined with Monte Carlo sample was calculated for the SUSY signal SU4 using a profile likelihood ratio provided by the RootStats package [361,362]. The estimated number of the SUSY signal SU4 and SM background events for the 2, 3 and 4 jet 0-lepton channels after applying all analyses cuts and a cut on $M_{\text{eff}} > 500$ GeV, as well as the determined p-value are summarised in Table 13.2.

channel	**system. uncertainty** [%]	**SU4 signal events**	**SM background events**	**p-value**
2 jet 0-lepton	30.0	11.78	6.24	0.031
2 jet 0-lepton	50.0	11.78	6.24	0.041
2 jet 0-lepton	80.0	11.78	6.24	0.064
3 jet 0-lepton	30.0	13.34	4.31	0.008
3 jet 0-lepton	50.0	13.34	4.31	0.011
3 jet 0-lepton	80.0	13.34	4.31	0.018
4 jet 0-lepton	30.0	13.6	3.45	0.007
4 jet 0-lepton	50.0	13.6	3.45	0.008
4 jet 0-lepton	80.0	13.6	3.45	0.012

Table 13.2: Expected 95% C.L. exclusion limits for the SUSY signal SU4 assuming an integrated luminosity of 2.95 pb^{-1} and different systematic uncertainties.

The p-value was calculated assuming the mentioned systematic uncertainties for the SM backgrounds. In addition to the JES systematic and the luminosity uncertainties, a systematic uncertainty of 30, 50 or 80% on the Standard Model background was considered.
If the systematic uncertainty is 50% or less, an average p-value of < 0.05 (95% confidence level) can be obtained for all three studied channel. The 4 jet channel seems to have the best exclusion power, even with an additional systematic uncertainty of 80%. This exclusion potential of the 4 jet 0-lepton channel with respect to lower jet multiplicities is somehow expected, since the SUSY signals typically have several high p_T jets. Based on the expected number of events and assuming that the measured events are already understood, the SUSY signal SU4 could be already excluded with this very low luminosity of $\mathscr{L} = 2.95\text{pb}^{-1}$.

The claim of a first discovery or the set of new exclusion limits strongly depends on the proper determination of the Standard Model backgrounds and the their experimental uncertainties. With larger datasets the ATLAS SUSY group is currently working on data-driven techniques to evaluate these more accurately.

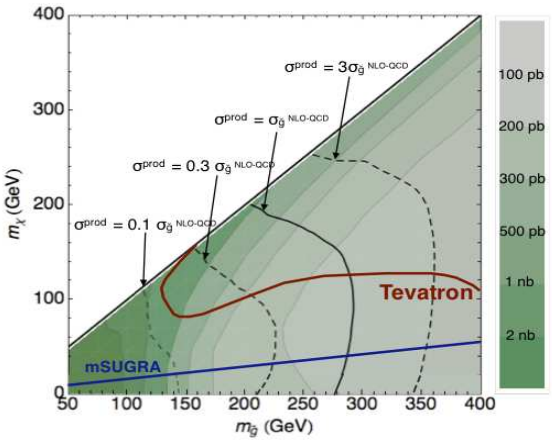

Figure 13.4: 95% C.L contours of the maximum allowed production cross section for $pp \to \tilde{g}\tilde{g}X$ in the gluino-neutralino mass plane for direct gluino decays into two quarks and a neutralino. The different contour values are specified in the colour scale. The dark lines show the possible exclusion boundary for models, where the gluino is produced through QCD alone with an NLO cross section, the dashed lines takes also other possible gluino decays into account ($BR(\tilde{g} \to qq\tilde{\chi}_1^0) < 1$). Figure is taken from Ref. [355].

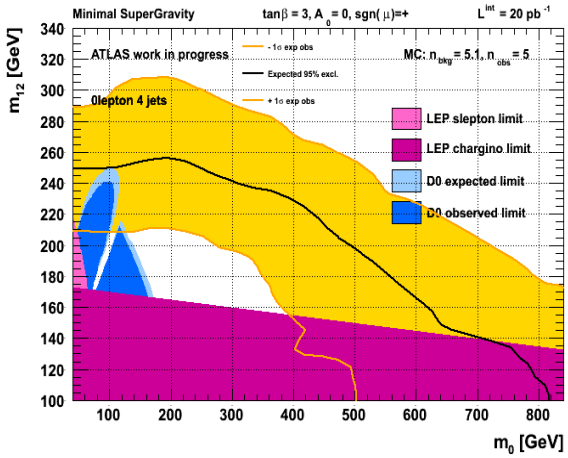

Figure 13.5: Expected 95% C.L. ATLAS exclusion limit for the 4 jet 0-lepton SUSY analysis in the mSUGRA $\tan\beta = 3$, $A_0 = 0$ and $\text{sign}(\mu) > 0$ parameter space assuming $\mathscr{L} = 20\ \text{pb}^{-1}$. Figure is taken from Ref. [364].

13.2.3. SUSY searches at the LHC in the coming years

If a "light" SUSY exists in nature, then it should be seen within the next year. In case a signature, consistent with SUSY, is established, the experimental focus will be to measure and understand the maximal possible information it contains to address the more fundamental questions like the couplings, the origin of the SUSY particle spins and the breaking mechanism or the relation to the Higgs mechanism. In any case, the definitive answers to these open questions will certainly require an interplay between the LHC and the next-generation of colliders.

A. SUSY benchmark points

In the following, the SUSY benchmark points (see Section 4.5.2), defined by the ATLAS SUSY group, are discussed. The tables and figures below give an overview of the main SUSY parameters, the cross sections, the masses of the SUSY particles and the main decay channels for the supersymmetric particles in the studied scenarios. In this thesis most figures show the SUSY signals SU3 and SU4 (see Chapter 8 till Chapter 11).

A.1. SUSY parameter

ATLAS has chosen a number of benchmark points in the mSUGRA parameter space which are roughly consistent with the observed cold dark matter density (see Section 6.3.1):

SU1 $m_0 = 70$ GeV, $m_{1/2} = 350$ GeV, $A_0 = 0$, $\tan\beta = 10$, $\text{sign}(\mu) > 0$. Coannihilation region with nearly degenerate $\tilde{\chi}_1^0$ and $\tilde{\ell}$.

SU2 $m_0 = 3550$ GeV, $m_{1/2} = 300$ GeV, $A_0 = 0$, $\tan\beta = 10$, $\text{sign}(\mu) > 0$. Focus point region near boundary with light higgsinos, very heavy squark and slepton masses. The $\tilde{\chi}_1^0$ has a high higgsino component.

SU3 $m_0 = 100$ GeV, $m_{1/2} = 300$ GeV, $A_0 = -300$ GeV, $\tan\beta = 6$, $\text{sign}(\mu) > 0$. Bulk region, relatively light sleptons enhance LSP annihilation.

SU4 $m_0 = 200$ GeV, $m_{1/2} = 160$ GeV, $A_0 = -400$ GeV, $\tan\beta = 10$, $\text{sign}(\mu) > 0$. Low mass point close to the Tevatron bound.

SU6 $m_0 = 320$ GeV, $m_{1/2} = 375$ GeV, $A_0 = 0$, $\tan\beta = 50$, $\text{sign}(\mu) > 0$. Funnel region with $2m_{\tilde{\chi}_1^0} \approx m_{A^0}$. Since $\tan\beta \gg 1$, A_0 is large and τ decays dominate.

SU8.1 $m_0 = 210$ GeV, $m_{1/2} = 360$ GeV, $A_0 = 0$, $\tan\beta = 40$, $\text{sign}(\mu) > 0$. Variant of coannihilation region with $\tan\beta \gg 1$, so that only $m(\tilde{\tau}_1) - m(\tilde{\chi}_1^0)$ is small.

A.2. SUSY particles masses, cross sections and available number of events

The LO and NLO cross sections (including filter and matching efficiencies, when applied), the samples ID, the available number of events for the SUSY benchmark points and the corresponding luminosity are detailed in Table A.1. For the studies at 10 TeV and 7 TeV only the benchmark point SU4 was used.

signal	**CSC ID**	σ_{eff} **(LO)** [pb]	σ **(NLO)** [pb]	**generated events**	**luminosity** [fb^{-1}]
SU1 (14 TeV)	005401	8.15	10.86	200 K	18.4
SU2 (14 TeV)	005402	5.17	7.18	50 K	7.0
SU3 (14 TeV)	005403	20.85	27.68	500 K	18.1
SU4 (14 TeV)	006400	294.46	402.19	200 K	0.5
SU6 (14 TeV)	005404	4.47	6.07	30 K	4.9
SU8.1 (14 TeV)	005406	6.48	8.70	50 K	5.7
SU4 (10 TeV)	106400	107.6	164.6	53 K	0.3
SU4 (7 TeV)	106484	42.3	59.9	50 K	0.8

Table A.1: Sample ID, production cross section at LO and NLO (including filter and matching efficiencies when applied), the available number of events and the corresponding luminosity produced for the SUSY benchmark points used for the 14 TeV, 10 TeV and 7 TeV studies.

The SUSY particle mass spectra (in GeV) of each benchmark point, generated for a $\sqrt{s}$ = 14 TeV, 10 and 7 TeV, are listed in Table A.2. The spectra were generated with ISAJET (see Section 4.2.1), the top quark mass was set to 175.0 GeV for 14 TeV and to 172.5 GeV for the centre-of-mass energies at 10 TeV and 7 TeV.

particle	particle mass [GeV]						
	SU1	SU2	SU3	SU4	SU6	SU8.1	SU4
	14 TeV	14 TeV	14 TeV	14 TeV	14 TeV	14 TeV	10/7 TeV
$\tilde{d}_L$	764.90	3564.13	636.27	419.84	870.79	801.16	425.93
$\tilde{u}_L$	760.42	3563.24	631.51	412.25	866.84	797.09	418.09
$\tilde{b}_1$	697.90	2924.80	575.23	358.49	716.83	690.31	361.29
$\tilde{t}_1$	572.96	2131.11	424.12	206.04	641.61	603.65	195.63
$\tilde{d}_R$	733.53	3576.13	610.69	406.22	840.21	771.91	411.95
$\tilde{u}_R$	735.41	3574.18	611.81	404.92	842.16	773.69	410.60
$\tilde{b}_2$	722.87	3500.55	610.73	399.18	779.42	743.09	408.94
$\tilde{t}_2$	749.46	2935.36	650.50	445.00	797.99	766.21	446.93
$\tilde{e}_L$	255.13	3547.50	230.45	231.94	411.89	325.44	231.98
$\tilde{\nu}_e$	238.31	3546.32	216.96	217.92	401.89	315.29	217.59
$\tilde{\tau}_1$	146.50	3519.62	149.99	200.50	181.31	151.90	200.52
$\tilde{\nu}_\tau$	237.56	3532.27	216.29	215.53	358.26	296.98	215.10
$\tilde{e}_R$	154.06	3547.46	155.45	212.88	351.10	253.35	212.69
$\tilde{\tau}_2$	256.98	3533.69	232.17	236.04	392.58	331.34	236.06
$\tilde{g}$	832.33	856.59	717.46	413.37	894.70	856.45	409.96
$\tilde{\chi}_1^0$	136.98	103.35	117.91	59.84	149.57	142.45	60.76
$\tilde{\chi}_2^0$	263.64	160.37	218.60	113.48	287.97	273.95	112.79
$\tilde{\chi}_3^0$	466.44	179.76	463.99	308.94	477.23	463.55	307.94
$\tilde{\chi}_4^0$	483.30	294.90	480.59	327.76	492.23	479.01	326.86
$\tilde{\chi}_1^+$	262.06	149.42	218.33	113.22	288.29	274.30	112.52
$\tilde{\chi}_2^+$	483.62	286.81	480.16	326.59	492.42	479.22	325.71
h^0	115.81	119.01	114.83	113.98	116.85	116.69	109.68
H^0	515.99	3529.74	512.86	370.47	388.92	430.49	369.81
A^0	512.39	3506.62	511.53	368.18	386.47	427.74	367.40
H^+	521.90	3530.61	518.15	378.90	401.15	440.23	378.12
t	175.00	175.00	175.00	175.00	175.00	175.00	172.5

Table A.2: Masses of the SUSY particles (in GeV) for the SUSY benchmark points. The spectra were generated with ISAJET, the top quark mass was set to 175.0 GeV for $\sqrt{s}$ = 14 TeV and to 172.5 GeV for 10 TeV and 7 TeV.

B. Comparison LO and NLO cross sections of the SUSY signals

For the MSSM grid with constraints as well as for the mSUGRA grid points at $\sqrt{s} = 10$ TeV (see Section 4.5.2) the total SUSY signal cross sections have been also calculated in next-to-leading order (NLO) using PROSPINO 2.1 [99–101] by summing up the squark pair, squark-anti-squark, gluino pair and gluino-squark production processes.

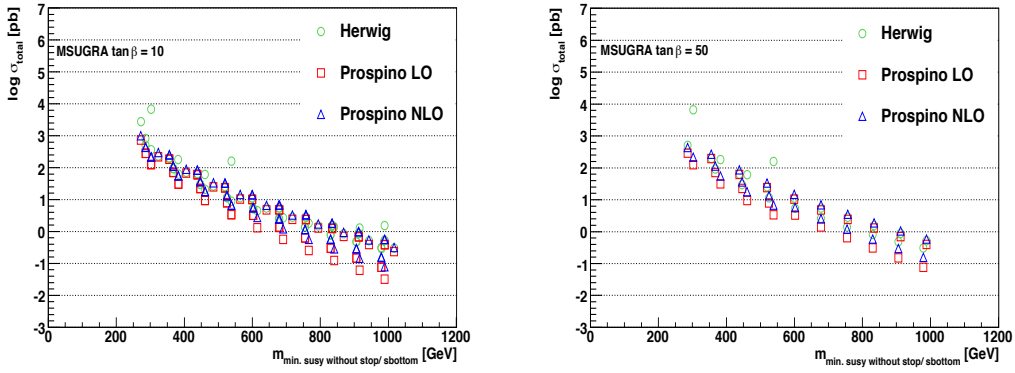

Figure B.1: Total cross section as derived by HERWIG (green points) as a function of $m_{\text{min. SUSY}}$ for the mSUGRA grid points with $\tan\beta = 10$ (left plot) and $\tan\beta = 50$ (right plot). The cross sections are compared to the sum of the squark pair production, squark-antisquark, gluino-pair and squark-gluino cross sections as derived in LO (red points) and NLO (blue points) with PROSPINO.

The PROSPINO option of free squark masses has been chosen, for example the cross sections for $\tilde{q}_L$ and $\tilde{q}_R$ production were calculated independently. The parton distribution CTEQ6M [365] was used. Figure B.1 shows the HERWIG (green points) and PROSPINO (LO -red points, NLO -blue points) cross sections for the mSUGRA grid and Figure B.2 shows the PYTHIA (green points) and PROSPINO (LO -red points, NLO -blue points) cross sections for the MSSM points with

constraints. A remarkable agreement for most points was achieved. Some points show larger differences between the HERWIG/PYTHIA and PROSPINO cross section. This is due to extra processes in HERWIG/PYTHIA that are not calculated with PROSPINO and that produce low mass charginos and neutralinos. This effect is compared to the total cross section quite small, but not negligible.

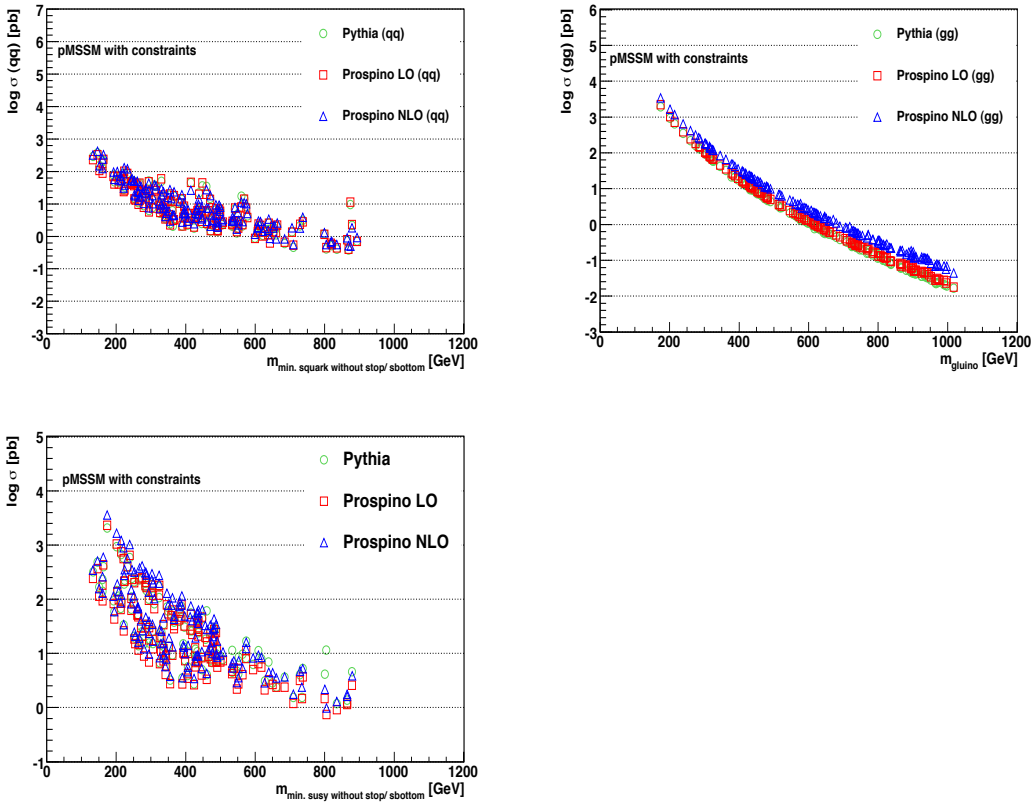

Figure B.2: The sum of all squark production cross sections as a function of the minimum squark mass (top left plot), the gluino pair production cross section as a function of the gluino mass (top right plot) and the total cross sections as a function of $m_{\text{min. SUSY}}$ = min. mass ($\tilde{u}, \tilde{d}, \tilde{s}, \tilde{c}, \tilde{g}$) (bottom plot) for the MSSM points with constraints. The LO cross sections calculated with PYTHIA (green points) are compared with the LO (red points) and NLO (blue points) PROSPINO cross sections. For the determination of the total cross section all subprocesses are summed up.

C. Studies for the LHC Chamonix workshop

Three different mSUGRA SUSY signals are analysed with the goal to estimate the luminosity required for a 5 σ discovery assuming a LHC centre-of-mass energy of 4, 6, 8, 10 and 14 TeV. Each of the three studied points has a minimum squark mass[1] m_{squark} that is equal to its gluino mass m_{gluino} and that is just beyond the Tevatron exclusion limits $m_{\text{squark}} = m_{\text{gluino}} > 392$ GeV ($A_0 = 0$, sign$(\mu) < 0$ and $\tan\beta = 5$ [237,291]):

$$m_{\text{squark}} = m_{\text{gluino}} = 400 \text{ GeV } (m_0 = 203, m_{1/2} = 152),$$
$$m_{\text{squark}} = m_{\text{gluino}} = 440 \text{ GeV } (m_0 = 223, m_{1/2} = 170),$$
$$m_{\text{squark}} = m_{\text{gluino}} = 480 \text{ GeV } (m_0 = 243, m_{1/2} = 166)$$

Further signal parameters are $A_0 = 0$, sign$(\mu) > 0$, $\tan\beta = 10$. The cross sections for the three different mSUGRA points, calculated with HERWIG and PROSPINO, are presented in Figure C.1 as a function of the LHC centre-of-mass energy. Every point was generated with ISAJET and simulated with ATLFAST2.

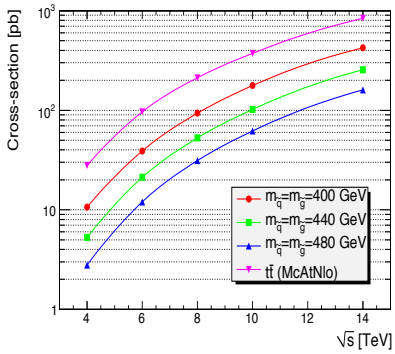

Figure C.1: PROSPINO NLO cross sections for the generated SUSY points and top pair production as a function of the LHC centre-of-mass energy.

[1] Minimum squark mass means here lightest mass of the four light squarks without stop and sbottom squarks.

Since the generation of QCD background for various LHC beam energies would have required too large computing resources, only the three jet channel with one lepton (muon or electron) has been studied with the main Standard Model backgrounds: $t\bar{t}$ and $W+$jets production. The 1-lepton channel has, compared to the 0-lepton channel, a slightly smaller discovery potential, but does not dependent on the early understanding of background from QCD processes with large fake missing transverse momentum. For the top background the MC@NLO generator was used, while the $W+$jets background was generated with the PYTHIA generator. Due to the time limit to give quickly input to the LHC operating strategy, all samples were reconstructed with ATLFAST1 and corrected in order to reproduce results obtained with the more detailed simulation ATLFAST2 (see discussion in Section 4.3.2). The studies are therefore based on simpler approximations than the studies presented in following Chapters 8-10.
The object and event selection criteria are the same as later discussed for the 10 TeV Monte Carlo studies (see Table 7.1 and 7.3) requiring at least three jets with $p_T > 100$ GeV for the first jet and $p_T > 40$ GeV for the second and third jet, large missing transverse energy $E_T^{miss} > 80$ *GeV* and exactly one lepton. The missing transverse momentum was required not to point in the direction of jets in ϕ within 0.2. In addition cuts to suppress the Standard Model backgrounds like a transverse mass cut $M_T > 100$ GeV are applied. For the significance calculation an conservative uncertainty estimate of $\pm 100\%$ in the normalisation of the total Standard Model background expectation for all intergrated luminosities and centre-of-mass energies has been used. Due to this assumption, the SUSY signals will only be visible at large centre-of-mass $\gtrsim 6$ TeV for integrated luminosities of $< 1\text{fb}^{-1}$.
The studied discovery reach depends on the number of Standard Model background events left after applying all event selection cuts. In order to validate the fast simulation of the SM backgrounds and to verify the SUSY discovery prospects with an improved background simulation based on better Monte Carlo generators and a better detector simulation, the background distributions obtained with the corrected Atlfast1 simulated samples are later compared with distributions produced with a ATLFAST2 detector simulations at centre-of-mass energy of 10 TeV. Moreover the $W+$jets generated with PYTHIA samples and based on $2 \rightarrow 2$ Matrix elements, are replaced by ALPGEN samples including up to 5 parton Matrix elements.

Results

The determined significance as a function of the LHC centre-of-mass energy for an integrated luminosity of 100 pb^{-1} is shown in Figure 6.13 (left plot) in Section 6.5, the integrated luminosity at which the significance exceeded 5σ as a function of the centre-of-mass energy can be seen in the right plot. From the figures it can be seen that the studied low SUSY mass points are clearly visible at 8 TeV for $\mathscr{L} \approx 100$ pb^{-1} including a 100% systematic error. With a luminosity of $O(100)\text{pb}^{-1}$ there is no chance to discover low mass SUSY with a centre-of-mass energy of 4 TeV. At a centre-of-mass energy of 7 TeV the current Tevatron exclusion limits could be reached with about 100 pb^{-1} integrated luminosity. The open symbols in the right figure are the results of the validation studies. It can be seen that the integrated luminosities needed for a 5σ discovery are only slightly increased when Atlfast2 background samples are used.

D. Standard Model Monte Carlo samples

The Standard Model samples generated for a centre-of-mass energy of $\sqrt{s} = 14$ TeV, 10 TeV, 7 TeV are detailed in Table D.1, D.2 and Table D.3 together with corresponding ATLAS identification number, generator used, effective cross section (including filter and matching efficiencies when applied) and corresponding luminosity produced. The given p_T values for the jet production via QCD processes (referred to as QCD) are the transverse momentum of the two partons involved in the hard scattering process. Showering, hadronisation and simulation of the underlying event was performed for the ALPGEN and MC@NLO samples by HERWIG generator, that was running together with the JIMMY generator (see Section 4.2.1).

Table D.1: Standard Model samples generated for a centre-of-mass energy of $\sqrt{s} = 14$ TeV. The corresponding ATLAS identification number, the generator used, the effective cross section including filter and the matching efficiencies when applied and the corresponding luminosity are presented.

background	**ATLAS ID**	**generator**	σ_{eff} [pb]	**luminosity** [pb^{-1}]
J4 (140-280 GeV)	08090_J4MET	PYTHIA	916.40	76.4
J5 (280–560 GeV)	08091_J5MET	PYTHIA	655.0	129.8
J6 (560–120 GeV)	08092_J6MET	PYTHIA	67.42	519.1
J7 (1120–2240 GeV)	08093_J7MET	PYTHIA	5.3	754.7
J8 ($>$ 2240 GeV)	08094_J8MET	PYTHIA	2.21×10^{-2}	181×10^{3}
W$e\nu$	05223_WenuNp2	ALPGEN	0.77	5.2×10^{3}
	05224_WenuNp3	ALPGEN	3.90	4.1×10^{3}
	05225_WenuNp4	ALPGEN	2.32	4.3×10^{3}
	05226_WenuNp5	ALPGEN	0.69	4.3×10^{3}
continued on next page				

Table D.1 - continued from previous page

background	**ATLAS ID**	**generator**	σ_{eff} [pb]	**luminosity** [pb^{-1}]
W$\mu\nu$	08203_WmunuNp3	ALPGEN	0.79	5.1×10^3
	08204_WmunuNp4	ALPGEN	2.13	4.7×10^3
	08205_WmunuNp5	ALPGEN	0.70	5.7×10^3
W$\tau\nu$	08208_WtaunuNp2	ALPGEN	0.61	4.9×10^3
	08209_WtaunuNp3	ALPGEN	3.27	4.3×10^3
	08210_WtaunuNp4	ALPGEN	3.08	4.5×10^3
	08211_WtaunuNp5	ALPGEN	0.94	5.3×10^3
Z$\nu\nu$	05124_ZvvNp3	ALPGEN	1.07	37.4×10^3
	05125_ZvvNp4	ALPGEN	3.06	15.7×10^3
	05126_ZvvNp5	ALPGEN	0.95	14.7×10^3
Zee	05161_ZeeNp1	ALPGEN	0.41	3.7×10^3
	05162_ZeeNp2	ALPGEN	4.15	11.8×10^3
	05163_ZeeNp3	ALPGEN	2.76	8.0×10^3
	05164_ZeeNp4	ALPGEN	0.70	8.6×10^3
	05165_ZeeNp5	ALPGEN	0.18	11.1×10^3
Z$\mu\mu$	08109_ZmumuNp3	ALPGEN	0.24	45.8×10^3
	08110_ZmumuNp4	ALPGEN	0.53	9.4×10^3
	08111_ZmumuNp5	ALPGEN	0.17	11.8×10^3
Z$\tau\tau$	08114_ZtautauNp2	ALPGEN	0.22	18.2×10^3
	08115_ZtautauNp3	ALPGEN	0.41	17.1×10^3
	08116_ZtautauNp4	ALPGEN	0.20	20.0×10^3
	08117_ZtautauNp5	ALPGEN	0.06	16.7×10^3
Weν	008270_Wenu	PYTHIA	49.05	1.02×10^3
W$\mu\nu$	008271_Wmunu	PYTHIA	28.64	1.05×10^3
W$\tau\nu$	008272_Wtaunu	PYTHIA	55.91	0.98×10^3
Zee	008194_Zee	PYTHIA	46.2	0.11×10^3
Z$\mu\mu$	008195_Zmumu	PYTHIA	9.60	0.52×10^3
Z$\tau\tau$	008191_Ztautau	PYTHIA	4.50	0.52×10^3
Z$\nu\nu$	008190_Znunu	PYTHIA	41.33	0.85×10^3

Table D.2: Standard Model samples generated for a centre-of-mass energy of $\sqrt{s} = 10$ TeV. The corresponding ATLAS identification number, the generator used, the effective cross section including filter and the matching efficiencies when applied and the corresponding luminosity are presented.

background	**ATLAS ID**	**generator**	σ_{eff} [pb]	**luminosity** [nb^{-1}]
WW	05985_WW	HERWIG	39.05	1.3×10^3
ZZ	05986_ZZ	HERWIG	2.83	17.7×10^3
WZ	05987_WZ	HERWIG	14.06	3.6×10^3
$t\bar{t}$	05200_toplepton	MC@NLO	450	1.3×10^3
	05204_tophad	MC@NLO	383	0.261×10^3
QCD bb J2	107360.AlpgenQcdbbJ2Np0	ALPGEN	317.91	11.01
QCD bb J2	107361.AlpgenQcdbbJ2Np1	ALPGEN	3892.93	8.09
QCD bb J2	107362.AlpgenQcdbbJ2Np2	ALPGEN	2117.86	10.86
QCD bb J2	107363.AlpgenQcdbbJ2Np3	ALPGEN	1193.72	10.05
QCD bb J3	107365.AlpgenQcdbbJ3Np0	ALPGEN	486.51	9.25
QCD bb J3	107366.AlpgenQcdbbJ3Np1	ALPGEN	10940.36	9.92
QCD bb J3	107367.AlpgenQcdbbJ3Np2	ALPGEN	10739.03	10.01
QCD bb J3	107368.AlpgenQcdbbJ3Np3	ALPGEN	6953.25	10.00
QCD bb J4	107310.AlpgenQcdbbJ4Np0	ALPGEN	147.90	10.14
QCD bb J4	107311.AlpgenQcdbbJ4Np1	ALPGEN	1078.60	10.20
QCD bb J4	107312.AlpgenQcdbbJ4Np2	ALPGEN	1430.00	10.14
QCD bb J4	107313.AlpgenQcdbbJ4Np3	ALPGEN	1021.20	10.28
QCD bb J4	107314.AlpgenQcdbbJ4Np4	ALPGEN	706.50	10.62
QCD bb J5	107315.AlpgenQcdbbJ5Np0	ALPGEN	3.20	312.50
QCD bb J5	107316.AlpgenQcdbbJ5Np1	ALPGEN	25.20	317.46
QCD bb J5	107317.AlpgenQcdbbJ5Np2	ALPGEN	50.00	310.00
QCD bb J5	107318.AlpgenQcdbbJ5Np3	ALPGEN	52.90	301.83
QCD bb J5	107319.AlpgenQcdbbJ5Np4	ALPGEN	55.50	306.31
QCD udsc J2	108372.AlpgenQcdJ2Np2	ALPGEN	76432.83	4.45
QCD udsc J2	108373.AlpgenQcdJ2Np3	ALPGEN	200925.83	8.25
QCD udsc J2	108374.AlpgenQcdJ2Np4	ALPGEN	75663.21	8.48
QCD udsc J2	108375.AlpgenQcdJ2Np5	ALPGEN	22035.01	8.52

continued on next page

Table D.2 - continued from previous page

background	**ATLAS ID**	**generator**	σ_{eff} [pb]	**luminosity**
			[pb]	[nb^{-1}]
QCD udsc J3	108377.AlpgenQcdJ3Np2	ALPGEN	102203.10	4.99
QCD udsc J3	108378.AlpgenQcdJ3Np3	ALPGEN	614746.50	0.59
QCD udsc J3	108379.AlpgenQcdJ3Np4	ALPGEN	332333.16	1.14
QCD udsc J3	108380.AlpgenQcdJ3Np5	ALPGEN	144597.07	0.97
QCD udsc J4	108362.AlpgenQcdJ4Np2	ALPGEN	31872.00	9.99
QCD udsc J4	108363.AlpgenQcdJ4Np3	ALPGEN	65508.90	10.01
QCD udsc J4	108364.AlpgenQcdJ4Np4	ALPGEN	49028.20	10.00
QCD udsc J4	108365.AlpgenQcdJ4Np5	ALPGEN	24249.30	9.96
QCD udsc J4	108366.AlpgenQcdJ4Np6	ALPGEN	116000	10.02
QCD udsc J5	108367.AlpgenQcdJ5Np2	ALPGEN	750.20	286.59
QCD udsc J5	108368.AlpgenQcdJ5Np3	ALPGEN	1944.80	190.25
QCD udsc J5	108369.AlpgenQcdJ5Np4	ALPGEN	2149.90	299.65
QCD udsc J5	108370.AlpgenQcdJ5Np5	ALPGEN	1392.80	300.11
QCD udsc J5	108371.AlpgenQcdJ5Np6	ALPGEN	972.60	299.97
W$e\nu$	107680.AlpgenJimmyWenuNp0	ALPGEN	10184.70	215.45
W$e\nu$	107681.AlpgenJimmyWenuNp1	ALPGEN	2112.30	182.50
W$e\nu$	107682.AlpgenJimmyWenuNp2	ALPGEN	676.00	461.54
W$e\nu$	107683.AlpgenJimmyWenuNp3	ALPGEN	203.30	221.35
W$e\nu$	107684.AlpgenJimmyWenuNp4	ALPGEN	56.10	2308.38
W$e\nu$	107685.AlpgenJimmyWenuNp5	ALPGEN	16.60	2680.72
W$\mu\nu$	107690.AlpgenJimmyWmunuNp0	ALPGEN	10125.70	142.03
W$\mu\nu$	107691.AlpgenJimmyWmunuNp1	ALPGEN	2155.50	28.30
W$\mu\nu$	107692.AlpgenJimmyWmunuNp2	ALPGEN	682.30	68.52
W$\mu\nu$	107693.AlpgenJimmyWmunuNp3	ALPGEN	202.00	215.35
W$\mu\nu$	107694.AlpgenJimmyWmunuNp4	ALPGEN	55.50	211.71
W$\mu\nu$	107695.AlpgenJimmyWmunuNp5	ALPGEN	16.30	2085.89

continued on next page

Table D.2 - continued from previous page

background	**ATLAS ID**	**generator**	σ_{eff} [pb]	**luminosity** [nb^{-1}]
$W\tau\nu$	107700.AlpgenJimmyWtaunuNp0	ALPGEN	10178.30	111.89
$W\tau\nu$	107701.AlpgenJimmyWtaunuNp1	ALPGEN	2106.90	28.72
$W\tau\nu$	107702.AlpgenJimmyWtaunuNp2	ALPGEN	672.80	228.52
$W\tau\nu$	107703.AlpgenJimmyWtaunuNp3	ALPGEN	202.70	2803.40
$W\tau\nu$	107704.AlpgenJimmyWtaunuNp4	ALPGEN	55.30	2689.87
$W\tau\nu$	107705.AlpgenJimmyWtaunuNp5	ALPGEN	17.00	2558.82
$Z\nu\nu$	107710.AlpgenJimmyZnunuNp0	ALPGEN	5254.00	27.12
$Z\nu\nu$	107711.AlpgenJimmyZnunuNp1	ALPGEN	1224.10	725.63
$Z\nu\nu$	107712.AlpgenJimmyZnunuNp2	ALPGEN	413.60	2352.51
$Z\nu\nu$	107713.AlpgenJimmyZnunuNp3	ALPGEN	121.00	2710.74
$Z\nu\nu$	107714.AlpgenJimmyZnunuNp4	ALPGEN	34.00	1169.09
$Z\nu\nu$	107715.AlpgenJimmyZnunuNp5	ALPGEN	9.60	2916.67
Zee	107650.AlpgenJimmyZeeNp0	ALPGEN	898.20	300.04
Zee	107651.AlpgenJimmyZeeNp1	ALPGEN	206.60	300.10
Zee	107652.AlpgenJimmyZeeNp2	ALPGEN	72.50	3000.00
Zee	107653.AlpgenJimmyZeeNp3	ALPGEN	21.10	2978.01
Zee	107654.AlpgenJimmyZeeNp4	ALPGEN	6.00	3083.33
Zee	107655.AlpgenJimmyZeeNp5	ALPGEN	1.70	3235.29
$Z\mu\mu$	107660.AlpgenJimmyZmumuNp0	ALPGEN	900.20	272.72
$Z\mu\mu$	107661.AlpgenJimmyZmumuNp1	ALPGEN	205.20	302.14
$Z\mu\mu$	107662.AlpgenJimmyZmumuNp2	ALPGEN	69.40	3004.32
$Z\mu\mu$	107663.AlpgenJimmyZmumuNp3	ALPGEN	21.60	3009.26
$Z\mu\mu$	107664.AlpgenJimmyZmumuNp4	ALPGEN	6.10	3032.79
$Z\mu\mu$	107665.AlpgenJimmyZmumuNp5	ALPGEN	1.70	3235.29
$Z\tau\tau$	107670.AlpgenJimmyZtautauNp0	ALPGEN	902.70	295.23
$Z\tau\tau$	107671.AlpgenJimmyZtautauNp1	ALPGEN	209.30	301.00
$Z\tau\tau$	107672.AlpgenJimmyZtautauNp2	ALPGEN	70.20	2998.55
$Z\tau\tau$	107673.AlpgenJimmyZtautauNp3	ALPGEN	21.10	118.48
$Z\tau\tau$	107674.AlpgenJimmyZtautauNp4	ALPGEN	6.00	3083.33
$Z\tau\tau$	107675.AlpgenJimmyZtautauNp5	ALPGEN	1.70	3235.29

continued on next page

Table D.2 - continued from previous page

background	**ATLAS ID**	**generator**	σ_{eff} [pb]	**luminosity** [nb^{-1}]
WW	106011.gg2WW0240	HERWIG	0.03	317258.88
WW	106012.gg2WW0240	HERWIG	0.03	111040.61
WW	106013.gg2WW0240	HERWIG	0.03	315672.59
WW	106014.gg2WW0240	HERWIG	0.03	315989.85
WW	106015.gg2WW0240	HERWIG	0.03	31694.16
WW	106016.gg2WW0240	HERWIG	0.03	317131.98
WW	106017.gg2WW0240	HERWIG	0.03	31725.89
WW	106018.gg2WW0240	HERWIG	0.03	111040.61
WW	106019.gg2WW0240	HERWIG	0.03	110596.45
WW	105921.McAtNlo0331	MC@NLO	0.79	5252.09
WW	105922.McAtNlo0331	MC@NLO	0.80	5145.62
WW	105923.McAtNlo0331	MC@NLO	0.77	2678.11
WW	105924.McAtNlo0331	MC@NLO	0.80	4527.50
WW	105925.McAtNlo0331	MC@NLO	0.79	2638.58
WW	105926.McAtNlo0331	MC@NLO	0.78	2706.56
WW	105927.McAtNlo0331	MC@NLO	0.80	4494.52
WW	105928.McAtNlo0331	MC@NLO	0.80	2622.51
WW	105929.McAtNlo0331	MC@NLO	0.80	21508.89
ZZ	105931.McAtNlo0331	MC@NLO	9.10	738.73
ZZ	105932.McAtNlo0331	MC@NLO	9.30	723.62
WZ	105941.McAtNlo0331	MC@NLO	18.70	195.14
WZ	105942.McAtNlo0331	MC@NLO	18.58	195.72
WZ	105971.McAtNlo0331	MC@NLO	10.75	1223.82
WZ	05972.McAtNlo0331	MC@NLO	11.01	331.99
$t\bar{t}$	105200.T1_McAtNlo	MC@NLO	202.86	16338.94
$t\bar{t}$	105204.TTbar_FullHad	MC@NLO	170.74	21587.10
single top	105502.AcerMC_tchan	AcerMC	14.41	693.89

Table D.3: The ATLAS identification number, the cross section times branching ratio and the equivalent integrated luminosity of the 7 TeV Standard Model Monte Carlo samples.

background	**ATLAS ID**	**generator**	σ_{eff} [nb]	**luminosity** [nb^{-1}]
Di-jets (QCD) $8 \leq p_T < 17\,\text{GeV}$	105009_J0_pythia_jetjet	PYTHIA	9.85×10^6	0.14
Di-jets (QCD) $17 \leq p_T < 35\,\text{GeV}$	105010_J1_pythia_jetjet	PYTHIA	6.78×10^5	2.06
Di-jets (QCD) $35 \leq p_T < 70\,\text{GeV}$	105011_J2_pythia_jetjet	PYTHIA	4.10×10^4	34.1
Di-jets (QCD) $70 \leq p_T < 140\,\text{GeV}$	105012_J3_pythia_jetjet	PYTHIA	2.20×10^3	636
Di-jets (QCD) $140 \leq p_T < 280\,\text{GeV}$	105013_J4_pythia_jetjet	PYTHIA	88	1.59×10^4
Di-jets (QCD) $280 \leq p_T < 560\,\text{GeV}$	105014_J5_pythia_jetjet	PYTHIA	2.35	5.96×10^5
Di-jets (QCD) $560GeV \leq p_T$	105015_J6_pythia_jetjet	PYTHIA	0.034	4.12×10^7
$W \to e\nu$	(107680–107685) AlpgenJimmyWenuNp(0-5)	ALPGEN	10.45	2.0×10^5
$W \to \mu\nu$	(107690–107695) AlpgenJimmyWmunuNp(0-5)	ALPGEN	10.45	2.0×10^5
$W \to \tau\nu$	(107700–107705) AlpgenJimmyWtaunuNp(0-5)	ALPGEN	10.45	2.0×10^5
$Z \to \nu\bar{\nu}$	(107710–107715) AlpgenJimmyZnunuNp(0-5)	ALPGEN	5.82	1.0×10^5
$Z \to e^+e^-$	(107650–107655) AlpgenJimmyZeeNp(0-5)	ALPGEN	0.79	5.0×10^5
$Z \to \mu^+\mu^-$	(107660–107665) AlpgenJimmyZmumuNp(0-5)	ALPGEN	0.79	5.0×10^5
$Z \to \tau^+\tau^-$	(107670–107675) AlpgenJimmyZtautauNp(0-5)	ALPGEN	0.79	5.0×10^5
$t\bar{t}$	105200.T1_McAtNlo_Jimmy	MC@NLO	0.164	7.0×10^6
	105204.TTbar_FullHad	MC@NLO	0.07	2.1×10^6

E. Searches for Supersymmetry at different centre-of-mass energies - additional material

E.1. Results of the 14 TeV Monte Carlo studies

The M_{eff} distributions for each applied cut for the 2 jet and 3 jet 0-lepton analyses are presented in Figure E.1 and Figure E.2. The corresponding number of the Standard Model background events and the number of the different SUSY signals events that are passing the applied event selection cuts are detailed in Table E.1 for the 4 jet 0-lepton channel, in Table E.1 for the 3 jet 0-lepton channel and in Table E.3 for the 2 jet 0-lepton channel. All numbers and figures are for a centre-of-mass energy of $\sqrt{s}$ = 14 TeV and an integrated luminosity of $\mathscr{L}$ = 1fb^{-1}.

E.2. Systematic uncertainties for the 14 TeV Monte Carlo studies

Different uncertainties are considered in order to estimate the systematic uncertainties for the Standard Model backgrounds determined with data-driven methods: An overall uncertainty on the jet energy scale of 5% was assumed and applied as a jet and E_T^{miss} global uncertainty, independently of jet p_T and η values and identically for light-quark jets and jets from b-quarks. For the jet energy resolution a residual uncertainty of 10% was considered. For the missing transverse energy uncertainty, calculated from the transverse vector sum of high p_T objects, the correlation with the jets is takes into account. For electrons an uncertainty on the identification efficiency of 0.5% is estimated as well as an uncertainty on the electron energy scale of 0.2% and on the energy resolution of 1%. For muons the determined uncertainty on the identification efficiency is 1% for $p_T < 100$ GeV and additional 3% extrapolation uncertainty for muons with a p_T of 1 TeV are assumed. Furthermore, an uncertainty on the muon p_T scale of 0.2%, 4% on the p_T resolution for muons below p_T =100 GeV and about 10% for muons with $p_T < 1$ TeV are considered. All these

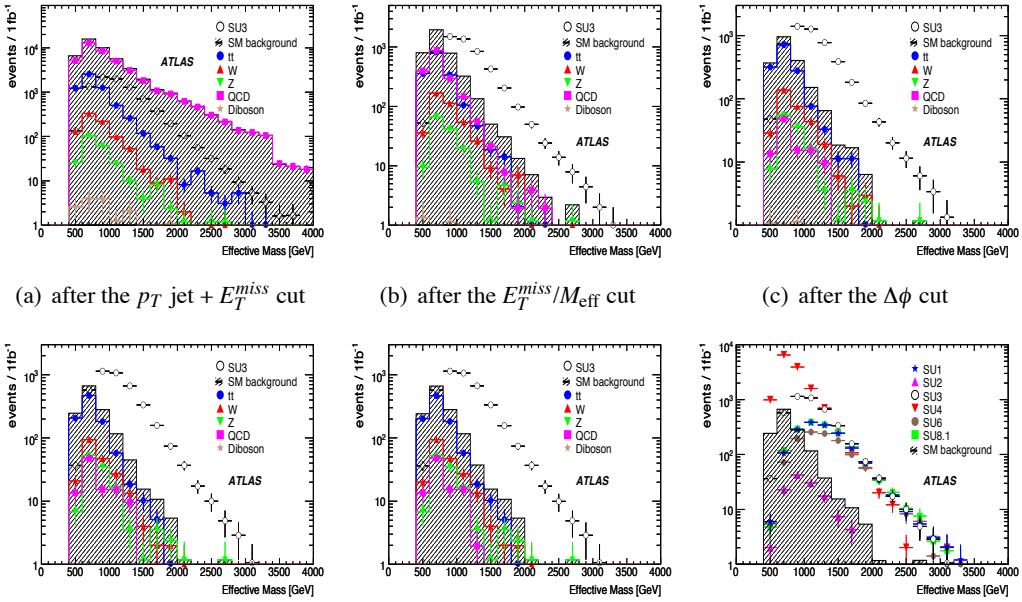

(a) after the p_T jet + E_T^{miss} cut (b) after the $E_T^{miss}/M_{\text{eff}}$ cut (c) after the $\Delta\phi$ cut

(d) after the lepton veto cut (e) after the trigger cut (f) after all cuts, different SUSY signals are presented

Figure E.1: Cut selection plots for the 3 jet 0-lepton analysis at $\sqrt{s} = 14$ TeV for $\mathscr{L} = 1$ fb^{-1}. All figures show signal (open circles), total Standard Model backgrounds (shaded histogram) and a breakdown of the background types. The cuts are described in the Table 7.1 and 7.3. The error bars reflect the statistical uncertainties of the Monte Carlo samples.

lepton uncertainties are assumed to be independent of η. Uncertainties from the use of Monte Carlo samples are estimated by comparing different event generators, particularly ALPGEN and MC@NLO and by the variation of generator parameters. As a result the total systematic uncertainties corresponding to $\sqrt{s} = 14$ TeV and $\mathscr{L} = 1\text{fb}^{-1}$ were assumed to be $\pm 50\%$ for QCD jet production and $\pm 20\%$ for the W, Z and $t\bar{t}$ backgrounds.

E.3. Results of the 10 TeV Monte Carlo studies

Distributions The effective mass and missing transverse energy distributions for the SUSY signal SU4 and the Standard Model backgrounds for the 2 jet (left plots) and 3 jet (right plots) 0-lepton channel are illustrated in Figure E.3. The effective mass, missing transverse momentum and the transverse mass (M_T) distributions for the 2 jet (left plots) and 3 jet (right plots) 1-lepton channel can be found in Figure E.4 and the effective mass distributions for the 2 and 3 jet channel with 2 leptons of opposite sign (OS) are presented in Figure E.5. For the missing transverse momentum and the M_T distributions all cuts are applied besides the cut on M_T.

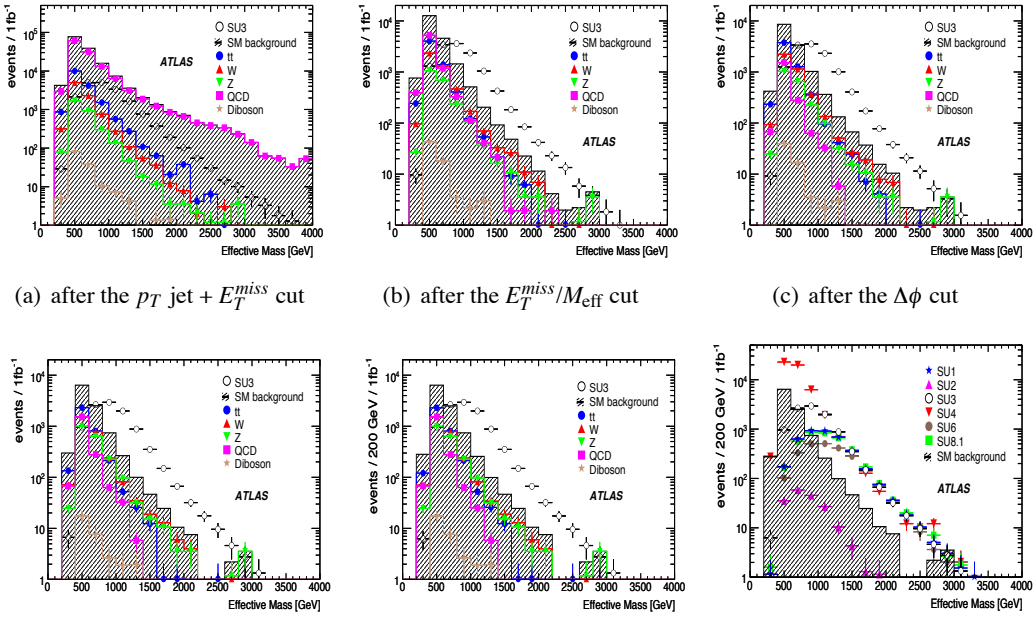

(a) after the p_T jet + E_T^{miss} cut

(b) after the $E_T^{miss}/M_{\text{eff}}$ cut

(c) after the $\Delta\phi$ cut

(d) after the lepton veto

(e) after the trigger cut

(f) after all cuts, different SUSY signals are presented

Figure E.2: Cut selection plots for the 2 jet 0-lepton analysis at $\sqrt{s} = 14$ TeV for $\mathscr{L} = 1$ fb^{-1}. All figures show the SUSY signa SU3 (open circles), the total Standard Model backgrounds (shaded histogram) and a breakdown of the background types. The cuts are described in the Table 7.1 and 7.3. The error bars reflect the statistical uncertainties of the Monte Carlo samples.

Cutflow tables The expected number of events at $\sqrt{s} = 10$ TeV for 200pb^{-1} after every applied 4 jet 0-lepton analysis cut are listed in Table E.4.

sample	p_T jet + E_T^{miss} cut	$E_T^{miss}/M_{\text{eff}}$ cut	S_T cut	$\Delta\phi$ cut	lepton veto cut	trigger cut	M_{eff} > 800 GeV
SU3	9600	7563	5600	5277	4311	4301	3349
SU4	79618	57803	46189	42408	34966	34336	8507
SU1	3485	2854	2004	1907	1401	1399	1229
SU2	604	369	308	279	169	167	131
SU6	2551	2062	1468	1383	1080	1078	956
SU8.1	3118	2540	1778	1686	1448	1447	1284
MC@NLO $t\bar{t}$	12861	8798	6421	5790	4012	3808	305
Pythia QCD	29230	7044	4667	848	848	773	13
Alpgen Z	1626	1045	732	660	644	632	162
Alpgen W	4066	2393	1654	1499	1147	1098	228
Herwig WZ	22	15	9	8	4	3	1
SM	47805	19294	13483	8806	6655	6315	708

Table E.1: Cutflow table for the 4 jets 0-lepton analysis at $\sqrt{s} = 14$ TeV. The events are normalised to 1 fb^{-1}. The applied cuts are discussed in Table 7.1 and 7.3.

sample	p_T jet + E_T^{miss} cut	$E_T^{miss}/M_{\text{eff}}$ cut	$\Delta\phi$ cut	lepton veto cut	trigger cut	M_{eff} > 800 GeV
SU3	8414.2	5391.4	4972.9	4126.8	4125.2	3514.0
SU4	43782.1	18634.1	16613.1	14149.4	14125.2	6657.4
SU1	3369.2	2329.3	2173.2	1644.7	1644.4	1531.6
SU2	519.1	240.2	211.1	129.2	129.0	104.2
SU6	2357.5	1619.7	1484.6	1175.5	1175.3	1098.1
SU8.1	3032.2	2092.4	1946.2	1689.1	1688.4	1565.8
MC@NLO $t\bar{t}$	6062.2	1721.3	1443.3	949.1	944.0	273.9
Pythia QCD	40537.0	1808.8	102.0	102.0	94.3	32.6
Pythia Z	243.7	153.6	128.5	124.0	124.0	64.4
Pythia W	872.3	417.5	317.1	211.5	210.5	96.3
Herwig WZ	16.1	3.7	2.8	1.4	1.4	0.6
SM	47731.3	4104.9	1993.7	1388.0	1374.2	467.7

Table E.2: Cutflow table for the 3 jet 0-lepton analysis at $\sqrt{s} = 14$ TeV for $\mathscr{L} = 1$ fb^{-1}. The applied cuts are discussed in Table 7.1 and 7.3.

sample	p_T jet + E_T^{miss} cut	$E_T^{miss}/M_{\text{eff}}$ cut	$\Delta\phi$ cut	lepton veto cut	trigger cut	M_{eff} > 800 GeV
SU3	18660.7	12519.8	12217.5	10055.2	10050.5	6432.2
SU4	123088	64740.5	62258.6	52327.1	52195.8	9422.2
SU1	7699.9	5427.5	5318.1	3996.8	3995.5	3196.0
SU2	642.4	319.7	301.2	185.1	184.8	90.4
SU6	4483.1	3133.5	3041.7	2418.5	2418.3	1987.0
SU8.1	6384.7	4482.5	4381.8	3804.5	3803.1	3067.7
MC@NLO $t\bar{t}$	17666.6	6273.8	5778.6	3556.7	3517.6	304.8
Pythia QCD	124513.9	7341.7	1983.7	1983.7	1976.0	107.6
Pythia Z	3222.5	2192.2	2109.5	2056.1	2056.1	391.6
Pythia W	8887.2	4504.5	4072.4	2775.5	2771.5	395.1
Herwig WZ	150.4	71.2	66.0	32.1	32.1	6.8
SM	154440.5	20383.4	14010.1	10404.1	10353.4	1205.8

Table E.3: Cutflow table for the 2 jet 0-lepton analysis at $\sqrt{s} = 14$ TeV. The events are normalised to $\mathscr{L} = 1$ fb^{-1} at $\sqrt{s} = 14$ TeV. The applied cuts are discussed in Table 7.1 and 7.3.

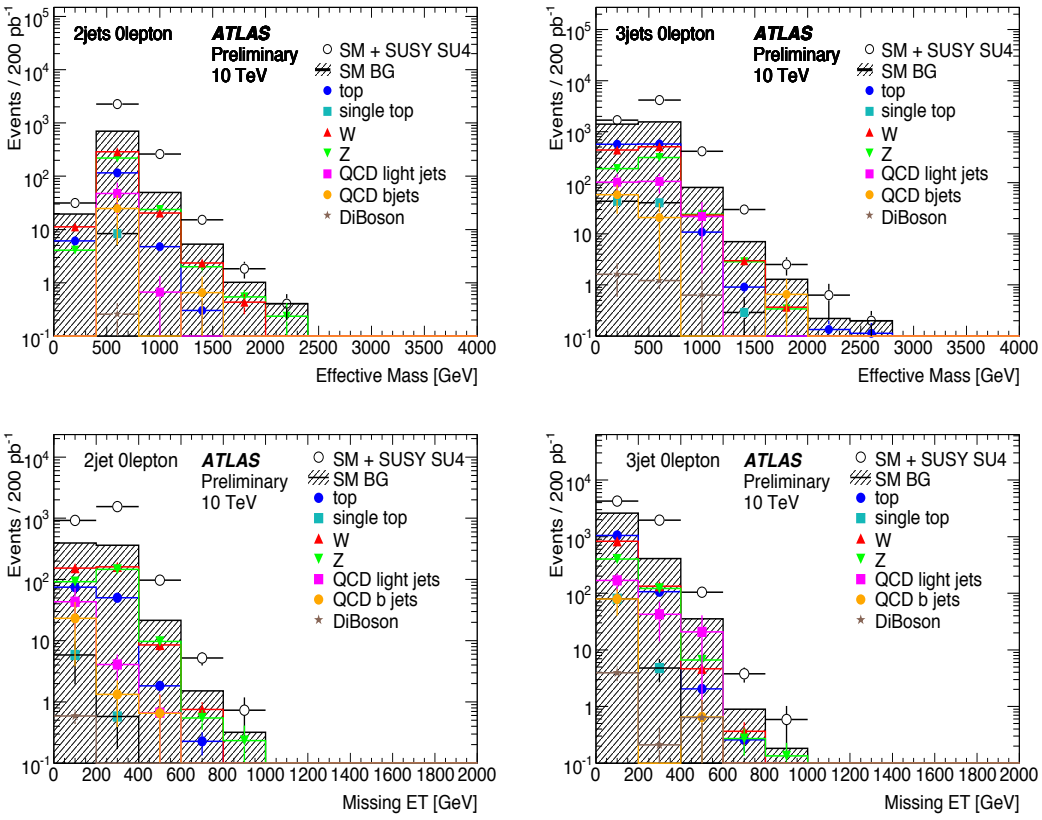

Figure E.3: Effective mass distributions (upper plots) and missing transverse energy distributions (bottom plots) for the 2 jet (left plots) and 3 jet (right plots) channel with 0 leptons at $\sqrt{s} = 10$ TeV for $\mathscr{L} = 200$ pb^{-1}. The applied cuts are discussed in Table 7.1 and 7.3.

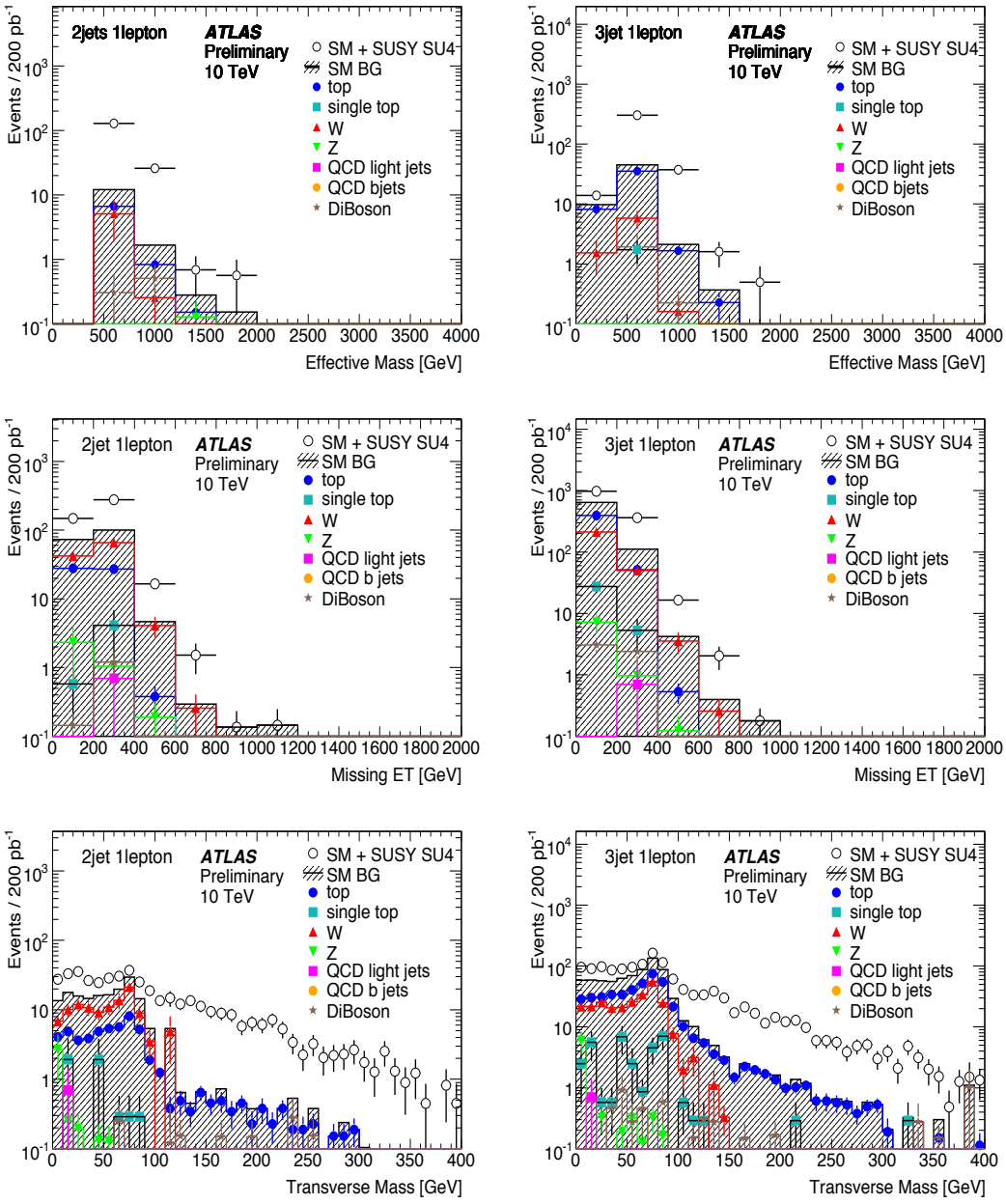

Figure E.4: Effective mass distributions (upper plots), missing transverse momentum (middle plots) and M_T distributions (bottom plots) for the 2 jet (left plots) and 3 jet channel (right plots) with 1 lepton at $\sqrt{s} = 10$ TeV for $\mathscr{L} = 200$ pb^{-1}.

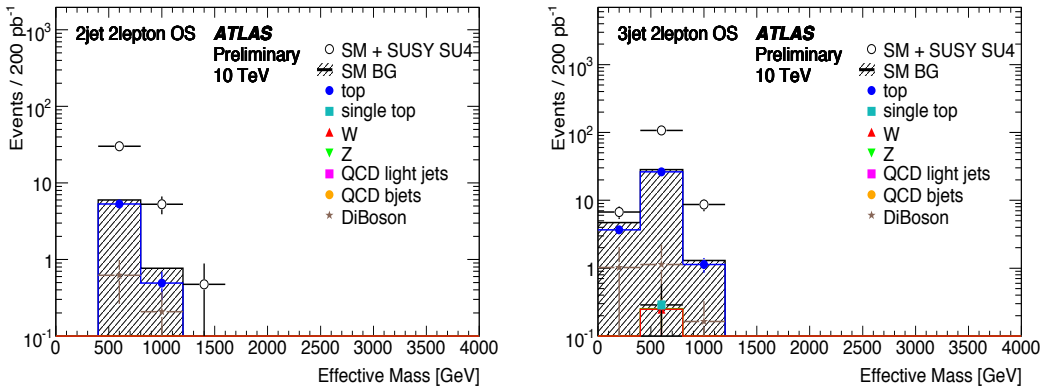

Figure E.5: Effective mass distributions for the 2 jet (left plot) and 3 jet (right plot) channel with 2 leptons of opposite sign (OS) at $\sqrt{s} = 10$ TeV for $\mathscr{L} = 200$ pb^{-1}.

sample	object selection	p_T *jet* + E_T^{miss} cut	$E_T^{miss}/M_{\text{eff}}$ cut	S_T cut	$\Delta\phi$ cut	lepton veto cut	$M_{\text{eff}} >$ 800 GeV
$Z \to ee$	229132.6	0.25	0.0	0.0	0.0	0.0	0.0
$Z \to \mu\mu$	240822.8	4.8	2.4	1.3	1.2	0.65	0.062
$Z \to \tau\tau$	241237.3	45.4	21.57	10.8	8.52	5.59	0.19
$Z \to \nu\nu$	223511.3	278.4	187.4	129.6	121.4	121.3	17.4
DiBoson	16326.3	9.90	6.11	3.44	3.19	0.86	0.60
$W \to e\nu$	2585333.2	298.4	169.2	110.9	99.9	66.3	4.81
$W \to \mu\nu$	2647330.4	243.7	139.1	99.6	93.3	45.4	5.4
$W \to \tau\nu$	2642019.8	532.8	324.8	212.4	182.4	168.0	15.6
QCD b-jets	7459336.9	1658.5	390.4	235.5	62.6	62.6	3.3
QCD light jets	228679374.4	4732.2	1023.8	411.6	209.8	208.5	2.4
single top	10974.6	121.2	80.2	67.2	61.9	38.8	0.0
top pairs	79290.0	2256.8	1466.5	1090.2	993.2	660.1	17.86
total SM	245054689.8	10182.4	3811.3	2372.8	1837.6	1378.1	67.6

Table E.4: Cutflow table for the 4 jet 0-lepton analysis. Listed are the expected number of events for $\mathscr{L} = 200$ pb^{-1} at $\sqrt{s} = 10$ TeV for the 4 jet 0 lepton analysis.

E.4. Reweighting of the 10 TeV Monte Carlo samples

The 10 TeV Monte Carlo studies have been repeated for a scenario assuming a LHC centre-of-mass collision energy $\sqrt{s} = 7$ TeV. For this the 10 TeV Standard Model and SUSY signal samples have been corrected using the LHAPDF software package [210], which calculates for every event an "event weight". This weight is obtained from the parton density functions (PDFs) (see Section 2.3.2 and Section 4.2.1) and calculated with the formula:

$$w = \frac{pdf(x_1', f_1, Q)pdf(x_2', f_2, Q)}{pdf(x_1, f_1, Q)pdf(x_2, f_2, Q)}$$

where x_i is the longitudinal momentum fraction of the proton taken by the interacting parton. The variable $x_i' = x_i \cdot E^{\text{old}}_{\text{beam}}/E^{\text{new}}_{\text{beam}}$ is the rescaled longitudinal momentum fraction of the proton taken by the interacting parton, f_i is the parton flavour and Q is the hard subprocess scale. The index i = 1, 2 refers to the first and second parton, which takes part in the hard subprocess.

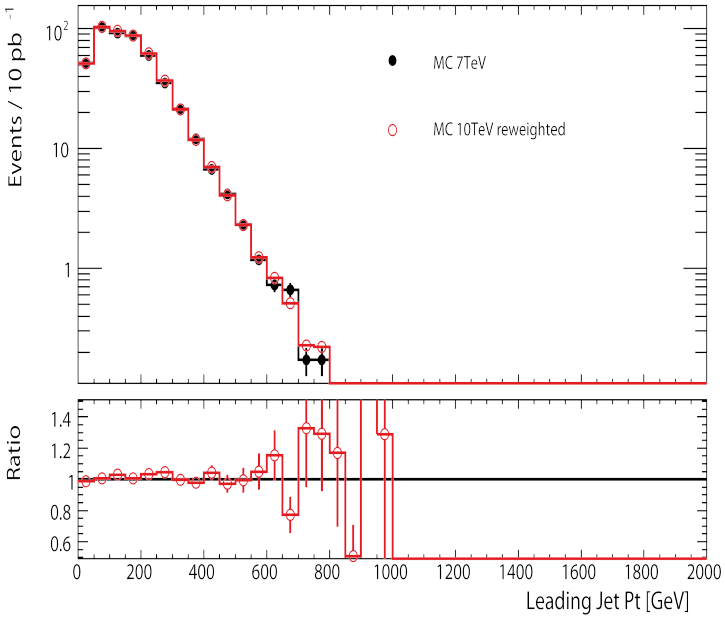

Figure E.6: Comparison between reweighted 10 TeV MC (red line) and 7 TeV MC samples (black line) for the SUSY signal SU4. The p_T distribution of the leading jet on generator level is presented. The lower plot presents the ratio between the reweighted 10 TeV and 7 TeV Monte Carlo distributions, that is consistent with one if the statistical errors are taken into account.

The applied procedure has been tested by comparing the reweighted 10 TeV Monte Carlo dis-

tributions with the 7 TeV Monte Carlo distributions. Figure E.6 shows, as an example, the p_T distribution of the leading jet on generator level for the SUSY sample SU4. The 7 TeV MC distribution (black line) is compared to the reweighted 10 TeV MC distribution (red line). As the ratio between 10 TeV and 7 TeV Monte Carlo distributions (lower plot) demonstrates, the method works very well within the given statistical errors.

E.5. Results of the 7 TeV MC studies

Figure E.7, Figure E.8 and Figure E.9 show the $\sqrt{s} = 7$ TeV transverse mass and effective mass distributions for the 2 and 3 jet 1-lepton channel, the effective mass distributions for the 2, 3 and 4 jet 2-lepton OS analyses and the missing transverse energy distributions for the 2 and 3 jet 0- and 1 lepton channel as well as for the 2, 3 and 4 jet 2-lepton OS analyses, respectively. All plots are normalised to $\mathscr{L} = 1$ fb^{-1}. The mSUGRA point SU4 and the Standard Model backgrounds are presented. For the missing transverse energy and the transverse mass distributions all cuts are applied beside the missing transverse energy and transverse mass cut, respectively. The same Monte Carlo samples as for the 10 TeV studies have been used, but they are reweighted to correct centre-of-mass energy.

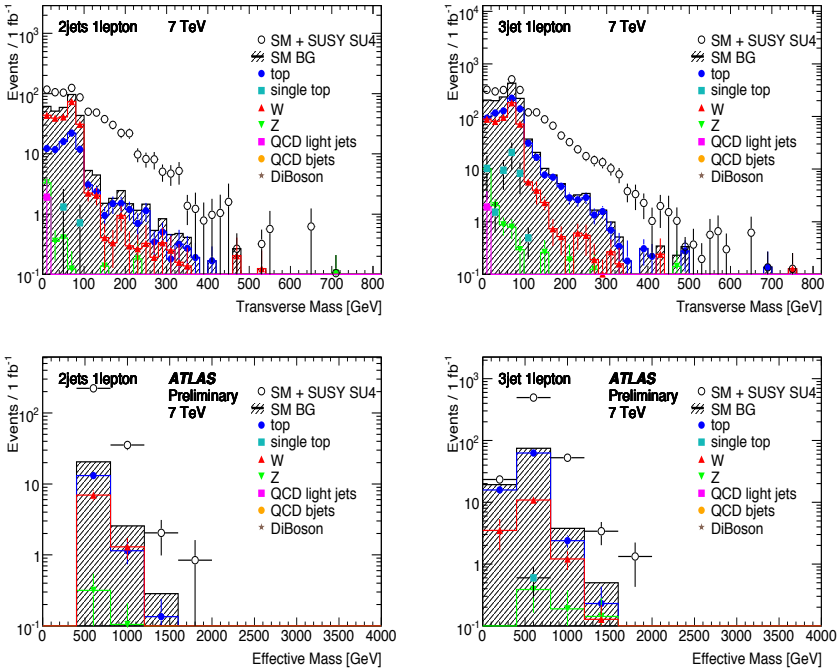

Figure E.7: Transverse mass (top plots) and effective mass (bottom plots) distributions for the 2 jet (left plot) and 3 jet (right plot) channel with one lepton at $\sqrt{s} = 7$ TeV for $\mathscr{L} = 1$ fb^{-1}. All cuts are applied beside the transverse mass cut.

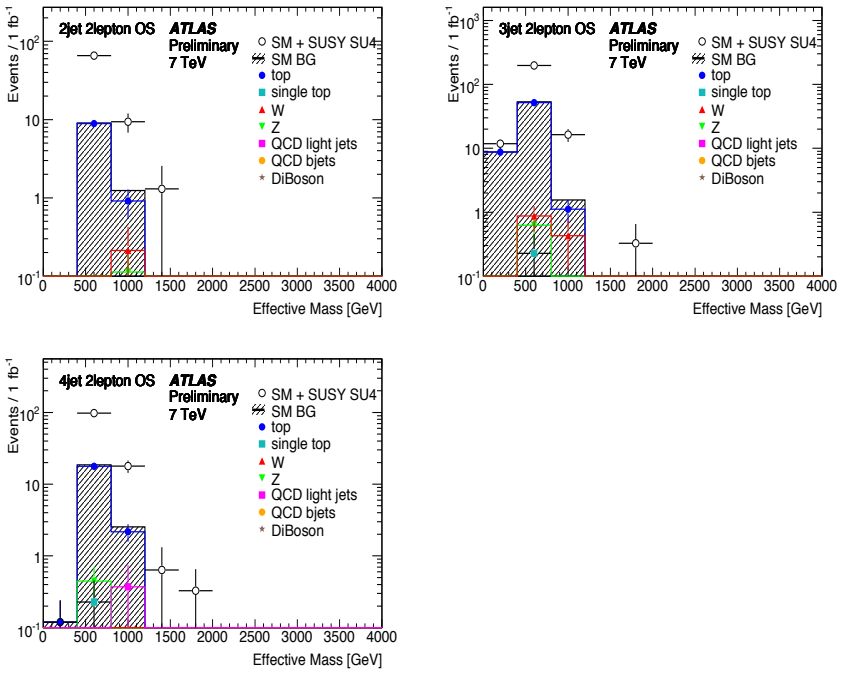

Figure E.8: Effective mass distributions for the 2 jet (left top plot), 3 jet (right top plot) and 4 jet channel (last row) 2 lepton OS assuming a centre-of-mass energy of $\sqrt{s} = 7$ TeV and $\mathscr{L} = 1$ fb^{-1}.

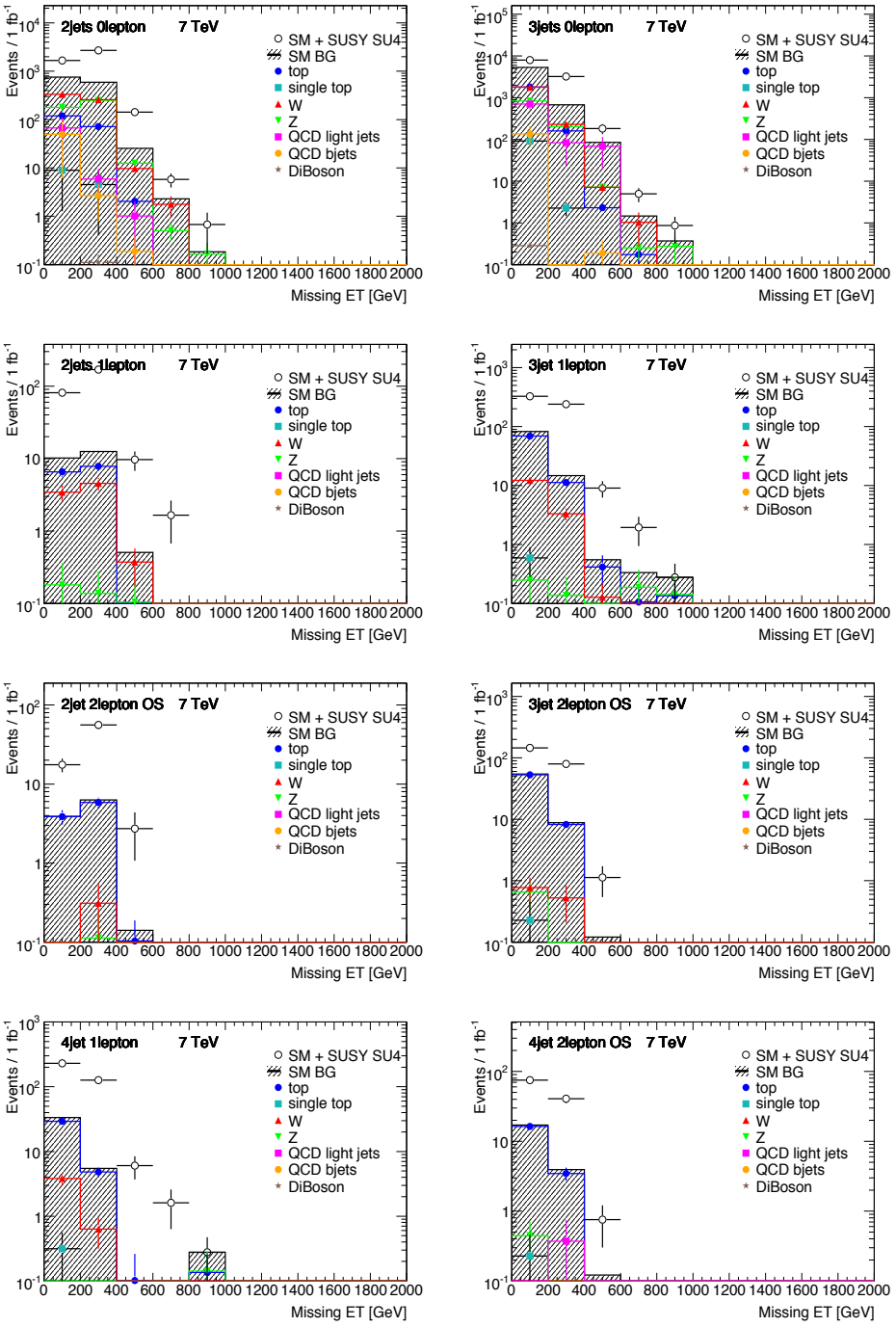

Figure E.9: Missing transverse energy distributions for the 2 jet (left plots), 3 jet (right plots) and 4 jet channel (last row) with 0 leptons (1st row), 1 lepton (2nd and 4th row) and 2 lepton OS (3rd and 4th row) for $\mathscr{L} = 1$ fb^{-1} at $\sqrt{s} = 7$ TeV.

E.6. Results of the first collision data events

The cutflow table E.5 shows the expected number of events normalised to 70pb^{-1} for every applied cut in the monojet, 2 jet, 3 jet and 4 jet 0-lepton analysis.

E.6.1. Event displays and cross checked events

Figure E.10 shows as an example the event display of an event (run 155669, event number 7405520), in which HEC noise (E_T^{miss} = 57.5 GeV) is overlaid with a jet with $p_T \approx 30$ GeV that is not rejected by the cleaning condition $f_{HEC} \geq 1 - f_{bad,Q}$.

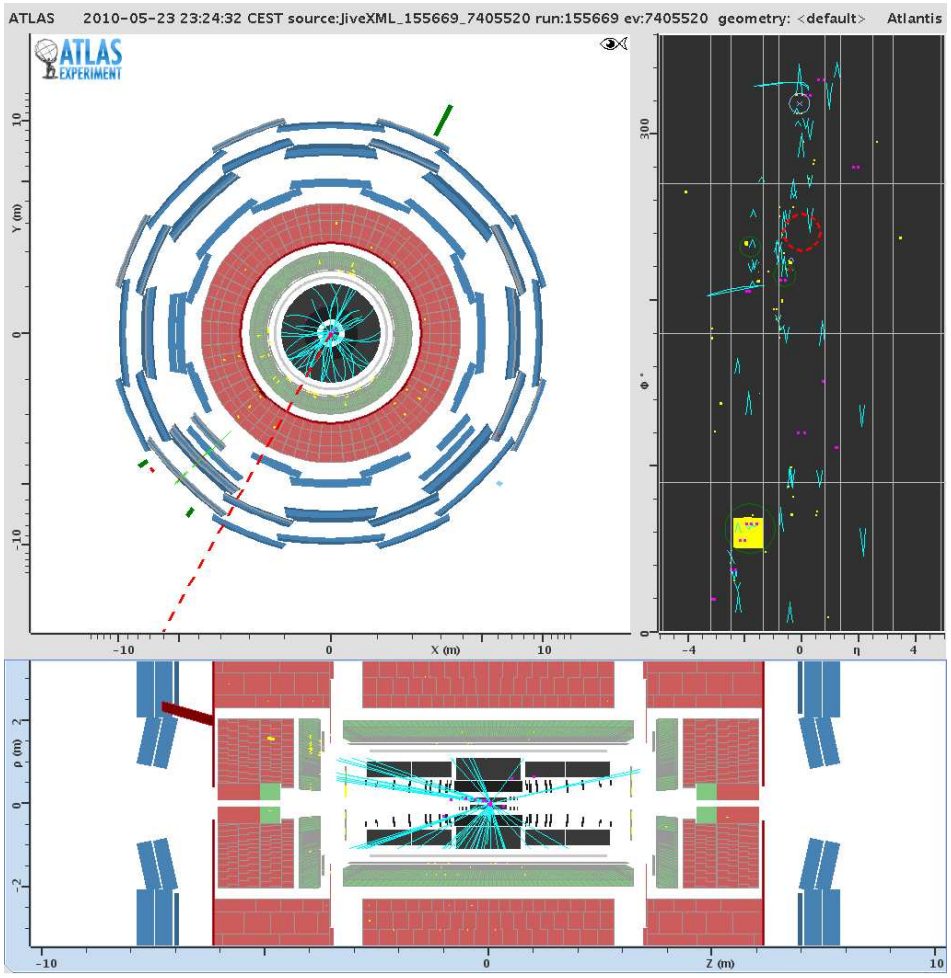

Figure E.10: Event display of the event run 155669, event number 7405520. It is a HEC noise overlaid event with missing transverse energy 69.9 GeV. Here one HEC cell (Id = 814522368) has the energy of $E_T = 57.5$ GeV and a quality factor of 65535 (overflow).

sample	p_T jet cut	after E_T^{miss} cut	$\Delta\phi$ cut	$E_T^{miss}/M_{\text{eff}}$ cut
1 jet 0 lepton				
SU4	0.05	0.05	-	-
Z + jets	6.7	6.0	-	-
W + jets	10.6	8.0	-	-
QCD	22743.2	32.2	-	-
top pairs	0.04	0.02	-	-
total SM	22760.5	46.2		
2 jet 0 lepton				
SU4	2.3	1.9	1.8	0.8
Z + jets	6.2	3.5	3.2	1.7
W + jets	16.4	7.4	6.7	2.6
QCD	108239	437.4	186.9	1.9
top pairs	5.9	1.3	1.2	0.3
total SM	108267.4	449.5	198.0	6.6
3 jet 0 lepton				
SU4	2.0	1.7	1.5	0.7
Z + jets	2.0	1.0	0.9	0.4
W + jets	5.3	2.5	2.1	0.7
QCD	30702.7	226.2	99.8	0.5
top pairs	5.6	1.2	1.0	0.3
total SM	30715.6	231.0	103.7	1.9
4 jet 0 lepton				
SU4	1.5	1.3	0.2	0.6
Z + jets	0.5	0.3	0.2	0.1
W + jets	1.3	0.7	0.6	0.2
QCD	5585.6	81.9	41.9	0.5
top pairs	4.5	0.8	0.6	0.2
total SM	5591.9	83.7	43.4	1.0

Table E.5: Cutflow table for the 4 jet 0-lepton analysis. Presented are the expected number of SM events for $\mathscr{L} = 70$ nb^{-1} at $\sqrt{s} = 7$ TeV.

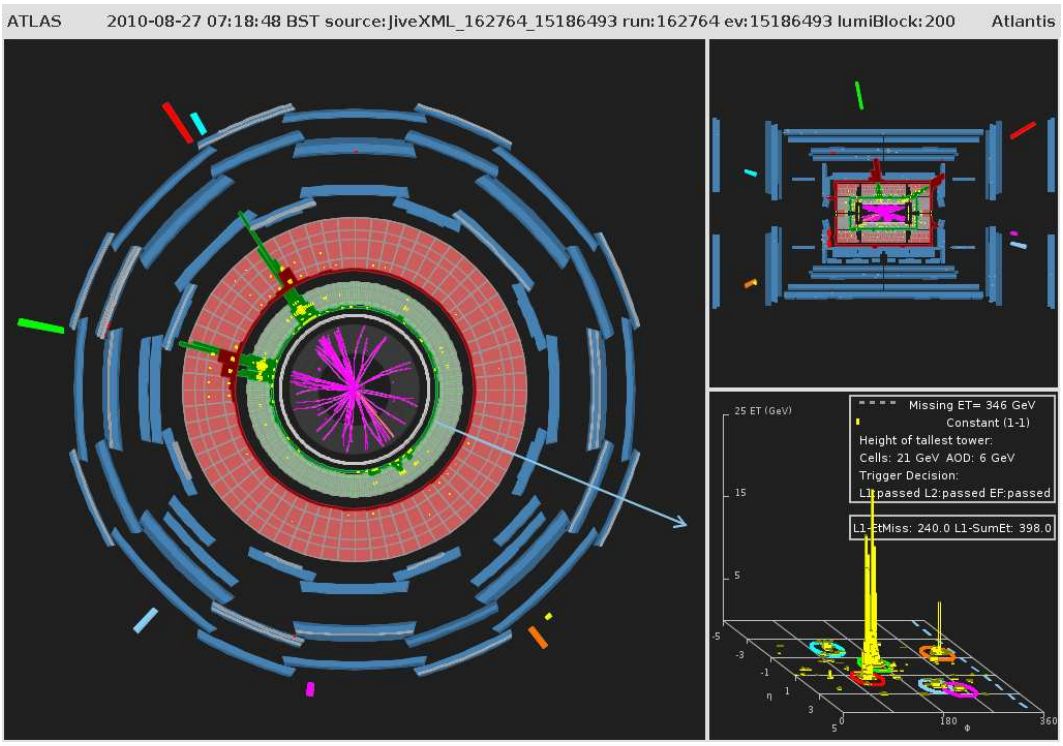

Figure E.11: Event display of the event run 162764, event number 15186493. It is a high M_{eff} event that passes all SUSY analysis cuts of the 2 jet, 3 jet and 4 jet 0-lepton channel.

Figure E.11 presents the event display for an event (run 162764, event number 15186493) with high M_{eff}:
$E_T^{miss} \approx 346$ GeV, $M_{\text{eff}} \approx 709$ GeV for the 2 jet 0-lepton channel, $M_{\text{eff}} \approx 754$ GeV for the 3 jet 0-lepton channel, $M_{\text{eff}} \approx 795$ GeV for the 4 jet 0-lepton channel that passes all 2 jet, 3 jet and 4 jet 0-lepton SUSY analysis cuts. The event numbers of the identified fake E_T^{miss} events coming from HEC noise and from other sources in the studied data sample ($\mathscr{L} = 70$ nb^{-1}) are summarised in Table E.6 and Table E.7. The events survived the standard data event cleaning cuts and have all $E_T^{miss} > 60$ GeV. The category represents one possible interpretation of the event.

E.6.2. Pile-up studies

Figure E.12 shows the distributions of E_T^{miss} (top left plot), M_{eff} (top right plot) and the azimuthal angular correlations between E_T^{miss} and the two leading jets (middle plots), as well as the distribution of the jet multiplicity (bottom plot) for events that pass the event cleaning cuts, vertex requirement and lepton veto. The 2 jet final state topology is considered for the E_T^{miss}, M_{eff} and $\Delta\phi$ distributions; no E_T^{miss} selection cut is applied for the M_{eff} and E_T^{miss} distribution. The

run number	event number	E_T^{miss} [GeV]	category
153565	16719787	88.2	HEC noise overlaid
153565	34054854	79.6	HEC noise overlaid
154817	1674739	246.3	HEC noise overlaid
154817	2908394	404	HEC coherent noise
155112	34821673	260.5	HEC coherent noise
155112	81162009	106.8	HEC noise overlaid
155112	22571186	80.9	HEC coherent noise
155697	16717957	62.9	HEC noise overlaid
155697	38988846	69.9	HEC noise overlaid

Table E.6: Events with $E_T^{miss} > 60$ GeV which survive the standard event cleaning cuts, but are rejected by the cleaning cut $f_{HEC} \geq 1 - f_{bad,Q}$.

$\Delta\phi(E_T^{miss}, \text{jet}_{1,2})$ plots are presented only for events with $E_T^{miss} > 40$ GeV. Jets are considered to have $p_T > 20$ GeV and $|\eta| < 2.5$. Two different run periods are compared: Periods A - C are periods with expected lower pile-up contribution (black line) and Period D (blue line) are runs where the luminosity was increased (higher pile-up). No significant differences are found in the shapes indicating that pile-up effects have for these measurements only a small impact on the analyses.

run number	event number	E_T^{miss} [GeV]	category	comments
153565	26794160	60.0	heavy flavour	with muon, $\Delta\phi(\text{track}, E_T^{miss}) < 0.01$
154813	14314654	94.9	resolution, crack	3 jet, a jet with $p_T = 306$ GeV, $\lvert\eta\rvert = 1.76$
154813	11658831	62.1	heavy flavour	muon with $p_T = 13.4$ GeV
154822	17159328	63.5	heavy flavour	no lepton, $\Delta\phi(\text{track}, E_T^{miss}) = 0.03$
154822	18132632	62.6	heavy flavour	muon with $p_T = 36.7$ GeV
155073	42829155	67.5	fake muon	muon with $p_T = 29.2$ GeV , $\Delta\phi(\text{muon}, E_T^{miss}) = 0.02$
155073	60290261	63.0	dead cell	3 jet, jet with f_{Cor}[a]= 0.15
155112	96514350	84.0	heavy flavour	no lepton, $\Delta\phi(\text{track}, E_T^{miss}) = 0.02$
155112	124107935	69.1	heavy flavour	muon with $p_T = 12.5$ GeV, $\Delta\phi(\text{muon}, E_T^{miss}) = 0.05$
155112	15039976	74.4	dead cell	3 jet, a jet with $f_{Cor} = 0.12$ and $\Delta\phi(\text{jet}, E_T^{miss}) = 0.07$
155112	23449229	83.8	$W \rightarrow \tau\nu + \text{jet}$	tau with $p_T = 20.7$ GeV
155112	45433614	60.5	heavy flavour	muon with $p_T = 58.4$ GeV
155160	36494374	90.4	heavy flavour	two-muons with $p_T = 24.7$ GeV and $p_T = 13.3$ GeV
155160	49382616	118	cosmic	jet with p_T = 148 GeV and n90 = 2 (t = 6.4 ns)
155160	59039343	77.1	heavy flavour	muon with p_T = 53.3 GeV

Table E.7: Events with $E_T^{miss} > 60$ GeV which survive the standard cleaning cut and the HEC noise cleaning cut $f_{HEC} \geq 1$ - $f_{bad,Q}$. The category represents one possible interpretation.

[a] f_{Cor} is the fraction of corrected energy for dead cells determined with the neighbour average method.

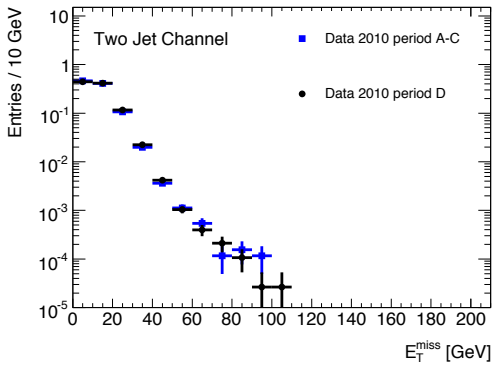

(a) E_T^{miss} for events with at least 2 jets

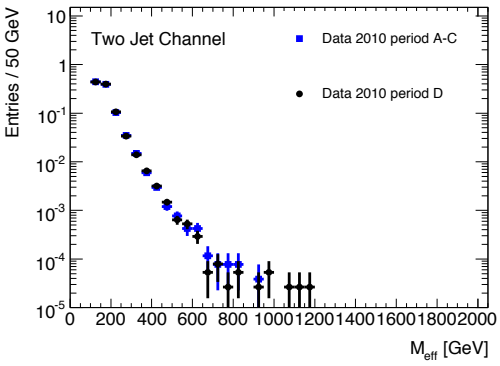

(b) M_{eff} for events with at least 2 jets

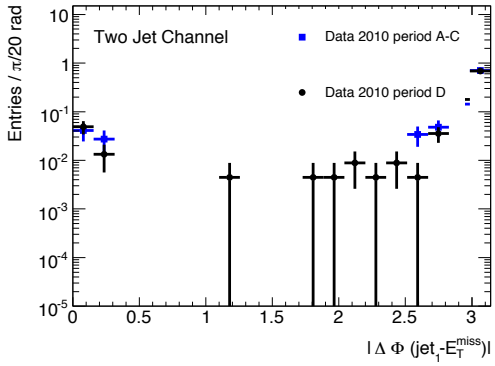

(c) $\Delta\phi(E_T^{miss},\ jet_1)$ for 2 jet events

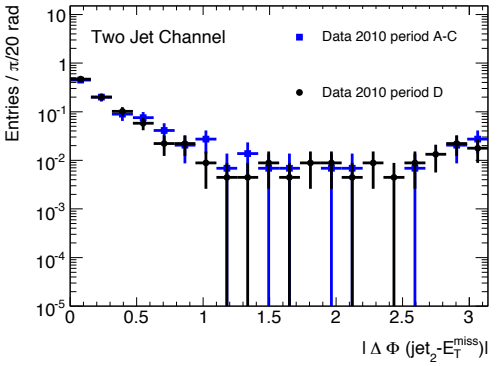

(d) $\Delta\phi(E_T^{miss},\ jet_2)$ for 2 jet events

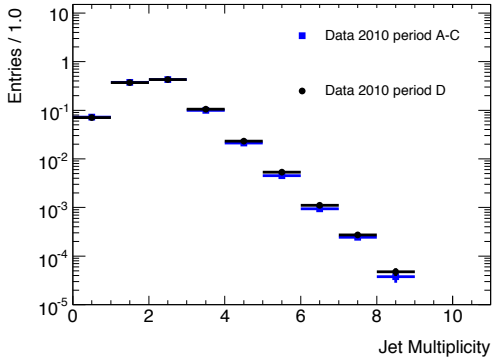

(e) jet multiplicity for 2 jet events

Figure E.12: Pile up studies for collision events of $\mathscr{L} = 70$ nb^{-1}. E_T^{miss} (top left plot, figure (a)), effective mass before E_T^{miss} selection (top right plot, figure (b)), $\Delta\phi(E_T^{miss}, jet_{1,2})$ distributions after the $E_T^{miss} > 40$ GeV selection (2nd row, figure (c) and figure (d)) for 2 jet 0-lepton events. The bottom plot (figure (e)) shows the jet multiplicity for jets with $p_T > 20$ GeV and $|\eta| < 2.5$. Events of high (black line) and low (blue line) pile-up runs are compared.

F. Jet reconstruction algorithms

In this chapter some details to the jet reconstruction algorithms, described in Section 5.2, are provided.

F.1. k_T algorithm

The k_T algorithm is based upon pair-wise clustering of the initial constituents (towers, clusters, partons, particles, etc.). All pairs of input objects are first listed and than analysed using a distance measure between the objects d_{ij} and also some condition upon which clustering should be terminated. The weighted distance measure between two objects (i, j) is calculated with the formula:

$$d_{ij} = min\left(k_{t,i}^{2p}, k_{t,j}^{2p}\right)\frac{\Delta R_{ij}^2}{R^2} d_{iB} = k_{T,i}^{2p} \tag{F.1}$$

where $\Delta R_{ij}^2 = (y_i - y_j)^2 + (\phi_i - \phi_j)^2$ is the distance between the two objects, $k_{t,i}$ and $k_{t,j}$ are the transverse momenta, ϕ_i and ϕ_j are the azimuthal angles and y_i, y_j are the rapidity of the objects i and j, respectively. R is a free parameter of the algorithm setting the resolution at which jets are resolved from each other as compared to the beam.
The algorithms proceeds as follows: Among all objects j the distance d_{ij} is calculated and the smallest distance $d_{i,min}$ is found. In the sense defined by the algorithm, the distance d_{iB} between two objects can be seen as the distance between object i and the beam.
If $d_{i,min}$ is of the "type" d_{iB} the object i is considered to be a jet by itself and removed from the list. Otherwise the corresponding objects i and j are combined into a new object k using four-momentum recombination. After this object i and j are removed from the list, object k is added and the list is remade. The procedure is repeated until also all resulting new sets of d_{ij} and d_{iB} are removed from the list.
For large values of R, the distances d_{ij} are smaller and thus more merging takes place before jets are complete.

F.2. anti-k_T algorithm

In addition to the radius R, a parameter p to govern the relative power of the energy/transverse momentum scale versus geometrical distance ΔR_{ij}, was added. For p = 1 one recovers the inclusive k_T algorithm. This means that within a jet the final merge is the hardest. Soft objects are either merged with nearby hard objects or left alone with low p_T ("merged" with the beam). For p > 0 the behaviour of the jet algorithm with respect to soft radiation is rather similar to that observed for the k_T algorithm, because the ordering between particles and R_{ij} have the biggest influence. The case of p = 0 corresponds to the so-called inclusive Cambridge/Aachen algorithm [259].
Since the behaviour with respect to soft radiation will be similar for all p < 0, for the "anti-k_T" jet-clustering algorithm p is set to be -1 in equation F.1. The consequence is that if $\Delta R <$R for a hard object, all softer objects will be merged with the harder object. Thus the jet boundary is unaffected by soft radiation. This means if a hard jet has no hard neighbours within a distance of 2R, then it will accumulate all soft particles within a circle of radius R and it will result in a perfectly conical jet. If two comparably hard objects are within R$< \Delta R_{ij} <$ 2R of each other, the energy will be shared between them depending upon their relative distance and $k_{t,i}$, e.g. for $k_{t,1} \gg k_{t,2}$ jet 1 will be conical and jet 2 will be partly conical, since it misses the overlapping part with jet 1. For hard objects within $\Delta R_{ij} <$ R of each other, a single jet will be formed containing both hard objects and the soft objects within their vicinity. The order of the merging is not important for this algorithm.

G. ATLAS data formats

The physics event informations are stored in different event formats, beginning with RAW and processing through reconstruction to ntuples used for the analysis [169–172].

RAW : data as recorded after the event filter (HLT); size: $\sim$ 1.6 MB/event

ESD : **E**vent **S**ummary **D**ata
output of the reconstruction process
content is intended to make access to RAW data (POOL ROOT files)
high-level objects: tracks, calorimeter clusters,
calorimeter cell energies, combined reconstruction objects etc.
stored in Tier-1s

AOD : **A**nalysis **O**bject **D**ata; derived from ESD
event reconstruction with "physics" objects of analysis interest:
electrons, muons, jets, vertices etc.
stored in Tier-1s and Tier-2s

DPD : **D**erived **P**hysics **D**ata; skimmed / slimmed / thinned events
performance (physics) DPDs are skims of ESDs (AODs) with selected events
and reduced event information
for performance studies/physics analysis
'user" data derived from AODs for end-user analysis and histogramming (n-tuples)
disk storage for group data is provided at Tier-1s and Tier-2s

TAG : event tags
short event summaries primarily for event selection to support efficient
identification/selection database (or ROOT files) used to quickly select
events in AOD and/or ESD files

List of Tables

List of Figures

Bibliography

[1] S. L. Glashow, *Partial symmetries of weak interactions*, Nucl. Phys. 22 (1961) 579-588.

[2] A. Salam and J. C. Ward, *Electromagnetic and weak interactions*, Phys. Lett. 13 (1964) 168-171.

[3] S. Weinberg, *A model of leptons*, Phys. Rev. Lett. 19 (1967) 1264-1266.

[4] A. Salam, *Gauge unification of fundamental forces*, Rev. Mod. Phys. 52 (1980) 525-538.

[5] Y.A. Golfand and E.P. Likhtman, *Extension of the algebra of poincare group generators and violation of p invariance*, JETP Lett. 13 (1971) 323.

[6] D. V. Volkov and V. P. Akulov, *Possible universal neutrino interaction*, JETP Lett. 16 (1972) 438.

[7] J. Wess and B. Zumino, *A Lagrangian model invariant under supergauge transformations*, Phys. Lett. B 49 (1974) 52.

[8] F. Halzen and A. D. Martin, *Quarks and leptons*, John Wiley & Sons, 1984.

[9] B. R. Martin and G. Shaw, *Particle physics*, John Wiley & Sons, 1997.

[10] D. Griffiths, *Introduction to elementary particles*, John Wiley & Sons, 1987.

[11] P. D. B. Collins, A. D. Martin and E. J. Squires, *Particle physics and cosmology*, John Wiley & Sons, 1989.

[12] M. E. Peskin and D. V. Schröder, *An introduction to quantum field theory*, West View Press, 1995.

[13] R. N. Mohapatra, *Unification and Supersymmetry*, Springer Verlag, 2003.

[14] H. Baer and X. Tata, *Weak scale Supersymmetry*, Cambrigde Univerity Press, 2006.

[15] J. Terning, *Modern Supersymmetry*, Oxford Science Publications, 2007.

[16] P. Binétruy, *Supersymmetry*, Oxford University Press, 2006.

[17] I. Aitchison, *Supersymmetry in particle physics*, Cambridge University Press, 2007.

[18] H. Kalka, G. Soff, *Supersymmetrie*, Teubner Studienbücher, 1997.

[19] E. Noether, *Invariante Variationsprobleme*, Nachr. d. Königl. Gesellsch. d. Wiss. zu Göttingen. Math.-Phys. Klasse (1918) 235-257.

[20] M. Gell-Mann, *A Schematic model of baryons and mesons*, Phys. Lett. 8 (1964) 214-215.

[21] M. Kobayashi and T. Maskawa, *CP violation in the renormalizable theory of weak interaction*, Prog. Theor. Phys. 49 (652-657) 1973.

[22] N. Cabibbo, *Unitary Symmetry and leptonic decays*, Phys. Rev. Lett. 10 (1963) 531-533.

[23] M. Ciuchini, *2000 CKM triangle analysis: A Critical review with updated experimental inputs and theoretical parameters*, JHEP 07 (2001) 013. arXiv: hep-ph/0012308.

[24] L. Euler, *Methodus Inveniendi Lineas Curvas Maximi Minive Proprietate Gaudentes*, Leonhardi Euleri Opera Omnia: Series I vol 24 (1744) 320.

[25] R. P. Feynman, *Space-time approach to non-relativistic quantum mechanics*, Rev. Mod. Phys. 20 (1948) 367-387.

[26] R. P. Feynman, *Mathematical formulation of the quantum theory of electromagnetic interaction*, Phys. Rev. 80 (1950) 440-457.

[27] P. W. Higgs, *Broken symmetries, massless particles and gauge fields*, Phys. Lett. 12 (1964) 132-133.

[28] P. W. Higgs, *Broken Symmetries and the masses of gauge bosons*, Phys. Rev. Lett. 13 (1964) 508-509.

[29] Abdelhak Djouadi, *The anatomy of electro-weak Symmetry breaking. I: The Higgs boson in the Standard Model*, Phys. Rept. 457 (2008) 1-216.

[30] *The Large Electron Positron collider*, CERN-ARCH-LEP-01-001 to 06-017 (1978-2000).

[31] *Fermi National Accelerator Laboratory*, `http://www.fnal.gov` (visited: 01.07.2010).

[32] *The LEP electroweak working group (LEPEWWG): Combined results from the ALEPH, DELPHI, L3, and OPAL detector collaborations*, `http://lepewwg.web.cern.ch/LEPEWWG/` (visited: 01.03.2010).

[33] R. Barate *et al.*, *Search for the Standard Model Higgs boson at LEP*, Phys. Lett. B 565 (2003) 61-75. arXiv: hep-ex/0306033.

[34] CDF collaboration and DØ collaboration, *Combined CDF and DØ upper limits on Standard Model Higgs boson production with up to 6.7 fb^{-1} of data*, FERMILAB-CONF-10-257-E (July, 2010). Preliminary Results prepared for the ICHEP 2010 Conference; arXiv: hep-ex/1007.4587.

[35] M. J. Herrero, *The Standard Model* (1998). lectures presented at the summer school: Techniques and concepts of high energy physics; arXiv: hep-ph/9812242v1.

[36] W. Greiner, S. Schramm and E. Stein, *Quantum chromodynamics*, Springer Verlag (2002).

[37] E. A. Paschos, *Electroweak theory*, Cambridge University Press, 2007.

[38] Y. Fukuda *et al*., *Evidence for oscillation of atmospheric neutrinos*, Phys. Rev. Lett. 81 (1998) 1562.

[39] G. Altarelli, R. Barbieri and F. Caravaglios, *Electroweak precision tests: A concise review*, Int. J. Mod. Phys. A 13 (1998) 1031.

[40] M. Planck, *On the law of distribution of energy in the normal spectrum*, Annalen der Physik 4 (1901) 553.

[41] J. R. Ellis, S. Kelley and D. V. Nanopoulos, *Probing the desert using gauge coupling unification*, Phys. Lett. B 260 (1991) 131-137.

[42] K. G. Begeman, A. H. Broeils and R. H. Sanders, *Extended rotation curves of spiral galaxies: Dark haloes and modified dynamics*, Mon. Not. Roy. Astron. Soc. 249 (1991) 523.

[43] G. Jungman, M. Kamionkowski, K. Griest, *Supersymmetric dark matter*, Phys. Rept. 267 (1996) 195-373. arXiv: hep-ph/9506380.

[44] C. L. Bennett *et al*., *Seven-Year Wilkinson Microwave Anisotropy Probe (WMAP) Observations: Sky Maps, systematic errors, and basic results*, submitted to Astrophysical Journal (2010). arXiv: astro-ph/1001.4744v1.

[45] J. Dunkley *et al*.(WMAP Collaboration), *Five-Year Wilkinson Microwave Anisotropy Probe (WMAP) Observations: Likelihoods and parameters from the WMAP data*, Astrophys. J. Suppl. 180 (2009) 306. arXiv: astro-ph/0803.0586.

[46] G. Bertone, D. Hooper and J. Silk, *Particle dark matter: Evidence, candidates and constraints*, Phys. Rept. 405 (2005) 279-390. arXiv: hep-ph/0404175.

[47] C. Amsler *et al*., *Particle Data Group: Review of particle physics*, Physics Letters B 667 (2008, partial update for the 2010) 1.

[48] P. Renton *et al*., *Global electroweak fits and the Higgs boson mass* (Philadelphia, July 2008). talk at the conference ICHEP08; arXiv: hep-ph/0809.4566.

[49] W. de Boer, *Grand unified theories and Supersymmetry in particle physics and cosmology*, Prog. Part. Nucl. Phys. 33 (1994) 201-302. arXiv: hep-ph/9402266v5.

[50] A. Djouadi, *The anatomy of electroweak Symmetry breaking. II: The Higgs bosons in the Minimal Supersymmetric Model*, Phys. Rept. 459 (2008) 1-241. arXiv: hep-ph/0503173.

[51] M. Drees *et al.*, *An introduction to Supersymmetry* (1996). arXiv: hep-ph/9611409.

[52] P. Langacker and M. Luo, *Implications of precision electroweak experiments for* m_t, ρ^0, $\sin^2\theta_W$, *and grand unification*, Phys. Rev. D 44 (1991) 817-822.

[53] J. R. Ellis, J. S. Hagelin, Dimitri V. Nanopoulos, Keith A. Olive, M. Srednicki, *Supersymmetric relics from the big bang*, Nucl. Phys. B 238 (1984) 453-476.

[54] H. Goldberg, *Constraint on the photino mass from cosmology*, Phys. Rev. Lett. 50 (1983) 1419-1422.

[55] S. Dimopoulos, *LHC, SSC and the universe*, Phys. Lett. B 246 (1990) 347-352.

[56] S. P. Martin, *A Supersymmetry primer*, arXiv: hep-ph/9709356.

[57] H. P. Nilles, *Supersymmetry, supergravity and particle physics*, Physics. Phys. Rept. 110 (1984) 1.

[58] H. E. Haber and G. L. Kane, *The search for Supersymmetry: Probing physics beyond the Standard Model*, Phys. Rept. 117 (1985) 75-263.

[59] J. Wess and J. Bagger, *Supersymmetry and supergravity*, 1992.

[60] C. Csaki, *The Minimal Supersymmetric Standard Model (MSSM)*, Mod. Phys. Lett. A 11 (1996) 599.

[61] H. E. Haber and G. L. Kane, *The search for Supersymmetry: Probing physics beyond the Standard Model*, Phys. Rep. 117 (1985) 75.

[62] H. Nilles, *Supersymmetry, supergravity and particle physics*, Phys. Rep. 110 (1984) 1.

[63] P. Nath and R. L. Arnowitt, *Generalized supergauge symmetry as a new framework for unified gauge theories*, Phys. Lett. B 56 (1975) 177.

[64] S. Ferrara, L. Girardello, F. Palumbo, *General mass formula in broken Supersymmetry*, Phys. Rev. D 20 (1979) 403-408.

[65] G. R. Farrar, P. Fayet, *Phenomenology of the production, decay, and detection of new hadronic states associated with Supersymmetry*, Phys. Letter B 76 (1978) 575.

[66] S. Prasad Das, A. Datta, M. Guchait *et al.*, *Probing R-parity violating models of neutrino mass at the Tevatron via top squark decays*, Phys. Rev. D 70 (2004) 015009. arXiv: hep-ph/0309168.

[67] M. Shiozawa *et al.*, *Search for proton decay via $p \to e^+\pi^0$ in a Large Water Cherenkov Detector*, Phys. Rev. Lett. 81 (1998) 3319.

[68] J. Ellis, K. A. Olive and Y. Santoso, *Constraining Supersymmetry*, New J. Phys. 4 (2002) 32.

[69] T. Falk, K. A. Olive, M. Srednicki, *Heavy sneutrinos as dark matter*, Phys. Lett. B 339 (1994) 248. arXiv: hep-ph/9409270.

[70] LEP Collaborations; SLD Electroweak Group and SLD Heavy Flavor Group, *A combination of preliminary electroweak measurements and constraints on the Standard Model*, CERN-EP/2003-091; LEP-EWWG/2003-02 (2004). arXiv: hep-ex/0312023v2.

[71] L. Girardello and Marcus T. Grisaru, *Soft breaking of Supersymmetry*, Nucl. Phys. B 194 (1982) 65.

[72] S. Dimopoulos and D. W. Sutter, *The Supersymmetric flavour problem*, Nucl. Phys. B 452 (1995) 496-512.

[73] F. E. Paige, S. D. Protopopescu, H. Baer, X. Tata, *ISAJET 7.69: A Monte Carlo event generator for pp, $p\bar{p}$, and e^+e^- reactions* (2003). arXiv: hep-ph/0312045.

[74] A. V. Gladyshev and D. I. Kazakov, *Supersymmetry and LHC* (2006). arXiv: hep-ph/0606288v1.

[75] G. Degrassi it et al., *Towards high-precision predictions for the MSSM Higgs sector*, Eur. Phys. J. C 28 (2003) 133.

[76] H. E. Haber and R. Hemping, *Can the mass of the lightest Higgs boson of the minimal supersymmetric model be larger than m(Z)?*, Phys. Rev. Lett. 66 (1991) 1815-1818.

[77] Y. Okada, M. Yamaguchi and T. Yanagida, *Upper bound of the lightest Higgs boson mass in the minimal supersymmetric Standard Model*, Prog. Theor. Phys. 85 (1991) 1-6.

[78] Y. Okada, M. Yamaguchi and T. Yanagida, *Renormalization group analysis on Higgs mass in the softly broken supersymmetric Standard Model*, Phys. Lett. B 262 (1991) 54-58.

[79] J. H. Lawrence, R. Rattazzi, U. Sarid, *The top quark mass in supersymmetric SO(10) unification*, Phys. Rev. D 50 (1994) 7048-7065.

[80] M. L. Brooks *et al.*, *New Limit for the family-number non-conserving decay $\mu^+ \to e^+\gamma$*, Phys. Rev. Lett. 83 (1999) 1521-1524.

[81] W. Buchmüller and D. Wyler, *CP Violation and R invariance in supersymmetric models of strong and electroweak interactions*, Phys. Lett. B 121 (1983) 321.

[82] A. Djouadi *et. all*, *The Minimal supersymmetric Standard Model: Group summary report* (1998). arXiv: hep-ph/9901246.

[83] A. Chamseddine *et al*, *Locally supersymmetric grand unification*, Phys. Rev. Lett. 49 (1982) 970.

[84] H. P. Nilles *et al*, *Supersymmetry, supergravity and particles*, Phys. Rep. 110 (1984) 1.

[85] M. Dine, Y. Shirman and A. Nelson, *Low energy dynamical Supersymmetry breaking simplified*, Phys. Rev. D 51 (1995) 1362.

[86] G. F. Giudice, R. Rattazzi, *Theories with gauge mediated Supersymmetry breaking*, CERN-TH/97-380 (1998). arXiv: hep-ph/9801271v2.

[87] G. F. Giudice, M. A. Luty, H. Murayama and R. Rattazzi, *Gaugino mass without singlets*, JHEP 9812 (1998) 027. arXiv: hep-ph/9810442.

[88] L. Randall and R. Sundrum, *Out Of this world Supersymmetry breaking*, Nucl. Phys. B 557 (1999) 1999. arXiv: hep-th/9810155.

[89] T. Gherghetta, G. F. Giudice, J. D. Wells, *Phenomenological consequences of Supersymmetry with anomaly-induced masses*, Nucl. Phys. B 559 (1999) 27. arXiv: hep-ph/9904378.

[90] J. Ellis, T. Falk, K. A. Olive, Y. Santoso, *Exploration of the MSSM with non-universal Higgs masses* (2002). arXiv: hep-ph/0210205v2.

[91] J. Pumplin*et al*., *New generation of parton distributions with uncertainties from global QCD analysis*, JHEP 07 (2002) 012. arXiv: hep-ph/0201195.

[92] M.A. Dobbs *et al*., *Les Houches guidebook to Monte Carlo generators for hadron collider physics*. arXiv: hep-ph/0403045.

[93] R. D. Field, *The underlying event in hard scattering processes*, FERMILAB-CONF-02-009-E (2002). arXiv: hep-ph/0201192.

[94] A. Moraes, C. Buttar, and I. Dawson, *Prediction for minimum bias and the underlying event at LHC energies*, Eur. Phys. J. C 50 (2007) 435-466.

[95] A. Moraes, *Modeling the underlying event: generating predictions for the LHC*, ATL-PHYS-PROC-2009-045 (2009).

[96] W. Beenakker (Leiden), R. Höpker, P. M. Zerwas (DESY), *SUSY-QCD decays of squarks and gluinos*, Phys. Lett. B 378 (1996) 159-166.

[97] M. Krämer *et al*., *Supersymmetric particle production at hadron colliders*, Nuclear Physics B 74 (1999) 80-84. arXiv: hep-ph/9809259v1.

[98] W. Beenakker, R. Höpker, *SUSY-QCD corrections in the squark-gluino sector*, Nucl. Phys. Proc. Suppl. C 51 (1996) 261-266. arXiv: hep-ph/9606290v1.

[99] W. Beenakker, R. Hopker, M. Spira, *PROSPINO: A program for the production of Supersymmetric Particles In Next-to-leading Order QCD* (1996). arXiv: hep-ph/9611232.

[100] W. Beenakker *et al*., *The production of charginos/neutralinos and sleptons at hadron colliders*, Phys. Rev. Lett. 83 (1999) 3780-3783. arXiv: hep-ph/9906298.

[101] *PROSPINO2*, `http://www.ph.ed.ac.uk/~tplehn/prospino/` (visited: 01.06.2010).

[102] M. Krämer, *Precise calculation for SUSY searches at the LHC*, talk in the ATLAS SUSY meeting; `http://indico.cern.ch/getFile.py/access?contribId=3&resId=0&materialId=slides&confId=108369` (visited: 28.10.2010), Cern, 6th of October 2010.

[103] ATLAS Collaboration, *ATLAS Detector and physics performance: Technical Design Report, volume 2*, CERN-TDR-015; CERN-LHCC-99-15 (1999).

[104] ATLAS Collaboration, *Expected performance of the ATLAS experiment - detector, trigger and physics*, CERN-OPEN-2008-020 (2008). arXiv: hep-ph/0901.0512.

[105] F. Ahles, B. Meirose, *Studying suppression of beam-induced and cosmic background to physics analyses*, ATL-PHYS-INT-2010-031 (2010).

[106] C. Lefevre, *The CERN accelerator complex*, `http://public.web.cern.ch/public/en/research/AccelComplex-en.html` (visited: 01.03.2010), 2006.

[107] *LHC website*, `http://lhc.web.cern.ch/lhc/` (visited: 01/07/2010).

[108] L. Evans and P. Byyant (editors), *LHC machine*, JINST 3:SO8001 (2008).

[109] O. S. Brüning, P. Collier, P. Lebrun, S. Myers, R. Ostojic, J. Poole, and P. Proudlock (editors), *LHC design report*, CERN-2004-003-V-1 volume 1: The LHC main ring (2004).

[110] O. S. Brüning, P. Collier, P. Lebrun, S. Myers, R. Ostojic, J. Poole, and P. Proudlock (editors), *LHC design report*, CERN-2004-003-V-2 volume 2: The LHC infrastructure and general services (2004).

[111] M. Benedikt, P. Collier, V. Mertens, J. Poole, and K. Schindl (editors), *LHC design report*, CERN-2004-003-V-3 volume 3: The LHC injector chain (2004).

[112] S. Myers, *Report on the LHC*, talk at the ICHEP conference, Paris, 26.07.2010.

[113] R. Assmann, *Status of LHC operations* (Geneva, 10.09.2010). talk in the LHC report meeting; `http://indico.cern.ch/conferenceDisplay.py?confId=103500` (visited: 01.10.2010).

[114] *Summary of the analysis of the 19 September 2008 incident at the LHC*, CERN press release (2008).

[115] G. Aad *et al*., *The ATLAS experiment at the CERN Large Hadron Collider*, JINST 3 SO8003 (2008).

[116] R. Adolphi *et al*., *The CMS experiment at the CERN LHC*, JINST 3 SO8004 (2008).

[117] A. A. Alves *et al*., *The LHCb detector at the LHC*, JINST 3 SO8005 (2008).

[118] K. Aamodt *et al*., *The ALICE experiment at the CERN LHC*, JINST 3 SO8002 (2008).

[119] O. Adriani *et al*., *The LHCf detector at the CERN Large Hadron Collider*, JINST 3 SO8006 (2008).

[120] G. Anelli *et al*., *The TOTEM experiment at the CERN Large Hadron Collider*, JINST 3 SO8007 (2008).

[121] *TOTEM experiment*, `http://totem-experiment.web.cern.ch/totem-experiment/` (visited: 01.03.2010).

[122] ATLAS Collaboration, *Technical proposal for a general-purpose p-p experiment at the Large Hadron Collider at CERN*, CERN-LHCC-94-43; LHCC-P-2 (1994).

[123] CDF Collaboration, *Observation of top quark production in $p\bar{p}$ collisions*, Phys. Rev. Lett. 74 (1995) 2626-2631. arXiv: hep-ex/9503002.

[124] S. Abachi *et al*. D0 Collaboration, *Observation of the top quark*, Phys. Rev. Lett. 74 (1995) 2632-2637. arXiv: hep-ex/9503003.

[125] ATLAS Collaboration, *Prospects for Supersymmetry discovery based on inclusive searches*, ATL-PHYS-PUB-2009-066 (2008).

[126] ATLAS Collaboration, *Prospects for Supersymmetry discovery based on inclusive searches at a 7 TeV centre-of-mass energy with the ATLAS detector*, ATL-PHYS-PUB-2010-010 (2010).

[127] ATLAS Collaboration, *ATLAS Detector and physics performance: Technical Design Report, volume 1*, CERN-TDR-014; CERN-LHCC-99-14 (1999).

[128] ATLAS Collaboration, *ATLAS Central Solenoid Technical Design Report*, CERN-LHCC-97-21 (1997).

[129] ATLAS Collaboration, *ATLAS Barrel Toroid Technical Design Report*, CERN-LHCC-97-19 (1997).

[130] ATLAS Collaboration, *ATLAS End-Cap Toroids Technical Design Report*, CERN-LHCC-97-20 (1997).

[131] ATLAS Collaboration, *ATLAS Inner detector Technical Design Report, volume 1*, CERN-LHCC-97-16 (1997).

[132] ATLAS Collaboration, *ATLAS Inner detector Technical Design Report, volume 2*, CERN-LHCC-97-17 (1997).

[133] ATLAS Collaboration, *ATLAS Pixel detector Technical Design Report*, CERN-LHCC-98-13 (1998).

[134] G. Aad *et al.*, *ATLAS Pixel detector electronics and sensors*, JINST 3 P07007 (2008).

[135] A. Ahmad *et al.*, *The Silicon microstrip sensors of the ATLAS semiconductor tracker*, Nucl. Instrum. Meth. A 578 (2007) 98-118.

[136] E. Abat *et al.*, *The ATLAS Transition Radiation Tracker (TRT) proportional drift tube: Design and performance*, JINST 3 P02013 (2008).

[137] Pixel Detector ATLAS webpage, `http://atlas.ch/pixel-detector.html` (visited: 01.03.2010).

[138] ATLAS Collaboration, *The ATLAS Inner Detector commissioning and calibration* (2010). accepted by EPJC; arXiv: physics.ins-det/1004.5293.

[139] ATLAS Collaboration, *Readiness of the ATLAS Tile Calorimeter for LHC collisions*, Tech. Rep. ATLAS-TCAL-2010-01-003; CERN-PH-EP-2010-024 (June, 2010). arXiv: physics.ins-det/1007.5423.

[140] ATLAS Collaboration, *Liquid argon calorimeter Technical Design Report*, CERN-LHCC-96-041 (1996). `http://cdsweb.cern.ch/record/331061` (visited: 01.03.2010).

[141] ATLAS Collaboration, *Tile Calorimeter Technical Design Report*, CERN-LHCC-96-042 (1996). `http://cdsweb.cern.ch/record/331062` (visited: 01.03.2010).

[142] ATLAS Collaboration, *ATLAS Collaboration. ATLAS Calorimeter Performance Technical Design Report*, CERN-LHCC-96-040 (1996).

[143] B. Aubert *et al.*, *Construction, assembly and tests of the ATLAS electromagnetic barrel calorimeter*, Nucl. Instrum. Meth. A 558 388 (2006).

[144] E. Abat *et al.*, *The ATLAS TRT Barrel Detector*, JINST 3 P02014 (2008).

[145] E. Abat *et al.*, *The ATLAS TRT End-Cap Detectors*, JINST 3 P10003 (2008).

[146] D.M. Gingrich *et al.*, *Construction, assembly and testing of the ATLAS hadronic end-cap calorimeter*, JINST 2 P05005 (2007).

[147] J. Ban *et al.*, *Cold electronics for the liquid argon hadronic end-cap calorimeter of ATLAS*, Nucl. Instrum. Meth. A 556 158 (2006).

[148] R. Ichimyia *et al.*, *Radiation qualification of electronics components used for the ATLAS level-1 muon endcap trigger system*, ATL-DAQ-CONF-2005-003. `http://cdsweb.cern.ch/record/812814` (visited: 01.04.2010).

[149] A. Artamonov *et al.*, *The ATLAS forward calorimeters*, JINST 3 P02010 (2008).

[150] ATLAS Collaboration, *Evidence for prompt photon production in p-p collisions at* $\sqrt{s}$ = *7 TeV with the ATLAS detector*, ATLAS-CONF-2010-077 (2010).

[151] ATLAS Collaboration, *ATLAS Muon Spectrometer Technical Design Report*, CERN-LHCC-97-22 (1997).

[152] S. Palestini *et al.*, *The muon spectrometer of the ATLAS experiment*, Nucl. Phys. 125 (Proc. Suppl.) 337 (2003).

[153] J. Wotschack *et al.*, *ATLAS Muon chamber construction parameters for CSC, MDT, and RPC chambers*, ATL-MUON-PUB-2008-006 (2008).

[154] ATLAS Collaboration, *Muon Performance in minimum bias p-p collision data at* $\sqrt{s}$ = *7 TeV with ATLAS*, ATLAS-CONF-2010-036 (2010).

[155] ATLAS Collaboration, *Charged-particle multiplicities in p-p interactions at* $\sqrt{s}$ *= 900 GeV measured with the ATLAS detector at the LHC*, Phys Lett B 688, Issue 1 (2010) 21-42.

[156] ATLAS Collaboration, *ATLAS forward detectors for measurement of elastic scattering and luminosity*, CERN-LHCC-2008-004 (2008). `http://cdsweb.cern.ch/record/1095847` (visited: 01.03.2010).

[157] ATLAS Collaboration, *ATLAS forward detectors for luminosity measurement and monitoring*, CERN-LHCC-2004-10; LHCC I-014 (2004). `http://cdsweb.cern.ch/record/721908` (visited: 01.03.2010).

[158] ATLAS Collaboration, *Zero degree calorimeters for ATLAS*, CERN-LHCC-2007-01; LHCC I-016 (2007). `http://cdsweb.cern.ch/record/1009649` (visited: 01.03.2010).

[159] Amaldi *et al.*, *The real part of the forward proton proton scattering amplitude measured at the CERN intersecting storage rings*, Phys. Lett. B 66 (1977) 390.

[160] ATLAS Collaboration, *Performance of the ATLAS detector using first collision data*, ATLAS-PERF-2010-01-003 (2010). accepted by JINST; arXiv: hep-ex/1005.5254v1.

[161] *ATLAS twiki pages: ATLAS Detector status*, `https://twiki.cern.ch/twiki/bin/view/Atlas/ApprovedPlotsATLASDetector` (visited: 01.03.2010).

[162] ATLAS Collaboration, *ATLAS High-Level Trigger, Data Aquisition and Controls Technical Design Report*, CERN-LHCC-2003-022 (2003).

[163] ATLAS Collaboration, *ATLAS First-Level Trigger Technical Design Report*, CERN-LHCC-98-14 (1998).

[164] A. Hamilton for the ATLAS Collaboration, *The ATLAS Trigger System commissioning and performance*, Poster at Hadron Collider Physics (2010). arXiv: physics.ins-det/1010.0017v2.

[165] ATLAS Collaboration, *Performance of the ATLAS jet trigger with pp collisions at* $\sqrt{s} =$ 900 GeV, ATLAS-CONF-2010-028 (July, 2010).

[166] ATLAS Collaboration, *The ATLAS missing* E_T *trigger performance with initial LHC runs at* $\sqrt{s} = 900$ GeV, ATLAS-CONF-2010-026 (July, 2010).

[167] *LHC webpage*, `http://public.web.cern.ch/public/en/lhc/Computing-en.html` (visited: 01.05.2010).

[168] *LCG webpage*, `http://lcg.web.cern.ch/lcg/` (visited: 01.05.2010).

[169] ATLAS Collaboration, *The ATLAS computing model*, ATL-SOFT-2004-007; CERN-LHCC-2004-037/G-085 (2004).

[170] *ATLAS computing model twiki page*, `https://twiki.cern.ch/twiki/bin/view/Atlas/WorkBookComputingModel;https://twiki.cern.ch/twiki/bin/view/Atlas/ComputingModel` (visited: 01.05.2010).

[171] ATLAS Collaboration, *The ATLAS computing Technical Design Report*, ATLAS-TDR-017; CERN-LHCC-2005-022 (2005).

[172] R. W. L. Jones, D. Barberis, *The evolution of the ATLAS computing model*, J. Phys. Conf. Ser. 219 072037 (2010). 17th International Conference on Computing in High Energy Physics and Nuclear Physics (CHEP 2009); `http://iopscience.iop.org/1742-6596/219/7/072037`.

[173] *Athena core software*, `http://atlas-computing.web.cern.ch/atlas-computing/packages/athenaCore/athenaCore.php` (visited: 01.05.2010).

[174] P. Calafiura, W. Lavrijsen, C. Leggett, M. Marino and D. Quarrie, *The Athena control framework in production, new developments and lessons learned*, 2005.

[175] ATLAS collaboration, *The ATLAS computing workbook*, `https://twiki.cern.ch/twiki/bin/view/Atlas/WorkBook` (visited: 01.05.2010).

[176] *MC generator ATLAS twiki page*, `https://twiki.cern.ch/twiki/bin/view/AtlasProtected/McGeneratorsForAtlas` (visited: 01.03.2010).

[177] T. Sjostrand, S. Mrenna, P. Skands, *PYTHIA 6.4 physics and manual*, JHEP 05 (2006) 026. arXiv: hep-ph/0603175.

[178] G. Corcella *et al.*, *HERWIG 6: An event generator for hadron emission reactions with interfering gluons (including supersymmetric processes)*, JHEP 01 (2001) 010. arXiv: hep-ph/0011363.

[179] G. Corcella *et al.*, *HERWIG 6.5 release note*, arXiv: hep-ph/0210213, 2002.

[180] J. Butterworth, J. Forshaw, M. Seymour, *Multiparton interactions in photoproduction at HERA*, Z. Phys. C72 (1996) 637-646. arXiv: hep-ph/9601371.

[181] G. Marchesini, B. Webber, G. Abbiendi, I. Knowles, M. Seymour, L. Stanco, *Herwig: A Monte Carlo event generator for simulating hadron emission reactions with interfering gluons*, Comput. Phys. Commun. 67 (1991) 465.

[182] T. Gleisberg *et al.*, *SHERPA 1.alpha, a proof-of-concept version*, JHEP 02 (2004) 056. arXiv: hep-ph/0311263.

[183] B. P. Kersevan, E. and Richter-Was, *The Monte Carlo event generator AcerMC version 2.0 with interfaces to PYTHIA 6.2 and HERWIG 6.5* (2004). arXiv: hep-ph/0405247.

[184] M. Mangano *et al.*, *ALPGEN, a generator for hard multiparton processes in hadronic collisions*, JHEP 07 (2003) 001. arXiv: hep-ph/0206293.

[185] T. Stelzer and W. Long, *Automatic generation of tree level helicity amplitudes*, Comput. Phys. Commun. 81 (1994) 357-371. arXiv: hep-ph/9401258.

[186] S. Frixione, B. R. Webber, *The MC@NLO 3.2 event generator* (2006). arXiv: hep-ph/0601192.

[187] S. Frixione, B. R. Webber, *Matching NLO QCD computations and parton shower simulations*, JHEP 06 029. arXiv: hep-ph/0204244.

[188] S. Moch, P. Uwer, *Heavy-quark pair production at two loops in QCD*, Nucl. Phys. Proc. Suppl. 183 75-80. arXiv: hep-ph/0807.2794.

[189] J. Alwalla *et al.*, *A standard format for Les Houches event files*, Comput. Phys. Commun. 176 (2007) 300-304. arXiv: hep-ph/0609017.

[190] S. Jadach, J. Kuhn, Z. Was, *TAUOLA: A Library of Monte Carlo programs to simulate decays of polarized tau leptons*, Comput. Phys. Commun. 64 (1990) 275-299.

[191] E. Barberio, B. van Eijk, Z. Was, *PHOTOS: A universal Monte Carlo for QED radiative corrections in decays*, Comput. Phys. Commun. 66 (1991) 115-128.

[192] A. Moraes *et al.*, *Prediction for minimum bias and the underlying events at LHC energies*, Eur. Phys. J. C 50 (2007) 435-466.

[193] CDF Collaboration, *Charged jet evolution and the underlying event in $p\bar{p}$ collisions at 1.8 TeV*, Phys. Rev. D 70 2004. arXiv: hep-ex/0404004.

[194] CDF Collaboration, *The underlying event in hard interactions at the Tevatron $p\bar{p}$ collider*, Phys. Rev. D 65 (2002) 092002.

[195] *JIMMY webpage*, `http://projects.hepforge.org/jimmy/` (visited: 01.03.2010).

[196] M. Bahr *et al.*, *Herwig++ physics and manual* (2008). arXiv: hep-ph/0803.0883.

[197] M. Bahr *et al.*, *Herwig++ 2.3 release note* (2008). arXiv: hep-ph/0812.0529.

[198] A. Sherstnev and R. S. Thorne, *Parton distributions for LO generators*, Eur. Phys. J. C 55 (2008) 553-575. arXiv: hep-ph/0711.2473.

[199] I. Borozan, M. Seymour, *An eikonal model for multiparticle production in hadron hadron 1938 interactions*, JHEP 09 (2002) 015. arXiv: hep-ph/0207283.

[200] J. Alwall *et al.*, *Comparative study of various algorithms for the merging of parton showers and matrix elements in hadronic collisions*, Eur. Phys. J. C53 (2008) 473-500.

[201] T. Binoth, M. Ciccolini, N. Kauer and M. Kramer, *Gluon-induced W-boson pair production at the LHC*, JHEP 12 (2006) 046. arXiv: hep-ph/0611170.

[202] H. Baer, *Computational Tools for Supersymmetry Calculations*, Chapter to appear in perspectives on Supersymmetry, edited by G. Kane (2009). arXiv: hep-ph/0912.3270v1.

[203] A. Djouadi, J. L. Kneur and G. Moultaka, *SuSpect: a fortran code for the supersymmetric and Higgs particle spectrum in the MSSM*, Comput. Phys. Commun. 176 (2007) 426. arXiv: hep-ph/0211331.

[204] B. C. Allanach, *SOFTSUSY: A C++ program for calculating supersymmetric spectra*, arXiv: hep-ph/0104145.

[205] F. E. Paige, S. D. Protopopescu, H. Baer, X. Tata, *Simulating Supersymmetry with ISAJET 7.0/ISASUSY 1.0*, proceedings of the workshop on Physics at Current Accelerators and Supercolliders, 1993.

[206] G. Belanger, F. Boudjema, A. Pukhov, A. Semenov, *Dark matter direct detection rate in a generic model with micrOMEGAs2.2*. arXiv: hep-ph/0803.2360.

[207] A. Djouadi, J.-L. Kneur, G. Moultaka, *SuSpect: a fortran code for the supersymmetric and Higgs particle spectrum in the MSSM*, arXiv: hep-ph/0211331, 2002.

[208] P. Skands *et al.*, *SUSY Les Houches Accord: Interfacing SUSY spectrum calculators, decay packages, and event generators*, JHEP 07 (2004) 036. arXiv: hep-ph/0311123.

[209] *Supersymmetry Les Houches Accord webpage*, `http://home.fnal.gov/~skands/slha/` (visited: 01.05.2010).

[210] M.R. Whalley, D. Bourilkov, R.C. Group, *The Les Houches accord PDFs (LHAPDF) and LHAGLUE* (2005). arXiv: hep-ph/0508110.

[211] W. Tung, H. Lai, J. Pumplin, P. Nadolsky, C. Yuan, *Global QCD Analysis and Collider Phenomenology-CTEQ* (2007). 15th International Workshop on Deep-Inelastic Scattering and Related Subjects; arXiv: hep-ph/0707.0275.

[212] *CTEQ webpage*, `http://www.phys.psu.edu/~cteq/` (visited: 01.06.2010).

[213] J. Pumplin *et al.*, *New generation of parton distributions with uncertainties from global QCD analysis*, JHEP 07 (2002) 012. arXiv: hep-ph/0201195.

[214] K. Assamagan *et al.*, *The ATLAS Monte Carlo Project*, ATL-SOFT-INT-2010-002 (2010).

[215] ATLAS collaboration, *ATLAS Monte Carlo tunes for MC09*, ATL-PHYS-PUB-2010-002 (2010).

[216] P. M. Nadolsky *et al.*, *Implications of CTEQ global analysis for collider observables*, Phys. Rev. D 78 (2008) 013004. arXiv: hep-ph/10.1103.

[217] S. Agostinelli *et al.*, *GEANT4: A simulation toolkit*, Nucl. Instrum. Meth. A 506 (2003) 250-303.

[218] D. Constanzo *et al.*, *ATLAS detector simulation: status and outlook- Technical Report*, ATL-SOFT-PUB-2005-004; ATL-COM-SOFT-2005-008; CERN-ATL-SOFT-PUB-2005-004 (2005).

[219] J. Allison *et al.*, *Geant4 developments and applications*, EEE Transactions on Nuclear Science Vol. 53, issue 1 (2006) 270-278.

[220] *Atlfast2 twiki page*, `https://twiki.cern.ch/twiki/bin/view/Atlas/AtlfastII` (visited: 01.06.2010).

[221] D. Cavalli *et al.*, *Performance of the ATLAS fast simulation ATLFAST*, ATL-PHYS-INT-2007-005; ATL-COM-PHYS-2007-012 (2007).

[222] D. Adams *et al.*, *The ATLFAST-II performance in release 14- particle signatures and selected benchmark processes*, ATL-COM-PHYS-2009-554 (2009).

[223] K. Edmonds, S. Fleischmann, T. Lenz, C. Magass, J. Mechnich, and A. Salzburger, *The Fast ATLAS Track Simulation (FATRAS),*, ATL-SOFT-PUB-2008-01; ATL-SOFT-PUB-2008-02 (2008).

[224] M. Dührssen, *The fast calorimeter simulation FastCaloSim*, ATL-PHYS-INT-2008-043; ATL-COM-PHYS-2008-093 (2008).

[225] D. Cavalli *et al.*, *Validation of the fast calorimeter simulation FastCaloSim against Athena release 10, 13.0.40 full simulation*, ATL-PHYS-INT-2009-073; ATL-COM-PHYS-2009-164 (2009).

[226] E. Richter-Was, D. Froidevaux, L. Poggioli, *Atlfast 2.0 a fast simulation package for ATLAS*, CERN-ATL-PHYS-98-131 (1998).

[227] S. Dean and P. Sherwood, *Athena Atlfast1*, `http://www.hep.ucl.ac.uk/atlas/atlfast/` (visited: 01.06.2010), 2008.

[228] ATLAS Collaboration, *Measurements from supersymmetric events*, ATL-PHYS-PUB-2009-067; ATL-COM-PHYS-2009-190 (2009). part of CSC book- CSC note5.

[229] *Duplicated events in mc08*, `http://groups.cern.ch/group/hn-atlas-susy-wg/Lists/Archive/` (visited: 01.03.2010).

[230] K. Melnikov, F. Pertriello, *Electroweak gauge boson production at hadron colliders through* $O(\alpha s2)$, Phys. Rev. D 74 (2006) 114017. arXiv: hep-ph/0609070.

[231] C. Anastasiou, L.J. Dixon, K. Melnikov, and F. Petriello, *High precision QCD at hadron colliders: Electroweak gauge boson rapidity distributions at NNLO*, Phys. Rev. D 69 (2004) 094008. arXiv: hep-ph/0312266.

[232] J. Campbell, J. Ellis, R. Keith, *An update on vector boson pair production at hadron colliders*, Phys. Rev. D 60 (1999) 113006. arXiv: hep-ph/9905386.

[233] *MCFM homepage*, `http://mcfm.fnal.gov/` (visited: 01.06.2010).

[234] ATLAS Collaboration, *Prospects for Supersymmetry and univeral extra dimensions discovery based on inclusive searches at a 10 TeV centre-of-mass energy with the ATLAS detector*, 2009.

[235] ATLAS collaboration, *Searching for Supersymmetry with two same-sign leptons, multi-jets plus missing transverse energy in ATLAS at* $\sqrt{s}$ *= 10 TeV*, ATL-PHYS-PUB-2009-085 (2009).

[236] B.C. Allanach *et al.*, *The Snowmass points and slopes: benchmarks for SUSY searches*, The European Physical Journal C Volume 25 Number 1 (2001) 113-123.

[237] T. Aaltonen *et al.* (CDF Collaboration), *Inclusive Search for squark and gluino production in* $p\bar{p}$ *collisions at* $\sqrt{s}$ *= 1.96 TeV* (2008). arXiv: hep-ex/0811.2512.

[238] DØ collaboration, *Search for squarks and gluinos in events with jets and missing transverse energy using 2.1*fb^{-1} *of* $p\bar{p}$ *collision data at* $\sqrt{s}$ *= 1.96 TeV*, Phys. Lett. B 660 (2008) 449.

[239] R. R. de Austri, R. Trotta and L. Roszkowski, *A Markov chain Monte Carlo analysis of the CMSSM*, JHEP 05 (2006) 002. arXiv: hep-ph/0602028.

[240] H. Baer *et al.*, *Neutralino relic density in minimal supergravity with co-annihilations*, Journal High Energy Phys 03 (2002) 042.

[241] WMAP Collaboration D. Spergel *et al.*, *Wilkinson Microwave Anisotropy Probe (WMAP) three year results: Implications for cosmology*, Astrophys. J. Suppl. 170 (2007) 377. arXiv: astro-ph/0603449.

[242] E. Barberio *et al.*, Heavy Flavour Averaging Group (HFAG) Collaboration, *Averages of b-hadron properties at the end of 2006* (2007). arXiv: hep-ph/0704.3575.

[243] A. Abulencia *et al.* (CDF Collaboration), *Search for $B_s^0 \to \mu^+\mu^-$ decays in $p\bar{p}$ collisions with CDF II*, Phys. Rev. Lett. 94 (2005) 221805.

[244] *Measurement of the positive muon anomalous magnetic moment to 0.7 ppm*, Phys. Rev. Lett. 89 (2002) 101804.

[245] *Measurement of the negative muon anomalous magnetic moment to 0.7 ppm*, Phys. Rev. Lett. 92 (2004) 161802.

[246] G. W. Bennett *et al.*, Muon g-2 Collaboration, *Measurement of the negative muon anomalous magnetic moment to 0.7-ppm*, Phys. Rev. Lett. 92 (2004) 161802. arXiv: hep-ex/0401008.

[247] M. Dine, A. E. Nelson, Y. Shirman, *Dynamical Supersymmetry breaking simplified*, Phys. Rev. D 51 (1994) 1362. arXiv: hep-ph/9408384.

[248] *SUSY grid twiki page*, `https://twiki.cern.ch/twiki/bin/view/AtlasProtected/SUSYSignalProduction` (visited: 01.04.2010).

[249] C. F. Berger, J. S. Gainer, J. L. Hewett, T. G. Rizzo, *Supersymmetry without prejudice*, JHEP 02 023. arXiv: hep-ph/0812.0980v3.

[250] G. Belanger, F. Boudjema, A. Pukhov, R. K. Singh, *Constraining the MSSM with universal gaugino masses and implication for searches at the LHC*, JHEP 11 026. arXiv: hep-ph/0906.5048.

[251] ATLAS Collaboration, *Calorimeter clustering algorithms: Description and performance*, ATL-LARG-PUB-2008-002; ATL-COM-LARG-2008-003 (2008).

[252] T.G. Cornelissen *et al.*, *Concepts, design and implementation of the ATLAS new tracking*, ATL-SOFT-PUB-2007-007 (2007).

[253] G. Blazey *et al.*, *Run II jet physics: proceedings of the run II QCD and weak boson physics workshop* (2000). arXiv: hep-ex/0005012v2.

[254] C. Buttar *et al.*, *Standard Model handles and candles working Group: Tools and jet*, Summary Report. 2008 (2008). arXiv: hep-ph/0803.0678.

[255] S. D. Ellis and D. E. Soper, *Successive combination jet algorithm for hadron collisions*, Phys. Rev. D 48 (1993) 3160-3166. arXiv: hep-ph/9305266.

[256] S. Catani, L. Y. Dokshitzer, M. H. Seymour, B. R. Webber, *Longitudinally invariant K_T clustering algorithms for hadron hadron collisions*, Nucl. Phys. B 406 (1993) 187-224.

[257] S. Catani, L. Y. Dokshitzer, M. H. Seymour, B. R. Webber, *The K-perpendicular clustering algorithm for jets in deep inelastic scattering and hadron collisions*, Phys. Lett. B 285 (1992) 291-29.

[258] S. D. Ellis, D. E. Soper, *Successive combination jet algorithm for hadron collisions*, Phys. Rev. D48 (1993) 3160-3166. arXiv: hep-ph/9305266.

[259] M. Cacciari and G. Salam, *Dispelling the N^3 myth for the k_T jet-finder*, Phys. Lett. B 641 (2006) 57-61. arXiv: hep-ph/0512210.

[260] M. Cacciari, G. P. Salam, G. Soyez, *The Anti-k(T) jet clustering algorithm*, JHEP 0804 (2008) 063; LPTHE-07-03. arXiv: hep-ph/0802.1189.

[261] L. Asquinth *et al*., *Performance of jet algorithms in the ATLAS detector*, ATLAS-COM-2009-630 (2009).

[262] B. Andrieu *et al*., *Results from pion calibration runs for the H1 liquid Argon calorimeter and comparisons with simulations*, Nucl. Instrum. Meth. A 336 (1993) 499.

[263] I. Abt *et al*., *The H1 detector at HERA*, Nucl. Instrum. Meth. A 386 (1997) 310-347.

[264] ATLAS Collaboration, *Jet energy scale and its systematic uncertainty in ATLAS for jets produced in proton-proton collisions at $\sqrt{s}$ = 7 TeV*, ATLAS-CONF-2010-056 (July, 2010).

[265] ATLAS Collaboration, *Jet reconstruction performance*, ATL-PHYS-PUB-2009-012; ATL-COM-PHYS-2009-114 (2009).

[266] ATLAS Collaboration, *Data-quality requirements and event cleaning for jets and missing transverse energy reconstruction with the ATLAS detector in proton-proton collisions at a center-of-mass energy of $\sqrt{s}$ = 7 TeV.*, ATLAS-CONF-2010-038 (May, 2010).

[267] ATLAS Collaboration, *Properties of jets and inputs to jet reconstruction and calibration with the ATLAS detector Using proton-proton collisions at $\sqrt{s}$ = 7 TeV*, ATLAS-CONF-2010-053 (July, 2010).

[268] ATLAS Collaboration, *Performance of the missing transverse energy reconstruction in minimum bias collisions at a center-of-mass energy of $\sqrt{s}$ = 7 TeV with the ATLAS detector*, ATLAS-CONF-2010-039 (June, 2010).

[269] ATLAS Collaboration, *Performance of the missing transverse energy reconstruction and calibration in proton-proton collisions at a center-of-mass energy of $\sqrt{s}$= 7 TeV with the ATLAS detector*, ATLAS-CONF-2010-057 (July, 2010).

[270] ATLAS Collaboration, *Data-quality requirements and event cleaning for jets and missing transverse energy reconstruction with the ATLAS detector in proton-proton collisions at a center-of-mass energy of $\sqrt{s}$ = 7 TeV*, ATLAS-CONF-2010-038 (June, 2010).

[271] ATLAS Collaboration, *Measurement of the missing transverse momentum based on tracks in proton-proton collisions at $\sqrt{s}$ = 900 GeV center-of-mass energy with the ATLAS detector*, ATLAS-CONF-2010-020 (2010).

[272] ATLAS Collaboration, *Reconstruction and identification of electrons in ATLAS*, ATL-PHYS-PUB-2009-004; ATL-COM-PHYS-2009-170 (2009).

[273] J. Dietrich *et al.*, *Prospects for SUSY discovery based on inclusive searches with the ATLAS detector at the LHC (Long Version)*, ATL-COM-PHYS-2009-261 (2009).

[274] D. E. Acosta *et al.*, *First measurements of inclusive W and Z cross sections from Run II of the Tevatron collider*, Phys. Rev. Lett. 94 (2005) 091803. arXiv: hep-ph/0406078.

[275] D. L. Adams, A. Ouraou, A. Poppleton, S. Willocq, *Muon reconstruction and identification performance in ATLAS: Studies with simulated Monte Carlo samples*, ATL-PHYS-PUB-2008-000 (2008).

[276] ATLAS Collaboration (muon group), *The ATLAS Muon Spectrometer Technical Design Report*, CERN/LHCC/97-22 (1997).

[277] S. Hassini *et al.*, *A Muon identification and combined reconstruction procedure for the ATLAS detector at the LHC using (Muonboy, STACO, MuTag) reconstruction package*, Nuclear Instr. and Methods A 572 (2007) 77-79.

[278] T. Lagouri *et al.*, *A muon identication and combined reconstruction procedure for the ATLAS detector at the LHC at CERN*, IEEE Trans. Nucl. Science 51 (2004) 3030-3033.

[279] D. Adams *et al.*, *Track Reconstruction in the ATLAS Muon Spectrometer with MOORE*, ATL-SOFT-2003-007; ATL-COM-MUON-2003-012 (2003).

[280] S. Tarem, Z. Tarem, N. Panikashvili, O. Belkind, *MuGirl - Muon identification in the ATLAS detector from the inside out*, Nuclear Science Symposium Conference Record 2007 1 (2007) 617-621.

[281] E. Eichten *et al.*, *Supercollider physics*, Rev. Mod. Phys. 56 (1984) 579.

[282] *LEP2 SUSY working group, ALEPH, DELPHI, L3 and OPAL experiments*, `http://lepsusy.web.cern.ch/lepsusy` (visited: 01.08.2010).

[283] *DØ new phenomena webpage*, `http://www-d0.fnal.gov/Run2Physics/np/` (visited: 01.08.2010).

[284] *CDF II exotics group public page*, `http://www-cdf.fnal.gov/physics/exotic/exotics_published.html` (visited: 01.08.2010).

[285] *LEP2 SUSY working group, ALEPH, DELPHI, L3 and OPAL experiments*, http://lepsusy.web.cern.ch/lepsusy/www/sleptons_summer04/slep_final.html (visited: 01.08.2010).

[286] M. Berggren *et al.*, *Selectron/Smuon/Stau results, 183-208 GeV* (2004). http://lepsusy.web.cern.ch/lepsusy/www/sleptons_summer04/slep_final.html (visited: 01.07.2010).

[287] *LEP2 SUSY working group, ALEPH, DELPHI, L3 and OPAL experiments*, http://lepsusy.web.cern.ch/lepsusy/www/inoslowdmsummer02/charginolowdm_pub.html (visited: 01.08.2010).

[288] *LEP Higgs working group*, http://lephiggs.web.cern.ch/LEPHIGGS/papers/index.html (visited: 01.08.2010).

[289] *LEP2 SUSY working group, ALEPH, DELPHI, L3 and OPAL experiments*, http://lepsusy.web.cern.ch/lepsusy/www/lspmsugra_summer02/02-06.2/mSUGRA_208.html (visited: 01.08.2010).

[290] DØ collaboration, *Search for associated production of charginos and neutralinos in the trilepton final state using 2.3* fb^{-1} *of data*, Phys. Lett. B 680 (2009) 34. arXiv: hep-ph/0901.0646.

[291] CDF collaboration, *Inclusive search for squark and gluino production in* $p\bar{p}$ *collisions at* $\sqrt{s}$ *= 1.96TeV*, Phys. Rev. Lett. 102 (2009) 221801.

[292] DØ Collaboration, *Search for scalar bottom quarks and third-generation leptoquarksin* $p\bar{p}$ *collisions at* $\sqrt{s}$ *= 1.96 TeV*, accepted by Phys. Lett. B (2010). arXiv: hep-ex/1005.2222.

[293] T. Aaltonen *et al.*, *Search for pair production of supersymmetric top quarks in dilepton events from* $p\bar{p}$ *collisions at* $\sqrt{s}$ *= 1.96 TeV*, Phys. Rev. Lett. 104 (2010) 251801. arXiv: hep-ex/0912.1308.

[294] ALEPH Collaboration, DELPHI Collaboration, L3 Collaboration, OPAL Collaboration, LEP Higgs Working Group, *Search for the Standard Model Higgs boson at LEP*, LHWG Note/2001-03 (2001). arXiv: hep-ex/0107029v4.

[295] *Search for Higgs bosons predicted in two-Higgs-doublet models via decays to tau lepton pairs in 1.96 TeV* $p\bar{p}$ *collisions*, Phys. Rev. Lett. 103 (2009) 201801.

[296] Tevatron New Physics Higgs Working Group (CDF Collaboration, DØ Collaboration), *Combined CDF and DØ upper limits on MSSM Higgs boson production in tau-tau final states with up to 2.2* fb^{-1} (2010). arXiv: hep-ex/1003.3363v3.

[297] John Ellis, Keith A. Olive, *Supersymmetric dark matter candidates*, CERN-PH-TH/2010-004, UMN-TH-2831/10, FTPI-MINN-10/02; from: Particle Dark Matter: Observations,

Models and Searches' edited by Gianfranco Bertone. Chapter 8 (2010). arXiv: hep-ph/1001.3651v1.

[298] John Ellis, *Prospects for new physics at the LHC*, CERN-PH-TH/2010-074 (Singapore, 24.02.2010). talk at the conference in honor of Murray Gell-Mann's 80th Birthday; arXiv: hep-ph/1004.0648v1.

[299] *HFAG: Rare B decay parameters (website)*, `http://www.slac.stanford.edu/xorg/hfag/rare/index.html;http://www.slac.stanford.edu/xorg/hfag/rare/ichep10/radll/btosg.pdf` (visited: 01.03.2010).

[300] M. E. Gómez, T. Ibrahim, P. Nath, S. Skadhauge, *An improved analysis of $b \to s\gamma$ in Supersymmetry*, Phys. Rev. D 74 (2006) 015015.

[301] V. M. Abazov *et al.*, *Search for $B_s \to \mu^+\mu^-$ at DØ*, Phys. Rev. D 76 (2007) 092001.

[302] T. Aaltonen *et al.*, *Search for $B_s \to \mu^+\mu^-$ decays with 2 fb^{-1} of $p\bar{p}$ collisions*, Phys. Rev. Lett. 100 (2008) 101802.

[303] M. Davier and W. J. Marciano, *The theoretical prediction for the muon anomalous magnetic moment*, Annual Review of Nuclear and Particle Science Vol. 54 (2004) 115-140.

[304] D. N. Spergel *et al.*, *First Year Wilkinson Anisotropy Probe (WMAP) Observations: Determination of cosmological parameters*, Astrophys. J. Suppl. 148 (2003) 175.

[305] C. L. Bennett *et al.*, *First Year Wilkinson Microwave Anisotropy Probe (WMAP) Observations: Beam profiles and window functions*, Astrophys. J. Suppl. 148 (2003) 39. arXiv: astro-ph/0302214v2.

[306] J. S. Bagla, H. K. Jassal, T. Padmanabhan, *Cosmology with tachyon field as dark energy*, Phys. Rev. D 67 (2003) 063504.

[307] A. Kusenko, *Color and charge breaking minima in the MSSM*, Nucl. Phys. Proc. Suppl. 52 A (1996) 67-69.

[308] U. De Sanctis *et al.*, *Perspectives for the detection and measurement of Supersymmetry in the focus point region of mSUGRA models with the ATLAS detector at LHC*, Eur. Phys. J. C 52 (2007) 743-758. arXiv: hep-ex/0704.2515.

[309] A. J. Barr, *Using lepton charge asymmetry to investigate the spin of supersymmetric particles at the LHC*, Phys. Lett. B 596 (2004) 205212. arXiv: hep-ph/0405052.

[310] G. Polesello and D. R. Tovey, *Constraining SUSY dark matter with the ATLAS detector at the LHC*, JHEP 0405 (2004) 071; ATL-PHYS-2004-008. arXiv: hep-ph/0403047.

[311] M. M. Nojiri and Y. Yamada, *Neutralino decays at the LHC*, Phys. Rev. D60 (1999) 015006. arXiv: hep-ph/9902201.

[312] C. Carli, *Proceedings of the 2009 Chamonix workshop on LHC performance*, Technical Report CERN-ATS-2009-001 (2009).

[313] ATLAS Collaboration, *ATLAS plots on Ecm dependence of physics reach*, ATL-COM-PHYS-2009-069 (2009). `https://twiki.cern.ch/twiki/bin/view/Atlas/AtlasResultsEcmDependence` (visited: 01.09.2010).

[314] J. Dietrich, P. de Jong, R. Bruneliere, S. Caron, G. Polesello, Z. Rurikova, *ATLAS prospects for the discovery of low mass SUSY for different LHC centre-of-mass energies*, ATL-PHYS-INT-2009-020 (2009).

[315] J. Dietrich, R. Bruneliere, S. Caron, Z. Rurikova, *Verification of the ATLAS Chamonix fast simulation SUSY results with a study based on a full detector simulation*, ATL-COM-PHYS-2010-063 (2010).

[316] *LHC -first-physics-webpage*, `http://public.web.cern.ch/press/pressreleases/Releases2010/PR07.10E.html` (visited: 01.05.2010).

[317] J.M. Butterworth *et al.*, *KtJet: A C++ implementation of the K(T) clustering algorithm*, Comput. Phys. Commun. 153 (2003) 85-96.

[318] ATLAS Collaboration. *Observation of prompt inclusive electrons in the ATLAS experiment at* $\sqrt{s}$ *= 7 TeV*. Technical Report ATL-COM-PHYS-2010-422, CERN, 2010.

[319] D. R. Tovey, *Measuring the SUSY mass scale at the LHC*, Phys. Lett. B 498 (2001) 1-10.

[320] D. R. Tovey, *Inclusive SUSY searches and measurements at ATLAS*, EPJ Direct 4 (2002) N4.

[321] C. G. Lester, D. J. Summers, *Measuring masses of semi-invisibly decaying particles pair produced at hadron colliders*, Phys. Lett. B 463 (1999) 99-103. arXiv: hep-ph/9906349.

[322] A. Barr, C. Gwenlan, *The race for Supersymmetry: using mT2 for discovery*, Phys. Rev. D 80 (2009) 074007. arXiv: hep-ph/0907.2713.

[323] H. Cheng, Z. Han, *Minimal kinematic constraints and mt2*, JHEP 12 (2008) 063. arXiv: hep-ph/10.1088.

[324] D. Tovey, *On measuring the masses of pair-produced semi-invisibly decaying particles at hadron colliders*, JHEP 04 (2008) 034. arXiv: hep-ph/10.1088.

[325] G. Polesello, D. R. Tovey, *Supersymmetric particle mass measurement with the boost-corrected contransverse mass*, JHEP 03 (2010) 030. arXiv: hep-ph/10.1007.

[326] S. Brandt, Ch. Peyrou, R. Sosnowski and A. Wroblewski, *The principal axis of jets – an attempt to analyse high-energy collisions as two-body processes*, Phys. Lett. 12 (1964) 57-61.

[327] N. P. Konstantinidis *et al.*, *The Atlantis event visualisation program for the ATLAS experiment* (2004). `http://cdsweb.cern.ch/record/865603?ln=en` (visited: 01.06.2010).

[328] *Atlantis twiki page*, `https://twiki.cern.ch/twiki/bin/view/Atlas/Atlantis` (visited: 01.10.2010).

[329] J. Dietrich, S. Caron, A. J. Barr *et al.*, *Details on 'Early Supersymmetry searches in channels with jets and missing transverse momentum with the ATLAS detector'*, ATL-COM-PHYS-2010-438 (2010).

[330] T.Carli, R. Teuscher, *Summary, action items and discussion about future directions*, `http://indico.cern.ch/getFile.py/access?contribId=131&sessionId=14&resId=0&materialId=slides&confId=91219` (visited: 01.10.2010).

[331] *Hadronic calibration workshop twiki page*, `http://indico.cern.ch/conferenceDisplay.py?confId=91219` (visited: 01.10.2010).

[332] ATLAS Collaboration, *Early Supersymmetry searches with jets, missing transverse momentum and one or more leptons with the ATLAS detector*, ATLAS-CONF-2010-066 (2010).

[333] *ATLAS Trigger menu twiki page*, `https://twiki.cern.ch/twiki/bin/view/Atlas/TriggerPhysicsMenu` (visited: 01.07.2010).

[334] B. Demirkoz, M. Martinez, E. Meoni, *Measurement of Level 1 Jet trigger efficiencies in ATLAS using p-p minimum bias data at $\sqrt{s}$ = 7 TeV*, ATL-DAQ-2010-114 (July, 2010).

[335] P. K. Sinervo, *Signal Significance in particle physics* (2002). to be published in the proceedings of the conference "Advanced Statistical Techniques in Particle Physics", Durham, England; arXiv: hep-ex/0208005v1.

[336] J. T. Linnemann, *Measures of significance in HEP and astrophysics* (2003). arXiv: physics/0312059v2.

[337] ATLAS Collaboration, *Data-driven determinations of W, Z, and top background to Supersymmetry*, ATL-PHYS-PUB-2009-064; ATL-COM-PHYS-2009-187 (2009). part of CSC book-CSC note 1,2.

[338] ATLAS Collaboration, *Estimation of QCD backgrounds to searches for Supersymmetry*, ATL-PHYS-PUB-2009-065; ATL-COM-PHYS-2009-188 (2009). part of CSC book-CSC note3.

[339] ATLAS Collaboration, *In-situ pseudorapidity intercalibration to evaluate jet energy scale uncertainty and calorimeter performance in the forward region*, ATLAS-CONF-2010-055 (July, 2010).

[340] ATLAS Collaboration, *Jet energy resolution and reconstruction efficiencies from in-situ techniques with the ATLAS detector using proton-proton collisions at a center-of-mass energy $\sqrt{s}$ = 7 TeV*, ATLAS-CONF-2010-054 (July, 2010).

[341] ATLAS Collaboration, *Luminosity determination using the ATLAS detector*, ATLAS-CONF-2010-060 (July, 2010).

[342] *ATLAS twiki page: Recommendation for jet quality and selection in events with pile-up*, `https://twiki.cern.ch/twiki/bin/view/AtlasProtected/JetQualityAndSelectionForPileup` (visited: 01.10.2010).

[343] ATLAS Collaboration, *Expected performance of the ATLAS detector in GMSB models with tau final states*, ATL-PHYS-PUB-2009-089 (2009).

[344] ATLAS Collaboration, *Early Supersymmetry searches in events with missing transverse energy and b-jets with the ATLAS detector* ATL-COM-PHYS-2010-580 (2010).

[345] ATLAS Collaboration, *Expected performance of the ATLAS experiment - Detector, trigger and physics*, CERN-OPEN-2008-020, page 397 (2008). arXiv: hep-ex/0901.0512.

[346] *Jet tag info:*, `http://alxr.usatlas.bnl.gov/lxr/source/atlas/PhysicsAnalysis/JetTagging/JetTagInfo/src/` (visited: 01.01.2010).

[347] *b-tagging twiki page:*, `https://twiki.cern.ch/twiki/bin/view/AtlasProtected/BTaggingFAQ;versionr13` (visited: 01.01.2010).

[348] ATLAS Collaboration, *Discovery potential for Supersymmetry with b-jet final states with the ATLAS detector*, ATL-PHYS-PUB-2009-075 (2009).

[349] ATLAS Collaboration, *Early Supersymmetry searches in events with missing transverse energy and b-jets with the ATLAS detector*, ATLAS-CONF-2010-079 (August, 2010).

[350] E. Farhi, *A QCD test for jets*, Phys. Rev. Lett. 39 (1977) 1587-1588.

[351] S. Catani and B. R. Webber, *Infrared safe but infinite: soft-gluon divergences inside the physical region*, JHEP 10 (1997) 005.

[352] A. Banfi, G. P. Salam, G. Zanderighi, *Phenomenology of event shapes at hadron colliders* (2010). arXiv: hep-ph/1001.4082v1.

[353] ATLAS Collaboration, *Early Supersymmetry searches in channels with jets and missing transverse momentum with the ATLAS detector*, July, 2010.

[354] J. Dietrich, S. Caron, *The ATLAS discovery reach for Supersymmetry in the pMSSM parameter space with universal gaugino masses and in the unconstrained pMSSM parameter space at a centre-of-mass energy of 10 TeV*, ATL-COM-PHYS-2010-029 (2010).

[355] D. S. M. Alves, E. Izaguirre, J. G. Wacker, *It's On: Early interpretations of ATLAS results in jets and missing energy searches* (August, 2010). arXiv: hep-ph/1008.0407v2.

[356] J. Alwall, M. Le, M. Lisanti and J. G. Wacker, *Model-independent jets plus missing energy searches*, Phys. Rev. D 79 (2009) 015005.

[357] J. Alwall, M. P. Le, M. Lisanti and J. G. Wacker, *Searching for directly decaying gluinos at the Tevatron*, Phys. Lett. B 666 (2008) 34. arXiv: hep-ph:/0803.0019.

[358] D. E. Kaplan, and M. D. Schwartz, *Constraining light colored particles with event shapes*, Phys. Rev. Lett. 101 (2008) 022002.

[359] T. Aaltonen *et al*. (CDF Collaboration), *Measurement of the cross section for W-boson production in association with jets in $p\bar{p}$ collisions at $\sqrt{s}$ = 1.96 TeV*, Phys. Rev. D 77 (2008) 011108. arXiv: hep-ex/0711.4044.

[360] V. Abazov *et al*. (DØ Collaboration), *Measurements of differential cross sections of Z/gamma + jets + X events in proton anti-proton collisions at $\sqrt{s}$ = 1.96 TeV*, Phys. Lett. B 678 (2009) 45-54.

[361] *RooStats::CombinedCalculator*, `http://root.cern.ch/root/html/RooStats__ProfileLikelihoodCalculator.html` (visited: 01.09.2010).

[362] *RooStats wiki page*, `https://twiki.cern.ch/twiki/bin/view/RooStats/WebHome` (visited: 01.10.2010).

[363] *ATLAS CMS Open Statistics Forum*, `http://indico.cern.ch/conferenceDisplay.py?confId=100458` (visited: 01.10.2010).

[364] G. Redlinger, *Paper preparation in the SUSY WG* (Cern, 08.10.2010). talk in the ATLAS week; `http://indico.cern.ch/conferenceDisplay.py?confId=66744`.

[365] D. Stump *et al*., *Inclusive jet production, parton distributions, and the search for new physics*, JHEP 10 (2003) 046. arXiv: hep-ph/0303013.